American Mineralogist, Volume 65, pages 821–836, 1980

Sapphirine + quartz association from Archean rocks in Enderby Land, Antarctica

EDWARD S. GREW

Department of Earth and Space Sciences
University of California
Los Angeles, California 90024

Abstract

Quartzites and granulites containing the sapphirine–quartz association are found in the pyroxene–granulite-facies Archean Napier complex in the Tula Mountains and Amundsen Bay areas of Enderby Land, Antarctica (50°30′ to 53°E; 67°S). Quartzites from the Tula Mountains consist of SiO_2, Al_2O_3, MgO, and FeO and contain virtually no alkalis or CaO. At the peak of metamorphism, the mineral assemblage in these quartzites is interpreted to be quartz–sapphirine–orthopyroxene–rutile±plagioclase. Cordierite is present, mostly as overgrowths on sapphirine, and appears to have formed from the reaction between sapphirine and quartz after the peak of metamorphism. Sapphirines are somewhat more siliceous than the $7MgO \cdot 9Al_2O_3 \cdot 3SiO_2$ composition and the proportion of the iron end member ranges from 6.8 to 23.5 mole %. Fe^{3+} contents do not exceed 18% of the total Fe in sapphirine. The proportion of Al to total cations in orthopyroxene ranges from 0.072 to 0.117, increases linearly with $FeSiO_3$ content, and is extrapolated to be 0.048 in a hypothetical iron-free orthopyroxene. On the basis of the compositions of coexisting pyroxenes, the Al content of hypothetical iron-free orthopyroxene associated with sapphirine, and the compositions of coexisting plagioclase and garnet, metamorphic temperatures and pressures are estimated to be 900°±30°C and 7±1 kbar. Colorless sapphirine (2.40 wt% FeO) with overgrowths of sillimanite is associated with orthopyroxene, quartz, biotite, and plagioclase in a magnesian quartzite (MgO = 4.24 wt%; Fe_2O_3 = 0.51 wt%) at Reference Peak, an exposure south of the Tula Mountains–Amundsen Bay areas. This association may represent the univariant reaction sapphirine + quartz = sillimanite + orthopyroxene in the iron-free system and may have crystallized at lithostatic pressures greater than 7 kbar and temperatures near 900°C.

Introduction

The rare mineral assemblage sapphirine–quartz, first reported by Dallwitz (1968) from Enderby Land, Antarctica, has to date been reported from four other areas worldwide (Table 1). Four of the five sapphirine–quartz localities, including Enderby Land, are in remote Precambrian granulite-facies complexes, and have not been studied in great detail; the fifth locality, where sapphirine and quartz occur in a xenolith in peridotite, was described only recently. Experimental studies of this assemblage in the system $MgO–SiO_2–Al_2O_3$ suggest that the sapphirine–quartz assemblage formed under high temperatures, high lithostatic pressures, and very low water pressures, conditions that may prevail in the Earth's lower crust. As some Enderby Land sapphirine–quartz rocks have a bulk chemistry approaching that of the simple system used by the experimentalists, a detailed study of these rocks may be a good test of the applicability of the laboratory results to the natural systems.

In this paper, I present data on sapphirine-bearing quartzites consisting largely of SiO_2, MgO, Al_2O_3, and FeO, and on associated rocks. My main aim is to estimate the physical conditions of metamorphism and to compare these estimates with experimental results. This study is based largely on samples I collected as U.S. exchange scientist with the Australian National Antarctic Research Expeditions (ANARE) in Enderby Land, including samples from Dallwitz' (1968) original locality.

General features of sapphirine–quartz rocks

Four of the five sapphirine–quartz localities are in regionally metamorphosed granulite-facies terrains of Precambrian age. The Chogar complex in eastern

0003–004X/80/0910–0821$02.00

Table 1. Reported occurrences of sapphirine–quartz associations

Locality	Main References
Enderby Land, Antarctica	Dallwitz (1968) Grew (1979a,b) Sheraton et al. (1980)
Cortlandt Complex, Peekskill, New York	Caporuscio and Morse (1978)
Red Wine Mountains-Wilson Lake area, Labrador	Leong and Moore (1972) Bourne (1978) Morse and Talley (1971)
Labwor Hills, Uganda	Nixon et al. (1973)
Chogar Complex, eastern Siberia	Karsakov et al. (1975)

Siberia, USSR (Karsakov *et al.,* 1975), Napier complex in Enderby Land (Grew and Manton, 1979; Sheraton *et al.,* 1980), and Watian suite in the Labwor Hills, Uganda (Clifford, 1974) were metamorphosed during the Archean [2500 million years (m.y.) or older]. By contrast, the Cortlandt complex is Ordovician (Dallmeyer, 1975). Here sapphirine and quartz occur in a hornfels xenolith and may have formed by reaction of the xenoliths with the enclosing olivine-rich magma under high oxygen fugacities (Barker, 1964; Caporuscio and Morse, 1978). However, temperature and lithostatic pressure may not have differed greatly from the granulite-facies conditions under which sapphirine and quartz were stabilized at the other localities.

The association sillimanite–orthopyroxene is characteristic of all the occurrences. It is commonly found in the same rock as sapphirine and quartz, typically as a breakdown product of this assemblage—*e.g.,* Labrador (Chatterjee and Schreyer, 1972), Cortlandt complex, New York (Caporuscio and Morse, 1978), and Chogar complex (Karsakov *et al.,* 1975). The converse is not true, as sapphirine–quartz is not found in some sillimanite–orthopyroxene terrains (*e.g.,* Chinner and Sweatman, 1968; Dougan, 1974). In the Strangway Ranges, Australia, sapphirine and quartz occur in the same rock, but not in direct contact (Woodford and Wilson, 1976).

The sapphirine–quartz rocks seem to differ from average metamorphosed pelitic rocks in having a higher Fe^{3+}/Fe^{2+} ratio or Mg/Fe ratio. High Fe^{3+}/Fe^{2+} ratios for the host rocks from Wilson Lake, Labwor Hills, and Cortlandt complex are indicated by relatively high Fe_2O_3 contents of 1.2 to 1.7 weight percent in associated sillimanite (Caporuscio and Morse, 1978; Grew, 1980), high Fe^{3+}/Fe^{2+} ratio in sapphirine (Merlino, 1973; Caporuscio and Morse, 1978; Sahama *et al.,* 1974), and presence of hematite. There is little evidence for a high Fe^{3+}/Fe^{2+} ratio in the Chogar complex rocks, as no hematite is reported by Karsakov *et al.* (1975), nor is there any evidence for it in the Napier complex rocks, which have above-average Mg/Fe ratios (see below).

Geological framework of the sapphirine–quartz rocks

The sapphirine–quartz association is found in the Tula Mountains and south to Amundsen Bay in western Enderby Land (Fig. 1), which is underlain by a Precambrian granulite-facies terrain mapped by Kamenev (1972) as the Napier zone. This zone, or metamorphic complex, is a highly deformed sequence of gneisses and granulites composed largely of quartz, feldspar, pyroxene, and garnet. These rocks can be grouped into four broad types: (1) charnockite and enderbite, (2) pyroxene granulite, (3) garnetiferous rocks, and (4) aluminous and siliceous rocks (Ravich and Kamenev, 1975; Kamenev, 1975; Grew, 1978; Sheraton *et al.,* 1980). The sapphirine–quartz association occurs in the last group of rocks. These rocks constitute no more than 5 percent of exposed rock and form well-layered sequences of granulites, quartzites, and gneisses. Garnet, sillimanite, biotite, cordierite, spinel (and rare corundum), sapphirine, orthopyroxene, osumilite, and graphite are characteristic of these sequences.

Petrography

Rocks containing the sapphirine–quartz association range from quartzites with scattered grains of sapphirine and orthopyroxene to aluminous granulites characterized by complex textures and symplectitic intergrowths (see also Dallwitz, 1968; Ellis *et al.,* 1980; Sheraton *et al.,* 1980).

This paper concerns seven samples of quartzite, six of which contain sapphirine, orthopyroxene, cordierite, rutile, and minor plagioclase, and the seventh sillimanite and biotite as well (Table 2). Six of the quartzites I collected in January 1978 from four localities in the Tula Mountains: 2064 and 2071 on Mount Hardy, 2048 on Gage Ridge, and 2042 at Spot Height 945 (Fig. 1). The rocks sampled at 2064 and at 2071 appear to be from the same layer offset by a fault.

Spot Height 945 is Dallwitz' (1968) original locality. Ellis *et al.* (1980) describe in detail sapphirine–quartz–osumilite granulites from this locality. J. W. Sheraton and his colleagues discovered the sapphirine–quartz association at Mount Hardy and Gage Ridge and provided me the information needed to find these localities in the field.

The sapphirine-bearing layers consist of granulite and quartzite 1.5 to 6 m thick that alternate with py-

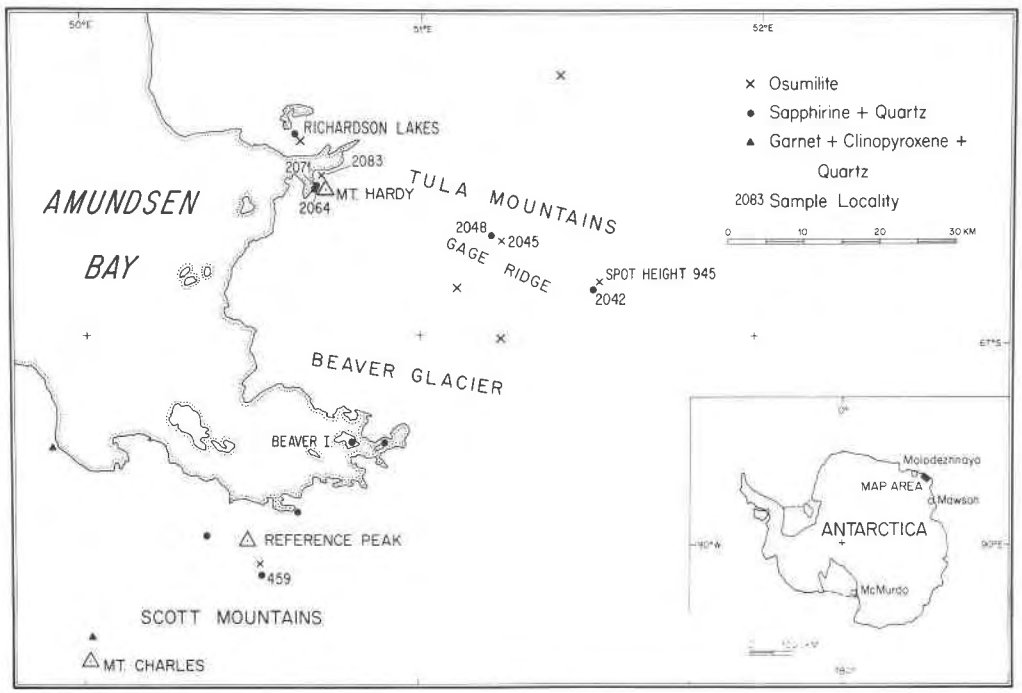

Fig. 1. Map of Tula Mountains–Amundsen Bay areas, Enderby Land, Antarctica, showing localities for critical minerals and mineral assemblages. Sources of data are Sheraton *et al.* (1980, Fig. 4), samples collected by geologists of the Australian Bureau of Mineral Resources (BMR) (provided by J. W. Sheraton), and samples I collected during the 1977–78 and 1979–80 field seasons. Minerals not reported by Sheraton *et al.* (1980) nor present in BMR samples are osumilite at Richardson Lakes, Reference Peak, and Mount Hardy, sapphirine + quartz at Richardson Lakes, and garnet + clinopyroxene + quartz at Mount Charles. Location of 459 (where sample 459A was collected) was provided by Ye. N. Kamenev (written communication, 1978). Numbers shown on map refer to sample localities; letters in text refer to individual samples, *e.g.*, 2064c is the third sample from locality 2064.

roxene granulite and garnetiferous rocks. Individual layers of quartzite are a few cm to 2 m thick. To take advantage of compositional variations, three quartzites were sampled at locality 2064. Quartzite containing sillimanite and biotite from locality 459, Reference Peak, south of Amundsen Bay (Fig. 1) was collected by Soviet geologists from a 100-m-thick unit in sillimanitic quartzite (Ravich and Kamenev, 1975, p. 146, and Table 40; Kamenev, written communication, 1978).

Readily visible in hand specimens of the six quartzites from the Tula Mountains are light- to dark-colored quartz which commonly has a blue opalescence, light to dark blue sapphirine, and light to dark brown orthopyroxene. In thin section, the quartzites consist of about 50 to 90% quartz, 10 to 40% sapphirine and orthopyroxene, and a trace to 10% cordierite (Table 2). Preferred orientation of flattened quartz and sapphirine grains is prominent only in sample 2048A. Quartz and orthopyroxene are commonly coarse (grains up to 15 mm across). Sapphirine is fine- to medium-grained (0.2–3 mm). Acicular inclusions, probably rutile, are abundant in quartz, which has a faint brown tint in transmitted light, and in orthopyroxene. Sapphirine is pleochroic in blue. I did not observe the brown absorption color described in sapphirine associated with quartz at Wilson Lake (Labrador), Labwor Hills (Uganda), or Peekskill, New York (Morse, 1971; Caporuscio and Morse, 1978; Sahama *et al.*, 1974; Nixon *et al.*, 1973).

Cordierite forms (1) independent grains, a few of which contain vermicular blebs of quartz, and (2) overgrowths around sapphirine. The overgrowth are present in all six samples of quartzite, but in samples 2048A and 2042E direct contacts of sapphirine and quartz are preserved. In the quartzites containing 3 to 10% cordierite (Mount Hardy) the cordierite overgrowths are 0.02–0.2 mm thick, and in the other two sections the overgrowths rarely exceed 0.04 mm in thickness. Sillimanite occurs in trace amounts in cordierite near sapphirine, commonly in close association with rutile; in one section a sillimanite overgrowth on sapphirine is present.

Quartz, sapphirine, and orthopyroxene appear to

Table 2. Modes of sapphirine–quartz rocks from Enderby Land (visual estimates)

Locality	Mt. Hardy				Gage Ridge	Spot Height 945	Reference Peak
Sample	2064C†	2064D†	2064F	2071C	2048A†	2042E	459A†
Quartz	52	71	72	73	88	82	51
Plagioclase	T	-	-	T	-	-	35*
Sillimanite	-	-	T	T	-	T	8*
Sapphirine	13*	4*	7*	2*	5*	8*	1*
Orthopyroxene	25*	20*	17*	20*	7*	8*	1*
Cordierite	10*	5*	3*	5	T*	1*	(?)
Zircon/Monazite	T	T	T	T	T	T	T
Rutile	T	T	1	T	T	1	T
Biotite	T	T	-	T	T	T	4*
Amphibole	-	-	-	-	T	-	-

T - Trace constituent
† - XRF Analysis of rock
* - Probe analysis
(?) - Optical identification uncertain

have crystallized in textural equilibrium in the Tula Mountain quartzites. Cordierite is interpreted to have formed by the reaction of sapphirine with quartz subsequent to the stabilization of the quartz–sapphirine–orthopyroxene association; the independent grains of cordierite are interpreted to have also grown at this time. Sillimanite may have formed from the reaction of sapphirine and quartz, as sapphirine has a higher $Al_2O_3/(MgO + FeO)$ ratio than cordierite. Biotite and amphiboles are fine-grained and appear to be derived from the alteration of other minerals, mostly orthopyroxene.

The quartzite from Reference Peak (sample 459A) has light brown (sillimanitic) and white layers mostly less than 1 cm thick. In thin section, the dominant constituents are medium-grained (0.05–2.5 mm) plagioclase ($Or_2Ab_{88}An_{10}$—microprobe analysis) with K-feldspar lamellae and quartz. The remainder of the rock consists of fine aggregates of prismatic sillimanite concentrated into layers, pale biotite, and colorless orthopyroxene (compare Ravich and Kamenev, 1975, p. 146). Acicular inclusions (rutile?) are abundant in orthopyroxene and quartz, and quartz and plagioclase have a faint brown tint. Biotite flakes (to 0.5 mm across) have an indistinct preferred orientation and do not appear to be derived from sapphirine or orthopyroxene. Colorless sapphirine, which was not reported by Ravich and Kamenev (1975), is generally surrounded by a sillimanite aggregate and no contacts with quartz were found. A few grains of sillimanite and sapphirine have overgrowths of a colorless mineral, either cordierite or plagioclase, which has a fibrous appearance in thin section due to abundant fine particles with a parallel orientation. Except possibly for these overgrowths, I found no cordierite in the two sections of this quartzite in my possession, nor is any cordierite reported by Ravich and Kamenev (1975). In this quartzite, sillimanite overgrowths on sapphirine imply that sapphirine has reacted with quartz to form sillimanite (and presumably orthopyroxene).

Analytical methods

Host rock compositions (Table 3) were determined by X-ray fluorescence (G. Stummer, analyst). Sample preparation followed the procedure described by Cortesogno *et al.* (1977).

Compositions of minerals (Tables 4–9) in carbon-coated polished thin sections were measured with a fully automated (Ni, F, and Cl on manual) ARL-EMX wavelength dispersive electron microprobe at UCLA and a fully automated JXA-5A wavelength-dispersive electron microprobe at the University of Melbourne (UM). The UM analyses are indicated by asterisks in Tables 4–7. Operating conditions on both microprobes were 15 kV and at UCLA about 20 nA sample current. Silicate and oxide minerals and glasses (halides for F and Cl) were used at UCLA,

Table 3. Compositions of Enderby Land quartzites (X-ray fluorescence analyses; G. Stummer, analyst) and of evaporitic mudstone from the Saharan Atlas, Northwest Africa (H. G. Kulke, quoted by Schreyer, 1977)

Rock Type	Quartzite				Evaporitic Mudstone	
Sample	2064C	2064D	2048A	459A	K-A015	K-AH2
Oxide	Weight Percent					
SiO_2	61.74	75.62	87.71	77.02	56.1	50.6
TiO_2	0.23	0.74	0.23	0.35	0.9	1.1
Al_2O_3	12.68	9.08	4.33	11.71	19.4	18.5
Fe_2O_3	3.18	6.28	3.41	0.51	3.0[1]	7.4[2]
MnO	0.019	0.040	0.027	0.005	n.r.	n.r.
MgO	21.29	7.09	3.47	4.24	17.8	21.5
CaO	0.17	0.32	0.07	0.92	0.5	0.4
K_2O	0.05	0.03	0.01	1.20	2.3	0.6
Na_2O	n.d.	n.d.	n.d.	3.36	0.1	0.0
P_2O_5	0.02	0.016	0.02	0.04	n.r.	n.r.
H_2O^+	n.a.	n.a.	n.a.	n.a.	10.2	8.2
Total	99.39	99.22	99.31	99.37	100.1	100.1
	ppm					
Cr	98	55	180	48	n.r.	n.r.
Ni	36	18	97	30	n.r.	n.r.
Rb	15	n.d.	8	23	n.r.	n.r.
Sr	20	8	14	93	n.r.	n.r.

n.a. - not analyzed
n.r. - not reported
n.d. - not detected
All Fe as Fe_2O_3

[1]Includes 1.2% Fe_2O_3 and 1.6% FeO
[2]Includes 2.3% Fe_2O_3 and 4.6% FeO

Table 4. Composition of sapphirine

	2064C AVE	2064D AVE	2064D GR	2064F* AVE	2071C AVE	2071C GR	2048A AVE	2048A GR	2042E* AVE	459A AVE	2042A AVE	2064H AVE
						Weight Percent						
SiO_2	14.75	13.80	13.31	13.78	14.20	13.87	13.69	14.25	13.61	13.59	14.40	14.27
TiO_2	0.06	0.06	0.05	0.10	0.05	0.02	0.06	0.06	0.11	0.02	0.05	0.05
Al_2O_3	62.07	61.89	62.50	61.08	61.76	62.57	60.08	59.52	61.01	63.75	59.48	61.30
Cr_2O_3	0.0	0.01	0.01	0.03	0.01	0.02	0.43	0.49	0.38	0.02	0.40	0.01
FeO[1]	2.98	8.14	7.73	7.98	7.38	6.81	9.53	9.68	6.51	2.40	9.86	6.21
MnO	0.01	0.03	0.03	0.02	0.04	0.03	0.09	0.09	0.02	0.02	0.07	0.03
MgO	20.10	16.99	16.78	17.19	17.43	17.33	15.72	15.95	17.02	19.43	15.93	18.41
CaO	0.07	0.10	0.08	0.02	0.08	0.06	0.11	0.12	0.01	0.07	0.08	0.08
K_2O	0.03	0.04	0.05	0.01	0.06	0.06	0.06	0.05	0.0	0.04	0.04	0.04
Na_2O	0.02	0.01	0.0	0.02	0.01	0.01	0.0	0.0	0.01	0.0	0.02	0.02
Total	100.09	101.05	100.53	100.30[2]	101.02	100.79	99.75	100.20	98.79[3]	99.35	100.31	100.41
						Atoms per 20 Oxygens						
Si	1.717	1.630	1.578	1.640	1.672	1.632	1.652	1.713	1.634	1.590	1.729	1.682
Ti	0.006	0.005	0.004	0.009	0.004	0.002	0.005	0.005	0.010	0.002	0.004	0.004
Al	8.517	8.620	8.734	8.569	8.572	8.679	8.550	8.435	8.637	8.793	8.420	8.518
Cr	0.0	0.000	0.001	0.003	0.001	0.002	0.041	0.047	0.036	0.001	0.038	0.000
Fe^{2+}	0.253	0.695	0.665	0.664	0.643	0.618	0.868	0.892	0.615	0.213	0.914	0.503
Fe^{3+}[4]	0.037	0.109	0.101	0.131	0.083	0.053	0.095	0.081	0.039	0.022	0.076	0.110
Mn	0.001	0.003	0.003	0.002	0.004	0.003	0.009	0.009	0.002	0.002	0.007	0.003
Mg	3.487	2.991	2.964	3.048	3.058	3.039	2.828	2.858	3.046	3.388	2.850	3.234
Total	14.019	14.054	14.050	14.065	14.037	14.026	14.047	14.040	14.019	14.011	14.038	14.055

AVE - Average for sample

GR - Single grain

1. All Fe as FeO
2. Includes 0.04 ZnO and 0.03 BaO
3. Includes 0.07 ZnO and 0·04 BaO
4. Calculated from stoichiometry (see text)

* Analysis done at University of Melbourne

and the UCLA microprobe data were corrected and reduced by the Bence–Albee method with an on-line PDP 11 computer. Metals, oxides, and silicates were used as standards at UM, and the data corrected by the computer program of Mason *et al.* (1969) modified for a PDP 8F on-line computer.

The compositions of the minerals analyzed at UCLA are in general an average of 3 or 4 grains per sample; each grain was analyzed at 3 points (two points for cordierite and plagioclase). Compositions of some grains or edges of grains of sapphirine and orthopyroxene that differ markedly from the overall sample average are also listed in Tables 4 and 5. Compositions measured at UM are an average of 3 grains per sample (2 for cordierite); each grain was generally analyzed at one point. Consequently, the analytical times involved in the UCLA analyses are considerably greater than those in the UM analyses. To estimate the precision of the UCLA analyses, two grains of sapphirine in sample 2045G from Gage Ridge were each analyzed 6 times at 3 or 4 points each time. Values for the 6 analyses range from 13.97 to 14.63 wt% and 13.84 to 14.27% SiO_2; 57.37 to 60.35% and 58.54 to 59.54% Al_2O_3; 0.59 to 0.62% and 0.90 to 1.00% Cr_2O_3; 9.09 to 9.64% and 8.57 to 8.99% FeO, and 15.93 to 16.31% and 16.07 to 16.44% MgO.

Table 5. Composition of orthopyroxene

	2064C Ave	2064C Edge	2064D Ave	2064F* Ave	2071C Ave	2071C Edge	2048A Ave	2042E* Ave	459A Ave
					Weight Percent				
SiO_2	54.36	55.51	49.32	49.86	50.45	52.14	47.78	49.51	54.25
TiO_2	0.10	0.06	0.15	0.19	0.17	0.10	0.25	0.26	0.07
Al_2O_3	7.17	6.08	9.58	9.48	8.47	5.97	10.98	9.27	7.10
Cr_2O_3	0.0	0.0	0.0	0.04	0.02	0.01	0.13	0.10	0.01
FeO[1]	6.99	7.23	16.07	15.55	15.32	15.49	18.10	14.07	6.33
MnO	0.03	0.02	0.08	0.05	0.08	0.08	0.17	0.04	0.06
MgO	32.73	33.06	24.93	25.43	25.68	26.37	22.79	25.54	33.06
CaO	0.19	0.18	0.09	0.07	0.13	0.13	0.11	0.01	0.07
K_2O	0.04	0.05	0.05	0.01	0.04	0.02	0.01	0.01	0.04
Na_2O	0.01	0.01	0.01	0.01	0.0	0.0	0.01	0.01	0.01
Total	101.62	102.18	100.28	100.78[2]	100.35	100.31	100.32	98.99[3]	100.99
					Atoms per 6 Oxygens				
Si	1.849	1.877	1.777	1.782	1.808	1.868	1.739	1.792	1.851
Ti	0.003	0.002	0.004	0.005	0.004	0.003	0.007	0.007	0.002
Al	0.287	0.242	0.407	0.400	0.358	0.252	0.471	0.396	0.286
Cr	0.000	0.000	0.000	0.001	0.001	0.000	0.004	0.003	0.000
Fe^{3+}[4]	0.011	0.000	0.032	0.025	0.017	0.007	0.035	0.005	0.010
Fe^{2+}	0.188	0.204	0.452	0.440	0.442	0.458	0.516	0.421	0.171
Mn	0.001	0.001	0.002	0.002	0.003	0.002	0.005	0.001	0.002
Mg	1.659	1.666	1.338	1.355	1.371	1.408	1.236	1.377	1.681
Ca	0.007	0.007	0.003	0.002	0.005	0.005	0.004	0.000	0.003
Na	0.001	0.001	0.000	0.001	0.000	0.000	0.001	0.001	0.001
Total	4.005	4.000	4.016	4.012	4.009	4.003	4.018	4.002	4.005

Ave - Average for sample Edge - Edge of a single grain
1. All Fe as FeO
2. Includes 0.07 ZnO and 0.03 BaO
3. Includes 0.10 ZnO and 0.06 BaO
4. From stoichiometry
* Analysis done at University of Melbourne

The ranges of values obtained for major components (>10%) are thus ±1–2.5% of the average value, and for minor components, ±3–5%.

Fe^{3+} contents of sapphirine and orthopyroxene were calculated from stoichiometry; the procedure outlined by Higgins *et al.* (1979) was used for sapphirine, except that Ti was included with Si for charge balance. As a check for this procedure, Wayne Dollase obtained Mössbauer spectra on coarse-grained sapphirine from locality 2064 (sample 2064H, Table 4) and 2042 (sample 2042A). Dollase (personal communication, 1979) estimates that the proportion of Fe^{3+} to total Fe is 17±3% in 2064H and 11.5±2% in 2042A. These values are consistent with estimates from stoichiometry—18±3% in 2064H and 7.7±3% in 2042A (Table 4). The uncertainty was estimated from the spread of Fe^{3+}/total Fe values calculated from repeated analyses of individual grains in samples 2045G, 2064H, and 2042A. Thus stoichiometry seems to provide a reasonable estimate of Fe^{3+}/total Fe ratio in sapphirine, as Higgins *et al.* reported.

Chemistry

Host rocks

Three of the quartzites from the Tula Mountains and the quartzite from Reference Peak were analyzed for 10 major elements and 4 trace elements (Table 3). The Tula Mountain quartzites consist almost exclusively of SiO_2, Al_2O_3, FeO, and MgO and contain little CaO (0.07–0.32 wt%), and almost no K_2O and Na_2O (0–0.05 wt%), while the quartzite from Reference Peak (459A) is notably sodic (3.4

Table 6. Composition of cordierite

	2064C*	2064D	2064F*	2048A	2042E*
	Weight Percent				
SiO_2	49.52	50.93	50.27	49.53	49.93
TiO_2	0.02	0.0	0.02	0.01	0.03
Al_2O_3	33.73	34.25	33.15	33.64	33.29
Cr_2O_3	0.02	0.02	0.01	0.0	0.04
FeO	0.95	2.62	2.53	3.37	2.15
MnO	0.03	0.03	0.04	0.04	0.01
MgO	12.83	12.24	12.06	11.56	12.01
CaO	0.01	0.08	0.01	0.09	0.0
K_2O	0.01	0.05	0.01	0.05	0.02
Na_2O	0.04	0.03	0.02	0.16	0.03
ZnO	0.09	-	0.09	-	0.16
BaO	0.02	-	0.01	-	0.0
Total	97.24	100.23	98.20	98.45	97.65
	Atoms per 18 Oxygens				
Si	4.987	5.009	5.046	4.983	5.033
Ti	0.002	0.000	0.002	0.001	0.002
Al	4.005	3.971	3.922	3.989	3.956
Cr	0.001	0.001	0.000	0.000	0.003
Fe	0.080	0.215	0.212	0.283	0.181
Mn	0.002	0.002	0.003	0.003	0.000
Mg	1.926	1.793	1.803	1.733	1.804
Ca	0.001	0.008	0.001	0.010	0.000
K	0.001	0.006	0.001	0.006	0.002
Na	0.007	0.005	0.004	0.032	0.006
Total	11.012	11.010	10.994	11.041	10.988

All Fe as FeO.

* Analysis done at the University of Melbourne.

wt%) and contains significant K_2O and CaO. All four quartzites are magnesian (Niggli mg ranges from 0.67 to 0.95).

The high Mg/Fe ratios, near absence of alkalis and of CaO in six quartzites, and high Na/K ratio in the seventh quartzite distinguishes these rocks from common sedimentary rocks, and from most igneous rocks. Examples of metamorphic rocks with similar compositions are a talc–yoderite schist (McKie, 1959), whiteschists (Schreyer, 1977), and sillimanite–orthopyroxene rocks (Chinner and Sweatman, 1968; Karsakov *et al.*, 1975). Protoliths suggested for these high Mg rocks low in alkalis are bentonitic sediments (McKie, 1959; Chinner and Sweatman, 1968), magnesian mudstones associated with evaporites (Schreyer, 1977), or pelitic rocks that have lost alkalis by removal of an anatectic melt (Nixon *et al.*, 1973; Lal *et al.*, 1978).

Schreyer's (1977) suggestion seems to be the most reasonable for the Enderby Land sapphirine–quartz rocks. Analyses of two evaporitic mudstones from northwest Africa (cited by Schreyer, 1977) are listed in Table 3 for comparison. The similarity in composition between these sedimentary rocks and the sapphirine–quartz rocks suggests that metasomatism or removal of anatectic melt need not be invoked to explain the composition of the magnesian pelitic rocks; sedimentary rocks of similar composition may very well have existed.

Table 7. Composition of biotite in Sample 459A

	Ave	Grain 1	Grain 2
	Weight Percent		
SiO_2	41.65	42.04	40.92
TiO_2	3.36	2.96	3.67
Al_2O_3	13.74	14.05	13.41
FeO	1.96	1.79	2.16
MnO	0.02	0.02	0.03
MgO	25.08	25.32	24.66
CaO	0.07	0.06	0.08
K_2O	10.44	10.45	10.33
Na_2O	0.12	0.14	0.10
BaO	0.25	0.22	0.29
F	3.98	4.12	3.77
Cl	0.07	0.07	0.08
Total[1]	99.04	99.48	97.90
	Based on 44 Anionic Charges (Foster, 1960)		
Si	5.776	5.795	5.750
Al^{IV}	2.224	2.205	2.222
Total	8.000	8.000	7.972
Al^{VI}	0.022	0.079	0.000
Ti	0.350	0.307	0.388
Fe	0.228	0.207	0.254
Mn	0.002	0.002	0.003
Mg	5.185	5.203	5.167
Total	5.787	5.798	5.812
Ca	0.011	0.009	0.012
K	1.848	1.838	1.852
Na	0.032	0.037	0.028
Ba	0.013	0.012	0.016
Total	1.904	1.896	1.908

[1]Corrected for oxygen equivalents of halogens

All Fe as FeO.

Sapphirine

Sapphirine analyzed in this study consists largely of MgO, SiO_2, Al_2O_3, and FeO; Cr_2O_3 is present in amounts greater than 0.1% in a few samples (Table 4). Values obtained on other oxides range from 0 to 0.12%, but only the values for MnO and TiO_2 are believed to be significant (*cf.* Higgins *et al.*, 1979).

Tula Mountain and Reference Peak sapphirines contain little ferric iron (0.02–0.13 Fe^{3+} per 20 oxygens, or no more than 18% of total Fe) by comparison with the Wilson Lake and Peekskill sapphirines, which contain 0.47 and 0.65 Fe^{3+} per 20 oxygen or 41–44% of all the iron present (Higgins *et al.*, 1979; Caporuscio and Morse, 1978).

Except for samples 2064C and 459A, the relative proportions of Si + Ti, Al + Cr + Fe^{3+}, and Fe^{2+} + Mg + Mn are nearly the same. The spread shown in Figure 2 of compositions for the five sapphirines is less than that for six repeated analyses of individual sapphirine grains in sample 2045G. Sapphirine in sample 2064C is significantly more siliceous, and that in sample 459A more aluminous, than the average of the other 5 sapphirines. The high Al content of sapphirine in sample 459A may be related to its association with sillimanite.

Sapphirine in a given sample is relatively homogeneous with respect to Mg/Fe ratio, and zoning was not detected. However, in some samples the composition of one of the analyzed grains differs markedly from the others in Al/Si ratio (Table 4). The differences appear to follow the substitution scheme Mg + Si = 2Al (Fig. 2) characteristic of many sapphirines (Schreyer and Abraham, 1975). Cr_2O_3 contents vary

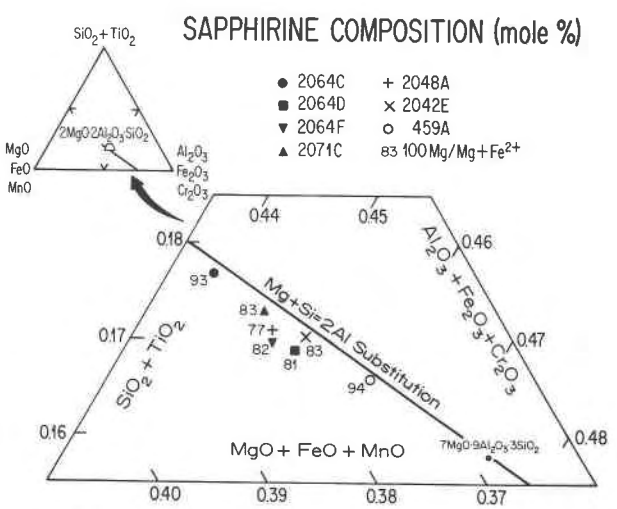

Fig. 2. Composition of sapphirine from Enderby Land. Fe^{3+} contents calculated from stoichiometry (Higgins *et al.*, 1979).

from grain to grain in some samples, *e.g.*, 0.2 to 0.5 wt% in 2048A.

Orthopyroxene

By comparison with the metamorphic orthopyroxenes listed by Deer *et al.* (1978, p. 41–47), the Enderby Land orthopyroxenes on the average contain more Al_2O_3 (7–11 wt%) and less CaO (0.1–0.2%) and TiO_2 (0.1–0.3%).

Orthopyroxene is homogeneous with respect to Fe/Mg ratio in a given sample. In a few samples, grains are zoned in Al_2O_3 content, which decreases from core to edge (*e.g.*, 2064C and 2071C, Table 5); a similar variation is reported by Chinner and Sweatman (1968) in orthopyroxene associated with sillimanite.

In contrast to sapphirine, the Al_2O_3 content of orthopyroxene increases markedly with Fe/Mg ratio or $FeSiO_3$ content (Fig. 3). Moreover, this relation appears to be a chemical feature of the orthopyroxene and does not reflect differences in the physical conditions of metamorphism among the localities, as Al contents of three orthopyroxenes from a single locality (2064) also increase with Fe/Mg ratio. The data for the Reference Peak orthopyroxene lie on the least-squares fit to data on the Tula Mountain orthopyroxenes (Fig. 3).

Cordierite, biotite, sillimanite

Cordierite is rich in the magnesium end member, contains negligible amounts of alkalis and CaO (except 2048A), and appears to be compositionally homogeneous (Table 6). Biotite in sample 459A (Table 7) is rich in TiO_2 (3.7 wt%) and fluorine (4%), but its Al_2O_3 content (13.7%) is low for biotite associated with sillimanite in granulite-facies rocks (*e.g.*, Dallmeyer and Dodd, 1971, and Dallmeyer, 1974, report 15 to 18%). The composition of this biotite varies widely from grain to grain. For the three grains analyzed in this study (analyses of two are shown in Table 7), the amounts of TiO_2 and Al_2O_3, and the amount of F and the Fe/Mg ratio, are inversely proportional.

Sillimanite in sample 459A contains 0.2 wt% Fe_2O_3, and in 2042A (a sapphirine–quartz rock) 0.4% Fe_2O_3. These sillimanites contain less Fe_2O_3 than most sillimanite from granulite-facies rocks elsewhere in Antarctica (0.3–1.4%; Grew, 1980) and significantly less than sillimanite associated with sapphirine and quartz in Wilson Lake, Labwor Hills, and Peekskill (1.2–1.7%; Caporuscio and Morse, 1978; Grew, 1980). The low Fe_2O_3 content of the sil-

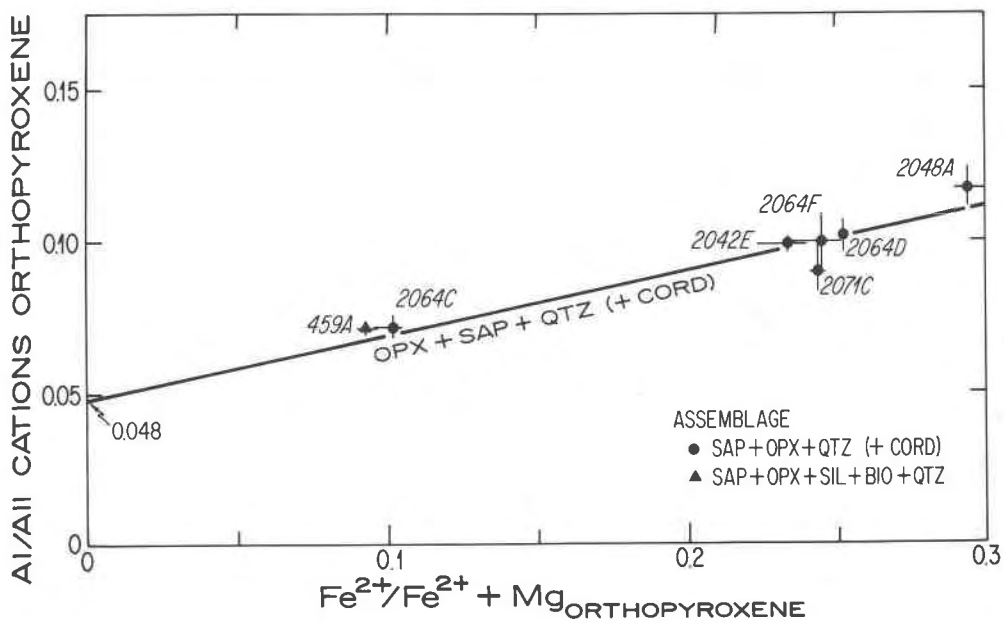

Fig. 3. Proportion of Al to all cations in orthopyroxene (Al/all cations) associated with sapphirine as a function of $Fe^{2+}/(Fe^{2+} + Mg)$ ratio. Average composition of orthopyroxene (exclusive of edges of grains) indicated by symbol. Approximate range in a given sample indicated by spread of values obtained on individual grains (generally 3 to 4 per sample). Line is a least squares fit of the average Al contents in the 6 orthopyroxenes from quartzites (sample 459A not included).

limanite is consistent with the low Fe^{3+}/total Fe ratio estimated for the associated sapphirine.

Chemical relations among the minerals

Data on Fe and Mg contents of coexisting sapphirine, cordierite, and orthopyroxene are summarized in Figure 4. The proportion of the iron end members, X_{Fe}, increases sympathetically in each of the minerals and with Fe/Mg ratio in the host rock composition (Table 3). Moreover, X_{Fe} is greatest in orthopyroxene and least in cordierite, a trend that is true for many parageneses (*e.g.*, Hensen, 1971; Higgins *et al.*, 1979). The regular trends and chemical homogeneity of these minerals imply that sapphirine and orthopyroxene crystallized in equilibrium with respect to Fe and Mg and that formation of cordierite also involved equilibration of Fe and Mg.

The proportion of Fe^{3+} to total Fe appears to be lower in orthopyroxene than in associated sapphirine, a relation also reported by Caporuscio and Morse (1978).

Physical conditions of metamorphism

Temperature

Temperatures at the peak of metamorphism, during which sapphirine + quartz was stable, were estimated from the compositions of coexisting pyroxenes in associated mafic and ultramafic rocks, and from the Al content of orthopyroxene in the Tula Mountain quartzites.

Four pairs of coexisting pyroxenes from Beaver Island (Amundsen Bay), Gage Ridge, and Spot Height 945 were analyzed (Table 8). Estimated temperatures range from 840–890°C from Wells' (1977) equation 5 and 890–1000°C from Wood and Banno's (1973) equation 27. These values are minimums, as both pyroxenes in each sample have exsolved lamellae of the other pyroxene.

Anastasiou and Seifert (1972) determined the Al_2O_3 contents of orthopyroxene coexisting with cordierite and sapphirine in the system MgO–Al_2O_3–SiO_2 at 900° and 1000°C at 5 kbar. In order to apply their experimental data to the Tula Mountains quartzite, we must first try to correct for the effect of Fe^{2+} on the Al content of orthopyroxene in the natural assemblages and then extrapolate Anastasiou and Seifert's Al isopleths to the stability field of sapphirine + quartz.

The measured values of Al in orthopyroxenes of varying Fe/Mg ratios have been used to estimate the Al content of a hypothetical Fe-free orthopyroxene by extrapolation of a least-squares fit to Al contents as a function of Fe/Mg ratios (Fig. 3). It is assumed that the temperature of crystallization did not differ greatly among the three localities (Mount Hardy,

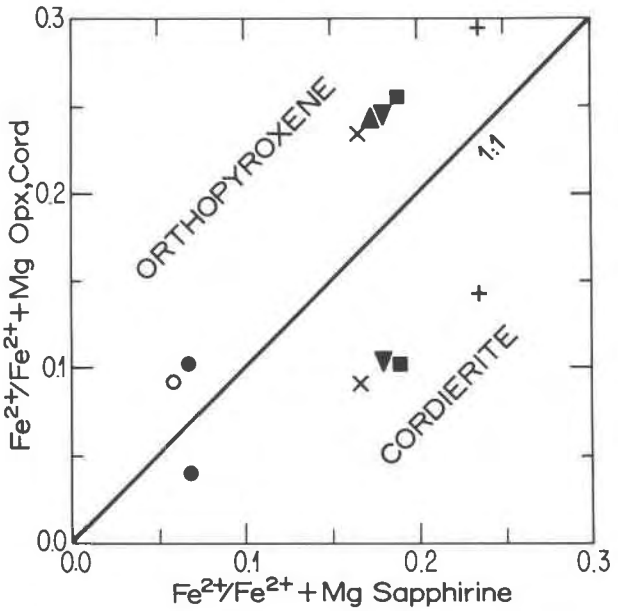

Fig. 4. $Fe^{2+}/(Fe^{2+} + Mg)$ contents of associated sapphirine and orthopyroxene, and of associated sapphirine and cordierite. Symbols designating samples are the same as those used in Fig. 2. 1:1 line is for no fractionation of Fe^{2+} and Mg, *i.e.* $K_D = 1$.

Gage Ridge, and Spot Height 945). This extrapolation gives a proportion of Al to all cations of 0.048 for a hypothetical Fe-free orthopyroxene associated with sapphirine and quartz.

For an orthopyroxene at 5 kbar coexisting with cordierite and sapphirine, a proportion of Al to all cations of 0.048 (close to 4.8 wt% Al_2O_3) indicates a temperature of crystallization of 930°C (Anastasiou and Seifert, 1972, Fig. 6). However, the Tula Mountain orthopyroxene crystallized with sapphirine and quartz at pressures greater than 6 kbar (see below). As Anastasiou and Seifert's Al isopleths in orthopyroxene associated with sapphirine and cordierite have steep negative slopes in *P–T* space, this temperature estimate is a maximum. A rough extrapolation of their isopleths to the estimated pressures of metamorphism indicates a metamorphic temperature near 900°C for the Tula Mountains quartzites.

More recent experiments and calculations by Danckwerth and Newton (1978, p. 196) and Ganguly and Ghose (1979) imply that the decrease with temperature of the Al_2O_3 content of enstatite associated with spinel and forsterite may be less than the decrease found experimentally by Anastasiou and Seifert. Anastasiou and Seifert's Al_2O_3 isopleths in the cordierite–sapphirine–enstatite field may also be too closely spaced, and consequently a temperature estimate based on their data at temperatures such as 900°C would be a maximum one (Newton, written communication, 1979).

The Al_2O_3 of the Reference Peak orthopyroxene plots close to the line representing a least-squares fit of the Tula Mountain orthopyroxenes (Fig. 3); thus the temperature of metamorphism at Reference Peak may not have differed significantly from that in the Tula Mountains.

Pressure

Pressures of metamorphism were estimated from the compositions of garnet and plagioclase associated with sillimanite and quartz (Ghent, 1976) in three

Table 8. Composition of pyroxenes used for geothermometry (wt.%)

Locality	Spot Height 945				Gage Ridge		Beaver Island	
Sample No.	2035A		2040B		2055B		2023A	
Mineral[1]	OPX	CPX	OPX	CPX	OPX	CPX	OPX	CPX
SiO_2	53.10	50.80	53.16	50.22	57.33	54.57	58.14	55.23
TiO_2	0.12	0.50	0.16	0.80	0.08	0.24	0.01	0.01
Al_2O_3	3.49	5.03	4.76	6.86	1.21	1.94	1.02	1.40
Cr_2O_3	0.13	0.25	0.27	0.42	0.30	0.64	0.25	0.77
FeO	17.46	7.15	14.18	5.54	8.33	2.74	5.72	1.63
MnO	0.28	0.15	0.35	0.19	0.16	0.08	0.22	0.10
MgO	26.07	14.28	27.82	14.36	33.71	17.43	35.38	17.82
CaO	0.73	22.66	0.49	23.26	0.45	23.57	0.34	24.15
Na_2O	0.01	0.61	0.01	0.48	0.01	0.53	0.01	0.45
NiO	0.09	0.04	0.06	0.02	0.15	0.06	0.26	0.13
Total	101.48	101.46	101.25	102.15	101.72	101.81	101.36	101.69

[1]OPX - orthopyroxene CPX - clinopyroxene
All Fe as FeO.

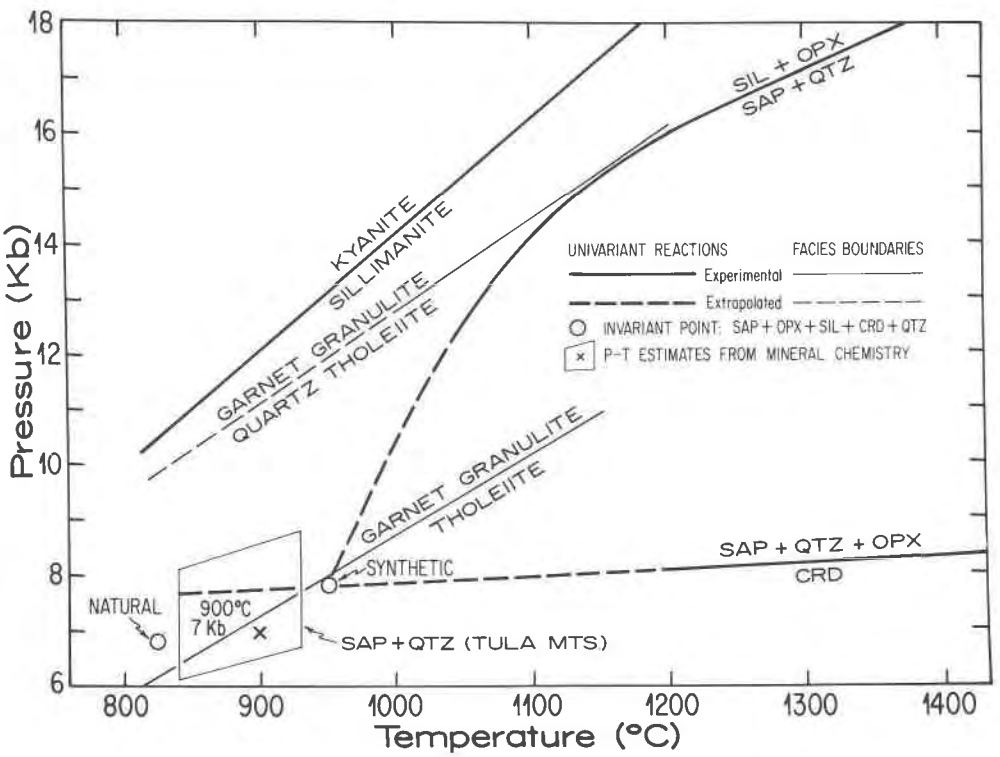

Fig. 5. Experimental curves relevant to rocks from western Enderby Land, Antarctica. Mineral abbreviations are kya—kyanite, sil—sillimanite, cpx—clinopyroxene, opx—orthopyroxene, sap—sapphirine, crd—cordierite, gar—garnet, olv—olivine, spl—spinel, plag—plagioclase, and qtz—quartz. Sources of data: kya–sil curve (Holdaway, 1971; extrapolated portions not indicated separately); sil + opx = sap + qtz (Hensen, 1972; Chatterjee and Schreyer, 1972; Newton, 1972; Newton *et al.*, 1974); sap + qtz + opx = crd (Newton, 1972; Newton *et al.*, 1974); invariant point sap + opx + sil + crd + qtz (Newton *et al.*, 1974); garnet granulite–quartz tholeiite transition (Green and Ringwood, 1967); garnet granulite–tholeiite transition (Ito and Kennedy, 1971). Outline indicates range of pressure–temperature estimates for Tula Mountains–Amundsen Bay area. Preferred values are 900°C and 7 kbar indicated by cross.

rocks (Table 9) at temperatures of 840° and 930°C.

In addition to temperature and composition, activity coefficients for the calcium components in plagioclase and garnet must be calculated (Table 10). For anorthite in plagioclase, a constant value of 1.28 was used (Orville, 1972). For grossular in garnet, we need to consider only three components: grossular, pyrope, and almandine. The interaction between grossular and spessartine may be ignored as spessartine contents are low. Andradite may also be ignored, as Fe^{3+} contents of the garnet are probably negligible. We can then treat garnet as a regular ternary solution and calculate the activity of grossular, γ_{Gr}, as follows (Newton, 1978, eq. 4): $RT \ln \gamma_{Gr} = W_{Gr\text{-}Py} X_{Py}^2 + X_{Py} X_{Am}(W_{Gr\text{-}Py} + W_{Gr\text{-}Am} - W_{Am\text{-}Py}) + W_{Gr\text{-}Am} X_{Am}^2$, where R = gas constant, Gr = grossular, Py = pyrope, Am = almandine, X = mole fraction, and W = Margules or interaction parameter between a given pair of the garnet components.

Unfortunately, there remains considerable disagreement on the values of the Margules parameters. For the present calculations, I have arbitrarily selected three cases (Table 10): (1) $W_{Gr\text{-}Py} = 3.8$, $W_{Gr\text{-}Am} = 0$, and $W_{Py\text{-}Am} = 2.5$ kcal (from Ganguly and Kennedy, 1974; Newton, 1978); (2) $W_{Gr\text{-}Py} = 7460 - 4.3\,T(°K)$ from Hensen *et al.* (1975), $W_{Gr\text{-}Am} = 0$, and $W_{Py\text{-}Am} = 2.5$ kcal; and (3) ideal solution (all $W = 0$). These cases should bracket the range of possible values; for example, O'Neill and Wood (1979) obtained $W_{Gr\text{-}Py} \approx 2.7 \pm 0.2$ kcal, $W_{Py\text{-}Am} \approx 0.2 \pm 0.2$ kcal, for $W_{Gr\text{-}Am} = 0$.

Pressures, P, were calculated from (1) Cressey *et al.*'s (1978, p. 401) equation adjusted to allow for a variable plagioclase composition: $-\ln K_D = -3RT \ln (\gamma_{Gr} X_{Gr} / \gamma_{An} X_{An}) = -1.2651(P_0 - P) + 2.878 \times 10^{-6}(P_0^2 - P^2)$, where P_0 is the pressure at which anorthite ($X_{An} = 1$), grossular ($X_{Gr} = 1$), sillimanite, and quartz are stable, and (2) Schmid and Wood's (1976)

Table 9. Compositions of garnet and plagioclase associated with sillimanite and quartz (used for geobarometry) (wt.%)

Locality	Gage Ridge		Mt. Hardy			
Sample Number	2045C		2083C		2083E	
Mineral[1]	Gar	Plag	Gar	Plag	Gar	Plag
SiO_2	39.31	58.59	40.54	55.47	39.61	54.09
TiO_2	0.05	0.03	0.08	0.02	0.05	0.01
Al_2O_3	23.18	26.14	22.85	29.30	22.76	28.34
FeO	25.13	0.01	22.50	0.08	22.69	0.02
MnO	0.44	0.0	0.42	0.01	0.42	0.01
MgO	12.55	0.0	14.57	0.0	13.54	0.01
CaO	1.00	7.71	1.39	11.56	1.47	10.74
Na_2O	0.01	7.15	0.01	5.18	0.04	5.52
K_2O	0.04	0.43	0.06	0.22	0.0	0.19
Cr_2O_3	n.a.	n.a.	0.08	0.0	0.06	0.01
Total	101.72	100.07[2]	102.51	101.83	100.63	98.93

[1]Gar - garnet Plag - plagioclase
All Fe as FeO
n.a. - not analyzed
[2]Includes BaO - 0.01%

equation 7: $\ln K_D = 5123/T - 16.02 + [(P - 1)0.6565]/T$. Goldsmith (1980) reports that Schmid and Wood's equation, which is based on the experimental work of Hays (1966), Newton (1966), and Hariya and Kennedy (1968), is in good agreement with his experimental redetermination of the Al_2SiO_5–grossular–anorthite–quartz reaction.

The calculated pressures are listed in Table 10. Assuming nonideal behavior in garnet (cases 1 and 2), pressures range from about 6.5 to 9 kbar at 930°C, and 6 to 8 kbar at 840°C, and for ideal behavior, 4.5 to 6 kbar for these temperatures. The calculated pressure increases with the estimated value of the activity coefficient of grossular.

Newton and Haselton (in press) calculated pressures of 6.9, 6.7, and 7.4 kbar for samples 2045C, 2083C, and 2083E, respectively, using my compositional data (Table 10) and a new calibration of the garnet–plagioclase–Al_2SiO_5–quartz geobarometer.

In summary, the temperature and pressure of metamorphism are estimated to be 840–1000°C and 4.2-9.2 kbar. Preferred values are 900±30°C and 7±1 kbar. Sheraton *et al.* (1980) report temperatures of 900° to 950°C and pressures of 8 to 10 kbar based on detailed studies at one locality in the Tula Mountains.

Partial pressure of water

Crystallization of the sapphirine + quartz association and its reaction to form sillimanite and orthopyroxene can be reproduced in the laboratory only under nearly anhydrous conditions (Newton, 1972). Moreover, the mineralogy of associated rocks in the Tula Mountains is consistent with this interpretation; for example, the quartz–K-feldspar–orthopyroxene association implies low water partial pressures given a lithostatic pressure of 7 kbar (Luth, 1967, p. 413). Additional evidence for low water partial pressures is the widespread occurrence of calcic mesoperthite and the limited extent of anatectic melting in quartzofeldspathic rocks (Sheraton *et al.*, 1980).

Comparison with experimental systems

Rocks rich in Al_2O_3 and MgO

Experimental results on the MgO–SiO_2–Al_2O_3 system (Newton, 1972; Hensen, 1972; Chatterjee and Schreyer, 1972; Newton *et al.*, 1974), which are summarized in Figure 5, can be applied to the quartzites. The major difficulties in comparing the laboratory data with natural assemblages are the effect of iron (Seifert, 1974, p. 196), and extrapolation of the reac-

Table 10. Calculation of pressure from compositions of coexisting garnet and plagioclase

	Composition (mole fraction)			
	Garnet			Plagioclase
Component	Gr	Am	Py	An
Sample				
2045C	0.0260	0.5106	0.4544	0.364
2083C	0.0351	0.4441	0.5123	0.546
2083E	0.0384	0.4618	0.4911	0.513

Pressures

Case 1. (Adapted from Ganguly and Kennedy, 1974)

	930°C				840°C			
Sample	γ_{Gr}	$\ln K_D$	P^1 Kb	P^2	γ_{Gr}	$\ln K_D$	P^1 Kb	P^2
2045C	1.575	-7.294	8.6	8.2	1.634	-7.184	7.9	7.2
2083C	1.718	-7.351	8.5	8.1	1.795	-7.220	7.8	7.1
2083E	1.660	-6.998	9.2	8.7	1.729	-6.874	8.4	7.7
Case 2. (Adapted from Hensen et al., 1975)								
2045C	1.194	-8.127	7.0	6.7	1.307	-7.854	6.7	6.0
2083C	1.260	-8.281	6.7	6.4	1.398	-7.968	6.4	5.9
2083E	1.234	-7.885	7.4	7.1	1.363	-7.589	7.0	6.5
Case 3. Ideal solution in garnet								
2045C	1.0	-8.658	6.0	5.7	1.0	-8.658	5.2	4.7
2083C	1.0	-8.974	5.3	5.1	1.0	-8.974	4.6	4.2
2083E	1.0	-8.517	6.2	5.9	1.0	-8.517	5.4	4.9

Case	W_{Gr-Py}	W_{Gr-Am} kcal	W_{Am-Py}	T°C
1	3.8	0	2.5	930,840
2	2.29	0	2.5	930
2	2.67	0	2.5	840
3	0	0	0	930,840

γ - activity coefficient; W - Margules parameter
Gr - grossular; Am - almandine; Py - pyrope
$K_D = (\gamma_{Gr}X_{Gr})^3_{Garnet}/(\gamma_{An}X_{An})^3_{plagioclase}$ where X - mole fraction
1. Cressey et al (1978) 2. Schmid and Wood (1976)

tion curves from the high temperatures used in the laboratory (mostly greater than 1000°C) to the lower temperatures estimated for the natural assemblages.

In the case of iron, some of the Enderby Land sapphirine–quartz rocks are more magnesian than the examples discussed by Seifert, and the shifts in the positions of reaction curves due to FeO and Fe_2O_3 may thus be relatively small compared to other ambiguities involved in applying experimental data to Enderby Land. Moreover, these shifts can be predicted qualitatively. The fractionation of Fe^{2+} and Mg illustrated in Figure 4 implies that the sillimanite–orthopyroxene field and sapphirine–quartz field (Fig. 5) expand to lower pressures in FeO-bearing rocks. The five-phase assemblage (sapphirine–sillimanite–orthopyroxene–cordierite–quartz) in such rocks is univariant and defines a *P–T* curve inferred to have a negative slope (Hensen, 1971, Fig. 1). Consequently, the temperature of the invariant point for this five-phase assemblage in the $MgO–SiO_2–Al_2O_3$ system is a minimum for the sapphirine–quartz association in FeO-bearing rocks. On the other hand, Fe_2O_3 would expand the sapphirine–quartz field and shift the invariant point to lower temperatures, as the Fe^{3+}/Fe^{2+} ratio of sapphirine is greater than those of associated orthopyroxene and cordierite (Caporuscio and Morse, 1978). The pressure of the five-phase assemblage would be lower in natural systems containing FeO or Fe_2O_3 relative to the $MgO–Al_2O_3–SiO_2$ system, while the temperature may not differ greatly.

The problem of extrapolating experimental data to geologic temperatures is more serious. The five-phase invariant point has not been located experimentally. Newton *et al.* (1974) estimated its position at 950°C and 8 kbar by extrapolating (with the help of thermochemical calculations) the two experimentally determined univariant reactions (cordierite = sapphirine + quartz + orthopyroxene, and sillimanite + orthopyroxene = quartz + sapphirine). If an allowance is made for possible differences in cation disorder between synthetic and natural sapphirine, as indicated by calorimetric measurements (Charlu *et al.*, 1975), the invariant point is shifted to 825°C (Newton *et al.*, 1974). Only the 825°C estimate is consistent with the temperatures of metamorphism in the Tula Mountains calculated from mineral compositions. This result could be interpreted as support for the suggestions of Newton *et al.* and Charlu *et al.* that the thermochemical properties of synthetic sapphirine differ considerably from those of natural sapphirines (not to be confused with the triclinic and monoclinic polytypes of sapphirine, S. Merlino, 1980). It could also signify that the curvature in the sillimanite + orthopyroxene = sapphirine + quartz reaction is less than that inferred by Newton *et al.*, and consequently, the intercept of the two univariant curves is at a temperature lower than 950°C.

The quartz–orthopyroxene–sillimanite (±sapphirine) association in the Reference Peak quartzite must have crystallized close to the univariant reaction involving these four minerals. As the temperature of crystallization at Reference Peak may have been similar to that for Tula Mountains, an increase in lithostatic pressure may be the cause of the change in mineralogy at Reference Peak. In contrast, Morse and Talley (1971) attribute the replacement of sapphirine–quartz by sillimanite–orthopyroxene to a decrease in temperature at nearly constant pressure.

The cordierite overgrowths on sapphirine in the Tula Mountain quartzites may be due to alteration following the most intense metamorphic event, and possibly reflect a decrease in both temperature and pressure. The reaction of sapphirine and quartz to cordierite probably occurs only under conditions of low water partial pressure (Newton, 1972).

Mafic rocks

The association garnet–clinopyroxene–orthopyroxene–plagioclase±quartz has not been found in mafic rocks of the Tula Mountains, although it does occur on Amundsen Bay (Sheraton *et al.*, 1980) and Mt. Charles (Fig. 1). Garnet and clinopyroxene at Mount Charles occur together in both olivine-normative and quartz-normative rocks having Niggli mg values of 0.3 to 0.5 (Grew, unpub. data). These rocks are thus more iron-rich than the materials used in the experimental determination of the tholeiite–garnet granulite transition (Fig. 5, from Green and Ringwood, 1967; Ito and Kennedy, 1971). These experimentalists agree that decreasing Mg/Fe ratio decreases the pressure of the first appearance of garnet in rocks of basaltic composition. The appearance of the garnet–clinopyroxene association at Mount Charles would be possible under the conditions estimated for the sapphirine–quartz association (Fig. 5), particularly if metamorphic pressures were higher at Mt. Charles than in the Tula Mountains, as Sheraton *et al.* (1980) suggest. An increase in pressure southwards of the Tula Mountains is also indicated by data on the Reference Peak quartzite.

Conclusion

The relatively rare assemblage sapphirine–quartz is exposed over a fairly large area in the Archean

(2500 m.y.) Napier complex of western Enderby Land. Textures and compositional relationships indicate that this association was in equilibrium at the peak of metamorphism. On the basis of mineral chemistry, metamorphic temperatures and pressures for the crystallization of sapphirine–quartz are estimated to be 900±30°C and 7±1 kbar. For the reaction of sapphirine and quartz to sillimanite and orthopyroxene, pressures may have been somewhat greater. Partial pressure of water during metamorphism was significantly less than lithostatic pressure. These pressure and temperature estimates are not entirely consistent with the development of sapphirine–quartz in Mg–Al-rich rocks as predicted from experimental results. This discrepancy could be explained by differences in the degree of cation disorder in synthetic and natural sapphirine (Newton *et al.,* 1974; Charlu *et al.,* 1975) or by inaccurate extrapolation to geologically reasonable temperatures of the experimentally derived reaction sapphirine + quartz = sillimanite + orthopyroxene.

Metamorphic pressures of 6 to 8 kbar are equivalent to depths of burial of 21 to 28 km. Corresponding thermal gradients lie in the range 30°C/km to 44°C/km, with 37°C/km the value based on the preferred *P–T* estimate of 900°C and 7 kbar. These values are comparable to the 18–35°C/km estimated for Archean granulites (Tarney and Windley, 1977; Weaver *et al.,* 1978) and to Lambert's (1976) suggested 36°C/km late Archean geotherm. However, the calculated pressure–temperature conditions cannot be unequivocally attributed to regional metamorphism (see Lambert, 1976). Although no plutonic bodies have been reported from the area shown in Figure 1, exposure is sufficiently poor that a plutonic rock may be present, but concealed by ice. Osumilite, normally a mineral of volcanic rocks, has been reported from granulite-facies contact aureoles of anorthositic complexes in Labrador (Berg and Wheeler, 1976) and in Norway (Maijer *et al.,* 1977). Osumilite in the Tula Mountains (Fig. 1) may also be related to concealed anorthositic bodies at depth (Sheraton *et al.,* 1980), and these authors report "thin anorthosite layers" at two localities in the Tula Mountains. In addition, Sheraton *et al.* (1980) note that a negative modified free-air gravity anomaly mapped by Wellman and Tingey (in press) roughly corresponds to the outcrop area of the sapphirine–quartz association and suggest that this anomaly may be associated with anorthosite. One difficulty in accepting a contact metamorphic origin of osumilite and of the sapphirine–quartz association in Enderby Land is their occurrence on a regional scale (Sheraton *et al.,* 1980). Possibly the distribution of osumilite and of the sapphirine–quartz association is not strictly regional. The presence of these minerals over a large area could be attributed to the partial coalescing of contact aureoles around small anorthosite bodies widely distributed throughout the Tula Mountains. An abundance of small anorthosite bodies could also explain Wellman and Tingey's (in press) gravity anomaly.

Acknowledgments

I thank the Antarctic Division of the Australian Department of Science and the Environment for the invitation to participate in the Australian National Antarctic Research Expeditions and for logistic support in the field; J. W. Sheraton, R. J. Tingey, I. F. Allison, and L. A. Offe for their assistance in planning and carrying out my field program; J. W. Sheraton and Ye. N. Kamenev for samples collected by Australian and Soviet geologists in Enderby Land, and for unpublished field data and information on sample locations; and J. F. Lovering for use of the electron microprobe at the University of Melbourne while I was there as a Senior Fulbright Scholar in 1978. G. Stummer performed the X-ray fluorescence analyses. This research was funded by NSF grant DPP 76-80957 to UCLA.

Thoughtful reviews of earlier versions of this manuscript by F. Chayes, R. C. Newton, W. Schreyer, F. Seifert, and R. J. Tingey have resulted in a substantial improvement, for which the author is very grateful.

References

Anastasiou, P. and F. Seifert (1972) Solid solubility of Al_2O_3 in enstatite at high temperatures and 1–5 kb water pressure. *Contrib. Mineral. Petrol., 34,* 272–287.

Barker, F. (1964) Reaction between mafic magmas and pelitic schist, Cortlandt, New York. *Am. J. Sci., 262,* 614–634.

Berg, J. H. and E. P. Wheeler (1976) Osumilite of deep-seated origin in the contact aureole of the anorthositic Nain complex, Labrador. *Am. Mineral., 61,* 29–37.

Bourne, J. H. (1978) Metamorphism in the eastern and southwestern portions of the Grenville Province. In J. A. Fraser and W. W. Heywood, Eds., *Metamorphism in the Canadian Shield,* p. 315–328. *Geol. Surv. Canada Pap. 78-10.*

Caporuscio, F. A. and S. A. Morse (1978) Occurrence of sapphirine plus quartz at Peekskill, New York. *Am. J. Sci., 278,* 1334–1342.

Charlu, T. V., R. C. Newton and O. J. Kleppa (1975) Enthalpies of formation at 970 K of compounds in the system MgO–Al_2O_3–SiO_2 from high temperature solution calorimetry. *Geochim. Cosmochim. Acta, 39,* 1487–1497.

Chatterjee, N. D. and W. Schreyer (1972) The reaction $enstatite_{ss}$ + sillimanite ⇄ $sapphirine_{ss}$ + quartz in the system MgO–Al_2O_3–SiO_2. *Contrib. Mineral. Petrol., 36,* 49–62.

Chinner, G. A. and T. R. Sweatman (1968) A former association of enstatite and kyanite. *Mineral. Mag., 36,* 1052–1060.

Clifford, T. N. (1974) Review of African granulites and related rocks. *Geol. Soc. Am. Spec. Pap. 156.*

Cortesogno, L., W. G. Ernst, M. Galli, B. Messiga, G. M. Pedemonte and G. B. Piccardo (1977) Chemical petrology of

eclogitic lenses in serpentinite, Gruppo di Voltri, Ligurian Alps. *J. Geol., 85,* 255–277.

Cressey, G., R. Schmid and B. J. Wood (1978) Thermodynamic properties of almandine–grossular garnet solid solutions. *Contrib. Mineral. Petrol., 67,* 397–404.

Dallmeyer, R. D. (1974) Metamorphic history of the northeastern Reading Prong, New York and northern New Jersey. *J. Petrol., 15,* 325–359.

——— (1975) $^{40}Ar/^{39}Ar$ release spectra of biotite and hornblende from the Cortlandt and Rosetown Plutons, New York, and their regional implications. *J. Geol., 83,* 629–643.

——— and R. T. Dodd (1971) Distribution and significance of cordierite in paragneisses of the Hudson Highlands, southeastern New York. *Contrib. Mineral. Petrol., 33,* 289–308.

Dallwitz, W. B. (1968) Co-existing sapphirine and quartz in granulite from Enderby Land, Antarctica. *Nature, 219,* 476–477.

Danckwerth, P. A. and R. C. Newton (1978) Experimental determination of the spinel peridotite to garnet peridotite reaction in the system $MgO–Al_2O_3–SiO_2$ in the range 900°–1100°C and Al_2O_3 isopleths of enstatite in the spinel field. *Contrib. Mineral. Petrol., 66,* 189–201.

Deer, W. A., R. A. Howie and J. Zussman (1978) *Rock-Forming Minerals, Vol. 2A, Single-Chain Silicates* (second ed.). Wiley, New York.

Dougan, T. W. (1974) Cordierite gneisses and associated lithologies of the Guri area, northwest Guayana Shield, Venezuela. *Contrib. Mineral. Petrol., 46,* 169–188.

Ellis, D. J., J. W. Sheraton, R. N. England and W. B. Dallwitz (1980) Osumilite–sapphirine–quartz granulites from Enderby Land Antarctica—mineral assemblages and reactions. *Contrib. Mineral. Petrol., 72,* 123–143.

Foster, M. D. (1960) Interpretation of the composition of trioctahedral micas. *U. S. Geol. Surv. Prof. Pap. 354-B.*

Ganguly, J. and S. Ghose (1979) Aluminous orthopyroxene: order–disorder, thermodynamic properties, and petrologic implications. *Contrib. Mineral. Petrol., 69,* 375–385.

——— and G. C. Kennedy (1974) The energetics of natural garnet solid solution. 1. Mixing of the aluminosilicate end-members. *Contrib. Mineral. Petrol., 48,* 137–148.

Ghent, E. D. (1976) Plagioclase–garnet–Al_2SiO_5–quartz: a potential geobarometer–geothermometer. *Am. Mineral., 61,* 710–714.

Goldsmith, J. R. (1980) The melting and breakdown reactions of anorthite at high pressures and temperatures. *Am. Mineral., 65,* 272–284.

Green, D. H. and A. E. Ringwood (1967) An experimental investigation of the gabbro to eclogite transformation and its petrological applications. *Geochim. Cosmochim. Acta, 31,* 767–833.

Grew, E. S. (1978) Petrologic study of the granulite-facies metamorphic rocks of Enderby Land, East Antarctica, with the Australian National Antarctic Research Expedition (ANARE), 1977–78. *Antarctic J., 13(4),* 2–3.

——— (1979a) Sapphirine + quartz from Archean rocks in Enderby Land, East Antarctica (abstr.). *Trans. Am. Geophys. Union, 60,* 423.

——— (1979b) Reactions involving sapphirine and sillimanite + orthopyroxene in quartz-bearing rocks of the 2.5 b.y. Napier complex, Enderby Land, East Antarctica (abstr.). *Geol. Soc. Am. Abstracts with Programs, 11,* 435–436.

——— (1980) Sillimanite and ilmenite from high-grade metamorphic rocks of Antarctica and other areas. *J. Petrol., 21,* 39–68.

——— and W. I. Manton (1979) Archean rocks in Antarctica: 2.5-billion-year uranium–lead ages of pegmatites in Enderby Land. *Science, 206,* 443–445.

Hariya, Y. and G. C. Kennedy (1968) Equilibrium study of anorthite under high pressure and high temperature. *Am. J. Sci., 266,* 193–203.

Hays, J. F. (1966) Lime–alumina–silica. *Carnegie Inst. Wash. Year Book, 65,* 234–239.

Hensen, B. J. (1971) Theoretical phase relations involving cordierite and garnet in the system $MgO–FeO–Al_2O_3–SiO_2$. *Contrib. Mineral. Petrol., 33,* 191–214.

——— (1972) Phase relations involving pyrope, enstatite$_{ss}$, and sapphirine$_{ss}$ in the system $MgO–Al_2O_3–SiO_2$. *Carnegie Inst. Wash. Year Book, 71,* 421–427.

———, R. Schmid and B. J. Wood (1975) Activity–composition relationships for pyrope–grossular garnet. *Contrib. Mineral. Petrol., 51,* 161–166.

Higgins, J. B., P. H. Ribbe and R. K. Herd (1979) Sapphirine 1. Crystal chemical contributions. *Contrib. Mineral. Petrol., 68,* 349–356.

Holdaway, M. J. (1971) Stability of andalusite and the aluminum silicate phase diagram. *Am. J. Sci., 271,* 97–131.

Ito, K. and G. C. Kennedy (1971) An experimental study of the basalt–garnet granulite–eclogite transition. In J. G. Heacock, Ed., *The Structure and Physical Properties of the Earth's Crust,* p. 303–314. *Am. Geophys. Union, Geophys. Monogr. 14.*

Kamenev, Ye. N. (1972) Geological structure of Enderby Land. In R. J. Adie, Ed., *Antarctic Geology and Geophysics,* p. 579–583. Universitetsforlaget, Oslo.

——— (1975) Geologiya Zemli Enderbi [Geology of Enderby Land]. *Antarktika Doklady Komissii, 14,* 34–58. Nauka, Moscow.

Karsakov, L. P., V. I. Shuldiner and A. M. Lennikov (1975) Granulitovyy kompleks vostochnoy chasti Stanovoy Skladchatoy Oblasti i Chogarskaya fatsiya glubinnosti [Granulite complex of the eastern part of the Stanovoy Fold Province and the Chogar facies of depth]. *Izvestiya Akad. Nauk SSSR, Ser. Geol. 1975(5),* 47–61

Lal, R. K., D. Ackermand, F. Seifert and S. K. Haldar (1978) Chemographic relationships in sapphirine-bearing rocks from Sonapahar, Assam, India. *Contrib. Mineral. Petrol., 67,* 169–187.

Lambert, R. St. J. (1976) Archean thermal regimes, crustal and upper mantle temperatures, and a progressive evolutionary model for the Earth. In B. F. Windley, Ed., *The Early History of the Earth,* p. 363–373. Wiley, London.

Leong, K. M. and J. M. Moore, Jr. (1972) Sapphirine-bearing rocks from Wilson Lake, Labrador. *Can. Mineral., 11,* 777–790.

Luth, W. C. (1967) Studies in the system $KAlSiO_4–Mg_2SiO_4–SiO_2–H_2O$: 1, Inferred phase relations and petrologic applications. *J. Petrol., 8,* 372–416.

Maijer, C., J. B. H. Jansen, J. Wevers and R. P. E. Poorter (1977) Osumilite, a mineral new to Norway. Contribution to the mineralogy of Norway, No. 63. *Norsk Geol. Tidssk., 57,* 187–188.

Mason, P. K., M. T. Frost and S. J. B. Reed (1969) Computer program for calculating corrections in quantitative X-ray microanalyses. *National Phys. Lab. (United Kingdom) I.M.S. Report 2.*

McKie, D. (1959) Yoderite, a new hydrous magnesium iron aluminosilicate from Mautia Hill, Tanganyika. *Mineral. Mag., 32,* 282–307.

Merlino, S. (1973) Polymorphism in sapphirine. *Contrib. Mineral. Petrol., 41,* 23–29.

——— (1980) Crystal structure of sapphirine-1Tc. *Z. Kristallogr., 151,* 91–100.

Morse, S. A. (1971) Reply. *Earth Planet. Sci. Lett., 12,* 357.

——— and J. H. Talley (1971) Sapphirine reactions in deep-

seated granulites near Wilson Lake, central Labrador, Canada. *Earth Planet. Sci. Lett., 10,* 325–328.

Newton, R. C. (1966) Some calc-silicate equilibrium relations. *Am. J. Sci., 264,* 204–222.

——— (1972) An experimental determination of the high-pressure stability limits of magnesian cordierite under wet and dry conditions. *J. Geol., 80,* 398–420.

——— (1978) Experimental and thermodynamic evidence for the operation of high pressures in Archaean metamorphism. In B. F. Windley and S. M. Naqvi, Eds., *Archaean Geochemistry,* p. 221–240. Elsevier, Amsterdam.

——— and H. T. Haselton (in press) Thermodynamics of the garnet–plagioclase–Al_2SiO_5–quartz geobarometer. In R. C. Newton, A. Navrotsky and B. J. Wood, Eds., *Thermodynamics of Minerals and Melts.* Springer-Verlag.

———, T. V. Charlu and O. J. Kleppa (1974) A calorimetric investigation of the stability of anhydrous magnesium cordierite with application to granulite facies metamorphism. *Contrib. Mineral. Petrol., 44,* 295–311.

Nixon, P. H., A. J. Reedman and L. K. Burns (1973) Sapphirine-bearing granulites from Labwor, Uganda. *Mineral. Mag., 39,* 420–428.

Orville, P. M. (1972) Plagioclase cation exchange equilibria with aqueous chloride solution: results at 700°C and 2000 bars in the presence of quartz. *Am. J. Sci., 272,* 234–272.

O'Neill, H. St. C. and B. J. Wood (1979) An experimental study of Fe–Mg partitioning between garnet and olivine and its calibration as a geothermometer. *Contrib. Mineral. Petrol., 70,* 59–70.

Ravich, M. G. and E. N. Kamenev (1975) *Crystalline Basement of the Antarctic Platform.* Wiley, New York.

Sahama, T. G., M. Lehtinen, and P. Rehtijärvi (1974) Properties of sapphirine. *Ann. Acad. Sci. Fennicae Ser. A. III. Geol.-Geogr. 114.*

Schmid, R. and B. J. Wood (1976) Phase relationships in granulitic metapelites from the Ivrea–Verbano zone (northern Italy). *Contrib. Mineral. Petrol., 54,* 255–279.

Schreyer, W. (1977) Whiteschists: their compositions and pressure–temperature regimes based on experimental, field, and petrographic evidence. *Tectonophysics, 43,* 127–144.

——— and K. Abraham (1975) Peraluminous sapphirine as a metastable reaction product in kyanite–gedrite–talc schist from Sar e Sang, Afghanistan. *Mineral. Mag., 40,* 171–180.

Seifert, F. (1974) Stability of sapphirine: a study of the aluminous part of the system MgO–Al_2O_3–SiO_2–H_2O. *J. Geol., 82,* 173–204.

Sheraton, J. W., L. A. Offe, R. J. Tingey and D. J. Ellis (1980) Enderby Land, Antarctica—an unusual Precambrian high-grade metamorphic terrain. *J. Geol. Soc. Aust., 27,* in press.

Tarney, J. and B. F. Windley (1977) Chemistry, thermal gradients and evolution of the lower continental crust. *J. Geol. Soc. London, 134,* 153–172.

Weaver, B. L., J. Tarney, B. F. Windley, E. B. Sugavanam and V. Venkata Rao (1978) Madras granulites: geochemistry and *P–T* conditions of crystallisation. In B. F. Windley and S. M. Naqvi, Eds., *Archaean Geochemistry,* p. 177–204. Elsevier, Amsterdam.

Wellman, P. and R. J. Tingey (in press) A gravity survey of Enderby and Kemp Lands, Antarctica. In C. Craddock, Ed., *Antarctic Geoscience,* University of Wisconsin Press, Madison, Wisconsin.

Wells, P. R. A. (1977) Pyroxene thermometry in simple and complex systems. *Contrib. Mineral. Petrol., 62,* 129–139.

Wood, B. J. and S. Banno (1973) Garnet–orthopyroxene and orthopyroxene–clinopyroxene relationships in simple and complex systems. *Contrib. Mineral. Petrol., 42,* 109–124.

Woodford, P. J. and A. F. Wilson (1976) Sapphirine, högbomite, kornerupine and surinamite from aluminous granulites, northeastern Strangways Range, central Australia. *Neues Jahrb. Mineral. Monatsh.,* 15–35.

Manuscript received, November 7, 1979;
accepted for publication, May 7, 1980.

American Mineralogist, Volume 65, pages 837–851, 1980

Significance of hornblende in calc-alkaline andesites and basalts

A. T. ANDERSON, JR.

Department of the Geophysical Sciences, The University of Chicago
5734 South Ellis Avenue
Chicago, Illinois 60637

Abstract

Hornblende occurs in some andesitic and basaltic rocks of calc-alkaline affinity, where it is commonly associated with olivine. The texture, eruption history, and composition are interpreted to indicate that hornblende commonly forms as a product of reaction between olivine and basaltic and andesitic liquids. The natural hornblendes probably formed within the crust at temperatures between 960° and 1080°C from liquids with less than about 6 weight percent H_2O. The formation of hornblende from basaltic liquid within the crust has implications for evolution of continental crust, as well as for the origin of andesite and thermal conditions in subduction zones.

Introduction

Boettcher (1973) and others (Mueller, 1969; Holloway and Burnham, 1972; Green, 1972; Helz, 1976; Cawthorn and O'Hara, 1976; Allen and Boettcher, 1978) argue that amphibole plays an important role in governing the compositions of calc-alkaline andesites. The mechanisms whereby amphibole supposedly exerts its role are not clear. Is it left behind in a crystalline residue—where is it: in the crust or in the mantle? Does amphibole crystallize and separate from a parental liquid—what are the composition and temperature of the parental liquid? Does amphibole crystallize from a derivative liquid which mixes with a parental liquid to yield andesite? Amphibole occurs in some calc-alkaline volcanic and plutonic rocks with basaltic and andesitic bulk compositions, but the significance of such occurrences is uncertain without textural evidence of how it got there: is the amphibole a primary igneous mineral or a product of alteration? If igneous, over what interval of crystallization did it form, and was the composition of the liquid in that interval andesitic, dacitic, or basaltic? If amphibole can be shown to have actually formed from a liquid with a certain composition, what does that portend for the concentration of H_2O in and the temperature of the liquid? My aim is to help point the way to answers to some of the above questions by critically examining evidence on the growth of amphibole from basaltic and andesitic liquids, both experimental and natural.

Definitions

In using the word liquid, I mean to refer to a single state of matter (a homogeneous liquid phase). It is vital to distinguish between the composition of a liquid (generally a residual liquid) and the composition of the bulk material. Petrographically a certain hornblende may be associated with a particular residual liquid. Experimentally a certain bulk composition may crystallize hornblende at or below the liquidus. The residual liquid associated with hornblende will generally differ in composition from the bulk. Thermodynamically the composition and temperature of a certain liquid can remain constant as the proportions of crystals and liquid vary. To interpret a given association of hornblende and liquid, the petrographer must seek experimental conditions which yield hornblende and liquid with compositions similar to those observed. If analogy is drawn with a particular bulk composition (and liquidus hornblende) the implied pressure (and concentration of H_2O in the liquid) is larger than if analogy is made with a residual liquid. The implications for temperature are complex and depend on the concentration of H_2O in the liquid as well as on compositional features such as Fe/Mg and concentrations of alkalis.

Hornblende in experimental products

Experimental studies yielding hornblende in products with either calc-alkaline bulk compositions or with residual liquids having analogous compositions

0003–004X/80/0910–0837$02.00

reveal: (1) Hornblende is a liquidus or near-liquidus mineral in some basaltic bulk compositions if P_{H_2O} exceeds about 10 kbar (Yoder and Tilley, 1962; Green and Ringwood, 1968; Allen *et al.*, 1975; Stern *et al.*, 1975) and if H_2O dissolved in liquid exceeds about 12 weight percent. (2) In some andesitic bulk compositions hornblende is a liquidus mineral if P_{H_2O} exceeds about 2 kbar (Piwinskii, 1973). (3) As P_{H_2O} decreases below P_{total}, the hornblende-out curve lies progressively farther below the liquidus (Robertson and Wyllie, 1971; Holloway and Burnham, 1972; Green, 1972; Eggler and Burnham, 1973; Allen and Boettcher, 1978). (4) The proportion and composition of residual liquid change dramatically over an interval of temperature less than 50°C after the beginning of crystallization of hornblende (Holloway and Burnham, 1972). (5) Near the liquidus low oxygen fugacity favors the crystallization of hornblende compared to pyroxene (Helz, 1973, 1976). (6) The reactions between hornblende, liquid and other crystals are complex (Bowen, 1928, p. 61, 85, 111; Helz, 1976). (7) Hornblende is stable to the highest temperatures and lowest concentrations of H_2O in liquid in systems (a) where olivine is present (Helz, 1976), (b) where $P_{H_2O} < P_{total}$ (Holloway, 1973), and (c) where significant F is present (Holloway and Ford, 1975).

The above relations are summarized on Figure 1. The coordinates of Figure 1 are qualitative. Quantitative values will vary with bulk composition. Lesser MgO and Mg/(Fe+Mg) will diminish the temperature of olivine, pyroxene, and hornblende liquidus surfaces. The field for liquidus hornblende will then extend farther into the vapor-absent portion of the diagram. Lesser concentrations of Al_2O_3 will shift more of the liquidus surface into the olivine and pyroxene fields and diminish the area of the liquidus field for plagioclase. Consequently, the combination of low Al_2O_3 and high MgO may obliterate the liquidus surface having hornblende, olivine, and plagioclase (see Bowen, 1928, p. 111). For a natural magma with CO_2 as well as H_2O, there will be a range in X_{H_2O} in addition to a boundary marking vapor-absent and vapor-present regions. Reactions between olivine, pyroxene, hornblende, and liquid add complications not shown on the diagram. Spinel and magnetite are probable additional liquidus minerals but are not shown. For simplicity only one pyroxene is depicted. Calcium-rich clinopyroxene is the liquidus pyroxene but is joined and/or replaced by orthopyroxene below the liquidus at temperatures below or near that of the appearance of hornblende. Except for such simplifications, the diagram is consistent with existing experimental and natural data.

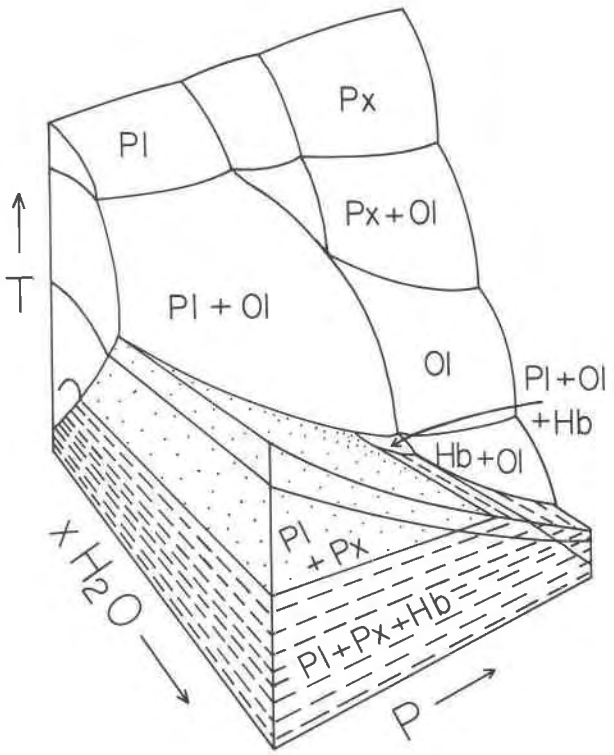

Fig. 1. Simplified hypothetical P–T–X_{H_2O} equilibrium diagram for a high-alumina basalt. The diagram is drawn in perspective. The origin is not shown. The concentration of H_2O refers to the bulk material. The stippled and dashed regions are saturated with vapor rich in H_2O. Below the liquidus surface the pyroxene (Px)-out and olivine (Ol)-in surfaces are assumed to coincide for simplicity. Fields for spinel and magnetite are omitted for simplicity. Hornblende (Hb) is a liquidus mineral in both vapor-absent and vapor-present regions. The liquidus hornblende is accompanied either by liquidus Ol or by both plagioclase (Pl) and Ol. Only one symbol is shown for pyroxene (Px). Liquidus Px is calcium-rich. Low-calcium pyroxene probably predominates if Hb is abundant.

It would be helpful to know the positions of surfaces of equal SiO_2 in the liquid (H_2O-free basis). At present the coordinates of such surfaces in Figure 1 are uncertain. Qualitatively, it is possible to give some limits. I consider a surface of $SiO_2 = 60$ weight percent on an anhydrous basis, corresponding roughly to andesite. Because the composition of the residual liquid changes steeply with temperature after the beginning of crystallization of hornblende (Holloway and Burnham, 1972), it is reasonable to expect the 60 percent SiO_2 surface to lie close to the hornblende-out surface. In the region of the diagram where hornblende is a liquidus mineral (hornblende-

out corresponds to liquidus), the 60 percent SiO_2 surface must lie below the hornblende-out surface. In the region of the diagram where the hornblende-out surface is far below the liquidus (for example, subaerial basalts with about 0.1 weight percent H_2O), residual liquids with more than 60 percent SiO_2 may develop in the absence of hornblende. Therefore, the 60 percent SiO_2 surface may intersect the hornblende-out surface, unless crystallization intervenes.

It is probable, but uncertain, that residual liquid in anhydrous high-alumina basalt attains 60 percent SiO_2 before complete crystallization if equilibrium is maintained. Residual glasses in natural high-alumina basalts have 62 (Fuego volcano, Guatemala—Rose *et al.,* 1978) and 67 (Hat Creek flow, California—Anderson and Gottfried, 1971) percent SiO_2. However, equilibrium is not maintained throughout the natural rocks. Because the minerals [plagioclase (An55), augite, olivine (Fo66), and magnetite] associated with the residual glass at Fuego are compositionally similar to the normative minerals [plagioclase (An50), pyroxene, olivine (Fo70), magnetite, and ilmenite, based on the weighted average composition with 1/3 of the iron trivalent], I conclude that anhydrous, calc-alkaline, high-alumina olivine tholeiites exemplified by Fuego probably yield equilibrium residual liquids with 60 percent or more SiO_2 before complete crystallization. Therefore the equilibrium surface for residual liquids with 60 percent SiO_2 probably intersects the hornblende-out surface.

The intersection of the 60 percent SiO_2 and hornblende-out surfaces may have major petrological significance. In a given bulk composition residual liquids with 60 percent SiO_2 will vary compositionally in accordance with the amounts of associated minerals, particularly hornblende. Many workers have pointed out that crystallization of hornblende can yield calc-alkaline residual liquids (Green and Ringwood, 1968; Boettcher, 1973; Holloway and Burnham, 1972; Helz, 1976; Cawthorn and O'Hara, 1976). Andesitic residual liquids not associated with hornblende may be alkalic or alkali-calcic. The residual liquid with 60 percent SiO_2 may have both a smaller ratio of Fe/(Mg+Fe) and a lower temperature if hornblende is present than if it is absent. For a given bulk composition the amount of hornblende associated with a residual liquid having 60 percent SiO_2 will be maximized: (1) if the initial concentration of H_2O is large; (2) if crystallization occurs at constant or increasing pressure; and (3) if equilibrium (reaction) is maintained. Consequently, many differences between various andesitic liquids may be explained by either contrasting initial concentrations of H_2O in parental high-alumina basaltic magma, variable depth of crystallization, or extent of reaction during crystallization.

Some natural calc-alkaline liquids associated with hornblende are less siliceous and hotter than most experimental analogs. The natural occurrences suggest that the field of liquidus hornblende extends to lower concentrations and partial pressures of H_2O than is indicated by most existing experimental results.

Hornblende associated with natural andesitic liquid

Many andesites have phenocrysts of hornblende (see for example, Moorhouse, 1959, p. 189–190; Turner and Verhoogen, 1960, p. 272–282) but most do not. Many, perhaps most, andesites contain clots of anhydrous crystals which may be reaction products of hornblende (Stewart, 1975); however, the occurrence of oscillatory zoned plagioclases within such clots suggests a different origin (Garcia and Jacobson, 1979).

Most hornblende andesites have more than about 60 percent SiO_2 (Kuno, 1950; Jakěs and White, 1972; Sakuyama, 1979); the groundmass probably is dacitic to rhyolitic in composition. The hornblendes commonly are rimmed or cored by crystals of pyroxene, plagioclase, and other minerals. The compositions of the hornblendes may be modified after crystallization. Thus the compositional relations between hornblende and andesitic liquid are difficult to infer from most occurrences.

Below I describe an association of hornblende and andesitic glass included in olivine from a lapillus of porphyritic andesite.

The 1783 eruption of Asama Volcano, Japan. Background: the eruption and its products

Asama volcano is a composite andesitic stratovolcano in central Honshu, Japan. Its geology is documented by Aramaki (1963) and briefly summarized by Anderson (1979).

The history of the 1783 eruption helps constrain the history of cooling and decompression which affected the extruded products. Although complex, this eruption probably is typical of the principal way Asama has grown. It involved a succession of Plinian explosions which produced about 0.17 km^3 of pyroclastic material (Minakami, 1942) and an equal volume of lava (Aramaki, 1956). The early products were air-fall pumice lapilli and ash; ash flows formed

on and after August 3 when the culminating blast occurred; an andesitic lava flow formed during the final phase of the eruption. The details are reported by Aramaki (1956, 1957), who interpreted the eruption sequence in terms of an initial vent-clearing phase between June 25 and August 2, 1783 followed by extrusion from a subvolcanic body of magma on and after August 3, 1783.

Petrography. The 1783 andesitic pumice lumps vary from light to medium brown; some have streaks of different shades of brown. Lapillus AM2-2 (Anderson, 1979) is medium brown. It was collected from a layer of air-fall lapilli which probably formed on or before August 2.

The pumice contains mm-sized phenocrysts of plagioclase, augite, hypersthene, magnetite, and ilmenite. Plagioclase is the principal phenocryst and makes up about 20 volume percent of the pumice on a void-free basis. Most of the plagioclases are subhedral to anhedral crystals with irregular cores sieved with vermicular inclusions of glass and gas. The cores are surrounded by a normally-zoned rim which is free of inclusions and 10 to 50 μm thick. Other plagioclases are poor in inclusions and oscillatory-zoned with skeletal protrusions. The augites contain inclusions of glass and lamellae of pyroxene in irregular, pale green cores. Some augites occur in clots where they are subhedral and irregular against each other. Commonly a zone of inclusions of plagioclase and pyroxene marks the boundary between a pale green core and deeper green rim. The rims are 50 to about 150 μm thick. Glasses included in pyroxene, plagioclase, and oxide phenocrysts range from about 70 to 79 weight percent SiO_2; the host glass outside of the phenocrysts has about 72 percent SiO_2 (Anderson, 1979).

Crystals of olivine (Fo79–Fo85) are rare. The olivines have 50-μm-thick rims of hypersthene or augite. There is more olivine in medium-brown pumice than in light brown pumice. Inclusions of glass in olivine crystals have 54 to 61 weight percent SiO_2 on an anhydrous basis (Anderson, 1979).

Hornblende associated with andesitic glass. Hornblende occurs together with andesitic glass included in an olivine crystal from the lapillus AM2-2 of medium-brown andesitic pumice (Fig. 2, Table 1). The hornblende is pale brown and faceted against glass. A second mineral (probably orthopyroxene) occurs with hornblende in the inclusion. It is colorless, long and prismatic, and has a refractive index close to that of the hornblende. The included glass has a round contact with the olivine host crystal. The microprobe

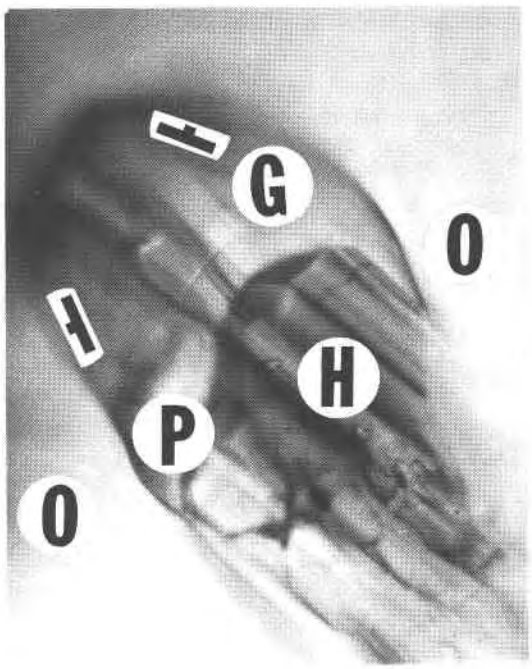

Fig. 2. Inclusion of glass (G), hornblende (H), and probable pyroxene (P) in olivine (O). The long dimension of the photograph is about 200 μm. Dip and strike symbols refer to the attitude of the contact between olivine and glass referred to the polished surface as horizontal. The olivine crystal is rimmed by orthopyroxene and is from a lump of pumice extruded from Asama volcano, probably on or before August 2, 1783.

analysis yields an estimated 4 percent of H_2O in the glass (Anderson, 1979).

A second, smaller inclusion in the same olivine crystal contains a pale brown crystal which is probably hornblende (Fig. 3). It comprises about 2 volume percent of the inclusion. Anisotropic and opaque crystals line the inside wall of the vapor bubble in the small inclusion.

The olivine host crystal of the hornblende-bearing inclusion is Fo83 (Table 1) compared to Fo79 to Fo85 for olivines from other lumps of pumice of the 1783 eruption (Anderson, 1979). The composition of the preserved glass (Table 1, column 2) is close to but more silicic than that of other inclusions in olivine which lack hornblende (Table 1, column 4).

Hornblende comprises about 30 volume percent of the large inclusion (Fig. 2), some of which was removed by sectioning. Probable orthopyroxene comprises about 10 volume percent. Most inclusions in Asama olivines are subspherical to ellipsoidal. The hornblende-bearing inclusion has walls which dip away from the inclusions at high angles (Fig. 2).

Attached phenocrysts of magnetite and ilmenite occur in the same lump of pumice. Their composi-

Table 1. Chemical compositions of hornblende and andesitic liquid with comparisons

Col.[1]	1	2	3	4	5	6	7	8	9
SiO_2	42.6	61.3	57.0	56.0	60.5	55.5	63.2	63.8	60.0
Al_2O_3	15.5	21.0	20.9	19.7	20.0	17.3	20.3	18.6	20.4
FeO[2]	8.2	3.4	3.6	6.9	4.2	8.5	3.0	4.3	4.5
MgO	15.6	2.6	3.4	3.0	1.1	3.4	0.3	0.7	4.3
CaO	12.7	5.5	8.9	10.0	8.4	9.2	7.4	6.9	7.5
Na_2O	2.6	4.3	4.0	2.9	3.2	2.8	3.0	2.8	0.9
K_2O	0.3	1.5	1.2	0.6	0.8	0.7	0.9	1.0	0.9
TiO_2	2.4	0.3	1.2	0.8	1.3	2.2	1.2	1.2	1.2
Cl	0.05	0.15	0.12	0.08	n.d.	n.d.	n.d.	n.d.	n.d.
Sum[3]	98.2	97.4		95.5	87.3	85.7	84.0	83.7	n.r.
H_2O[4]	3	4		3	10	10	10	6	?10
T[5]	1080-960	1080-960		1080-960	1015	1045	1050	999	1010
P[6]	0.1-1?	0.1-1?		0.1-1?	5	5	8.0	5.2	13
Assoc.[7]	Fo83,Px?	Hb,Fo83, Px?		Fo79	Hb,Cpx, Ol	Hb,Cpx, Ol,Ox	Hb,Cpx, Ol,Mt	Cpx,Hb, Ol,Mt	Hb,Cpx Ox

[1]See key to columns below.

[2]All iron as FeO.

[3]Sum of the original analysis. Reported analyses are recalculated to 100 percent except for rounding errors. Original sum for column 9 is not published. Sums are H_2O-free.

[4]Estimated concentration of H_2O. Estimated by difference (Anderson, 1973) for columns 1, 2, 4; estimated from pressure, gas composition and solubility otherwise.

[5]Estimated temperature in degrees Celsius. See text for columns 1, 2, 4. Otherwise published run temperature.

[6]Estimated pressure in Kbar. See text for 1 and 2. Otherwise run pressure (total pressure not necessarily same as P_{H_2O}).

[7]Coexisting minerals: Fo = olivine with atomic ratio of 100 Mg/(Mg+Fe); Hb = hornblende, Px = pyroxene, Cpx = calcium-rich pyroxene, Ol = olivine, Mt = magnetite, Ox = oxide.

Key to Columns:

1 = Hornblende included in olivine together with glass of column 2 (analysis 9 of Table 3 of Anderson, 1979).

2 = Andesitic glass included in olivine, Asama 1783 (analysis 8 of Table 3 of Anderson, 1979).

3 = Result of adding 0.4 parts hornblende (column 1), 0.7 parts glass (column 2), and 0.1 part of orthopyroxene (stoichiometric En83) and subtracting 0.2 parts olivine (Fo83).

4 = Andesitic glass included in olivine, Asama 1783 (analysis 10 of Table 3 of Anderson, 1979).

5 = Synthetic andesitic glass (analysis 15a of Table 7b of Helz, 1976).

6 = Synthetic andesitic glass (analysis 16a of Table 7b of Helz, 1976).

7 = Synthetic andesitic glass (from Table 8 of Holloway and Burnham, 1972).

8 = Synthetic andesitic glass (from Table 8 of Holloway and Burnham, 1972).

9 = Synthetic andesitic glass (average of analyses 21 and 22 of Table 6a of Allen and Boettcher, 1978).

tions (Hm24, Usp34) suggest a temperature of equilibration of 1080°C, according to the unpublished geothermometer of Lindsley and Rumble (1977). The same compositions suggest a temperature of 1060° to 1070°C, according to my visual interpolation of data by Buddington and Lindsley (1964) and Taylor (1964). Similar compositions but lower temperatures (990°–1020°C) were reported by Oshima (1976).

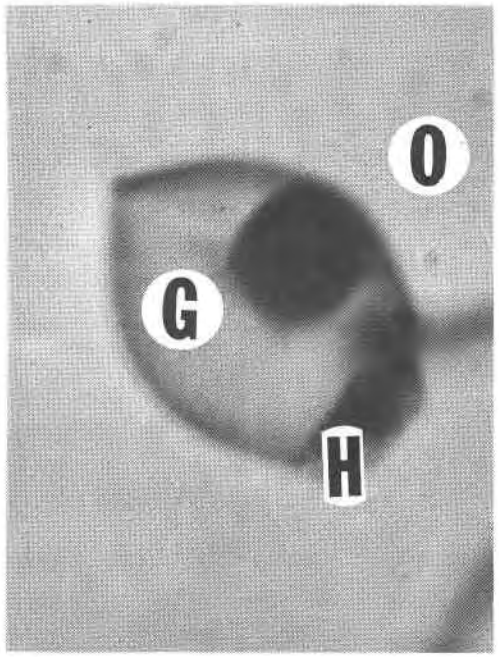

Fig. 3. Photograph of a second, smaller inclusion in the same crystal as that shown in Fig. 2. The inclusion is about 30 μm long and contains a pale brown crystal of probable hornblende (H) and a dark bubble of vapor.

Interpretation

The andesitic glass (Table 2, column 1) probably is in a state of quenched equilibrium with olivine (about Fo83) and hornblende, because the pumice lump in which it occurs was explosively erupted and cooled in air before falling to the ground. The inclusion probably cooled from about 1080°C to a few hundred degrees C in a few minutes, judging from the Plinian explosions which probably erupted it in late July or early August of 1783 (Aramaki, 1956; written communication, 1979). Possibly the inclusion was contained in a froth of magma at a few hundred atmospheres or less for a few days, because it was extruded during the early part of the eruption when the vent probably was intermittently filled with froth.

I interpret the textural, compositional, and historical facts to suggest that andesitic or basaltic liquid carried crystals of olivine into a crystal-rich body of andesitic magma during or before the early stages of the eruption (May 9 to August 2). The irregular anhedral cores of many plagioclase crystals suggest fragmentation. The abundance of gas in the sieved cores suggests that fragmentation was accompanied by and/or caused by effervescence. The rims on the crystals of plagioclase, pyroxene, and olivine indicate that reaction and crystallization took place after fragmentation. The faceted (not skeletal) shape and size of hornblende included in olivine suggest it to be a daughter crystal or reaction product rather than a quench crystal or product of devitrification. The round contact between the olivine and glass associated with hornblende is consistent with a reaction relation between olivine, liquid, and hornblende. Crystals intergrown with a residual rhyolitic liquid were broken apart and overgrown probably because invading, olivine–porphyritic magma caused effervescence of the interstitial liquid (due to pressure release and/or temperature increase) and contaminated the liquid with relatively refractory constituents.

Liquids trapped within the olivine crystals became modified in composition as a result of growth of daughter crystals of hornblende and/or pyroxene and reaction with olivine, because the temperature decreased from that in the initial environment to near that of the invaded andesitic magma with residual rhyolitic liquid.

The initial composition of the trapped liquid before crystallization of hornblende and pyroxene can be estimated by adding 0.4 parts hornblende, 0.1 parts pyroxene and 0.7 parts andesitic glass, and subtracting 0.2 parts olivine. The result (Table 1, column 3) is somewhat similar in composition to other inclusions of andesitic glass in olivines which lack hornblende (Table 1, column 4). If other minerals are included in the calculation, the similarity can be increased. Some inclusions of glass in the Asama 1783 olivines have as little as 54 percent SiO_2 (Anderson, 1979). It is not possible to relate all the glasses to a common precursor without including either minerals not now in contact with the glasses, or residual rhyolitic liquids as mixing components, or both. The origins of the glasses included in the olivines are complex if considered in detail. Such detail is beyond the scope of this paper. Subtraction of olivine in the above calculation corresponds to resorption of olivine concomitant with crystallization of hornblende and pyroxene from a less silicic liquid precursor. Probably the andesitic liquid was in equilibrium with hornblende, pyroxene, and olivine at the temperature of eruptive quenching; however, the relation with olivine probably was one of reaction.

Two kinds of experimental results can be compared with the natural association of hornblende, pyroxene, olivine, and andesitic liquid. Consequently, it is possible to obtain two estimates of the temperature and the concentration of H_2O in the silicate liquid. In the first case comparison is made with the liquidus

Table 2. Chemical compositions of hornblendes and associated basaltic materials

Col.[1]	1	2	3	4	5	6	7	8	9
SiO_2	42.8	54.5	51.0	42.1	51.7	41.4	54.0	40.7	55.5
Al_2O_3	13.6	18.1	19.1	14.3	18.4	16.5	17.7	13.3	17.3
FeO[2]	10.5	9.4	10.0	10.8	9.7	12.4	9.2	14.2	8.5
MgO	15.3	3.5	5.4	15.6	5.3	14.1	4.8	13.0	3.4
CaO	12.2	8.3	9.3	11.8	10.3	11.0	8.3	10.7	9.3
Na_2O	2.3	3.7	3.0	2.5	2.9	2.6	3.8	2.0	2.8
K_2O	0.4	1.0	0.6	0.3	0.5	0.1	0.8	0.5	0.7
TiO_2	2.7	1.2	1.1	2.1	1.0	1.8	1.3	4.4	2.2
Cl	0.05	0.12	0.09	n.d.	n.d.	n.d.	n.d.	n.d.	n.d.
Sum[3]	98.9	93.8	94.3	99.8	99.8	98.7	99.8	98.7	85.7
H_2O[4]	1	4	4	1.8	n.d.	n.d.	n.d.	n.d.	8
T[5]	1030	1030	1030	n.d.	n.d.	1000	1000	1045	1045
p[6]	1-2	1-2	1-2	8	8	12-30	12-30	5	5
Assoc.[7]	An92	An86	Fo79	Ol,Cpx, Pl,Mt	Ol,Cpx Hb,Pl, Mt	Fo83	Ol,Pl	Fo82-84 Cr,Cpx	Fo82-84 Hb,Cr,Cpx

Key to Columns (see Table 1 for footnotes):

1 = Hornblende included in core of plagioclase phenocryst from Fuego (analysis reported in legend to Figure 16, p. 20 of Rose et al., 1978).

2 = Glass included in rim of plagioclase phenocryst (An83) of column 7 (analysis No. 6 of Table 6 of Rose et al., 1978).

3 = Glass included in olivine (Fo79) from Fuego (analysis 4 of Table 6 of Rose et al., 1978, and close in composition to the weighted average of the 1974 erupted ash).

4 = Hornblende from gabbroic block, La Soufrière, St. Vincent (analysis 1 of Table 6 of Lewis, 1973a).

5 = Fine grained, interstitial material from same gabbroic block as column 9 (analysis 1 of Table 4 of Lewis, 1973b).

6 = Hornblende inclusions in olivine phenocrysts, Little Mt. Hoffman basalt, California (column 2, Table 2 of Mertzman, 1978).

7 = Groundmass of Little Mt. Hoffman basalt (calculated by subtracting 10 percent olivine [Fo80] and 25 percent plagioclase [An70] from the bulk rock--analysis 1 of Table 1 of Mertzman, 1978).

8 = Synthetic hornblende (Helz, 1976, Table 13a, No. 2, p. 192).

9 = Synthetic liquid associated with hornblende (column 8) calculated by Helz (1976, Table 7b, analysis No. 16a, p. 152).

phases of an andesitic bulk composition. In the second case comparison is made with the residual liquid in a basaltic bulk composition.

For the first comparison two assumptions are necessary: (1) the hornblende is a hydroxy-hornblende; (2) the minerals in contact with the natural andesitic liquid are thermodynamically equivalent to the liquidus phases of a system composed of the liquid alone.

The first assumption is justifiable because: (1) the natural hornblende contains negligible chlorine; (2) its pale color suggests a negligible concentration of oxycomponent; and (3) its fluorine content is unknown, but probably small, because fluorine is a minor constitutent of most magmas. The second assumption may be questioned because olivine probably is in a reaction relation. For the present purposes I assume that the presence of olivine may be ignored. Consequently, I seek experimental conditions which yield hornblende and pyroxene on the liquidus of andesite. The compilation of Stern *et al.* (1975) suggests that compositionally similar andesitic

liquids have hornblende and clinopyroxene on the liquidus if the temperature is below about 980°C and the liquid contains more than about 10 weight percent H_2O. The results of Allen and Boettcher (1978) on andesitic bulk compositions are consistent with the above estimate: more than 10 weight percent H_2O in the liquid.

For the second comparison only one assumption is necessary: the hornblende is a hydroxy-hornblende (justified above). I now seek experimental conditions which yield hornblende, pyroxene, and andesitic liquid in a reaction relation with olivine. Holloway and Burnham (1972) and Helz (1973, 1976) encountered andesitic residual liquidus associated with hornblende, pyroxene, and olivine (and in some cases magnetite) at temperatures between about 1000 and 1050°C and with about 6 to 10 weight percent H_2O in the silicate liquid (Table 1, columns 5–8). Allen and Boettcher (1978) found a comparable residual liquid (Table 1, column 9, but no olivine). However, the compositions of residual liquids are difficult to establish for experimental products. The detailed assessment by Helz (1976) suggests that the residual liquids at temperatures greater than about 1015°C (at P_{H_2O} = 5 kbar) are less siliceous than the natural liquid. The results of Allen and Boettcher (1978) reveal that the maximum temperature of hornblende stability increases from about 990° to 1050°C as the mole fraction of H_2O in the gas decreases from 1 to about 0.25, consistent with the findings of Holloway (1973). At the mole fraction of 0.25 and a total pressure of 10 kbar, the partial pressure of H_2O would be about 2.5 kbar and there would be about 6 weight percent H_2O dissolved in the liquid. The Hawaiian basalt investigated by Holloway and Burnham (1972), Helz (1973, 1976) and Allen and Boettcher (1978) probably is neither appropriate nor optimal for the generation of natural andesitic residual liquids because of its low concentrations of Al_2O_3 and alkalis. Consequently, it is likely that high-alumina basalt would yield andesitic residual liquids associated with hornblende, pyroxene, and olivine at pressures less than 5 kbar and with P_{H_2O} less than P_{total} at temperatures greater than that found for Hawaiian tholeiite at 5 kbar = P_{H_2O} = P_{total} (namely, greater than about 1015°C).

The above comparisons suggest that andesitic liquids and hornblende are stable to higher temperatures and lesser concentrations of H_2O in basaltic bulk compositions than in andesitic bulk compositions. Probably the availability of olivine (or augite) as a reactant is a principal cause of the greater stability of hornblende in basaltic systems. Other compositional differences [greater Al_2O_3 (Bowen, 1928, p. 111), and alkalis (Cawthorn and O'Hara, 1976)] may help stabilize hornblende, but they cannot be evaluated quantitatively with published information. In sum, comparison of the natural andesitic liquid and associated minerals with experimental products suggests that the natural liquid contained less than 6 weight percent H_2O and quenched from a temperature greater than 1015°C.

Sekine *et al.* [1979] studied experimentally the Asama 1783 andesite. They found no hornblende on or near the liquidus, but did estimate that the residual dacitic liquid (69–72 weight percent SiO_2) of this andesite contained 3.3 weight percent of H_2O at 960°C before extrusion.

Could the concentration and fugacity of H_2O in the included andesitic liquid exceed that of the surrounding residual dacitic liquid? Roedder's (1965) work reveals that olivines are strong enough at 1200°C to contain excess pressures of a few thousand atmospheres in an inclusion. However, a significant gradient of H_2O fugacity from inclusion to rim of crystal would probably disappear by diffusion in a few days or weeks at temperatures near 1000°C, judging from data on Fe, Mg, and O diffusivity in olivine (Buening and Buseck, 1973; Muehlenbachs and Kushiro, 1975). The diffusion of H_2O probably is comparable to that of oxygen because of the similarity in size. The concentration of H_2O (or OH^-) in olivine probably is low in comparison to oxygen; consequently, the concentration gradient and diffusion of H_2O in olivine may be small. Laboratory heating experiments on natural olivines with inclusions of glass suggest that diffusive transfer of H_2O is effective over tens of microns in a few hours at temperatures above 1000°C (Anderson, 1974). Probably both temperature and the fugacity of H_2O in the trapped andesitic liquid associated with hornblende are similar to those in the surrounding melt. Consequently, the most probable conditions for growth of the hornblende from the trapped andesitic liquid are 1080° (Fe–Ti oxides) to 960°C and 100 atm (plausible pressure of froth in vent) to about 1000 atm of H_2O pressure (Sekine *et al.*, 1979).

In sum, the eruptive history, texture, and compositional relations of the hornblende-bearing inclusion suggest that its glass represents an andesitic liquid quenched from a temperature of 1020±60°C and a partial pressure of H_2O between about 100 and 1000

atm. The liquid was in equilibrium with hornblende, probably orthopyroxene, and olivine. The andesitic liquid probably contained a few percent H_2O.

Hornblende associated with natural calc-alkaline basaltic liquid

Observational data

Hornblendes associated with calc-alkaline basaltic material are known from La Soufrière, St. Vincent (Lewis, 1973a,b), Fuego (Rose *et al.*, 1978), and Medicine Lake Volcano, California (Mertzman, 1978). Analyses of these hornblendes and related materials are compared in Table 2. The compositions of the hornblendes are similar and have 13.6 to 16.5 weight percent Al_2O_3, 2.3 to 2.6 weight percent Na_2O, and 1.8 to 2.7 weight percent TiO_2 on an anhydrous basis.

Interpretation

It is uncertain whether any of these hornblendes are in a state of quenched equilibrium with basaltic liquids, because the textural relationships are not definitive and because quenched basaltic matrix is termed andesite by some workers. A case-by-case analysis and interpretation is necessary.

Fuego volcano, Guatemala

The analyzed hornblende (Table 2, column 1) is in the anorthitic core (An92) of a plagioclase phenocryst (An92 to An80). The most closely associated analyzed glass (column 2, Table 2) is an inclusion in the rim of the same crystal. The glass and the hornblende are not in contact. The crystal is depicted in Figure 16 of Rose *et al.* (1978). The glass in the plagioclase is transitional in composition between basalt and andesite.

Rose *et al.* suggested that the hornblende included in the anorthitic core actually grew from a liquid with a more basaltic composition than the inclusion of glass found within the rim of the plagioclase. Their reasoning was as follows: many cores of anorthite from the same eruption contain inclusions of olivine. Subhedral crystals of anorthite (An92–90) are common in olivine phenocrysts. The anorthitic cores of the plagioclase phenocrysts have round corners, comprise a low proprotion of the total plagioclase, are subequant and little zoned. Most of the Fuego plagioclase is oscillatory zoned. The textures of the anorthite cores suggest that it is an early mineral to form in the Fuego magma. Some olivine phenocrysts contain inclusions of basaltic glass (51 percent SiO_2) which are close to the weighted average composition of the bulk rock extruded in the October eruption. The basaltic inclusions and bulk rock probably are similar in composition to the parental liquid from which the earliest crystals formed. The anorthitic cores and the included hornblende probably formed from a liquid with a composition near that of the basaltic glasses (Table 2, column 3).

The temperature of the parental basaltic liquid was about 1030°C; it contained about 4 weight percent H_2O (Rose *et al.*, 1978). Subsequently, Harris (1979) has directly measured 1.6 to 3.2 weight percent of H_2O in inclusions of glass in olivine phenocrysts from Fuego. The lower concentration of 1.6 weight percent H_2O applies to parental liquid in Fo77 olivine. Accordingly, a revised estimate of 1030±50°C and 1.6 weight percent H_2O is preferable for the Fuego liquid which probably precipitated the hornblende.

La Soufrière, St. Vincent

Lewis's (1973a,b) descriptions show that vesicular and microcrystalline dark interstitial material touches hornblende as well as olivine, plagioclase, pyroxene, and magnetite in xenolith 770. The interstitial material (termed scoria by Lewis) analyzed by him is basaltic in composition (column 5, Table 2). Lewis (written communication, 1979) considers his separate to be a good one, little affected by products of weathering and contaminating pieces of the crystals from the gabbro. His analyses show that interstitial scoria from different blocks differ in composition, consistent with an indigenous origin of the interstitial material. The most siliceous interstitial scoria comes from a block of gabbro lacking hornblende but containing olivine, plagioclase, pyroxene, and magnetite. I would expect progressive solidification to increase the number of minerals, stabilize hornblende, and enrich the residual liquid in K_2O and SiO_2. Possibly the gabbro with the most siliceous interstitial material originates from a lesser depth. Lewis's data suggest the crystallization of hornblende from basaltic liquid.

Little Mt. Hoffman, California

Olivine phenocrysts in a basaltic lava from a vent of Modoc Basalt (Powers, 1932) contain subround to irregular inclusions of hornblende (Mertzman, 1978). Olivine phenocrysts in the scoria of the cinder cone (Little Mt. Hoffman) at the source of the flow have round inclusions of devitrified glass, but no hornblende (A. T. Anderson, unpublished data). The compositions of the hornblende and the groundmass

of the basalt are given in Table 2, columns 6 and 7.

Because the hornblende occurs included in olivine phenocrysts in basaltic lava, Mertzman (1978) reasonably argued that the hornblende formed from basaltic liquid. The occurrence of hornblende included in olivine together with andesitic glass (see Asama, above) suggests possible alternative interpretations: (1) the olivines with hornblende are xenocrysts derived from an andesitic environment, (2) the hornblendes are daughter crystals which crystallized after the trapped melt attained an andesitic composition by crystallizing olivine. Mertzman's figures show that the hornblende is associated with microcrystalline material (probably formerly liquid). Because of its round shape and association with microcrystalline material, it is likely that the hornblende grew from trapped liquid after it had crystallized olivine. Growth of hornblende from supercooled liquid at a pressure less than 1000 atmospheres is a third possibility. The composition of the liquid from which the hornblende in the Little Mt. Hoffman basalt formed is uncertain. Mertzman (written communication, 1979) notes that the 0.1 weight percent of K_2O in the Little Mt. Hoffman hornblendes suggests that the liquid from which they formed had less than about 0.5 percent K_2O. Possibly the groundmass of the Little Mt. Hoffman basalt is enriched in K_2O by contamination (compare studies of East Sand Butte and cinder cone M39 of Anderson, 1976). Additional work on the Little Mt. Hoffman materials is needed to evaluate the alternatives. I suggest that the liquid from which the hornblende grew was richer in SiO_2 than is the bulk rock because of crystallization of olivine. Probably the liquid was similar in composition to that of the calculated groundmass given as column 7 of Table 2. The composition is that of a basaltic andesite.

Mertzman (1978) extrapolated the results of Yoder and Tilley (1962) on the Warner high-alumina basalt to estimate that the hornblende initially formed at pressures greater than about 12 kbar. In my judgement Mertzman's application and extrapolation of Yoder and Tilley's work is not justified, because the hornblende in question probably grew from a more siliceous liquid with a greater Fe/(Fe + Mg) ratio than the Warner basalt.

Summary

Evidence for the crystallization of hornblende from natural calc-alkaline liquids at least as basic as basaltic andesite (about 54 weight percent SiO_2) is compelling. The data of Rose *et al.* (1978) and Lewis (1973a,b) on ejecta of Fuego and Soufrière volcanoes, respectively, suggest that hornblende grows stably from some high-alumina basalt liquids with about 51 weight percent SiO_2 at temperatures near 1030°C. The basaltic melts are comparatively rich in Fe and poor in Mg and crystallize anorthitic plagioclase (commonly greater than An85), olivine (Fo84 to 66), and magnetite, as well as hornblende.

Experimental results (Helz, 1973, 1976) demonstrate the crystallization of hornblende at crustal pressures from basaltic andesite but not from basaltic liquids. As argued above for andesitic liquids, the crystallization of hornblende is fostered by greater concentrations of alumina and alkalis and $P_{total} > P_{H_2O}$ probable for natural high-alumina basaltic liquids compared to the Hawaiian basalt studied by Helz. The Warner high-alumina basalt studied by Yoder and Tilley (1962) has atypically greater MgO, MgO/(MgO + FeO), and low alkalis for basaltic members of calc-alkaline magma series. Rose *et al.* (1978) argued that the smaller MgO/MgO + FeO) ratio for Fuego high-alumina basalt would have the effect of making its olivine liquidus temperature about 80°C less than that of the Warner basalt. The difference might permit liquidus hornblende for basalt with a concentration of about 5 percent H_2O in the liquid if $P_{H_2O} = P_{total}$. Experimental results are not consistent with crystallization of hornblende from some natural high-alumina basaltic liquids with less than a few weight percent H_2O.

General discussion

The facts and interpretations outlined above suggest that hornblende crystallizes from andesitic and basaltic liquids at crustal pressures. Most such hornblende probably is a product of a reaction between liquid and olivine, as first suggested by Bowen (1928, p. 61). The field and textural evidence of plutonic rocks is consistent with crustal formation of hornblende by reaction between liquid and olivine (Miller, 1938; Best and Mercy, 1967; Lewis, 1973b, Ikeda, 1976; Walawender, 1976; Mullan and Bussell, 1977). The 10^4- to 10^6-year lifetimes of subduction-zone volcanoes (McBirney *et al.*, 1974; Rose *et al.*, 1977; Mertzman, 1977; McBirney, 1978), the shorter-term variations in compositions of extruded products (Crandell and Mullineaux, 1973; Crandell *et al.*, 1962; Newhall, 1979), and the 1 km^3 and smaller volumes of products of most individual eruptions, as well as the larger volumes of rare caldera-forming eruptions (Smith, 1979), suggest that the roots of subduction zone volcanoes have thicknesses less than

about 1 km and solidify (and differentiate) on time scales appropriate for cold (crustal) environments. Geophysical models of Cenozoic island arcs suggest they consist mostly of rock denser than andesite (for example, see Grow, 1973). Gabbroic rocks, including hornblende gabbro, have appropriate densities consistent with Kuno's (1968) model of a gabbroic crust in island arcs. Dominant hornblende gabbro in island arcs is particularly appealing because it can yield derivative magmas with the calcium-rich cores of plagioclase crystals, the isotopic ratios of strontium and lead, and the bulk compositions typical of many rocks in granodioritic batholiths (Piwinskii and Wyllie, 1968; Faure and Powell, 1972; Doe, 1967; Wyllie, 1977). The basaltic and andesitic liquids from which hornblende forms appear to contain 1.6±0.3 (Harris, 1979) to 4±2 weight percent of H_2O (Rose *et al.*, 1978; Anderson, 1979). The temperature at which hornblende forms in such liquids is probably between 1080° and 960°C (see above).

Various factors probably contribute to the crystallization of hornblende from natural basaltic and andesitic liquids with smaller concentrations of H_2O than the minimum of about 6 weight percent suggested by experiments (Yoder and Tilley, 1962; Holloway and Burnham, 1972; Green, 1972; Helz, 1973, 1976; Stern *et al.*, 1975; Allen and Boettcher, 1978): (1) olivine commonly is present as a reactant in natural associations; (2) natural liquids have some CO_2 in addition to H_2O (Harris, 1979), consequently $P_{H_2O} < P_{total}$; (3) natural basaltic liquids associated with calc-alkaline magma series have greater concentrations of alumina and alkalis than Hawaiian basalts used in experiments; (4) natural calc-alkaline basaltic liquids have smaller MgO/(MgO + FeO) and greater concentrations of alkalis than the Warner basalt used in experiments. All these differences probably enlarge the field of stability of hornblende beyond that found in experiments. Reaction with olivine and other factors probably foster the crystallization of hornblende in some natural basaltic and andesitic liquids with less than 6 weight percent of H_2O, as suggested by the natural occurrences described above.

Reaction between olivine and liquid yielding hornblende acts to minimize the increase in Fe/(Mg + Fe) ratio in derivative liquids. Two factors are significant in minimizing the increase in Fe/(Mg + Fe): (1) reaction between liquid and olivine; (2) crystallization of a hornblende-bearing assemblage of minerals in place of an equivalent anhydrous assemblage.

The effect of reaction was emphasized by Bowen (1928, p. 61). With reaction magnesium-rich olivine tends to buffer the Fe/(Mg + Fe) ratio of crystallizing minerals and residual liquid. Helz (1976) noted that the Fe/(Mg + Fe) ratio of pyroxenes and residual liquids *decreases* with crystallization in part of the range of solidification of hornblende, for example. Reaction with magnesium-rich minerals is an effective mechanism which minimizes increases in the Fe/(Mg + Fe) ratio of residual liquids.

The influence on Fe/(Mg + Fe) of the crystallization of a hornblende-bearing assemblage in place of an equivalent anhydrous assemblage of minerals is complex and disputed (see Ringwood, 1974 and Allen and Boettcher, 1978 for contrasting views). What is meant by "equivalent"? Consider the hornblende-out surface of Figure 1. The mineralogy above the surface and the composition of the liquid on the surface vary with P, T and X_{H_2O}. Many definitions of "equivalent" are possible. I adopt the following definition because it seems consistent with most petrological discussions regarding the role of hornblende in the formation of calc-alkaline rock series: on any surface marking identical bulk compositions of liquids, regions with different solids are equivalent.

For a given increment of crystallization how do the Fe/(Mg + Fe) ratios of residual liquids in two equivalent fields compare? For a given bulk composition (H_2O-free), the liquidus surface is one (and possibly the only) surface with identical compositions of liquids. Consider the difference between the Ol + Pl and the Ol + Hb fields. I assume that the equilibrium composition of olivine on the liquidus is everywhere the same (Roeder and Emslie, 1970). In general the Fe/(Mg + Fe) of hornblende is greater than for associated olivine (Helz, 1973; Lewis, 1973a,b). However, the effect on Fe/(Mg + Fe) of the residual liquid depends on the proportions of the crystallizing minerals as well as on their compositions. The net iron enrichment caused by crystallization of Ol + Hb possibly is greater than that for Ol + Pl. Probably the variation of Fe/(Mg + Fe) of residual liquids with equilibrium crystallization of equivalent hornblende-free and hornblende-bearing assemblages is complex, but not as large as the variations caused by fractional (as opposed to equilibrium) crystallization. I agree, therefore, with Cawthorn and O'Hara (1976) that the omission of iron from their experiments probably is not crucial to an evaluation of the role of hornblende. My emphasis is on reaction, however, rather than fractionation.

Minor increase in Fe/(Mg + Fe) is a characteristic feature of calc-alkaline magma series (Fenner, 1926; Kuno, 1950; Miyashiro, 1974). Consequently, the

spectrum of rock series found in subduction zone environments (Peacock, 1931; Kuno, 1950, 1959) can be related in part to variable reaction between olivine and liquid yielding hornblende: in general the more hornblende, the more calcic and the less iron-enriched (less tholeiitic) the series. Many tholeiitic series are calcic, however (for example Higashiyama, Isshiki, 1963) and have basaltic members with small concentrations of alkalis. The concentration of alkalis in the parental liquid is important. Series lacking hornblende probably are tholeiitic or alkalic and tend to have groundmass pigeonite. Variable production of hornblende by reaction between liquid and olivine can help explain variable iron-enrichment and lime-alkali index of many subduction zone magma series.

Implications

The probable crystallization of hornblende within the crust from subduction zone basaltic liquids with less than 6 weight percent H_2O has implications for: (1) the genesis of andesite, (2) the temperature above the Benioff zone, (3) dehydration of subducted oceanic crust, and (4) the origin of continental crust.

Genesis of andesite within the crust is implied by the crustal formation of hornblende gabbro. As discussed above, the Fe/(Mg + Fe) ratio and calc-alkalic index for subduction zone magma series are explicable according to crystallization of hornblende by reaction between olivine and liquid. Although the storage and release of H_2O in and from hornblende in subducted oceanic crust may be important in initiating subduction-zone magmatism, reactions between hornblende and liquids in the Benioff zone probably have no direct influence on the characteristics of magma series in subduction zones (compare Green and Ringwood, 1968; Green, 1972; Boettcher, 1973, with Stern *et al.*, 1975; Cawthorn and O'Hara, 1976; Allen and Boettcher, 1978).

Temperatures greater than about 1000°C are implied by basaltic liquids with less than about 6 weight percent H_2O. If subduction zone basaltic liquids originate between the Benioff zone and the surface, then the temperature must be at least as high as 1000°C somewhere in the interval. Geophysical models of subduction zone processes generally yield lesser temperatures, particularly close to the relatively cold Benioff zone (compare Andrews and Sleep, 1974; Anderson *et al.*, 1976, with Hasebe *et al.*, 1970; Ito, 1978). In order to be consistent with volcanological and geological data, geophysical models should yield temperatures in excess of 1000°C in the magma path between the Benioff zone and the volcanic front, as has been emphasized by Hasebe *et al.* (1970).

Some of the H_2O subducted as oceanic crust is probably not returned to the surface by the outgassing of parental basaltic liquids in subduction zones. There is an average of about 1 to 2 weight percent of mineralogically-bound H_2O in the combined oceanic crustal layers 2 (Melson *et al.*, 1968; Humphris and Thompson, 1978) and 3 (Melson and Thompson, 1971; Prinz *et al.*, 1976; Ito, 1979; Anderson *et al.*, 1979). Parental basaltic liquids of subduction zones probably contain an average of about 2 to 4 weight percent H_2O (Eggler, 1972; Anderson, 1973, 1979; but see also Marsh, 1976; Garcia *et al.*, 1979; and Sekine *et al.*, 1979, who estimate lower concentrations of H_2O). The ratio of mass production of crust in subduction zones (continental growth) to that at oceanic ridges is about 0.2 (Anderson, 1974), based on the ratios of cross-sectional areas of Cenozoic oceanic island arcs (Murauchi *et al.*, 1968; Grow, 1973) and the estimated cross-sectional areas of subducted oceanic crust implied by late Cenozoic local rates of plate convergence (Chase, 1972). If all the H_2O bound in subducted oceanic crust returns to the surface by first entering into basaltic parental liquids, the expected concentration of H_2O in the liquids ranges from 5 (1/0.2) to 10 (2/0.2) weight percent. The estimates of H_2O actually present (2 to 4 percent) are uncertain, but are consistent with the notion (Anderson *et al.*, 1979) that H_2O is released from dehydrating chlorite (the principal mineralogical residence of H_2O in oceanic crust) at too shallow a depth (Delany and Helgeson, 1978, but see Jenkins, 1979) to contribute to melting in subduction zones. The H_2O associated with the parental liquids of subduction zone magmas is similar in amount to the H_2O supplied by amphiboles in the oceanic crust (Ito, 1979).

A complex origin of continental crust is implied by parental basaltic liquid and hornblende gabbro in subduction zones. A principal idea regarding the formation of continental crust involves the postulated production and accretion of andesitic island arcs (Wilson, 1954, p. 206), because average continental crust is andesitic in composition (Goldschmidt, 1933; Taylor, 1967). The chemical composition of the bulk and lower continental crust is uncertain and debated (see Taylor and McLennan, 1979, and Tarney and Windley, 1979 for contrasting views). If the bulk of Cenozoic island arcs is composed of hornblende gabbro, then how can the andesitic composition of average continental crust be explained? The implication

of dominant hornblende gabbro in island arcs is that continental crust either was made differently before Cenozoic times or is further differentiated by additional processes.

Note added in proof

The following important article appeared after this paper was accepted for publication: Ritchey, J. L. (1980) Divergent magmas at Crater Lake, Oregon: products of fractional crystallization and vertical zoning in a shallow, water-undersaturated chamber. *J. Volcanol. Geothermal Res., 7,* 373–386.

Acknowledgments

I thank P. J. Wyllie for helpful discussion and review of an early version of this paper. C. Bacon (Menlo Park) provided a helpful review. I have benefited from rock samples and advice contributed by Shigeo Aramaki and Naoki Onuma (Asama) and by W. I. Rose (Fuego). The work reported here was supported by NSF grant EAR76-15016 A01.

References

Allen, J. C. and A. L. Boettcher (1978) Amphiboles in andesite and basalt: II. Stability as a function of P–T–f_{H_2O}–f_{O_2}. *Am. Mineral., 63,* 1074–1087.

———, ———, and G. Marland (1975) Amphiboles in andesite and basalt: I. Stability as a function of P–T–f_{O_2}. *Am. Mineral., 60,* 1069–1085.

Anderson, A. T. (1973) The before-eruption water content of some high-alumina magmas. *Bull. Volcanol., 37,* 530–552.

——— (1974) Chlorine, sulfur, and water in magmas and oceans. *Geol. Soc. Am. Bull., 85,* 1485–1492.

——— (1976) Magma mixing: petrological process and volcanological tool. *J. Volcanol. Geotherm. Res., 1,* 3–33.

——— (1979) Water in some hypersthenic magmas. *J. Geol., 87,* 509–531.

——— and D. Gottfried (1971) Contrasting behavior of P, Ti and Nb in a differentiated high-alumina olivine tholeiite and a calc-alkaline andesitic suite. *Geol. Soc. Am. Bull., 82,* 1929–1942.

———, D. M. Harris and E. Ito (1979) Toward geologic cycles for H_2O, CO_2, Cl and S. (abstr.). *Int. Union Geodesy and Geophysics Assembly, Canberra, Interdisciplinary Abstr.,* 26.

Anderson, R. N., S. Uyeda and A. Miyashiro (1976) Geophysical and geochemical constraints at converging plate boundaries. Part I. Dehydration in the downgoing slab. *Geophys. J. R. Astron. Soc., 44,* 333–357.

Andrews, D. J. and N. M. Sleep (1974) Numerical modelling of tectonic flow behind Island Arcs. *Geophys. J. R. Astron. Soc., 38,* 237–251.

Aramaki, S. (1956) The 1783 activity of Asama volcano, Part 1. *Jap. J. Geol. Geogr., 27,* 189–229.

——— (1957) The 1783 activity of Asama volcano, Part 2. *Jap. J. Geol. Geogr., 28,* 11–33.

——— (1963) Geology of Asama volcano. *J. Fac. Sci. Univ. Tokyo, 14,* 229–443.

Best, M. G. and E. L. P. Mercy (1967) Composition and crystallization of mafic minerals in the Guadalupe igneous complex, California. *Am. Mineral., 52,* 436–474.

Boettcher, A. L. (1973) Volcanism and orogenic belts—the origin of andesites. *Tectonophysics, 17,* 223–240.

Bowen, N. L. (1928) *The Evolution of the Igneous Rocks.* Dover, New York.

Buddington, A. F. and D. H. Lindsley (1964) Iron-titanium oxide minerals and synthetic equivalents. *J. Petrol., 5,* 310–357.

Buening, D. K. and P. R. Buseck (1973) Fe–Mg lattice diffusion in olivine. *J. Geophys. Res., 78,* 6852–6862.

Cawthorn, R. G. and M. J. O'Hara (1976) Amphibole fractionation in calc-alkaline magma genesis. *Am. J. Sci., 276,* 309–329.

Chase, C. G. (1972) The N plate problem of plate tectonics. *Geophys. J. Roy. Astron. Soc., 29,* 117–122.

Crandell, D. W. and D. R. Mullineaux (1973) Pine Creek volcanic assemblage at Mount St. Helens, Washington. *U.S. Geol. Surv. Bull., 1383A,* 1–23.

———, R. D. Miller and M. Rubin (1962) Pyroclastic deposits of Recent age at Mount Rainier, Washington. *U.S. Geol. Surv. Prof. Pap., 450-D,* D64–D68.

Delany, J. M. and H. C. Helgeson (1978) Calculation of the thermodynamic consequences of dehydration in subducting oceanic crust to 100 kb and >800°C. *Am. J. Sci., 278,* 638–686.

Doe, B. R. (1967) The bearing of lead isotopes on the source of granitic magma. *J. Petrol., 8,* 51–83.

Eggler, D. H. (1972) Water-saturated and undersaturated melting relations in a Paricutin andesite and an estimate of water content in the natural magma. *Contrib. Mineral. Petrol., 34,* 261–271.

——— and C. W. Burnham (1973) Crystallization and fractionation trends in the system andesite–H_2O–CO_2–O_2 at pressures to 10 Kb. *Geol. Soc. Am. Bull., 84,* 2517–2532.

Faure, G. and J. L. Powell (1972) *Strontium Isotope Geology.* Springer-Verlag, Berlin.

Fenner, C. N. (1926) The Katmai magmatic province. *J. Geol., 34,* 673–772.

Garcia, M. O. and S. S. Jacobson (1979) Crystal clots, amphibole fractionation and the evolution of calc-alkaline magmas. *Contrib. Mineral. Petrol., 69,* 319–327.

———, N. W. K. Liu and D. W. Muenow (1979) Volatiles from submarine volcanic rocks from the Mariana Island arc and trough. *Geochim. Cosmochim. Acta, 43,* 305–312.

Goldschmidt, V. M. (1933) Grundlagen der quantitativen Geochemie. *Fortschr. Mineral. Kristollogr. Petrogr., 17,* 112–156.

Green, T. H. (1972) Crystallization of calc-alkaline andesite under controlled high-pressure conditions. *Contrib. Mineral. Petrol., 34,* 150–166.

——— and A. E. Ringwood (1968) Genesis of the calc-alkaline igneous rock suite. *Contrib. Mineral. Petrol., 18,* 105–162.

Grow, J. A. (1973) Crustal and upper mantle structure of the central Aleutian arc. *Geol. Soc. Am. Bull., 84,* 2169–2192.

Harris, D. M. (1979) Pre-eruption variations of H_2O, S and Cl, in a subduction zone basalt (abstr.). *EOS, 60,* 968.

Hasebe, R., N. Fujii and S. Uyeda (1970) Thermal processes under island arcs. *Tectonophysics, 10,* 335–355.

Helz, R. T. (1973) Phase relations of basalts in their melting range at P_{H_2O} = 5 kb as a function of oxygen fugacity. *J. Petrol., 14,* 249–302.

——— (1976) Phase relations of basalts in their melting ranges at P_{H_2O} = 5 kb. Part II. Melt compositions. *J. Petrol., 17,* 139–193.

Holloway, J. R. (1973) The system pargasite–H_2O–CO_2: a model for melting of a hydrous mineral with a mixed volatile fluid. I. Experimental results to 8 kbar. *Geochim. Cosmochim. Acta, 37,* 651–666.

——— and C. W. Burnham (1972) Melting relations of basalt with equilibrium water pressure less than total pressure. *J. Petrol., 13,* 1–29.

——— and C. E. Ford (1975) Fluid-absent melting of the fluorohydroxy amphibole pargasite to 35 kilobars. *Earth Planet. Sci. Lett., 25,* 44–48.

Humphris, S. E. and G. Thompson (1978) Hydrothermal alteration of oceanic basalts by seawater. *Geochim. Cosmochim. Acta, 42,* 107–126.

Ikeda, Y. (1976) Petrology and mineralogy of the Iritono basic intrusive rocks, central Abukuma plateau. *J. Fac. Sci. Univ. Tokyo, 19,* 229–251.

Isshiki, N. (1963) Petrology of Hachijo-jima volcano group, Seven Izu Islands, Japan. *J. Fac. Sci. Univ. Tokyo, 15,* 91–134.

Ito, E. (1979) High-temperature alteration of oceanic gabbros from the mid-Cayman rise (abstr.). *Geol. Soc. Am. Abstracts with Programs, 11,* 449.

Ito, K. (1978) Ascending flow between the descending lithosphere and the overlying asthenosphere. *J. Geophys. Res., 83,* 262–268.

Jakěs, P. and A. J. R. White (1972) Hornblendes from calc-alkaline volcanic rocks of island arcs and continental margins. *Am. Mineral., 57,* 887–902.

Jenkins, D. M. (1979) Experimental phase relations of chlorite- and amphibole-bearing peridotites (abstr.). *Geol. Soc. Am. Abstracts with Programs, 11,* 451.

Kuno, H. (1950) Petrology of Hakone volcano and the adjacent areas, Japan. *Geol. Soc. Am. Bull., 61,* 957–1020.

——— (1959) Origin of Cenozoic petrographic provinces of Japan and surrounding areas. *Bull. Volcanol., 20,* 37–76.

——— (1968) Origin of andesite and its bearing on the island arc structure. *Bull. Volcanol., 32,* 141–176.

Lewis, J. F. (1973a) Mineralogy of ejected plutonic blocks of the Soufrière volcano, St. Vincent: olivine, pyroxene, amphibole and magnetite paragenesis. *Contrib. Mineral. Petrol., 38,* 197–220.

——— (1973b) Petrology of ejected plutonic blocks of the Soufrière volcano, St. Vincent, West Indies. *J. Petrol., 14,* 81–112.

Lindsley, D. H. and D. Rumble, III (1977) Thermodynamic solution model for coexisting Ti-magnetite plus ilmenite (abstr.). *EOS, 58,* 519.

Marsh, B. D. (1976) Some Aleutian andesites: their nature and source. *J. Geol., 84,* 27–46.

McBirney, A. R. (1978) Volcanic evolution of the Cascade range. *Am. Rev. Earth Planet. Sci., 6,* 437–456.

———, J. F. Sutter, H. R. Naslund, K. G. Sutton and C. M. White (1974) Episodic volcanism in the central Oregon Cascade Range. *Geology, 2,* 585–589.

Melson, W. G. and G. Thompson (1971) Petrology of a transform zone and adjacent ridge segments. *R. Soc. Lond. Phil. Trans., 268,* 423–441.

——— and T. H. van Andel (1968) Volcanism and metamorphism in the mid-Atlantic ridge, 22°N latitude. *J. Geophys. Res., 73,* 5925–5941.

Mertzman, S. A., Jr. (1977) The petrology and geochemistry of the Medicine Lake volcano, California. *Contrib. Mineral. Petrol., 62,* 221–247.

——— (1978) A tschermakite-bearing high-alumina olivine tholeiite from the southern Cascades, California. *Contrib. Mineral. Petrol., 67,* 261–265.

Miller, F. S. (1938) Hornblendes and primary structures of the San Marcos gabbro. *Geol. Soc. Am. Bull., 49,* 1213–1232.

Minakami, T. (1942) On the distribution of volcanic ejecta (Part 2). The distribution of Mt. Asama pumice in 1783. *Bull. Earthq. Res. Inst., 20,* 93–106.

Miyashiro, A. (1974) Volcanic rock series in island arcs and active continental margins. *Am. J. Sci., 274,* 321–355.

Moorhouse, W. W. (1959) *The Study of Rocks in Thin Section.* Harper and Row, New York.

Muehlenbachs, K. and I. Kushiro (1975) Measurements of oxygen diffusion in silicates (abstr.). *EOS, 56,* 459.

Mueller, R. F. (1969) Hydration, oxidation, and the origin of the calc-alkali series. *NASA TN, D-5400,* 1–27.

Mullan, H. S. and M. A. Bussell (1977) The basic rock series in batholithic associations. *Geol. Mag., 114,* 265–280.

Murauchi, S., N. Den, S. Asano, H. Hotta, T. Yoshii, T. Asanuma, K. Hagiwara, K. Ichikawa, T. Sato, W. J. Ludwig, J. I. Ewing, N. T. Edgar and R. E. Houtz (1968) Crustal structure of the Philippine Sea. *J. Geophys. Res., 73,* 3143–3171.

Newhall, C. G. (1979) Temporal variation in the lavas of Mayon volcano, Philippines. *J. Volcanol. Geothermal. Res., 6,* 61–83.

Oshima, O. (1976) Fe–Ti oxide minerals of the 1973 eruption of Asama volcano. *Univ. Tokyo, Coll. of Gen. Educ., Sci. Pap., 26,* 39–50.

Peacock, M. A. (1931) Classification of igneous rock series. *J. Geol., 39,* 54–67.

Piwinskii, A. (1973) Experimental studies of granitoids from the central and southern Coast Ranges, California. *Tschermaks Mineral. Petrogr. Mitt., 20,* 107–130.

——— and P. J. Wyllie (1968) Experimental studies of igneous rock series: a zoned pluton in the Wallowa batholith, Oregon. *J. Geol., 76,* 205–234.

Powers, H. A. (1932) The lavas of the Modoc lava bed quadrangle, California. *Am. Mineral., 17,* 253–293.

Prinz, M., K. Keil, J. A. Green, A. M. Reid, E. Bonatti and J. Honnorez (1976) Ultramafic and mafic dredge samples from the equatorial mid-Atlantic Ridge and fracture zone. *J. Geophys. Res., 81,* 4087–4103.

Ringwood, A. E. (1974) The petrological evolution of island arc systems. *Geol. Soc. Lond. J., 130,* 183–204.

Robertson, J. K. and P. J. Wyllie (1971) Rock–water systems with special reference to the water-deficient region. *Am. J. Sci., 271,* 252–277.

Roedder, E. (1965) Liquid CO_2 inclusions in olivine-bearing nodules and phenocrysts from basalts. *Am. Mineral., 50,* 1746–1782.

Roeder, P. L. and R. F. Emslie (1970) Olivine–liquid equilibrium. *Contrib. Mineral. Petrol., 29,* 275–289.

Rose, W. I., Jr., A. T. Anderson, Jr., L. G. Woodruff and S. B. Bonis (1978) The October 1974 basaltic tephra from Fuego volcano: description and history of the magma body. *J. Volcanol. Geotherm. Res., 4,* 3–53.

———, N. K. Grant, G. A. Hahn, I. M. Lange, J. L. Powell, J. Easter and J. M. Degraff (1977) The evolution of Santa Maria volcano, Guatemala. *J. Geol., 85,* 63–87.

Sakuyama, M. (1979) Lateral variations of H_2O contents in Quaternary magmas of northeastern Japan. *Earth Planet. Sci. Lett., 43,* 103–111.

Sekine, T., T. Katsura and S. Aramaki (1979) Water saturated phase relations of some andesites with application to the estimation of the initial temperature and water pressure at the time of eruption. *Geochim. Cosmochim. Acta, 43,* 1367–1376.

Smith, R. L. (1979) Ash-flow magmatism. *Geol. Soc. Am. Spec. Pap., 180,* 5–27.

Stern, C. R., W. L. Huang and P. J. Wyllie (1975) Basalt–andesite–rhyolite–H_2O: crystallization intervals with excess H_2O and

H_2O-undersaturated liquidus surfaces to 35 kilobars, with implications for magma genesis. *Earth Planet. Sci. Lett., 28,* 189–196.

Stewart, D. C. (1975) Crystal clots in calc-alkaline andesites as breakdown products of high-Al amphiboles. *Contrib. Mineral. Petrol., 53,* 195–204.

Tarney, J. and B. F. Windley (1979) Continental growth, island arc accretion and the nature of the lower crust—a reply to S. R. Taylor and S. M. McLennan. *Geol. Soc. Lond. J., 136,* 501–504.

Taylor, R. W. (1964) Phase equilibria in the system FeO–Fe_2O_3–TiO_2 at 1300°C. *Am. Mineral., 49,* 1016–1030.

Taylor, S. R. (1967) The origin and growth of continents. *Tectonophysics, 4,* 17–34.

——— and S. M. McLennan (1979) Discussion on "Chemistry, thermal gradients and evolution of the lower continental crust. In J. Tarney and B. F. Windley, Eds., *Geol. Soc. Lond. J., 136,* 497–500.

Turner, F. J. and J. Verhoogen (1960) *Igneous and Metamorphic Petrology.* McGraw-Hill, New York.

Walawender, M. J. (1976) Petrology and emplacement of the Los Pinos pluton, southern California. *Can. J. Earth Sci., 13,* 1288–1300.

Wilson, J. T. (1954) The development and structure of the crust. In G. P. Kuiper, Ed., *The Earth as a Planet,* p. 138–214. University of Chicago Press, Chicago, Illinois.

Wyllie, P. J. (1977) Crustal anatexis: an experimental review. *Tectonophysics, 43,* 41–71.

Yoder, H. S. and C. E. Tilley (1962) Origin of basalt magmas: an experimental study of natural and synthetic rock systems. *J. Petrol., 3,* 342–532.

Manuscript received, October 27, 1979;
accepted for publication, March 25, 1980.

American Mineralogist, Volume 65, pages 854-866, 1980

The thermal-compositional dependence of Fe^{2+}–Mg distributions between coexisting garnet and pyroxene: applications to geothermometry[1]

PETER S. DAHL

Department of Geology, Kent State University
Kent, Ohio 44242

Abstract

The thermal–compositional dependence of Fe^{2+}–Mg distributions between coexisting garnet and pyroxene in diverse metamorphic lithologies from two small areas in the Ruby Range, southwestern Montana, has been studied by electron microprobe and multiple linear regression techniques. For coexisting garnet–clinopyroxene, this dependence, which is inferred from independent metamorphic P–T estimates for two areas and thirteen mineral-pair analyses, is summarized by the equation

$$RT \ln K_D = (2482\pm845) + (1509\pm1392)(X_{Fe}-X_{Mg})^{Gar} + (2810\pm954)(X_{Ca}^{Gar}) + (2855\pm792)(X_{Mn}^{Gar})$$

where $K_D = (X_{Fe}/X_{Mg})^{Gar}/(X_{Fe}/X_{Mg})^{Cpx}$, X = mole fraction, $2482 = 2324 + 0.022P = -\Delta G_T^P$(cal) for the gar–cpx Fe–Mg exchange reaction, and the coefficients represent regressed values for garnet mixing parameters (w_{ij}^{Gar}). The regressed parameters for Ca and Mn agree well with those calculated by Ganguly (1979); however, the regressed value of w_{FeMg}^{Gar} is intermediate to those of Ganguly and O'Neill and Wood (1979).

For nine garnet–orthopyroxene pairs, the best-fit equation is identical to that given above except that $-\Delta G_T^P = 1391\pm288$ cal for the gar–opx Fe–Mg exchange reaction.

The garnet–clinopyroxene geothermometers of Ganguly (1979) and Saxena (1979) yield anomalously high temperatures for the Ruby Range. If this result is observed in other upper-amphibolite to lower-granulite facies terrains, more realistic temperatures may be obtained from the gar–cpx equation presented here. The gar–opx equation can be used as a relative (but not absolute) geothermometer.

Introduction

The temperature dependence of Fe^{2+}–Mg distributions between coexisting ferromagnesian silicates has been used extensively in the calibration of mineral-pair geothermometers. Such distributions are a function not only of temperature, however, but depend also upon composition of the exchanging minerals and—to a lesser extent—upon load pressure. This paper examines the compositional dependence of Fe^{2+}–Mg distributions for garnet–clinopyroxene and garnet–orthopyroxene pairs in natural assemblages from the Ruby Range, southwestern Montana (Fig. 1). Potentially the most useful field areas for such a study are those that contain a diversity of lithologic units, yet are sufficiently small that uniformity of metamorphic P–T conditions can be reasonably assumed. If, in addition, coexisting garnets and pyroxenes crystallized under equilibrium conditions, then it follows that any variation in Fe^{2+}–Mg distributions between these minerals must be compositionally controlled. With these considerations in mind, two small areas in the Ruby Range were chosen for study. These areas, designated in Figure 1 as the Kelly and Carter Creek areas, are 1 km² and 9 km², respectively.

Coexisting garnets and pyroxenes in 17 rocks representing six metamorphic lithologies in the Kelly and Carter Creek areas were analyzed by electron microprobe. The distribution of Fe^{2+} and Mg between coexisting minerals, usually expressed by a distribution coefficient K_D, is defined here as

$$K_D\ (\text{Fe/Mg; gar–pyrox}) = (X_{Fe}/X_{Mg})^{Gar}/(X_{Fe}/X_{Mg})^{Pyrox} \quad (1)$$

[1] Contribution No. 211, Department of Geology, Kent State University, Kent, Ohio.

0003–004X/80/0910–0852$02.00

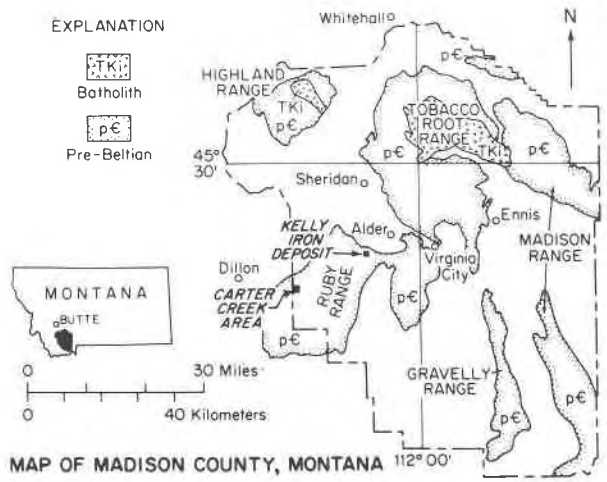

Fig. 1. Map showing exposures of Precambrian metamorphic rocks and Tertiary intrusives in Madison County, Montana (after Cordua, 1973). The Kelly and Carter Creek areas of the Ruby Range are the primary sample sites for this study. One sample is from the Stone Creek area, located approximately halfway between the two main areas.

where the X terms denote mole fractions. In this paper, thermodynamic modeling of thermal and compositional effects on K_D is done by two methods. The first approach utilizes Ganguly's (1979) binary mixing parameters for garnet and Dahl's (1979) estimates of peak metamorphic temperatures in the Kelly and Carter Creek areas; the second approach involves multiple linear and step-wise regression techniques, utilizing the 17 Montana samples as the data base. The results are evaluated in terms of earlier studies by Banno (1970), Berg (1975, 1977), Davidson (1969), Davidson and Mathison (1973), Dougan (1974), Ganguly (1979), O'Neill and Wood (1979), Råheim and Green (1974), and Saxena (1968, 1969, 1976, 1979).

Methods of study

Garnet–pyroxene-bearing rocks collected in the Ruby Range were studied by standard optical and electron microprobe techniques. Mineral assemblages and compositional data for these rocks are summarized in Tables 1 and 2, respectively. Chemical analyses of all minerals were performed on polished thin sections using a 3-spectrometer ETEC Autoprobe; operating conditions and analytical conditions were identical to those described by Klein (1974). Only mean analyses, based on 3–10 individual analyses and generally uncorrected for small amounts of Fe^{3+}, were used in the calculation of distribution coefficients (K_D) and graphical data points. The averaging procedure did not significantly alter trends observed by plotting data from single analyses, but served only to reduce analytical scatter. Core and rim analyses of mineral grains, although not significantly different in most cases, were averaged separately; only rim analyses were used in this study, however.

Multiple linear and step-wise regressions were performed using a Hewlett-Packard model 9845A computer.

Geologic setting

The Precambrian metamorphic core of the Ruby Range is underlain by sillimanite–K feldspar-zone assemblages, except in the extreme northeast, where the orthopyroxene isograd is exceeded. Both the Kelly and Carter Creek areas contain a thick sequence of marbles, mafic gneisses, iron-formations, pelitic and semi-pelitic rocks, and quartzites. These rocks, collectively termed "Cherry Creek" rocks by Heinrich (1960), probably attained their high-grade metamorphic character approximately 2750 m.y. ago, during the Beartooth orogeny (James and Hedge, 1980).

Table 1. Summary of iron-formation and mafic gneiss assemblages in samples from the Ruby Range

Sample	Unit	gar	cpx	opx	hb	bi	plag	qtz	ilm	mag	other
RMK-13	GN	x	x		x		x	x	–		(zirc)
RMK-17	GN	x	x				x	x			
RMS-22	GN	x	x	x	x		x	x	–		
RMK-26	GN	x	x		x		x		–		
RMK-27$_1$	GN	x	x		x	x	x	x	–		
RMK-27$_2$	GN	x	x			–	x	x	x	–	(apa)
RMK-27$_3$	GN	x	–	x	x	–	x	x	x	–	
RMK-77	GN	x	x		x		x		x	–	
RMK-122	GN		x	x	x		x				
RMK-51	GQ	x	–	x	x	x	x	x	–		(zirc)
RMK-46	GIF	x	x	x				x		x	
RMK-76	GIF	x	x	x				x		x	(cal)
RMK-82	GIF	x	x	x				x		x	
RMK-37$_1$	QIF	x	x	x				x	–	–	
RMK-37$_2$	QIF	x	x	x				x		–	
RMK-48	QIF	–		x				x		x	
RMC-1$_1$	DGN	x	x		x			–			mic, sph, cal, scp, (zirc)
RMC-1$_2$	DGN	x	x		x			–			
RMC-71	AM	x	x				x				cal, scp

RMK and RMC samples are from the Kelly and Carter Creek areas, respectively. Subscripts on sample numbers denote compositional bands within a polished thin section. Sample RMS-22 is from the Stone Creek area, located directly between the two main sample areas. Lithologic designations (James et al., 1969; James and Wier, 1972a, 1972b) : GN = mafic granulite gneiss; GQ = garnet quartzite; GIF = garnet iron-formation; QIF = quartz iron-formation; DGN = diopside gneiss; AM = amphibolite. The term mafic gneiss (in table title and text) includes all lithologies except GIF and QIF. Symbols: x = major constituent; ( ) or - = minor or trace component (less than 3 modal %). Abbreviations: hb = hornblende; cum = cummingtonite; mag = magnetite; apa = apatite; mic = microcline; sph = sphene; cal = calcite; scp = scapolite; bi = biotite; plag = andesine or labradorite.

Table 2. Fe-Mg K_D values and compositional data for the subassemblage garnet±clinopyroxene±orthopyroxene in samples from the Ruby Range

		K_D(Fe/Mg)			Cations per 12 oxygens in garnet				Cations per 6 oxygens in clinopyroxene				Cations per 6 oxygens in orthopyroxene			
Sample	Unit	gar-cpx	gar-opx	cpx-opx	Fe	Mg	Ca	Mn	Fe	Mg	Ca	Mn	Fe	Mg	Ca	Mn
RMK-27$_2$	GN	6.80			1.890	0.453	0.697	0.038	0.445	0.621	0.861	0.003				
RMK-13^2	GN	6.48			1.720	0.511	0.778	0.042	0.352	0.678	0.878	0.002				
RMK-27$_3$	GN	*	3.52	0.53	1.927	0.526	0.559	0.056	0.364	0.660	0.828	0.005	0.995	0.957	0.020	0.012
RMK-17^3	GN	7.33			1.734	0.277	1.059	0.060	0.461	0.540	0.951	0.005				
RMS-22	GN	*	3.65	0.55	1.965	0.411	0.578	0.062	0.461	0.597	0.844	0.012	1.071	0.877	0.023	0.017
RMK-51	GQ	*	3.87	0.51	1.763	0.671	0.557	0.063	0.265	0.764	0.907	0.003	0.807	1.187	0.019	0.010
RMK-122	GN			0.55					0.260	0.761	0.888	0.012	0.740	1.201	0.017	0.019
RMK-77	GN	7.17			1.785	0.462	0.766	0.080	0.359	0.666	0.901	0.005				
RMK-26	GN	6.84			1.710	0.458	0.810	0.099	0.368	0.674	0.872	0.006				
RMK-76	GIF	7.29	4.37	0.60	1.920	0.322	0.574	0.269	0.475	0.581	0.862	0.022	1.103	0.808	0.026	0.053
RMK-82	GIF	7.65	4.34	0.57	2.021	0.173	0.613	0.313	0.655	0.429	0.882	0.029	1.390	0.516	0.033	0.066
RMK-46	GIF	8.45	4.96	0.60	1.710	0.297	0.533	0.563	0.432	0.634	0.827	0.042	0.999	0.874	0.027	0.110
RMK-37$_2$	QIF	9.08	5.40	0.60	1.486	0.137	0.517	0.978	0.576	0.482	0.821	0.120	1.147	0.571	0.040	0.235
RMK-37$_1$	QIF	8.95	5.79	0.65	1.499	0.125	0.497	1.006	0.618	0.461	0.796	0.124	1.190	0.575	0.034	0.235
RMK-48	QIF		5.61		**1.078	0.109	0.482	1.315					0.985	0.555	0.046	0.411
RMC-71	AM	11.54			**1.037	0.121	1.632	0.229	0.390	0.525	0.958	0.016				
RMC-1$_1$	DGN	11.47			1.566	0.113	1.073	0.280	0.545	0.451	0.904	0.022				
RMC-1$_2$	DGN	11.41			1.503	0.168	1.083	0.311	0.446	0.569	0.970	0.019				

*Subscripts on sample numbers denote compositional bands within a polished thin section. See Table 1 for explanation of lithologic symbols. *K_D not reported because gar and cpx were not found in contact. **These values have been corrected for relatively large amounts of Fe^{3+} using the computer program of Friberg (1976). All other Fe values are uncorrected for Fe^{3+}. Although not discussed in the text, cpx-opx K_D values (calculated from gar-cpx and gar-opx K_D values) approximately correlate with Fe^{Cpx} and Mn^{Cpx}. The Fe trend parallels a similar trend observed and explained by Davidson (1968) for Australian pyroxene pairs.*

Estimated *P–T* conditions of metamorphism for the two areas, based upon geothermometric and mineral assemblage data, are shown in Figure 2. Assemblage data and six mineral-pair geothermometers yielded concordant temperature estimates of 745±50°C (Kelly) and 675±45°C (Carter Creek) (Dahl, 1979). Because sillimanite is the stable aluminosilicate polymorph in pelitic rocks throughout the Ruby Range (Dahl, 1977), these estimates, coupled with Holdaway's (1971) determination of aluminosilicate *P–T* stabilities, constrain the maximum load pressures for the two areas (see Fig. 2). Minimum load pressures cannot have been too far below the sillimanite–kyanite univariant, or kyanite—a metastable relict in some pelitic rocks—would probably not have persisted. Thus, load pressures for the two areas are tentatively estimated at 7.2±1.2 kbar (Kelly) and 6.2±1.2 kbar (Carter Creek). The *P–T* ranges shown in Figure 2 are consistent with geothermal gradients of 30° to 35°C/km.

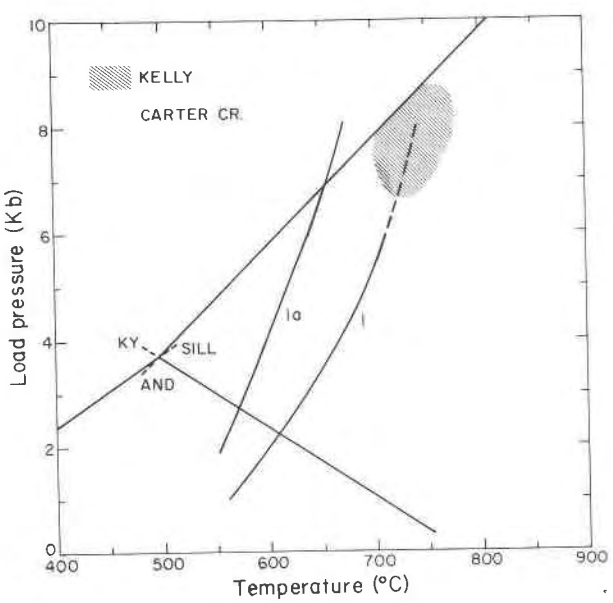

Fig. 2. *P–T* diagram showing probable peak metamorphic conditions for the Kelly and Carter Creek areas. Curves 1 and 1a represent the reaction mu + qtz ⇄ Al_2SiO_5 + ksp + H_2O at X_{H_2O} = 1 (Chatterjee and Johannes, 1974) and X_{H_2O} = 0.5 (Kerrick, 1972), respectively. Wintsch (1975) has calculated that Kerrick's experimental X_{H_2O} may correspond to $a_{H_2O} \simeq 0.25$.

The common association of microcline and sillimanite in metapelites indicates muscovite breakdown, and it appears from Figure 2 that the activity of water a_{H_2O} was significantly less than 1—and perhaps as low as or lower than 0.25—for pelitic rocks in the Carter Creek area; such was probably also the case for the higher-temperature pelitic rocks in the Kelly area. These conclusions are consistent with the lack of widespread partial melting in pelitic rocks throughout the Ruby Range.

Local alteration of prograde assemblages indicates that Precambrian greenschist to lower amphibolite facies metamorphism occurred in the Ruby Range

(1) during the waning stages of the 2750 m.y. event and/or (2) during a separate event at 1600 m.y., inferred from mineral dates of Giletti (1966).

Additional details on the stratigraphy, structure, and petrology of the "Cherry Creek" rocks in the Ruby Range are given in Garihan (1979), Heinrich (1960), James *et al.* (1969), James and Wier (1972a,b), Okuma (1971), and Dahl (1977, 1979).

Attainment of chemical equilibrium

The thermodynamic models presented in the following section assume that (1) chemical equilibrium between garnet and coexisting pyroxene was attained during the 2750 m.y. metamorphism, (2) garnet–pyroxene pairs within a given area equilibrated at the same (or similar) temperature regardless of lithology, and (3) evidence of this equilibrium was preserved (*i.e.*, was not partly obliterated by local retrograde effects). Evidence supporting the validity of these assumptions is presented below.

In support of assumption (1), no assemblage in Table 1 has negative variance; most assemblages are either di- or tri-variant. Second, coexisting garnets and pyroxenes typically exhibit smooth grain boundaries, suggesting textural equilibrium (Dahl, 1977). Third, element distributions between grain edges of coexisting garnets and pyroxenes are orderly, as exemplified by Mn and Al distributions in Figures 3A, B, C. Orderly element distributions also support assumption (2).

Assumption (3) is supported by the general lack of retrograde zoning among coexisting garnets and pyroxenes (Dahl, 1977). Furthermore, these minerals are typically free of retrograde alteration products; some grains, however, exhibit incipient alteration to minerals such as chlorite or actinolitic hornblende. Only pyroxenes in mafic granulite gneisses (the GN unit) from the Kelly area exhibit slight zoning. The GN unit may have originated as a gabbroic magma (Dahl, in preparation); zoning in Na, Al, Fe^{2+}, and Mg, therefore, is thought to reflect re-equilibration of the pyroxenes from igneous to high-grade metamorphic conditions. Rim compositions of coexisting garnets and pyroxenes in this unit are thus thought to reflect the latter conditions.

Thermodynamic models

Garnet–clinopyroxene

The exchange of Fe^{2+} and Mg between garnet and clinopyroxene can be represented by the equilibrium

$$\underset{\text{HD}}{CaFeSi_2O_6} + 1/3\underset{\text{PY}}{Mg_3Al_2Si_3O_{12}} \leftrightarrows \underset{\text{DI}}{CaMgSi_2O_6} + 1/3\underset{\text{ALM}}{Fe_3Al_2Si_3O_{12}} \quad (2)$$

Assuming (1) a substitutional solution model [*cf.* Kerrick and Darken (1975)] and (2) no Fe^{2+} or Mg in the *M2* site of clinopyroxene, the equilibrium constant $K(P,T)$ in terms of activities a, mole fractions X, and activity coefficients γ is given by

$$K(P,T) = \frac{(a_{Fe}^{Gar})^{1/3}(a_{Mg}^{Cpx})}{(a_{Mg}^{Gar})^{1/3}(a_{Fe}^{Cpx})} = \frac{(X_{Fe}^{Gar})(X_{Mg}^{Cpx})}{(X_{Mg}^{Gar})(X_{Fe}^{Cpx})} \cdot \frac{(\gamma_{Fe}^{Gar})(\gamma_{Mg}^{Cpx})}{(\gamma_{Mg}^{Gar})(\gamma_{Fe}^{Cpx})} \quad (3)$$

where the term composed of mole fractions is equivalent to the Fe–Mg distribution coefficient K_D. The equilibrium constant $K(P,T)$ is related to the Gibbs free energy change ΔG_T^P for the exchange reaction by the expression

$$\Delta G_T^P = -RT \ln K(P,T) \quad (4)$$

where R is the gas constant. Substitution of equation (4) into equation (3) and rearrangement of terms yields the relationship

$$RT \ln K_D = -\Delta G_T^P - RT \ln (\gamma_{Fe}^{Gar}/\gamma_{Mg}^{Gar}) + RT \ln (\gamma_{Fe}^{Cpx}/\gamma_{Mg}^{Cpx}) \quad (5)$$

Ganguly and Kennedy (1974) used the "simple mixture" approximation of Guggenheim (1967, p. 54–57) to derive the following expression for the activity coefficients of Fe^{2+} and Mg in garnet:

$$RT \ln (\gamma_{Fe}^{Gar}/\gamma_{Mg}^{Gar}) \simeq w_{FeMg}(X_{Mg}^{Gar} - X_{Fe}^{Gar}) + (w_{FeCa} - w_{MgCa})(X_{Ca}^{Gar}) + (w_{FeMn} - w_{MgMn})(X_{Mn}^{Gar}) \quad (6)$$

The w_{ij} are binary solution interaction parameters which express the non-ideality of mixing between components i and j in garnet. Applying multivariate regression methods to published analyses of garnet and coexisting biotite in staurolite-zone assemblages, Ganguly and Kennedy derived w_{ij} values for garnet. Revised values presented by Ganguly (1979) are: $w_{FeMg} = 2710$ cal/mole; $w_{FeCa} - w_{MgCa} = -3152$ cal/mole; and $w_{FeMn} - w_{MgMn} = -2600$ cal/mole. Substitution of these values into equation (6) permits calculation of the activity term for garnet in equation (5). Equation (5) thus becomes

$$RT \ln K_D = -\Delta G_T^P + 2710(X_{Fe}^{Gar} - X_{Mg}^{Gar}) + 3152(X_{Ca}^{Gar}) + 2600(X_{Mn}^{Gar}) + RT \ln (\gamma_{Fe}^{Cpx}/\gamma_{Mg}^{Cpx}) \quad (7)$$

Table 3. Compositional effects on K_D (Fe–Mg) predicted by equation (9) for garnet–clinopyroxene pairs in samples from the Ruby Range

Sample	$2710(X_{Fe} - X_{Mg})^{Gar}$ (cal/mole)	+ $3152(x_{Ca}^{Gar})$ (cal/mole)	+ $2600(x_{Mn}^{Gar})$ (cal/mole)	= *Sum(X)* (cal/mole)	K_D predicted	K_D measured
RMK-27_2	1266	712	31	2009	6.82	6.80
RMK-13	1073	804	36	1913	6.50	6.48
RMK-17	1260	1065	49	2374	8.17	7.33
RMK-77	1160	782	68	2010	6.82	7.17
RMK-26	1103	829	83	2015	6.84	6.84
RMK-76	1404	586	226	2216	7.55	7.29
RMK-82	1604	618	260	2482	8.61	7.65
RMK-46	1233	542	471	2246	7.67	8.45
RMK-37_2	1173	523	816	2512	8.74	9.08
RMK-37_1	1190	501	837	2528	8.81	8.95
RMC-71	821	1705	198	2724	11.48	11.54
RMC-1_1	1298	1116	239	2653	11.06	11.47
RMC-1_2	1182	1113	263	2658	11.09	11.41

Ganguly (1979) has used a simplified activity term for clinopyroxene of the form

$$RT \ln (\gamma_{Fe}^{Cpx}/\gamma_{Mg}^{Cpx}) = \Delta w(X^{Jd} + X^{Ac})^{Cpx} \quad (8)$$

where Δw is the difference between the simple-mixture interaction parameters in the jadeite–hedenbergite and jadeite–diopside joins and the X terms represent mole fractions of jadeite and acmite in clinopyroxene. Although a reliable estimate for Δw is lacking in the 700–800°C range ($\Delta w \simeq 0$ at 1000°C; Ganguly, 1979), the magnitude of the activity term is probably near zero for clinopyroxenes from the Kelly area, judging from their extremely low and uniform Na contents ($X_{Na}^{M2-Cpx} = 0.02$–0.06 at grain edges). With this approximation, equation (7) can be simplified to the form

$$RT \ln K_D = -\Delta G_T^P + 2710(X_{Fe}^{Gar} - X_{Mg}^{Gar}) + 3152(X_{Ca}^{Gar}) + 2600(X_{Mn}^{Gar}) \quad (9)$$

Equation (9) approximates the dependence of K_D(Fe/Mg; gar–cpx) on mineral composition and temperature. Calculated values for the compositional terms in equation (9) are presented in Table 3 for garnet–clinopyroxene-bearing samples from the Ruby Range; for a given sample, the sum of the three compositional terms is denoted by the quantity *sum*(X).

The approximate validity of equation (9) can be tested in several ways. First, the equation predicts that increases in X_{Fe}^{Gar}, X_{Ca}^{Gar}, or X_{Mn}^{Gar} cause sympathetic increases in K_D(Fe/Mg; gar–cpx). Indeed, all three effects have been reported in the literature; data of D. H. Green plotted by Banno (1970) indicate very weak Fe and Ca effects, whereas Saxena (1968, 1969) infers a strong Mn and relatively weak Ca effect.

Second, equation (9) predicts that any increase in *sum*(X) effects a corresponding increase in K_D, all other factors equal. Indeed, for samples RMK-27_2 through RMK-37_1 (listed in Table 3 in order of increasing Mn content in garnet), the general trend of increasing *sum*(X) values is paralleled by an increase in measured K_D values. Note that the *sum*(X) values for the Carter Creek samples are distinctly higher than those for the Kelly samples. These higher values, which are due partly to increased Ca concentrations in garnet (Table 3, column 3), are consistent with the higher K_D values measured in the Carter Creek samples. The other factor contributing to the higher K_D values is the lower metamorphic temperature for the Carter Creek area (see Fig. 2).

The most rigorous test involves a comparison of K_D values predicted from equation (9) and values actually measured for the 13 samples from the Ruby Range. The first step in predicting K_D values is the calculation of ΔG_T^P for equation (2). A mean value of -1874 ± 240 cal (95 percent confidence limits) for ΔG_T^P is obtained from equation (9) by averaging the 13 values obtained for the difference between RT ln K_D and *sum*(X). Despite the inferred P–T difference between the Kelly and Carter Creek areas (Fig. 2), ΔG_T^P values calculated for the two areas by the above method are not significantly different. Furthermore, values for ΔG_{1018}^{7200} (P = 7200 bars and T = 1018°K) and ΔG_{948}^{6200}—calculated from molar enthalpy, entropy, heat capacity, and volume data in Robie *et al.* (1978), Helgeson *et al.* (1978), and Zen (1973)—are different by only 0.8 percent. Hence, the −1874 cal value is retained for all 13 samples from the Ruby

Range (Table 3). Inferred values for ΔG^p_T, *sum*(X), and T can now be substituted into equation (9) to predict K_D.

K_D values predicted thereby are presented in Table 3 for garnet–clinopyroxene-bearing mafic gneisses and iron-formations from the Ruby Range. The model appears to over-correct for the high Ca and Fe contents in samples RMK-17 and RMK-82, respectively, but for most other samples there is good agreement between predicted and measured K_D values. Linear regression of predicted *vs.* measured K_D values in Table 3 yields a line of slope 0.90 and a correlation coefficient (r) of 0.97. This level of correlation lends credence to Ganguly's (1979) mixing parameters for garnet and to the temperature estimates inferred for the Kelly and Carter Creek areas. Furthermore, it indicates—for the Montana clinopyroxenes at least—that any clinopyroxene mixing terms have nearly constant, or negligible, value.

Although equation (9) closely defines the thermal and compositional dependence on K_D observed in garnet–clinopyroxene pairs from the Ruby Range, it is possible to use the 13 Ruby Range samples themselves as the data base for multiple linear regression. Accordingly, regression was performed by computer on 13 equations in the form of equation (9), where $RT \ln K_D$ was chosen as the dependent variable, the three X terms as the independent variables, and ΔG^p_T as the regression constant. Regressed coefficients derived from the Ruby Range samples are included in Table 4; substitution of these values into equation (9) yields

$$RT \ln K_D = 2482 + 1509(X^{Gar}_{Fe} - X^{Gar}_{Mg}) + 2810(X^{Gar}_{Ca}) + 2855(X^{Gar}_{Mn}) \quad (10)$$

Measured K_D values and values predicted from equation (10) are compared in Table 5. Linear regression (as before) yields a line slope of 0.89 (*cf.* unity for a perfect model) and an r value of 0.97. This regression is plotted in Figure 4.

In Table 4, the regressed coefficients and thermal–compositional data base of this study are compared to data of Ganguly and Kennedy (1974), Ganguly (1979), and O'Neill and Wood (1979). Despite its relatively small size, the Montana data base comprises a broader range of composition—particularly for X^{Gar}_{Ca}—than that of Ganguly and Kennedy. Furthermore, analysis of variance indicates that equation (10)—derived from the 13 Montana samples—accounts for 89 percent of the total variance in $RT \ln K_D$ actually observed in this data base, whereas similar analysis (by this writer) of Ganguly and Kennedy's (1974) model (data base of 30 samples) reveals a 55 percent accounting of the total variance they observed in $RT \ln K_D$. The remaining 45 percent of variance is probably explained by (1) temperature differences among samples included in their data base, (2) the effects of variable Al^{3+}, Fe^{2+}, Fe^{3+}, and Ti^{4+} in biotite on K_D [see Goldman and Albee (1977)], and (3) the analytical uncertainty in determining Fe^{2+} and Fe^{3+} concentrations in biotites. The Montana model, on the other hand, is based on samples from two very small areas whose respective peak temperatures were probably uniform (see Dahl, 1979). Also, points (2) and (3) above are much less of a problem for the Montana clinopyroxenes, as they contain very low amounts of Na, Al^{3+}, Fe^{3+}, and Ti^{4+} (Dahl, 1977). Furthermore, mixing of Fe^{2+} and Mg in the clinopyroxenes is confined largely to a single site (*M1*), unlike in biotite. The remaining 11 percent of variance in the Montana model may be explained by (1) analytical error, (2) non-ideal mixing among Fe^{2+}, Mg, Ca, and Mn in clinopyroxenes, and (3) small yet variable amounts of Fe^{3+} among garnets. However, the small data base precludes meaningful consideration of more than the three independent variables.

The first three sets of interaction parameters w_{ij} given in Table 4 all correctly predict the effects of X^{Gar}_{Ca} and X^{Gar}_{Mn} on K_D, but the relatively low value of w_{FeMg} derived from the Montana data base suggests a lesser effect of X^{Gar}_{Fe} on K_D than that predicted by Ganguly's (1979) revised model. Furthermore, the low value and high uncertainty in w_{FeMg}, relative to the other w_{ij} computed from the Montana data base, indicate that variable X^{Gar}_{Fe} has a lesser effect on K_D than comparable variations in X^{Gar}_{Ca} or X^{Gar}_{Mn}. This conclusion is supported by a stepwise linear regression of $RT \ln K_D$ for the Montana data base. In this regression, variation in X^{Gar}_{Mn} alone is found to explain 33 percent of the variance observed in $RT \ln K_D$; X^{Gar}_{Mn} and X^{Gar}_{Ca} together explain 82 percent of the variance, and all three variables together account for 89 percent of the total variance. This result indicates that X^{Gar}_{Mn} is the most important variable affecting K_D in the Montana samples, whereas $X^{Gar}_{Fe} - X^{Gar}_{Mg}$ is the least important (of the three considered).

Data in Table 4 suggest that the value of w_{FeMg} may be temperature dependent. However, this observation contradicts Ganguly and Kennedy (1974), who concluded on the basis of thermodynamic and crystal-chemical reasoning that the w_{ij} for garnet should be insensitive to temperature. For equilibration temperatures greater than 675°C, I believe that only w_{FeMg} values significantly lower than 2710 cal/

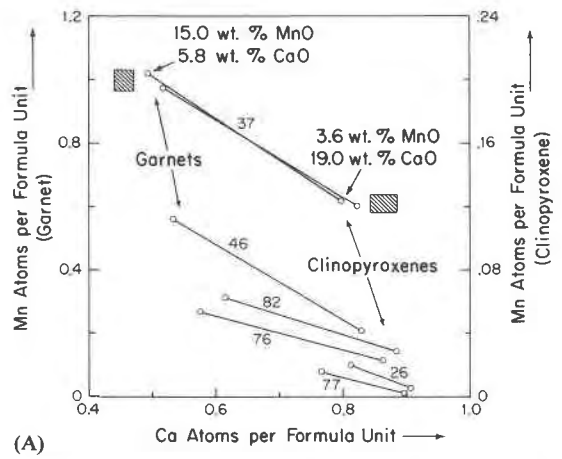

(A)

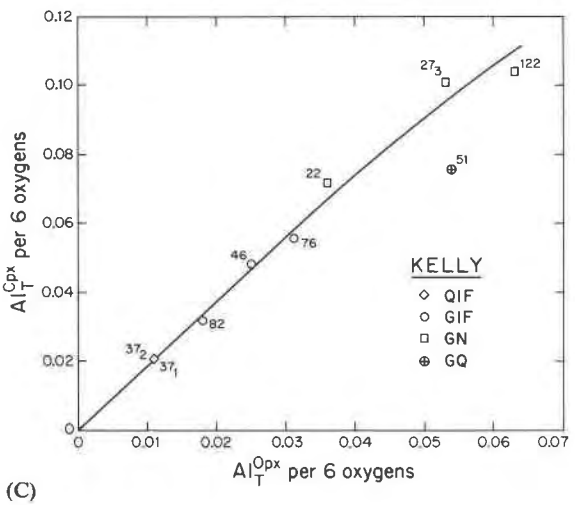

(C)

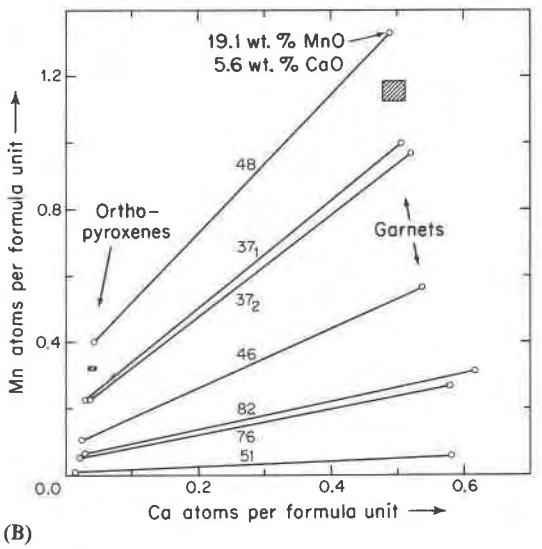

(B)

Fig. 3. (A, B) Partitioning of Mn and Ca between coexisting garnet and pyroxene in iron-formations (GIF, QIF) and mafic granulite gneiss (GN) from the Kelly area of the Ruby Range. Formula units based upon 12 oxygens for garnet and 6 oxygens for pyroxene. Error blocks (2σ) are given for the data points of sample RMK-37 (Fig. 3A) and sample RMK-48 (Fig. 3B). Errors for other data points are comparable. (C) Roozeboom plot of total Al (Al_T) between coexisting pyroxenes from the Kelly and Stone Creek areas. Lithologic abbreviations are defined in Table 1. RMK (or RMS) sample numbers are adjacent to tie lines and data points. All data points are computed from averaged electron microprobe analyses.

mole are realistic, for two reasons: (1) variable $X_{Fe}^{Gar} - X_{Mg}^{Gar}$ explains only a small percentage of the total variance observed in $RT \ln K_D$ for the Montana samples, and (2) neither experimental studies (*e.g.*, Råheim and Green, 1974) nor statistical studies (*e.g.*, Saxena, 1969) concerning P, T, or X dependences of K_D(Fe/Mg; gar–cpx) reveal significant effects of variable X_{Fe}^{Gar} or X_{Mg}^{Gar} on K_D.

There is, however, good agreement between Ganguly's (1979) w_{ij} for Ca and Mn and those calculated in this study, and despite the discrepancy in w_{FeMg} values both equations (9) and (10) closely approximate the thermal–compositional dependence of K_D(Fe/Mg; gar–cpx) for the Ruby Range samples.

Garnet–orthopyroxene

The exchange of Fe^{2+} and Mg between garnet and orthopyroxene can be represented by the equilibrium

$$\underset{\text{FS}}{FeSiO_3} + 1/3\underset{\text{PY}}{Mg_3Al_2Si_3O_{12}} \rightleftarrows \underset{\text{EN}}{MgSiO_3} + 1/3\underset{\text{ALM}}{Fe_3Al_2Si_3O_{12}} \qquad (11)$$

Treatment of this exchange equilibrium in a manner similar to that of the garnet–clinopyroxene equilibrium yields an expression analogous to equation (10) that approximates the thermal–compositional dependence of the distribution coefficient K_D(Fe/Mg; gar–opx). This expression is

$$RT \ln K_D = -\Delta G_T^P + sum(X) \qquad (12)$$

where $sum(X)$ is the sum of the three compositional terms in equation (10) and incorporates the same w_{ij} values derived earlier from the Montana garnet–clinopyroxene data base. The term ΔG_T^P is the Gibbs free energy change for equation (11) at the P and T of interest.

One limitation inherent in equation (12), in addition to those cited earlier for equation (10), is its failure to account for non-ideality of mixing between

Table 4. Thermal-compositional data bases and regressed thermochemical values from different studies

Parameter	Ganguly and Kennedy (1974)	Ganguly (1979)	This study	O'Neill and Wood (1979)
number of samples	30		13	
$(X_{Fe}-X_{Mg})^{Gar}$	0.348-0.665		0.303-0.592	
X^{Gar}_{Ca}	0.004-0.24		0.159-0.541	
X^{Gar}_{Mn}	0.04-0.27		0.012-0.322	
$T(^{\circ}C)$	630±40		745±50** 675±45***	1150±250
W_{FeMg}	2979±369	2710±200	1509±1392	195±430
$W_{MgCa}-W_{FeCa}$	4603±2117	3152±720	2810±954	2676±402
$W_{MgMn}-W_{FeMn}$	2308±1508	2600±850	2855±792	
ΔG^{7200}_{1018}		-1874±240*	-2482±845	

*The term $\Delta G(P,T)$ refers to the Fe-Mg exchange reaction (equation (2)). Values for $\Delta G(P,T)$ and the w_{ij} are expressed in cal and cal/mole, respectively, and quoted uncertainties reflect 95 percent confidence limits. *calculated in this study using data from Ganguly (1979) (see text for explanation). Temperature estimates for the Kelly (**) and Carter Creek (***) areas are from Dahl (1979).*

Fe^{2+} and Mg in the *M1* site of orthopyroxene; Saxena and Ghose (1971) reported a value of 1956 cal/mole (at 700°C) for the Fe–Mg interaction parameter for this site. However, site occupancies of Fe and Mg in the Montana orthopyroxenes were not determined in this study. Mixing between Fe^{2+} and Mg in these pyroxenes is probably further complicated by their high Mn^{2+} contents (Table 2). For these reasons, and given the small data base, compositional terms for orthopyroxene are not considered in equation (13), and the distribution coefficient K_D(Fe/Mg; gar–opx) is based on total Fe and Mg in orthopyroxene. The consequences of these simplifications are discussed further in this and later sections.

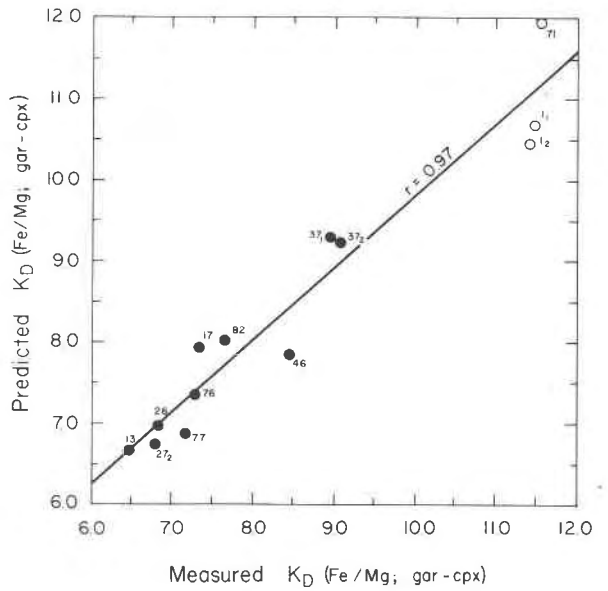

Fig. 4. Correlation between K_D(Fe/Mg; gar–cpx) values predicted from equation (10) and values measured in samples from the Ruby Range (see Table 5). RMK and RMC sample numbers are adjacent to data points. Solid circles represent Kelly samples; open circles represent Carter Creek samples.

A mean value for ΔG^P_T in equation (12) can be obtained from the difference between known values of $RT \ln K_D$ and $sum(X)$ for the nine garnet–orthopyroxene pairs from the Kelly area, using the same procedure described earlier for garnet–clinopyroxene pairs. For the Kelly area, the computed value of ΔG^{7200}_{1018} is −1391±288 cal (95 percent confidence limits). Equation (12) can now be rewritten in the form

$$RT \ln K_D = 1391 + 1509(X^{Gar}_{Fe} - X^{Gar}_{Mg}) + 2810(X^{Gar}_{Ca}) + 2855(X^{Gar}_{Mn}) \quad (13)$$

Table 5. Compositional effects on K_D (Fe,Mg) predicted by equation (10) for garnet–clinopyroxene pairs in samples from the Ruby Range

Sample	$1509(X_{Fe}-X_{Mg})^{Gar}$ (cal/mole)	+ $2810(X^{Gar}_{Ca})$ (cal/mole)	+ $2855(X^{Gar}_{Mn})$ (cal/mole)	= $Sum(X)$ (cal/mole)	K_D predicted	K_D measured
RMK-27_2	705	635	34	1374	6.73	6.80
RMK-13	598	717	40	1355	6.66	6.48
RMK-17	702	950	54	1706	7.93	7.33
RMK-77	646	697	74	1417	6.87	7.17
RMK-26	614	739	91	1444	6.97	6.84
RMK-76	782	523	248	1553	7.35	7.29
RMK-82	893	551	286	1730	8.02	7.65
RMK-46	687	483	517	1687	7.85	8.45
RMK-37_2	653	467	897	2017	9.25	9.08
RMK-37_1	663	447	919	2029	9.30	8.95
RMC-71	457	1520	217	2194	11.98	11.54
RMC-1_1	723	995	263	1981	10.69	11.47
RMC-1_2	658	992	288	1938	10.45	11.41

Table 6. Compositional effects on K_D (Fe,Mg) predicted by equation (13) for garnet–orthopyroxene pairs in samples from the Ruby Range

Sample	$1509(X_{Fe}-X_{Mg})^{Gar}$ (cal/mole)	+ $2810(X_{Ca}^{Gar})$ (cal/mole)	+ $2855(X_{Mn}^{Gar})$ (cal/mole)	= Sum(X) (cal/mole)	K_D predicted	K_D measured
RMK-27_3	690	511	51	1252	3.69	3.52
RMS-22	779	540	60	1379	3.93	3.65
RMK-51	539	511	60	1110	3.44	3.87
RMK-76	782	523	248	1553	4.29	4.37
RMK-82	893	551	286	1730	4.68	4.34
RMK-46	687	483	517	1687	4.58	4.96
RMK-37_2	653	467	897	2017	5.39	5.40
RMK-37_1	663	447	919	2029	5.42	5.79
RMK-48	489	455	1259	2203	5.91	5.61

This expression permits an independent check on the validity of the three compositional terms derived earlier, insofar as K_D(Fe/Mg; gar–opx) values predicted by equation (13) can be compared to values actually measured for the nine garnet–orthopyroxene-bearing samples from the Kelly area. Predicted and measured K_D values, as well as compositional trends in the garnets, are presented in Table 6. Linear regression of predicted *vs.* measured K_D values yields a line of slope 0.92 and a correlation coefficient r of 0.93. This regression is plotted in Figure 5. The near-unity slope and high level of correlation in Figure 5 not only corroborate the w_{ij} used in equations (10) and (12), but also suggest that any mixing terms for orthopyroxene in equation (12) have nearly constant or negligible value for the nine samples of the data base. Furthermore, the w_{ij} appear to be applicable beyond the X_{Mn}^{Gar} range of the original data base, to at least X_{Mn}^{Gar} equal to 0.441. This level of Mn content, found in sample RMK-48, is the highest yet reported in the literature for garnet coexisting with orthopyroxene (*cf.* Davidson and Mathison, 1973).

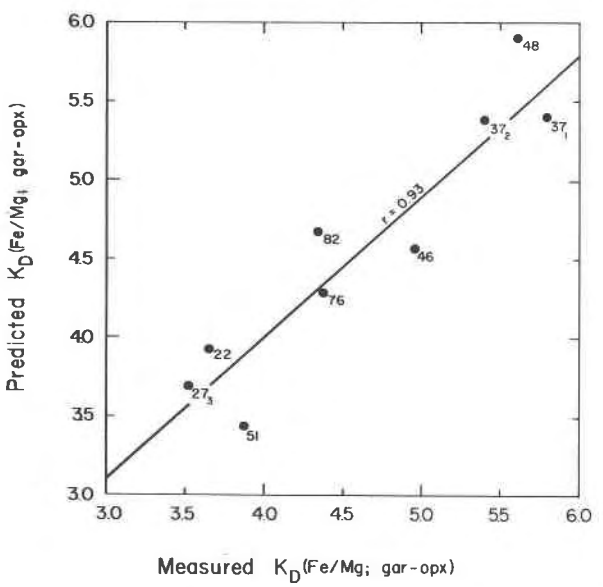

Fig. 5. Correlation between K_D(Fe/Mg; gar–opx) values predicted from equation (13) and values measured in samples from the Ruby Range (see Table 6). RMK (and RMS) sample numbers are adjacent to data points.

I conclude that equation (13) closely approximates the thermal–compositional dependence of K_D(Fe/Mg; gar–opx) for the Ruby Range samples. This dependence is comparable to that of garnet–clinopyroxene K_D values.

Similar analysis using Ganguly's (1979) interaction parameters in equation (13) yields a ΔG_{1018}^{7200} value of −896±425 cal for equation (11) (95 percent confidence limits); linear regression of predicted *vs.* measured K_D(Fe/Mg; gar–opx) values results in a line with a slope of only 0.70 and a correlation coefficient r of 0.85.

Accuracy of ΔG_T^P calculations

The ΔG_T^P values for garnet–pyroxene Fe–Mg exchange reactions, calculated from the thermodynamic models presented in earlier sections, vary widely from values calculated using thermochemical data in Robie *et al.* (1978), Helgeson *et al.* (1978), and Zen (1973). For example, for gar–cpx pairs [equation (2)], the model yielded $\Delta G_{1018}^{7200} \simeq \Delta G_{948}^{6200} = -2482\pm845$ cal. The published thermochemical data, on the other hand, when applied to the equation

$$\Delta G_T^P = \Delta H_{298}^\circ - T\Delta S_{298}^\circ + \int_{298}^{T} \Delta C_p^\circ dT - T\int_{298}^{T} \frac{\Delta C_p^\circ}{T} dT + \int_1^P \Delta V^\circ dP \qquad (14)$$

yield $\Delta G_{1018}^{7290} = -14018 \pm 4000$ cal and $\Delta G_{948}^{6200} = -13905 \pm 4000$ cal. Substitution of the latter values into

equation (10) yields metamorphic temperatures that are completely unreasonable for the Kelly area (*ca.* 3700°C!). It is highly unlikely that additional compositional terms (*e.g.*, for clinopyroxene) in equation (10) could account for the −11500 cal/mole that would be necessary in this case to render the equation a reliable temperature indicator, since (1) the sum of all compositional terms for garnet accounts for only 1000 to 2000 cal/mole (ee Table 5) and (2) the model presented earlier accounts for 89 percent of the compositional variance observed in $RT \ln K_D$. Thus, I conclude that the discrepancy in ΔG_T^P values is due at least partly to inaccuracies in some of the published enthalpy and entropy values for garnet and clinopyroxene end-members. For garnet–orthopyroxene pairs, the discrepancy is even greater, and the conclusion is the same.

The validity of the regressed ΔG_T^P values for equations (2) and (11) can be tested by determining the degree of internal consistency among K_D and ΔG_{1018}^{7200} values for gar–cpx, gar–opx, and cpx–opx Fe–Mg exchange equilibria. Because the cpx–opx exchange reaction

$$\underset{\text{FS}}{FeSiO_3} + \underset{\text{DI}}{CaMgSi_2O_6} \rightleftarrows \underset{\text{EN}}{MgSiO_3} + \underset{\text{HD}}{CaFeSi_2O_6} \quad (15)$$

is obtained by subtraction of equations (2) and (11), the ΔG_{1018}^{7200} values for the three equilibria must be related by

$$(\Delta G_{1018}^{7200})_{\text{gar–opx}} - (\Delta G_{1018}^{7200})_{\text{gar–cpx}} = (\Delta G_{1018}^{7200})_{\text{cpx–opx}}$$

$$(-1391 \pm 288 \text{ cal}) - (-2482 \pm 845 \text{ cal}) = (1091 \pm 893 \text{ cal}) \quad (16)$$

where $(\Delta G_{1018}^{7200})_{\text{cpx–opx}}$ refers to equation (15). We can state that

$$(\Delta G_T^P)_{\text{cpx–opx}} \simeq -RT \ln K_D(\text{Fe/Mg; cpx–opx}) \quad (17)$$

Now, if the calculated value of 1091 cal for $(\Delta G_{1018}^{7200})_{\text{cpx–opx}}$ in equation (17) is accurate, then the K_D(Fe/Mg; cpx–opx) value we can compute from this equation must agree with K_D values observed in natural assemblages at 1018°K (745°C). Indeed, equation (17) yields a K_D value of 0.58, which compares with the mean K_D(Fe/Mg; cpx–opx) value of 0.57 for nine pyroxene pairs reported in Table 2. This internal consistency corroborates not only the three ΔG_T^P values, but also the validity of equations (10) and (13) and the basic correctness of the interaction parameters w_{ij} contained therein.

However, internal consistency of ΔG_T^P values calculated using Ganguly's (1979) mixing parameters can also be demonstrated by equations (16) and (17). In this case, the computed value of ΔG_{1018}^{7200} for equation (15) is 1042 cal [*i.e.*, −896 cal − (−1938 cal)], and for K_D (Fe/Mg; cpx–opx) a value of 0.60 is obtained. Thus I conclude that only the *difference* in calculated ΔG_T^P values for equations (2) and (11) can truly be tested by the above method, and *not* their absolute values.

Applications to geothermometry

Garnet–clinopyroxene

Measured ln K_D (Fe/Mg; gar–cpx) and calculated *sum*(X) values from Table 5 are plotted in Figure 6. The line representing garnet–clinopyroxene pairs from the Kelly area defines a 745°C isotherm. Because the Carter Creek samples plot at significantly higher K_D than the Kelly samples at equivalent *sum*(X) values, the former probably represent part of a lower-temperature isotherm. This conclusion is consistent with (1) the known divergence of K_D (Fe/Mg; gar–cpx) from unity with declining temperature (*e.g.*, see Banno, 1970, and Råheim and Green, 1974) and (2) the lower peak temperature estimate of 675±45°C inferred for the Carter Creek area by Dahl (1979).

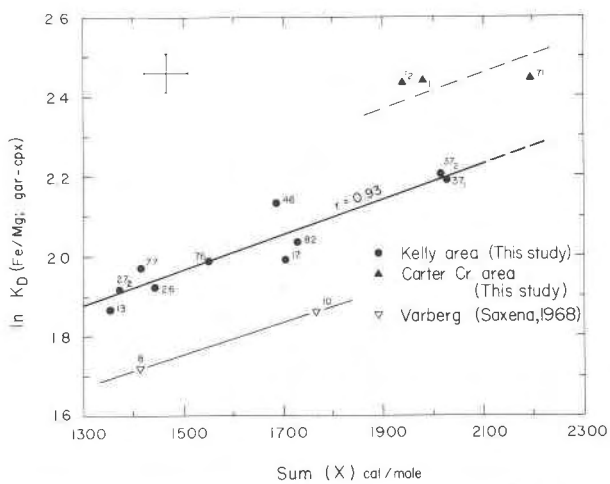

Fig. 6. Variations in ln K_D(Fe/Mg; gar–cpx) as a function of *sum*(X) [as defined in equation (10)] for gar–cpx pairs in samples from the Ruby Range and from Varberg, Sweden (Saxena, 1968; only unzoned samples plotted). Kelly and Carter Creek samples define two distinct isotherms for the Ruby Range, with the Carter Creek samples indicating the lower apparent temperature (higher K_D). $K_D = (\text{Fe/Mg})^{\text{Gar}}/(\text{Fe/Mg})^{\text{Cpx}}$. Total Fe used to calculate K_D except for sample RMC-71, whose garnets contain relatively high Fe^{3+}. Cross in upper left represents uncertainties (2σ) in the data points for sample RMK-37; uncertainties in all other Ruby Range data points are smaller.

Similar reasoning suggests that the charnockites from Varberg, Sweden (Saxena, 1968), reached metamorphic temperatures higher than the 745±50°C for the Kelly area. Indeed, Saxena (1976, p. 651) has estimated temperatures of 801±60°C for the Varberg area, using pyroxene geothermometry.

Because the Carter Creek, Kelly, and Varberg garnet–clinopyroxene pairs define isotherms or parts of isotherms whose temperatures have been independently estimated, Figure 6 provides the basis for geothermometry in other upper-amphibolite to granulite facies terrains. As more chemical data from other localities become available, additional isotherms can be added to Figure 6.

Reconstruction (not shown) of Figure 6, using instead Ganguly's (1979) mixing parameters for garnet, results in no change in the relative positions of isotherms and data points shown.

Figure 6 illustrates the marked effects of composition on K_D (Fe/Mg; gar–cpx) and underscores the danger inherent in the application of any mineral-pair geothermometer without due consideration of this potential complication. For example, routine application of Råheim and Green's (1974) calibrated garnet–clinopyroxene geothermometer to the Kelly area results in temperatures ranging from 653°C [low K_D, low *sum*(X)] down to 584°C [high K_D, high *sum*(X)]. These estimates are low and falsely indicate variations in peak temperature for the Kelly area. Application of this calibration to the Kelly area is valid only if, along the Kelly isotherm, a range of K_D values is chosen that corresponds to the range of *sum*(X) values characteristic of Råheim and Green's experimentally-derived garnets. Their chemical analyses indicate a *sum*(X) value of 379±200 cal/mole (95 percent confidence limits), which, upon substitution into the line equation for the Kelly isotherm

$$\ln K_D = 0.00044\ sum(X) + 1.30010 \qquad (18)$$

yields a compositionally corrected K_D value of 4.34±0.40. This value, in turn, when applied to Råheim and Green's calibration, gives a temperature estimate of 752±44°C (at P = 7200±1200 bars) for the Kelly area. This estimate is concordant with the independent estimate of 745±50°C reported earlier. Thus, by correcting for compositional effects on K_D, a reliable temperature estimate is obtained. Clearly, the application of this technique to other localities requires samples sufficient to define adequately an isothermal line equation.

Yet a third approach to geothermometry involves solution of equation (10) for T. A pressure term can be incorporated by first evaluating the volume term in equation (14), using garnet–clinopyroxene volume data from Takahashi and Liu (1970) and Rutstein and Yund (1969). For a load pressure of 7200 bars (Kelly area), the volume term for the Fe–Mg exchange reaction [equation (2)] equals −158 cal. Thus, included in the calculated ΔG^{7200}_{1018} value of −2482 cal is −2324 cal (ΔG°_{T}) and a volume term of −158 cal [*i.e.*, $-0.022P$(bars) for the Kelly area]. Equation (10) can now be rewritten in the form

$$T(°\mathrm{K}) = [2324 + 0.022P(\mathrm{bars}) + 1509(X^{Gar}_{Fe} - X^{Gar}_{Mg}) + 2810(X^{Gar}_{Ca}) + 2855(X^{Gar}_{Mn})]/(1.987 \ln K_D) \qquad (19)$$

Recent gar–cpx geothermometers of Ganguly (1979) and Saxena (1979) work very well for peridotites, high-temperature eclogites, and upper-granulite facies rocks. However, both methods yield temperatures for the Kelly and Carter Creek areas that are significantly higher than the consensus estimates reported earlier (see Table 7). Equation (19) may find general application to (1) upper-amphibolite and lower-granulite facies rocks in which pyroxenes are low in Na and Al and (2) rocks that are high in Mn. Reliable application of equation (19) to other localities is based upon the assumption that ΔG°_{T} is nearly constant over a broad temperature range. This assumption is reasonable because (1) the heat capacity integrals in equation (14) virtually cancel out, regardless of temperature, and (2) the value of ΔS°_{298} for equation (2) is nearly zero; a value of +1.013 cal/°K is obtained using S°_{298} data from Robie *et al.* (1978)

Table 7. Peak metamorphic temperature estimates for the Ruby Range

Sample	Ganguly (1979) T°C	Saxena (1979) T°C	this paper (eqn. 10) T°C	Råheim and Green (1974) T°C	
RMK-27$_2$	811	809	739	643	Kelly area
RMK-13	832	792	760	653	
RMK-17	833	827	785	627	
RMK-77	810	812	723	632	
RMK-26	827	800	755	641	
RMK-76	803	791	749	628	
RMK-82	799	803	769	618	
RMK-46	791	836	710	598	
RMK-37$_2$	809	790	753	584	
RMK-37$_1$	811	795	763	587	
mean T =	813±14	806±16	751±22	621±24	
RMC-71	811	671	685	536	Carter Creek area
RMC-1$_1$	761	671	643	536	
RMC-1$_2$	764	674	636	537	
mean T =	779±28	672±2	655±27	536±1	

Equation (18) yields an independent temperature estimate of 752±22°C for the Kelly area. Consensus estimates for the Ruby Range are 745±50°C (Kelly) and 675±45°C (Carter Creek). (Dahl, 1979).

and Helgeson *et al.* (1978). If this value is correct, then a 100°K change in temperature results in only a 101 cal (or 4.6 percent) change in ΔG_T° (= −2324 cal).

Garnet–orthopyroxene

Measured ln K_D (Fe/Mg; gar–opx) and calculated *sum*(X) values for garnet–orthopyroxene pairs from the Kelly area (Table 6) and other localities are plotted in Figure 7. The relative positions of the data points representative of these localities should, in principle, permit tentative determination of their relative metamorphic temperatures. Line B represents the Kelly isotherm (745±50°C). Line C is an isotherm defined by compositions in garnet–orthopyroxene–cordierite gneisses from a 43-km² area in the Guayana Shield region, Venezuela (Dougan, 1974). The proximity of lines B and C suggests little or no temperature difference between the Kelly and Venezuelan localities. On the basis of several geothermometers, Dougan inferred a metamorphic temperature of 760±40°C for the Venezuelan locality, which indeed is concordant with estimates for the Kelly area.

The three points comprising group D in Figure 7 define part of an isotherm for highly metamorphosed iron-formations from a small area near Quairading, Western Australia (Davidson and Mathison, 1973). Group D plots at significantly lower ln K_D than line B, suggesting that peak temperatures in the Quairading area exceeded 745°C. To test this conclusion, coexisting pyroxenes from the two localities are compared in the pyroxene quadrilateral shown in Figure 8. The Quairading pyroxenes plot at a higher temperature (*ca.* 800°C) on the pyroxene solvus than those from the Kelly area. Thus, two independent methods result in the same relative temperature estimate for the two localities.

Line E in Figure 7 represents core compositions for garnet–orthopyroxene–cordierite-bearing anorthosites from a 10000-km² area in the Nain Province, Labrador (Berg, 1975, 1977). The eight samples included in Figure 7 represent those for which Berg obtained his highest (concordant) garnet–cordierite and garnet–biotite temperatures—858±60°C. Lines E and B barely overlap, so that thermal comparison of the Kelly and Nain areas is possible only at *sum*(X) values near 1100 cal/mole. The lower ln K_D for line E at this *sum*(X) is consistent with the higher temperatures inferred by Berg for the Nain area.

The five scattered points labelled group A in Figure 7 represent rim compositions for some of the eight high-temperature Nain samples. Berg concluded, on the basis of antithetic Fe–Mg profiles at grain edges of both garnets and coexisting orthopyroxenes, that the rim K_D values reflect retrograde metamorphic conditions; for these conditions, he estimated temperatures in the range of 547±25°C. It is not surprising, therefore, that the group A data points cluster well above all isotherms in Figure 7.

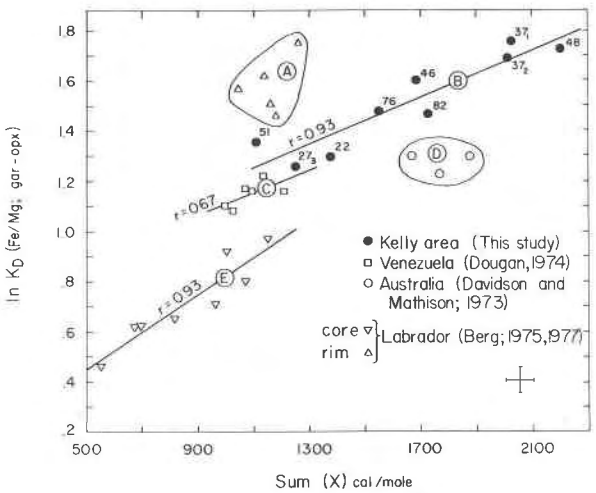

Fig. 7. Dependence of K_D(Fe/Mg; gar–opx) on *sum*(X) [as defined in equation (13)] for garnet–orthopyroxene pairs from several localities. Labeled lines delineate trends for each locality. Lines B, C, and E represent distinct isotherms; groups A and D represent parts thereof (see text). Lower K_D isotherms probably represent higher metamorphic temperatures. $K_D = (Fe/Mg)^{Gar}/(Fe/Mg)^{Opx}$. Ruby Range samples are all from the Kelly area except for sample RMS-22, which is from Stone Creek. Total Fe was used in the K_D calculations for Labrador and Ruby Range samples, except for sample RMK-48. All other K_D values were corrected for Fe^{3+} in the published analyses. Cross in lower right represents uncertainties (2σ) in the data point for sample RMK-48; uncertainties in all other data points in line B are smaller.

Reconstruction (not shown) of Figure 7, using instead Ganguly's (1979) mixing parameters for garnet, results in no change in the relative positions of isotherms and data points shown, although the slope for line E parallels the other lines better.

The ΔG_T° component of ΔG_T^P in equation (13) is not constant over a broad range of temperature, inasmuch as a ΔS_{298}° value of +13.9 cal/°K is obtained for equation (13), using S_{298}° data from Robie *et al.* (1978) and Helgeson *et al.* (1978). This shortcoming precludes the use of equation (13) as an absolute geothermometer, but does not affect the use of K_D (Fe/Mg; gar–opx) as a relative geothermometer, as in Figure 7.

Limitations

Figures 6 and 7 represent attempts to normalize the compositional effects on ln K_D (Fe/Mg; gar–cpx) and ln K_D (Fe/Mg; gar–opx) so that meaningful geothermometry can be done. However, there are several limitations inherent in their application. First, thermal comparisons between areas may be invalid unless their respective isotherms (or portions thereof) overlap in *sum*(X) values. Thus in Figure 7 direct comparison of lines C or E with group D is not advisable.

Second, in both figures the effects of load pressure P on ln K_D are ignored. All samples plotted in these figures were metamorphosed to pressures in the range 4.5–8.5 kbar, according to estimates available from the literature. Råheim and Green's (1974) experiments suggest that an increase in P from 4.5 to 8.5 kbar results in a 4 percent increase in ln K_D (Fe/Mg; gar–cpx) at 750°C. Thus, normalization for pressure effects in Figures 6 and 7 may result in slight shifts among the isotherms, but these shifts are probably not significant enough to alter the relative temperatures inferred earlier.

Third, and perhaps most important, the reliability of Figures 6 and 7 is contingent on the inherent correctness of the respective thermodynamic models [*i.e.,* equations (10) and (13)]. Although the models do account for most of the variance in RT ln K_D observed for the Montana garnet–pyroxene pairs, they do not account for the possible effects of variable Fe^{3+} in garnet or variable Na, Al, Ca, or Mn in pyroxene; nor do they account for the non-ideality of mixing between Fe and Mg in pyroxene *M1–M2*

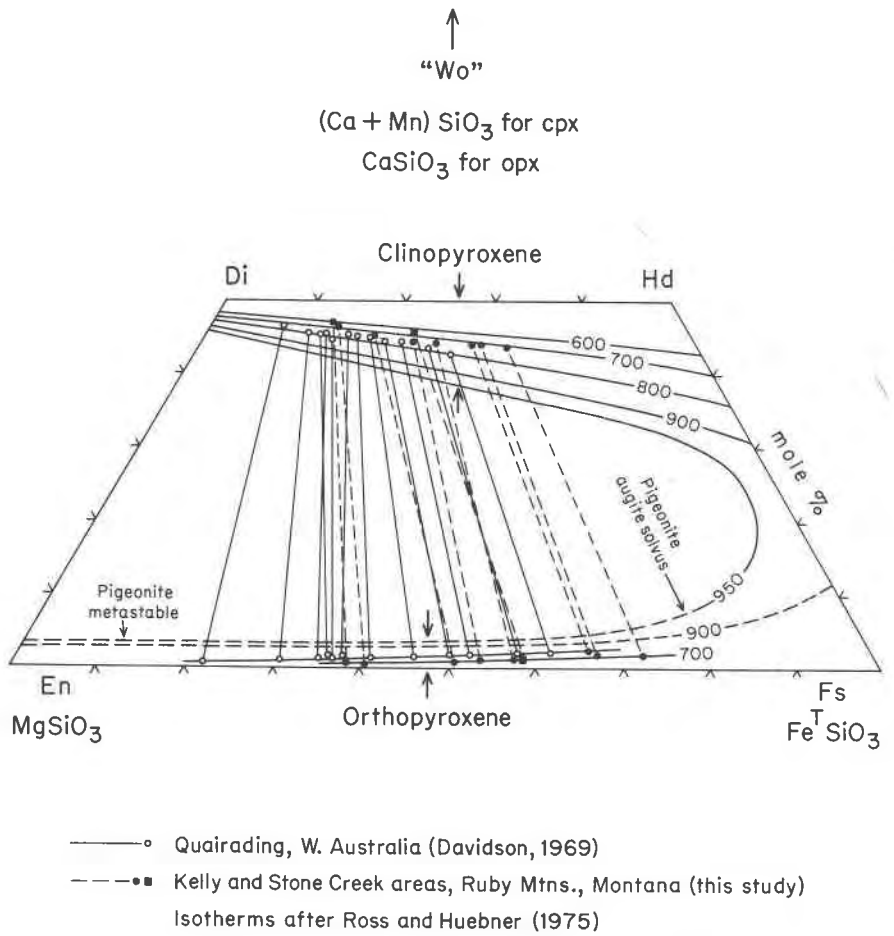

Fig. 8. Pyroxene pairs from the Ruby Range (single, not averaged, analyses plotted) compared with those from the Quairading district of Western Australia (Davidson, 1969). Superimposed is the experimentally-determined pyroxene solvus of Ross and Huebner (1975). It is assumed that Ca and Mn occupy the *M2* site of clinopyroxene; the relative position of the two curves is not changed, however, if Mn is plotted with Fe^T (total iron) instead of with Ca. Ross and Huebner place a ±100°C uncertainty on temperatures estimated by their method.

sites. These limitations can be removed only when larger data bases incorporating broad variations in diverse components are studied. Such data bases are most likely to be found in highly metamorphosed terrains containing garnet–pyroxene pairs in diverse lithologies.

Conclusions

The Ruby Range, southwestern Montana, has been used as a natural laboratory to model the *P–T–X* dependences of garnet–pyroxene K_D (Fe/Mg) values. The major conclusions of this study are summarized below.

(1) Petrographic and geothermometric data indicate that peak metamorphic *P–T* conditions for the Kelly and Carter Creek areas were 7.2±1.2 kbar, 745±50°C and 6.2±1.2 kbar, 675±45°C, respectively.

(2) The excellent correlation between measured garnet–clinopyroxene K_D values and those predicted using Ganguly's (1979) garnet mixing parameters (Table 3) supports the general validity of his parameters and confirms the temperature difference inferred between the Kelly and Carter Creek areas. The correlation also indicates that within a given area, garnet–pyroxene pairs in diverse lithologies last equilibrated at the same or nearly the same temperature.

(3) Garnet–pyroxene K_D (Fe/Mg) values are highly dependent on composition—particularly on X_{Mn}^{Gar} and X_{Ca}^{Gar}. Meaningful geothermometry, therefore, requires that such compositional effects be taken into account, such as is done in equations (9), (10), (13), (18), and (19), and in Figures 6 and 7.

(4) Multiple linear regression of the Ruby Range data base in conjunction with known temperatures of metamorphism yields new and internally consistent values of $\Delta G_{948-1018}^{6200-7200}$ for Fe^{2+}–Mg exchange reactions involving garnet–clinopyroxene [equation (2)], garnet–orthopyroxene [equation (11)], and clinopyroxene–orthopyroxene [equation (15)]. Because all three values are much closer to zero than values obtained using thermochemical data from Robie *et al.* (1978), Helgeson *et al.* (1978), and Zen (1973), they are more compatible with the known dependences of K_D values on temperature.

The regression also yields new values for the garnet mixing parameters (Table 4). These results corroborate those reported by Ganguly (1979), except that the w_{FeMg} inferred in my study is intermediate to Ganguly's and O'Neill and Wood's (1979) values. This discrepancy may reflect a temperature dependence for this parameter.

(5) Equation (19) may be applied as a geothermometer to upper-amphibolite and lower-granulite facies rocks or to rocks high in Mn. Both Ganguly's (1979) and Saxena's (1979) garnet–clinopyroxene thermometers yield high temperatures for such rocks (Table 7), although they appear to work extremely well for eclogites, peridotites, and upper-granulite facies rocks.

(6) Larger data bases from the Ruby Range and other terrains are required in order to evaluate the possible effects on K_D of components other than those considered in this study. Such components include Fe^{3+} in garnet and Na, Al, Ca, and Mn in pyroxene. Also, an accounting for the non-ideal mixing of Fe and Mg in pyroxene *M1–M2* sites is desired. Despite these omissions, the thermodynamic models presented in this paper explain up to 89 percent of the variance actually observed in K_D (Fe/Mg) values for garnet–pyroxene-bearing mafic gneisses and iron-formations from the Ruby Range.

Acknowledgments

Part of this work was included in a doctoral dissertation presented to Indiana University. I am most grateful to Dr. C. Klein, Jr., for his support and advice during this investigation. Drs. R.G. Craig, H.L. James, D.F. Palmer, D.G. Towell, and R.P. Wintsch read earlier versions of the manuscript and made many helpful suggestions. Special thanks are due to Drs. S.K. Saxena and J.M. Ferry for their careful reviews, which greatly improved the quality of the manuscript. I thank Mr. Kevin Zak for drafting, and Lynn V. Dahl and Susan B. Hoak for typing of the manuscript.

Field and laboratory support for this study were provided by NSF grants DES-72-01665 and EAR-76-11740 to Professor Klein. The electron microprobe was obtained on NSF grant GA-37109 to Professor Klein, with joint funds from the Indiana University Foundation.

References

Banno, S. (1970) Classification of eclogites in terms of physical conditions of their origin. *Phys. Earth Planet. Interiors, 3,* 405–421.

Berg, J. H. (1975) Quantitative regional geobarometry of the anorthositic Nain complex (abstr.). *Int. Conf. Geothermometry and Geobarometry,* The Pennsylvania State University, University Park, Pennsylvania

——— (1977) Regional geobarometry in the contact aureoles of the anorthositic Nain complex. *J. Petrol. 18,* 399–430.

Chatterjee, N. D. and W. Johannes (1974) Thermal stability and standard thermodynamic properties of synthetic $2M_1$-muscovite, $KAl_2AlSi_3O_{10}(OH)_2$. *Contrib. Mineral. Petrol., 48,* 89–114.

Cordua, W. S. (1973) *Precambrian Geology of the Southern Tobacco Root Mountains, Madison Co., Montana.* Ph.D. Thesis, Indiana University, Bloomington, Indiana.

Dahl, P. S. (1977) *The Mineralogy and Petrology of Precambrian Metamorphic Rocks from the Ruby Mountains, Southwestern*

Montana. Ph.D. Thesis, Indiana University, Bloomington, Indiana.

——— (1979) Comparative geothermometry based on major-element and oxygen isotope distributions in Precambrian metamorphic rocks from southwestern Montana. *Am. Mineral., 64,* 1280–1293.

Davidson, L. R. (1968) Variation in ferrous iron–magnesium distribution coefficients of metamorphic pyroxenes from Quairading, Western Australia. *Contrib. Mineral. Petrol., 19,* 239–259.

——— (1969) Fe^{++}–Mg^{++} distribution in coexisting metamorphic pyroxenes. *Spec. Publ. Geol. Soc. Aust., 2,* 333–339.

——— and C. I. Mathison (1973) Manganiferous orthopyroxenes and garnets from metamorphosed iron formations of the Quairading district, Western Australia. *Neues Jahrb. Mineral. Monatsh.,* 47–57.

Dougan, T. W. (1974) Cordierite gneisses and associated lithologies of the Guri area, Northwest Guayana Shield, Venezuela. *Contrib. Mineral. Petrol., 46,* 169–188.

Friberg, L. M. (1976) *Petrology of a Metamorphic Sequence of Upper-amphibolite Facies in the Central Tobacco Root Mountains, Southwestern Montana,* Ph.D. Thesis, Indiana University, Bloomington, Indiana.

Ganguly, J. (1979) Garnet and clinopyroxene solid solutions, and geothermometry based on Fe–Mg distribution coefficient. *Geochim. Cosmochim. Acta, 43,* 1021–1029.

——— and G. C. Kennedy (1974) The energetics of natural garnet solid solution. I. Mixing of the aluminosilicate end-members. *Contrib. Mineral. Petrol., 48,* 137–148.

Garihan, J. M. (1979) Geology and structure of the central Ruby Range, Madison County, Montana. *Bull. Geol. Soc. Am., 90,* 695–788.

Giletti, B. J. (1966) Isotopic ages from southwestern Montana. *J. Geophys. Res., 71,* 4029–4036.

Goldman, D. S. and A. L. Albee (1977) Correlation of Mg/Fe partitioning between garnet and biotite with $^{18}O/^{16}O$ partitioning between quartz and magnetite. *Am. J. Sci., 277,* 750–767.

Guggenheim, E. A. (1967) *Thermodynamics.* North-Holland, Amsterdam.

Heinrich, E. W. (1960) Pre-Beltian geology of the Cherry Creek and Ruby Mountains areas, southwestern Montana. *Mont. Bur. Mines and Geol. Mem., 38,* 15–40.

Helgeson, H. C., J. M. Delany, H. W. Nesbitt and D. K. Bird (1978) Summary and critique of the thermodynamic properties of rock-forming minerals. *Am. J. Sci., 278-A,* 1–229.

Holdaway, M. J. (1971) Stability of andalusite and the aluminum silicate phase diagram. *Am. J. Sci., 271,* 97–131.

James, H. L. and C. E. Hedge (1980) Age of the basement rocks of southwest Montana. *Geol. Soc. America Bull., Part I, 91,* 11–15.

——— and K. L. Wier (1972a) Geologic map of the Kelly iron deposit. *U.S. Geol. Surv. Misc. Field Studies Map MF-349.*

——— and ——— (1972b) Geologic map of the Carter Creek iron deposit. *U.S. Geol. Surv. Field Studies Map MF-359.*

———, ——— and K. W. Shaw (1969) Map showing lithology of Precambrian rocks in the Christensen Ranch and adjacent quadrangles, Madison and Beaverhead Counties, Montana. *U.S. Geol. Surv. Open-File Report.*

Kerrick, D. M. (1972) Experimental determination of muscovite + quartz stability with $P_{H_2O} < P_{total}$. *Am. J. Sci., 272,* 946–959.

——— and L. S. Darken (1975) Statistical thermodynamic models for ideal oxide and silicate solid solutions, with application to plagioclase. *Geochim. Cosmochim. Acta, 39,* 1431–1442.

Klein, C., Jr. (1974) Greenalite, stilpnomelane, minnesotaite, crocidolite, and carbonates in a very low grade metamorphic Precambrian iron-formation. *Can. Mineral., 12,* 475–498.

Okuma, A. F. (1971) *Structure of the Southwestern Ruby Range Near Dillon, Montana.* Ph.D. Thesis, The Pennsylvania State University, University Park, Pennsylvania.

O'Neill, H. St.C. and B. J. Wood (1979) An experimental study of Fe–Mg partitioning between garnet and olivine and its calibration as a geothermometer. *Contrib. Mineral. Petrol., 70,* 59–70.

Råheim, A. and D. H. Green (1974) Experimental determination of the temperature and pressure dependence of the Fe–Mg partition coefficient for coexisting garnet and clinopyroxene. *Contrib. Mineral. Petrol., 48,* 179–203.

Robie, R. A., B. S. Hemingway and J. R. Fisher (1978) Thermodynamic properties of minerals and related substances at 298.15 K and 1 bar (10^5 pascals) pressure and at higher temperatures. *U.S. Geol. Surv. Bull. 1452.*

Ross, M. and J. S. Huebner (1975) A pyroxene geothermometer based on composition–temperature relationships of naturally occurring orthopyroxene, pigeonite, and augite (abstr.). *Int. Conf. Geothermometry and Geobarometry,* The Pennsylvania State University, University Park, Pennsylvania.

Rutstein, M. S. and R. A. Yund (1969) Unit-cell parameters of synthetic diopside–hedenbergite solid solutions. *Am. Mineral., 54,* 238–245.

Saxena, S. K. (1968) Distribution of iron and magnesium between coexisting garnet and clinopyroxene in rocks of varying metamorphic grade. *Am. Mineral., 53,* 2018–2024.

——— (1969) Silicate solid solutions and geothermometry. 4. Statistical study of chemical data on garnets and clinopyroxene. *Contrib. Mineral. Petrol., 23,* 140–156.

——— (1976) Two-pyroxene geothermometer: a model with an approximate solution. *Am. Mineral., 61,* 643–652.

——— (1979) Garnet–clinopyroxene geothermometer. *Contrib. Mineral. Petrol., 70,* 229–235.

——— and S. Ghose (1971) Mg^{2+}–Fe^{2+} order–disorder and the thermodynamics of the orthopyroxene crystalline solution. *Am. Mineral., 56,* 532–559.

Takahashi, T. and L. G. Liu (1970) Compression of ferromagnesian garnets and the effect of solid solutions on the bulk modulus. *J. Geophys. Res., 71,* 5757–5766.

Wintsch, R. P. (1975) Solid–fluid equilibria in the system $KAlSi_3O_8$–$NaAlSi_3O_8$–Al_2SiO_5–SiO_2–H_2O–HCl. *J. Petrol., 16,* 57–79.

Zen, E-an (1973) Thermochemical parameters of minerals from oxygen-buffered hydrothermal equilibrium data: method, application to annite and almandine. *Contrib. Mineral. Petrol., 39,* 65–80.

Manuscript received, August 4, 1978;
accepted for publication, March 14, 1980.

American Mineralogist, Volume 65, pages 867–884, 1980

Structure and redox equilibria of iron-bearing silicate melts

BJØRN O. MYSEN, FRIEDRICH SEIFERT[1] AND DAVID VIRGO

Geophysical Laboratory, Carnegie Institution of Washington
Washington, D.C. 20008

Abstract

Redox equilibria and coordination states of iron in silicate melts have been determined with Mössbauer spectroscopy. The anionic structure of the silicate network of the melts has been determined with laser Raman spectroscopy.

Mössbauer spectroscopic data indicate that in all quenched melts in the system Na_2O–FeO–Fe_2O_3–SiO_2 at 1 atm pressure, ferric iron is in tetrahedral coordination, probably as an $NaFeO_2$ complex. For example, melt of $NaFe^{3+}Si_2O_6$ composition quenched from 1400°C has a three-dimensional network structure. In all melts, the Fe^{2+} is octahedrally coordinated with oxygen.

Both Fe^{3+} and Fe^{2+} are network modifiers in the system CaO–MgO–FeO–Fe_2O_3–SiO_2, probably because $CaFe_2O_4$ and $MgFe_2O_4$ complexes are not stable in molten silicates. Only alkali metals can stabilize ferric iron in tetrahedral coordination.

Quenched melts along joins such as Na_2SiO_3–$NaFeSi_2O_6$ become progressively more polymerized as the acmite content of the system increases. Under $f(O_2)$ conditions more reducing than that of air, $Fe^{2+}/\Sigma Fe$ of the melts also increases with increasing acmite content (increasing degree of polymerization) of the melt. At fixed bulk composition iron-bearing melts of alkali silicates become depolymerized with decreasing $f(O_2)$ because $NaFeO_2$ complexes in the silicate network are transformed to $Fe^{2+}O_6^{10-}$ octahedra, whereby ferrous iron becomes a network modifier.

The Raman spectra are interpreted to suggest that the anionic structure of quenched metasilicate melts on the join $CaSiO_3$–$MgSiO_3$ predominantly consists of three structural units—separate SiO_4^{4-} tetrahedra, $Si_2O_5^{2-}$ and $Si_2O_6^{4-}$ units. The proportions of SiO_4^{4-} and $Si_2O_5^{2-}$ units increase relative to that of $Si_2O_6^{4-}$ units as the Ca/(Ca + Mg) of the melt increases. In melts on this join with 5 mole % $FeSiO_3$ component added, the $Fe^{2+}/\Sigma Fe$ decreases with increasing Ca/(Ca + Mg). This decrease is related to the increased degree of proportionation of the $Si_2O_6^{4-}$ units to SiO_4^{4-} and $Si_2O_5^{2-}$ units with increasing Ca/(Ca + Mg).

Provided that sufficient alkali metal is available in rock-forming silicate melts for local charge balance of Fe^{3+}, the ferric iron will be in the network. A progressive decrease of M^+/M^{2+} of a magma (as a result of fractional crystallization, for example) will result in ferric iron shifting from IV to VI coordination, thus changing the anionic structure of the melt. This change will also change some properties of the melt such as viscosity and density and the activity coefficients of trace elements.

Introduction

The redox ratio of iron in rock-forming silicate melts is often used as an indicator of petrogenetic history (*e.g.*, Fudali, 1965). Its partitioning behavior between melts and crystals has also been used to deduce the petrogenetic history of basaltic and derivative melts (Osborn, 1959, 1962, 1977; Carmichael, 1967; Buddington and Lindsley, 1964; Roeder and Emslie, 1970).

Recent experimental work has been devoted to determining the influence of both intensive and extensive variables on the redox ratio of iron in silicate melts (Lauer, 1977; Lauer and Morris, 1977; Schreiber *et al.*, 1978; Mysen and Virgo, 1978). The problem is complex because iron may not simply respond to variations in melt structure; rather it may affect

[1] Present address: Mineralogisch-Petrographisches Institut und Museum der Universität Kiel, Olshaussenstrasse 40–60, 2300 Kiel, West Germany.

0003–004X/80/0910–0867$02.00

the melt structure in important ways. Furthermore, the iron component in a melt can play a dual role because Fe can be both tetrahedrally and octahedrally coordinated. The structural role of iron is controlled by an involved interrelationship between degree of polymerization of the host, types of cations present, amount of iron present and its oxidation state (Waff, 1977). In an attempt to understand these problems, a study of the anionic structure of quenched Fe-bearing silicate melts has been undertaken. In this report the structural role of iron as a function of oxygen fugacity and bulk composition of the melt is emphasized.

Experimental techniques

Bulk compositions were chosen to determine the relations between redox states of iron and the ratio of nonbridging to bridging oxygen in the melt (NBO/BO) and the effect of different modifying cations on the structural role of ferric and ferrous iron. Such an effect is most conveniently studied in systems like Na_2O–FeO–Fe_2O_3–SiO_2(NFFS) and CaO–MgO–FeO–Fe_2O_3–SiO_2 (CMFFS) because structural data on melts in portions of these systems are already available (Brawer and White, 1975, 1977; Etchepare, 1972; Brown *et al.*, 1978; Mysen and Virgo, 1978, in preparation; Seifert *et al.*, 1979a,b; Mysen *et al.*, 1979; Virgo *et al.*, 1980). The NBO/BO varies as a systematic function of Na content of melts on the join Na_2O–SiO_2, for example (Brawer and White, 1975). It is also known that the anionic structure of quenched metasilicate melts is similar for a larger variety of network-modifying cations (Brawer and White, 1975, 1977; Verweij and Konijnendijk, 1976; Virgo *et al.*, 1980; Mysen *et al.*, 1980).

The starting materials were prepared from spectroscopically pure (Johnson and Matthey) SiO_2, Fe_2O_2, MgO, $CaCO_3$, and reagent grade Na_2CO_3.

The mixtures, (10–30 mg) were held at 1400–1585°C as beads on the Pt-wire loops in air or in a gas mixing furnace for time periods ranging from 6 to 1/2 hr, depending on the temperature of the experiment. Mysen and Virgo (1978) determined redox ratios of iron in melts on the join $NaAlSi_2O_6$–$NaFe^{3+}Si_2O_6$ as a function of time at 1450°C, and found that at that temperature a sample of about 50 mg would equilibrate with the surrounding atmosphere in about 1/2 hr. The present samples generally are less viscous than those studied by Mysen and Virgo. It is likely, therefore, that >1/2 hr run durations are sufficient to attain equilibrium.

The samples are quenched in air, mercury, or liquid nitrogen to produce glasses of the appropriate compositions. The compositions given here are nominal values.

The Mössbauer spectroscopic techniques were identical with those of Mysen and Virgo (1978). Except for the magnetic spectra (see below), a maximum of three lines were visually resolved when both ferric and ferrous iron were present in the quenched glasses, and only up to three lines of Lorentzian shape were fitted to the spectra. The absence of any splitting or even significant broadening of the low-velocity line indicates that the position of the low-velocity component of the ferric doublet closely matches that of the low-velocity component of the ferrous doublet, so that the sum of these two lines can be treated numerically as a single line. Further justification for this procedure can be derived from the position of the low-velocity line in largely ferrous and completely ferric samples. For instance, in glass of acmite composition the velocity changes from −0.132 mm/sec (relative to metallic iron) in the reduced sample to −0.237 mm/sec in the oxidized sample, a small change compared with the half-width of these absorption lines (about 0.60 mm/sec).

The $Fe^{2+}/\Sigma Fe$ values have been calculated from the area ratios of the ferrous and ferric doublets (see also Mysen and Virgo, 1978). When only two lines (due to the ferrous doublet) can be observed, any deviation of the $Fe^{2+}/\Sigma Fe$ value from 1 will be reflected in the inequality of peak areas. An example of this effect is the relation between $f(O_2)$ and $Fe^{2+}/\Sigma Fe$, as discussed further below. The $Fe^{2+}/\Sigma Fe$ is calculated from the difference of the peak areas. The reliability of $Fe^{3+}/\Sigma Fe$ of glasses determined with Mössbauer spectroscopy was discussed in some detail by Mysen and Virgo (1978), who also reported comparative studies using wet-chemical analysis as an additional technique. Comparative studies using wet-chemical and Mössbauer techniques for determination of $Fe^{3+}/\Sigma Fe$ were also conducted by Bancroft and Burns (1969) and Bancroft *et al.* (1969). In those studies, there generally was agreement between the results with the two methods. Whenever discrepancies arose, the wet-chemical technique gave higher $Fe^{3+}/\Sigma Fe$. Replicate wet-chemical analysis of such samples brought the results into agreement. It should be mentioned in this context that the wet-chemical techniques used are oxidation techniques. It is not surprising, therefore, that if there are discrepancies, they tend to be on the side of too much ferric iron. Kurkjian (1970) used published redox ratios of iron-bearing glasses on the join Na_2O–SiO_2–

FeO–Fe_2O_3 based on wet-chemical analysis (where no report on technique for wet-chemical analysis is given) and compared the results from those uncharacterized samples with Mössbauer results obtained by him on a new set of samples. In that study, results with both higher and lower $Fe^{3+}/\Sigma Fe$ values were reported. Inasmuch as the samples used in that study were not described appropriately, one cannot assess the quality of either the wet-chemical or the Mössbauer results. Therefore, the conclusions drawn by Kurkjian (1970) are open to question.

The Raman spectra were taken on small chips of quenched melts (~ 0.5–1.0 mm cubes) that were free of bubbles. The spectra were recorded with a Jobin–Yvon optical system, holographic grating, double monochromator (HG25), and a photon-counting detection system. The spectra were recorded at about 3 cm^{-1}/sec. The iron-free samples were excited with the 488.0 nm line of an Ar^+ laser, using a laser power of 200–400 mW at the sample with a 90° scattering geometry. The iron-bearing samples were excited with the 647.1 nm line of the Kr^+ ion laser also operated at 200–400 mW. Polarized spectra were obtained with the focused exciting beam parallel to the horizontal spectrometer slit and with the electric vector of the exciting radiation in a vertical orientation. A sheet of polarizer disk in front of an optical scrambler was used to record separately the parallel and perpendicular components of the scattered radiation.

As a matter of routine, replicate spectra from the same chips, from different chips of the same experimental run product, and from replicate experimental run products were also taken.

Results and discussion

Mössbauer spectroscopy

The hyperfine parameters calculated from the Mössbauer data on quenched melts in the system Na_2O–FeO–Fe_2O_3–SiO_2 are shown in Table 1. Spectra of crystalline acmite, composition $NaFe^{3+}Si_2O_6$ (Bowen *et al.*, 1930) and a ferrous-bearing akermanite (50 mole percent FeAk–50 mole percent Ak) were also taken (Table 2), in order to determine the hyperfine parameters for ferric iron in octahedral coordination and ferrous iron in tetrahedral coordination.

In all quenched melts on the join Na_2SiO_3–$NaFe^{3+}Si_2O_6$ (NS–Ac) in air, the absence of any absorption peak at about 1.8 mm/sec and the equal intensity and half-width of the two-component peaks of the doublet indicate that more than 95 percent of the iron is in the ferric state (Fig. 1). In quenched melts with 6 mole percent or less Ac (NS94Ac6), an additional line is observed at about 1.5 mm/sec (Fig. 2) and the tail region of the envelope extends to at least 7.5 mm/sec. In spectra taken at 77K (Fig. 2B) individual lines appear in this tail region, which constitutes a broadened magnetic sextet pattern superimposed on a doublet. The magnetic splitting supposedly arises from long relaxation times of spin–spin interactions of Fe^{3+} at these low iron concentrations (Bhargava *et al.*, 1979).

Table 1. Hyperfine parameters of ferric iron of quenched melts on the join Na_2SiO_3–$NaFe^{3+}Si_2O_6$ at 1400°C in air (mm/sec)

Composition	IS(Fe^{3+})	QS(Fe^{3+})
NS85Ac15	0.264	0.847
NS75Ac25	0.232	0.832
NS50Ac50	0.227	0.732
NS25Ac75	0.249	0.906
Ac100	0.249	0.971

IS(Fe^{3+}), isomer shift of Fe^{3+} relative to metallic iron. QS(Fe^{3+}), quadrupole splitting of Fe^{3+}.

The quenched melts on the join NS–Ac with more than 6 mole percent acmite component but with $Na_2O < SiO_2$, quenched in air, show similar features. We conclude, therefore, that all iron is in the ferric state (within the detection limit, <95%) in the melts in the system Na_2O–Fe_2O_3–SiO_2 when equilibrated in air.

The Mössbauer spectra of the melts in the system Na_2O–Fe_2O_3–SiO_2 show a visually resolved doublet (Fig. 1) with isomer shifts in the range between 0.23 and 0.26 mm/sec and quadrupole splitting from 0.79 to 0.97 mm/sec (Table 1). These values compare with isomer shift values of 0.38–0.40 mm/sec and quadrupole splitting of 0.30 mm/sec, respectively, for the two crystalline phases with Fe^{3+} in octahedral coordination (Fig. 1; see also Table 2).

Only compositions with small amounts of sodium metasilicate component have been investigated at low oxygen fugacity because of excessive sodium loss from the depolymerized melts close to the Na_2SiO_3 composition (Seifert *et al.*, 1979a). Even in the more Si- and Fe-rich compositions some loss of sodium to the CO_2/CO vapor phase of the furnace may have taken place, and the compositions studied may therefore not lie exactly on the join.

As the oxygen fugacity is lowered, the ferric doublet in the Mössbauer spectra becomes asymmetric, and eventually a new line at ~1.8mm/sec is ob-

Table 2. Hyperfine parameters of iron-bearing crystalline materials (mm/sec)

Composition	IS(Fe^{3+})	IS(Fe^{2+})	QS(Fe^{3+})	QS(Fe^{2+})
$NaFe^{3+}Si_2O_6$	0.399	...	0.301	...
$Na_5Fe^{3+}Si_4O_{12}$	0.377	...	0.300	...
$(CaFe^{2+}_2Si_2O_7)_{50\ mole\ \%}(CaMg_2Si_2O_7)_{50\ mole\ \%}$	...	0.958	...	2.394

IS(Fe^{3+}), isomer shift of Fe^{3+} relative to Fe metal. IS(Fe^{2+}), isomer shift of Fe^{2+} relative to Fe metal QS(Fe^{3+}), quadrupole splitting of Fe^{3+}. QS(Fe^{2+}), quadrupole splitting of Fe^{2+}.

served. The intensity of this new line increases as the oxygen fugacity decreases (Fig. 3). Concomitantly, the intensity of the high-velocity component of the ferric doublet decreases until only two lines of nearly equal area are observed (Fig. 3, Table 3), as also discussed above. The low-velocity component of this doublet is more intense and has smaller line width than the high-velocity component. The isomer shift of the latter doublet (~0.95 mm/sec) is typical of ferrous iron, and the $Fe^{2+}/\Sigma Fe$ values could be determined from its area, as described in the section on experimental techniques. The $Fe^{2+}/\Sigma Fe$ values thus derived show systematic relationships to both bulk composition and oxygen fugacity (Fig. 4). At constant oxygen fugacity the $Fe^{2+}/\Sigma Fe$ increases as the acmite content of the quenched melt is increased from 50 mole percent Ac toward pure acmite. At constant bulk composition the $Fe^{2+}/\Sigma Fe$ increases with decreasing oxygen fugacity.

The Mössbauer spectra of quenched melts in the system CaO–MgO–FeO–Fe_2O_3–SiO_2 are shown in Figures 5 and 6 (see also Table 4). In all samples, except the two at $MgSiO_3$ + 5 mole percent $FeSiO_3$ at 1585°C and $CaMgSi_2O_6$ + 1 mole percent $FeSiO_3$ at 1425°C, a ferric iron doublet is visually resolved. The line widths of the component peaks of the Mössbauer

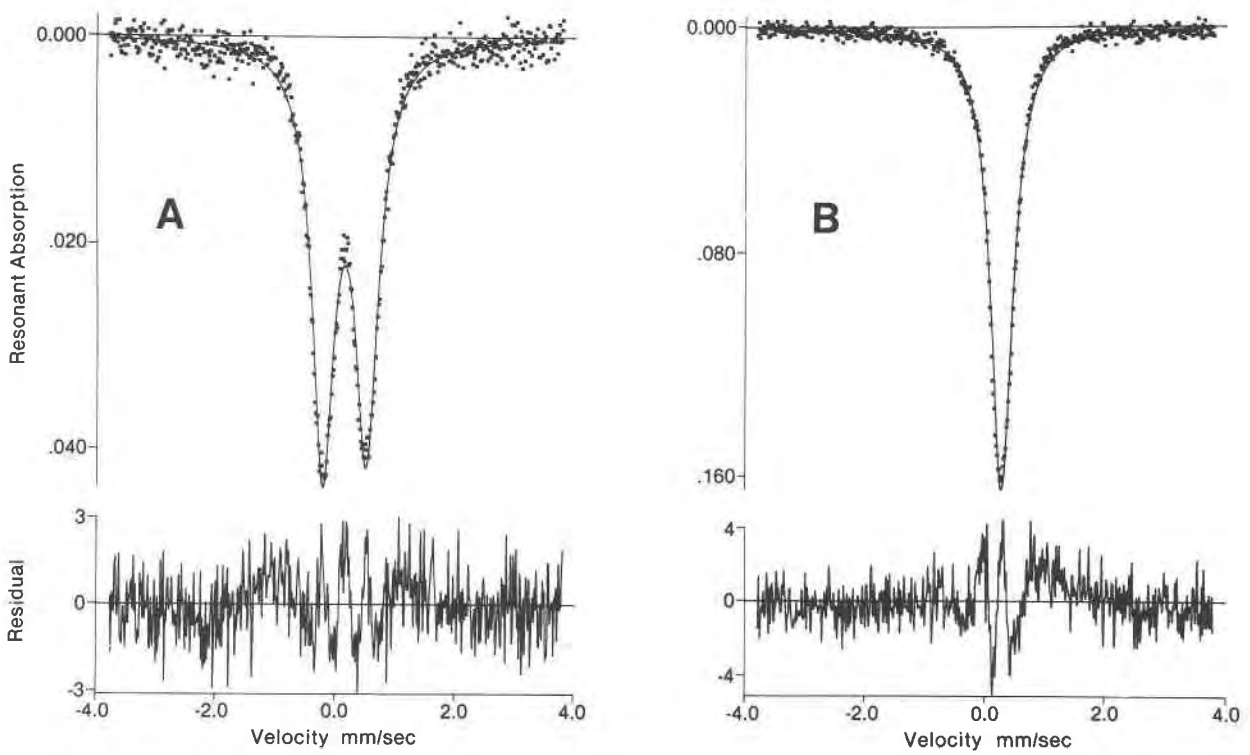

Fig. 1. ^{57}Fe Mössbauer spectra of the composition NFS518 (50 mole percent Na_2SiO_3–50 mole percent $NaFe^{3+}Si_2O_6$) in air. (A) Quenched melt. (B) Crystalline.

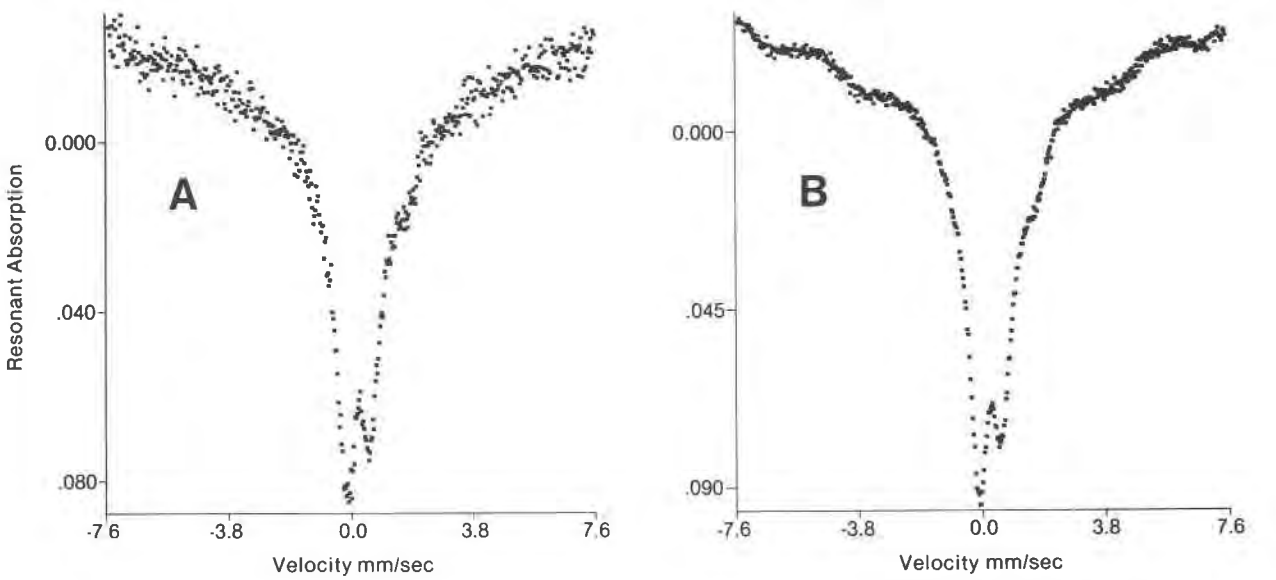

Fig. 2. ^{57}Fe Mössbauer spectra of quenched melt of Na_2SiO_3 composition with 1 mole percent $NaFe^{3+}Si_2O_6$. (A) 298K. (B) 77K.

spectra of quenched metasilicate melts of the alkaline earths are generally greater (0.8–0.9 mm/sec) than those of alkali metasilicate melts with similar amounts of iron present (0.5–0.6 mm/sec).

The isomer shift of ferric iron [IS(Fe^{3+})] of melts in the system CMFFS is greater than 0.37 mm/sec and generally greater than 0.45 mm/sec (Table 4). That of ferrous iron [IS(Fe^{2+})] is about 1 mm/sec for all compositions studied. The quadrupole splitting of ferric iron is about 1 mm/sec and that of ferrous iron is about 2 mm/sec.

The $Fe^{2+}/\Sigma Fe$ of quenched melts of alkaline earth metasilicate melts as a function of temperature and Ca/(Ca + Mg) and $FeSiO_3$ content of the starting material in air is shown in Figures 7–9. No evidence for a magnetic component was found in the Mössbauer spectra of metasilicate melts of the alkaline earths with low iron content. The $Fe^{2+}/\Sigma Fe$ of melts with 5 mole percent $FeSiO_3$ component added to the starting material increases with decreasing Ca/(Ca + Mg) in air at 1585°C (Fig. 8). Even the most oxidized sample, however, contains about 50 percent ferrous

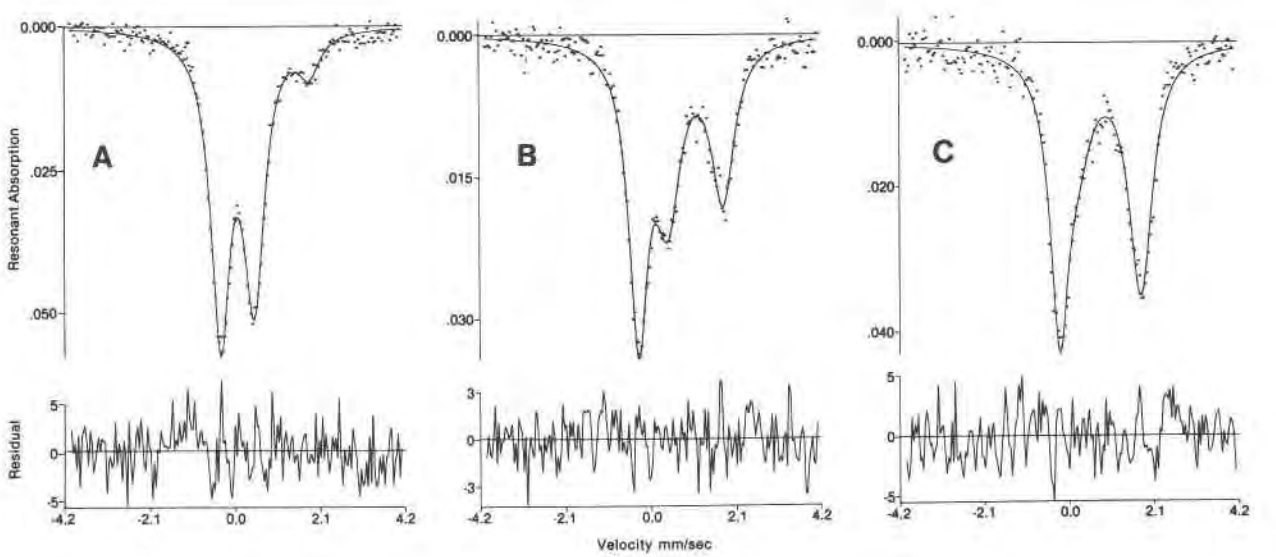

Fig. 3. ^{57}Fe Mössbauer spectra of quenched melts of composition NFS518 (see Fig. 1) as a function of $f(O_2)$ at 1400°C. (A) $f(O_2) = 10^{-4}$ atm. (B) $f(O_2) = 10^{-6}$ atm. (C) $f(O_2) = 10^{-8}$ atm.

Table 3. Hyperfine parameters and area ratios of glasses in the system sodium metasilicate–acmite–$Na_2O{\cdot}2FeO{\cdot}4SiO_2$ under reducing conditions

Composition, mole % acmite	Log $f(O_2)$, atm	Fe^{3+}				Fe^{2+}				$Fe^{2+}/\Sigma Fe$
		IS, mm/sec	QS, mm/sec	$FWHH_L$	$FWHH_H$	IS, mm/sec	QS, mm/sec	$FWHH_L$	$FWHH_H$	
50	-4	0.253	0.833	0.556	0.603	0.938	2.194		0.539	0.126
	-6	0.264	0.744	0.568	0.732	0.938	2.091		0.628	0.435
	-8	0.182	0.468	0.534	0.898	0.956	2.044		0.699	0.750
75	-4	0.260	0.879	0.583	0.591	0.925	2.209		0.592	0.117
	-6	0.283	0.759	0.609	0.720	0.940	2.060		0.696	0.505
	-8					0.991	1.955	0.755	0.754	0.889
	-10					0.993	1.943	0.681	0.746	0.916
100	-4	0.249	0.884	0.593	0.611	0.888	2.148		0.811	0.228
	-6	0.302	0.691	0.618	0.699	0.956	2.033		0.722	0.656
	-8					0.937	1.937	0.682	0.787	0.927

The compositions are given in terms of the oxidized system.
IS, isomer shift relative to metallic iron. QS, quadrupole splitting. FWHH, full width at half height. Indices H and L, high- and low-velocity component peaks.

iron. The $Fe^{2+}/\Sigma Fe$ also increases with increasing temperature (Fig.9). We also noted that at similar temperature, oxygen fugacity, and iron content, about 50 percent of the iron is ferrous in quenched matasilicate melts of the alkaline earths whereas all the iron is ferric in sodium metasilicate melts (Figs. 4 and 9).

The structural role of iron in the quenched melts can be determined to a large extent from its coordination to oxygen, which is reflected by the hyperfine parameters of the Mössbauer spectra. Tetrahedral and octahedral Fe^{3+} show well-defined ranges of isomer shifts in crystalline phases (0.19–0.30 mm/sec and 0.36–0.50 mm/sec, respectively; Annersten and Hålenius, 1976; Kurkjian, 1970; Taneja *et al.*, 1973; Annersten and Olesch, 1978). The isomer shifts observed for Fe^{3+} in the quenched melts of sodium metasilicate–acmite composition (about 0.25 mm/sec) are therefore typical of ferric iron in tetrahedral coordination. In addition, the rather sharp lines and the absence of any distinct asymmetry preclude the existence of significant amounts of octahedral Fe^{3+}. Further support for this interpretation is found in the large difference in IS(Fe^{3+}) of melts and crystals of $NaFe^{3+}Si_2O_6$ and $Na_5Fe^{3+}Si_4O_{12}$ compositions (0.23–0.26 mm/sec and 0.38–0.40 mm/sec, respectively; Tables 1 and 2). Note that Brown *et al.* (1978) concluded that the Fe^{3+} is in tetrahedral coordination, based on EXAFS analysis.

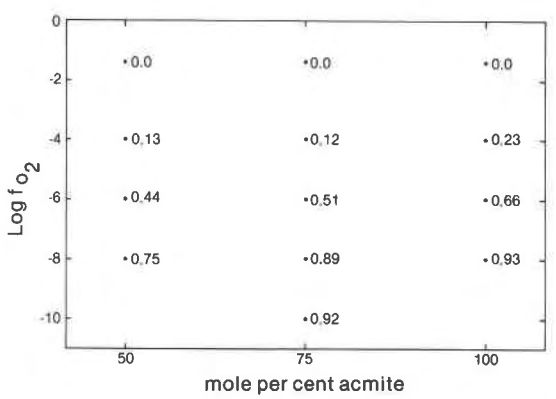

Fig. 4. $Fe^{2+}/\Sigma Fe$ of melts on the join Na_2SiO_3–$NaFe^{3+}Si_2O_6$ at 1400°C as a function of $f(O_2)$ and acmite component.

The isomer shifts of alkaline-earth metasilicate melts for ferric iron are generally in the range of 0.45–0.50 mm/sec (Table 4), which is well within the range of IS(Fe^{3+}) of ferric iron in octahedral coordination in crystalline materials (Annersten and Hålenius, 1976; Annersten and Olesch, 1978; see also Mysen and Virgo, 1978). We conclude, therefore, that tetrahedrally-coordinated ferric iron is unstable relative to octahedrally-coordinated ferric iron in quenched alkaline-earth metasilicate melts.

The hyperfine parameters of ferrous-iron quenched melts apparently are less sensitive to oxygen coordination number than those of ferric iron. In crystalline ferrous akermanite (50 mole percent)–akermanite (50 mole percent), the IS(Fe^{2+}) is about 0.95 mm/sec and the quadrupole splitting is about 2.35 mm/sec.

The isomer shifts of ferrous iron in the present quenched melts are between that of octahedral (generally greater than 1.10 mm/sec) and tetrahedral (about 0.90 mm/sec) ferrous iron in crystalline com-

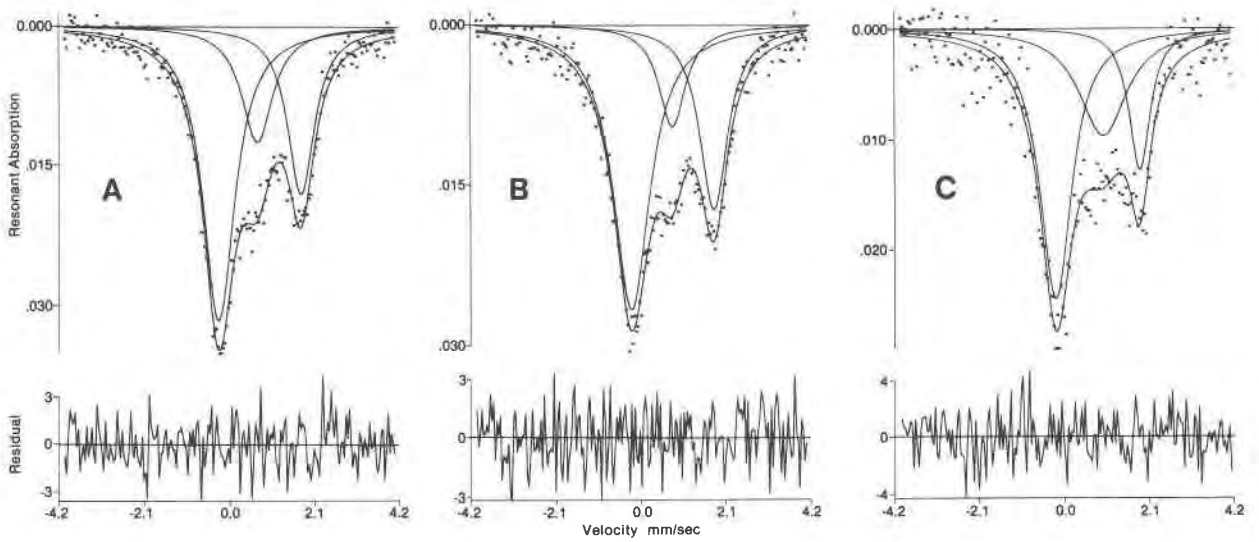

Fig. 5. ^{57}Fe Mössbauer spectra of quenched melts on the join $CaSiO_3$–$MgSiO_3$ with 5 mole percent $FeSiO_3$ component at 1585°C and 1 atm in air. (A) $CaSiO_3$. (B) $CaMgSi_2O_6$. (C) $MgSiO_3$.

pounds. Octahedral ferrous iron seems to exhibit systematically lower isomer shifts in quenched melts compared with crystals, however, as exemplified by the isomer shift of Fe^{2+} in synthetic quenched melts (1.04–1.07 mm/sec) where Fe^{2+} is known to occupy octahedral positions from optical absorption studies (Mao *et al.*, 1973; Bell and Mao, 1974).

These low values might be related to the decrease of the IS(Fe^{2+}) with increasing distortion of the octahedron (Seifert and Olesch, 1977). The quadrupole splitting of Fe^{2+} also indicates distorted sites.

We conclude, therefore, that at least a major fraction of ferrous iron in the quenched melts we studied is incorporated into octahedral positions. Ferric iron is in tetrahedral coordination in quenched melts with alkali metals. In quenched melts in which alkaline earths are the dominant modifying components, ferric iron is in octahedral coordination. Ferrous iron is in octahedral coordination in both types of melts.

Raman spectroscopy

In order to provide a framework for band-assignments in the melts under consideration, the Raman

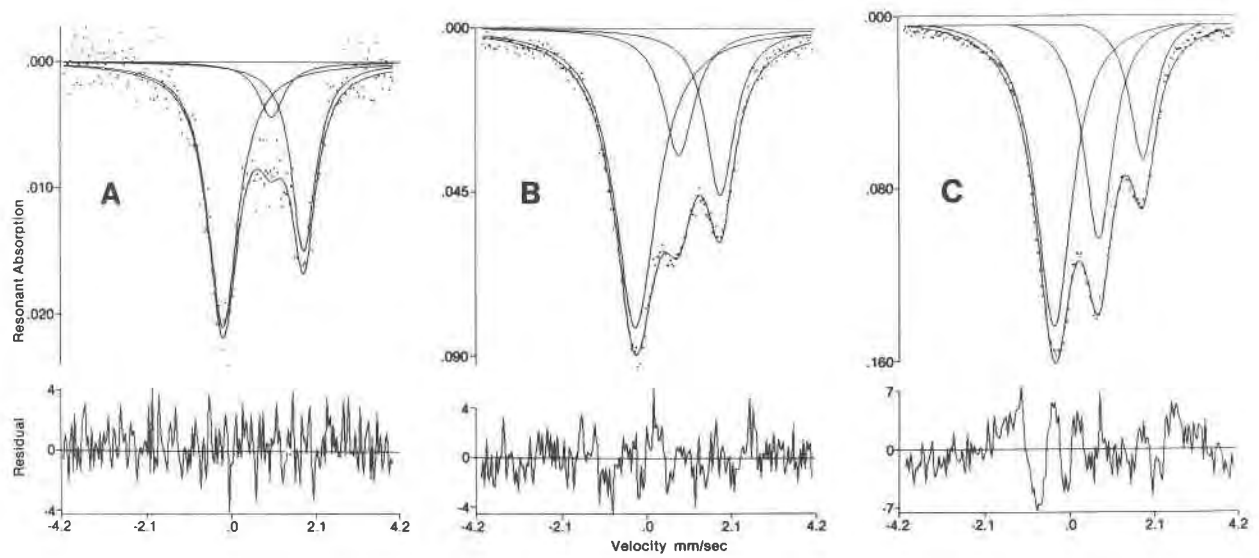

Fig. 6. ^{57}Fe Mössbauer spectra of quenched melts on the join $CaMgSi_2O_6$–$FeSiO_3$ at 1425°C and 1 atm in air. (A) 1 mole percent $FeSiO_3$. (B) 5 mole percent $FeSiO_3$. (C) 10 mole percent $FeSiO_3$.

Table 4. Mössbauer data on quenched melts in the system $CaO–MgO–FeO–Fe_2O_3–SiO_2$

Composition	Temp., °C	$f(O_2)$	Fe^{3+}		Fe^{2+}		$Fe^{2+}/\Sigma Fe$
			IS, mm/sec	QS, mm/sec	IS, mm/sec	QS, mm/sec	
Di + 1% Fs*	1425	air	...	...	1.014	1.918	0.82
Di + 2.5% Fs	1425	air	0.524	1.073	0.998	2.011	0.60
Di + 5% Fs	1425	air	0.479	1.027	0.982	2.032	0.58
Di + 10% Fs	1425	air	0.372	1.114	0.921	2.214	0.36
DW50 + 5% Fs	1525	air	0.449	1.028	0.980	2.057	0.55
DW50 + 5% Fs	1525	O_2	0.453	1.064	0.956	2.071	0.47
Di + 5% Fs	1525	air	0.492	1.060	0.984	2.048	0.61
DE50 + 5% Fs	1525	air	0.532	1.053	0.987	2.003	0.64
DE50 + 5% Fs	1525	O_2	0.473	1.026	0.977	2.035	0.60
WO + 5% Fs	1585	air	0.422	0.965	0.961	2.044	0.51
WO + 10% Fs	1585	air	0.382	0.939	1.048	1.904	0.35
DW50 + 5% Fs	1585	air	0.500	1.002	0.999	2.002	0.60
Di + 5% Fs	1585	air	0.484	1.024	1.024	2.046	0.60
DE50 + 5% Fs	1585	air	0.510	1.001	1.051	2.034	0.867
En + 5% Fs*	1585	air	...	...	0.923	1.835	0.78

**Two-line fit.*

IS, isomer shift relative to Fe metal; QS, quadrupole splitting; Di, $CaMgSi_2O_6$; DW50, 50 mole % $CaMgSi_2O_6$–50 mole % $Ca_2Si_2O_6$; DE50, 50 mole % $CaMgSi_2O_6$–50 mole % $Mg_2Si_2O_6$; En, $MgSiO_3$; Fs, $FeSiO_3$ (added as a component with Fe_2O_3 in the starting material).

spectra of quenched melts on various metal oxide–silica joins as a function of metal oxide/silica ratio and type of metal oxide must be considered. A considerable amount of data is already available (Brawer and White, 1975, 1977; Furukawa *et al.*, 1978; Verweij, 1979a,b; Virgo *et al.*, 1980; Mysen *et al.*, 1980; Virgo and Mysen, in preparation). The data base provided by these authors includes NBO/Si (nonbridging oxygen per silicon) from near 4 (orthosilicate) to 0 (three-dimensional network), and cations such as K^+, Na^+, Li^+, Ca^{2+}, Mg^{2+}, and Pb^{2+}. In summarizing these data, Brawer and White (1977) and Virgo *et al.* (1980) concluded that the Raman spectra of melts with given metal oxide/silica ratio do not depend on the type of metal cation. They inferred from this conclusion that the anionic structure of binary metal oxide–silicate melts does not depend on the type of metal cation.

The most accurate spectroscopic information on the structure of such binary melts can be obtained

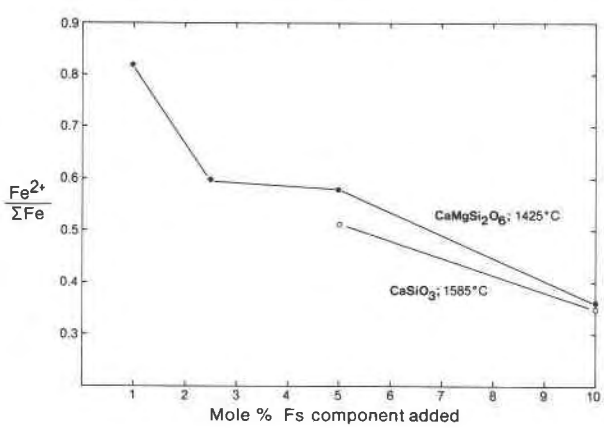

Fig. 7. $Fe^{2+}/\Sigma Fe$ of quenched melts on the join $CaSiO_3$–$MgSiO_3$–$FeSiO_3$ as a function of Fs content.

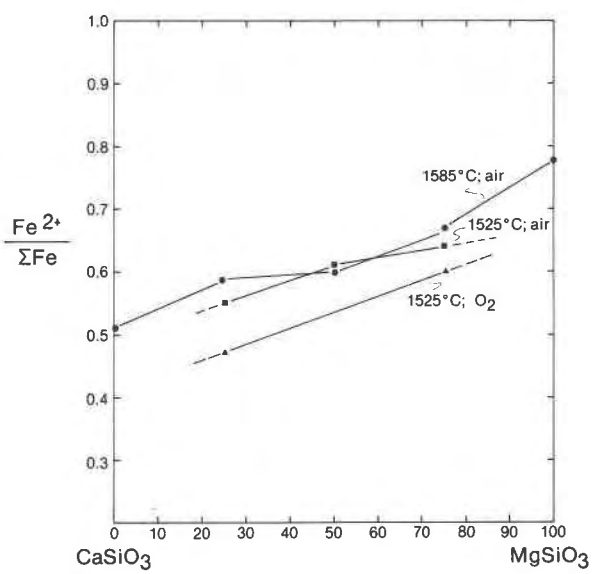

Fig. 8. $Fe^{2+}/\Sigma Fe$ of quenched melts on the join $CaSiO_3$–$MgSiO_3$ with 5 mole percent Fs component added.

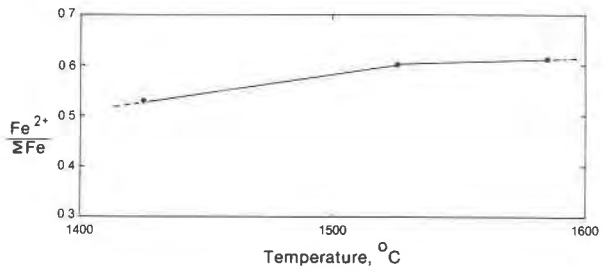

Fig. 9. $Fe^{2+}/\Sigma Fe$ of quenched melt of $CaMgSi_2O_6$ + 5 mole percent $FeSiO_3$ component as a function of temperature in air.

from alkaline-earth silicate melts, as such melts are not significantly hygroscopic and do not suffer potential metal-cation volatilization during preparation (Kracek, 1930). Among the joins of alkaline-earth silicates, the join with the widest range of M/Si is $CaO–MgO–SiO_2$ (Ca/Mg = 1) (Virgo *et al.*, 1980; Mysen *et al.*, 1980). Eight spectra from melts on that join are reproduced in Figure 10 (see also Table 5). Compositionally, these melts differ only in (Ca + Mg)/Si, as indicated in Figure 10.

The dominant feature of each spectrum is the intense, slightly asymmetric band in the region between 600 and 670 cm^{-1} combined with an intense, high-frequency envelope in the region between 800 and 1100 cm^{-1}. All these bands are strongly polarized. All the bands, with the exception of that in the region 600–670 cm^{-1}, remain at the same frequency as M/Si varies (Fig. 10). The latter bands shift to higher frequency as a systematic function of increasing M/Si.

In melts with M/Si between 1.9 (DM 95) and 1.18 (DM 25), there is a very strong sharp band near 870 cm^{-1} and a less intense band near 900 cm^{-1}. The 870 cm^{-1} band remains in all spectra of melt compositions from DM 95 to SD 40. The 900 cm^{-1} band disappears somewhere between DM 25 and Di composition (M/Si = 1.18 and 1.0, respectively). It appears that the intensity of the 900 cm^{-1} band passes through a maximum for melt compositions near DM 58. The intensity of the 870 cm^{-1} decreases as a continuous function of decreasing M/Si. Both bands remain polarized in the entire compositional range.

The 870 cm^{-1} band is by far the most intense band in crystalline orthosilicates (Furukawa *et al.*, 1978; Verweij and Konijnendijk, 1976). Furukawa *et al.* (1978), Verweij and Konijnendijk (1976), Verweij (1979a,b) and Furukawa and White (1980) assigned this band to symmetric stretch vibrations of nonbridging oxygen bonds in separate SiO_4^{4-} tetrahedra (symbol: $Si–O^{2-}$). This assignment is retained here.

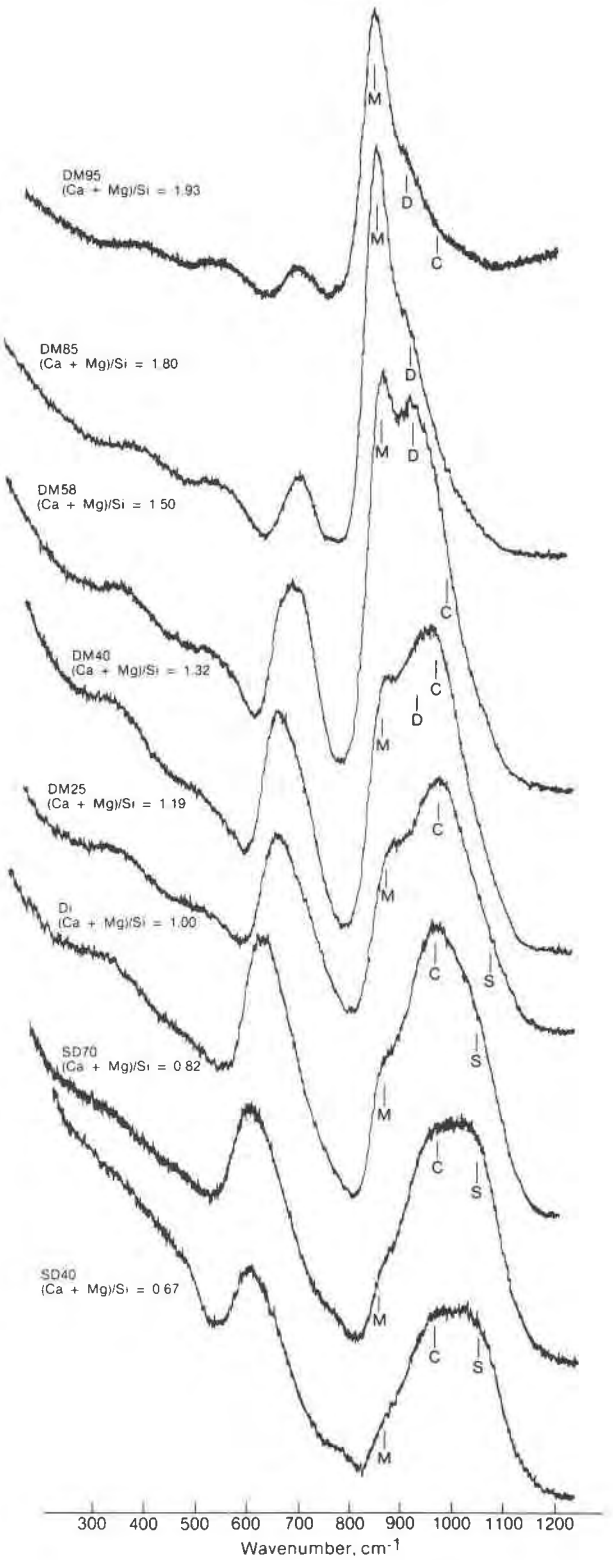

Fig. 10. Raman spectra of quenched melts on the join $CaO–MgO–SiO_2$ (Ca/Mg = 1) at 1 atm and 1650°C. M, D, C, S: band positions of symmetric stretch bands derived from vibrations in structural units with NBO/Si = 4, 3, 2, and 1, respectively.

Table 5. Raman data of quenched melts on the join CaO–MgO–SiO_2 (Ca/Mg = 1) at 1 atm and 1650°C

Composition	Wavenumber, cm^{-1}							
DM95	380w,p(bd)	530m,p(bd)	700w,p	–	848s,p	903m,p	977mw,p	–
DM85	380w,p(bd)	527m,p(bd)	700w,p	–	847s,p	903m,p	978m, p	–
DM58	343w,p(bd)	513m,p(bd)	686w,p	–	860s,p	910s,p	973m,p	–
DM40	340w,p(bd)	500m,p(bd)	660m,p	–	863s,p	908m,p	973m,p	–
DM25	340w,p(bd)	–	655m,p	–	860s,p	913w,p	973s,p	–
DI	340w,p(bd)	–	630m,p	770vw(sh)	867m,p	–	967s,p	1060m,p
SD70	–	–	622s,p	770,w	873w,p	–	959s,p	1063m,p
SD40	–	500vw,(sh)	610s,p	–	873vw	–	955s,p	1063m,p

Symbols: vw - very weak, w - weak, mw - medium to weak, m - medium, ms - medium to strong, s - strong
p - polarized, (bd) - broad, (sh) - shoulder.
Uncertainties: Strong to weak bands - ± 5 cm^{-1}. Very weak bands - ∿ 10 cm^{-1}. Shoulders - ± 15-20 cm^{-1}
Compositions are defined in Fig. 10.

The 900 cm^{-1} band is the major band in crystalline pyrosilicates (Lazarev, 1972; Sharma and Yoder, 1979). Since its frequency is higher than that of the symmetric $Si–O^{2-}$ stretch band (870 cm^{-1}), it is polarized, and its frequency coincides with the main band in crystalline pyrosilicates, this band is interpreted as due to the presence of dimer structural units in the melt ($Si_2O_7^{6-}$). Its frequency is independent of the melt composition. We conclude, therefore, that the NBO/Si of this structural unit does not change with changing composition of the melt. Further support for this interpretation is found in the observation that the maximum intensity of the 900 cm^{-1} band is found in melts with a stoichiometry close to that of a dimer (NBO/Si = 3).

The high-frequency envelope (Fig. 10) also contains a band near 970 cm^{-1} (found in all compositions on this join) and one near 1070 cm^{-1} (found in melt compositions with M/Si equal to or less than that of metasilicate). Both bands are polarized. The intensity of the 970 cm^{-1} band increases relative to the other bands in the high-frequency envelope in the compositional range between DM 95–Di and decreases as the M/Si is decreased further. The intensity of the 1070 cm^{-1} band increases as a function of decreasing M/Si at M/Si<1. The frequencies of both bands are independent of M/Si. Note that the frequency of the band between 600 and 670 cm^{-1} decreases from about 650 cm^{-1} in metasilicate melt (M/Si = 1) to near 600 in SD 40 melt (M/Si = 0.67).

On the basis of frequencies, polarization characteristics, and analogy with crystalline meta- and disilicates (Etchepare, 1972; Furukawa and White, 1980), we conclude that the 970 cm^{-1} band is a symmetric $^-O–Si–O^-$ stretch band and the 1070 band is a symmetric $^-O–Si–O^0$ stretch band. The associated deformation bands are those at 650 and 600 cm^{-1}, respectively. This conclusion accords with that of Verweij (1979a,b) and Furukawa and White (1980). The $^-O–Si–O^-$ stretch vibration may be derived from structural units with NBO/Si = 2 (*e.g.*, chain) and the $^-O–Si–O^0$ from structural units with NBO/Si = 1 (*e.g.*, sheet). The exact structural assignments will be discussed below.

The most important observation made from the above assignments of the Raman spectra is that there appears to be a unique set of coexisting anionic structural units in specific ranges of NBO/Si of the melts. The proportions of the individual structural units vary as a function of bulk NBO/Si (M/Si), but the NBO/Si of each unit does not. In Table 6, the anionic units are defined on the basis of the average NBO/Si, using the data summarized above in conjunction with the published data summarized by Virgo *et al.* (1980) and Mysen *et al.* (1980). Several aspects of these conclusions warrant further comment. In comparison to some models of melt structure (*e.g.*, Masson, 1977), the model is strikingly simple. This simplicity should not be surprising, since when comparing with crystal structures of silicates only a few anionic structures can be found (see Dent Glasser, 1979, for review). The same structural units have been found in silicate melts. In silicate crystal chemistry, the metal cations are considered important in controlling the type of polymers that will occur. Polymer theory as applied to silicates (*e.g.*, Masson, 1977) does not take the metal cations into account.

Table 6. Raman frequencies of the stretch vibrations of specific Si-rich anionic structural units in silicate melts (after Virgo *et al.*, 1980)

Structural unit	NBO/Si	Frequency (cm^{-1})	Characteristics of vibrational mode
SiO_4^{4-}	4	850–880	Symmetric stretch
$Si_2O_7^{6-}$	3	900–920	Symmetric stretch
$Si_2O_6^{4-}$	2	950–980	Symmetric stretch
$Si_2O_5^{2-}$	1	1050–1100	Symmetric stretch
SiO_2	0	1060,1190	antisymmetric stretch

Previous models of melt structure include features such as trimers, tetramers, pentamers, *etc.*, in addition to rings and branched chains. The experimental basis for most of these models is from organic chemistry. As applied to silicates, the experimental basis has been chromatographic data derived from trimethylsilyl derivatives of the silicates (TMS-derivatives). Limitations and inconsistencies of such data have been discussed elsewhere (*e.g.*, Masson, 1977; Kuroda and Kato, 1979) and are not pursued here. It is merely concluded that structural data of silicate melts derived from TMS-derivatives are not reliable.

Polymer theory predicts that there is a positive correlation between the number of silicons in the polymers and the proportion of various types of polymers and the NBO/Si of the melt. In Raman spectroscopic studies, such a correlation would result in a successive increase of the frequency of Si–O stretch bands as a function of decreasing NBO/Si (M/Si) (*e.g.*, Lazarev, 1972; Brawer and White, 1975; Furukawa and White, 1980; see also Table 6). On this basis it would be expected that if anionic structural units with degree of polymerization between chains and dimers were formed in the melts in the various binary metal oxide–silicate joins, new bands would occur between 900 and 970 cm^{-1} or bands such as that at 900 cm^{-1} would shift to higher frequency as a function of decreasing M/Si of the melt. No such spectroscopic evidence is present in our data, nor in any related published data (Brawer and White, 1975, 1977; Furukawa *et al.*, 1978; Verweij, 1979a,b; Verweij and Konijnendijk, 1976; Furukawa and White, 1980; Mysen *et al.*, 1980). We conclude, therefore, that structural units with NBO/Si between that of a dimer and that of a chain (3 and 2, respectively) do not exist in significant amounts in silicate melts.

The structural units with NBO/Si = 2 have been referred to as a chain. Simple rings have, however, the same NBO/Si. The idea of ring structures in silicate melts has experimental support in the TMS-derivative work (as summarized by Masson, 1977). Ring structures have also been suggested in melts on binary metal oxide–silicate joins on the basis of the viscous behavior of such melts (*e.g.*, MacKenzie, 1960; Bockris and Reddy, 1970). Spectroscopic evidence relevant to ring structures is scarce. Lazarev (1972) discussed spectroscopic imprints of ring structures with up to 6 silicons. In the simple $Si_3O_9^{6-}$ ring, there is a strong silicon–oxygen deformation band near 750 cm^{-1}. No such band exists in the data in Figure 10 and other relevant data discussed elsewhere, and therefore this type of ring probably does not occur. Larger ring structures show stretch bands slightly above 1100 cm^{-1}. On a spectroscopic basis alone it is not likely, but not impossible, that the 1070 cm^{-1} band could, in fact, be such a band (*e.g.*, S-band in Fig. 10). Mass-balance considerations require, however, that in metasilicate melts, for example, the existence of structural units with NBO/Si = 4 and 2 also requires the existence of structural units with NBO/Si < 2. Careful analysis by, in particular, Verweij (1979a,b) and Furukawa and White (1980) resulted in the conclusion that the band between 1070 and 1100 in their melts (Na_2O–SiO_2 join) was due to a band with NBO/Si = 1. Inasmuch as this band also exists in alkaline-earth metasilicates, it is attractive to assign this band to that structural unit. One might suggest, however, that the ^-O–Si–O^0 vibrational mode stems from end units in a linear structure. Such an interpretation does not provide for structural units in the melt that would satisfy the mass-balance requirements, and neither would the ring-structure assignment. It might also be suggested that the presence of branched chains or multiple chains could constitute the structural unit(s) with NBO/Si < 2. The end result of such branching is, of course, a sheet. Intuitively, it would be expected that branching would be continuously increasing as the M/Si of the melt decreased. If the S-band in Figure 11 were such a band, for example, one would expect its frequency to increase. It does not. Furthermore, according to survey of silicate mineral structures (Dent Glasser, 1979), branched chains do not exist, presumably for energetical reasons. There is no reason, therefore, why one would expect such structures in a melt. Instead, chains and sheets are formed.

An option that does exist to explain the 1070 cm^{-1} band is multiple chains (finite sheet). It cannot be established from the Raman data whether the S-band (Fig. 10) is due to such a finite sheet or due to an infinite sheet. The simplest interpretation is an infinite

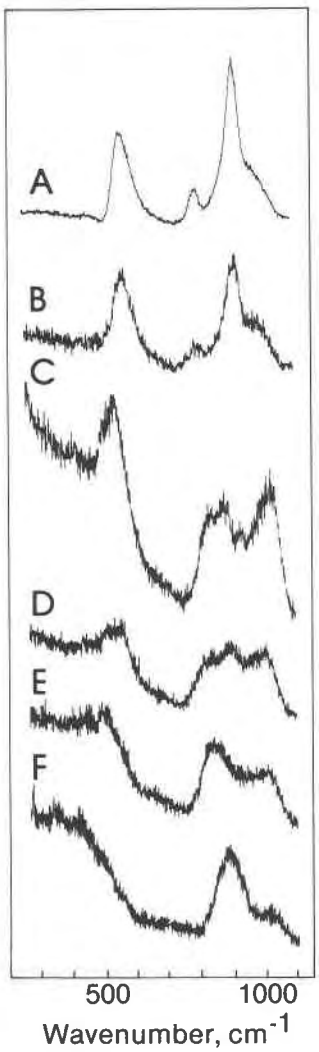

Fig. 11. Unpolarized Raman spectra of quenched melts on the join Na_2SiO_3–$NaFe^{3+}Si_2O_6$ in air at 1400°C. (A) NS. (B) NS94Ac6. (C) NS85Ac15. (D) NS75Ac25. (E) NS50Ac50. (F) Ac100. (Kr^+ ion laser with 200–400 mW power.)

sheet (NBO/Si = 1) and this interpretation is adhered to here. This conclusion is not absolutely certain, however.

Iron was added to metasilicate melts of Na^+(NS), Ca^{2+} (Wo), $(Ca,Mg)^{2+}$ (Di) and Mg^{2+} (En). The Raman spectra of these melts will be discussed first (Fig. 11A, 12; see also Tables 7 and 8). The high-frequency envelopes of these spectra were deconvoluted into individual bands (Fig. 13), in order to get an impression of the relative intensities of the bands in the high-frequency envelopes. In the deconvolution procedure, we assumed that the bands were Gaussian, were symmetric, and that the background was horizontal. The Gaussian line-shape was derived from selected portions of the high- and low- frequency limbs of the high-frequency envelopes. Extrapolation of the Rayleigh tail from frequencies less than 500 cm^{-1}, using exponential functions, to the spectral region of the high-frequency envelope indicates that the assumption of horizontal background is appropriate. Finally, bands were only fitted when indicated by the form of the raw Raman, high-frequency envelope.

With the exception of the broad, weak band near 350 cm^{-1} in quenched Wo melt (Fig. 12), the same Raman bands are found in all four metasilicate melts. The spectra consist of a strong, somewhat asymmetric band in the region between 620 and 650 cm^{-1}, a distinct band or shoulder near 870 cm^{-1}, a strong band near 970 cm^{-1} and a shoulder between 1050 and 1100 cm^{-1}. These bands are polarized. All the bands were discussed under Figure 10 (see also Tables 5 and 6), and no further discussion is necessary. The additional band near 350 cm^{-1} in quenched Wo melt was also noted by Brawer and White (1977)

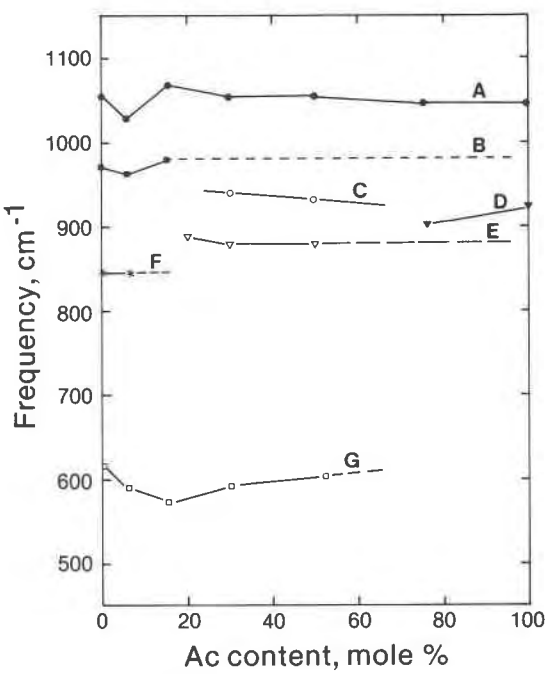

Fig. 12. Frequency shift of unpolarized Raman bands as a function of Ac content [(Fe)Si]O^0 on the join Na_2SiO_3–$NaFeSi_2O_6$ at 1400°C in air. (A) (Si, Fe)–O^0 stretch mode. (B) (Si, Fe)–O^- stretch mode; dashed line denotes inferred extension (see discussion in text). (C) Mixed (Fe,Si)–O^- and (Fe,Si)–O^0 stretch modes (see discussion in text). (D) Mixed (Fe, Si)–O^0 and (Fe,Si)–O^- stretch modes (see discussion in text). (E) (Fe,Si)–O^- stretch mode; dashed line denotes inferred extension (see discussion in text). (F) Si–O^{2-} stretch mode. (G) (Si,Fe)–O^0 rocking mode.

Table 7. Vibrational frequencies and band assignments of quenched melts on the join Na_2SiO_3–$NaFe^{3+}Si_2O_6$ at 1400°C in air

Composition	Wavenumber, cm^{-1}							
NS	...	...	619,s,p	847,w,p	...	...	970,s,p	1070,m(sh),p
NS94Ac6	...	...	591,s,p	847,w,p	...	...	962,s,p	1032,m(sh),p
NS85Ac15	...	...	577,s,p	...	887,m,p	928,m,p	978,m,p	1065,m,p
NS75Ac25	...	551,m,p	590,s,p	...	877,m,p	...	940,m,p	1052,m,p
NS50Ac50	480,w,p	540,s,p	605(sh),p	...	882,m,p	...	931,m,p	1053,s,p
NS25Ac75	477,s,p	540,m(sh),p	...	...	...	897,m,p	...	1047,m,p
Ac100	451,s,p	541,m(sh),p	...	...	...	925,s,p	...	1047,m,p

Symbols: w, weak; m, medium; s, strong; (sh), shoulder; p, polarized.
The uncertainty is 10 cm^{-1} for weak bands, 5-6 cm^{-1} for medium bands and 3-4 cm^{-1} for strong bands. For shoulder add 100% to uncertainty.

and is probably due to vibrations within Ca–O polyhedra.

The Raman data for metasilicate melts indicate, therefore, that the anionic structural units are SiO_4^{4-} (NBO/Si = 4), $Si_2O_6^{4-}$ (NBO/Si = 2), and $Si_2O_5^{2-}$ (NBO/Si = 1). Our interpretation suggests, therefore, that in metasilicate melts the chain units are partially disproportionated into monomers (SiO_4^{4-}) and sheets ($Si_2O_5^{2-}$):

$$3Si_2O_6^{4-} \rightleftharpoons 2SiO_4^{4-} + 2Si_2O_5^{2-} \quad (1)$$

Raman spectroscopic measurements have been carried out on quenched melts on the join Na_2SiO_3–$NaFe^{3+}Si_2O_6$ (NS–Ac) (Table 7) where the Mössbauer data indicated that within the detection limit of the Mössbauer technique all iron was present in the ferric state. No spectra could be taken on samples with ferrous iron because of oxidation of Fe^{2+} to Fe^{3+} due to surface heating by the laser, photo-oxidation, or both. Consequently, Raman data for iron-bearing alkaline-earth metasilicate melts could not be acquired.

The Raman spectrum of acmite melt formed in air and quenched from 1400°C is shown in Figure 11 and band assignments are shown in Table 7. The spectrum consists of four bands. The strongest band is at 925 cm^{-1} and a weaker one is at 1047 cm^{-1}. In addition, there is a shoulder near 540 cm^{-1} and another one near 450 cm^{-1}.

The results of Mössbauer (Table 1), EXAFS, and radial distribution analysis (Brown *et al.*, 1978) have shown that Fe^{3+} is in tetrahedral coordination in melts of $NaFe^{3+}Si_2O_6$ composition when quenched in air. This conclusion implies that in the absence of Fe^{2+} quenched Ac melt has a three-dimensional network structure. In compositions analogous to those on the joins $NaAlO_2$–SiO_2, $CaAl_2O_4$–SiO_2, $NaFeO_2$–SiO_2, and $NaGaO_2$–SiO_2 (Virgo *et al.*, 1979), it was shown that at least two high-frequency (Si,Al)–O^0, (Si,Fe)–O^0, and (Si,Ga)–O^0 stretch bands occur. Their frequencies and intensities shift systematically with Si/(Si + T), where T = Al, Fe, or Ga. In light of these observations, we suggest that the two high-frequency bands in quenched Ac melt are due to antisymmetric (Si,Fe)–O^0 and (Fe,Si)–O^0 stretching.[2]

In addition to the two characteristic high-frequency bands, a distinct shoulder occurs near 450 cm^{-1}. This shoulder is probably an (Si,Fe)–O^0 rocking mode. The band characteristically occurs in the spectral region between 450 and 500 cm^{-1} in all three-dimensional melts in the system Na_2O–CaO–Ga_2O_3–Al_2O_3–SiO_2 (Bates *et al.*, 1974; Virgo *et al.*, 1979).

The Raman spectra of quenched melts of compositions on the join Na_2SiO_3–$NaFe^{3+}Si_2O_6$ are also shown in Figure 11, and the band assignments are given in Table 7. The frequency shifts of the important bands as a function of bulk composition of the quenched melt are shown in Figure 14.

Mixing of Na_2SiO_3 and $NaFe^{3+}Si_2O_6$ components constitutes combining a three-dimensional network unit with characteristic bands at 1047, 925, 540, and 451 cm^{-1} and a less polymerized melt that consists of

Table 8. Vibrational frequencies and band assignments of melts on the join $CaSiO_3$–$MgSiO_3$

Composition	Wavenumber, cm^{-1}			
$CaSiO_3$	637,s,p	979,s,p	981,s,p	1070,s(sh),p
$CaMgSi_2O_6$	640,s,p	877,m(sh),p	980,s,p	1070,s(sh),p
$MgSiO_3$	640,s,p	882,m(sh),p	975,s,p	1058,m(sh),p

Symbols and uncertainty as in Table 5.

[2] The notations (Si,Fe)–O^0 and (Fe,Si)–O^0, respectively, imply Si-rich and Fe-rich (Si,Fe)–O–(Si,Fe) stretch vibrations. The analogous rotations for nonbridging oxygen bands are (Si,Fe)–O^- and (Fe,Si)–O^-.

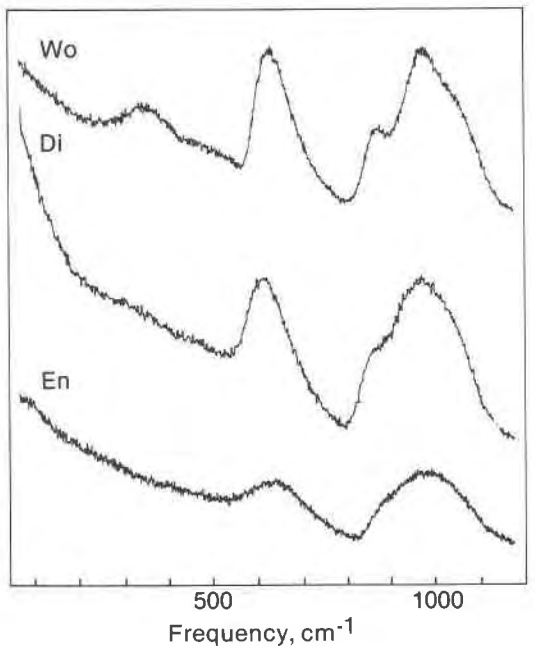

Fig. 13. Unpolarized Raman spectra of quenched (1585°C) melts on the join $CaSiO_3$–$MgSiO_3$. Wo, $CaSiO_3$; Di, $CaMgSi_2O_6$; En, $MgSiO_3$. (Al^+ ion laser with 200–400 mW power.)

monomer, chain, and sheet units with characteristic bands at 1070, 970, 850, and 618 cm^{-1} (Fig. 11, Table 7). Addition of 25 mole percent NS component to Ac results in resolved bands at 1047, 897, 540, and 477 cm^{-1}. The band at 897 cm^{-1} is asymmetric and much broader than the 925 cm^{-1} band in quenched Ac melt. The asymmetry of this band may indicate that it, in fact, consists of two unresolved bands. One band may be the 925 cm^{-1} band of quenched Ac melt [(Fe,Si)–O^0 stretch]. The other band is new and occurs at a wave number between 800 and 900 cm^{-1}. If this interpretation of the asymmetric 897 cm^{-1} band is correct, this latter band may be due to nonbridging oxygen in the melt and could be either an ^-O–(Fe,Si)–O^0 or an ^-O–(Fe,Si)–O^- stretch vibration. The 1047 cm^{-1} band in NS25Ac75 is more intense relative to the rest of the high-frequency envelope than in quenched Ac melt. Inasmuch as the proportion of Ac component is decreased in NS25Ac75 melt relative to that of pure Ac composition, probably the 1047 cm^{-1} band in quenched NS25Ac75 melt either reflects a new vibrational mode or is a combination of two modes. In the latter case, one mode may be the (Si,Fe)–O^0 stretch vibration of Ac melt and the other vibration may reflect a nonbridging oxygen. We suggest that the increased intensity of the 1047 cm^{-1} band is due to ^-O–(Si,Fe)–O^0 stretching. Its frequency is lower than that for pure NS quenched melt (Fig. 14) because of (Si,Fe) coupling. As a result of this band assignment, it must be concluded that the unresolved low-frequency component of the 894 cm^{-1} band is a highly coupled ^-O–(Fe,Si)–O^- stretch vibration. In conclusion, quenched melt of NS25Ac75 composition consists of a combination of structural units with NBO/T (where T = Si + Fe) = 0, 1, and 2.

In quenched NS50Ac50 melt, the two low-frequency bands suggested for NS25Ac75 melt (as a result of the asymmetric 897 cm^{-1} band) are partially resolved (Fig. 11). One band is found at 882 cm^{-1} and the other near 930 cm^{-1}. In this melt composition, the 1047 cm^{-1} band is shifted to 1053 cm^{-1}, and its intensity relative to the rest of the high-frequency envelope has increased further compared with that of quenched NS25Ac75 melt. The intensity increase is a result of more sheet units in the more NS-rich quenched melt. The location of the 882 cm^{-1} band in the spectrum is probably still somewhat influenced by the weakened (Fe,Si)–O^0 stretch vibration at 925 cm^{-1}. The shoulder on this band also indicates the presence of a second band near 930 cm^{-1}. This band

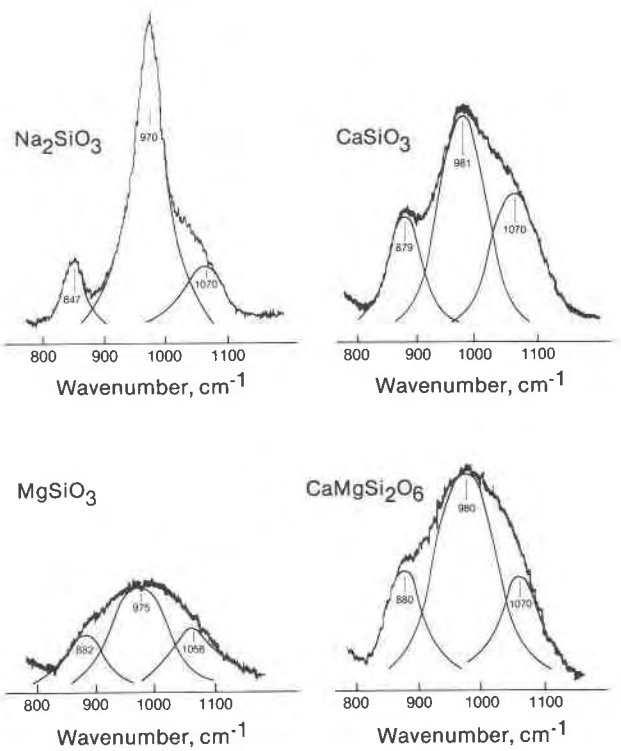

Fig. 14. High-frequency envelope of Raman spectra of quenched metasilicate melts with Gaussian curves fitted inside the envelope to match positions and total area of high-frequency envelope.

could be the (Fe,Si)–O^0 stretch vibration with a slightly lowered Fe content. Alternatively, it could be another band that has appeared. If the latter suggestion is correct the frequency of this band might shift to a higher wave number as the NS content of the quenched melt is increased, as indicated by the data in Figure 14. This feature will be discussed below. A shoulder occurs near 600 cm^{-1} in quenched melt of NS50Ac50 composition. Its frequency is near the 620 cm^{-1} band, corresponding to the deformation mode of pure metasilicate melt (Figs. 11 and 12), and may be due to a similar vibration. In conclusion, quenched melt of NS50Ac50 composition consists of the same structural units as quenched NS25Ac75 melt (3D: NBO/T = 0, sheet: NBO/T = 1 and chain: NBO/T = 2). The chain and sheet units are more pronounced and the 3D unit less pronounced in this melt than in quenched melt of NS25Ac75 composition, as would also be expected because of the higher NS content of this quenched melt.

The high-frequency envelope of quenched NS75Ac25 melt shows the same bands as quenched NS50Ac50 melt except that their frequencies and intensities are slightly different (Figs. 11 and 14). The highest frequency band (1052 cm^{-1}) is at the same position as in quenched NS50Ac50 melt, but it has become more intense (Fig. 11). The 931 cm^{-1} band in quenched NS50Ac50 melt has shifted to 940 cm^{-1} and is now clearly resolved. We suggest that this band is a combination of the 925 cm^{-1} band of (Fe,Si)–O^0 stretching and a new band at higher frequency, which probably is the 970 cm^{-1} band found in pure NS melt, a band assigned to ^-O–Si–O^- stretching. The higher frequency of this band compared with the ^-O–(Fe,Si)–O^- stretch band below 900 cm^{-1} indicates much less extensive (Fe,Si) coupling. With the exception of this conclusion, the band assignments of the high-frequency envelope of the Raman spectrum of quenched NS75Ac25 melt are the same as for quenched NS50Ac50 melt. The greater intensities of the bands assigned to depolymerized units are due to the greater proportion of NS component in this quenched melt. In fact, except for the above discussion concerning the 925 cm^{-1} band, no clear evidence exists for the presence of a 3D unit in quenched melt of NS75Ac25 composition.

In quenched melt of NS85Ac15 composition the band at 940 cm^{-1} in NS75Ac25 occurs at 978 cm^{-1} and is clearly resolved. We conclude, therefore, that the band that first occurs at 931 cm^{-1} in NS50Ac50 composition now is at 978 cm^{-1}. It is not clear whether this evolution is a result of diminished interference from the 925 cm^{-1} band as the Ac content decreases and increased intensity as the NS content increases, or a result of diminished (Si,Fe) coupling of this vibration as the Fe content of the quenched melts decreases. Note, however, that the other band assigned to ^-O–(Si,Fe)–O^- stretch vibration (880 cm^{-1}) does not change its frequency significantly as a function of Ac content of the melt; only its intensity decreases. We suggest that the same behavior takes place for the 970 cm^{-1} band. Its frequency remains constant as the bulk composition changes, but the intensity increases at the expense of the more (Si,Fe)-coupled vibrations.

The diminished influence of Fe on the band frequencies of quenched NS85Ac15 melt is also indicated by the increased frequency of the 1050 cm^{-1} band, now found at 1065 cm^{-1}. The 1065 cm^{-1} frequency is nearly the same as for pure NS melt (Fig. 11, Table 7). This band is probably due to ^-O–Si–O^0 stretching with insignificant (Si,Fe) coupling.

The spectrum of quenched NS94Ac6 melt closely resembles that of quenched melt of NS100 composition (Fig. 11) and differs substantially from the spectra of more Fe-rich compositions. The same bands are observed in the spectra of quenched NS100 and NS94Ac6 melts, although there are systematic frequency shifts (Fig. 14). The 1070 cm^{-1} band in pure NS occurs at 1032 cm^{-1}, and the strong band at 970 cm^{-1} is found at 962 cm^{-1}. The weak band at 847 cm^{-1} in quenched NS melt is at 847 cm^{-1} in NS94Ac6 melt as well. The 619 cm^{-1} band in pure NS melt is at slightly lower frequency in NS94Ac6 melt, probably reflecting a slightly higher degree of polymerization (Brawer, 1975). The 1032 cm^{-1} band in quenched NS94Ac6 melt is assigned to ^-O–(Si,Fe)–O^0 stretching (sheet), and the 962 cm^{-1} band to ^-O–(Si,Fe)–O^- stretching (chain). The 847 cm^{-1} band reflects the presence of isolated SiO_4^{4-} tetrahedra in the quenched melt. There is no evidence for additional Raman bands that may be ascribed to isolated $NaFeO_4^{4-}$ tetrahedra. The intensity of the 1032 cm^{-1} band relative to that at 962 cm^{-1} is greater than the intensity ratio of the analogous bands in pure quenched NS melt. We conclude, therefore, that even though monomers, chains, and sheets are present in both quenched melts, the proportion of sheet units is greater in NS94Ac6 quenched melt than in NS melt.

In summary, mixing of Na_2SiO_3 (NS) and $NaFe^{3+}Si_2O_6$ (Ac) components results in a melt that to a first approximation resembles mixing of SiO_2 and Na_2SiO_3 when the NS melt becomes more po-

lymerized as the Ac content of the melt is increased. Ferric iron is distributed among all structural units in the melts, with the possible exception of isolated tetrahedra. The latter structural unit has a limited stability field, however, as it is not observed in melts with more than 15 mole % Ac component.

The spectra are also interpreted to indicate that the stretch vibrations of the various structural units occur in pairs—one indicates greater Si(Fe)-coupling than the other. This observation may indicate that both Fe-rich and Si-rich structural units occur in these melts.

The anionic structures of these melts differ in the extent of disproportionation, which can be expressed with the intensity ratios $I(970)/I(870)$ and $I(970)/I(1070)$ (Table 9). The larger the extent of disproportionation, the smaller the intensity ratios. Tables 9 and 10 show that the extent of disproportionation of metasilicate melts increases in the order NS < En < Di < Wo.

Redox equilibria

Despite the similarity of the anionic silicate units in metasilicate melts, ferric iron enters tetrahedral coordination only in the presence of Na^+. Metasilicate melts of the alkaline earths have ferric iron in octahedral coordination. In all other alkali silicate melts investigated so far (Mysen and Virgo, 1978; Brown *et al.*, 1978: Seifert *et al.*, 1979b), ferric iron enters tetrahedral coordination, probably as an $NaFeO_2$ complex, in analogy with the $NaAlO_2$ complex found in Al-bearing melts (Virgo *et al.*, 1979; Brawer and White, 1977). It may be inferred, therefore, that in alkali-bearing melts, Fe^{3+} and Al^{3+} often play similar structural roles.

Solution of Ac component in NS melt in air (no detectable ferrous iron) results in the formation of structural units with $NBO/Fe^{3+} = 1$ and 2 ($Fe_2O_5^{4-}$ and $Fe_2O_6^{6-}$, respectively), in addition to the structural units expressed with equation 1. As $f(O_2)$ is lowered below that of air, ferrous iron is formed in these melts. Our data and published information (Mao *et al.*, 1973; Bell and Mao, 1974; Boon and Fyfe, 1972; Mysen and Virgo, 1978) indicate that Fe^{2+} is a network modifier. The redox equilibrium involving ferric iron in tetrahedral coordination and ferrous iron in octahedral coordination may be expressed with the equation:

$$4Fe(IV)O_2^- + 36O^-(NBO) \rightleftarrows 4Fe(VI)O_6^{10-} + O_2 \quad (2)$$

The nonbridging oxygen (NBO) required to form the octahedral ferrous ion complex, FeO_6^{10-}, may be derived from the anionic silicate structural units. Equation 1 may be combined with equation 2, therefore, in order to describe the interaction between redox equilibria of iron and the anionic structure of silicate melts:

$$72Si_2O_6^{4-} + 4Fe(IV)O_2^- \rightleftarrows 54Si_2O_5^{2-} + 36SiO_4^{4-} + 4Fe(VI)O_6^{10-} + O_2 \quad (3)$$

The $Fe^{3+}/\Sigma Fe$ of such melts depends, therefore, not only on $f(O_2)$, but also on the NBO/T of the melt, a conclusion also made by Lauer (1977) and Lauer and Morris (1977).

We concluded above, on the basis of the isomer shifts of ferric iron, that Fe^{3+} will not be a network former in melts where there is only alkaline-earth metal network modifier for local charge balance. The redox equilibria of network modifiers in such melts do, however, also depend on the anionic structure of the silicate melts, as also shown by Lauer and Morris (1977). Those authors concluded, for example, that the redox equilibrium for a network-modifying cation shifts to a more reduced state as the size of the network-modifying cations in the melt decreases. This conclusion accords with our observation for iron oxides in melts on the join $MgSiO_3$–$CaSiO_3$ (Fig. 8), where the $Fe^{3+}/\Sigma Fe$ decreases as Ca/(Ca + Mg) decreases. Lauer and Morris (1977) expressed such relationships with a Φ-function that could be determined experimentally without further consideration for the structure of the silicate melts. We may discuss this dependence in terms of the disproportionation of anionic polymers such as shown in equation 1. According to the results summarized in Table 8, equation 1 shifts to the left as Ca/(Ca + Mg) of the melt

Table 9. Intensity ratios $I(970)/I(870)$ and $I(970)/I(1070)$, in quenched silicate melts

Composition	$I(970)/I(870)$	$I(970)/I(1070)$
$MgSiO_3$	3.95	3.53
$CaSiO_3$	2.69	1.77
$CaMgSi_2O_6$	3.57	2.53
Na_2SiO_3	8.17	5.15

Table 10. Percentage change of $I(970)/I(870)$ and $I(970)/I(1070)$ of quenched melts on the join $CaSiO_3$–$MgSiO_3$ relative to quenched melt of Na_2SiO_3 composition

Composition	$I(970)/I(870)$	$I(970)/I(1070)$
$CaSiO_3$	-67	-65
$CaMgSi_2O_6$	-56	-51
$MgSiO_3$	-52	-31

decreases. Whether this is because both the monomer and the sheet unit are affected by the decreasing size of the cation or only one of these units are affected cannot be ascertained from our data. Dent Glasser (1979) noted, however, that in silicate minerals the stability of highly polymerized silicate polymers is lowered as the network modifier becomes smaller. It is tempting to suggest, therefore, that similar relationships may apply to melts.

The redox equilibrium in alkaline-earth metasilicates can be expressed by combining equation 1 with one that describes the redox equilibrium of iron oxides as network modifiers.

$$2Fe(VI)O_6^{9-} + 2O^-(NBO) \leftrightarrows 2Fe(VI)O_6^{10-} + O_2 \quad (4)$$

to give:

$$8Si_2O_6^{4-} + 4Fe(VI)O_6^{9-} \leftrightarrows 4SiO_4^{4-} + 6Si_2O_5^{2-} + 4Fe(VI)O_6^{10-} + O_2 \quad (5)$$

Equation 5 shows that as the degree of proportionation of the metasilicate chains increases at constant $f(O_2)$, $Fe^{3+}/\Sigma Fe$ will increase.

The equilibrium constants from equations 3 and 5 are:

$$K_1 = C^9[Fe(VI)O_6^{10-}/Fe(IV)O_2^-]^4 f(O_2) \quad (6)$$

and

$$K_2 = C[Fe(VI)O_6^{10-}/Fe(VI)O_6^{9-}]^4 f(O_2) \quad (7)$$

where

$$C = [(Si_2O_5^{2-})^6(SiO_4^{4-})^4]/Si_2O_6^{4-})^8 \quad (8)$$

Equations 6 and 7 demonstrate that the redox ratio of iron is much less sensitive to the extent of disproportionation when ferric iron is a network modifier than when it is a network former.

The value of C (eq. 8) for a given alkali metal or alkaline earth increases with increasing temperature and with decreasing pressure (Mysen *et al.*, 1980). Consequently, at constant $f(O_2)$, $Fe^{3+}/\Sigma Fe$ will increase with increasing temperature and will decrease with increasing pressure. The pressure and temperature dependence of the redox ratio is more pronounced in melts with ferric iron as a network former than in melts with ferric iron as a network modifier. The $f(O_2)$ dependence of $Fe^{3+}/\Sigma Fe$ is the same regardless of whether ferric iron is an network former or a network modifier.

Petrological applications

The above summary shows that changes of extensive and intensive variables affect physical and chemical properties of iron-bearing, rock-forming silicate melts because of the complex structural role of iron in the melts. Acidic melts such as andesite, dacite, and granite (rhyolite) will have a large excess of M^+ over M^{2+} melt modifiers. As a result, variations of redox ratios of iron will alter the degree of polymerization of the melt and therefore the viscosity and cation diffusion coefficients. It is expected, for example, that increasing $f(O_2)$ will result in increasing viscosity of the melt. Cation diffusion coefficients in silica-rich, iron-bearing melt will most likely decrease with increasing oxygen fugacity. Notably, the experimental data (Seifert *et al.*, 1979b) indicate that the activity coefficients of the Fe^{3+} and Fe^{2+} complexes do not change with oxygen fugacity. As a result, partition coefficients of ferrous and ferric iron between acidic melts and minerals in equilibrium with the melt will not be affected by the oxygen fugacity.

Physical properties of basaltic melts will be affected less by changing redox ration of iron than silica-rich melts because alteration of redox states results in smaller changes of NBO/BO. It is notable, however, that as a result of fractional crystallization of a basaltic melt to more silicic compositions, the physical properties of the magma will gradually change as the influence of redox ratios of iron on the degree of polymerization of the melt increases with increasing M^+/M^{2+}.

Acknowledgements

Critical reviews by C. M. Scarfe, H. S. Yoder, Jr., H. S. Waff, and G. Waychunas are appreciated. This research was partially supported by NSF grant EAR-7911313 and partially by the Carnegie Institution of Washington.

References

Annersten, H. and U. Hålenius (1976) Ion distribution in pink muscovite: a discussion. *Am. Mineral., 61,* 1045–1050.

——— and M. Olesch (1978) Distribution of ferrous and ferric iron in clintonite and the Mössbauer characteristics of ferric iron in tetrahedral coordination. *Can. Mineral., 16,* 199–204.

Bancroft, G. M. and R. G. Burns (1969) Mössbauer absorption spectral study of alkali amphiboles. *Mineral. Soc. Am. Spec. Pap., 2,* 137–151.

———, P. G. L. Williams and E. J. Essene (1969) Mössbauer spectra of omphacite. *Mineral Soc. Am. Spec. Pap., 2,* 59–67.

Bates, J. B., R. W. Hendricks and L. B. Shaffer (1974) Neutron irradiation effects and structure of non-crystalline SiO_2. *J. Chem. Phys., 61,* 4163–4176.

Bell, P. M. and H. K. Mao (1974) Crystal-field spectra of Fe^{2+} and Fe^{3+} in synthetic basalt glass as a function of oxygen fugacity. *Carnegie Inst. Wash. Year Book, 73,* 496–497.

Bhargava, S. C., J. E. Knudsen and S. Mørup (1979) Mössbauer study of spin–spin relaxation of Fe^{3+} ions in the presence of other paramagnetic ions. *J. Phys. Chem. Solids, 40,* 45–53.

Bockris, J. O'M. and A. K. N. Reddy (1970) *Modern Electrochemistry, Vol. 1.* Plenum Press, New York.

Bowen, N. L., J. F. Schairer and H. W. V. Willems (1930) The ternary system Na_2SiO_3–Fe_2O_3–SiO_2. *Am. J. Sci., 20,* 405–455.

Brawer, S. A. (1975) Theory of the vibrational spectra of some network and molecular glasses. *Phys. Rev. B., 11,* 3173–3194.

——— and W. B. White (1975) Raman spectroscopic investigation of the structure of silicate glasses. I. The binary silicate glasses. *J. Chem. Phys., 63,* 2421–2432.

——— and ——— (1977) Raman spectroscopic study of the structure of silicate glasses. II. Soda-alkali earth-alumina ternary and quaternary glasses. *J. Non-Cryst. Solids, 23,* 261–278.

Brown, G. E., K. D. Keefer and P. M. Fenn (1978) Extended X-ray fine structure (EXAFS) study of iron-bearing silicate glass (abstr.). *Geol. Soc. Am. Abstracts with Programs, 10,* 373.

Buddington, A. F. and D. H. Lindsley (1964) Iron–titanium oxide minerals and synthetic equivalents. *J. Petrol., 5,* 310–357.

Carmichael, I. S. E. (1967) The iron–titanium oxides of salic volcanic rocks and their associated ferromagnesian silicates. *Contrib. Mineral. Petrol., 14,* 36–64.

Dent Glasser, L. S. (1979) Non-existent silicates. *Z. Kristallogr., 149,* 291–305.

Etchepare, J. (1972) Study by Raman spectroscopy of crystalline and glassy diopside. In R. W. Douglas and B. Ellis, Eds., *Amorphous Materials,* p. 337–346. Wiley, New York.

Fudali, R. F. (1965) Oxygen fugacity of basaltic and andesitic magmas. *Geochim. Cosmochim. Acta, 29,* 1063–1075.

Furukawa, T. and W. B. White (1980) Raman spectroscopic investigation of the structure of silicate glasses. III. Alkali–silica–germanates. *J. Chem. Phys.,* in press.

———, S. A. Brawer and W. B. White (1978) The structure of lead silicate glasses determined by vibrational spectroscopy. *J. Mater. Sci., 13,* 268–282.

Kracek, F. C. (1930) The system sodium oxide–silica. *J. Phys. Chem., 34,* 1583–1598.

Kurkjian, C. R. (1970) Mössbauer spectroscopy in inorganic glasses. *J. Non-Cryst. Solids, 3,* 157–194.

Kuroda, K. and C. Kato (1979) Trimethylsilylation of hemimorphite. *J. Nucl. Inorg. Chem., 41,* 947–951.

Lauer, H. V. (1977) Effect of glass composition on major element redox equilibria: Fe^{2+}–Fe^{3+}. *Phys. Chem. Glasses, 18,* 49–52.

——— and R. V. Morris (1977) Redox equilibria of multivalent ions in silicate glasses. *J. Am. Ceram. Soc., 60,* 443–451.

Lazarev, A. N. (1972) *Vibrational Spectra and Structure of Silicates.* Consultants Bureau, New York.

MacKenzie, J. D. (Ed.) (1960) *Modern Aspects of the Vitreous State.* Butterworth's, Washington, D. C.

Mao, H. K., D. Virgo and P. M. Bell (1973) Analytical study of the orange soil returned by the Apollo 17 astronauts. *Carnegie Inst. Wash. Year Book, 72,* 631–638.

Masson, C. R. (1977) Anionic constitution of glass-forming melts. *J. Non-Cryst. Solids, 1,* 1–42.

Mysen, B. O. and D. Virgo (1978) Influence of pressure, temperature and bulk composition on melt structures in the system $NaAlSi_2O_6$–$NaFe^{3+}Si_2O_6$. *Am. J. Sci., 278,* 1307–1322.

———, ——— and F. Seifert (1979) Redox equilibria and melt structure in the system CaO–MgO–FeO–Fe_2O_3–SiO_2. *Carnegie Inst. Wash. Year Book, 78,* 519–526.

———, ——— and C. M. Scarfe (1980) Relations between anionic structure and viscosity of silicate melts—a Raman spectroscopic study at 1 atmosphere and at high pressure. *Am. Mineral. 65,* 690–710.

Osborn, E. F. (1959) Role of oxygen pressure in the crystallization and differentiation of basaltic magmas. *Am. J. Sci., 257,* 609–647.

——— (1962) Reaction series for subalkaline igneous rocks based on different oxygen pressure conditions. *Am. Mineral., 47,* 211–226.

——— (1977) Origin of calc-alkali magma series of Santorini volcano type in light of recent experimental phase-equilibrium studies. *Proceedings of the International Congress on Thermal Waters, Geothermal Energy and Vulcanism of the Mediterranean Area, Athens, October 1976, 3,* 154–167.

Roeder, P. L. and R. F. Emslie (1970) Olivine–liquid equilibrium. *Contrib. Mineral. Petrol., 29,* 275–289.

Schreiber, H. D., T. Thanyashiri, J. J. Lach and R. A. Legere (1978) Redox equilibria of Ti, Cr and Eu in silicate melts: reduction potentials and mutual interactions. *Phys. Chem. Glasses, 19,* 126–140.

Seifert, F. and M. Olesch (1977) Mössbauer spectroscopy of grandidierite, $(Mg,Fe)Al_3BSiO_9$. *Am. Mineral., 62,* 547–553.

———, D. Virgo and B. O. Mysen (1979a) Sodium loss from sodium metasilicate melts in CO_2 and CO atmospheres. *Carnegie Inst. Wash. Year Book, 78,* 679.

———, ——— and ——— (1979b) Melt structures and redox equilibria in the system Na_2O–FeO–Fe_2O_3–Al_2O_3–SiO_2. *Carnegie Inst. Wash. Year Book, 78,* 511–519.

Sharma, S. K. and H. S. Yoder (1979) Structural study of glasses of akermannite, diopside and sodium melilite compositions by Raman spectroscopy. *Carnegie Inst. Wash. Year Book, 78,* 526–532.

Taneja, S. P., C. W. Kimball and J. C. Schaffer (1973) Mössbauer spectroscopy of amorphous semiconductors and glasses containing antimony, tin and iron: a review. *Mössbauer Effect Methodology, 8,* 41–69.

Verweij, H. (1979a) Raman study of the structure of alkali germanosilicate glasses. I. Sodium and potassium metagermanosilicate glasses. *J. Non-Cryst. Solids, 33,* 41–53.

——— (1979b) Raman study of the structure of alkaligermanosilicate glasses. II. Lithium, sodium and potassium digermanosilicate glasses. *J. Non-Cryst. Solids, 33,* 55–69.

——— and W. L. Konijnendijk (1976) Structural units in K_2O–PbO–SiO_2 glasses by Raman spectroscopy. *J. Am. Ceram. Soc., 59,* 517–521.

Virgo, D., B. O. Mysen and I. Kushiro (1980) Anionic constitution of silicate melts quenched from 1 atm from Raman spectroscopy: implications for the structure of igneous melts. *Science,* in press.

———, F. Seifert and B. O. Mysen (1979) Three-dimensional network structures of melts in the systems $CaAl_2O_4$–SiO_2, $NaAlO_2$–SiO_2, $NaFeO_2$–SiO_2 and $NaGaO_2$–SiO_2 at 1 atm. *Carnegie Inst. Wash. Year Book, 78,* 506–511.

Waff, H. S. (1977) The structural role of ferric iron in silicate melts. *Can. Mineral., 15,* 198–199.

Manuscript received, September 28, 1979;
accepted for publication, May 2, 1980.

American Mineralogist, Volume 65, pages 885–899, 1980

Solubility mechanisms of carbon dioxide in silicate melts: a Raman spectroscopic study

BJØRN O. MYSEN AND DAVID VIRGO

Geophysical Laboratory, Carnegie Institution of Washington
Washington, D.C. 20008

Abstract

Determinations of carbon dioxide solubility in melts of $CaMgSi_2O_6$ and $NaCaAlSi_2O_7$ composition at high pressure and temperature have been combined with Raman spectroscopic measurements of quenched melts to determine the structural role of CO_2 in silicate melts.

Carbon dioxide solubility increases with increasing temperature under isobaric conditions between 1450° and 1700°C and decreases as a function of increasing temperature below 1450° and above 1700°C. We suggest that these contrasting temperature dependences are a result of similar contrasting behavior of the fugacity of CO_2.

Carbon dioxide dissolves in silicate melts predominantly as CO_3^{2-}. This anion is most likely closely associated with one or more network-modifying cations. In the present melts we suggest that $(CaCO_3)^0$ complexes are formed.

The CO_2 contents of the quenched melts are systematically correlated with structural changes of the network of the melts. The anionic structure of alkaline earth metasilicate melts is predominantly a combination of structural units that, on the average, have 4, 2, and 1 nonbridging oxygens per silicon (NBO/Si). These structures are referred to as monomers, chains, and sheets. The formation of carbonate is associated with a lowering of the proportion of monomers in the melt and an increase of the proportions of chain and sheet units.

The principles of CO_2 solubility mechanisms derived from melt of $CaMgSi_2O_6$ composition also apply to melt of $NaCaAlSi_2O_7$ composition. The solubility mechanisms in the two types of melts differ in detail, however, as the latter melt contains a large proportion of aluminum in tetrahedral coordination, which combined with the silicon results in a higher degree of polymerization of the melt. The $NaCaAlSi_2O_7$ melt consists of structural units that, on the average have 2, 1, and 0 nonbridging oxygens per tetrahedrally coordinated cation (NBO/T). These units are referred to as chains, sheets, and three-dimensional network structures, respectively. When CO_2 is dissolved in such melt, the three-dimensional network units become more dominant at the expense of chain units.

We suggest that the $NaCaAlSi_2O_7$ melt composition is a better model for natural basalt magma than $CaMgSi_2O_6$ melt. On the basis of our observations, we conclude, however, that the predictions of CO_2 solubility behavior in natural basalt melt based on studies with binary silicate systems provide an accurate basis for understanding the role of CO_2 in silicate melts.

Introduction

The presence of CO_2 during the formation and evolution of igneous rocks is well documented. Carbon dioxide is one of the major components of volcanic gases (Gerlach and Nordlie, 1975). It is also a major volatile component in glass and fluid inclusions in phenocrysts in basalts (Roedder, 1965; Green, 1972; Delaney *et al.*, 1978). Its presence in the upper mantle during partial melting is documented (McGetchin and Besancon, 1973; see also Irving and Wyllie, 1975, for review of data).

Phase-equilibrium measurements on CO_2-bearing systems relevant to igneous processes in the upper mantle have shown that the presence of CO_2 results in enhanced stability of more polymerized minerals relative to those observed in the absence of CO_2 (Eggler, 1975; Huang and Wyllie, 1976; Eggler and Rosenhauer, 1978; Eggler *et al.*, 1979). As a result, partial melts of peridotite + CO_2 are more basic than those formed by partial melting of CO_2-free peridotite (Wendlandt and Mysen, 1978).

On the basis of the data summarized above and in-

0003–004X/80/0910–0885$02.00

frared measurements of quenched, CO_2-saturated silicate melts (Mysen *et al.*, 1976; Brey and Green, 1976; Eggler *et al.*, 1979), it has been suggested that CO_2 is dissolved in silicate melts primarily as CO_3^{2-}. It has also been suggested that the silicate melt becomes more polymerized as a result of the formation of this carbonate anion. The effect on the melt structure of solution of CO_2 has not, however, been determined. In order to determine the structural role of CO_2 in rock-forming silicate melts under conditions relevant to magma formation and evolution, Raman spectroscopy of silicate melts with and without CO_2 has been used in conjunction with solubility determinations on selected melt compositions.

Starting materials

Two melt compositions were chosen for CO_2 solubility studies (compositions: $CaMgSi_2O_6$—Di melt, and $NaCaAlSi_2O_7$—Sm melt). In addition, six CO_2-free compositions on the join Ca_2SiO_4–SiO_2 were studied in order to substantiate the band assignments in the CO_2-bearing samples. This join was chosen because of its chemical simplicity; only Si^{4+} is in tetrahedral coordination. The overall ratio of nonbridging oxygens to tetrahedral cation (NBO/T) is a simple function, therefore, of the Ca/Si (atomic) ratio. Furthermore, there are other published data on melt compositions where Ca^{2+} is substituted with other alkaline earth and alkali metal cations.

For the CO_2 solubility studies, Di melt was used, in part because of the significant amount of available experimental data on Di-bearing systems and also because no amphoteric oxides exist in Di melt. A direct correlation between dissolved carbonate anions and their influence on the Si-O network may result. Sm melt was chosen because of the presence of a large proportion of aluminum, which may act as both a network former and a network modifier. In volatile-free Sm melt, all Al is probably a part of the silicate network where Al exist as $(CaAl_2O_4)^0$ or as $(NaAlO_2)^0$ complexes (Virgo *et al.*, 1979). The possibility exists, therefore, that with the formation of CO_3^{2-} anions as $CaCO_3$ or Na_2CO_3 a portion of the aluminate complexes may dissociate, as some of the modifying cations in the aluminate complexes are needed to form carbonate complexes. As a result of this mechanism, some Al may no longer be in the network, and the melt must depolymerize because of dissolved CO_2.

Experimental technique

The starting materials were mixtures of Johnson–Matthey spectroscopically pure SiO_2, Al_2O_3, MgO, and $CaCO_3$, and reagent grade Na_2CO_3. All high-pressure experiments were conducted in solid-media, high-pressure apparatus (Boyd and England, 1960) using sealed Pt containers of 3 mm O.D. in a furnace assembly of 0.5″ diameter. Inasmuch as the furnace parts must be kept dry to avoid formation of H_2 with the resultant formation of reduced carbon species in the experimental charges (Eggler *et al.*, 1974), the furnace parts were dried thoroughly prior to each experiment.

All experiments were carred out with the piston-out technique and with no pressure correction for friction (Boyd and England, 1963). The uncertainty of the pressure is about ±1 kbar. Thermocouples were Pt–Pt90Rh10 with no correction on the electromotive force for pressure. The uncertainty of the temperature due to this simplification is 6°–10°C, depending on the temperature (Mao *et al.*, 1971). Quenching rates were of the order of 250°C/sec.

Selected high-pressure experiments had run durations up to 1 hour at 1700°C. The thermocouple drift at such high temperatures depends, to a large extent, on the purity of the alumina thermocouple insulators (Mao *et al.*, 1971; Presnall *et al.*, 1973). In the present studies, McDanel grade 998 alumina was used in all experiments. With this high-purity alumina, the thermocouple drift is about 10° per hour at 1700°C. Inasmuch as the uncertainty of the temperature is already about 10°C due to the largely unknown influence of pressure of the emf, no further refinement of the temperature monitoring system was carried out.

High-pressure experiments of CO_2-free melts of Di and Sm composition were carried out with glass starting materials. The run durations were the same as for the CO_2-bearing samples at the same temperature and pressure. The one-atm glasses were quenched after 30 minutes at 1500°C. All samples were contained in Pt capsules (sealed).

The six melt compositions on the join Ca_2SiO_4–SiO_2 were prepared at 1650°C in a vertical quench furnace with molybdenum disilicide heating elements. In order to avoid contamination of the samples by conventional quenching in water or mercury, the samples were quenched in a Pt crucible standing in liquid nitrogen. The quenching rate with this technique is on the order of 500°/sec over the first 1000°C.

The CO_2 contents of the quenched melts were measured with beta-track mapping (Mysen and Seitz, 1975), using carbon-14 as source of the beta activity. This activity was recorded on K-5 nuclear emulsions supplied by Ilford Co., England. The stan-

dard was synthetic calcite. The reliability of this method has been tested against determinations by several other techniques (*e.g.*, Kadik and Eggler, 1975; Mysen *et al.*, 1976; Eggler *et al.*, 1979) and is reliable to within less than 5% of the CO_2 content of the sample.

The Raman spectra were taken on small chips of quenched bubble-free melt (about 0.5–1.0 mm cubes). The spectra were recorded with a Jobin-Yvon optical system, holographic grating, double monochromator (HG25), and a photon-counting detection system. The spectra were recorded at 3 cm^{-1}/sec. The samples were excited with the 488.0 mn line of an Ar^+ laser, using a laser power of 200–400 mW at the sample with 90° scattering geometry. Polarized spectra were obtained with the focused exciting beam parallel to the horizontal spectrometer slit and with the electric vector of the exciting radiation in a vertical orientation. A sheet of polarizer disk in front of an optical scrambler was used to record separately the parallel and perpendicular components of the scattered radiation.

As a matter of routine, replicate spectra from the same chips, from different chips of the same experimental run product, and from duplicate experiments were also taken.

Equilibrium considerations

The experiments were routinely conducted with a finely ground oxide + carbonate mixture (1 μm grain size). The carbonate was the source of CO_2. Mysen *et al.* (1976) conducted solubility measurements at fixed pressure and temperature but with run durations varying from 1 to 60 min. They found that in a viscous melt such as that of $NaAlSi_3O_8$ composition, less than 5 min was needed to reach equilibrium CO_2 concentrations at 1450°C and 20 kbar. Longer run durations did not affect the results. In the present study experiments of 5 min or longer were always used. In addition, reversal experiments at 20 kbar and 1685°C were carried out. These conditions were chosen because the forward experiments indicated that melts quenched from this temperature and pressure contained the largest amount of CO_2. In the reversal experiments the sample was first subjected to 10 kbar and 1650°C for 10 min, where the forward experiments indicated that the solubility was less than 50 percent of that at 20 kbar and 1685°C. The conditions were then changed to 20 kbar and 1685°C. About 60 min under these conditions was needed to reach the same CO_2 concentrations as in the initial experiment. Shorter run durations resulted in heterogeneous charges. The much longer run lengths needed to achieve equilibrium in the reversal experiments can be understood by considering the diffusion distances of CO_2 in the two types of experiment. During a forward experiment, CO_2 needs to move only a few micrometers to become thoroughly mixed with the oxide components because of the fine-grained, thoroughly mixed nature of the starting material. The CO_2 that does not dissolve in the melt enters a separate vapor phase. During a reversal experiments some of the CO_2 that initally entered the vapor phase must redissolve in the melt and move perhaps several hundred micrometers into the liquids, thus requiring longer time for equilibration.

This agreement between the forward and reversal experiments indicates that the run durations used for the routine experiments were sufficient to attain equilibrium CO_2 contents of the melts.

Results

CO_2 solubility

The carbon dioxide solubilities in the melts and other experimental details are shown in Table 1. The reversal experiment is marked with an asterisk. Carbon dioxide contents of quenched melts of Di composition as a function of temperature and pressure are shown in Figure 1. The solubilities agree with those of Mysen *et al.* (1976) in the pressure and temperature ranges also studied by them. Whereas Mysen *et al.* (1976) suggested essentially no temperature dependence of the solubility at 10 kbar, the present data may indicate a very slight decrease in CO_2 content with increasing temperature above 1600°C at this pressure. At 20 kbar the CO_2 solubility in Di melt increases rapidly from 1580° to about

Table 1. Run data

Sample No.	Composition	Pressure, kbar	Temp., °C	Run Duration, min	Wt % CO_2
997	Di + CO_2	10	1550	10	1.55 ± 0.02
1014	Di + CO_2	10	1600	10	2.00 ± 0.06
995	Di + CO_2	10	1650	10	1.95 ± 0.05
1018	Di + CO_2	10	1725	5	1.85 ± 0.07
1036	Di + CO_2	20	1580	15	3.1 ± 0.1
1000	Di + CO_2	20	1650	5	3.38 ± 0.08
1023	Di + CO_2	20	1685	5	4.8 ± 0.2
1002	Di + CO_2	20	1725	5	2.71 ± 0.09
1004	Di + CO_2	25	1725	5	3.6 ± 0.1
1039*	Di + CO_2	20	1685	60	5.0 ± 0.2
1056	Sm + CO_2	10	1275	60	5.2 ± 0.2
1073	Sm + CO_2	10	1460	15	3.9 ± 0.2
1074	Sm + CO_2	10	1550	10	3.8 ± 0.1
1062	Sm + CO_2	20	1325	30	4.9 ± 0.2
1068	Sm + CO_2	20	1460	15	4.4 ± 0.2
1072	Sm + CO_2	20	1550	10	5.9 ± 0.3

*Reversal.

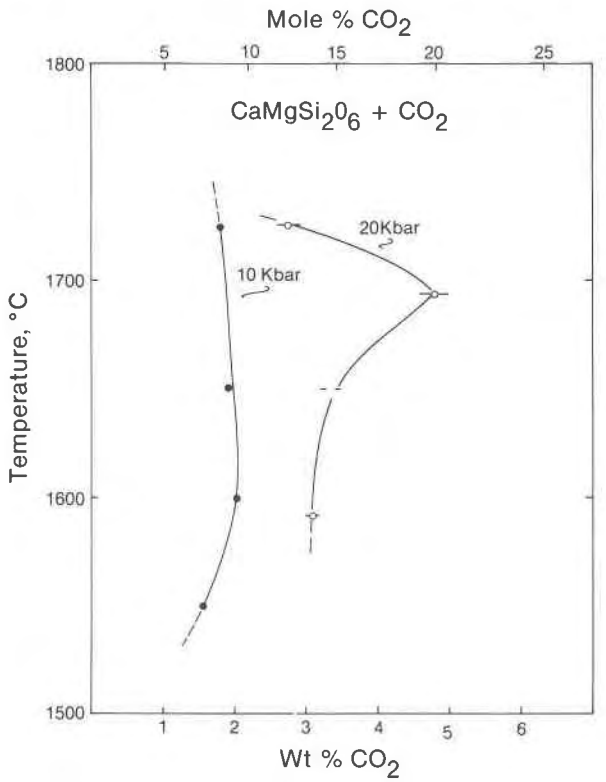

Fig. 1. Carbon dioxide solubility in Di melt as a function of temperature and pressure.

1700°C. As the temperature is raised further, the CO_2 content of the melt is lowered. There is therefore a maximum of the CO_2-solubility curve for Di melt at 20 kbar. The CO_2 solubility at 1685°C and 20 kbar was confirmed by replicate experiments, time studies, and reversal experiments. This maximum CO_2 solubility was not observed by Mysen *et al.* (1976) because they did not extend their experiments to sufficiently high temperatures. Holloway *et al.* (1976) found, however, that CO_2 solubilities in melts on the join Ca_2SiO_4–Mg_2SiO_4 also reached a maximum and then decreased as the temperature was raised above 1700°C at 20 kbar, and they suggested a structural interpretation for this observation. The CO_2 solubility in a melt of natural nephelinite composition (Mysen *et al.*, 1975) also passed through a maximum near 1700°C at 20 kbar (Mysen and Eggler, unpublished data, 1977).

Inasmuch as the structures of ortho- and metasilicate melts differ substantially in the degree of polymerization (Brawer and White, 1975; Verweij and Konijnendijk, 1976; Furukawa *et al.*, 1978), it is not likely that the hypothesis of Holloway *et al.* (1976), suggesting that the melt must be nearly completely depolymerized at 1700°C, can be used to explain the data.

The carbon dioxide solubility in Sm melt displays a more complex behavior with temperature than is the case for Di melt (Figs. 1 and 2). At both 10 and 20 kbar the solubility decreases with increasing temperature immediately above the liquidus (above about 1300°C). At 10 kbar the rate of decrease diminishes as the temperature is increased, whereas at 20 kbar the CO_2 solubility in Sm melt passes through a minimum with increasing temperature at about 1450°C. At high temperature the CO_2 solubility increases.

Data on carbon dioxide solubility in silicate melts at temperatures below 1460°C are scarce. It is not possible to decide, therefore, whether the unusual temperature dependence of the solubility in the temperature range below 1450°C in Sm melt is due to the thermodynamic properties of CO_2 or to the structural features of Sm melt in this temperature range.

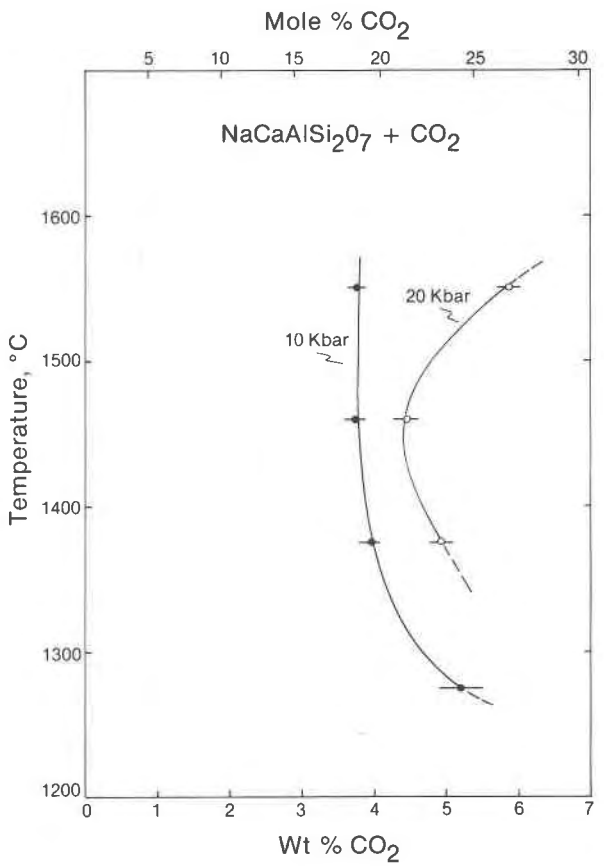

Fig. 2. Carbon dioxide solubility in Sm melt as a function of temperature and pressure.

Raman spectroscopy

In order to provide a framework for Raman spectroscopic band assignments, Virgo *et al.* (1980) acquired spectra of 14 quenched melts on the joins Ca_2SiO_4–SiO_2 and $CaMgSiO_4$–SiO_2. These spectra were also compared with the published data on the joins Li_2O–SiO_2, Na_2O–SiO_2, K_2O–SiO_2, CaO–SiO_2, and PbO–SiO_2 (Brawer and White, 1975, 1977; Verweij and Konijnendijk, 1976; Verweij, 1979a,b; Furukawa *et al.*, 1978; Furukawa and White, 1980). A result of this comparative study was that for all these compositions, at given metal cation to silicon ratio, the same Raman bands occur. The spectra differ somewhat in resolution, however, presumably because of variations in local disorder (Brawer, 1975).

The spectra with the best resolution of important stretch bands are found on the join Ca_2SiO_4–SiO_2 (Fig. 3; see also Table 2). The dominant feature of each spectrum is the intense, slightly asymmetric band in the region 610–673 cm^{-1} combined with an intense, high-frequency envelope in the region 830–1060 cm^{-1}. All these bands are strongly polarized. The Raman spectra on the join $CaMgSiO_4$–SiO_2 are similar to those of analogous melts along the join Ca_2SiO_4–SiO_2 (Virgo *et al.*, 1980).

On the basis of comparison with appropriate crystalline analogues, and experimental and theoretical considerations (Lazarev, 1972; Etchepare, 1972; Brawer, 1975; Brawer and White, 1975, 1977; Furukawa *et al.*, 1978; Furukawa and White, 1980; Verweij, 1979a,b; Sharma *et al.*, 1979; Virgo *et al.*, 1980), we conclude that the band assignments summarized in Table 3 represent the best interpretation of the Raman data summarized above and exemplified with Figure 3 and Table 2.

The most important observation made from the above assignment of the Raman spectra is that there is a unique set of coexisting anionic structural units for specific ranges of the ratio of nonbridging oxygen to silicon. In Table 3, the anionic units are defined on the basis of average NBO/Si. There are several aspects of these conclusions that warrant further comment. In comparison to other models of melt structure (*e.g.*, Masson, 1968), the present model is strikingly simple. This simplicity should not be surprising in view of the fact that when comparing the crystal structures of silicate minerals, only a few anionic structural arrangements can be found (see Dent Glasser, 1979, for review).

Previous models of silicate melt structures involve features such as trimers, tetramers, pentamers *etc.* in addition to rings and branched chains. The experimental basis for most of those models has been chromatographic data derived from trimethylsilyl derivatives of the silicate polymers (TMS derivatives). When applying that method to glass structural determinations, certain apparent inconsistencies appear. First, when comparing results from TMS-derivative studies to structural data derived from Raman spectroscopy of the same materials, the results differ (compare, for example, the results of Lentz, 1964

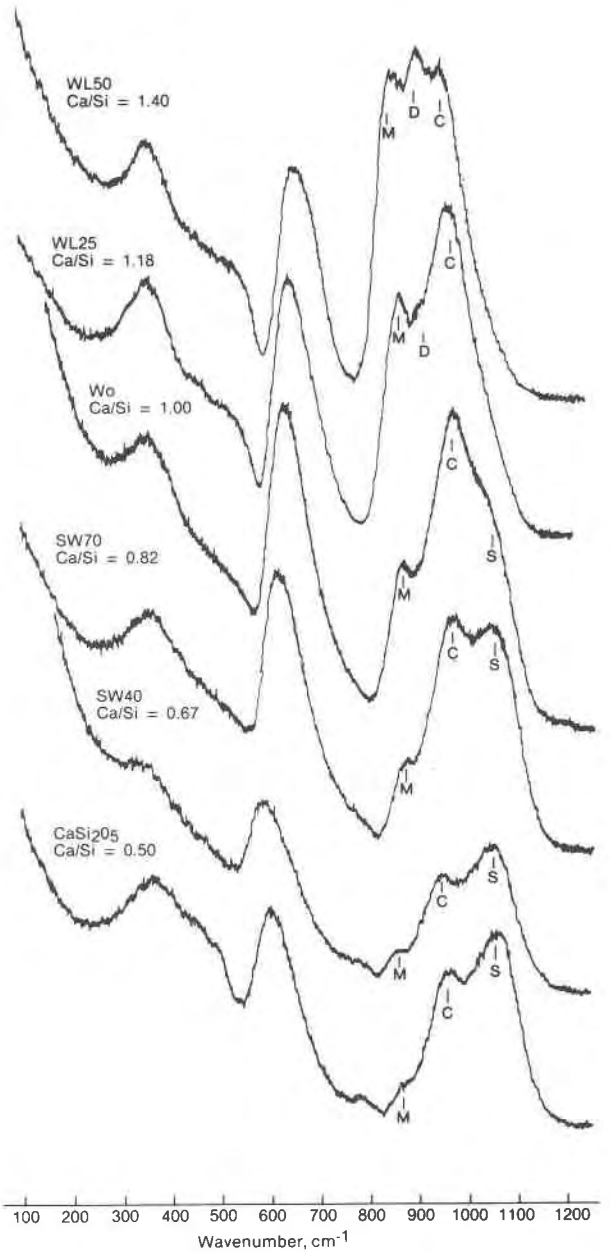

Fig. 3. Unpolarized Raman spectra of quenched melts on the join Ca_2SiO_4–SiO_2. All samples were quenched from 1650°C at 1 atm pressure after 30 minutes. (Ar^+ laser, 200–400 mW power.)

Table 2. Raman data on quenched melts in the system Ca_2SiO_4–SiO_2

Composition	Wavenumber, cm^{-1}						
WL 50	352m,p	547(Sh)	670s,p	830s,p	900s,p	960s,p	...
WL 25	350s,p	547(Sh)	647s,p	853s,p	927m,p	970s,p	...
Wo	345m,p(bd)	...	620s,p	867s,p	...	962s,p	1050m,p
SW 70	343w(bd)	...	613s,p	869w,p	...	963s,p	1051s,p
SW 40	341w(bd)	...	586s,p	863vw	...	957s,p	1055s,p
$CaSi_2O_5$	355m(bd)	...	593s,p	861vw	...	958s,p	1057s,p

Symbols: *WL 50, Ca/Si = 1.40; WL 25, Ca/Si = 1.18; Wo, Ca/Si = 1.00; SW 70, Ca/Si = 0.82; SW 40, Ca/Si = 0.67 $CaSi_2O_5$, Ca/Si = 0.50. All ratios are atomic ratios.*

vw, very weak; w, weak; m, medium; s, strong; (bd), broad; (Sh), shoulder; p, polarized Uncertainty on each measurement is about ± 5 cm^{-1} except for (Sh) where the uncertainty is near 15 cm^{-1}.

with Brawer and White, 1975 for the system Na_2O–SiO_2, and the data of Smart and Glasser, 1979 with those of Furukawa *et al.*, 1978 for the system PbO–SiO_2). Second, results obtained with the TMS derivatives are internally inconsistent. For compositions Pb_2SiO_4 and Na_4SiO_4, the melts have NBO/Si = 4. The results from the work with TMS derivatives indicate that NBO/Si is less than 3 (Smart and Glasser, 1979; Lentz, 1964). We suggest that the reason for this discrepancy is condensation of silicate polymers taking place during solution of the glasses in acid solutions to form the TMS derivatives.

Another feature of most models of melt structure is a positive correlation between order and proportion of silicate polymers and bulk NBO/Si of the melt. In Raman spectroscopic studies, such an evolution would result in a successive increase of the frequency of Si–O stretch bands as the number of Si^{4+} cations in the polymers increases (*e.g.*, Lazarev, 1972; Brawer and White, 1975; Furukawa and White, 1980; see also Table 3). On this basis it would be expected that if anionic structural units with degree of polymerization between dimers and chains were formed on the various binary silicate joins indicated above (see also Fig. 3), new bands would develop or bands such as that near 900 cm^{-1} (Fig. 3; Table 2) would shift to higher frequency as the M/Si of the melt decreased. There is no spectroscopic evidence for such developments. We conclude, therefore, that structural units with NBO/Si between that of a dimer and that of a chain do not exist in significant amounts in silicate melts.

The structural unit with NBO/Si = 2 has been referred to as a chain structure. Ring structures have, however, the same NBO/Si. The idea of the presence of ring structures in silicate melts has experimental support in studies of TMS derivatives of silicate melts (*e.g.*, Masson, 1968). In view of the discussion above, it is not clear whether such data give an accurate description of the structure of the melt itself. Spectroscopic data relevant to the formation of ring structures are scarce. Lazarev (1972) discussed spectroscopic imprints of ring structures with up to 6 silicons. The simple $Si_3O_9^{6-}$ ring has a strong deformation band near 750 cm^{-1}. No such band occurs in the spectra discussed here and elsewhere. This type of a

Table 3. Raman frequencies of the stretch vibrations of specific Si-rich anionic units in silicate melts

Structural unit	NBO/Si	Frequency (cm^{-1})	Characteristics of vibrational mode
SiO_4^{4-}	4	850–880	symmetric stretch
$Si_2O_7^{6-}$	3	900–930	symmetric stretch
$Si_2O_6^{4-}$	2	950–970	symmetric stretch
$Si_2O_5^{2-}$	1	1050–1100	symmetric stretch
SiO_2	0	1065–1200	antisymmetric stretch

Data from Virgo et al. (1980). See text for further discussion.

ring probably does not occur in these melts, therefore. Larger rings (*e.g.*, $Si_4O_{12}^{8-}$–$Si_6O_{18}^{12-}$) show vibrational bands at or slightly above 1100 cm^{-1} (Lazarev, 1972). On a spectroscopic basis alone it is not likely, but not impossible, that the S-band indicated in Figure 3 is such a band, as its frequency is near 1070 cm^{-1}. Furthermore, mass balance considerations indicate that the Raman band in this spectroscopic region reflects vibrations in structural units with NBO/Si less than 2. Consider, for example, the spectrum Wo ($CaSiO_3$) in Figure 3. The Wo composition has bulk NBO/Si = 2. The strong 870 cm^{-1} and an even stronger 970 cm^{-1} band reflect the presence in the melt of structural units with NBO/Si = 4 and 2, respectively. In order to maintain mass balance of oxygen and silicon, there must be structural units in this melt that have NBO/Si less than 2. Careful analysis by in particular Verweij (1979a,b) and Furukawa and White (1980) and also by Virgo *et al.* (1980) has led to the conclusion that the band in the frequency range between 1070 and 1100 cm^{-1} in the MO–SiO_2 and M_2O–SiO_2 melts most likely is a stretch vibration from a unit that has NBO/Si = 1. One might suggest that such a vibrational mode could stem from end units in a linear structure. Such an interpretation does not, however, provide for structural units that satisfy the mass balance of the melt. It might also be suggested that the presence of branched chains or multiple chains in the melt constitutes the structural unit(s) with NBO/Si less than 2. The end result of the evolution of such branching is, of course, an infinite sheet. The frequency of the band in question (denoted S in Fig. 3) does not shift with changes in M/Si. Its intensity increases with decreasing M/Si, however. On this basis, we conclude that the NBO/Si of this structural unit does not vary with changes of bulk NBO/Si of the melt. The possibility of a branched chain is considered unlikely for two reasons. First, there is no experimental evidence for the presence of such structures in silicate melts (branched chains with NBO/Si less than 2). Second, according to a survey by Dent Glasser (1979), branched chains do not occur in minerals. Instead, chains or sheets are formed. There is no clear reason, therefore, why one would expect such a structure in a melt.

A possible explanation for the 1070 cm^{-1} band is multiple chains. The Raman data do not establish whether the S-band (Fig. 3) is an infinite sheet or a finite sheet (multiple chains). In view of the data summarized above, the structural unit probably has an average NBO/Si near 1 (infinite sheet), and the structural units represented by this Si–O stretch band in the Raman spectra will be referred to as a sheet.

Because the relative integrated intensities of the bands assigned to the different anionic species may not be linearly related to NBO/Si, only a general discussion of their relative abundances in these silicate melts is possible at this time. We suggest that monomers are the most abundant species in the melts near the orthosilicate composition and that they become increasingly unstable with increasing NBO/Si, but are still present in the $CaSi_2O_5$ sheet composition. In contrast, the dimer unit has a restricted range of stability, with an apparent maximum in its abundance between the ortho- and metasilicate compositions. The instability of the dimer species appears to coincide with the appearance of the sheet unit, and with increasing NBO/Si the sheet and chain species increase in abundance relative to the monomer units.

In view of the above results and mass-balance considerations, we propose that the equilibria relating the coexisting anionic species are the following disproportionation reactions, which correspond to the specific ranges of NBO/Si indicated above:

$$2Si_2O_7^{6-} = 2SiO_4^{4-} + Si_2O_6^{4-} \quad (1)$$

and

$$3Si_2O_6^{4-} = 2SiO_4^{4-} + 2Si_2O_5^{2-} \quad (2)$$

$CaMgSi_2O_6 + CO_2$

Raman spectra of volatile-free Di melt at several temperatures and pressures are shown in Figure 4, and band assignments are given in Table 4. The spectra show an overall similarity in that the same bands occur at all temperatures and pressures. All bands are polarized.

The spectra of quenched Di melt consist of a broad envelope between 850 and 1105 cm^{-1}, containing at least three bands. The strongest band is at 970–980 cm^{-1} and does not change frequency appreciably with changing temperature or pressure. A higher-frequency band of strong intensity occurs as a shoulder near 1050 cm^{-1}. A third band of intermediate intensity is between 860 and 880 cm^{-1}. This band occurs as a shoulder under all conditions. In addition to the high-frequency envelope, there is a strong band near 640 cm^{-1} that shifts to slightly lower frequency with decreasing temperature. The spectra closely resemble that of Wo melt in Figure 3.

Three bands of Gaussian form were fitted inside the high-frequency envelope of the spectra shown in Figure 4. Although the presence of more than three

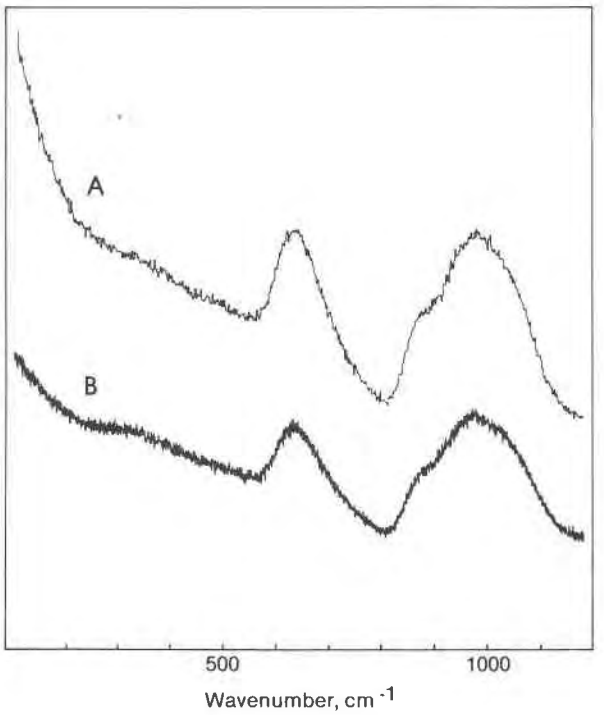

Fig. 4A. Unpolarized Raman spectra of quenched Di melt at 1 atm and 1550°C (*A*) and 1400°C (*B*). (Ar^+ laser, 200–400 mW power.)

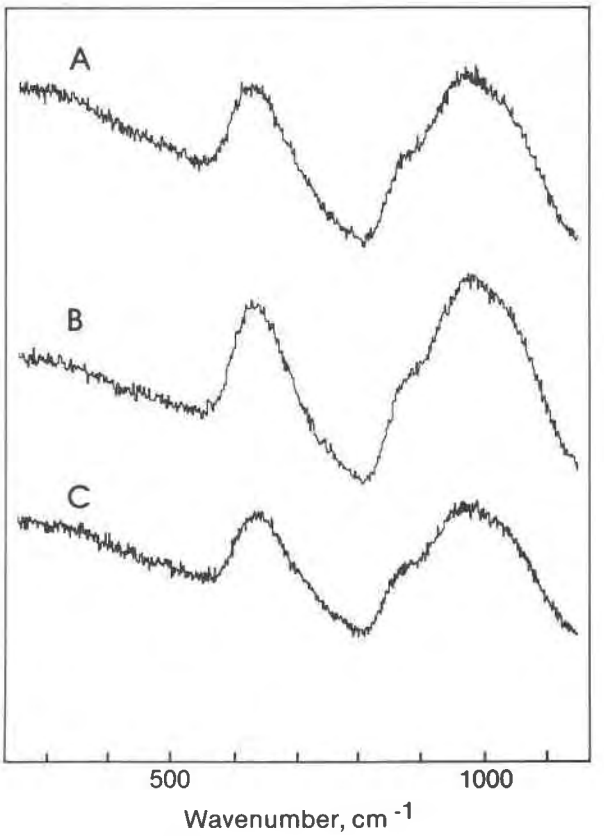

Fig. 4B. Unpolarized Raman spectra of quenched Di melt at 10 kbar and 1550°C (*A*), 10 kbar and 1650°C (*B*), and 20 kbar and 1685°C (*C*). (Ar^+ ion laser, 4880 A line, 200–400 mW power.)

bands cannot be ruled out, the spectra shown here (Figs. 3 and 4), as well as data from other relevant systems discussed or referred to above, indicate that only three bands are present. When the data were fitted, the maximum of the high-frequency envelope was initially assumed to coincide with the maximum of the strongest band, and the lower portion of the low-frequency limb of the high-frequency envelope was set to coincide with the low-frequency limb of a band near 870 cm^{-1} (its presence is indicated by the shoulder in Fig. 4). The cumulative area of the three bands thus fitted within the high-frequency envelope equals the area of the envelope within the statistical uncertainty of the spectra themselves. The results of this fitting procedure for quenched Di melts as a function of pressure and temperature are shown in Figure 5. The frequencies of all bands are independent of pressure and temperature. It should be emphasized that the existence and frequency of the stretch bands in the high-frequency envelope are also evident from the raw Raman data. The curve fitting was carried out simply in an attempt to get a better impression of the intensity ratios and a more accurate determination of the frequencies of the individual bands. Consequently, the structural interpretation of the Raman spectra insofar as the individual structural units are concerned is not affected by the curve-fitting procedure. The procedure will, however, give an impression about how the proportions of the individual structural units vary.

The Raman spectra of quenched Di melt indicate, therefore, that such melts consist of anionic structural units with an average of 4, 2, and 1 NBO/Si. The equilibrium between these units may be expressed with equation 2 above. The proportions of the units in a quenched melt are related to the relative intensities of the bands at 870 cm^{-1} (monomer), 970 cm^{-1} (chain), and 1070 cm^{-1} (sheet). As a melt becomes more disproportioned, the intensity ratios $I(970)/I(870)$ and $I(970)/I(1070)$ will decrease. The rate of change of these intensity ratios is not linearly related to molar proportions of the structural units, however, because the molar scattering coefficients differ for the different vibrations considered. The intensity ratios are listed in Table 4. These data show that both intensity ratios decrease with decreasing

Table 4. Raman spectroscopic data, $CaMgSi_2O_6 + CO_2$

Sample No.	Composition	P, kbar	T, °C	Wavenumber, cm^{-1}								$\frac{I(970)}{I(870)}$	$\frac{I(970)}{I(1070)}$
1007	Di	0.001	1585	...	632s,p	880m,p	983s,p	1070m,p	...	...	...	...	3.57	2.53
1006	Di	0.001	1425	...	633s,p	880m,p(sh)	980s,p	1068m,p(sh)	...	...	...	...	5.33	5.61
1013	Di	10	1650	...	629s,p	873m,p(sh)	975s,p	1070m,p(sh)	...	...	...	...	3.70	2.36
1017	Di	20	1650	...	629s,p	873m,p(sh)	975s,p	1070m,p	...	...	...	...	5.63	4.59
1024	Di	20	1685	...	636s,p	872m,p(sh)	978s,p	1066m,p	...	...	...	...	3.55	2.66
997	Di + CO_2	10	1550	...	630s,p	874m,p	965s,p	1040m,p	1075s,p	...*	...*	...*	...	...
1014	Di + CO_2	10	1600	...	630s,p	873m,p	970s,p	1035m,p	1075s,p	...*	...*	...*	...	...
995	Di + CO_2	10	1650	...	630s,p	874m,p	963s,p	1035m,p	1078s,p	...*	...*	...*	3.72	3.29
1000	Di + CO_2	20	1650	...	628s,p	862m,p(sh)	965s,p	1038w,p	1073s,p	...*	...*	...*	5.55	5.05
1023	Di + CO_2	20	1685	467m,p(sh)	605s,p	863vw,p(sh)	963s,p	1023w,p	1070s,p	1420vw,p	1525vw,p	1730vw,p	17.0	17.0
1002	Di + CO_2	20	1725	...	624s,p	865m,p	964s,p	1030w,p	1073s,p	...*	...*	...*	4.59	5.39
1004	Di + CO_2	25	1725	...	610s,p	879w,p	964s,p	1040w,p	1073s,p	...*	...*	...*	5.75	3.64

*Band present, but too weak for assignment.
Uncertainty ± 5 cm^{-1}.
Symbols: s, strong; m, medium; w, weak; vw, very weak; p, polarized; (sh), shoulder.

temperature under isobaric conditions and with decreasing pressure under isothermal conditions. The temperature effect is greater at 20 kbar than at 1 atm, because the percentage change of both intensity ratios is similar between 1425° and 1585°C at 1 atm and between 1650° and 1685°C at 20 kbar. The proportion of chain relative to monomer and sheet decreases by about the same amount between 20 and 10 kbar at 1650°C as between 1650° and 1685°C at 20 kbar for quenched, volatile-free Di melt (Table 4).

Addition of CO_2 to quenched Di melt results in new bands at 1080, 1450, 1525, and 1730 cm^{-1} (see Fig. 6 and Table 4). Furthermore, the 650 cm^{-1} band has developed an asymmetry toward higher frequency. This asymmetry may be caused by another unresolved band near 700 cm^{-1}. These bands are characteristic of the carbonate ion (White, 1974; Verweij *et al.*, 1977), the only difference being two bands at 1450 and 1525 cm^{-1} rather than one or only a minor splitting into two. This large band separation (75 cm^{-1}) may be due to deformation of the CO_3^{2-} anionic complex relative to the highly symmetric CO_3^{2-}

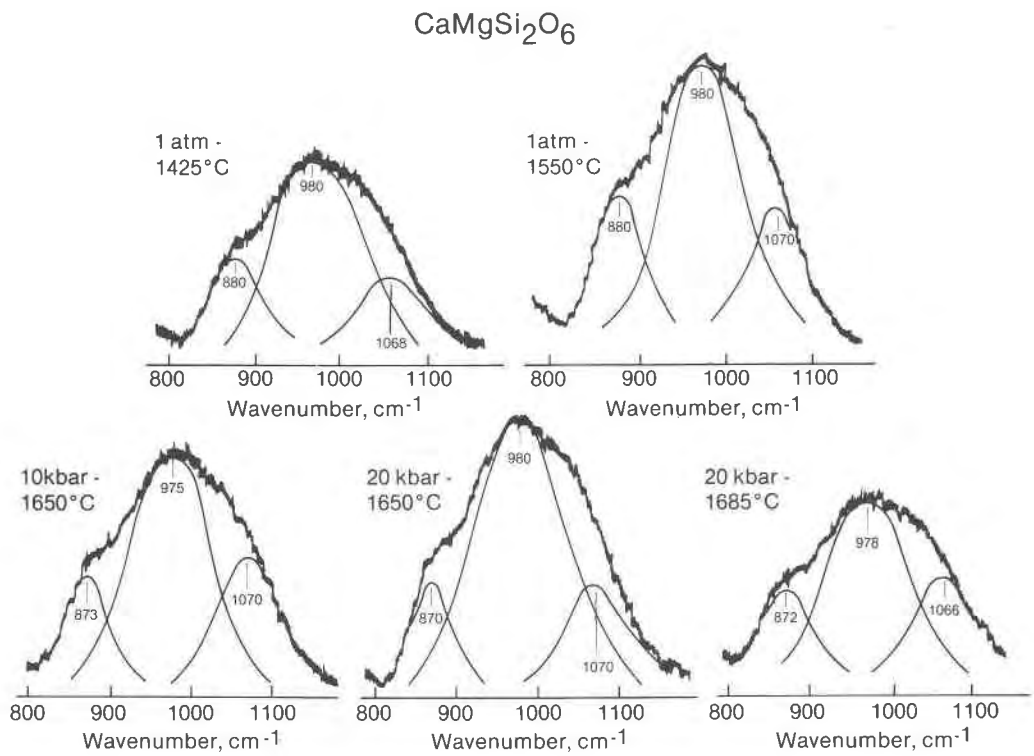

Fig. 5. Results of fitted lines inside the high-frequency envelope of Raman spectra of quenched Di melt as a function of temperature and pressure (see text for procedure).

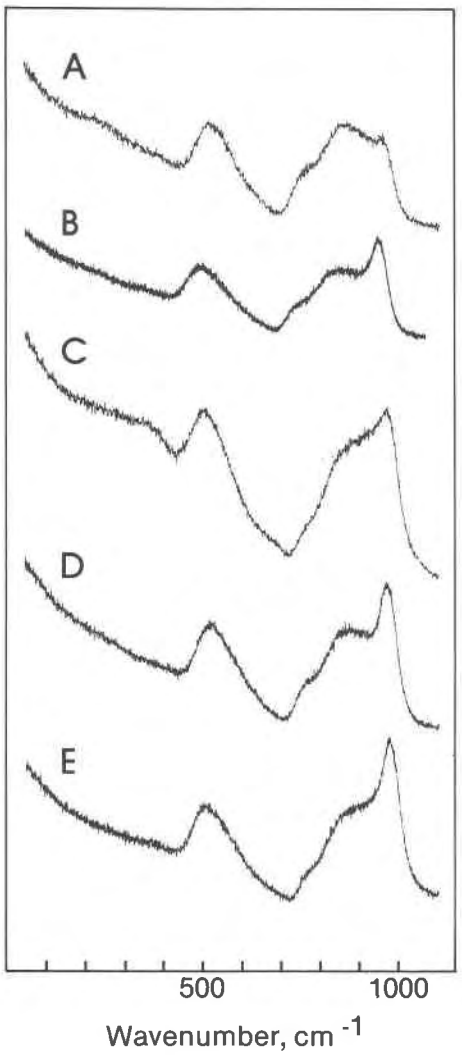

Fig. 6. Unpolarized Raman spectra of Di + CO_2 melts at 10 kbar and 1650°C (*A*), 20 kbar and 1650° (*B*), 20 kbar and 1685°C (*C*), 20 kbar and 1725°C (*D*), and 25 kbar and 1725°C (*E*). (Ar^+ ion laser, 4880 A line with 200–400 mW power.)

found in crystalline $CaCO_3$, for example. There is no evidence in the Raman spectra to indicate the reason for such deformation.

The spectra reflecting the silicate anionic network of CO_2-saturated, quenched Di melts resemble those of CO_2-free melts (Figs. 4–6). There are, however, systematic shifts of frequencies and intensity ratios as a function of CO_3^{2-} of the quenched melts.

At 10 kbar the CO_2 solubility is about 2 wt. percent (9 mole percent CO_3^{2-}), with only minor temperature dependence. The 630 cm^{-1} band (Si–O^0 bending characteristic of $Si_2O_6^{4-}$ chains) remains near 630 cm^{-1} at 10 kbar pressure. In the high-frequency envelope three bands near 880, 970, and 1070 cm^{-1} can be discerned in the raw Raman data (Fig. 6). The 1070 cm^{-1} C–O stretch band occurs at nearly the same frequency as the stretch band indicative of sheet structural units in the CO_2-free melt (Tables 2–4). This is also the frequency region where antisymmetric stretch bands from structural units with NBO/Si = 0 are anticipated (Table 3). A three-dimensional array of SiO_4 tetrahedra also results in two deformation bands between 430 and 480 cm^{-1} (*e.g.*, Bates *et al.*, 1974). Such bands do not occur in the present spectra (Fig. 6; see also Table 4). We conclude, therefore, that three-dimensional network units do not occur in Di melt with several wt. percent CO_2 in solution. In view of the overall similarity of the Raman spectra resulting from vibrations in silicate tetrahedral complexes, it seems reasonable to assume that there is another Raman band near (perhaps at the same frequency as) the C–O stretch band at 1070 cm^{-1}.

The data in Figure 6 (see also Tables 1 and 4) show that as the CO_2 content of the Di melt increases, the intensity of the band near 870 cm^{-1} decreases. Consequently, we conclude that the proportion of monomers in the melt structure decreases relative to the other structural units as the CO_2 content of the melt increases.

As the CO_2 content of the melt is increased, the frequency of the band near 650 cm^{-1} shifts toward 600 cm^{-1}. This observation is interpreted to mean that the proportion of structural units with NBO/Si less than 2 becomes more important relative to other structural units as the CO_2 content of the melt is increased.

$NaCaAlSi_2O_7 + CO_2$

Provided that Al is in tetrahedral coordination in Sm melt, this melt has the same number of nonbridging oxygens per tetrahedrally coordinated oxygen as sodium trisilicate melt ($Na_2Si_3O_7$). According to available data (*e.g.*, Taylor and Brown, 1979, Virgo *et al.*, 1979), Al is tetrahedrally coordinated in silicate melts provided that sufficient metal cations are present to maintain a local charge of 4+ near the tetrahedral cation. This requirement will be referred to as local charge balance.

It has been shown (*e.g.*, Virgo *et al.*, 1979) that tetrahedrally coordinated Al in a given structural unit results in a downward shift of the frequency of the associated stretch band that is positively correlated with the Si/(Si + Al) of the structural unit under consideration. In addition to this effect, such Si(Al) coupling results in loss of spectroscopic resolution,

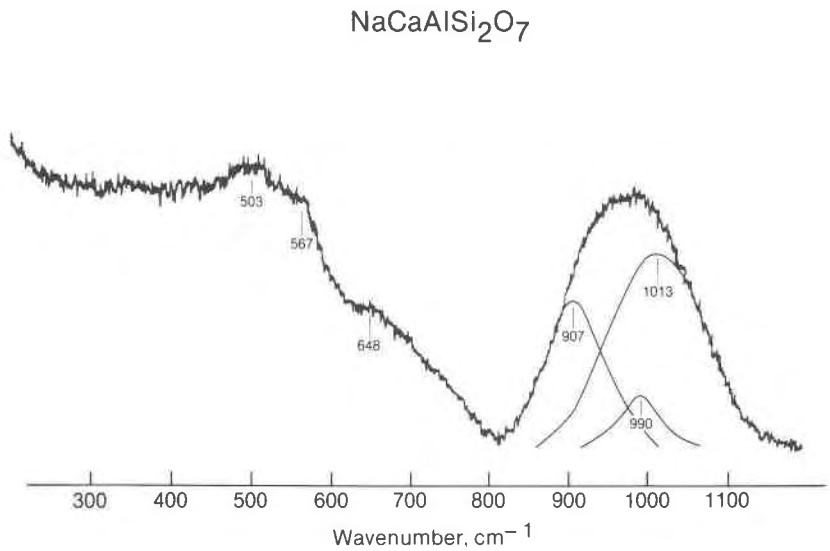

Fig. 7. Unpolarized Raman spectrum of volatile-free Sm melt at 10 kbar and 1275°C. See text for discussion of suggested line-fitting in the high-frequency envelope. (Ar^+ laser, 200–400 mW power.)

probably because of increased local disorder. Consequently, the interpretation of the Raman spectra of Sm melt (19.74 wt. percent Al_2O_3) is difficult. In view of the similar stoichiometry of $Na_2Si_3O_7$ and Sm melt compositions, published Raman spectroscopic results from the former composition (Furukawa and White, 1979) will be used as an aid in interpreting the Sm spectra. Furukawa and White (1980), in a careful analysis of the band assignments in the Raman spectrum of $Na_2Si_3O_7$ melt, concluded that the sheet unit was the major structural unit in the melt. In addition, there is a band near 950 cm^{-1} which is assigned to a structural unit with NBO/Si = 2 (chain). From a mass-balance point of view, quenched melt of $Na_2Si_3O_7$ composition (NBO/Si = 0.67) must also contain at least one structural unit with NBO/Si considerably less than 1. Virgo *et al.* (1980) found evidence for this unit in the existence of rocking bands near 450 cm^{-1} and a bending band near 800 cm^{-1}. These frequencies correspond to those found for three-dimensional structural units. The associated Si–O stretch band most likely occurs near 1060 cm^{-1}. Its spectroscopic signature is, however, probably obliterated by the intense 1100 cm^{-1} band in this composition.

The Raman spectrum of Sm melt is shown in Figure 7 (see also Table 5). The band near 500 cm^{-1} is near the same frequency as the (Si,Al)–O^0 rocking (deformation) band observed in melts with a three-dimensional network structure on the joins $CaAl_2O_4$–SiO_2 and $NaAlO_2$–SiO_2 (Brawer and White, 1977; Virgo *et al.*, 1979), and is considered characteristic of melts with a three-dimensional network unit. The band near 650 cm^{-1} is assigned to (Si,Al)–O^0 bending and at this frequency is characteristic of a chain unit (see also above).

The high-frequency envelope is asymmetric and indicates the presence of at least two bands. This fre-

Table 5. Raman spectroscopic data, $NaCaAlSi_2O_7 + CO_2$

Sample No.	Composition	P, kbar	T, °C	Wavenumber, cm^{-1}									
1059	Sm	0.001	1460	...	493m,p	560m,p	651m,p	...	...	900w,p(sh)	980s,p	...	...	...	...
1057	Sm	10	1275	...	500m,p	553m,p	662m,p	...	...	900w,p(sh)	980s,p	...	...	...	...
1056	Sm + CO_2	10	1275	...	493s,p	566m,p	683m,p†	716w,p	860w,p(sh)	942s,p	1000s,p	1070s,p	1413vw,p	1513vw,p	1737vw
1073	Sm + CO_2	10	1460	...	497s,p	557m,p	670m,p†	707w,p(sh)	860w,p(sh)	930s,p(sh)	993s,p	1070s,p	...*	...*	...*
1074	Sm + CO_2	10	1550	...	490s,p	557m,p	650w,p	683w,p	860vw,p(sh)	922m,p	990s,p	1070s,p	...*	...*	...*
1062	Sm + CO_2	20	1325	279m	482s,p	550m,p(sh)	...	700m,p	860vw,p(sh)	942s,p	997s,p	1075s,p	n.m.	n.m.	n.m.
1068	Sm + CO_2	20	1460	...	493s,p	560m,p	627vw,p	700m,p	860vw,p(sh)	940s,p	1006s,p	1075s,p	n.m.	n.m.	n.m.
1072	Sm + CO_2	20	1550	...	490s,p	560m,p	...	707m,p	860w,p(sh)	950s,p	1010s,p	1070s,p	n.m.	n.m.	n.m.

*Band present, but too weak for assignment.
†Broad.
Uncertainty ±5 cm^{-1}.
Symbols: n.m., not measured; others as in Table 2.

quency region differs considerably from that obtained for crystalline $NaCaAlSi_2O_7$ (Sharma, 1979) where the major band is very near 900 cm^{-1} (Si_2O_7 dimer in crystalline material). In analogy with the conclusions for quenched $Na_2Si_3O_7$ melt, the main band in the high-frequency envelope should stem from stretch vibrations in a structural unit with an average NBO/T = 1. The above interpretations, which are independent of the data contained in the high-frequency envelope, indicate that three-dimensional structural units as well as units with NBO/T = 2 also occur in this melt. These conclusions imply that at least three stretch bands must be located in the high-frequency envelope. Curve-fitting involving unresolved bands should be carried out with great caution, and the curves inserted in the high-frequency envelope in Figure 7 should only be considered as a suggestion. In deriving this suggested solution it was assumed that Al was randomly distributed between the three structural units and that the influence of Si(Al) coupling on the frequencies of the relevant stretch bands is relatively similar. A consequence of this assumption is that all the stretch bands should be at a lower frequency than the analogous bands in the Al-free $Na_2Si_3O_7$ melt composition. If the calibration of Virgo *et al.* (1979) for frequency shift of antisymmetric stretch bands in three-dimensional network structures on the joins $NaAlO_2$–SiO_2 and $CaAl_2O_4$–SiO_2 as a function of Si/(Si + Al) were used, each stretch band in the Sm melt composition would shift by approximately 70 cm^{-1} relative to their positions in $Na_2Si_3O_7$. Finally, the location of the two shoulders on the high-frequency envelope were taken as an indication of approximate position of the two strongest bands in the envelope, and the form of the high- and low-frequency limbs of the envelope was used as a guide for the form of the high- and low-frequency limbs of these two bands. With all these considerations in mind, the curve-fitting shown in Figure 7 was produced. With this interpretation, the strong 1013 cm^{-1} band is an Si(Al)-coupled stretch band from a structural unit with, on the average, NBO/T = 1. The 990 cm^{-1} band stems from a three-dimensional structural unit and the 907 cm^{-1} band from a structural unit with about 2 nonbridging oxygens per tetrahedrally coordinated cation.

The three structural units are denoted T_2O_6, T_2O_5, and TO_2, where T = Si + (NaAl) + ($1/2CaAl_2$). The equilibrium between the three structural units may be expressed with the equation

$$2T_2O_5^{2-}\ (\text{sheet}) = T_2O_6^{4-}\ (\text{chain}) + 2TO_2\ (3D) \quad (3)$$

Addition of carbon dioxide to Sm melt results in the appearance of the characteristic carbonate bands (1070, 1420, 1520, and 1740 cm^{-1}; White, 1974) seen in Figure 7 (see also Table 5). In addition to these bands, a weak band occurs near 700 cm^{-1}. This band is characteristic of the in-plane deformation mode of the CO_3^{2-} anion (Verweij *et al.*, 1977; White, 1974). It cannot be observed in CO_2-bearing Di melt (Fig. 5) because it lies beneath the high-frequency limb of the strong Si–O^0 bending band at 650 cm^{-1}.

Systematic changes of vibrational frequencies and intensity ratios of important bands occur as a result of dissolved CO_2 in quenched Sm melt (Figs. 7 and 8; Table 5). The spectroscopic features near 500 cm^{-1} remain unaltered with addition of CO_2. In view of the discussion above, this observation is interpreted to mean that three-dimensional structural units occur in CO_2-bearing Sm melts with the CO_2 contents used here (Table 1). The band near 650 cm^{-1} also remains as CO_2 is added except in the two most CO_2-rich samples (5.9 and 5.2 wt. percent CO_2; Table 1), which indicates that chain units also remain in the CO_2-bearing melt. The data do indicate, however, that the proportion of such units may have decreased as CO_2 is dissolved in the melt.

In the high-frequency envelope (Figs. 7 and 8), generally there are at least three bands in addition to the C–O stretch band near 1070 cm^{-1}. The strongest band is near 1000 cm^{-1} and probably corresponds to an Al-bearing structural unit with NBO/T near 1 (sheet). In addition, there is a medium to strong band near 930–940 cm^{-1} and a very weak band near 860 cm^{-1}. In view of the diminished intensity of the 650 cm^{-1} band with the addition of CO_2 to the melt, we suggest that the 860 cm^{-1} band is the associated stretch band (chain). Its lower frequency compared with the CO_2-free melt may indicate lower Si/(Si + Al) of this structural unit. Its lower intensity relative to the other bands in the high-frequency envelope indicates lower abundance.

The remaining band in the high-frequency envelope may be the stretch band associated with the occurrence of aluminous, three-dimensional structural units in the melt. The other evidence for such units is the band near 500 cm^{-1}. The 500 cm^{-1} band frequency corresponds to that of the rocking band in three-dimensional aluminosilicate melts such as those of $NaAlSiO_4$ and $CaAl_2Si_2O_8$ composition. The frequencies of the Si(Al) coupled stretch bands are also similar (Virgo *et al.*, 1979). The lower frequency of this band compared with its position in CO_2-free Sm melt indicates a decrease in Si/(Si + Al). Its

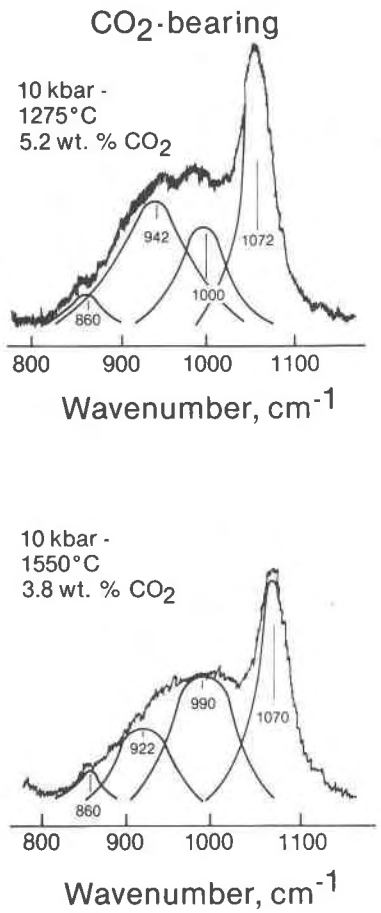

Fig. 8. High-frequency envelope of CO_2-bearing Sm quenched melt. (Ar^+ laser, 200–400 mW power.)

greater intensity relative to the other bands in the high-frequency envelope compared with the CO_2-free samples (Figs. 7 and 8) indicates that the abundance of three-dimensional structural units in the melt has increased as the result of dissolved CO_2.

Solubility mechanisms

$CaMgSi_2O_6 + CO_2$

According to our data, solution of CO_2 in Di melts to form carbonate complexes is accompanied by a reduction of isolated SiO_4^{4-} tetrahedra relative to chain and sheet units in the melt. There are no indications that new silicate units have been formed with the amounts of CO_2 added to these experiments (see Table 1).

Inasmuch as the CO_2 solubility is positively correlated with Ca/(Ca + Mg) in meta- and orthosilicate melts (Holloway *et al.*, 1976), it appears that the CO_3^{2-} anion is closely associated with Ca^{2+} in the melt by formation of $CaCO_3$. The increasing degree of polymerization of the melt with increasing carbonate content is in response to the formation of such complexes. The CO_2 solubility is controlled primarily by the activity of Ca^{2+}, and not by the degree of polymerization of the melt as suggested by Holloway *et al.* (1976).

Eggler and Rosenhauer (1978) surveyed the data on the influence of CO_2 on silicate phase equilibria and its solubility in silicate melts. They concluded that in melts that contain nonbridging oxygens, the principle of the solubility mechanism may be illustrated with the expression:

$$CO_2(gas) + 2O^-(NBO) = CO_3^{2-}\ (melt) + O^0\ (BO) \quad (4)$$

This mechanism is consistent with our conclusions. The nonbridging oxygen (NBO) to form bridging oxygen (BO) may be derived from $Si_2O_6^{4-}$ or $Si_2O_5^{2-}$ units or both:

$$2SiO_4^{4-}\ (melt) + 2CO_2(gas) = Si_2O_6^{4-}\ (melt) + 2CO_3^{2-}\ (melt) \quad (5)$$

and

$$2SiO_4^{4-}\ (melt) + 3CO_2\ (gas) = Si_2O_5^{2-}\ (melt) + 3CO_3^{2-}\ (melt) \quad (6)$$

Chains could also be transformed to sheets:

$$Si_2O_6^{4-}\ (melt) + CO_2\ (gas) = Si_2O_5^{2-}\ (melt) + 2CO_3^{2-}\ (melt) \quad (7)$$

The spectroscopic data cannot be used to determine whether sheets are formed at the expense of chains, or whether equations 4 or 5 represent the most accurate description of the interaction between the anionic network of the melt and CO_2 in solution in the melt. Note, however, that Dent Glasser (1979), in a review of crystal structures of silicates, concluded, on the basis of charge density considerations relating to modifying cations that $Si_2O_5^{2-}$ (sheet) structures are less stable than $Si_2O_6^{4-}$ (chain) structures when balanced with alkaline earth cations. In fact, alkaline earth sheet structures do not occur in a crystallized form. We suggest, therefore, that equation 5 probably describes the interaction between the melt and CO_2 most accurately. This equation may then be combined with equation 2 to describe the solubility mechanism in metasilicate melts such as those of Di composition:

$$5Si_2O_6^{4-}\ (melt) + 2\ CO_2\ (gas) = 2SiO_4^{4-}\ (melt) + 4Si_2O_5^{2-}\ (melt) + 2CO_3^{2-}\ (melt) \quad (8)$$

$NaCaAlSi_2O_7 + CO_2$

The influence of dissolved CO_2 on the anionic complexes in Sm melt is less well defined than in Di melt, partly because Sm melt is a combination of more polymerized units such as three-dimensional network, sheets, and chains, whereas Di melt also has a large proportion of orthosilicate and little or no three-dimensional network component. As a result, Raman spectra are less sensitive to the changes of Sm melt structure than of Di melt structure.

The Raman data (Figs. 7 and 8; Table 5) indicate that the formation of CO_3^{2-} complexes in the melt results in polymerization of the silicate network, as the proportion of three-dimensional structural units has increased substantially relative to chain and sheet units.

The principles governing the solubility of CO_2 in Sm melt are, therefore, similar to those for CO_2 in Di melt. The main difference is that the expression that illustrates the interaction between CO_2 and the silicate network must take into account the different structural units in the two melts.

There are two reasons why $(CaCO_3)^0$ rather than $(Na_2CO_3)^0$ type complexes probably are formed in Sm melt. First, as also summarized above, solubility studies of CO_2 in silicate melts always indicate that carbonate complexes are associated with Ca^{2+} cations rather than other monovalent or divalent cations in the melt. Second, as suggested by Bottinga and Weill (1972) and also pointed out by Virgo *et al.* (1980), MAl^{4+} complexes are more stable than $M_{0.5}Al^{4+}$ complexes.

Inasmuch as three-dimensional structural units appear to become more abundant as CO_2 is dissolved in Sm melt, the solubility mechanism may now be illustrated with the equation:

$$T_2O_6^{4-}\text{ (melt)} + 2CO_2\text{ (gas)} = 2TO_2\text{ (melt)} + 2CO_3^{2-}\text{ (melt)} \quad (9)$$

Equation 9 may be combined with equation 3 to give the complete reaction:

$$4T_2O_5^{2-}\text{ (melt)} + 2CO_2\text{ (gas)} = T_2O_6^{4-}\text{(melt)} + 6TO_2\text{ (melt)} + 2CO_3^{2-}\text{ (melt)} \quad (10)$$

where $T = Si^{4+} + (NaAl)^{4+}$ and the carbonate is associated with Ca^{2+}.

Applications

Most phase-equilibrium studies of the role of CO_2 in the formation and evolution of magma at high pressures and temperatures have been conducted in systems that do not contain amphoteric oxides. These studies (Eggler, 1973, 1974, 1975, 1976, 1978; Eggler and Rosenhauer, 1978, Huang and Wyllie, 1976) have shown that the addition of CO_2 results in the liquidus boundary between two minerals of different degree of polymerization (*e.g.*, forsterite and enstatite) shifting toward the silica-deficient portion of the systems. The solubility mechanism of CO_2 in simple silicate melts without amphoteric oxides also indicates that more polymerized minerals would precipitate from the CO_2-saturated silicate melts, because the concentration of more polymerized species in the melt increases with increasing CO_2 content.

Even though the Di composition is useful to demonstrate the solubility mechanism of CO_2 in silicate melts that contain nonbridging oxygens, this composition is a gross oversimplification of natural magma. The greatest difference is the absence of amphoteric oxides such as Al_2O_3 and Fe_2O_3. The Sm composition contains 19.74 wt. percent Al_2O_3 and about 46 wt. percent SiO_2. Basaltic rocks usually contain about 18–21 wt. percent total amphoteric oxides (Chayes, 1975). Consequently, with the assumption that the structural roles of Al^{3+} and Fe^{3+} are similar in basaltic magma, the Sm composition represents a closer approximation of the natural magma. Our data indicate that the solubility mechanism of CO_2 in simple binary silicate melts resembles that of the more complex Sm composition. We conclude, therefore, that the data acquired in such simple systems provide an accurate basis on which to provide information on the influence of CO_2 on natural basaltic magma.

Acknowledgments

Critical reviews by G. E. Brown, S. A. Brawer, J. R. Holloway, W. Harrison, F. J. Ryerson, and H. S. Yoder, Jr. are appreciated. This research was partially supported by NSF grant EAR 7911313 and partially by the Carnegie Institution of Washington.

References

Bates, J. B., R. W. Hendricks and L. B. Shaffer (1974) Neutron irradiation effects and structure of non-crystalline SiO_2. *J. Chem. Phys., 61,* 4163–4176.

Bottinga, Y. and D. F. Weill (1972) The viscosity of magmatic silicate liquids: a model for calculation. *Am. J. Sci., 272,* 438–475.

Boyd, F. R. and J. L. England (1960) Apparatus for equilibrium measurements at pressures up to 50 kilobars and temperatures up to 1750°C. *J. Geophys. Res., 65,* 741–748.

——— and ——— (1963) Effect of pressure on the melting of diopside, $CaMgSi_2O_6$, and albite, $NaAlSi_3O_8$, in the range up to 50 kb. *J. Geophys. Res., 68,* 311–323.

Brawer, S. A. (1975) Theory of the vibrational spectra of some network and molecular glasses. *Phys. Rev. B, 11,* 3173–3194.

——— and W. B. White (1975) Raman spectroscopic investigation of the structure of silicate glasses. I. The binary silicate glasses. *J. Chem. Phys., 63,* 2421–2432.

——— and ——— (1977) Raman spectroscopic investigation of the structure of silicate glasses. II. Soda-alkali earth-alumina ternary and quaternary glasses. *J. Non-Cryst. Solids, 23,* 261–278.

Brey, G. P. and D. H. Green (1976) Solubility of CO_2 in olivine melilitite at high pressure and the role of CO_2 in the earth's upper mantle. *Contrib. Mineral. Petrol., 55,* 217–230.

Chayes, F. (1975) Average composition of the commoner Cenozoic volcanic rocks. *Carnegie Inst. Wash. Year Book, 75,* 547–549.

Delaney, J. R., W. W. Muenow and D. G. Graham (1978) Abundance and distribution of water, carbon and sulfur in the glassy rims of submarine pillow basalts. *Geochim. Cosmochim. Acta, 42,* 581–594.

Dent Glasser, L. S. (1979) Non-existent silicates. *Z. Kristallogr., 149,* 291–305.

Eggler, D. H. (1973) Role of CO_2 in melting processes in the mantle. *Carnegie Inst. Wash. Year Book, 72,* 457–467.

——— (1974) Application of a portion of the system $CaAl_2Si_2O_8$–$NaAlSi_3O_8$–SiO_2–MgO–Fe–O_2–H_2O–CO_2 to genesis of the calc-alkaline suite. *Am. J. Sci., 274,* 297–315.

——— (1975) Peridotite–carbonatite relations in the system CaO–MgO–SiO_2–CO_2. *Carnegie Inst. Wash. Year Book, 74,* 468–474.

——— (1976) Does CO_2 cause partial melting in the low-velocity layer of the mantle? *Geology, 2,* 69–72.

——— (1978) The effect of CO_2 upon partial melting in the system Na_2O–CaO–Al_2O_3–MgO–SiO_2–CO_2 to 35 kb, with an analysis of melting in a peridotite–H_2O–CO_2 system. *Am. J. Sci., 278,* 305–343.

——— and M. Rosenhauer (1978) Carbon dioxide in silicate melts. II. Solubility of CO_2 and H_2O in $CaMgSi_2O_6$ (diopside) liquids and vapors at pressures to 40 kb. *Am. J. Sci., 278,* 64–94.

———, B. O. Mysen and T. C. Hoering (1974) Gas species in sealed capsules in solid-media, high-pressure apparatus. *Carnegie Inst. Wash. Year Book, 73,* 228–232.

———, J. R. Holloway and T. C. Hoering (1979) The solubility of carbon monoxide in silicate melts at high pressures and its effect on silicate phase relations. *Earth Planet. Sci. Lett., 43,* 321–330.

Etchepare, J. (1972) Study by Raman spectroscopy of crystalline and glassy diopside. In R. W. Douglas and B. Ellis, Eds., *Amorphous Materials,* p. 337–346. Wiley, New York.

Furukawa, T. and W. B. White (1980) Raman spectroscopic investigation of the structure of silicate glasses. III. Alkali–silico–germanates. *J. Chem. Phys.,* in press.

———, S. A. Brawer and W. B. White (1978) The structure of lead silicate glasses determined by vibrational spectroscopy. *J. Mater. Sci., 13,* 268–282.

Gerlach, T. M. and G. E. Nordlie (1975) The C–O–H–S system. Part I. Compositional limits and trends in basaltic glasses. *Am. J. Sci., 275,* 353–376.

Green, H. W., II (1972) A CO_2 charged asthenosphere. *Nature, 238,* 2–5.

Holloway, J. R., B. O. Mysen and D. H. Eggler (1976) The solubility of CO_2 in liquids on the join CaO–MgO–SiO_2–CO_2. *Carnegie Inst. Wash. Year Book, 75,* 626–631.

Huang, W. L. and P. J. Wyllie (1976) Melting relationships in the systems CaO–CO_2 and MgO–CO_2 to 33 kilobars. *Geochim. Cosmochim. Acta, 40,* 129–132.

Irving, A. J. and P. J. Wyllie (1975) Subsolidus and melting relationships for calcite, magnesite on the join $CaCO_3$–$MgCO_3$ to 36 kb. *Geochim. Cosmochim. Acta, 39,* 35–53.

Kadik, A. A. and D. H. Eggler (1975) Melt–vapor relations on the join $NaAlSi_3O_8$–H_2O–CO_2. *Carnegie Inst. Wash. Year Book, 74,* 479–484.

Lazarev, A. N. (1972) *Vibrational spectra and structure of silicates.* Consultants Bureau, New York.

Lentz, C. W. (1964) Silicate minerals as sources of trimethylsilyl silicates and silicate structure analysis of sodium silicate solutions. *Inorg. Chem., 3,* 574–579.

Mao, H. K., P. M. Bell and J. L. England (1971) Tensional errors and drift of thermocouple electromotive force in the single-stage, piston–cylinder apparatus. *Carnegie Inst. Wash. Year Book, 70,* 281–287.

Masson, C. R. (1968) Ionic equilibria in liquid silicates. *J. Am. Ceram. Soc., 51,* 134–143.

McGetchin, T. R. and J. R. Besancon (1973) Carbonate inclusions in mantle-derived pyropes. *Earth Planet. Sci. Lett., 18,* 408–410.

Mysen, B. O. (1976) The role of volatiles in silicate melts: solubility of carbon dioxide and water in feldspar, pyroxene and feldspathoid melts to 30 kb and 1626°C. *Am. J. Sci., 276,* 969–996.

——— and M. G. Seitz (1975) Trace element partitioning determined by beta-track mapping—an experimental study using carbon and samarium as examples. *J. Geophys. Res., 80,* 2627–2635.

———, D. H. Eggler, M. G. Seitz and J. R. Holloway (1976) Carbon dioxide in silicate melts and crystals. I. Solubility measurements. *Am. J. Sci., 276,* 455–479.

Presnall, D. C., N. L. Brenner and T. H. O'Donnell (1973) Thermocouple drift of PtPt10Rh and W3Re/W25Re thermocouples in single stage piston–cylinder apparatus. *Am. Mineral., 58,* 771–777.

Roedder, E. (1965) Liquid CO_2 inclusions in olivine-bearing nodules and phenocrysts from basalts. *Am. Mineral., 50,* 1746–1782.

Sharma, S. K. (1979) Structure and solubility of carbon dioxide in silicate glasses of diopside and sodium melilite compositions at high pressures from Raman spectroscopic data. *Carnegie Inst. Wash. Year Book, 78,* 532–537.

Smart, R. M. and F. P. Glasser (1978) Silicate anion constitution of lead silicate glasses and crystals. *Phys. Chem. Glasses, 19,* 95–102.

Taylor, M. and G. E. Brown (1979) Structure of mineral glasses. I. The feldspar glasses $NaAlSi_3O_8$, $KAlSi_3O_8$, $CaAl_2Si_2O_8$. *Geochim. Cosmochim. Acta, 43,* 61–77.

Verweij, H. (1979a) Raman study of the structure of alkali germanosilicate glasses. I. Sodium and potassium metasilicate glasses. *J. Non-Cryst. Solids, 33,* 41–53.

——— (1979b) Raman study of the structure of alkali germanosilicate glasses. II. Lithium, sodium and potassium digermanosilicate glasses. *J. Non-Cryst. Solids, 33,* 55–69.

——— and W. L. Konijnendijk (1976) Structural units in K_2O–PbO–SiO_2 glasses by Raman spectroscopy. *J. Am. Ceram. Soc., 59,* 517–521.

———, H. Van Den Boom and R. E. Breemer (1977) Raman scattering of carbonate ions dissolved in potassium silicate glasses. *J. Am. Ceram. Soc., 60,* 529–534.

Virgo, D., B. O. Mysen and I. Kushiro (1980) Anionic constitution of silicate melts quenched at 1 atm from Raman spectroscopy: implications for the structure of igneous melts. *Science,* in press.

———, F. Seifert and B. O. Mysen (1979) Three-dimensional network structures of melts in the systems $CaAl_2O_4$–SiO_2, $NaAlO_2$–SiO_2, $NaFeO_2$–SiO_2, and $NaGaO_2$–SiO_2 at 1 atm. *Carnegie Inst. Wash. Year Book, 78,* 506–511.

White, W. B. (1974) The carbonate minerals. In V. C. Farmer, Ed., *The Infrared Spectra of Minerals,* p. 227–284. Mineralogical Society, London.

Wyllie, P. J. and W.-L. Huang (1976) Carbonation and melting reactions in the system CaO–MgO–SiO_2–CO_2 at mantle pressures with geophysical and petrological applications. *Contrib. Mineral. Petrol., 54,* 79–104.

Manuscript received, October 1, 1979;
accepted for publication, June 2, 1980.

American Mineralogist, Volume 65, pages 900–914, 1980

Solubility mechanisms of H_2O in silicate melts at high pressures and temperatures: a Raman spectroscopic study

BJØRN O. MYSEN, DAVID VIRGO, WENDY J. HARRISON AND CHRISTOPHER M. SCARFE[1]

Geophysical Laboratory, Carnegie Institution of Washington
Washington, D.C. 20008

Abstract

Raman spectroscopy has been employed to determine the solubility mechanisms of H_2O in silicate melts. In melts that have a three-dimensional network structure (*e.g.*, melts on the join Na_2O–Al_2O_3–SiO_2), water reacts with bridging oxygens to form two OH groups per broken oxygen bond. At the same time some of the three-dimensional network is broken down to chain units, accompanied by the expulsion of Al^{3+} from tetrahedral coordination. In melts that have nonbridging oxygen (NBO), water reacts with both nonbridging oxygen and network modifiers (*e.g.*, Na^+) to form Si–OH bonds and M(OH) or $M(OH)_2$ complexes. The anhydrous portion of the network becomes more polymerized.

The formation of chain units at the expense of three-dimensional network units in melts implies that the liquidus boundaries involving pyroxenes and silica minerals or feldspar minerals shift to higher silica contents. Liquidus fields of silica minerals or feldspar minerals are depressed relative to those of pyroxene minerals. This prediction is supported by published observations of phase relations in hydrous basalt and andesite systems. Similar logic can be used to explain the formation of partial melts of andesitic bulk composition from hydrous peridotite in the upper mantle.

We propose that trace-element crystal–liquid partition coefficients involving highly polymerized melts will decrease with increasing water content because of the formation of the less polymerized chain units in the melt. Partition coefficients involving less polymerized melts (*e.g.*, picrite and komatiite) may increase because the degree of polymerization of the melt is increased as a result of dissolved water.

Introduction

Water is one of the most important volatiles in magmas. The presence of H_2O in the source region of partial melts in the upper mantle results in a more silica-rich liquid than in its absence (*e.g.*, Kushiro *et al.*, 1968; Kushiro, 1969, 1972; Yoder, 1969). For this reason, for example, water is required to produce andesitic partial melts from peridotite (Kushiro *et al.*, 1972; Mysen and Boettcher, 1975). Water in magma also affects crystallization paths. The liquidus fields of feldspars are depressed relative to those of pyroxenes, and the liquidus fields of pyroxenes relative to those of olivine (Yoder, 1969, 1973; Eggler, 1972; Kushiro, 1972). The redox equilibria of iron and hence the phase equilibria of iron-bearing minerals also depend on the water content of magma (Osborn, 1959).

Physical properties of magma such as viscosity and electrical conductivity are affected by water (Lebedev and Khitarov, 1964; Kushiro, 1978; Kushiro *et al.*, 1976). It has also been suggested that activity coefficients of trace elements and therefore crystal–liquid partition coefficients depend on the water content of the liquid (Drake and Holloway, 1977; Hart and Davis, 1978).

As a result of the important petrological influence of H_2O in silicate melts, the solubility behavior of H_2O in a variety of melts and under a variety of physical conditions has been studied extensively (Goranson, 1931; Kennedy *et al.*, 1962; Burnham, 1974, 1975; Burnham and Jahns, 1962; Burnham and Davis, 1971, 1974; Hamilton *et al.*, 1964; Eggler and Rosenhauer, 1978). Solubility models of H_2O in silicate melts based on solubility data and thermodynamic properties of hydrous melts have been proposed (Burnham, 1974, 1975).

[1] On leave from the University of Alberta, Edmonton, Canada.

0003–004X/80/0910–0900$02.00

Despite the importance of H_2O in petrogenetic processes, data on the structural role of H_2O in silicate melts are scarce. Orlova (1964) and Velde and Kushiro (1976) determined that OH groups exist in highly polymerized, water-bearing melts on the join $NaAlSiO_4$–SiO_2. Hodges (1974) suggested that molecular water may occur as well. Data on the structural role of the OH groups in silicate melts are rare (Adams and Douglas, 1959). No data appear to exist for melts formed at both high temperature and high pressure. Such data are necessary to understand the influence of H_2O on chemical and physical processes of magma formation and evolution. In the present report, Raman spectroscopy has been used to determine (1) the chemical and structural forms of dissolved water in silicate melts and (2) the interaction between water-bearing structural units and the remaining anionic structure of silicate melts.

Experimental methods

The Raman spectra were acquired on small chips (~1 mm) of quenched melts. A discussion of the application of such data to the structures of melts was provided by Mysen *et al.* (1980). The problem was also discussed by Taylor and Brown (1979) and Sharma *et al.* (1978). They concluded that the structural features of liquids that are discernible with Raman spectroscopy can be quenched at least with the quenching rates employed here (250°–500°C/sec).

An added complexity in the present experiments is the mobility of H_2O in silicate melts and the tendency of water-bearing melts not to form a glass. Instead, minerals precipitate from the melt during quenching. In melts with a three-dimensional network structure [*e.g.*, $NaAlSi_2O_6$ (Jd) and $NaAlSi_3O_8$ (Ab) compositions in the present study] it has been suggested that liquids with up to about 5 wt. percent H_2O can be quenched at high pressure (Burnham, 1975). No more than about 5 wt. percent H_2O was therefore added to these melts. Whether H_2O could be quenched in these melts was also assessed by monitoring the intensity of the Si–OH and HOH stretch bands in the Raman spectra (see below).

Less is known about melts that are less polymerized than those that have a three-dimensional network (NBO/T > 0).[2] In fact hydrous melts of metasilicate composition cannot even be quenched to a glass. Di- and trisilicate of sodium [$Na_2Si_2O_5$ (NS2) and $Na_2Si_3O_7$ (NS3)] can be quenched to clear, bubble-free glass at least with water contents up to 4–5 wt. percent. Inasmuch as the intensity of Raman bands of Si–OH stretch vibrations of such melts increases with increasing H_2O content of the quenched melt, we conclude that in these melts (NS2 and NS3) the H_2O content can be quenched. Melts of $Na_2Si_2O_5$ and $Na_2Si_3O_7$ composition were used, therefore, to study solubility mechanisms of H_2O in silicate melts with a significant number of nonbridging oxygens.

The starting materials for high-pressure experiments were glasses made at 1 atm. The glasses were produced from spectroscopically pure (Johnson and Matthey) SiO_2 and Al_2O_3 and reagent-grade Na_2CO_3 (Fisher). Water was double-distilled H_2O, added to the samples with a microsyringe with 0.03 μl precision. Deuterium oxide (MSD isotope products, Canada) was 95 percent D_2O and 5 percent H_2O.

The samples were contained in sealed Pt capsules of 2 or 3 mm O.D. In order to ensure that the desired amount of water was in the charge during an experiment, the capsules were weighed before and after welding and again after 1–2 hr at 110°C. The accuracy of the amount of water reported is 4–7 percent (depending on the concentration of H_2O in the melt).

All experiments were carried out in solid-media, high-pressure apparatus (Boyd and England, 1960) using the piston-out technique with a −4 percent correction for friction (calibrated against the quartz–coesite transition). The temperatures were measured with Pt–Pt90Rh10 thermocouples. The uncertainties were ±1 kbar and ±6°–10°C (Eggler, 1977; Mao *et al.*, 1971).

The Raman spectra were taken on small chips of quenched melt (about 0.5–1.0 mm cubes) free of bubbles. The spectra were recorded with a Jobin-Yvon optical system, holographic grating, double monochromator (HG25) with a photon-counting detection system. The spectra were recorded at 3 cm^{-1}/sec. The samples were excited with the 488.0 nm line of an Ar^+ laser using laser power of 200–400 mW at the sample with 90° scattering geometry. Polarized spectra were obtained with the focused exciting beam parallel to the horizontal spectrometer slit and with the electric vector of the exciting radiation in a vertical orientation. A sheet of polarizer disk in front of an optical scrambler was used to record separately the parallel and perpendicular components of the scattered radiation.

Several of the high-frequency envelopes of the

[2] NBO/T denotes nonbridging oxygen per tetrahedral cation. The tetrahedral cation can be Si^{4+}, Ti^{4+}, P^{5+}, Al^{3+}, and Fe^{3+}. With Fe^{3+} and Al^{3+}, local charge balance is attained with an alkali metal or an alkaline earth to form complexes such as $MAlO_2$, $MFeO_2$ and MAl_2O_4. MFe_2O_4 complexes are not stable in silicate melts (Mysen *et al.*, 1979a). The notation NBO/Si is used when T = Si.

Table 1. Raman spectroscopic data on the system Na_2O–SiO_2–D_2O–H_2O at 1300°C and 20 kbar

Composition	Mole % H_2O (D_2O)	Wavenumber, cm^{-1}							$\frac{I(1100)}{I(1060)}$	$\frac{I(1100)}{I(950)}$
$Na_2Si_2O_5$	...	573s,p	763w,p	948m,p	...	1055m,p	1103s,p	...	4.52	3.47
$Na_2Si_2O_5$	33.6 (D_2O)	573s,p	770w,p	943w,p(bd)	...	1057s,p	1098s,p	...	2.12	4.10
$Na_2Si_2O_5$	8.1	579s,p	764w,p	939mw,p	983w	1061s,p	1098s,p	...	1.61	4.19
$Na_2Si_2O_5$	14.4	574s,p	767w,p	940w,p(bd)	983w(bd)	1070s,p	1100s,p	...	1.11	3.64
$Na_2Si_3O_7$	...	542s,p	775w,p	942w,p	...	1065m,p	1093s,p	...	0.81	...
$Na_2Si_3O_7$	44.8 (D_2O)	538s,p	780w,p	...	...	1050s,p(bd)	1097s,p	1152m,p	3.89	...
$Na_2Si_3O_7$	8.6	539s,p	777w,p	...	972w(bd)	1061m,p(bd)	1101s,p	1173w(bd)	1.82	...
$Na_2Si_3O_7$	24.3	546s,p	773w,p	...	978m,p	1056s,p	1093s,p	1152m,p	0.96	...
$Na_2Si_3O_7$	37.9	546s,p	773w,p	...	973m	1062s,p	1093s,p	1147m,p	0.81	...

Abbreviations: s, strong; m, medium; mw, medium to weak; w, weak; vw, very weak; (bd), broad; (sh), shoulder; p. polarized. Band positions above 1200 cm^{-1} not accurately measured. For detailed positions of such bands (HOH and DOD stretch bands), see Table 2.

spectra were attempted deconvoluted into individual peaks. The details of the procedures used are described by Mysen *et al.* (1980).

Results

Volatile-free melts

The structural interpretation of volatile-free, quenched NS2 and NS3 melts at 1 atm and at high pressure has been presented elsewhere (Brawer and White, 1975; Furukawa and White, 1980; Mysen *et al.*, 1980). Only a summary of the band positions (Table 1) and interpretation of the Raman spectra are given here. The Raman spectrum of quenched NS2 melt consists of three polarized bands that are important for the present discussion. The strong band near 1100 cm^{-1} is due to ^-O–Si–O^0 stretching[3] (diagnostic of sheet units in the melt). The band near 950 cm^{-1} is due to ^-O–Si–O^- stretching (diagnostic of chain units), and that near 1060 cm^{-1} is due to Si–O^0 stretching (three-dimensional network unit). Other bands near 570 and 770 cm^{-1}, respectively, are due to Si–O^0 rocking and bending motions.

In volatile-free melt of $Na_2Si_2O_5$ composition, the following expression can be used to describe the equilibrium between the anionic structural units of the melt (Mysen *et al.*, 1980):

$$2Si_2O_5^{2-}\ (\text{sheet}) = Si_2O_6^{4-}\ (\text{chain}) + SiO_2\ (3D) \quad (1)$$

The same bands occur in volatile-free, quenched NS3 melt as in volatile-free NS2 melt (Table 1). Mysen *et al.* (1980) concluded, therefore, that quenched NS2 and NS3 melts contain the same structural units and that the equilibrium expressed with equation 1 applies to both melt compositions. The two melts differ, however, in that chain units are more dominant in NS2 than in NS3 melts, as indicated by the intensity ratios of diagnostic bands.

Virgo *et al.* (1980) found that analogous expressions could be derived for binary melts with greater NBO/Si than NS2. In those cases, the expressions were :

for NBO/Si between 1.0 and 2.0:

$$3Si_2O_6^{4-}\ (\text{chain}) = 2Si_2O_4^{2-}\ (\text{sheet}) + 2SiO_4^{4-}\ (\text{monomer}) \quad (2)$$

and for NBO/Si between 4.0 and 2.0:

$$2Si_2O_7^{6-}\ (\text{dimer}) = Si_2O_6^{4-}\ (\text{chain}) + 2SiO_4^{4-}\ (\text{monomer}) \quad (3)$$

Mysen *et al.* (1980) noted that the same expressions hold true regardless of the type of network-modifying cation. They also concluded that this structural model does not agree with models based on polymer theory, and presented arguments as to why this would be expected. This model is, however, consistent with rheological data on silicate melts (Bockris *et al.*, 1956). The interested reader is referred to Mysen *et al.* (1980) for a complete discussion of the present and other models.

The distinct assignments to monomers, dimers, chain, and sheets were also discussed in some length by Mysen *et al.* (1980), and no further discussion of those assignments is presented here.

The anionic structures of the two melts with three-dimensional network structure at 20 kbar (Jd and Ab melt) are also known (Virgo *et al.*, 1979a; Mysen *et al.*, 1980). Only band positions of volatile-free,

[3] O^{2-}, O^-, and O^0 denote free oxygen, nonbridging, and bridging oxygens, respectively. The notation Si–O^0 indicates that the vibration is from a bridging oxygen bond. In ^-O–Si–O^0, one oxygen (out of four) is nonbridging. In ^-O–Si–O^-, two oxygens per silicon are nonbridging.

Table 2. Band positions of Raman spectra from quenched melts in the system Na_2O–Al_2O_3–SiO_2–D_2O–H_2O at 1500°C and 20 kbar

Composition	Mole % H_2O (D_2O)	Wavenumber, cm^{-1}									$\frac{I(1100)}{I(870)}$	$\frac{I(1100)}{I(970)}$	$\frac{I(1100)}{I(1000)}$
$NaAlSi_2O_6$	...	470s,p	566w,p	784w,p	...	...	950m,p	1062s,p	...	2175s 2300w	...	...	...	...	2.17
$NaAlSi_2O_6$	27.4	480s,p	570p(sh)	773w,p	871w,dp	983w(bd)	966m,p	1058s,p	...*	...* ...*	...	...*	12.28	...	2.30
$NaAlSi_2O_6$	40.0	484s,p	561p(sh)	770w,p	862w,dp	985w(bd)	961m,p	1068s,p	...*	2180s 2300w	...	...*	8.34	10.[illegible]	2.42
$NaAlSi_2O_6$	51.9	484s,p	563p(sh)	770w,p	860w,dp	985w(bd)	940m,p	1062s,p	...*	...* ...*	...	...*	3.18	6.3[illegible]	2.63
$NaAlSi_3O_8$	...	468s,p	573w,p	794w,p	...	...	1000m,p	1100s,p	...	2175s 2300w	...	...	...	...	0.72
$NaAlSi_3O_8$	40.9 (D_2O)	465s,p	579p(sh)	806w,p	886w,dp	...	1000m,p	1100s,p	...	...* ...*	2583s(bd)	3566s(bd)	1.63	...	2.27
$NaAlSi_3O_8$	15.5	472s,p	573p(sh)	776w,p	874w,dp	976vw(bd)	1004m,p	1100s,p	...*	...* ...*	...	...*	16.7	10.8	1.23
$NaAlSi_3O_8$	27.5	476s,p	569p(sh)	790w,p	885w,dp	983w(bd)	1000m,p	1100s,p	1368w(bd)	...* ...*	...	3535s(bd)	3.6	8.0	1.37
$NaAlSi_3O_8$	38.9	484s,p	570p(sh)	785w,p	893w,dp	983mw(bd)	1000m,p	1100s,p	1374w(bd)	...* ...*	...	3530s(bd)	3.6	7.4	1.51

Abbreviations and uncertainties as in Table 1.
**Present but not determined accurately.*

quenched Jd and Ab melts are given (Table 2). Briefly, the high-frequency envelope consists of two (Si,Al)–O^0 stretch bands. Their frequencies are lowered with increasing Al content of the melt. The two stretch bands reflect two different three-dimensional network units in the melt. According to Mysen *et al.* (1980), these two units differ in average Si/(Si + Al), where the lowest frequency band is due to the most Si-rich unit. In addition, the Raman spectra show bands near 800, 570, and 470 cm^{-1}, which are due to Si–O^0 bending, decoupled defects, and Si–O^0 rocking, respectively (Bates *et al.*, 1974; Stolen and Walrafen, 1976). The three bands at these positions are diagnostic of the presence of three-dimensional network units in the quenched melts (Virgo *et al.*, 1979a).

In addition, the Raman spectra of all the samples, whether volatile-free or volatile-bearing, show two sharp bands near 2300 and 2200 cm^{-1}, respectively (Fig. 1). These two bands are due to N_2 and N_2^+ (Hartwig, 1977; Nakamoto, 1978) from air, and are

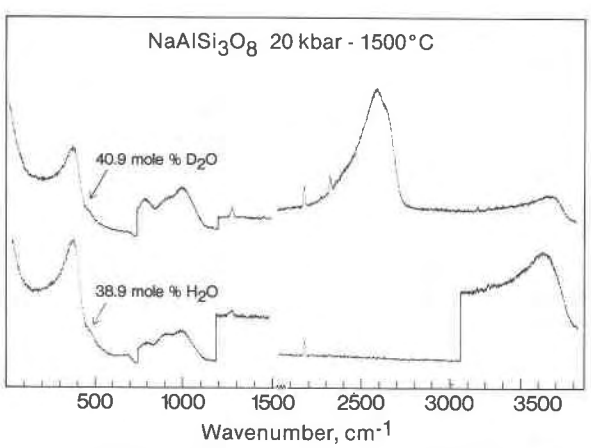

Fig. 1. Raman spectra (unpolarized) of quenched Ab + H_2O and Ab + D_2O melt.

of no consequence for the interpretation of the spectroscopic features under consideration. This observation is important because these two bands occur in the frequency region of Si–H stretching and could be misinterpreted as a result of such bonds. The two bands do not shift their frequency with composition, however, as would be expected if they were due to Si–H stretching (Lucovsky, 1979; Lucovsky *et al.*, 1979). Furthermore, no Si–H bands could be detected in the frequency region between 800 and 900 cm^{-1}.

Silicate melts with H_2O

Before the spectra of H_2O-bearing silicate melts are discussed, it is instructive to discuss the D_2O-bearing samples, because Si–OH stretch vibrations are expected in the frequency region near 950 cm^{-1} (Stolen and Walrafen, 1976). The Si–O stretch vibrations also occur in this frequency region. The analogous Si–OD bands are at frequencies that are lower than those of the OH vibrations by a factor of $\sqrt{2}$ (Van der Steen and Van den Boom, 1977; Hartwig, 1977).

The Raman spectrum of quenched Ab melt with 40.9 mole percent D_2O (calculated on the basis of 8 oxygens) is shown in Figure 1. The high-frequency envelope of this spectrum is compared with that of volatile-free and H_2O-bearing Ab melt in Figure 2. Detailed band positions are given in Table 2. The strong, broad, and asymmetric band near 2600 cm^{-1} is due to D–O–D stretching (Van der Steen and Van den Boom, 1977). The two sharp bands on the low-frequency shoulder of the 2600 cm^{-1} band are due to N_2 and N_2^+ from the air (see above). There is also a weak band near 3570 cm^{-1}, which is due to H–O–H stretching (*e.g.*, Stolen and Walrafen, 1976). This band is expected because the D_2O also contained about 5 percent H_2O.

Several changes have occurred in the high-fre-

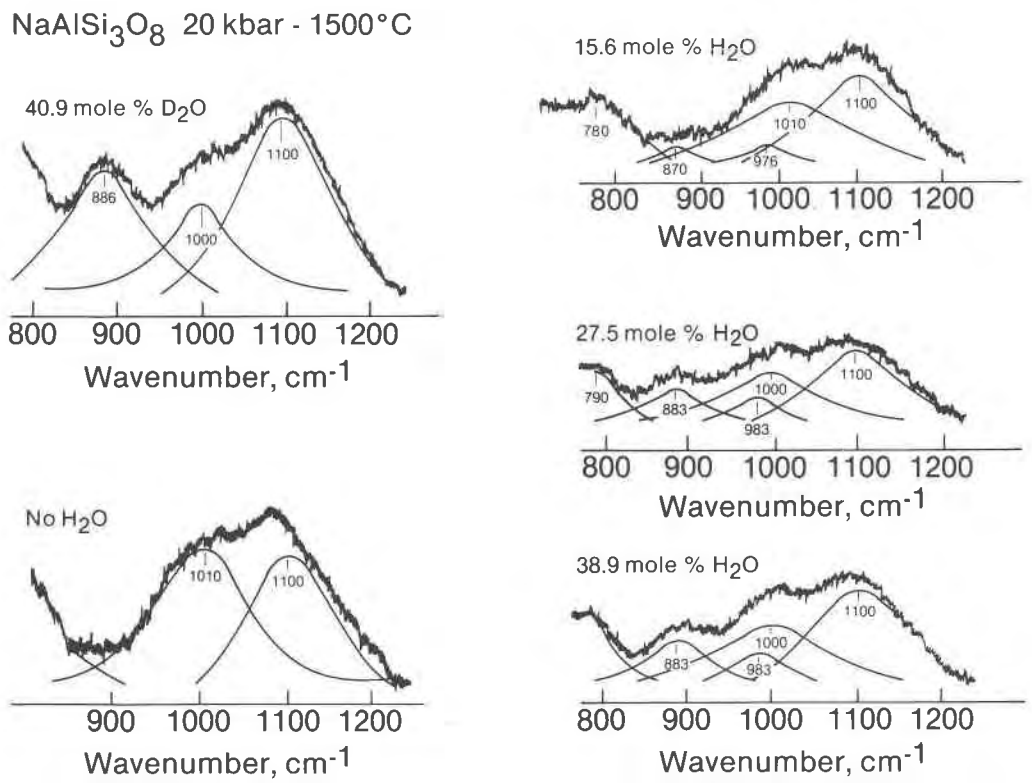

Fig. 2. High-frequency envelope of Raman spectra (unpolarized) of quenched Ab melt as a function of volatile content.

quency envelope of the spectrum from Ab + D_2O compared with the envelope of volatile-free Ab melt (Figs. 1 and 2). The two (Si,Al)–O^0 stretch bands remain in the same positions (about 1000 and 1100 cm^{-1}) as for the volatile-free melt. The intensity of the band near 1000 cm^{-1} is considerably weakened, however, relative to the 1100 cm^{-1} band [I(1100)/I(1000) is about 2.3 compared with 0.7 for volatile-free Ab melt; see also Table 2]. We conclude, therefore, that the proportion of Si-rich, three-dimensional network unit (3D) in Ab melt has been substantially reduced as a result of dissolved D_2O. It is emphasized, however, that the average Si/(Si + Al) of the two three-dimensional units is the same. Only the proportion of the Si-rich unit has been reduced.

A new band at 886 cm^{-1} occurs in deuterated, quenched Ab melt at 20 kbar and 1500°C (Fig. 2, Table 2). The D_2O contains only a very small amount of H_2O and the position and intensity of the 886 cm^{-1} band do not change appreciably whether 40 mole percent H_2O or 40 mole percent D_2O (with 5 percent H_2O) has been dissolved in the melt. It is not likely, therefore, that this band is due to vibrations involving D, H, OH, or OD-groups, as their intensities and frequencies would depend on concentration and type of volatile component added to the melt. We conclude, therefore, that the 880 cm^{-1} band cannot be assigned to Si–H, Si–D, Al–H, Al–D, Si–OH, Si–OD, Al–OH, or Al–OD vibrations. In addition, there are other arguments in favor of another interpretation. The Al–H, Al–D, Si–H, and Si–D vibrations may have bands that occur in the frequency range between 700 and 900 cm^{-1} (*e.g.*, Ryskin, 1974; Hartwig, 1977; Lucovsky, 1979; Lucovsky *et al.*, 1979; Peri, 1966). The band near 880 cm^{-1} could be due to Al–O^0, $^-$O–(Si,Al)–O^0 or $^-$O–(Si,Al)–O^- stretching. If it were due to Al–O^0 stretch vibrations, clusters of AlO_4 tetrahedra without nonbridging oxygens would be expected in the melt. This hypothesis is ruled out for the following reasons. In vibrational spectra known to contain AlO_4 clusters, Al–O^0 stretch vibrations result in one or more bands at 800 cm^{-1} or lower frequency (Tarte, 1967; Serna *et al.*, 1977, 1979; Virgo and Seifert, unpublished data, 1979), and no such bands are found in the hydrated samples. It is not likely, therefore, that the 880 cm^{-1} band found in the Ab + D_2O spectrum results from AlO_4 clusters. The band between 750 and 800 cm^{-1} found in the spectra of quenched Ab and Jd melts (Table 2) also

occurs at this frequency in Al-free melts with three-dimensional network units. The band in the deuterated and hydrated melts is not significantly affected by D_2O or H_2O content. This band is assigned to Si–O^0 bending, as also suggested by Bates *et al.* (1974) for quenched SiO_2 melt. No new bands occur in the spectral region below 800 cm^{-1} as a result of added volatiles. The presence of AlO_4 clusters is therefore ruled out.

The 880 cm^{-1} band changes its frequency with H_2O and Al content (Table 2) and hence is most likely a coupled (Si,Al) vibration. The intensity of the band relative to the (Si,Al)–O^0 stretch bands is so large, however, that it is unlikely that the 880 cm^{-1} band reflects vibrations of a bridging oxygen (see also Furukawa and White, 1980, for further discussion of such intensity considerations).

The 880 cm^{-1} band is polarized and thus is probably a symmetric $^-$O–(Si,Al)–O^- stretch vibration rather than an asymmetric $^-$O–(Si,Al)–O^0 stretch vibration. Mysen and Virgo (1979) noted that in quenched melts of $NaCaAlSi_2O_7$ composition [Si/(Si + Al) = 0.33 as compared with 0.25 in $NaAlSi_3O_8$ composition] the $^-$O–Si–O^- stretch band found near 950 cm^{-1} was shifted to near 900 cm^{-1} as a result of (Si,Al) coupling. In the system $NaAlSi_3O_8$ + D_2O, the average Si/(Si + Al) is greater than in $NaCaAlSi_2O_7$. As discussed further below, the Si/(Si + Al) of the anhydrous portion of the melt is less than this average value, however, because some of the Si of the melt is no longer part of the anhydrous network (owing to the formation of Si–OH- or Si–OD-containing structural units in the melt). The Si–OD band (stretch) is expected near 600 cm^{-1}. This is a weak band, however (Stolen and Walrafen, 1976; Van der Steen and Van den Boom, 1977), and is unresolved beneath the asymmetric band with a maximum near 500 cm^{-1} (Fig. 2). As a result of these considerations, we conclude that the 880 cm^{-1} band in quenched Ab + D_2O melt is due to symmetric $^-$O–(Si,Al)–O^- stretching. The (Si,Al) coupling is more extensive than indicated by the average Si/(Si + Al) of the melt. This band is, therefore, diagnostic of anhydrous (or undeuterated) chain units in the quenched Ab melt with 40.9 mole percent D_2O in solution.

The Raman spectra of quenched Ab + H_2O melt are shown in Figures 1 and 2, and band positions are given in Table 2. All spectra show the same features as the spectrum for Ab + D_2O, except that the H–O–H and Si–OH vibrations occur at different frequencies because of the different mass of H compared with D (Van der Steen and Van den Boom, 1977). A broad, asymmetric band near 3520 cm^{-1} is assigned to H–O–H stretching (Stolen and Walrafen, 1976). The asymmetry toward lower frequency is probably due to weak OH···O hydrogen bonds (Serratosa and Vinas, 1964; Peri, 1966). Hydrogen bonds between outer hydroxyl groups and neighboring oxygen are frequently observed in micas, for example (Serna *et al.*, 1977, 1979).

There are no bands at higher frequency than the H–O–H band; thus the presence of molecular H_2 in the quenched Ab + H_2O melt is ruled out (Lucovsky *et al.*, 1979). The absence of a band near 1600 cm^{-1} rules out the possibility of a contribution of molecular H_2O in solution in any of these melts (Lucovsky *et al.*, 1979). The two sharp bands near 2200 and 2300 cm^{-1} are due to N_2^+ and N_2 from the air (see also above). The weak band near 1380 cm^{-1} (Fig. 2) is due to H–O–H bending (Ryskin, 1974).

We note that the intensity of the band near 570 cm^{-1} [due to defects (broken oxygen bridges) in the three-dimensional network structure (Bates *et al.*, 1974; Stolen and Walrafen, 1976)] is lower in the spectra of melts with H_2O (and D_2O) than in those of melts without volatiles (Fig. 3). Stolen and Walrafen (1976) made similar observations in the system SiO_2–H_2O. They concluded that H^+ reacted with defects in the three-dimensional network structure (Si–O^-···Si–O–Si^-) to form OH, thereby diminishing the intensity of this band. The same mechanism explains the reduced intensity of the 570 cm^{-1} band in the spectra shown here. Stolen and Walrafen (1976) noted, however, that only about 1000 ppm H_2O can dissolve in fused SiO_2 according to this mechanism, and it is

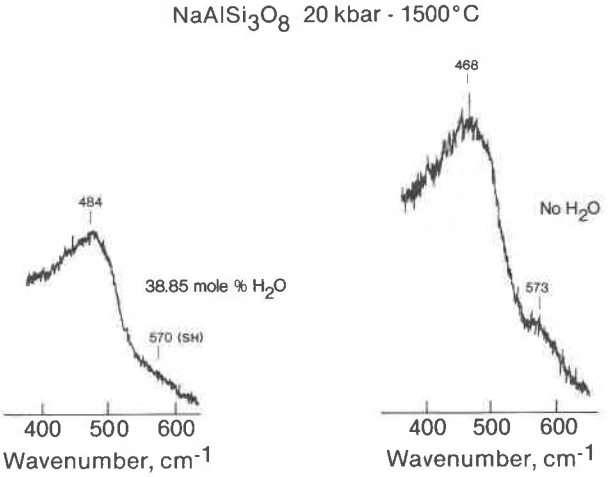

Fig. 3. Low-frequency region of volatile-free and H_2O-bearing quenched Ab melt.

therefore not considered the major mechanism for solution of several weight percent H_2O.

The band near 880 cm^{-1} in quenched Ab + D_2O melt also occurs in quenched Ab + H_2O melt (Fig. 2) and is at nearly the same position (within experimental uncertainty).

The 1000 cm^{-1} shoulder in Ab + H_2O spectra is stronger than in the spectrum from Ab + D_2O (Fig. 2). This higher intensity is caused by the presence of two bands in the frequency region near 1000 cm^{-1}. One is due to (Si,Al)–O^0 stretching from the silica-rich, three-dimensional network unit (1000 cm^{-1}). The other band (near 980 cm^{-1}) is an Si–OH stretch vibration. It may be argued that the 980 cm^{-1} band may also be due to Al–OH stretching. This possibility is considered unlikely because (1) the band occurs at the same frequency in Al-free samples (*e.g.*, Stolen and Walrafen, 1976; see also below) and (2) several Al–OH bending and rocking vibrations would be expected in the frequency region between 950 and 750 cm^{-1} (Ryskin, 1974). No such bands were found in our samples.

The 880 cm^{-1} band may shift to slightly higher frequency with increasing water content of quenched Ab melt (Fig. 4). The frequencies of the 1000 and 1100 cm^{-1} bands are not affected by the presence of water in the melt. The frequency increase of the 880 cm^{-1} band with increasing water content indicates that the average Si/(Si +Al) of this structural unit in quenched Ab melt increases slightly with increasing H_2O content.

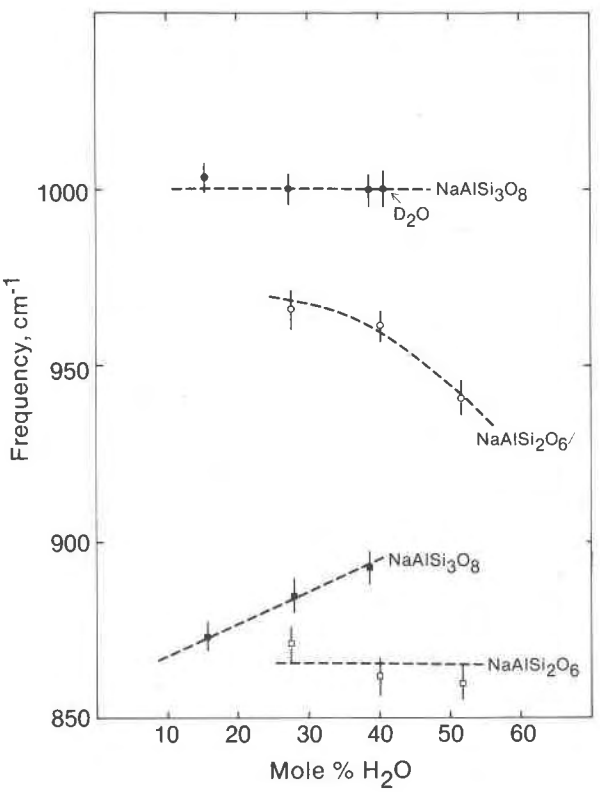

Fig. 4. Frequency shifts of critical Raman bands as a function of water content.

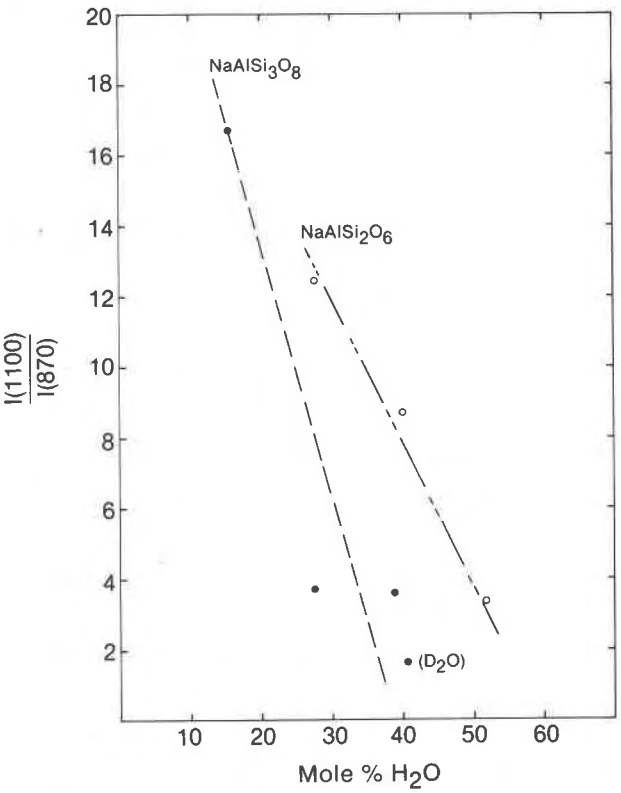

Fig. 5. Raman band intensity ratios $I(1100)/I(870)$, of volatile-free and volatile-bearing quenched Ab and Jd melts.

The intensities of both the 880 and 980 cm^{-1} bands increase relative to those of the 1100 and 1000 cm^{-1} (Al,Si)–O^0 stretch bands as the water content of the Ab melt is increased (Fig. 5; see also Table 2). We conclude, therefore, that more chain units and Si–OH bands are formed as the water content of the melt is increased. Finally, the intensity ratio, $I(1100)/I(1000)$, increases with increasing water content (Fig. 6). This increase implies that the Si–OH groups are formed as a result of interaction between the H_2O and the most silica-rich of the two three-dimensional network units in melt of $NaAlSi_3O_8$ composition.

The high-frequency envelope of the Raman spectra of quenched melts of $NaAlSi_2O_6$ and $NaAlSi_2O_6 + H_2O$ composition are shown in Figure 7 (see also Table 2). The portions of these spectra at higher

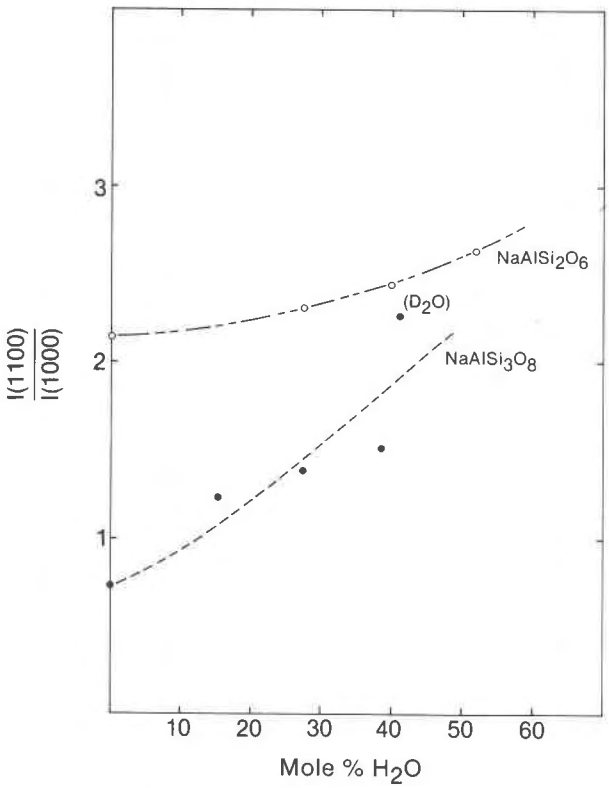

Fig. 6. Raman band intensity ratios, $I(1100)/I(1000)$, of volatile-free and volatile-bearing quenched Ab and Jd melts.

and lower frequencies than those shown in Figure 7 are identical with the same regions in the spectra of quenched Ab + H_2O melt and are not included. The exact band positions from these regions are given in Table 2.

The structure of quenched anhydrous Jd melt at high pressure has been described by Mysen *et al.* (1980). Briefly, the structure closely resembles that of quenched anhydrous Ab melt except that the two three-dimensional network units are more Al-rich in the Jd than in the Ab melt. The proportion of the most Si-rich unit relative to the Al-rich unit is also smaller in Jd melt.

Addition of water to Jd melt results in the same changes in the high-frequency envelope of the Raman spectra of both Ab and Jd melts (Figs. 2 and 7). A new, polarized band occurs near 860 cm^{-1}. This band is analogous to the 880 cm^{-1} band in quenched Ab + H_2O melt and is assigned to symmetric ^-O–(Al,Si)–O^- stretching, as in quenched Ab + H_2O melt. Its slightly lower frequency in Jd + H_2O melt is a result of the smaller Si/(Si + Al) of Jd compared with Ab melt. The intensity of this band relative to the (Si,Al)–O^0 stretch bands increases with increasing water content of the melt, as was also the case for Ab + H_2O melt (Fig. 5). A new band near 980 cm^{-1} is assigned to Si–OH stretching. This band most likely does not reflect Al–OH stretching, for the same reasons as outlined above for Ab + H_2O melt. Finally, the intensity ratio, $I(1060)/I(950)$, increases with increasing water content (Fig. 6). This intensity increase corresponds to the intensity increase of $I(1100)/I(1000)$ for Ab + H_2O melt, and is interpreted to mean that the proportion of the Si-rich, three-dimensional network unit decreases relative to the Al-rich unit as the water content of quenched Jd melt is increased.

In summary, solution of H_2O in melts of $NaAlSi_3O_8$ and $NaAlSi_2O_6$ has similar effects on the anionic structure of the melts. First, water is bound in the structure as Si–OH, resulting in a decrease in the average Si/(Si + Al) of the anhydrous portion of the melt. The three-dimensional network portion of the melt responds to this decrease by an increase in the proportion of the Al-rich unit relative to the Si-rich, three-dimensional network unit. Second, (Si,Al)-coupled chains of the type $NaAlSiO_6^{4-}$ are formed. No OH groups are attached to the chain units. Third, aluminum is not attached to hydroxyl in any complex in the melt. Fourth, it is not possible to determine from the Raman spectra whether complexes involving Na^+ and OH^- occur in the melt. This unidentified complex is referred to as $Na(OH)^0$ in the remainder of the text.

A comparison of the high-frequency envelopes of the Raman spectra of quenched melts of $Na_2Si_3O_7$ and $Na_2Si_3O_7$ + 44.8 mole percent D_2O (based on the chemical formula—7 oxygens) is shown in Figure 8, and detailed data are given in Table 1. A comparison of the spectra of the volatile-free samples with the deuterated sample is conducted first, to avoid interferences from OH bands in the high-frequency envelope (see also above).

Three features are evident from the comparison of the volatile-free and the deuterated samples. First, the 940 cm^{-1} band diagnostic of chain units in anhydrous NS3 melt cannot be discerned in the deuterated sample. Second, a new band near 1150 cm^{-1} is observed in the Raman spectrum of quenched NS3 + D_2O. We suggest that this is the band found at 1200 cm^{-1} in quenched SiO_2 melt and assigned to Si–O^0 stretching (Bates *et al.*, 1974). Brawer and White (1975, 1977) noted that this band shifts from 1200 cm^{-1} to near 1150 cm^{-1} as Na_2O is added to SiO_2 melt on the join Na_2O–SiO_2. The band disappears at

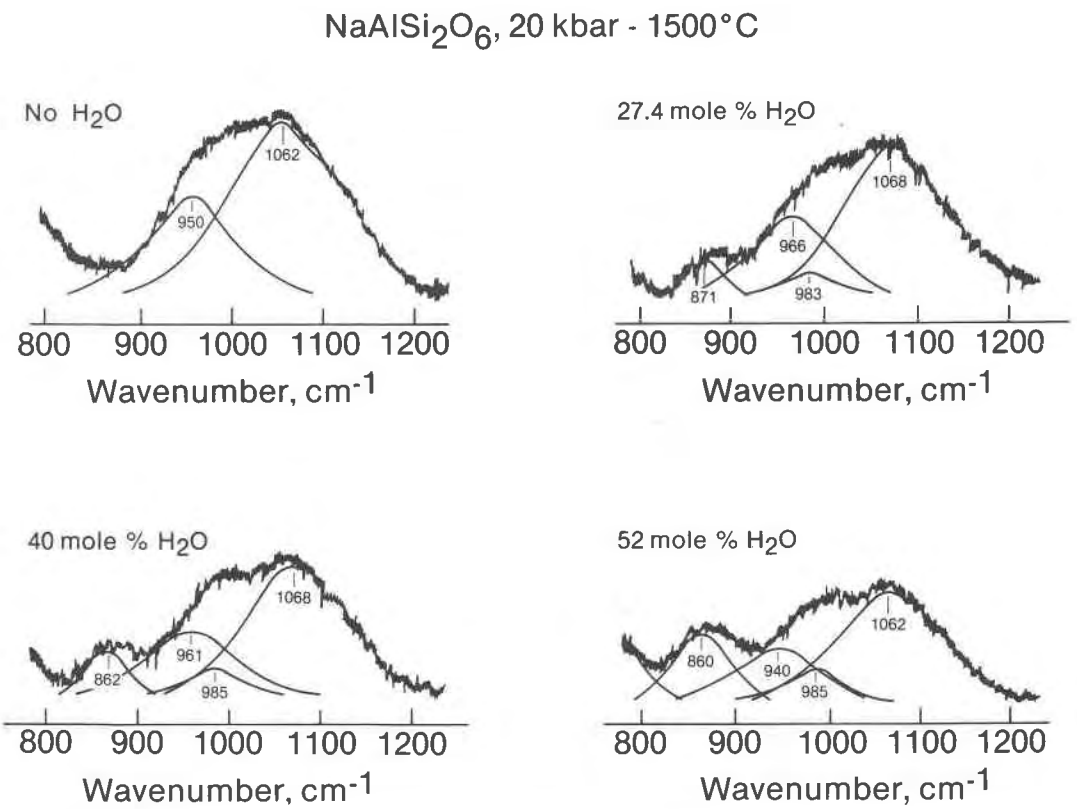

Fig. 7. High-frequency region of Raman spectra of volatile-free and volatile-bearing quenched Jd melt.

Na_2O/SiO_2 = 1/3–1/4. The reappearance of this band with the addition of D_2O to quenched melt of NS3 composition (Na_2O/SiO_2 = 1/3) indicates that the proportion of bridging oxygen is greater in deuterated than in volatile-free melt of NS3 composition. Third, the intensity of the 1100 cm^{-1} band (indicating that sheet units may be present in the melt; Mysen *et al.,* 1980) relative to the intensity of the 1050 cm^{-1} band (Si–O^0 antisymmetric stretch band; Furukawa and White, 1980; Mysen *et al.,* 1980) has decreased. This observation also implies that deuterated NS3 melt is more polymerized than D_2O-free, quenched melt of $Na_2Si_3O_7$ composition.

The high-frequency envelopes of the Raman spectra of hydrated quenched NS3 melt are shown in Figure 9 (see also Table 1). When curves were fitted to the high-frequency envelope (see Mysen *et al.,* 1980, for the fitting procedure), the bands near 1050, 1100, and 1150 cm^{-1} were retained. In order to fulfill this requirement, a broad band near 970 cm^{-1} also had to be included. This band becomes more intense with increasing water content, and because of this relation and its frequency, it is assigned to Si–OH stretching.

The intensity ratio of the 1100 and 1050 cm^{-1} bands is plotted as a function of H_2O content of the melt in Figure 10. These data show that the 1050 cm^{-1} band becomes more intense as the water content of the melt increases. This observation is interpreted to mean that the solution of H_2O in melt of $Na_2Si_3O_7$ composition results in the formation of Si–OH bonds with a concomitant decrease of NBO/Si of the melt.

The effect of dissolved H_2O and D_2O on the high-frequency envelope of the Raman spectra of quenched NS2 melt is shown in Figure 11. A comparison of the spectra of volatile-free, D_2O-bearing, and H_2O-bearing NS2 melt shows the same bands in all cases (940 cm^{-1}, $Si_2O_6^{4-}$ chains; 1060 cm^{-1}, SiO_2 three-dimensional network; 1100 cm^{-1}, $Si_2O_6^{2-}$ sheets). It is clear, however, that the intensity ratio $I(1100)/I(1060)$ has decreased and $I(1100)/I(940)$ has increased (Table 1; see also Fig. 10). As for hydrous melt of NS3 composition, these changes are interpreted to mean that the proportion of bridging oxygen in the melt has increased as water is dissolved. This change is reflected in an increased ratio of three-dimensional network units to sheet units, and an in-

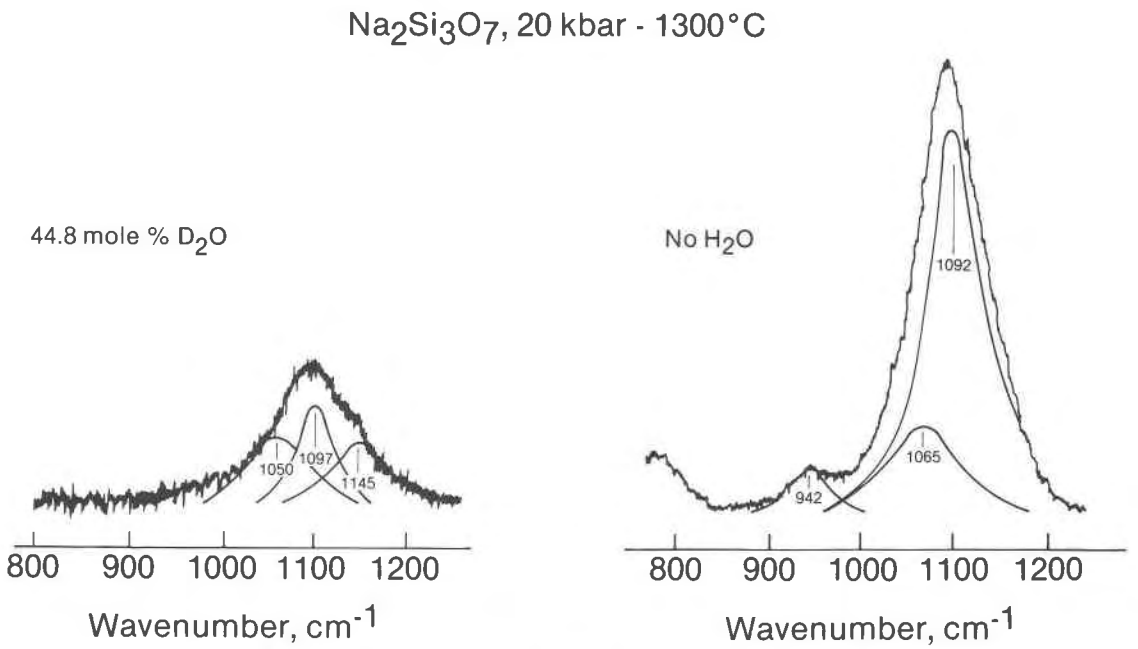

Fig. 8. High-frequency region of volatile-free and D_2O-bearing quenched melt of $Na_2Si_3O_7$ composition.

crease of sheet units relative to chain units in the melt.

Addition of H_2O to quenched NS2 melt results in an additional change of the high-frequency envelope. A new band occurs near 980 cm^{-1}, which is the Si–OH stretch band also found in all the other compositions.

In summary, the influence of dissolved water on the structure of melts in the system Na_2O–SiO_2 appears similar for all compositions studied. Water is attached to the network with Si–OH bonds, and the hydroxyl-free portion of the network has become more polymerized. As in the systems Ab + H_2O and Jd + H_2O, it cannot be determined from the Raman spectra whether $Na(OH)^0$ occurs in the melts; however, mass-balance considerations require its presence. This conclusion contrasts with that for the other two compositions, in which $Na(OH)^0$ does not occur.

Solubility mechanisms

Even though H_2O reacts with silicate melts to form Si–OH bonds, two distinctly different solubility mechanisms are necessary to explain the spectroscopic observations, depending on whether the silicate melt contains nonbridging oxygen. Most solubility models for H_2O have been based on studies of melts with a three-dimensional network structure, and this type of melt is considered first.

The Raman spectra of hydrous Jd and Ab melt show the existence of four structural units. First, there are units that involve only Si and OH. Whether Si–O–Si bonds also exist in these structural units cannot be discerned from the Raman spectra. Second, there are chain units without OH but with both Si and Al. The Al^{3+} must be locally charge-balanced with Na^+. The exact proportion of Si and Al in the chain unit cannot be determined. In the present discussion, the chain unit is described by the formula $NaAlSiO_6^{4-}$, where Al, therefore, is in tetrahedral coordination. Third, a portion of the three-dimensional network units is not affected by the presence of H_2O in the melt. The proportion of the latter two units and the OH/Si of the hydroxylated silicate unit depends on the H_2O content of the melt. Fourth, Burnham (1975) noted that the equimolal solubility of H_2O in $NaAlSi_3O_8$ melt is about 10 percent greater than in Si_4O_8. This additional water is dissolved as OH^-, locally charge-balanced by Na^+. This configuration in the melt is referred to as $Na(OH)^0$ in this text. This notation is not meant to imply that such complexes actually occur in the melt.

A consequence of the formation of chain units from a three-dimensional network structure is the expulsion of some Al^{3+} from tetrahedral coordination. There is no evidence that either this or any other Al^{3+} is coordinated with OH groups. An equivalent amount of Na^+ must also be transformed from its charge-balancing role to become a network modifier.

The extra Al^{3+} is referred to simply as Al^{3+} in the

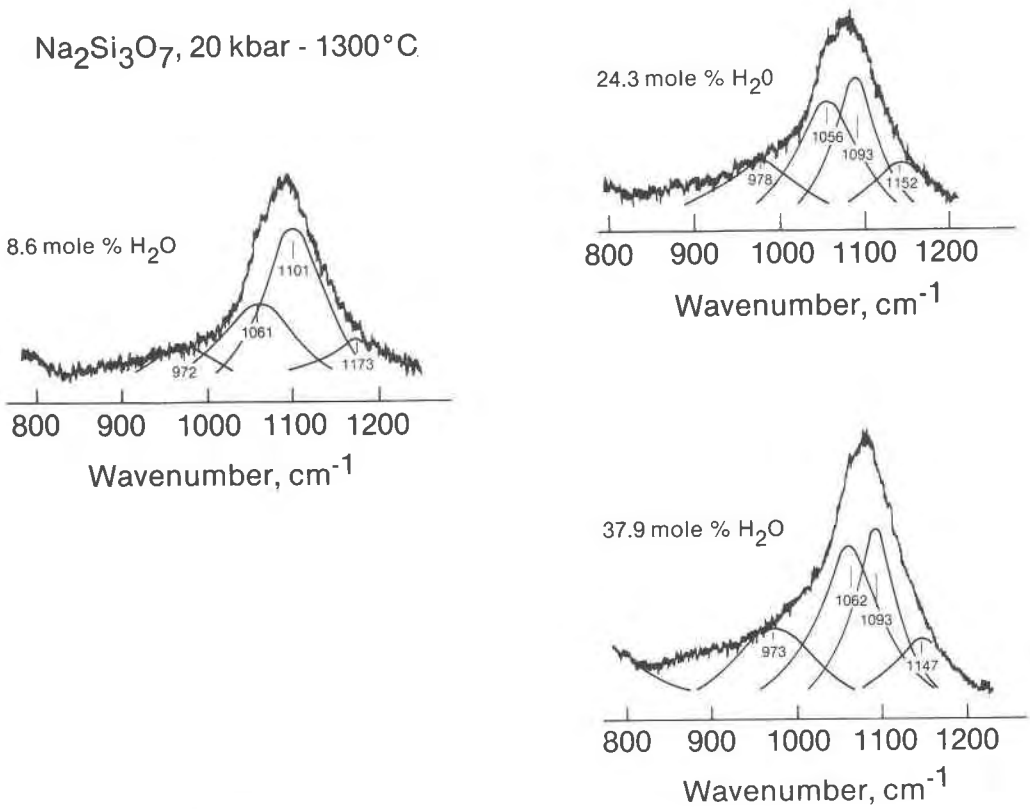

Fig. 9. High-frequency region of water-bearing, quenched melt of $Na_2Si_3O_7$ composition.

expressions below. This notation is meant to indicate the proportion of aluminum in the melt that is no longer in tetrahedral coordination. Instead, this proportion of the total amount of aluminum in the melt has become a network-modifier.

The formation of Si–OH bonds from bridging oxygen is visualized as follows:

$$\text{–Si–O–Si– (melt)} + H_2O\ \text{(vapor)} = \text{–Si–OH . . . HO–Si– (melt)} \quad (4)$$

The principle illustrated with this expression was also proposed by Kurkjian and Russell (1957), Wasserburg (1957), Adams and Douglas (1959), and Uys and King (1963). The formation of two OH groups per molecule of H_2O was indicated by the fact that the H_2O solubility was proportional to $[f(H_2O)]^{1/2}$ (Kurkjian and Russell, 1957).

In view of the above observations and discussion, an idealized expression that describes the solubility mechanism of H_2O in melt of $NaAlSi_3O_8$ composition can be written:

$$14NaAlSi_3O_8\ \text{(melt)} + 13xH_2O\ \text{(vapor)} = 9Si_4O_{8-x}(OH)_{2x}\ \text{(melt)} + 8Na(OH)^0\ \text{(melt)} + 8Al^{3+}\ \text{(melt)} = 6NaAlSiO_6^{4-} \quad (5)$$

The Al^{3+} in equation 5 reflects the proportion of aluminum that is now a network modifier. With x = 2, 4, 6, and 8, the hydroxylated silicate is respectively a sheet, chain, dimer, and monomer. The corresponding amount of H_2O that can be dissolved in Ab melt with these values for x is given in Table 3. The results of the latter calculations (Table 3) show that in our quenched melts the hydroxylation probably did not proceed beyond sheets $[Si_4O_6(OH)_4]$.

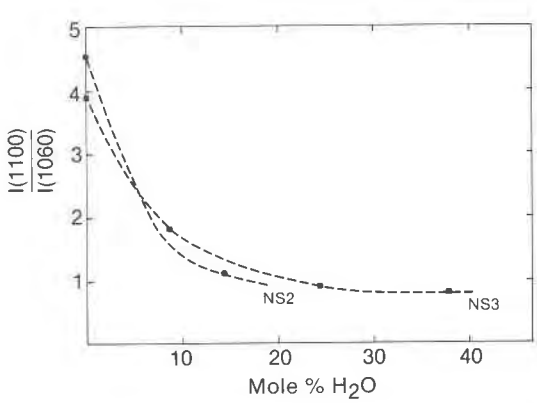

Fig. 10. Raman band intensity ratio, $I(1100)/I(1060)$, of quenched NS3 and NS2 melts as a function of water content.

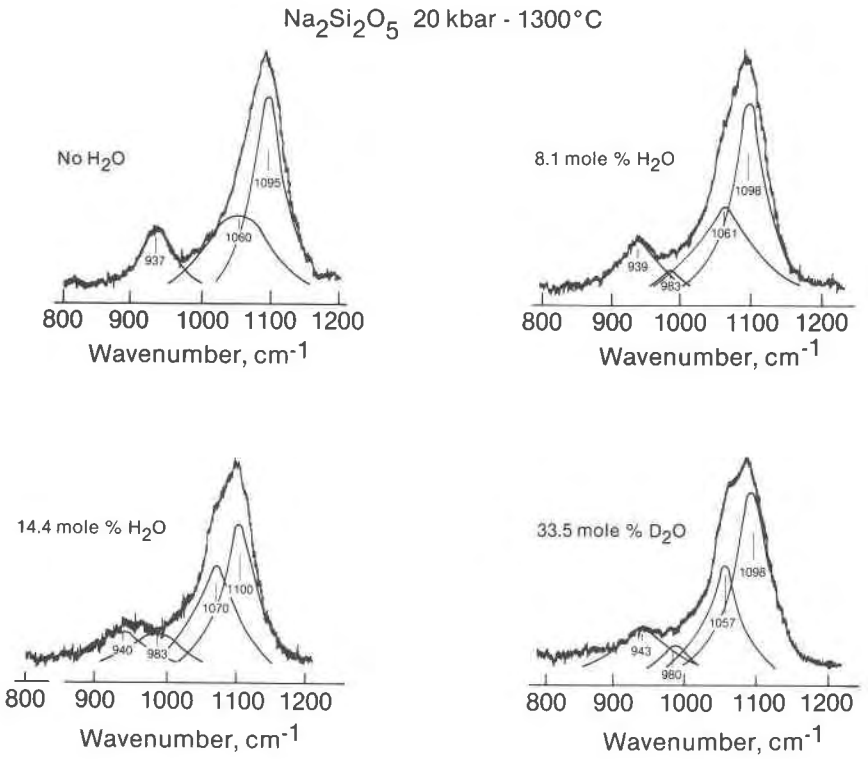

Fig. 11. High-frequency region of volatile-free and water-bearing quenched melt of $Na_2Si_2O_5$ composition.

The Raman spectra of quenched hydrated melt of $NaAlSi_2O_6$ composition indicate that the solubility mechanism for H_2O in such melts in similar to that in Ab melt. The analogous expression is

$$28NaAlSi_2O_6\ (melt) + 15xH_2O\ (vapor) = 11Si_4O_{8-x}(OH)_{2x}\ (melt) + 16Na(OH)^0\ (melt) + 16Al^{3+}\ (melt) + 12NaAlSiO_6^{4-}\ (melt) \quad (6)$$

The maximum solubilities of H_2O corresponding to x = 2, 4, 6, and 8 are shown in Table 3.

We suggest that analogous mechanisms control the solubility of H_2O in melts with three-dimensional network structures but with other melt modifiers (*e.g.*, K or alkaline earths) or amphoteric cations (*e.g.*, Fe^{3+}). The solubility mechanisms of H_2O in silicate melts with nonbridging oxygen indicate the formation of Si–OH bonds with a concomitant decrease in NBO/Si of the melt. The formation of an Si–OH bond from $Si–O^-$ indicates that one H^+ has taken the place of an Na^+. The Na^+ released can be neutralized by forming $Na(OH)^0$, a model also advanced by Kurkjian and Russell (1957) on the basis of solubility studies on $Na_2O–SiO_2$ melts. In fact, the formation of $Na(OH)^0$ complexes is a consequence of the spectroscopic observation that $SiO_2/Si_2O_5^{2-}$ increases with increasing water content of the melts.

Table 3. Maximum water solubility in silicate melts as a function of the number of OH groups attached to Si

Composition	Wt % H_2O			
	x=2 (sheet)	x=4 (chain)	x=6 (dimer)	x=8 (monomer)
$NaAlSi_3O_8$	9.7	17.8	24.5	30.2
$NaAlSi_2O_6$	8.2	15.2	21.1	26.3
$Na_2Si_3O_7$	11.0	19.9	27.1	33.2
$Na_2Si_2O_5$	14.2	24.8	33.1	39.7

The complete reactions for melts of $Na_2Si_3O_7$ and $Na_2Si_2O_5$ compositions may be written:

$$6Na_2Si_3O_7\ (melt) + 5xH_2O\ (vapor) = 2Si_4O_{8-x}\ (OH)_{2x}\ (melt) + 6SiO_2\ (melt) + 12Na(OH)^0\ (melt) \quad (7)$$

and

$$6Na_2Si_2O_5\ (melt) + 5xH_2O\ (vapor) = 2Si_4O_{8-x}\ (OH)_{2x}\ (melt) + 4SiO_2\ (melt) + 12Na(OH)^0\ (melt) \quad (8)$$

The maximum water solubilities for given values of x (Table 3) show that for given x the water solubility increases with increasing Na_2O/SiO_2, as also concluded by Uys and King (1963) on the basis of water solubility studies on melts on alkali–silica joins.

We suggest that solution mechanisms similar to those shown in equations 7 and 8 also operate in

metasilicate melts. In those melts, chain units are the predominant units, and the hydroxylated units can be no more polymerized than that.

In summary, the Raman spectra of quenched hydrated melts with a three-dimensional network structure show that nonbridging oxygens are formed in addition to hydroxylated silicate units. In melts with nonbridging oxygen, the Raman spectra show an increase in the degree of polymerization of the network. Water is bonded in the structure as both Si–OH and complexes of the type $M(OH)^0$, where M is a modifying cation.

Applications

Water affects the melting relations of silicate mineral assemblages. Kushiro (1969) has shown, for example, that in the system $CaO–MgO–SiO_2–H_2O$ the pyroxene–silicate mineral liquidus boundary shifts significantly toward the silica-rich portion of the system with the addition of H_2O. This observation is understandable in the light of the solubility mechanisms for water in highly polymerized melts where $X(T_2O_6)/(XTO_2)$ increases as a function of increasing water content of the melt.[4] If it is assumed that the relative changes of concentration of the structural units in the melt can be approximated with the relative changes of their activities (activity coefficient ratios are constant), the stability field of the most silica-rich mineral is reduced simply because $X(TO_2)/[X(TO_2) + X(T_2O_6)]$ has decreased.

The plagioclase stability field shrinks at the expense of pyroxene stability fields as H_2O is added to natural and synthetic andesite systems (*e.g.*, Kushiro, 1972; Eggler, 1972). These changes can also be directly related to the increased importance of T_2O_6 units in the melts with increasing water content.

Partial melts from hydrous peridotite in the upper mantle are more siliceous than those from anhydrous peridotite (*e.g.*, Kushiro *et al.*, 1972; Mysen and Boettcher, 1975). Carmichael *et al.* (1974) explained such observations by stating that the activity of silica in the hydrous partial melts is lower than in the anhydrous partial melts. The reason for this lowering of silica activity is the lowering of $X(TO_2)/[X(TO_2) + X(T_2O_6)]$ as water is added to the system.

Melt structure (bulk composition) affects crystal–liquid partition coefficients (Watson, 1976, 1977; Hart and Davis, 1978; Mysen *et al.*, 1979c). The most important feature of the melt structure affecting the partition coefficients is the ratio of nonbridging to bridging oxygen in the melt. The crystal–liquid partition coefficients of both transition metals and rare earth elements decrease with increasing NBO/T of the melt (Mysen *et al.*, 1979c). Solution of H_2O in highly polymerized melts (*e.g.*, basalt, andesite and granite) results in an increase of NBO/T. We suggest, therefore, that crystal–liquid partition coefficients will decrease with increasing water content. In melts with a large value of NBO/T (*e.g.*, picrite, komatiite, and basanite), it is likely that solution of H_2O results in decreased NBO/T. In such cases, the relevant crystal–liquid partition coefficients (*e.g.*, Ni between olivine and melt) will increase with increasing water content of the melt.

Iron is likely to play a similar role in silicate melts to aluminum (Seifert *et al.*, 1979). That is, in hydrous basaltic melts some ferric iron is a network modifier and some is a network former. The proportion of ferric iron in tetrahedral coordination will depend on the water content of the melt. The activity of ferric iron complexed in octahedral coordination in melts is greater than when ferric iron is in tetrahedral coordination (Seifert *et al.*, 1979; Mysen *et al.*, 1979b). Consequently, the stability fields of iron oxides on the liquidi of hydrous basalt differ from those of anhydrous basaltic melts not only because water affects the fugacity of hydrogen (*e.g.*, Osborn, 1959), but also because it affects the structural role of ferric iron in the melt.

Physical properties of silicate melts (*e.g.*, electrical conductivity and viscosity) depend on their water content (Lebedev and Khitarov, 1964; Shaw, 1963; Kushiro, 1978; Kushiro *et al.*, 1976). In anhydrous melts of basaltic and more acidic composition, NBO/T is less than 1 (Bottinga and Weill, 1972; Scarfe *et al.*, 1979; Mysen *et al.*, 1979a). In such melts, the flow units during viscous flow are SiO_2-rich, three-dimensional clusters (Mysen *et al.*, 1979a). The clusters are bonded with T–O bonds, where the T cation is tetrahedrally coordinated Al^{3+}, Ti^{4+}, and Fe^{3+}. The viscosity of such melts depends on the strength of the T–O bond (*e.g.*, Taylor and Rindone, 1970). In melts with NBO/T > 1, the flow units are isolated SiO_4 tetrahedra and modifying cations (*e.g.*, Bockris *et al.*, 1955). The viscosity of such melts depends on the number of oxygen bridges that must be broken to form the flow units. Furthermore, only a portion of the melt participates in the viscous flow at any given time. In this case, the viscosity of a melt with a sheet structure, for example, is greater than that of one

[4] The notations $X(TO_2)$, $X(T_2O_5)$ and $X(T_2O_6)$, respectively, denote proportions of melt units with a three-dimensional network, sheet, and chain structure. The T cation can be Si^{4+}, Ti^{4+}, P^{5+}, $(NaAl)^{4+}$, $(½CaAl)^{4+}$, and $(NaFe)^{4+}$.

with a chain structure, and so on. The viscosity of such melts is also lower than in melts with three-dimensional network structure because of the smaller size of the flow units. We suggest that viscous flow of hydrous basaltic and more silica-rich melts is controlled by the latter mechanism, whereas in the anhydrous equivalents the viscous flow is controlled by the former mechanism. Hence hydrous melts are more fluid than anhydrous, highly polymerized melts.

We may also speculate that because H_2O in effect increases NBO/T in less polymerized melts, the viscosity of melts of picrite, komatiite, and basanite composition may increase as a result of the dissolution of water.

Acknowledgments

Critical reviews by D. H. Eggler, E. Takahashi, W. B. White, and H. S. Yoder, Jr. are appreciated. Scarfe acknowledges support from the Carnegie Institution of Washington and Canadian NSERC grant A 8394. This research was partially supported by NSF grant EAR 7911313 and partially by the Carnegie Institution of Washington.

References

Adams, R. V. and R. W. Douglas (1959) Infrared studies on various samples of fused silica with special reference to the bands due to water. *J. Soc. Glass Technol., 42,* 147–158.

Bates, J. B., R. W. Hendricks and L. B. Shaffer (1974) Neutron irradiation effects and structure of non-crystalline SiO_2. *J. Chem. Phys., 61,* 4163–4176.

Bockris, J. O'M., J. D. MacKenzie and J. A. Kitchner (1955) Viscous flow in silica and binary liquid silicates. *Trans. Faraday Soc., 51,* 1734–1748.

Bottinga, Y. and D. F. Weill (1972) The viscosity of magmatic silicate liquids: a model for calculation. *Am. J. Sci., 272,* 438–475.

Boyd, F. R. and J. L. England (1960) Apparatus for phase equilibrium measurements at pressures up to 50 kilobars and temperatures up to 1750°C. *J. Geophys. Res., 65,* 741–749.

Brawer, S. A. and W. B. White (1975) Raman spectroscopic investigation of the structure of silicate glasses. I. The binary silicate glasses. *J. Chem. Phys., 63,* 2421–2432.

——— and ——— (1977) Raman spectroscopic investigation of the structure of silicate glasses. II. Soda–alkaline earth–alumina ternary and quaternary glasses. *J. Non-Cryst. Solids, 23,* 261–278.

Burnham, C. W. (1974) $NaAlSi_3O_8$–H_2O solutions: a thermodynamic model for hydrous magmas. *Bull. Soc. fr. Mineral. Cristallogr., 97,* 223–230.

——— (1975) Thermodynamics of melting in experimental silicate–volatile systems. *Geochim. Cosmochim. Acta, 39,* 1077–1084.

——— and N. F. Davis (1971) The role of H_2O in silicate melts. I. *P-V-T* relations in the system $NaAlSi_3O_8$–H_2O to 10 kilobars and 1000°C. *Am. J. Sci., 271,* 54–79.

——— and ——— (1974) The role of H_2O in silicate melts. II. Thermodynamic and phase relations in the system $NaAlSi_3O_8$–H_2O to 10 kilobars, 700° to 1100°C. *Am. J. Sci., 274,* 902–940.

——— and R. H. Jahns (1962) A method for determining the solubility of water in silicate melts. *Am. J. Sci., 260,* 721–745.

Carmichael, I. S. E., F. J. Turner and J. Verhoogen (1974) *Igneous Petrology.* McGraw-Hill, New York.

Drake, M. J. and J. R. Holloway (1977) Partitioning of samarium between plagioclase, clinopyroxene, amphibole and hydrous silicate liquid at high pressure: preliminary results. In *Papers Presented at the International Conference on Experimental Trace Element Geochemistry, Sedona, Arizona,* 21–23.

Eggler, D. H. (1972) Water-saturated and water-undersaturated melting relations in a Paricutin andesite and an estimate of water contents in natural magma. *Contrib. Mineral. Petrol., 34,* 261–271.

——— (1977) Calibration of a Pyrex solid-media assembly. *Carnegie Inst. Wash. Year Book, 76,* 656–658.

——— and M. Rosenhauer (1978) Carbon dioxide in silicate melts. II. Solubilities of CO_2 and H_2O in $CaMgSi_2O_6$ (diopside) liquids and vapors at pressures to 40 kb. *Am. J. Sci., 278,* 64–94.

Furukawa, T. and W. B. White (1980) Raman spectroscopic investigation of the structure of silicate melts. III. Alkali–silico–germanates. *J. Chem. Phys.,* in press.

Goranson, R. W. (1931) The solubility of water in granitic magmas. *Am. J. Sci., 22,* 481–502.

Hamilton, D. L., C. W. Burnham and E. F. Osborn (1964) The solubility of water and effects of oxygen fugacity and water content on crystallization in mafic magmas. *J. Petrol., 5,* 21–39.

Hart, S. R. and K. E. Davis (1978) Nickel partitioning between olivine and silicate melt. *Earth Planet. Sci. Lett., 40,* 203–220.

Hartwig, C. M. (1977) The radiation-induced formation of hydrogen and deuterium compounds in silica as observed by Raman scattering. *J. Chem. Phys., 66,* 227–239.

Hodges, F. N. (1974) The solubility of H_2O in silicate melts. *Carnegie Inst. Wash. Year Book, 73,* 251–255.

Kennedy, G. C., G. J. Wasserburg, H. C. Heard and R. C. Newton (1962) The upper three-phase region in the system SiO_2–H_2O. *Am. J. Sci., 260,* 501–521.

Kurkjian, C. R. and L. E. Russell (1957) The solubility of water in molten alkali silicates. *J. Soc. Glass Technol., 41,* 130–144.

Kushiro, I. (1969) The system forsterite–diopside–silica with and without water at high pressures. *Am. J. Sci., 267A,* 269–294.

——— (1972) Effect of water on the composition of magmas formed at high pressures. *J. Petrol., 13,* 311–334.

——— (1978) Density and viscosity of hydrous calc-alkalic andesite magma at high pressure. *Carnegie Inst. Wash. Year Book, 77,* 675–678.

———, H. S. Yoder, Jr. and B. O. Mysen (1976) Viscosities of basalt and andesite melts at high pressures. *J. Geophys. Res., 81,* 6351–6356.

———, ——— and M. Nishikawa (1968) Effect of water on the melting of enstatite. *Geol. Soc. Am. Bull., 79,* 1685–1692.

———, N. Shimizu, Y. Nakamura and S. Akimoto (1972) Composition of coexisting liquid and solid phases formed upon melting of natural garnet and spinel lherzolites at high pressures: a preliminary report. *Earth Planet. Sci. Lett., 14,* 19–25.

Lebedev, E. E. and N. I. Khitarov (1964) The dependence of electrical conductivity of granite melt and the beginning of granite melting on high pressures of water. [in Russian] *Geokhimiya, 3,* 195–201.

Lucovsky, G. (1979) Chemical effects on the frequencies of Si–H vibrations in amorphous solids. *Solid State Commun., 29,* 571–576.

———, R. J. Nemanich and J. C. Knights (1979) Structural inter-

pretation of the vibrational spectra of α-Si:H alloys. *Phys. Rev. B, 19,* 2064–2073.

Mao, H. K., P. M. Bell and J. L. England (1971) Tensional errors and drift of thermocouple electromotive force in the single-stage, piston–cylinder apparatus. *Carnegie Inst. Wash. Year Book, 70,* 281–287.

Mysen, B. O. and A. L. Boettcher (1975) Melting of a hydrous mantle. II. Geochemistry of crystals and liquids formed by anatexis of mantle peridotite at high pressures and high temperatures as a function of controlled activities of water, hydrogen and carbon dioxide. *J. Petrol., 16,* 549–590.

———, D. Virgo and C. M. Scarfe (1980) Relations between the anionic structure and viscosity of silicate melts: a Raman spectroscopic study at 1 atmosphere and at high pressure. *Am. Mineral., 65,* 690–710.

———, ——— and F. Seifert (1979a) Melt structures and redox equilibria in the system CaO–MgO–FeO–Fe_2O_3–SiO_2. *Carnegie Inst. Wash. Year Book, 78,* 519–526.

———, ——— and ——— (1979b) Influence of melt structure on element partitioning between olivine and melt and between clinopyroxene and melt at 1 atm. *Carnegie Inst. Wash. Year Book, 78,* 542–547.

Nakamoto, K. (1978) *Infrared and Raman Spectra of Inorganic and Coordination Compounds,* 3d ed. Wiley, New York.

Orlova, G. P. (1964) The solubility of water in albite melts. *Int. Geol. Rev., 6,* 254–258.

Osborn, E. F. (1959) The role of oxygen pressure in the crystallization and differentiation of basaltic magma. *Am. J. Sci., 257,* 609–647.

Peri, J. B. (1966) Infrared study of OH and NH_2 groups on the surface of dry silica aerogel. *J. Phys. Chem., 70,* 2937–2945.

Ryskin, Ya. I. (1974) The vibrations of protons in minerals: hydroxyl, water and ammonium. In V. C. Farmer, Ed., *The Infrared Spectra of Minerals,* p. 137–183. Mineralogical Society, London.

Scarfe, C. M., B. O. Mysen and D. Virgo (1979) Changes in viscosity and density of melts of sodium disilicate, sodium metasilicate and diopside composition with pressure. *Carnegie Inst. Wash. Year Book, 78,* 547–551.

Seifert, F., D. Virgo and B. O. Mysen (1979) Melt structures and redox equilibria in the system Na_2O–FeO–Fe_2O_3–Al_2O_3–SiO_2. *Carnegie Inst. Wash. Year Book, 78,* 511–519.

Serna, C. J., B. D. Velde and J. L. White (1977) Infrared evidence of order–disorder in amesites. *Am. Mineral., 62,* 296–303.

———, J. L. White and B. D. Velde (1979) The effect of aluminum on the infrared spectra of trioctahedral minerals. *Mineral. Mag., 43,* 141–148.

Serratosa, J. M. and J. M. Vinas (1964) Infrared investigations of the OH-band in chlorites. *Nature, 202,* 999.

Sharma, S. K., D. Virgo and B. O. Mysen (1978) Structure of glasses and melts of $Na_2O \cdot xSiO_2$ (x = 1, 2, 3) composition from Raman spectroscopy. *Carnegie Inst. Wash. Year Book, 77,* 649–652.

Shaw, H. R. (1963) Obsidian–H_2O viscosities at 1000 and 2000 bars in the temperature range 700° to 900°C. *J. Geophys. Res., 68,* 6337–6343.

Stolen, R. H. and G. E. Walrafen (1976) Water and its relation to broken bond defects in fused silica. *J. Chem. Phys., 64,* 2623–2631.

Tarte, P. (1967) Infrared spectra of inorganic aluminates and characteristic vibrational frequencies of AlO_4 tetrahedra and AlO_6 octahedra. *Spectrochim. Acta, 23A,* 2127–2143.

Taylor, M. and G. E. Brown (1979) Structure of mineral glasses. I. The feldspar glasses $NaAlSi_3O_8$, $KAlSi_3O_8$, $CaAl_2Si_2O_8$. *Geochim. Cosmochim. Acta, 43,* 61–77.

Taylor, T. D. and G. E. Rindone (1970) Properties of soda aluminosilicate glasses. V. Low-temperature viscosities. *J. Am. Ceram. Soc., 53,* 692–695.

Uys, J. M. and T. B. King (1963) The effect of basicity on the solubility of water in silicate melts. *Trans. Metall. Soc. AIME, 227,* 492–500.

Van der Steen, G. H. A. M. and H. Van den Boom (1977) Raman study of hydrogen-containing vitreous silica. *J. Non-Cryst. Solids, 23,* 279–286.

Velde, B. D. and I. Kushiro (1976) Infrared spectra of high-pressure quenched silicate liquids. *Carnegie Inst. Wash. Year Book, 75,* 618–621.

Virgo, D., B. O. Mysen and F. Seifert (1979a) Structures of quenched melts in the system $NaAlSiO_4$–$CaMgSi_2O_6$–Mg_2SiO_4–SiO_2 at 1 atm. *Carnegie Inst. Wash. Year Book, 78,* 502–506.

———, F. Seifert and B. O. Mysen (1979b) Three-dimensional network structures of glasses in the systems $CaAl_2O_4$–SiO_2, $NaAlO_2$–SiO_2, $NaFeO_2$–SiO_2, and $NaGaO_2$–SiO_2 at 1 atm. *Carnegie Inst. Wash. Year Book, 78,* 506–511.

Wasserburg, G. J. (1957) The effects of H_2O in silicate systems. *J. Geol., 65,* 15–23.

Watson, E. B. (1976) Two-liquid partition coefficients: experimental data and geochemical implications. *Contrib. Mineral. Petrol., 56,* 119–134.

——— (1977) Partitioning of manganese between forsterite and silicate liquid. *Geochim. Cosmochim. Acta, 41,* 1363–1374.

Yoder, H. S., Jr. (1969) Calc-alkalic andesites: experimental data bearing on the origin of their assumed characteristics. In A. R. McBirney, Ed., *Proceedings of the Andesite Conference, Oreg. Dep. Geol. Miner. Ind. Bull., 65,* 77–89.

——— (1973) Contemporaneous basaltic and rhyolitic magmas. *Am. Mineral., 58,* 153–171.

Manuscript received, October 9, 1979;
accepted for publication, May 28, 1980.

American Mineralogist, Volume 65, pages 915–919, 1980

Experimental evidence at high pressure for potassic metasomatism in the mantle of the Earth[1]

I. D. RYABCHIKOV

Institute of Geology of Ore Deposits
35 Staromonetny
Moscow, 109017, U.S.S.R.

AND A. L. BOETTCHER

Institute of Geophysics and Planetary Physics
and Department of Earth and Space Sciences
University of California, Los Angeles
Los Angeles, California 90024

Abstract

To assess the concentration of potassium in aqueous fluids as a model for metasomatism of the mantle of the Earth, we experimentally determined the solubility of potassium in an aqueous vapor in equilibrium with phlogopite and other phases to pressures of 30 kbar at 1100°C. The concentration of potassium (in grams of K_2O per 100 g H_2O) is 4 at 11 kbar, 7 at 20 kbar, and 25 at 30 kbar. Such values are sufficient to transfer from the interior of the Earth all of the K_2O to the continental crust during formation of the hydrosphere by outgassing. However, it is likely that most of this transport was by silicate-rich liquids.

Introduction

A number of investigators have suggested that primary alkaline magmas and particularly highly potassic melts are formed by partial melting of mantle material that was previously enriched in potassium and other components by precursory metasomatic processes (Sobolev, 1977; Ryabchikov and Green, 1979; Lloyd and Bailey, 1975; Boettcher and O'Neil, 1980). The present work was designed to provide a quantitative check on the possibility of such processes by experimentally measuring K_2O concentrations in aqueous vapors in equilibrium with phlogopite-bearing mineral assemblages typical of the mantle at high pressures and temperatures.

Earlier studies (Wendlandt, 1977; Yoder and Kushiro, 1969) revealed that subsolidus experiments at 20 kbar for the composition joins phlogopite–H_2O and phlogopite–H_2O–CO_2 quenched to an assemblage containing phlogopite plus forsterite. This demonstrates that incongruent solubility of phlogopite in an aqueous vapor under these conditions is significant and that K_2O and Al_2O_3 dissolve in the vapor in excess of that in phlogopite composition. In this work we extended the investigation of phlogopite-containing joins to higher H_2O concentrations and determined the H_2O contents at various pressures where phlogopite became unstable, dissolving entirely in the vapor, enabling us to determine K_2O contents of fluids in equilibrium with phlogopite, olivine, and some other phases typical of mantle assemblages.

Experimental procedures

Starting materials

A mixture of oxides of anhydrous phlogopite composition was prepared by sintering and partial melting at about 1100°C. Fired gels of pyrope and forsterite compositions were added to anhydrous phlogopite powder for some of our experiments.

Experiments were performed in sealed platinum capsules on mixtures of known proportions of silicate components and water.

[1] Institute of Geophysics and Planetary Physics Contribution No. 1916.

0003–004X/80/0910–0915$02.00

Apparatus

All the experiments were in piston–cylinder apparatus similar to that described by Boyd and England (1960). The experimental method was described earlier (Allen and Boettcher, 1978).

Identification

After sealing, the capsules were folded in such a way that the starting mixtures were contained in one half of each of the capsules. During the run, however, the second half of each capsule was filled with vapor phase, which precipitated quench material during fast isobaric cooling at the end of an experiment (see Fig. 1). Comparison of the material from both halves of the capsules was very useful for the distinction of primary and quench phlogopite crystals.

The nature of quench material changed considerably with pressure. Between 10 and 14 kbar, it was mainly an amorphous, glass-like phase forming spheres, rods, and coatings on primary crystals (Fig. 2). At these pressures, quench phlogopite occurred in minor amounts as small (<5 μm), thin flakes.

At 20 kbar the proportion of quench phlogopite was noticeably greater, forming large (>20 μm), thin plates with uneven extinction and some skeletal morphology. The spheres of amorphous material were typically situated along the growth figures of quench phlogopite. At 30 kbar, large (700 μm), euhedral (but thin) phlogopite plates were part of the quench material and were overgrown by irregular aggregates of phlogopite and amorphous material (Fig. 2). Primary phlogopites at all pressures were euhedral, relatively thick crystals (Fig. 3).

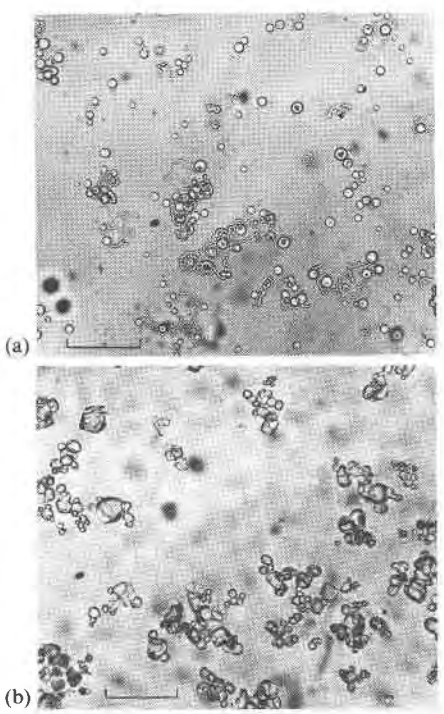

Fig. 1. Photomicrographs of products of run 33; (a) quench vapor in folded part of capsule, (b) forsterite + quench vapor in main part of capsule. Bars are 100 μm.

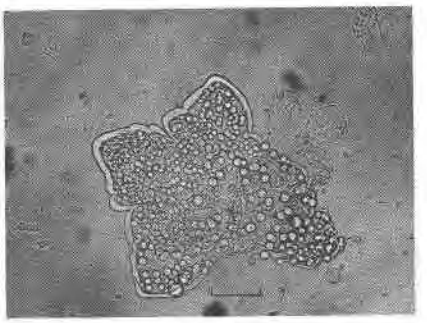

Fig. 2. Photomicrograph of quench vapor in products of run 26. Bar is 100 μm.

Olivines occurred in all our run products. They were typically euhedral, tabular grains whose average size increased with increasing pressure, ranging from 10 μm at 10 kbar to 500×150 μm at 30 kbar. Some olivines contained fluid inclusions.

The run products for the join phlogopite–pyrope–water contained orthopyroxene and spinel in addition to phlogopite and olivine.

Experimental results

The results of our experiments are summarized in Table 1. Their interpretation is based on the following reasoning. In the runs in which the products did not include primary phlogopite, all the K_2O was incorporated into the fluid phase, inasmuch as the co-

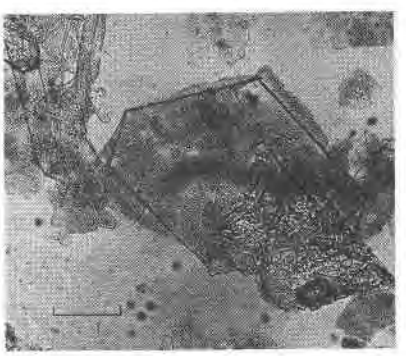

Fig. 3. Photomicrograph of thin plates of quench phlogopite and other quench products in run 24. Bar is 200 μm.

Table 1. Experimental data

Run	Pres (kbars)	Temp (°C)	Bulk composition	g K_2O / 100 g H_2O	Time (hrs)	Run products
32	10	1100	$Aph_{17}Fo_{35}W_{48}$	4.2	9	Fo+Ph+Q
33	12	1100	$Aph_{18}Fo_{36}W_{46}$	4.7	11.5	Fo+Q
30	14	1100	$Aph_{17}Fo_{35}W_{48}$	4.3	9	Fo+Q
23	20	1100	$Aph_{33}W_{67}$	5.8	13	Fo+Q
26	20	1100	$Aph_{37}W_{63}$	7.0	9	Fo+(Ph)+Q
3	20	1100	$Aph_{42}W_{58}$	8.7	8	Fo+Ph+Q
14	20	1100	$Aph_{42}W_{55}$	9.6	10	Fo+Ph+Q
11	20	1100	$Aph_{76}W_{24}$	36.6	8	Fo+Ph+Q
22	20	1050	$Aph_{10}Py_{40}W_{50}$	2.2	9	Opx+Sp+Q
25	20	1050	$Aph_{20}Py_{30}W_{50}$	4.8	11	Fo+Opx+Sp+Q
29	20	1050	$Aph_{24}Py_{24}W_{52}$	5.6	12	Fo+Opx+Sp+Q
27	20	1050	$Aph_{30}Py_{20}W_{50}$	7.2	12	Fo+(Opx)+Sp+Ph+Q
21	30	1100	$Aph_{47}W_{53}$	10.3	12	Fo+Q
19	30	1100	$Aph_{54}W_{46}$	13.8	8	Fo+Q
24	30	1100	$Aph_{57}W_{43}$	15.8	8.5	Fo+Q
31	30	1100	$Aph_{65}W_{35}$	21.9	10	Fo+Q
37	30	1100	$Aph_{71}W_{29}$	28	8.5	Fo+Ph+Q

Abbreviations: Aph is anhydrous phlogopite composition ($KMg_3AlSi_3O_{11}$); Fo is forsterite (Mg_2SiO_4); W is water (H_2O); Py is pyrope composition ($Mg_3Al_2Si_3O_{12}$); Ph is phlogopite; Opx is orthopyroxene; Sp is spinel; Q is quench material (amorphous substance and quench mica); parentheses indicate minor amount.

existing crystalline phases (olivine or olivine + orthopyroxene + spinel) contain only negligible amounts of this element. Interpolating between the compositions of two adjacent runs with and without primary phlogopite, we deduce the K_2O/H_2O ratio in the fluid coexisting with the traces of phlogopite in addition to forsterite or forsterite + orthopyroxene + spinel. In this manner, we estimated the values of K_2O concentrations (in grams of K_2O per 100 g of H_2O) in equilibrium with assemblages containing phlogopite and forsterite in 1100°C to be as follows: 4 at 11 kbar, 7 at 20 kbar, and 25 at 30 kbar.

The run products for the join phlogopite–pyrope–water at 20 kbar and 1100°C were buffered with respect to the chemical potential of SiO_2 (μ_{SiO_2}) by the presence of both forsterite and orthopyroxene and with respect to $\mu_{Al_2O_3}$ by olivine, orthopyroxene, and spinel. These compositions are more nearly representative of the chemistry of mantle material than are the joins phlogopite–water and phlogopite–forsterite–water. The concentration of K_2O in the vapor in equilibrium with phlogopite, forsterite, orthopyroxene, and spinel at 1050°C and 20 kbar was estimated from these experiments as 6 g K_2O per 100 g H_2O, only slightly lower than that for phlogopite + forsterite phase assemblages at the same pressure but at 1100°C.

Thus our experimental data permit us to evaluate K_2O/H_2O ratios in aqueous fluids. The same reasoning is also applicable to Al_2O_3 concentrations, inasmuch as this component also occurs in olivines only in trace amounts. It is also clear that the K_2O/Al_2O_3 ratios of our solutions were always close to unity (the same as in phlogopite). Unfortunately, it is not possible to estimate MgO and SiO_2 concentrations in aqueous solutions from our experimental data alone. However, from the results of Modreski and Boettcher (1973), who analyzed quenched vapor in equilibrium with forsterite, enstatite, and phlogopite at 1050°C and 10 kbar, we conclude that the MgO content of aqueous fluid at these conditions is negligible. Therefore, it is rather safe to assume that concentrations of magnesium in the fluid in our runs at 1100°C and 11 kbar are also very low, because the pressure–temperature conditions of these runs and those of Modreski and Boettcher (1973) are similar. From this we estimate the K_2O (3.4 wt%), Al_2O_3 (3.7 wt%), and SiO_2 (6.6 wt%) concentrations in the aqueous phase in equilibrium with forsterite and phlogopite at 1100°C and 11 kbar, with the total content of dissolved oxides being approximately 14 wt%. At higher pressures MgO concentrations in fluids coexisting with phlogopite-containing phase assemblages must be substantial, judging from the increasing amount of quench phlogopite.

Eggler and Rosenhauer (1978) determined the solubility of diopside in an aqueous fluid at 20 and 30 kbar and approximately 1200°C to be approximately 10 wt%, which corresponds to about 2.5 wt% of MgO in solution. We assume that in our experiments at the same pressures the MgO content of fluid was the same or higher because the chemical potential of MgO for a forsterite-containing phase assemblage must be higher than in the presence of diopside alone. Assuming 2.5 wt% as a minimum value, we estimate the concentrations of other components, and the results of these calculations show that the total

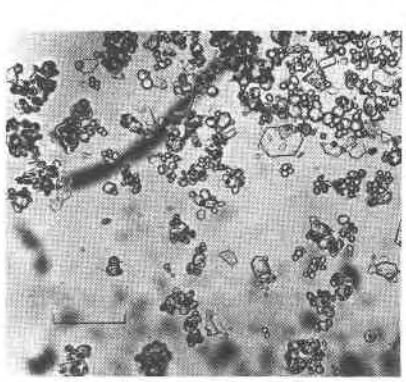

Fig. 4. Photomicrograph of primary phlogopite and forsterite in the products of run 32. Bar is 100 μm.

contents of dissolved silicate components in aqueous fluids in equilibrium with phlogopite and forsterite at 1100°C and pressures of 20 and 30 kbar are about 25 wt% and 50 wt%, respectively. It is clear that at 30 kbar fluids in equilibrium with phlogopite-containing phase assemblages are near critical conditions.

Table 2 illustrates that the proportion of solute in the vapor is a function of pressure, ranging from about 14 wt% at 11 kbar to about 55 wt% at 30 kbar. At 30 kbar, our vapors contain approximately 25 wt% dissolved solids. This is about twice the value for the solubility of diopside in a vapor containing 95 wt% H_2O and 5 wt% CO_2, determined by Eggler (1975). Experiments by Nakamura and Kushiro (1974) at 15 kbar reveal that aqueous vapor coexisting with forsterite and enstatite dissolves about 18 wt% SiO_2 at 1280°C and 22 wt% SiO_2 at 1310°C; the vapor coexisting with only enstatite contains up to 40 wt% SiO_2 at 1280°C and 15 kbar.

Petrological applications

Our experimental data were obtained for compositions with H_2O as the only volatile component. However, vapors in the mantle contain other volatile species, and experiments have shown that addition of components such as CO_2 and H_2 that lower the fugacity of H_2O will reduce the solubility of silicates in an aqueous vapor (for example, Shettel, 1973; Nakamura, 1974). Comparison of P–T coordinates for continental shield geotherms with the positions of vapor-phase isopleths for divariant assemblages corresponding to the following reactions (in the presence of H_2O and CO_2) shows that under these conditions H_2O/CO_2 values in vapors are high, particularly at depths below those of the stability of amphibole:

$$2Fo + Di + 2CO_2 = Do + 4En;$$
$$Fo + CO_2 = Mc + En$$

(Newton and Sharp, 1975; Eggler, 1977; Wyllie, 1979)

Our results show that under these conditions fluids may be very efficient agents for transporting K_2O. For example, temperatures of about 1050°C are reached under continental shields at depths of about 130 km corresponding to pressures of 40 kbar, from the geotherm of Clark and Ringwood (1964). Extrapolation of our results to 1050°C and 40 kbar clearly shows that the vapors in equilibrium with phlogopite would contain in excess of 30 g K_2O per 100 g of H_2O. If we accept 10 g K_2O/100 g H_2O as a conservative estimate, and if we assume that all the water in the present hydrosphere was transferred from the deep levels of the mantle of the Earth, then vapor could have transported $1.4 \cdot 10^{23}$ g of K_2O, which is approximately the amount in the continental crust. However, the shield geotherm intersects the peridotite–H_2O solidus at about 100 km, and it is more likely that much of the K_2O was transported in a silicate liquid.

It may be noted that the high mobility of K_2O-rich fluids under conditions of continental shield geotherms is consistent with the fact that only on continents do we find evidence for enrichment of mantle-derived magmatic rocks that commonly bring to the surface xenoliths of phlogopite-bearing ultramafic rocks. Under the higher temperature conditions of the deep oceanic lithosphere, vapor may have a higher value of CO_2/H_2O if carbonates are unstable (Eggler, 1978). Mysen *et al.* (1978) have experimentally investigated the mobility of H_2O in peridotite under mantle conditions. These preliminary results do suggest that the rate of migration of H_2O-rich fluids is sufficiently rapid to permit mobilization of K_2O and other components. However, high mobility of K_2O in aqueous fluids is necessary but not sufficient for intensive mantle metasomatism. There must also exist certain mechanisms for fixation of dissolved K_2O. One obvious method to precipitate K_2O is to decrease the pressure and temperature of the ascending vapor. The change in the CO_2/H_2O ratio of the vapor during ascent (Wyllie, 1979) would also affect the solubility of K_2O and other solutes. Crystallization of amphiboles at depths of about 60 km would certainly increase CO_2/H_2O, and the K_2O, Al_2O_3, and other components previously dissolved in the fluid would take part in metasomatic reactions.

Some K_2O is fixed in the upper levels of the mantle at depths of about 50 km, as evidenced by metasomatism of lherzolite xenoliths in alkali basalts (Boettcher and O'Neil, 1980; Stewart and Boettcher, 1977; Wilshire *et al.*, 1980). However, the abundance of phlogopite in kimberlites and in xenoliths in kimberlites suggests that considerable amounts of K_2O reside at depths greater than 50 km.

Acknowledgments

This research was supported by NSF grant EAR78-16413 to ALB. Chris West and Dave Klimberg provided valuable technical assistance in the laboratory; Harriett Arnoff typed the manuscript. The reviews by D. H. Eggler and B. O. Mysen are appreciated.

References

Allen, J. C. and A. L. Boettcher (1978) Amphiboles in andesites and basalt: II. Stability as a function of P–T–f_{H_2O}–f_{O_2}. *Am. Mineral., 63,* 1074–1087.

Boettcher, A. L. and J. R. O'Neil (1980) Stable isotope, chemical, and petrographic studies of high-pressure amphiboles and micas: evidence for metasomatism in the mantle source regions of alkali basalts and kimberlites. *Am. J. Sci.*, in press.

Boyd, F. R. and J. L. England (1960) Apparatus for phase-equilibrium measurements at pressures up to 50 kilobars and temperatures up to 1750°C. *J. Geophys. Res., 65,* 741–748.

Clark, S. P. and A. E. Ringwood (1964) Density distribution and constitution of the mantle. *Rev. Geophys., 2,* 35–88.

Eggler, D. H. (1975) CO_2 as a volatile component of the mantle: the system Mg_2SiO_4–SiO_2–H_2O–CO_2. In L. H. Ahrens *et al.*, Eds., *Physics and Chemistry of the Earth, 9,* p. 869–881. Pergamon Press, New York.

——— (1977) The principle of the zone of invariant vapor composition: an example in the system CaO–MgO–SiO_2–CO_2–H_2O and implications for the mantle-solidus. *Carnegie Inst. Wash. Year Book, 76,* 428–435.

——— (1978) Stability of dolomite in a hydrous mantle, with implications for the mantle solidus. *Geology, 6,* 397–400.

——— and M. Rosenhauer (1978) Carbon dioxide in silicate melts: II. Solubilities of CO_2 and H_2O in $CaMgSi_2O_6$ (diopside) liquids and vapors at pressures to 40 kb. *Am. J. Sci., 278,* 64–94.

Lloyd, F. E. and D. K. Bailey (1975) Light element metasomatism of the continental mantle: the evidence and the consequences. In L. H. Ahrens *et al.*, Eds., *Physics and Chemistry of the Earth,* 9, p. 389–416. Pergamon Press, New York.

Modreski, P. J. and A. L. Boettcher (1973) Phase relationships of phlogopite in the system K_2O–MgO–CaO–Al_2O_3–SiO_2–H_2O to 35 kilobars: a better model for micas in the interior of the Earth. *Am. J. Sci., 273,* 385–414.

Mysen, B. O., I. Kushiro and T. Fujii (1978) Preliminary experimental data bearing on the mobility of H_2O in crystalline upper mantle. *Carnegie Inst. Wash. Year Book, 77,* 793–797.

Nakamura, Y. (1974) The system SiO_2–H_2O–H_2 at 15 kbar. *Carnegie Inst. Wash. Year Book, 73,* 259–263.

——— and I. Kushiro (1974) Composition of the gas phase in Mg_2SiO_4–SiO_2–H_2O at 15 kbar. *Carnegie Inst. Wash. Year Book, 73,* 255–258.

Newton, R. C. and W. E. Sharp (1975) Stability of forsterite + CO_2 and its bearing on the role of CO_2 in the mantle. *Earth Planet. Sci. Lett., 26,* 239–243.

Ryabchikov, I. D. and D. H. Green (1979) A study of the origin of potassic magmas. *Contrib. Mineral. Petrol.*, in press.

Shettel, D. L. (1973) Solubility of quartz in H_2O–CO_2 fluids at 5 kb and 500°–900°C. *EOS, 54,* 480.

Sobolev, N. V. (1977) Deep-seated inclusions in kimberlites and the problem of the composition of the upper mantle. *Am. Geophys. Union,* Washington, D. C.

Stewart, D. C. and A. L. Boettcher (1977) Chemical gradients in mantle xenoliths (abstr.). *Geol. Soc. Am. Abstracts with Programs, 9,* 1191–1192.

Wendlandt, R. F. (1977) The system K_2O–MgO–Al_2O_3–SiO_2–H_2O–CO_2: stability of phlogopite as a function of vapor composition and high pressures and temperatures. *Carnegie Inst. Wash. Year Book, 76,* 441–448.

Wilshire, H. G., J. E. N. Pike, C. E. Meyer and E. C. Schwarzman (1980) Kaersutite veins in lherzolite xenoliths, Dish Hill and Deadman Lake, California. *Am. J. Sci.*, in press.

Wyllie, P. J. (1979) Magmas and volatile components. *Am. Mineral., 64,* 469–500.

Yoder, H. S., Jr. and I. Kushiro (1969) Melting of a hydrous phase: phlogopite. *Am. J. Sci., 267-A,* 558–582.

Manuscript received, June 26, 1979;
accepted for publication, March 3, 1980.

American Mineralogist, Volume 65, pages 920–930, 1980

Structure and elastic properties of quartz at pressure

LOUISE LEVIEN[1], CHARLES T. PREWITT AND DONALD J. WEIDNER

Department of Earth and Space Sciences
State University of New York
Stony Brook, New York 11794

Abstract

Unit cells and crystal structures were determined on a single crystal of quartz at seven pressures from 1 atm to 61.4 kbar. Unit-cell parameters are $a = 4.916(1)$ and $c = 5.4054(4)$Å at 1 atm, and $a = 4.7022(3)$ and $c = 5.2561(2)$Å at 61.4 kbar. Structural changes observed over this pressure range include a decrease in the Si–O–Si angle from 143.73(7)° to 134.2(1)°, a decrease in the average Si–O bond distance from 1.6092(7) to 1.605(1)Å, and an increase in distortion of the silicate tetrahedron. Several O–O distances show very large changes (11%) that can be related to the unit-cell-edge compression. As pressure is increased, the geometry of the SiO_2 (quartz) structure approaches that of the low-pressure GeO_2 (quartz) structure.

The structural changes that take place with increased temperature are not the inverses of those that occur with increased pressure; changes in the Si–O–Si angle and the tetrahedral tilt angle control thermal expansion, whereas smaller changes in the Si–O–Si angle and tetrahedral distortion control isothermal compression.

By constraining the zero-pressure bulk modulus to be equal to that calculated from acoustic data [$K_T = 0.371(2)$ Mbar], the pressure derivative of the bulk modulus at zero pressure [$K'_T = 6.2(1)$] has been calculated by fitting the P–V data to a Birch-Murnaghan equation of state. The anomalously low value of Poisson's ratio in quartz can be explained by the low ratio of the off-diagonal shear moduli to the pure-shear moduli. This small ratio reflects the easily expanding or contracting spirals of tetrahedra that behave like coiled springs.

Introduction

The literature on the crystal structure and compressibility of quartz leaves many questions about its changes with pressure. As high-pressure structural refinements have not been as precise as those performed under ambient conditions, these studies report large changes (*e.g.,* the Si–O–Si interbond angle); however, subtle ones have not been previously resolvable. Recent experimental developments in our laboratory offer the potential of providing improved resolution in high-pressure structural data.

The crystal structure of quartz at room temperature and pressure has been refined many times (Young and Post, 1962; Smith and Alexander, 1963; Zachariasen and Plettinger, 1965; Le Page and Donnay, 1976; Jorgensen, 1978; d'Amour *et al.,* 1979), with the Young and Post and the Smith and Alexander papers reporting the first quality refinements of positional parameters and thermal ellipsoids. Zachariasen and Plettinger improved upon these studies by applying a secondary-extinction correction to their refinement. The Le Page and Donnay refinement again improved the R value; however, no corrections for crystal X-ray absorption or extinction were made. Both Jorgensen and d'Amour *et al.* collected intensity data for room-pressure structural refinements with crystals already loaded in high-pressure cells; these refinements are of lower precision than the others.

Static-compressibility studies on quartz were first carried out by Adams and Williamson (1923) and Bridgman (1925; 1928), and then greatly improved by Bridgman (1948a,b; 1949) and others (McWhan, 1967; Vaidya *et al.,* 1973; Olinger and Halleck, 1976; Jorgensen, 1978; d'Amour *et al.,* 1979). McWhan measured the compression of quartz in a modified Bridgman-anvil apparatus with Guinier geometry

[1] Present address: Division of Geological and Planetary Sciences, California Institute of Technology, Pasadena, California 91125.

0003–004X/80/0910–0920$02.00

X-ray cameras, using NaCl as both a pressure-transmitting medium and a calibration standard. The experiments were carried out to 150 kbar and no evidence of a phase transition was seen, despite the fact that the sample had been subjected to pressures higher than required to transform quartz to coesite and stishovite at high temperature. The Vaidya *et al.* compressibility data were collected in a piston–cylinder apparatus with indium, a low shear-strength metal, as the pressure-transmitting medium. Displacement of a piston was measured to determine the volume change; therefore, the data at low pressures, where voids are being closed, are not as accurate as the higher-pressure data. The Olinger and Halleck study was performed in a modified Bridgman-anvil apparatus, using a 4:1 methanol:ethanol mixture as the hydrostatic pressure-transmitting fluid. Jorgensen collected hydrostatic high-pressure neutron-diffraction data on a powdered sample, determining changes in both unit cell and crystal structure. The d'Amour *et al.* work, the only previous compressional study of quartz using single-crystal X-ray techniques, also gave unit-cell parameters and structural data.

Experimental techniques

A clear crystal of natural quartz was broken, and a platy fragment (70 μm × 50 μm × 30 μm) used for this study, with c approximately normal to the plane of the plate. Although precession and Weissenberg X-ray photographs showed the crystal to be of high quality, intensity data were collected on the crystal before it was loaded into the diamond cell. The refinement of these data were used both for comparison purposes and to check for Dauphiné twinning, which cannot be distinguished easily with film techniques because it is only recognizable as increased or decreased intensity of a certain class of reflections (Young and Post, 1962). We refined the structure both with the entire set of structure factors and with the structure factors not affected by Dauphiné twinning (*hhl* and *hk*0). Having found essentially identical refinements for these two sets of data, we decided not to make a correction for Dauphiné twinning of the sample. Room-pressure and 31-kbar data were collected with Ag$K\alpha$ radiation, which has two potential advantages over Mo$K\alpha$ radiation for diamond-cell work: its shorter wavelength makes more of the reciprocal lattice accessible, and its linear-absorption coefficients are smaller than those for Mo$K\alpha$. However, the lower intensity of the incident Ag$K\alpha$ radiation and the poorer counting efficiency of the scintillation detector more than offset the above advantages and make Ag$K\alpha$ less desirable. The refinement of the 31-kbar structure, collected with Ag$K\alpha$ radiation, resulted in R values three times those of the Mo$K\alpha$ data sets and has therefore been omitted from this report.

The quartz crystal was mounted in a Merrill-Bassett design single-crystal diamond-anvil cell (Merrill and Bassett, 1974). The diamonds (1/8 carat each) had 0.65 mm faces (culet), and the gasketing material [250 μm thick Inconel X750 (spring)] had a 300 μm hole. The crystal was attached to one diamond face with the alcohol-insoluble fraction of petroleum jelly, and a 4:1 methanol:ethanol mixture was used as the pressure-transmitting medium (Finger and King, 1978; Piermarini *et al.*, 1973). A small ruby crystal (10 μm; 0.5 wt.% Cr) (Piermarini *et al.*, 1975) in the cell was used for pressure calibration, which was performed both before and after X-ray data were collected. The pressure-calibration system, based on the shift of the fluorescence spectrum of ruby, is similar to that described by Barnett *et al.* (1973) but modified by King (1979). The diamond cell was then mounted on a specially designed goniometer head (Hazen and Finger, 1977; Finger and King, 1978), which was in turn mounted on a four-circle X-ray diffractometer. Both before and after intensity data were collected at each pressure, unit-cell parameters were determined, using King and Finger's (1979) method of avoiding systematic errors resulting from an uncentered crystal.

With the exception of the room-pressure determination, an entire sphere of integrated intensities in reciprocal space ($2° < 2\theta < 90°$) was collected with crystal-monochromatized Mo$K\alpha$ radiation; a hemisphere of intensities ($2° < 2\theta < 45°$) (Ag$K\alpha$) was collected on the crystal at room pressure. Intensities were measured using a quasi-constant-precision counting scheme with reflections less than $2\sigma_I$ considered unobserved; σ_F's were calculated by adding to the constant-precision value an additional factor that reflects the fluctuation of the incident beam (Baldwin and Prewitt, in preparation). Structure factors were corrected for X-ray absorption of the diamond cell (Finger and King, 1978) and crystal X-ray absorption. Several reflections with exceptionally high or asymmetrical background counts were rejected from each of the high-pressure data sets because of overlap with diamond reflections. None of the reflections with 2θ values near or on the 2θ values of beryllium metal were collected. Symmetrically equivalent reflections were averaged, yielding between 198 and

Table 1. Intensity information for quartz at six pressures

	Total # data	# after av.*	$\#>2\sigma_I$**	wR	R	Ext.x10^{-4}***	$\delta^\dagger$
1 atm	663	210	194	0.019	0.016	0.11(1)	-16.37
20.7(5)†† kbar	390	198	170	0.029	0.029	0.32(4)	-19.54
37.6(5) kbar	438	215	190	0.031	0.032	0.34(4)	-21.58
48.6(5) kbar	440	217	196	0.032	0.034	0.37(4)	-22.46
55.8(5) kbar	432	214	200	0.028	0.026	0.34(3)	-23.05
61.4(5) kbar	426	215	191	0.031	0.034	0.23(3)	-23.47

*Number of data after symmetrically equivalent reflections were averaged.
**Number of data accepted in the refinement. All were greater than $2\sigma_I$.
***Refined secondary extinction parameters.
†The tetrahedral tilt parameter from Grimm and Dorner (1975).
††Parenthesized figures represent esd's of least units cited.

218 independent reflections at each pressure. Anisotropic refinements of the structure were executed using the least-squares program RFINE4 with a $1/\sigma^2$ weighting scheme (Finger and Prince, 1975). In the high-pressure data sets, all observed reflections were accepted; two reflections were rejected from the room-pressure refinement. The final weighted R values range from 0.019 to 0.032 (Table 1). Observed and calculated structure factors are listed in Table 2[2]; positional parameters and temperature factors are reported in Table 3; interatomic distances and angles are given in Table 4; and unit-cell parameters are listed in Table 5.

Room-pressure structural study

The refined positional parameters, bond distances and angles of our room-pressure study (Tables 3 and 4) are in better agreement with the Zachariasen and Plettinger (1965) refinement than with the more recent refinement of Le Page and Donnay (1976). Le Page and Donnay suggest that the large discrepancy between their x and y oxygen parameters and those of Zachariasen and Plettinger may be due to the limited $\sin\theta/\lambda$ range of the latter study. Data for our room-pressure refinement were collected to a maximum $\sin\theta/\lambda$ of 0.68Å^{-1} and fall closer to the 0.64Å^{-1} Zachariasen and Plettinger value than to that of Le Page and Donnay (0.99Å^{-1}). Le Page and Donnay based their decision not to make a secondary extinction correction on a calculation derived from Zachariasen (1963). To determine the effect of extinction on a reflection, its transmission factor is required. Transmission factors are commonly determined during the crystal X-ray absorption correction, but no such correction was made by Le Page and Donnay because of the crystal's odd shape. Therefore, their calculation to determine the necessity of an extinction term must have been made assuming equal transmission factors for all reflections. This incorrect assumption may have biased their calculation, and therefore improperly suggested that no extinction term was necessary. In addition, this model tests only type I extinction, and Zachariasen (1967) showed that the quartz crystal he studied in 1965 suffers from type II extinction as well. The refinement of a secondary-extinction parameter for our data brought even the largest F_{obs} ($10\bar{1}$) (which was rejected in the two prior studies) into excellent agreement with its F_{calc} (Tables 1 and 2), and decreased the R values of all six of our refinements at the 0.005 significance level (Hamilton, 1974). The temperature factors in our 1 atm refinement are larger than in the other 1 atm refinements or our high-pressure refinements (performed with Mo$K\alpha$ radiation and over a larger $\sin\theta/\lambda$ range). The thermal ellipsoid for Si is nearly spherical, as shown by the approximately equal RMS amplitudes [0.085(1), 0.085(1), 0.095(1)] and the very large (~105°) errors on the angles that describe the thermal ellipsoid's orientation relative to the crystallographic axes.

Grimm and Dorner (1975) suggest that the α–β transition in quartz can be described as a simultaneous tilting of the tetrahedra around the twofold axes perpendicular to c. They derive the following equation to quantify the tilt angle, δ, in the quartz structure,

$$\tan\theta = \frac{2\sqrt{3}}{9}\,\frac{c}{a}\,\frac{6z-1}{x}$$

[2] To receive a copy of Table 2, order Document AM-80-140 from the Business Office, Mineralogical Society of America, 2000 Florida Avenue, N.W., Washington, D.C. 20009. Please remit $1.00 in advance for the microfiche.

Table 3. Positional and thermal parameters of quartz at pressure

	1 atm	20.7*	37.6	48.6	55.8	61.4
x(Si)	0.4697(1)**	0.4630(2)	0.4581(2)	0.4551(2)	0.4537(2)	0.4526(2)
x(O)	0.4135(3)	0.4111(6)	0.4079(6)	0.4061(6)	0.4047(5)	0.4034(6)
y(O)	0.2669(2)	0.2795(4)	0.2867(5)	0.2912(5)	0.2926(4)	0.2952(5)
z(O)	0.1191(2)	0.1095(2)	0.1039(3)	0.1012(3)	0.0998(2)	0.0987(3)
B(Si)	0.62(2)	0.44(2)	0.47(2)	0.51(2)	0.49(2)	0.49(2)
B(O)	1.05(2)	0.86(3)	0.88(3)	0.84(3)	0.80(2)	0.79(3)
β_{11}(Si)†	0.93(2)	0.70(4)	0.79(4)	0.87(4)	0.82(3)	0.84(4)
β_{22}(Si)	0.78(2)	0.57(5)	0.68(5)	0.70(5)	0.74(4)	0.69(5)
β_{33}(Si)	0.49(2)	0.35(2)	0.35(2)	0.39(2)	0.36(2)	0.39(2)
β_{13}(Si)	-0.001(7)	0.02(1)	-0.05(1)	-0.03(1)	-0.02(1)	-0.02(1)
β_{11}(O)	1.90(6)	1.48(9)	1.55(10)	1.50(10)	1.53(8)	1.48(10)
β_{22}(O)	1.44(5)	1.08(8)	1.23(9)	1.28(10)	1.17(7)	1.21(9)
β_{33}(O)	0.83(3)	0.76(3)	0.69(3)	0.65(3)	0.62(3)	0.64(3)
β_{12}(O)	1.06(5)	0.75(8)	0.75(10)	0.78(10)	0.79(8)	0.80(10)
β_{13}(O)	-0.25(3)	-0.34(6)	-0.40(6)	-0.42(6)	-0.32(4)	-0.27(6)
β_{23}(O)	-0.35(3)	-0.29(4)	-0.32(4)	-0.31(4)	-0.30(3)	-0.26(4)

Pressures reported in kbar unless otherwise stated.
**Parenthesized figures represent esd's of least units cited.*
†*All anisotropic temperature factors, β's, are given x 10^2.*
β_{12} *and* β_{23} *for Si are constrained to be 1/2* β_{22} *and 2* β_{13}*, respectively.*

Table 4. Selected interatomic distances and angles of quartz at pressure

	1 atm	20.7*	37.6	48.6	55.8	61.4
Intra-tetrahedral distances						
Si-O (Å)**	1.605(1)	1.604(2)	1.601(3)	1.601(2)	1.600(2)	1.603(2)
Si-O (Å)	1.614(1)	1.610(2)	1.610(2)	1.609(2)	1.611(1)	1.607(2)
<Si-O> (Å)	1.6092(7)	1.607(1)	1.605(1)	1.605(1)	1.605(1)	1.605(1)
Inter-tetrahedral distances						
Si-Si (Å)	3.05853(8)	3.0193(3)	2.9899(3)	2.9743(3)	2.9666(3)	2.9575(2)
Intra-tetrahedral distances						
O-O (Å)	2.645(1)	2.645(3)	2.650(4)	2.655(3)	2.659(3)	2.664(3)
O-O (Å)	2.631(2)	2.634(3)	2.631(3)	2.625(3)	2.625(3)	2.619(3)
O-O (Å)	2.6171(7)	2.603(1)	2.592(2)	2.586(2)	2.584(1)	2.580(2)
O-O (Å)	2.612(2)	2.618(3)	2.614(4)	2.618(4)	2.614(3)	2.619(4)
Inter-tetrahedral distances						
O-O (Å)	3.331(2)	3.151(3)	3.038(3)	2.982(3)	2.953(3)	2.925(3)
O-O (Å)	3.411(1)	3.260(2)	3.165(3)	3.114(3)	3.092(2)	3.064(2)
Inter-tetrahedral angle						
Si-O-Si (deg)	143.73(7)	139.9(2)	137.2(2)	135.8(2)	135.1(1)	134.2(1)
Intra-tetrahedral angles						
O-Si-O† (deg)	110.52(6)	110.7(1)	111.3(1)	111.6(1)	111.8(1)	112.2(1)
O-Si-O† (deg)	108.81(2)	108.15(4)	107.67(5)	107.31(5)	107.22(4)	106.97(5)
O-Si-O (deg)	108.93(9)	109.4(2)	109.5(2)	109.7(2)	109.6(1)	109.5(2)
O-Si-O (deg)	109.24(8)	109.7(1)	109.5(2)	109.4(2)	109.2(1)	109.1(2)
Quad. Elong.	1.00019	1.00035	1.00067	1.00094	1.00112	1.00139
SiO_4^{4-} Vol. (Å^3)	2.138	2.129	2.122	2.119	2.120	2.118

All pressures are reported in kbar unless otherwise noted.
**Parenthesized figures represent esd's of least units cited.*
†*This angle is one of two symmetrically equivalent angles within the tetrahedron.*

Table 5. Unit-cell parameters of quartz at pressure

	a (Å)	c (Å)	V (Å^3)
1 atm	4.916 (1)*	5.4054(4)	113.13(3)
20.7(5) kbar	4.8362(5)	5.3439(4)	108.24(2)
31. (1) kbar	4.785 (3)	5.307 (2)	105.26(8)
37.6(5) kbar	4.7736(7)	5.3010(4)	104.61(2)
48.6(5) kbar	4.739 (1)	5.2785(5)	102.66(3)
55.8(5) kbar	4.7222(5)	5.2673(6)	101.72(3)
61.4(5) kbar	4.7022(3)	5.2561(2)	100.65(3)

* *Parenthesized figures represent esd's of least units cited.*

where c and a are unit-cell parameters and x and z are oxygen coordinates. The values for this angle are essentially equivalent for all three room-pressure data sets (Table 1).

High-pressure structural studies

The changes in the crystal structure observed in our experiments are consistent with the two previous studies (Jorgensen, 1978; d'Amour *et al.*, 1979), but, in addition, our increased precision has allowed us to observe changes not seen in the other two experiments (Table 4). Because we have determined individual Si–O bond distances at pressure to a precision of ±0.002Å, we observe a small change in the average Si–O bond length from 1.6092(7)Å at one atm to 1.605(1)Å at 61.4 kbar (Fig. 1). Both unique Si–O bonds compress at about the same rate (Table 4). We would not have expected Jorgensen's refinements to show this change, as his data are collected only to 28 kbar and his Si–O bond-distance errors are approximately 0.005Å; these errors may partially reflect the effects of Dauphiné twinning on his samples. The d'Amour *et al.* data were collected to high enough pressures (68 kbar) to determine the Si–O bond compression; however, their errors on the Si–O distances were ±0.02Å. The diamond cell used by d'Amour *et al.* contained a sphere of Be (4 cm in diameter) with holes drilled in it so that the crystal could be viewed while under pressure. The spherical shape was used so that a correction for X-ray absorption of the cell would not be necessary; however, the holes in the Be caused large enough deviations from a spherical shape that an absorption correction should have been made (Schulz and d'Amour, personal communication). This problem, combined with the fact that their data were only collected out to 50° 2θ, were responsible for the larger errors. In addition, their crystal/gasket-hole size ratio is small when compared to those normally used in our experiments. When a crystal is too close to the gasket-hole edge, either the incident or diffracted beam can be shielded, causing systematic decreases in the intensities of some reflections.

The compressions of the five shortest non-tetrahedral Si–O distances do not suggest structural movement toward a six-coordinated Si site. The change in the Si···Si distance (Table 4) is nearly linear over the pressure range studied, 3.0585(1)Å at one atm and 2.9575(2)Å at 61.4 kbar. Several pairs of O–O distances decrease more than 0.34Å, or about eleven percent (Fig. 2). At 61.4 kbar these distances, 3.064(2)Å and 2.925(3)Å, are rapidly approaching 2.7Å, the average O–O distance in many silicates at ambient conditions. The common occurrence of this value suggests that there may be a large increase in repulsive energy when oxygens are forced closer than 2.7Å.

The O–O distances within the silicate tetrahedron diverge from the value for a regular tetrahedron as pressure is increased (Table 4). The difference between the longest and shortest distances is 0.033Å at one atm and 0.084Å at 61.4 kbar. This increased tetrahedral distortion is also reflected in the O–Si–O internal tetrahedral angles, which are plotted in Figure 3 along with a dashed line at 109.47°, the internal angle of a regular tetrahedron. The difference between the largest and smallest of the four symmetrically distinct angles is 1.7° at one atm and becomes 5.2° at 61.4 kbar. This increased distortion is consistent with the tetrahedral distortion observed in Jorgensen's (1978) study, but was not observed in the d'Amour *et al.* (1979) work. If distortion of the tetrahedron is measured by quadratic elongation (Robinson *et al.*, 1971) (Table 4), the percent increase gets

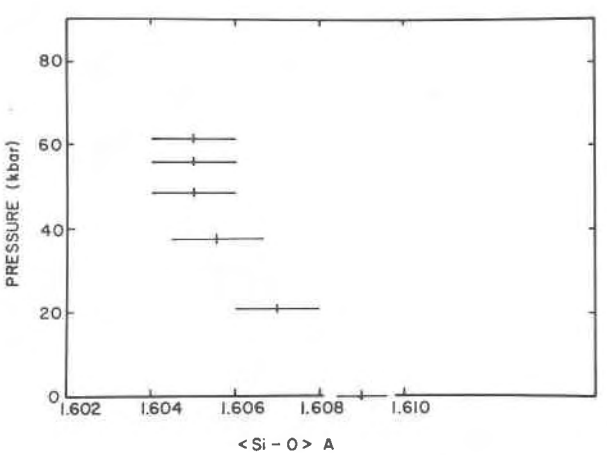

Fig. 1. The change caused by pressure on the average Si–O bond length of quartz.

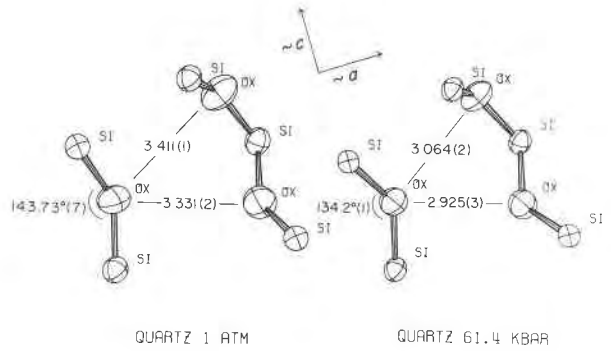

Fig. 2. The effect of pressure on the cavities in the quartz structure. The Si–O–Si angle compresses from 143.73° at 1 atm to 134.2° at 61.4 kbar. The shortening of two long O–O interatomic distances shown in this figure appears to be partially responsible for the difference in compressibilities along the *a* and *c* crystallographic directions.

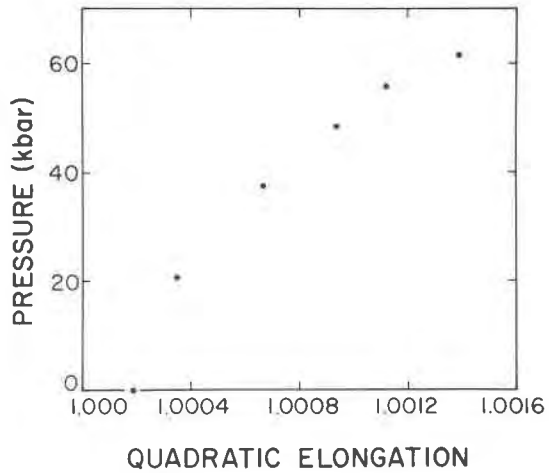

Fig. 4. Increase in tetrahedral distortion with pressure as indicated by quadratic elongation. The curvature of the data indicates that the amount of distortion per kbar is greater at higher prssures than at lower pressures.

larger at higher pressures (Fig. 4), *i.e.*, more distortion takes place between 50 and 60 kbar than between 1 atm and 10 kbar. Because a regular tetrahedron occupies the greatest volume for any tetrahedron of that average size, as it distorts its volume must decrease. Our experiments were not precise enough to show the change in volume due to distortion (Table 4), but we would predict that at higher pressure this volume change would become significant. The structural element responsible for the anomalously high compressibility of quartz is the Si–O–Si interbond angle, which decreases non-linearly by ten degrees over the pressure range from 1 atm to 61 kbar (Figs. 2 and 5). At higher pressures the Si–O–Si angle is responsible for less volume compression; however, the atomic rearrangement that causes the tetrahedron to distort gradually accounts for more compression.

Finally, there is no significant change in the equivalent isotropic temperature factor or orientation of the thermal ellipsoid of Si with pressure; there may be a small decrease in the size of the thermal ellipsoid of O (Table 3). The temperature factor for Si does become more anisotropic as pressure is increased (in our lowest-pressure run), which is consistent with the increased distortion of the tetrahedron.

Unit-cell and elasticity data

Pressure–volume data for quartz (McWhan, 1967; Vaidya *et al.*, 1973; Olinger and Halleck, 1976; Jor-

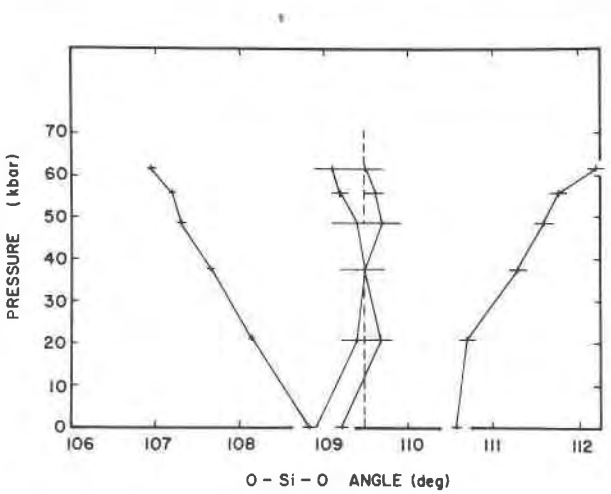

Fig. 3. The pressure dependence of the four unique internal tetrahedral angles (O–Si–O).

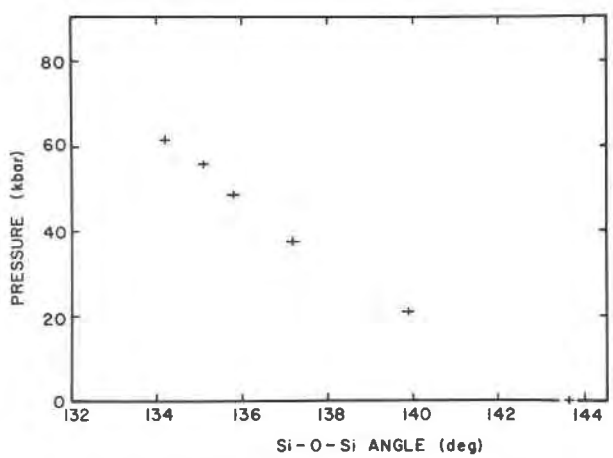

Fig. 5. The pressure dependence of the flexible Si–O–Si angle. The curvature of the data indicates a tapering off of the change in this angle as pressure is increased.

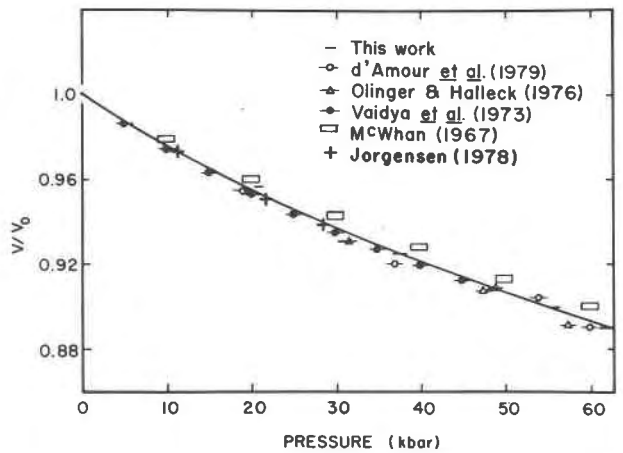

Fig. 6. Unit-cell volume normalized to the ambient unit-cell volume for six compressibility studies of quartz.

gensen, 1978; d'Amour *et al.*, 1979), plotted in Figure 6, show good agreement with the Birch-Murnaghan curve calculated from the ultrasonically determined values of the bulk modulus, K_S, and the pressure derivative of the bulk modulus, K'_S (McSkimin *et al.*, 1965). Isothermal (K_T and K'_T) values have been calculated by fitting the P–V data to a Birch-Murnaghan equation of state for each data set, with all pressures converted to Decker (1971) equation of state values to facilitate comparison (Table 6). Values of K_T and K'_T calculated for the McWhan and Vaidya *et al.* studies may differ from the others because both used solid pressure-transmitting media, NaCl and indium metal, respectively. However, calculations of K_T and K'_T and graphs of V/V_0 *vs.* P do not give a sufficiently accurate picture of the internal consistency of the data.

In Figure 7 the c/a cell-parameter ratio is plotted *vs.* P, with all symbols approximately the same size, so errors in data are not represented. For the c/a ratio to increase with pressure, the c direction must be elastically stiffer than a. Using the single-crystal elastic moduli and the pressure derivatives of these moduli from McSkimin *et al.* (1965), the c/a ratio can be calculated for high pressures. To make these calculations, lattice parameters are expressed as polynomial expansions, which give notoriously bad lattice-parameter extrapolations to higher pressures. For quartz, such a calculation predicts that with increased pressure the c/a ratio reaches a maximum and then decreases at less than 100 kbar. Therefore, on Figure 7 we have used Thurston's (1967) extrapolation formula, which is essentially linear over this pressure range, although it does show a small amount of similar curvature to our data and those of d'Amour *et al.* (1979). The Thurston (solid line) curve diverges from the data at pressures as low as 60 kbar. This discrepancy reflects the need for either second derivatives with respect to pressure of single-crystal elastic moduli, or better extrapolation formulae. The dashed–dotted curve on Figure 7 has been drawn through the data from this study (crosses) and those of Jorgensen (1978) (closed circles), and the dashed curve has been drawn through the d'Amour *et al.* data (open circles) and shows a parallel but systematically offset trend. The excellent agreement at low pressures of our data and the curve predicted by the elastic moduli gives us additional confidence that our experiments were hydrostatic, and that parameters such as bond distances and an-

Table 6. Elasticity data for quartz

Investigator	Technique	K_T (Mbar)*	K'_T
Levien et al.	Single-crystal	0.38 (3)**	6. (2)
d'Amour et al.	Single-crystal	0.365(9)	5.9(4)
Jorgensen	Neutron-powder	0.364(5)	6.3(4)
Olinger and Halleck	Bridgman-anvil	0.38 (1)	5.4(4)
Vaidya et al.	Piston-cylinder	0.347(1)	7.7(1)
McWhan	Bridgman-anvil	0.445(2)	3.6(1)
McSkimin et al.	Ultrasonic	0.371(2)	6.3(3)

*All values for K_T and K_T' determined from pressure-volume data were calculated from a least-squares fit of the P-V data to a Birch-Murnaghan equation of state.

$P = 3/2\ K_T(y^{-7/3} - y^{-5/3})\ [1 - 3/4(4 - K_T')(y^{-2/3} - 1)]$,

$y = V/V_O$.

**Parenthesized figures represent esd's of least units cited.

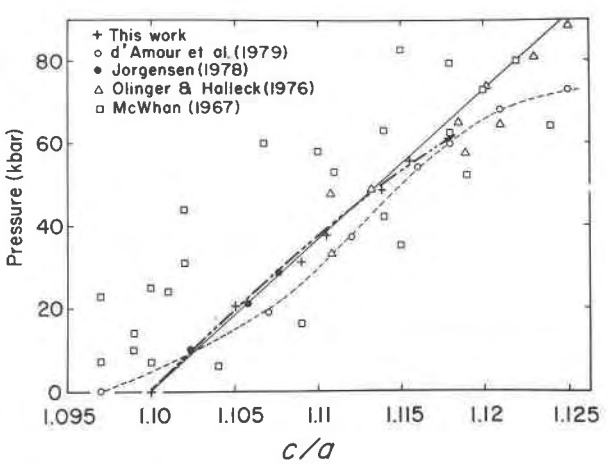

Fig. 7. The c/a unit-cell parameter ratio as a function of pressure for five compressibility studies of quartz. The solid line has been determined from Thurston's (1967) extrapolation formula for the McSkimin *et al.* (1965) elastic moduli. The dashed curve is drawn through the d'Amour *et al.* (1979) data, and the dashed–dotted curve is drawn through the data from this study and that of Jorgensen (1978).

gles are consistent with the ultrasonic data. The systematic differences between the high-pressure d'Amour *et al.* unit-cell parameter ratios and ours may have been caused by their crystal being poorly centered (d'Amour, personal communication). The Olinger and Halleck (1976) data (triangles), although showing the proper trend, do not fall along a curve, and the non-hydrostatic McWhan (1967) data (squares) again give the correct general trend, but show a great deal of scatter. Compensating errors in these last two studies gave reasonable values for unit-cell volumes, but only approximate unit-cell edges.

Discussion

Comparison of SiO_2 and GeO_2

As pressure is increased, the geometry of the Si-quartz structure becomes more like the room-pressure Ge-quartz structure. The Si–O–Si angle goes from 143.73° at one atm to 134.2° at 61 kbar, approaching the room-pressure Ge–O–Ge angle of 130° (Smith and Isaacs, 1964). The tetrahedral tilt angle, δ, changes from −16.37° to −23.47°, as compared to the room-pressure Ge-quartz δ of −26.55°. Finally, the O–Si–O angles within the tetrahedron become more like those of the Ge structure under ambient conditions. By 61 kbar the difference between the largest and smallest O–Si–O angles has increased from 1.7° to 5.2°, approaching the 6.8° difference in the one-atm Ge analogue. Therefore, rather than two different structural elements (Si–O–Si angle bending and tetrahedral distortion) controlling the compression of the two crystals, as suggested by Jorgensen (1978), we actually see a continuum. For the quartz structure, substituting Ge for Si appears to have the same effect on the geometry of the structure as increasing the pressure has. Because we see Si–O bond shortening, we would predict some compression of the Ge–O bonds; this was not observed in the Jorgensen study.

Systematic changes in stereochemistry of quartz

Hill and Gibbs (1979) describe an apparent structural interdependence between the Si–O–Si angles and both d(Si–O) and d(Si···Si) in silica polymorphs as well as in silicates. The first relationship, −sec(Si–O–Si) ∝ d(Si–O), suggests that as the Si–O–Si angle decreases the Si–O distance will increase. If true at high pressures, it would predict that Si–O distances might actually increase. In Figure 8 we have plotted the regression line for the room-pressure data (Hill and Gibbs) and the six points (crosses) determined in this study; this correlation does not persist with increased pressure because a coupled decrease in the Si–O–Si angle and the Si–O distance is observed.

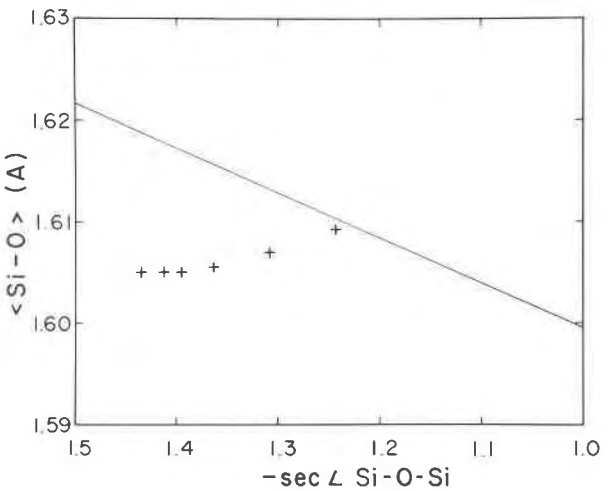

Fig. 8. Si–O bond length as a function of −sec(Si–O–Si) for the silica minerals. The line represents the trend shown in Hill and Gibbs (1979) for the polymorphs measured under ambient conditions; the crosses represent the data for quartz from this study at six pressures, including room pressure. This relationship does not persist at high pressure.

The second relationship in Hill and Gibbs, log sin[(Si–O–Si)/2] ∝ log d(Si···Si), suggests that longer Si···Si separations are associated with wider Si–O–Si angles. In Figure 9 the Hill and Gibbs regression line for this relationship is drawn with our high-pressure data (crosses). This relationship seems to hold better than the first when applied to data other than those obtained under ambient conditions. More structural data are needed on the silica polymorphs to test the validity of this relationship and the importance of non-bonded Si···Si interactions on structural changes under general P–T conditions.

The structural changes that take place during thermal expansion and isothermal compression are not simple inverses. Although the quartz structure is often thought of as compressing and expanding solely through changes in the Si–O–Si angle, as if it behaved like a simple spring, this is not the case. Figures 10 and 11 compare structural changes at elevated temperatures and pressures by plotting unit-cell volume, at P or T divided by the ambient unit-cell volume, against the Si–O–Si angle and the tetrahedral tilt angle, δ, respectively. For these calculations unit-cell data at elevated temperatures were taken from Ackermann and Sorrell (1974), and high-temperature structural data were taken from Young (1962). In Figure 10 there is a break in the slope of the lines

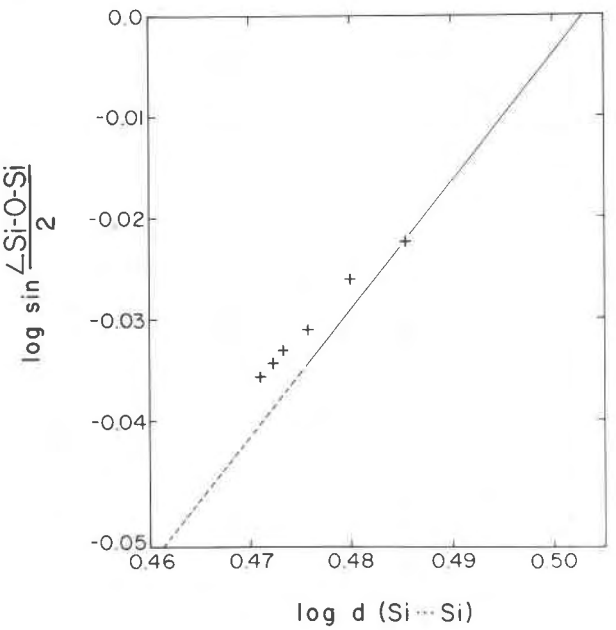

Fig. 9. Plot of log d(Si ··· Si) *vs.* log sin[Si–O–Si)/2] for the silica polymorphs. The line represents the trend shown in Hill and Gibbs (1979) for the silica minerals measured under ambient conditions. The crosses represent the data for quartz from this study, measured at six pressures including room pressure. This relationship may hold for general *P–T* conditions.

connecting the high-temperature and high-pressure points, suggesting that in these two regimes at least partially different structural changes must be responsible for the change of volume. In Figure 11 a hyperbolic curve shows that δ increases rapidly as the α–β transition is approached, but decreases in magnitude more slowly as unit-cell volume is decreased. Although the high-temperature work is not definitive, we conclude that the silicate tetrahedron does not show inverse effects. As temperature is increased, there may be a small increase in distortion (Young); when pressure is increased, tetrahedral distortion increases considerably. It thus appears that the volume increase with temperature is accomplished through changes in the Si–O–Si angle and δ, whereas compression seems to be accomplished by the Si–O–Si angle and increasingly by tetrahedral distortion.

Systematic changes in elasticity of quartz

Several methods have recently been used to investigate the bulk and single-crystal elastic properties of quartz from structural considerations. *Ab initio* calculations, made by modeling quartz from smaller molecules, have determined a bulk modulus for quartz close to the experimental values (O'Keeffe *et al.*, 1980). We have investigated how atomic rearrangements reflect single-crystal elastic properties. The structural reason for the changing c/a cell-parameter ratio (Fig. 7) can be seen in Figure 2, on which we have drawn approximate crystallographic axes. One of the rapidly changing O–O distances is nearly parallel to a; the other is approximately 45° between a and c. Hence there is more compression of these distances in the a direction than in the c direction, explaining the stiffer elastic nature of c.

The errors on the bulk modulus, K_T, and the pressure derivative of the bulk modulus, K'_T, listed in Table 6, are based on the assumption that the scatter of the data from the curve being fit accurately represents the errors on the pressure and volume of each point; this is often not the case (Bass *et al.*, 1979). When the errors associated with each point of our quartz data are included in the analysis, K_T and K'_T are very poorly constrained. Therefore, Bass *et al.* have fixed the value of K_T equivalent to the Reuss bound, calculated from the acoustically determined single-crystal elastic moduli (McSkimin *et al.*, 1965) and corrected for the difference between isothermal and adiabatic experiments. Using a weighted fit of our data, holding $K_T = 0.371(2)$ Mbar, they calculate $K'_T = 6.2(1)$, in excellent agreement with McSkimin *et al.*'s acoustic value of 6.3(3).

Using any two bulk elastic moduli, the elastic character of an isotropic material (an ideal polycrystal) can be described. A common pair of such moduli are Young's modulus, E, and Poisson's ratio,

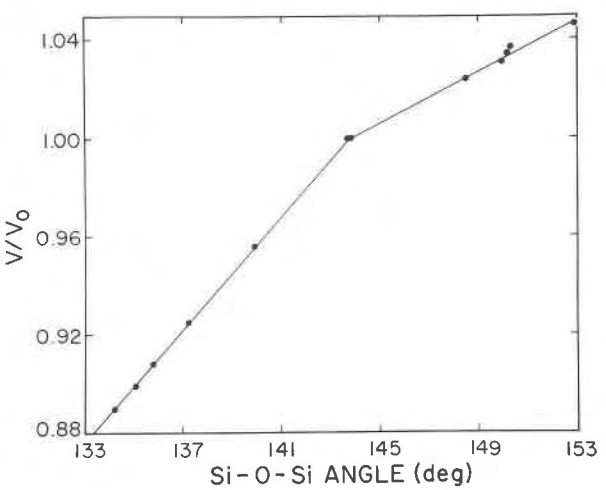

Fig. 10. The Si–O–Si angle of quartz as a function of unit-cell volume at temperature or pressure normalized to room-pressure–temperature volume. The break in slope at the room-temperature–pressure point suggests that different structural changes cause the volume change for increased temperature or pressure.

σ, which describe the lengthening and necking of a rod under tensile stress. Poisson's ratio can be written in terms of K, the bulk modulus, and μ, the shear modulus: $\sigma = (3K - 2\mu)/2(3K + \mu)$. The Voigt bound of K can be expressed as 1/9[a + 2b] where, for the case of quartz, $a = 2c_{11} + c_{33}$ and $b = 2c_{13} + c_{12}$ (c_{ij}'s are single-crystal elastic moduli); μ can be written as 1/15[a − b + 3c] where a and b are as above, and $c = 2c_{44} + c_{66}$. Therefore $\sigma = [a + 4b - 2c]/[4a + 6b + 2c]$. The value of σ for quartz is 0.056, yet for most minerals $\sigma \simeq 0.25$. To understand why σ commonly equals 0.25, we assumed $\sigma = 0.25$ and solved this equation. The result is that b equals c. Therefore, for most minerals the sum of the pure-shear elastic moduli (c) is approximately equal to the sum of the off-diagonal shear moduli (b). In quartz the ratio of b/c is 0.2 instead of 1.0 (McSkimin *et al.*, 1965).

Single-crystal elastic moduli each describe the structural deformation that takes place when a given stress is applied to a crystal. The pure-shear elastic moduli (c_{44} and c_{66}) indicate the amount of shear stress required to produce a unit shear strain in the *a*–*c* plane (c_{44}) and the a_1–a_2 plane (c_{66}). One of the off-diagonal elastic moduli, c_{13}, describes the stress induced in the *c* direction due to a strain parallel to *a*; the other, c_{12}, describes the similar coupling between a_1 and the direction perpendicular to a_1 and *c*. When a coil spring is shortened parallel to its axis, very little stress is induced in a direction perpendicular to the axis. Exactly such a change can be easily accommodated by the quartz structure which is comprised of tetrahedra repeated along threefold screw axes parallel to *c* (Fig. 12). When a length change occurs parallel to *c*, the small value of c_{13} suggests that there is a small concomitant change in *a*. In addition, if a length change occurs parallel to a_1, a small change in the direction perpendicular to a_1 and *c* results. This behavior dominates the elastic behavior of a polycrystal. We therefore believe the small value for Poisson's ratio is caused by the easily expanding and contracting spirals of tetrahedra which behave like coiled springs. Thus for this relatively simple structure the shear moduli can be rationalized from structural considerations. Although this work provides only a beginning, we hope that additional detailed studies of crystal structures at high pressures, and the relationships of structural changes to the single-crystal elastic properties of the same materials, will eventually lead to general empirical relationships that may help us to predict elastic properties of minerals as they exist within the Earth.

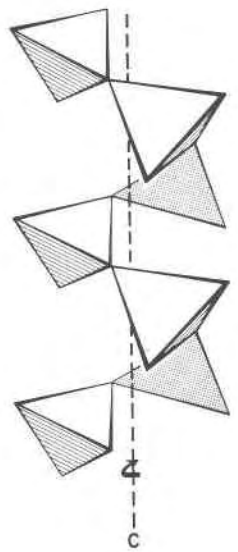

Fig. 12. Spirals of silicate tetrahedra parallel to *c*. These easily expanding and contracting spirals behave like coiled springs and are, therefore, responsible for the low value of Poisson's ratio in quartz.

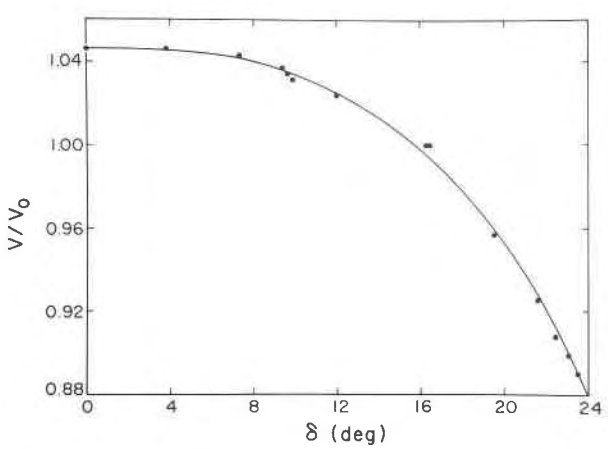

Fig. 11. The tetrahedral tilt parameter for quartz, δ, as a function of unit-cell volume at temperature or pressure normalized to the room-temperature–pressure volume. The hyperbolic shape of this curve suggests that tetrahedral tilting is important to the change in unit-cell volume as the α–β transition is approached but has less effect as unit-cell volume decreases.

Acknowledgments

We thank J. D. Bass for developing the program to calculate the elastic parameters, and J. D. Bass and R. C. Liebermann for helpful discussions about the elasticity sections of this paper. This research was supported by NSF grant EAR77-13042. The first author also gratefully acknowledges a pre-doctoral fellowship awarded to her by the American Association of University Women Educational Foundation.

References

Ackermann, R. J. and C. A. Sorrell (1974) Thermal expansion and the high–low transformation in quartz. I. High-temperature X-ray studies. *J. Appl. Crystallogr., 7,* 461–467.

Adams, L. H. and E. D. Williamson (1923) Compressibility of minerals and rocks at high pressure. *J. Franklin Inst., 195,* 475–529.

Barnett, J. D., S. Block and G. J. Piermarini (1973) An optical fluorescence system for quantitative pressure measurement in the diamond-anvil cell. *Rev. Sci. Instrum., 44,* 1–9.

Bass, J. D., R. C. Liebermann, D. J. Weidner and S. J. Finch (1979) Elasticity data from acoustic and volume compression experiments (abstr.). *Trans. Am. Geophys. Union, 60,* 386.

Bridgman, P. W. (1925) Linear compressibility of fourteen natural crystals. *Am. J. Sci., 10,* 483–498.

——— (1928) The linear compressibility of thirteen natural crystals. *Am. J. Sci., 15,* 287–296.

——— (1948a) The compression of 39 substances to 100,000 kg/cm^2. *Proc. Am. Acad. Arts Sci., 76,* 55–70.

——— (1948b) Rough compressions of 177 substances to 40,000 kg/cm^2. *Proc. Am. Acad. Arts Sci., 76,* 71–87.

——— (1949) Linear compression to 30,000 kg/cm^2, including relatively incompressible substances. *Proc. Am. Acad. Arts Sci., 77,* 189–234.

d'Amour, H., W. Denner and H. Schulz (1979) Structure determination of α-quartz up to 68×10^8 Pa. *Acta Crystallogr., B35,* 550–555.

Decker, D. L. (1971) High-pressure equation of state for NaCl, KCl, and CsCl. *J. Appl. Phys., 42,* 3239–3244.

Finger, L. W. and E. Prince (1975) A system of Fortran IV computer programs for crystal structure computations. *U. S. Natl. Bur. Stand. Tech. Note 854.*

——— and H. King (1978) A revised method of operation of the single-crystal diamond cell and the refinement of the structure of NaCl at 32 kbar. *Am. Mineral., 63,* 337–342.

Grimm, H. and B. Dorner (1975) On the mechanism of the α–β phase transformation of quartz. *J. Phys. Chem. Solids, 36,* 407–413.

Hamilton, W. C. (1974) Tests for statistical significance. In J. A. Ibers and W. C. Hamilton, Eds., *International Tables for X-Ray Crystallography,* Vol. IV, p. 285–310. Kynoch Press, Birmingham, England.

Hazen, R. M. and L. W. Finger (1977) Modifications in high-pressure single-crystal diamond-cell techniques. *Carnegie Inst. Wash. Year Book, 76,* 655–656.

Hill, R. J. and G. V. Gibbs (1979) Variation in d(T–O), d(T···T) and <TOT in silica and silicate minerals, phosphates and aluminates. *Acta Crystallogr., B35,* 25–30.

Jorgensen, J. D. (1978) Compression mechanisms in α-quartz structures—SiO_2 and GeO_2. *J. Appl. Phys., 49,* 5473–5478.

King, H. E., Jr. (1979) *Phase Transitions in FeS at High-Temperatures and High-Pressures.* Ph.D. Thesis, State University of New York, Stony Brook, New York.

——— and L. W. Finger (1979) Diffracted beam crystal centering and its application to high-pressure crystallography. *J. Appl. Crystallogr., 12,* 374–378.

Le Page, Y. and G. Donnay (1976) Refinement of the crystal structure of low-quartz. *Acta Crystallogr., B32,* 2456–2459.

McSkimin, H. J., P. Andreatch, Jr. and R. N. Thurston (1965) Elastic moduli of quartz versus hydrostatic pressure at 25° and −195.8°C. *J. Appl. Phys., 36,* 1624–1632.

McWhan, D. B. (1967) Linear compression of α-quartz to 150 kbar. *J. Appl. Phys., 38,* 347–352.

Merrill, L. and W. A. Bassett (1974) Miniature diamond anvil pressure cell for single crystal X-ray diffraction studies. *Rev. Sci. Instrum., 45,* 290–294.

O'Keefe, M., M. D. Newton and G. V. Gibbs (1980) Ab initio calculation of interatomic force constants in $H_6Si_2O_7$ and the bulk modulus of α-quartz and α-cristobalite. *Phys. Chem. Mineral.,* in press.

Olinger, B. and P. M. Halleck (1976) The compression of α quartz. *J. Geophys. Res., 81,* 5711–5714.

Piermarini, G. J., S. Block and J. D. Barnett (1973) Hydrostatic limits in liquids and solids to 100 kbar. *J. Appl. Phys., 44,* 5377–5382.

———, ———, ——— and R. A. Forman (1975) Calibration of the pressure dependence of the R_1 ruby fluorescence line to 195 kbar. *J. Appl. Phys., 46,* 2774–2780.

Robinson, K., G. V. Gibbs and P. H. Ribbe (1971) Quadratic elongation: a quantitative measure of distortion in coordination polyhedra. *Science, 172,* 567–570.

Smith, G. S. and L. E. Alexander (1963) Refinement of the atomic parameters of α-quartz. *Acta Crystallogr., 16,* 462–471.

——— and P. B. Isaacs (1964) The crystal structure of quartz-like GeO_2. *Acta Crystallogr., 17,* 842–856.

Thurston, R. N. (1967) Calculation of lattice-parameter changes with hydrostatic pressure from third-order elastic constants. *J. Acoust. Soc. Am., 41,* 1093–1111.

Vaidya, S. N., S. Bailey, T. Pasternack and G. C. Kennedy (1973) Compressibility of fifteen minerals to 45 kilobars. *J. Geophys. Res., 78,* 6893–6898.

Young, R. A. (1962) Mechanism of phase transition in quartz. *AFOSR-2569 (Final Report, Project No. A-447) Engineering Experimental Station, Georgia Institute of Technology.*

——— and B. Post (1962) Electron density and thermal effects in alpha quartz. *Acta Crystallogr., 15,* 337–346.

Zachariasen, W. H. (1963) The secondary extinction correction. *Acta Crystallogr., 16,* 1139–1144.

——— (1967) A general theory of X-ray diffraction in crystals. *Acta Crystallogr., 23,* 558–564.

——— and H. A. Plettinger (1965) Extinction in quartz. *Acta Crystallogr., 18,* 710–714.

Manuscript received, May 31, 1979;
accepted for publication, April 18, 1980.

American Mineralogist, Volume 65, pages 931–935, 1980

The crystal structure of klebelsbergite, $Sb_4O_4(OH)_2SO_4$

SILVIO MENCHETTI AND CESARE SABELLI

CNR, Istituto di Mineralogia dell'Università
Via La Pira 4, 50121 Firenze, Italy

Abstract

Klebelsbergite is an antimony sulfate found at Felsöbánia, Hungary, and recently at Pereta, Tuscany, Italy. Crystal data are: $a = 5.766(2)$, $b = 11.274(2)$, $c = 14.887(2)$Å; space group $Pca2_1$; $Z = 4$. The atomic positions were determined by direct methods and refined by least-squares calculations to an R index of 0.045 for 1111 observed reflections.

The basic structural units are the Sb^{III}–O polyhedra and the SO_4 tetrahedron. Antimony polyhedra show, as usual, intermediate features between the SbO_3E tetrahedron and the SbO_4E trigonal bipyramid, where E indicates the unshared lone pair of electrons. These polyhedra are connected to each other by edge sharing to form Sb–O sheets parallel to (001). Adjacent sheets are linked together by SO_4 tetrahedra and, indirectly, by H-bonds. Taking into account anions and lone pairs, the volume occupied by each anion is similar to that found in close-packed structures. A marked pseudosymmetry (towards the centric group *Pcan*) is present in the Sb–O sheet.

Introduction

Klebelsbergite from Felsöbánia, Hungary, was first described by Zsivny (1929); however, the first complete description of the mineral is by Nakai and Appleman (1980). A second occurrence of klebelsbergite, at Pereta mine (Tuscany, Italy), is reported by Cipriani *et al.* (1980a). A synthetic compound equivalent to klebelsbergite was prepared by Nakai and Appleman by boiling Sb_2O_3 with sulfuric acid. The same compound was also obtained by researchers of the Laboratoire de Chimie-Physique, Besançon, France (Douglade, personal communication).

In recent years several Sb^{3+}–O compounds have been structurally studied and much attention has been directed towards the stereochemistry of elements with one unshared electron pair. Our work was undertaken in order to contribute to the crystal-chemistry knowledge of these compounds. Another question was the full knowledge of the chemical composition of klebelsbergite and if the true crystal-chemical formula was $Sb_4O_4(OH)_2SO_4$ or $Sb_4O_5SO_4 \cdot H_2O$.

Experimental

For our study a small (approx. $0.1 \times 0.1 \times 0.5$ mm) colorless crystal was chosen from a sample we collected at Pereta. Crystal data are: $a = 5.766(2)$, $b = 11.274(2)$, $c = 14.887(2)$Å, $V = 967.7$Å^3; $Z = 4$, $D_x = 4.67$ g cm^{-3}, formula weight 681.1. The space group, determined from the extinctions, is *Pcam* or $Pca2_1$. The latter is the correct one on the basis of the structure determination.

Intensities were collected with a Philips *PW 1100* four-circle computer-controlled diffractometer (Centro di Cristallografia Strutturale del C.N.R., Pavia, Italy), with Mo$K\alpha$ radiation and the ω–2θ scan technique. A total of 1469 independent reflections, in the range $2 < \theta < 30°$ were measured; only 1111 were considered to be actually observed according to the criterion $F_o > 5\sigma(F_o)$. Intensities were corrected for Lorentz-polarization effects; an absorption correction was carried out on the basis of the semiempirical method proposed by North *et al.* (1968).

Structure determination and refinement

As statistical tests did not give a clear indication on the absence of the symmetry center, the first attempts to solve the crystal structure of klebelsbergite were performed in the centric space group *Pcam*, which was later found to be incorrect. Other difficulties were presented by the incomplete knowledge of the chemical composition. The structure was solved by direct methods, using MULTAN (Main *et al.*, 1974). However, many successive three-dimensional Fou-

0003–004X/80/0910–0931$02.00

Table 1. Klebelsbergite: fractional atomic coordinates and thermal parameters

Atom	x	y	z	B eq.*	β_{11}	β_{22}	β_{33}	β_{12}	β_{13}	β_{23}
Sb(1)	0.4789(2)	0.3596(2)	0.25	1.18	59(3)	29(1)	14(1)	5(2)	4(1)	1(1)
Sb(2)	0.3917(2)	0.0874(2)	0.0914(2)	0.86	60(3)	19(1)	9(1)	4(2)	0(1)	0(1)
Sb(3)	0.1526(2)	0.4078(2)	0.4322(2)	0.84	56(3)	20(1)	9(1)	5(2)	-2(1)	1(1)
Sb(4)	0.0483(2)	0.1412(2)	0.2673(1)	1.13	71(3)	26(1)	13(1)	8(2)	6(1)	-2(1)
S	0.6780(7)	0.2595(8)	0.5083(7)	1.18	64(12)	34(4)	11(2)	-1(7)	-7(6)	2(2)
O(1)	0.8525(25)	0.2505(14)	0.4312(14)	2.13	191(47)	65(16)	6(6)	4(22)	15(17)	13(10)
O(2)	0.6400(27)	0.3877(12)	0.5285(10)	2.27	288(57)	17(12)	24(8)	-2(21)	-32(17)	-1(7)
O(3)	0.4627(26)	0.2026(19)	0.4849(11)	3.87	137(47)	149(25)	25(8)	-106(29)	2(15)	-35(11)
O(4)	0.7742(25)	0.2015(15)	0.5899(13)	2.94	128(45)	125(18)	9(8)	77(22)	15(17)	28(12)
O(5)	0.2856(30)	0.4627(15)	0.1823(15)	1.50	166(53)	20(13)	15(9)	44(20)	1(17)	6(8)
O(6)	0.3077(24)	0.2026(17)	0.1821(12)	1.02	77(46)	26(13)	8(8)	-17(19)	22(14)	1(8)
O(7)	0.4238(30)	0.4919(18)	0.3657(13)	1.42	53(42)	61(16)	5(7)	-41(22)	13(16)	-12(8)
O(8)	0.1178(24)	0.0069(16)	0.1642(14)	0.73	26(40)	18(13)	10(8)	6(18)	-13(13)	5(8)
O(9)	0.2723(34)	0.0515(16)	0.3413(16)	2.22	268(59)	36(13)	14(10)	-26(23)	-58(18)	1(9)
O(10)	0.1994(26)	0.3088(15)	0.3213(12)	1.04	98(45)	16(12)	11(8)	-19(18)	21(13)	-13(8)
H(1)	0.301	0.513	0.129	4.00						
H(2)	0.337	0.101	0.389	4.00						

*Equivalent isotropic B (Å^2) calculated from anisotropic temperature factors, except for H(1) and H(2) where B was not refined.

Form of anisotropic temperature factors (x10^4): $\exp -(\beta_{11}h^2+\beta_{22}k^2+\beta_{33}l^2+2\beta_{12}hk+2\beta_{13}hl+2\beta_{23}kl)$

rier syntheses were necessary to locate all non-hydrogen atoms. Some cycles of isotropic full-matrix least-squares refinement led to $R = 0.07$. A weight $W = 1/\sigma^2(F_o)$ with σ derived from counting statistics was given to all observed reflections. Two more least-squares cycles with the introduction of anisotropic thermal parameters were carried out. A difference Fourier synthesis at this stage did not give sure indication for H atoms. The latter were therefore located on the basis of crystal-chemical considerations, along the donor–acceptor alignment at about 1.0Å from the donor oxygen atom. The positional and thermal parameters of hydrogens were not refined. The final R value was 0.045 for the observed reflections and 0.071 including "less thans." Seven reflections were considered to be affected by secondary extinction and therefore excluded from least-squares calculations. Scattering-factor curves for all atoms and the anomalous dispersion coefficient for heavy atoms were taken from *International Tables for X-ray Crystallography* (1974, p. 99–101, 148–151).

The atomic positional and thermal parameters are listed in Table 1, and a list of observed and calculated structure factors appears in Table 2.[1]

Discussion

The basic structural units of klebelsbergite are the Sb^{3+}–O polyhedra and the SO_4 tetrahedron.

It is well known from the literature that anions linked to an Sb^{3+} atom are arranged all to one side of the cation so that it is out of the center of its coordination polyhedron. This usually happens for ns^2-elements which have one unshared electron pair. Two ideal coordination polyhedra for Sb^{3+} are the tetrahedron and the trigonal bipyramid. In both instances a vertex is supposed to be occupied by the lone pair of electrons (E) which has the same volume as that of

[1] To receive a copy of Table 2, order Document AM-80-138 from the Business Office, Mineralogical Society of America, 2000 Florida Avenue, N.W., Washington, D.C. 20009. Please remit $1.00 in advance for the microfiche.

an anion (Galy *et al.*, 1975). Taking into consideration anions and lone pairs, the structures of many oxides and fluorides of ns^2-elements can be considered as close packed. In the SbO_3E model (tetrahedron) there are three strong Sb–O bonds with distances of 2.0Å. In the SbO_4E model (trigonal bipyramid) there are two equatorial and two axial Sb–O bonds. According to Galy *et al.* (1975) the theoretical distances are 2.0 and 2.27Å respectively, while the corresponding theoretical angles are 92.2 and 151.5°. According to the same authors it is also possible to calculate the theoretical position of the center of the lone pair *E*, which should be approximately 1.1Å distant from the Sb atom.

Bovin (1976) has collected the experimental Sb–O distances found in 28 compounds; the analysis of these values and of others found in subsequently solved structures shows that the experimentally found polyhedra show intermediate features between the tetrahedron and the trigonal bipyramid. Indeed only a slight displacement of the Sb atom out of the equatorial plane of the trigonal bipyramid is necessary to change four- to three-coordination.

Selected interatomic distances and angles in klebelsbergite are reported in Table 3. As also shown in Figure 1, each of the four independent Sb atoms is bound to four O atoms with distances ranging from 1.90 to 2.48Å. The four polyhedra have very similar Sb–O mean distances (from 2.10 to 2.14Å), and all exhibit arrangements intermediate between the SbO_3E and SbO_4E models. However, the Sb(3) polyhedron resembles more a distorted tetrahedron than a trigonal bipyramid, while the contrary happens for the other three polyhedra. Two of the shortest distances (1.90 and 1.98Å) are related to the hydroxyl oxygens O(5) and O(9) which are linked to only one Sb atom. Within the upper limit of 3.0Å there are few other Sb–O distances, not so far taken into consideration: however, they are very long and likely refer to very weak bonds.

The Sb–O polyhedra are tightly connected to each other by edge sharing so as to form layers parallel to (001). The values of the Sb–Sb distances between contacting polyhedra, 3.5Å or less, are similar to those found in other structures, *e.g.* in $Sb_6O_7(SO_4)_2$ (Bovin, 1976). In the unit cell there are two parallel Sb–O sheets connected by means of SO_4 tetrahedra, and indirectly by means of H-bonds. Oxygens belonging to the SO_4 group are of two kinds: O(1) and O(4) are linked also to an Sb atom, while O(2) and O(3) are acceptors of a H-bond. Consequently, S–O(1) and S–O(4) distances should be longer than S–

Table 3. Klebelsbergite: selected interatomic distances (Å) and angles (°)

Sb(1)		**Sb(3)**	
Sb(1)-O(5)	1.90(2)	Sb(3)-O(7)	2.08(2)
Sb(1)-O(6)	2.26(2)	Sb(3)-O(10)	2.01(2)
Sb(1)-O(7)	2.30(2)	Sb(3)-O(1,2)	2.48(2)
Sb(1)-O(10)	2.01(2)	Sb(3)-O(7,9)	2.00(2)
average	2.12	average	2.14
Sb(1)-O(5,7)	2.86(2)*	Sb(3)-O(2,9)	2.72(1)*
O(5)-O(6)	2.94(3)	O(7)-O(10)	2.52(3)
O(5)-O(7)	2.86(3)	O(7)-O(1,2)	4.38(3)
O(5)-O(10)	2.75(3)	O(7)-O(7,9)	2.89(2)
O(6)-O(7)	4.31(3)	O(10)-O(1,2)	2.67(2)
O(6)-O(10)	2.47(3)	O(10)-O(7,9)	2.83(3)
O(7)-O(10)	2.52(3)	O(1,2)-O(7,9)	3.09(2)
O(5)-Sb(1)-O(6)	89.2(7)	O(7)-Sb(3)-O(10)	76.2(7)
O(5)-Sb(1)-O(7)	85.4(8)	O(7)-Sb(3)-O(1,2)	148.1(7)
O(5)-Sb(1)-O(10)	89.1(7)	O(7)-Sb(3)-O(7,9)	90.2(7)
O(6)-Sb(1)-O(7)	141.3(6)	O(10)-Sb(3)-O(1,2)	72.0(6)
O(6)-Sb(1)-O(10)	70.4(6)	O(10)-Sb(3)-O(7,9)	89.8(7)
O(7)-Sb(1)-O(10)	71.2(7)	O(1,2)-Sb(3)-O(7,9)	86.6(7)
Sb(2)		**Sb(4)**	
Sb(2)-O(6)	1.94(2)	Sb(4)-O(6)	2.08(2)
Sb(2)-O(8)	2.12(2)	Sb(4)-O(8)	2.19(2)
Sb(2)-O(4,5)	2.32(2)	Sb(4)-O(9)	1.98(2)
Sb(2)-O(8,8)	2.00(2)	Sb(4)-O(10)	2.23(2)
average	2.10	average	2.12
Sb(2)-O(3,6)	2.89(2)*	Sb(4)-O(1,2)	2.96(2)*
		Sb(4)-O(9,10)	2.91(2)*
O(6)-O(8)	2.48(3)	O(6)-O(8)	2.48(3)
O(6)-O(4,5)	2.77(2)	O(6)-O(9)	2.93(3)
O(6)-O(8,8)	2.97(2)	O(6)-O(10)	2.47(3)
O(8)-O(4,5)	4.28(3)	O(8)-O(9)	2.83(3)
O(8)-O(8,8)	2.89(2)	O(8)-O(10)	4.16(3)
O(4,5)-O(8,8)	2.67(3)	O(9)-O(10)	2.95(2)
O(6)-Sb(2)-O(8)	75.2(7)		
O(6)-Sb(2)-O(4,5)	80.9(6)	O(6)-Sb(4)-O(8)	70.8(7)
O(6)-Sb(2)-O(8,8)	98.1(8)	O(6)-Sb(4)-O(9)	92.3(8)
O(8)-Sb(2)-O(4,5)	149.6(7)	O(6)-Sb(4)-O(10)	70.0(7)
O(8)-Sb(2)-O(8,8)	88.9(7)	O(8)-Sb(4)-O(9)	85.2(8)
O(4,5)-Sb(2)-O(8,8)	76.0(6)	O(8)-Sb(4)-O(10)	140.0(6)
		O(9)-Sb(4)-O(10)	88.7(7)
Hydroxyls		**S**	
O(5)-O(2,3)	2.88(3)	S-O(1)	1.53(2)
O(5)-H(1)	0.98	S-O(2)	1.49(2)
H(1)...O(2,3)	1.90	S-O(3)	1.44(2)
		S-O(4)	1.49(2)
O(9)-O(3)	2.95(3)	average	1.49
O(9)-H(2)	0.98		
H(2)...O(3)	1.97	O(1)-O(2)	2.45(2)
		O(1)-O(3)	2.45(2)
		O(1)-O(4)	2.47(3)
		O(2)-O(3)	2.41(2)
		O(2)-O(4)	2.42(2)
		O(3)-O(4)	2.38(2)
Cation-cation distances (<3.8 Å)			
Sb(1)-Sb(3)	3.35(2)		
Sb(1)-Sb(4)	3.51(2)	O(1)-S-O(2)	108.2(9)
Sb(2)-Sb(4)	3.34(3)	O(1)-S-O(3)	110.9(9)
Sb(2)-Sb(2,8)	3.49(3)	O(1)-S-O(4)	109.8(9)
Sb(2)-Sb(4,8)	3.78(3)	O(2)-S-O(3)	110.7(9)
Sb(3)-Sb(3,7)	3.56(2)	O(2)-S-O(4)	108.4(9)
		O(3)-S-O(4)	108.8(9)
S-Sb(2,4)	3.38(2)		
S-Sb(3,1)	3.40(2)		
S-Sb(3)	3.64(2)		

The equivalent positions (referred to Table 1) are designated by the second number in parentheses and are (1) = 1+x,y,z; (2)=-1+x,y,z; (3)=1-x,1-y,-1/2+z; (4)=3/2-x,y,1/2+z; (5)=3/2-x,y,-1/2+z; (6)=1/2-x,y,-1/2+z; (7)=1/2+x,1-y,z; (8)=1/2+x,-y,z; (9)=-1/2+x,1-y,z; (10)=-1/2+x,-y,z.

*Largest Sb-O distances (<3 Å).

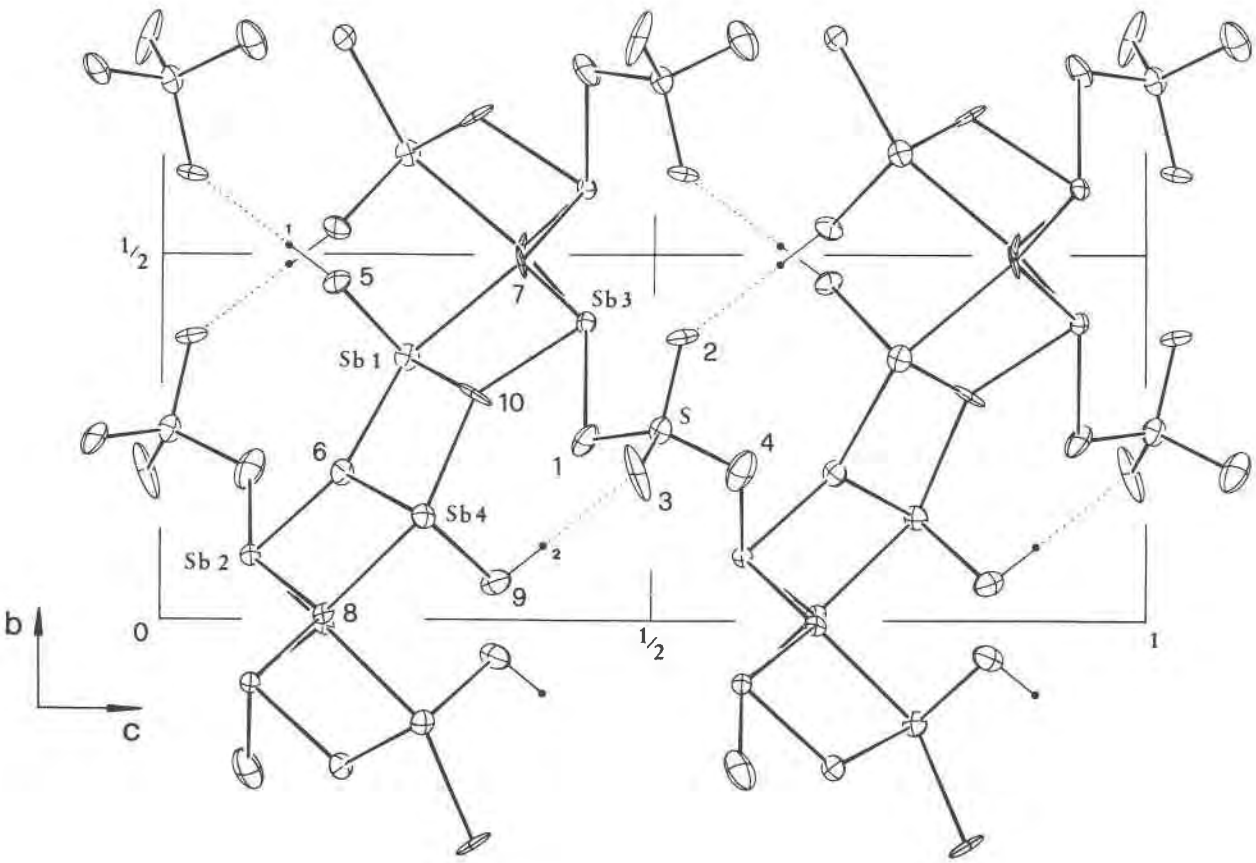

Fig. 1. Klebelsbergite: a projection of the structure down the *a* axis.

O(2) and S–O(3). However, this is not entirely fulfilled, as S–O(2) and S–O(4) distances have the same length of 1.49Å, which correspond to the S–O mean value. On the other hand, other "very weak" bonds (distances greater than 2.7Å) are present between antimony and oxygen atoms. The analysis of O–S–O angles and of O–O edges shows some distortion in the SO_4 tetrahedron. On the basis of an IR spectrum Nakai and Appleman (1980) concluded that there are several kinds of S–O bonds in klebelsbergite and that the SO_4 tetrahedron is significantly distorted. This statement is in agreement with our structural results.

As mentioned above, the connection between the sheets is also achieved by means of H-bonds between the hydroxyl oxygens O(5) and O(9) and the sulfate oxygens O(2) and O(3) respectively. The O–O distances are 2.88 and 2.95Å, so they can be considered as weak H-bonds. The interlayer bonding should on the whole be strong enough to generate good cohesion also in this direction; in fact, the mineral has no distinct cleavage (Nakai and Appleman, 1980).

This structure can be also considered on the basis of the volume occupied by each anion. For this calculation, according to Andersson *et al.* (1973), the volume of the unit cell can be simply divided by the number of anions and lone pairs. The value found in klebelsbergite, 17.3Å^3, compares well with 16.6Å^3 found in orthorhombic Sb_2O_3 (Svensson, 1974), 16.8Å^3 in $Sb_2O_3 \cdot 2SO_3$ (Mercier *et al.*, 1975), and 16.3Å^3 in $Sb_2(OH)_2(SO_4)_2 \cdot 2H_2O$ (Douglade *et al.*, 1978). Therefore in klebelsbergite anions and lone pairs are close-packed.

The electrostatic valence balance (see Table 4), computed according to Brown and Kun Wu (1976), is not fully satisfactory, especially for O(1) and O(10), which appear to be underbonded and overbonded respectively.

Klebelsbergite and the new mineral peretaite, $CaSb_4O_4(OH)_2(SO_4)_2 \cdot 2H_2O$ (Cipriani *et al.*, 1980b) are the only naturally-occurring Sb sulfates. Among the synthetic compounds, at least three anhydrous and one hydrated Sb sulfates are structurally known. None of the above compounds, however, has an

Table 4. Klebelsbergite: electrostatic valence balance

Atom	Sb(1)	Sb(2)	Sb(3)	Sb(4)	S	H(1)	H(2)	Sum
O(1)			0.33	0.15	1.31			1.79
O(2)			0.22		1.47	0.18		1.87
O(3)		0.16			1.73		0.15	2.04
O(4)		0.43			1.49			1.92
O(5)	1.07 0.17					0.82		2.06
O(6)	0.49	0.96		0.71				2.16
O(7)	0.45		0.87 0.73					2.05
O(8)		0.82 0.63		0.56				2.01
O(9)				0.90 0.16			0.85	1.91
O(10)	0.82		0.85	0.52				2.19
Sum	3.00	3.00	3.00	3.00	6.00	1.00	1.00	

atomic arrangement which, on the whole, resembles the present structure. This point is discussed in the paper dealing with the structure of peretaite (Menchetti and Sabelli, 1980).

A final noteworthy point is the presence of a marked pseudosymmetry in the Sb–O sheet. The pseudosymmetry element is an inversion center (at approximately 1/4, 1/4, 1/4 in Fig. 1) which refers Sb(1) to Sb(4), Sb(2) to Sb(3), O(6) to O(10), and so on. It is interesting to compare some "symmetrical" distances or angles. The only atoms which do not obey this "symmetry" are the sulfate oxygens, especially O(2) and O(3). The pseudocenter, of course, implies a pseudo glide plane parallel to (001), with translation $1/2\ a + 1/2\ b$, located at $c = 0$ and $1/2$ in Figure 1. With these additional elements the symmetry should be the corresponding centrosymmetrical group *Pcan*. Actually the intensities of reflections $hk0$ with $h + k = 2n$ are stronger than the intensities of the reflections with $h + k = 2n + 1$. In conclusion, with the exception of a few oxygens, the structure of klebelsbergite can be regarded as centrosymmetrical. Should this structure be twinned, as generally occurs when such a pseudosymmetry is present, the (001) plane would be the twinning plane.

References

Andersson, S., A. Åström, J. Galy and G. Meunier (1973) Simple calculation of bond lengths and bond angles in certain oxides, fluorides or oxide fluorides of Sb^{3+}, Te^{4+} and Pb^{2+}. *J. Solid State Chem., 6,* 187–190.

Bovin, J.-O. (1976) The crystal structure of the antimony (III) oxide sulfate $Sb_6O_7(SO_4)_2$. *Acta Crystallogr., B32,* 1771–1777.

Brown, I. D. and K. Kun Wu (1976) Empirical parameters for calculating cation–oxygen bond valences. *Acta Crystallogr., B32,* 1957–1959.

Cipriani, N., S. Menchetti and C. Sabelli (1980a) Klebelsbergite and another antimony mineral from Pereta, Tuscany, Italy. *Neues Jahrb. Mineral. Monatsh.*, 223–229.

———, ———, P. Orlandi and C. Sabelli (1980b) Peretaite, $CaSb_4O_4(OH)_2(SO_4)_2 \cdot 2H_2O$, a new mineral from Pereta, Tuscany, Italy. *Am. Mineral., 65,* 936–939.

Douglade, J., R. Mercier and H. Vivier (1978) Structure cristalline de $Sb_2(OH)_2(SO_4)_2 \cdot 2H_2O$. *Acta Crystallogr., B34,* 3163–3168.

Galy, J., G. Meunier, S. Andersson and A. Åström (1975) Stéréochimie des éléments comportant des paires non liées: Ge(II), As(III), Se(IV), Br(V), Sn(II), Sb(III), Te(IV), I(V), Xe(VI), Tl(I), Pb(II) et Bi(III) (oxydes, fluorures et oxyfluorures). *J. Solid State Chem., 13,* 142–159.

International Tables for X-ray Crystallography, Vol. IV (1974) Kynoch Press, Birmingham, England.

Main, P., M. M. Woolfson, L. Lessinger, G. Germain and J. P. Declercq (1974) *MULTAN 74. A System of Computer Programs for the Automatic Solution of Crystal Structures from X-ray Diffraction Data.* Universities of York, England, and Louvain-la-Neuve, Belgium.

Menchetti, S. and C. Sabelli (1980) Peretaite, $CaSb_4O_4(OH)_2(SO_4)_2 \cdot 2H_2O$: its atomic arrangement and twinning. *Am. Mineral., 65,* 940–946.

Mercier, R., J. Douglade and F. Theobald (1975) Structure cristalline de $Sb_2O_3 \cdot 2SO_3$. *Acta Crystallogr., B31,* 2081–2085.

Nakai, I. and D. E. Appleman (1980) Klebelsbergite, $Sb_4O_4(OH)_2SO_4$: redefinition and synthesis. *Am. Mineral., 65,* 499–505.

North, A. C. T., D. C. Phillips and F. S. Mathews (1968) A semi-empirical method of absorption correction. *Acta Crystallogr., A24,* 351–359.

Svensson, C. (1974) The crystal structure of orthorhombic antimony trioxide, Sb_2O_3. *Acta Crystallogr., B30,* 458–461.

Zsivny, V. (1929) Klebelsbergit, egy új ásvány Felsöbányáról. *Mat. Termès. Ért., 46,* 19–24. (Abstract in *Mineral. Abstr., 4,* 150, 1929).

Manuscript received, April 2, 1980;
accepted for publication, April 22, 1980.

American Mineralogist, Volume 65, pages 936-939, 1980

Peretaite, $CaSb_4O_4(OH)_2(SO_4)_2 \cdot 2H_2O$, a new mineral from Pereta, Tuscany, Italy

NICOLA CIPRIANI, SILVIO MENCHETTI

Istituto di Mineralogia dell'Università
Via La Pira 4, 50121 Firenze, Italy

PAOLO ORLANDI

Istituto di Mineralogia e Petrografia dell'Università
Via S. Maria 53, 56100 Pisa, Italy

AND CESARE SABELLI

CNR Centro di Studio per la Mineralogia e le Geochimica dei sedimenti
Istituto di Mineralogia dell'Università
Via La Pira 4, 50121 Firenze, Italy

Abstract

Peretaite, a new calcium and antimony sulfate mineral, occurs as aggregates of colorless tabular crystals in the antimony-bearing vein at Pereta, Tuscany, Italy. It is monoclinic, space group $C2/c$, with $a = 24.641$, $b = 5.598$, $c = 10.180$Å, $\beta = 95.95°$. The calculated density is 4.06 g cm^{-3}. The cleavage {100} is perfect. Crystals are always twinned (100). Peretaite is biaxial (+) with mean refractive index 1.841. The five strongest lines in the X-ray diffraction pattern are (d in Å, I, hkl): 12.19 *100* 200; 6.12 *21* 400; 3.10 *24* $\bar{5}12$; 3.06 *67* 800; 2.451 *31* 10.00. On the basis of the wet-chemical analysis, the IR spectroscopy, the TGA spectrum, and especially the structure determination, the chemical formula is $CaSb_4O_4(OH)_2(SO_4)_2 \cdot 2H_2O$.

Introduction

In a paper dealing with a new find of klebelsbergite (Cipriani *et al.*, 1980), some of us pointed out that a new mineral is present among the accessory minerals of the antimony-bearing vein at Pereta, Tuscany, Italy. Further study fully confirmed the thesis.

The new species, $CaSb_4O_4(OH)_2(SO_4)_2 \cdot 2H_2O$, is named peretaite for the locality. Both the mineral and the name have been approved by the Commission on New Minerals and Mineral Names, IMA. Type specimens are deposited in the mineralogical museums of Florence University (regional collection, #164/I) and Pisa University.

Occurrence and paragenesis

The environment where peretaite was found has been described by Cipriani *et al.* (1980). Peretaite occurs, in small quantities, as aggregates of tabular crystals in the geodes of a deeply silicified limestone from "Calcare Cavernoso," and also in the cavities of columnar stibnite. Crystals of peretaite associated with acicular crystals of klebelsbergite are shown in Figure 1. Other associated minerals are stibnite, quartz, calcite, pyrite, valentinite, kermesite, sulfur, and gypsum. Aggregates of klebelsbergite crystals and rarely of peretaite are often red from incrustations of valentinite. Unlike klebelsbergite, which was found rather abundantly in the fissures of the stibnite veinlets, peretaite occurs closer to the boundary with limestones. The mineral, as well as klebelsbergite, has apparently been formed by the action of sulfuric acid on stibnite; the source of the calcium in peretaite is likely the limestone of the country rock.

Chemistry

Preliminary qualitative analyses of peretaite were made with an ORTEC X-ray microanalyzer and an ARL SEMQ electron microprobe. However, since the crystals decompose under the electron beam, microprobe results were considered not reliable for a quan-

0003-004X/80/0910-0936$02.00

Fig. 1. Crystals of peretaite associated with acicular crystals of klebelsbergite; the largest crystal is 1.5 mm long (photo P. B. Scortecci).

titative determination, especially for sulfur. Therefore a wet-chemical analysis was performed. About 20 mg of purified material was dissolved in 1:5 HCl and diluted to 25 ml with distilled water. Calcium was determined by atomic absorption spectrometry, using a Perkin Elmer 303 instrument. Antimony was determined by alternating current anodic stripping voltammetry, on hanging-drop mercury electrode in 1M HCl. Total sulfur was potentiometrically titrated with $Pb(ClO_4)_2$ and an ORION 94-82 lead ion electrode. The water content was inferred from a TGA spectrum. The result, given in Table 1, corresponds

Table 1. Chemical analysis of peretaite. All values are weight percent

Oxide	(1)	(2)
Sb_2O_3	68.31	69.09
CaO	6.58	6.44
SO_3	18.78	17.62
H_2O	6.33	6.0
	100.00	99.15

(1) Ideal peretaite

(2) From analytical results

Table 2. X-ray powder diffraction data for peretaite; *d* values are in Å

I/I_o	d_{obs}	d_{calc}	h k l	I/I_o	d_{obs}	d_{calc}	h k l
100	12.19	12.254	2 0 0	31	2.451	2.451	10 0 0
21	6.12	6.127	4 0 0			2.449	9 1 0
16	5.45	5.457	1 1 0	17	2.068	2.066	8 2 0
5	4.85	4.851	-1 1 1			2.070	11 1 0
4	4.76	4.758	1 1 1	3	2.059	2.059	-8 0 4
5	4.08	4.085	6 0 0			2.058	6 0 4
5	3.68	3.688	5 1 0	16	1.878	1.878	-2 2 4
2	3.55	3.556	-5 1 1			1.877	0 2 4
11	3.51	3.516	-3 1 2	3	1.858	1.859	8 0 4
3	3.38	3.381	5 1 1			1.860	-10 0 4
5	3.35	3.354	-6 0 2	5	1.844	1.844	10 2 0
12	3.31	3.316	3 1 2	4	1.710	1.710	-14 0 2
24	3.10	3.098	-5 1 2	3	1.699	1.700	3 3 2
67	3.06	3.064	8 0 0	4	1.684	1.684	-11 1 4
4	3.03	3.029	6 0 2	2	1.668	1.668	-5 3 2
4	2.967	2.968	7 1 0	1	1.609	1.609	-12 2 2
14	2.874	2.876	5 1 2	2	1.604	1.604	14 0 2
12	2.799	2.799	0 2 0	2	1.582	1.582	-5 1 6
13	2.727	2.729	2 2 0	2	1.556	1.556	3 1 6
5	2.696	2.698	0 2 1	2	1.549	1.549	8 2 4
20	2.532	2.532	-2 0 4	6	1.532	1.532	16 0 0
		2.531	0 0 4	1	1.511	1.510	-16 0 2
				4	1.397	1.396	17 1 0

to $Ca_{1.01}Sb_{4.17}S_{1.94}O_{16}H_{5.86}$ on the basis of 16 oxygens, or ideally $CaSb_4^{3+}O_4(OH)_2(SO_4)_2 \cdot 2H_2O$ from the structural results and the infrared spectrum. Indeed, both the structural determination and the IR spectroscopy gave clear indications, the first without any doubt, on the presence of sulfate groups as well as of H-bonded water molecules and hydroxyl groups.

Crystallography

X-ray single-crystal study (Weissenberg camera and single-crystal diffractometer) indicated Laue symmetry $2/m$. Systematic extinctions are consistent with the space groups $C2/c$ or Cc. The former, however, is the correct one from the structural study (Menchetti and Sabelli, 1980b). All the examined crystals appeared to be twinned with (100) as twin plane.

The X-ray powder diffraction pattern (Table 2) was obtained by means of a Philips diffractometer, with Co$K\alpha$ radiation, NaF as internal standard, and 0.25° per min scanning speed. Indexing was per-

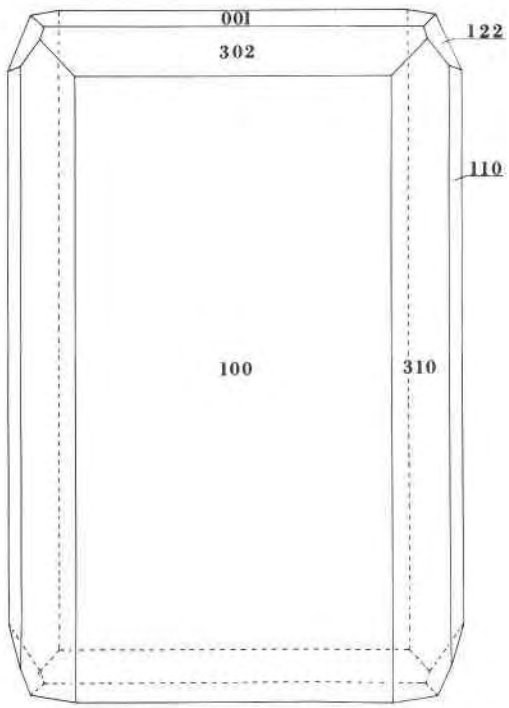

Fig. 2. Typical habit of a peretaite crystal.

formed on the basis of single-crystal data and taking into account the intensities of the reflections collected for the structural study. In the powder pattern there is a systematic enhancement of the intensities of $h00$ reflections because of a preferential orientation due to the {100} cleavage. The unit-cell parameters, determined from powder data by means of least-squares calculations, are: $a = 24.641(2)$, $b = 5.598(2)$, $c = 10.180(1)$Å, $\beta = 95.95(1)°$.[1]

Peretaite crystals appear flattened (100) and sometimes elongated [001]. Two typical habits of peretaite are shown in Figures 2 and 3. The observed forms are {100}, {310}, {110}, {122}, {001}, {010}, {210}, {$\bar{2}$01}, {302}, and {601}. The largest crystals have dimensions up to 5 × 2 × 0.5 mm.

Physical properties

Crystals of peretaite are transparent and colorless, with vitreous luster and {100} cleavage. A density >3.8 g cm^{-3} was determined by the heavy-liquid method; crystals seem to float in Clerici solution with a density of about 4.0 g cm^{-3}. The calculated density (for the ideal formula) is 4.06 g cm^{-3}. The microindentation hardness (VHN) with a 15-g load is between 170 and 190 kg mm^{-2}.

Crystals are optically biaxial positive (+) with a very large axial angle. The value of $2E\alpha$ measured with a universal stage, using hemispheres with refraction index of 1.649, is nearly 102°. The optical plane is parallel to (010). By the prism method [(100) ∧ ($\bar{3}$10)] a first index of refraction of 1.841(1) was measured. The corresponding vibration direction makes an angle of about 28° with the b axis. A second index of 1.935(1) was measured for a vibration direction almost parallel to c. The mean index of refraction calculated from the Gladstone–Dale relationship, using the ideal chemical formula, the calculated density, and the constants given by Mandarino (1976), is 1.841.

The TGA spectrum (taken under nitrogen atmosphere) shows a weight loss of about 6%, which is attributed to a dehydration reaction including both H_2O and OH. The tracing is not very sharp; however, it seems possible to identify two successive steps in the temperature range 200–240°C. This temperature is about 60–70°C lower than that found for the corresponding effect in klebelsbergite. In the latter, however, only OH groups are present.

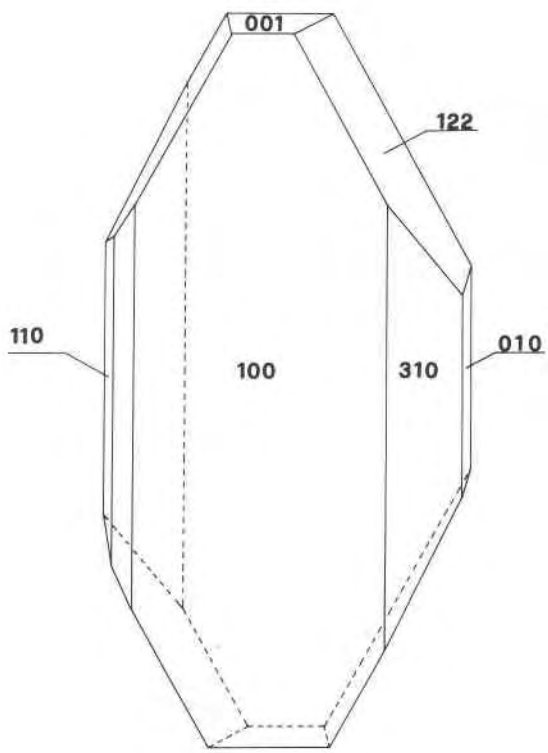

Fig. 3. Another frequently encountered crystal habit. Sometimes the form {001} is lacking.

[1] Lattice parameters used in the crystal structure determination are those measured with a single-crystal diffractometer. They are $a = 24.665(4)$, $b = 5.6006(9)$, $c = 10.185(1)$Å, $\beta = 95.98(1)°$.

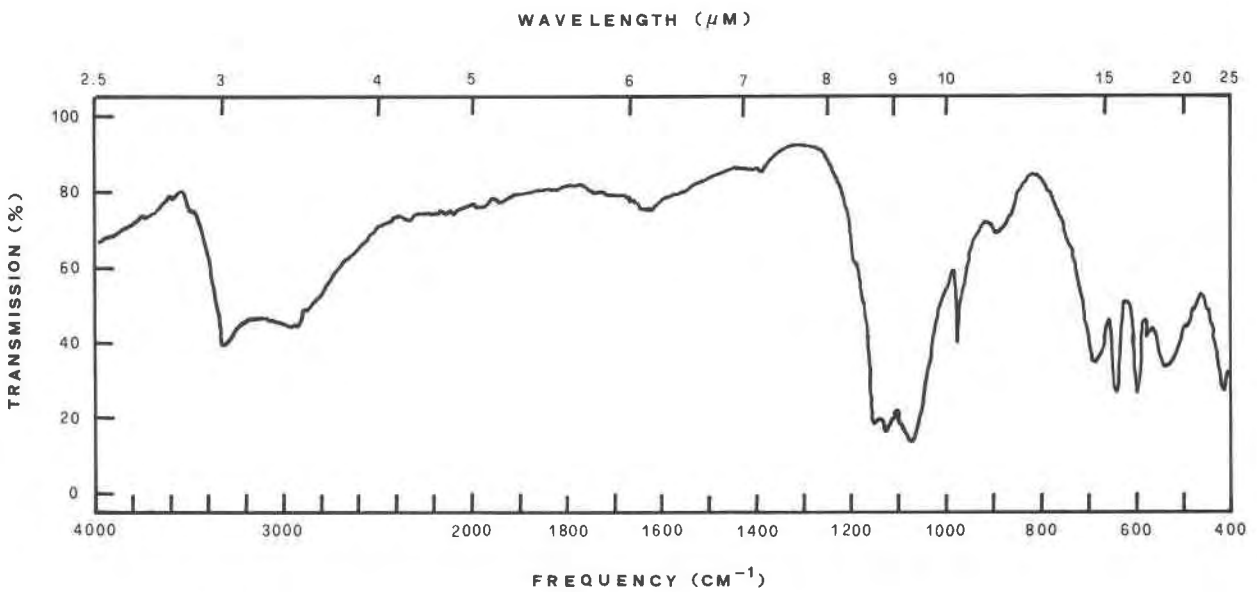

Fig. 4. Infrared absorption spectrum of peretaite.

The infrared spectrum was obtained from a potassium bromide disc containing peretaite. The pellet was heated at 120°C for two hours. The spectrum, taken from 4000 to 400 cm^{-1}, is shown in Figure 4. The sharp absorption at 3310 cm^{-1} due to the O–H stretching mode supports the presence of hydroxyl groups, with H-bonds stronger than that of klebelsbergite, which has the same peak at 3435 cm^{-1}. The occurrence of a very broad band, ranging from 3500 to 2500 cm^{-1} with a maximum at about 3000 cm^{-1}, and of a weak band at 1640 cm^{-1}, indicates the presence of water of hydration with strong H-bonds. In klebelsbergite the corresponding peaks are absent: in the structure of this mineral there are no water molecules (Menchetti and Sabelli, 1980a). Of the SO_4^{2-} stretching vibrations, ν_3, ν_1, and ν_4 were observed, at frequencies slightly different from klebelsbergite. The presence of ν_1 (at 975 cm^{-1}) shows that the sulfate tetrahedron is distorted. In addition ν_1 appears as a single peak and ν_3 shows fewer structures than in klebelsbergite: this may be due to the presence of the inversion center in the structure of peretaite and to more strict selection rules.

Acknowledgments

We thank the SAMIN SpA Company (F. Principato) for sampling permission, G. Sbrana and V. Schettino for obtaining and interpreting the infrared spectrum, and A. Bencini, P. Cellini Legittimo, and G. Piccardi for the chemical analysis.

References

Cipriani, N., S. Menchetti and C. Sabelli (1980) Klebelsbergite and another antimony mineral from Pereta, Tuscany, Italy. *Neues Jahrb. Mineral. Monatsh.*, 223–229.

Mandarino, J. A. (1976) The Gladstone–Dale relationship—Part I. Derivation of new constants. *Can. Mineral., 14,* 498–502.

Menchetti, S. and C. Sabelli (1980a) The crystal structure of klebelsbergite, $Sb_4O_4(OH)_2SO_4$. *Am. Mineral., 65,* 931–935.

——— and ——— (1980b) Peretaite, $CaSb_4O_4(OH)_2(SO_4)_2 \cdot 2H_2O$: its atomic arrangement and twinning. *Am. Mineral., 65,* 940–946.

Manuscript received, April 2, 1980;
accepted for publication, April 22, 1980.

American Mineralogist, Volume 65, pages 940-946, 1980

Peretaite, $CaSb_4O_4(OH)_2(SO_4)_2 \cdot 2H_2O$: its atomic arrangement and twinning

SILVIO MENCHETTI AND CESARE SABELLI

CNR, Istituto di Mineralogia dell'Università
Via La Pira 4, 50121 Firenze, Italy

Abstract

Peretaite, $CaSb_4O_4(OH)_2(SO_4)_2 \cdot 2H_2O$, crystallizes in the monoclinic space group $C2/c$, with $a = 24.665$, $b = 5.6006$, $c = 10.185$Å, $\beta = 95.98°$. The structure was determined by Patterson and direct methods and refined by least-squares technique to a final R index of 0.037. The dominant structural feature is the arrangement of the two independent Sb polyhedra into sheets parallel to (100). The Ca ion is coordinated by six O and two H_2O in a square antiprism. These polyhedra are edge- and corner-linked to SO_4 groups into chains which run parallel to the Sb–O sheets. The hydroxyl groups form hydrogen bonds between Sb–O sheets and Ca–S chains; these bonds provide for the three-dimensional cohesion of the structure. An interpretation of twinning with (100) as twin plane is given.

Introduction

Peretaite is a new sulfate of antimony and calcium found at Pereta, Tuscany, Italy. Its chemical formula, $CaSb_4O_4(OH)_2(SO_4)_2 \cdot 2H_2O$, and other mineralogical data have been reported in the preceding article (Cipriani *et al.*, 1980). It occurs as aggregates of tabular crystals, associated with quartz, pyrite, calcite, sulfur, gypsum, and other antimony minerals, stibnite, valentinite, kermesite, and klebelsbergite. Klebelsbergite and peretaite are the only two Sb sulfate minerals so far known.

This study was undertaken to solve the crystal structure of peretaite and to investigate its possible crystal-chemical relationships with the structures of klebelsbergite (Menchetti and Sabelli, 1980) and of other synthetic Sb sulfates such as the anhydrous $Sb_2O_3 \cdot 2SO_3$ (Mercier *et al.*, 1975), $Sb_2O_3 \cdot 3SO_3$ (Mercier *et al.*, 1976), $Sb_6O_7(SO_4)_2$ (Bovin, 1976), and the hydrate $Sb_2(OH)_2(SO_4)_2 \cdot 2H_2O$ (Douglade *et al.*, 1978).

Experimental

For the X-ray structure analysis a small tabular crystal (approx. $0.1 \times 0.4 \times 0.2$ mm) was taken from an original sample of peretaite. Monoclinic symmetry and possible space groups $C2/c$ and Cc were determined by Weissenberg photographs. The centrosymmetric space group $C2/c$ was chosen for the structure determination and was subsequently found to be correct. The unit-cell dimensions, determined from 25 high-angle reflections measured on a four-circle automatic diffractometer, are $a = 24.665(4)$, $b = 5.6006(9)$, $c = 10.185(1)$Å, $\beta = 95.98(1)°$.

The sample used for intensity data collection and all other crystals tested for X-ray work were found to be twinned. Figure 1 reports the reflection population due to the whole twinned crystal and referred to reciprocal lattice levels with $k = 2n$ (levels with $k = 2n+1$ can be represented by a similar scheme with h-odd lattice points occupied instead of h-even ones). One can readily see that overlapping of points from the two individuals takes place only in the lattice rows with $l = 4n$. From the intensities of 363 pairs of well-separated reflections (with $l = 4n + 2$) the relative volumes of the two members of the twin were easily computed. The knowledge of the volume ratio so determined (A/B = 3.55±0.02) allowed the composite intensities of the overlapped reflections to be subdivided into the intensities of A and B individuals, by solving the following equations:

$$I_{hkl} = I^{A}_{hkl} + I^{B}_{h'k'l'}$$

$$I_{h'k'l'} = I^{A}_{h'k'l'} + I^{B}_{hkl}$$

where I is the observed intensity of the twinned crystal and I^A and I^B are the intensities of the two superimposed reflections; h,k,l are the Miller indices of reflections belonging to the A individual and $h' = -(h + \frac{l}{2})$, $k' = k$, $l' = l$ those of overlapped reflections of the B individual of the twin. In conclusion, according to Friedel's (1926) notation, the crystals of peretaite

0003–004X/80/0910–0940$02.00

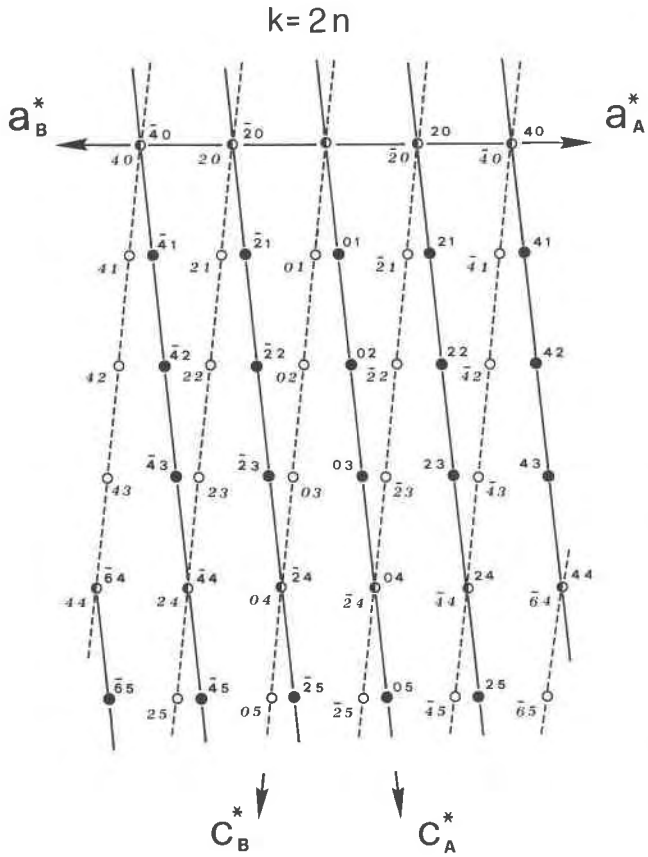

Fig. 1. A layer of the reciprocal lattice of the twinned peretaite. Numbering refers to h and l Miller indices, with $k = 2n$. The black-dotted lattice belongs to a member of the twin (A individual), the open-circled lattice to the other (B individual).

are twinned by pseudo-merohedry, with twin plane (100), twin index 4, and twin obliquity 0.05°.

Intensities were collected on a Philips PW-1100 four-circle computer-controlled diffractometer (Centro di Cristallografia Strutturale del CNR, Pavia, Italy), with graphite-monochromated Mo$K\alpha$ radiation, ω–2θ scan technique, integration width of 1.5° and scan speed of 0.1°/sec.

A total of 2044 symmetry-independent reflections were measured within the limit of $2\theta \leq 30°$; only 1808 reflections with $F_o > 5\sigma(F_o)$, with σ derived from counting statistics, were regarded as observed. The intensities were corrected for Lorentz and polarization factors and for absorption, the latter being carried out on the basis of the semiempirical method proposed by North *et al.* (1968).

Structure determination and refinement

The four heavy-atom positions were determined by direct methods using the computer program MULTAN (Main *et al.*, 1974). The 250 largest normalized structure amplitudes ($E > 1.52$) were selected as input for the phase determination. Because of their particular coordinates, the heavy atoms (mainly the antimony atoms) contribute, in the structure-factor calculation, almost entirely to the reflections with $l = 2n$. For this reason, in order to derive indications about the oxygen atom locations, a three-dimensional Patterson synthesis with l-odd reflections only was computed. The introduction of the oxygen positions, recognized in this map, in the structure-factor calculation allowed the l-odd reflections also to take a sign. In the next Fourier map all missing oxygen atoms were located and two cycles of isotropic full-matrix least-squares refinement led to $R = 0.07$. The observed structure factors were weighted by $1/\sigma^2(F_o)$. A difference Fourier synthesis calculated after a cycle of anisotropic refinement ($R = 0.037$) yielded the positions of hydrogen atoms. Subsequent least-squares refinement was carried out using isotropic temperature factors fixed at 4Å^2 for hydrogen atoms. Because of inconsistencies in their shifts, the hydrogen atom positions could not be refined. The last cycle achieved convergence at $R = 0.035$ for the observed reflections and $R = 0.041$ including "less thans." The scattering factors for all atoms and the anomalous dispersion coefficients for heavy atoms were taken from *International Tables for X-ray Crystallography* (1974, p. 99–101, 148–151).

The atomic positional and thermal parameters are listed in Table 1, and a list of observed and calculated structure factors appears in Table 2.[1]

Description and discussion of the structure

There has been remarkable interest in recent years in the coordination of the Sb atom in Sb^{3+}–O compounds. For a general treatment of this matter we refer to the works by Andersson *et al.* (1973) and Galy *et al.* (1975), and also to the discussions of the structures of $Sb_6O_7(SO_4)_2$ (Bovin, 1976) and of klebelsbergite $Sb_4O_4(OH)_2SO_4$ (Menchetti and Sabelli, 1980).

Taking into account the lone pairs of electrons (E) in peretaite, the volume per oxygen and E is 17.4Å^3. This figure compares well with the values found in many Sb^{3+}–O compounds, and in this way peretaite also can be described as a structure having a close-packing of anions and lone pairs.

[1] To receive a copy of Table 2, order Document AM-80-139 from the Business Office, Mineralogical Society of America, 2000 Florida Avenue, N.W., Washington, D.C. 20009. Please remit $1.00 in advance for the microfiche.

Table 1. Peretaite: fractional atomic coordinates and thermal parameters

Atom	x	y	z	B eq.*	β_{11}	β_{22}	β_{33}	β_{12}	β_{13}	β_{23}
Sb(1)	0.29249(2)	0.50504(7)	0.51525(4)	0.79	2(0)	72(1)	23(1)	1(0)	2(0)	16(1)
Sb(2)	0.31537(2)	0.05196(6)	0.26706(4)	0.65	3(0)	48(1)	18(1)	2(0)	2(0)	-1(1)
Ca	0.50	0.1856(3)	0.25	0.92	3(0)	83(5)	22(2)	-	1(1)	-
S	0.4201(1)	-0.0163(2)	0.5184(1)	0.94	3(0)	83(4)	23(1)	-1(1)	1(1)	4(2)
O(1)	0.3600(2)	0.0049(9)	0.5276(5)	2.00	3(1)	253(18)	49(5)	3(3)	3(2)	1(8)
O(2)	0.4296(2)	0.0463(8)	0.3829(4)	1.55	6(1)	142(15)	36(4)	1(3)	4(2)	28(6)
O(3)	0.4511(2)	0.1391(8)	0.6159(4)	1.70	8(1)	121(14)	40(5)	3(3)	-3(2)	-23(6)
O(4)	0.4378(2)	-0.2635(7)	0.5487(4)	1.52	10(1)	65(12)	33(4)	1(3)	-1(2)	7(6)
O(5)	0.4446(2)	0.5206(7)	0.3043(4)	1.30	5(1)	90(13)	39(4)	-4(2)	3(1)	-5(6)
O(6)	0.2609(2)	0.1778(7)	0.3871(4)	0.59	1(1)	68(11)	18(4)	-2(2)	4(1)	-1(5)
O(7)	0.2625(2)	0.1787(6)	0.1146(4)	0.56	2(1)	52(11)	11(3)	-3(2)	-1(1)	3(5)
O(8)	0.3394(2)	0.3860(7)	0.2667(4)	1.05	3(1)	66(11)	41(4)	-3(2)	2(1)	1(6)
H(1)	0.450	0.600	0.210	4.00						
H(2)	0.450	0.660	0.380	4.00						
H(3)	0.382	0.420	0.285	4.00						

*Equivalent isotropic B ($Å^2$) calculated from anisotropic temperature factors, except for H(1), H(2) and H(3) where B was not refined.

Form of anisotropic temperature factors ($\times 10^4$): $\exp -(\beta_{11}h^2+\beta_{22}k^2+\beta_{33}l^2+2\beta_{12}hk+2\beta_{13}hl+2\beta_{23}kl)$

Selected interatomic distances and angles are reported in Table 3. In peretaite there are two crystallographically distinct Sb polyhedra. The Sb(1) polyhedron (of SbO_4E type) shows a trigonal bipyramidal arrangement with one of the equatorial corners occupied by the lone pair *E*. The two axial Sb–O distances are somewhat different (2.206 and 2.336Å), but their mean value of 2.271Å, as well as the values of 98.0° and 141.0° (equatorial and axial angles) correspond well to 2.27Å, 92.2°, and 151.5°, the respective values of the theoretically derived model (Galy *et al.*, 1975).

On the contrary, the Sb(2) polyhedron is of the SbO_3E type and can be described as a tetrahedron with the lone pair at one corner and O(6), O(7), and O(8) on the others. As one can see in Table 1, both Sb–O and O–O distances show a narrow range of variation, as well as O–Sb–O and O–O–O angles; this constancy agrees with a tetrahedral approximation of the polyhedron.

Each Sb(1) polyhedron shares edges with two symmetry-equivalent Sb(1) polyhedra (through the symmetry centers at 1/4, 1/4, 1/2 and 1/4, 3/4, 1/2), to form edge-by-edge chains running in the *b* direction. The oxygens of Sb(2) polyhedron are: O(6) belonging to a chain, O(7) of the adjacent chain, and the hydroxyl oxygen O(8). In this way Sb(1) chains result cross-linked by the Sb(2) polyhedra, to make dense Sb–O sheets. These sheets, two per unit cell and parallel to (100), account for the platy habit of the crystals. A view of the structure looking along the sheets is shown in Figure 2.

The calcium atom, on the two-fold axis, binds three pairs of sulfate oxygens and one pair of water oxygen, to form a distorted square antiprism (Fig. 2). Ca–O distances range from 2.419 to 2.508Å. Each Ca polyhedron is connected to four surrounding SO_4 groups by edge and corner sharing. This linkage produces Ca–S zig-zag chains running in the *c* direction (Fig. 3). Connections between Ca–S are provided by H-bonds, with O(5) water oxygen acting as donor and O(3) and O(4) as acceptors.

The formula unit of peretaite can be regarded as the summation of a formula unit of klebelsbergite

Table 3. Peretaite: selected interatomic distances (Å) and angles (°)

Sb(1)			
Sb(1)-O(6,3)	2.011(4)		
Sb(1)-O(7,5)	2.040(4)		
Sb(1)-O(7,6)	2.206(4)		
Sb(1)-O(6)	2.336(4)		
average	2.148		
Sb(1)-O(8,6)	2.766(4) ◆		
Sb(1)-O(8)	2.967(5) ◆		
O(6)-O(6,3)	2.547(6)		
O(6)-O(7,5)	2.863(5)		
O(6)-O(7,6)	4.283(6)		
O(6,3)-O(7,5)	3.056(6)		
O(6,3)-O(7,6)	2.854(5)		
O(7,5)-O(7,6)	2.484(5)		
O(6)-Sb(1)-O(6,3)		71.3(1)	
O(6)-Sb(1)-O(7,5)		81.4(1)	
O(6)-Sb(1)-O(7,6)		141.0(1)	
O(6,3)-Sb(1)-O(7,5)		98.0(2)	
O(6,3)-Sb(1)-O(7,6)		85.0(2)	
O(7,5)-Sb(1)-O(7,6)		71.5(1)	

Sb(2)			
Sb(2)-O(8)	1.963(4)		
Sb(2)-O(6)	2.035(4)		
Sb(2)-O(7)	2.048(4)		
average	2.015		
Sb(2)-O(1)	2.778(5) ◆		
Sb(2)-O(1,8)	2.796(5) ◆		
Sb(2)-O(2)	2.938(5) ◆		
O(8)-O(6)	2.666(6)		
O(8)-O(7)	2.594(6)		
O(6)-O(7)	2.779(5)		
O(8)-Sb(2)-O(6)		83.6(2)	
O(8)-Sb(2)-O(7)		80.6(2)	
O(6)-Sb(2)-O(7)		85.8(2)	
O(7)-O(6)-O(8)		56.9(1)	
O(6)-O(7)-O(8)		59.3(1)	
O(6)-O(8)-O(7)		63.8(2)	

Ca			
2 Ca-O(5)	2.419(5)		
2 Ca-O(2)	2.440(5)		
2 Ca-O(4)	2.468(4)		
2 Ca-O(3,2)	2.508(5)		
average	2.459		
O(5)-Ca-O(2)		70.7(2)	
O(5)-Ca-O(4,2)		89.4(2)	
O(5)-Ca-O(3,2)		133.6(1)	
O(5)-Ca-O(2,4)		145.8(2)	
O(5)-Ca-O(4,8)		74.7(1)	
O(5)-Ca-O(3,8)		115.8(2)	
O(5)-Ca-O(5,4)		78.3(2)	
O(2)-Ca-O(4,2)		90.7(2)	
O(2)-Ca-O(3,2)		78.2(2)	
O(2)-Ca-O(2,4)		142.7(2)	
O(2)-Ca-O(4,8)		95.7(2)	
O(2)-Ca-O(3,8)		74.9(2)	
O(4,4)-Ca-O(3,2)		56.9(1)	
O(4,4)-Ca-O(4,8)		159.6(2)	
O(4,4)-Ca-O(3,8)		143.4(2)	
O(3,4)-Ca-O(3,8)		87.0(2)	

S			
S-O(2)	1.466(5)		
S-O(3)	1.473(5)		
S-O(4)	1.475(4)		
S-O(1)	1.500(5)		
average	1.479		
O(2)-O(3)	2.433(6)		
O(2)-O(4)	2.415(6)		
O(2)-O(1)	2.387(7)		
O(3)-O(4)	2.396(6)		
O(3)-O(1)	2.449(7)		
O(4)-O(1)	2.429(7)		
O(2)-S-O(3)		111.8(3)	
O(2)-S-O(4)		110.4(3)	
O(2)-S-O(1)		107.2(3)	
O(3)-S-O(4)		107.0(3)	
O(3)-S-O(1)		111.0(3)	
O(4)-S-O(1)		109.5(3)	

H(1)-O(5)-H(2) water		
O(5)-O(3,7)	2.721(6)	
O(5)-H(1)	1.08	
H(1)...O(3,7)	1.75	
O(5)-O(4,1)	2.789(6)	
O(5)-H(2)	1.10	
H(2)...O(4,1)	1.83	
O(3,7)-O(5)-O(4,1)		109.8(2)
H(1)-O(5)-H(2)		108
O(5)-H(1)...O(3,7)		147
O(5)-H(2)...O(4,1)		144

O(8)-H(3) hydroxyl		
O(8)-O(5)	2.691(6)	
O(8)-H(3)	1.07	
H(3)...O(5)	1.64	
O(8)-H(3)...O(5)		170

Cation-cation distances (<3.8 Å)	
Sb(1)-Sb(1,9)	3.447(2)
Sb(1)-Sb(1,3)	3.538(2)
Sb(1)-Sb(2,6)	3.571(2)
Sb(1)-Sb(2,3)	3.650(2)
Sb(1)-Sb(2)	3.997(2)
Sb(1)-Sb(2,5)	3.718(2)
Sb(2)-S	3.463(2)
Ca-S(,2)	3.063(2)
Ca-S	3.709(2)

The equivalent positions (referred to Table 1) are designated by the second number in parentheses and are (1) = x,1+y,z; (2) = 1-x,-y,1-z; (3) = 1/2-x,1/2-y,1-z; (4) = 1-x,y,1/2-z; (5) = 1/2-x,1/2+y,1/2-z; (6) = x,1-y,1/2+z; (7) = x,1-y,-1/2+z; (8) = x,-y,-1/2+z; (9) = 1/2-x,3/2-y,1-z.

◆Largest Sb-O distances (<3 Å).

with a formula unit of gypsum. Each calcium atom in gypsum, as in peretaite, is surrounded by one pair of water molecules and by three pairs of oxygen atoms belonging to SO_4 groups. Moreover the *a* axis of gypsum (5.670Å) is comparable with the *b* axis of peretaite (5.6006Å). However, there are no other similarities between the structures of these two minerals. In gypsum (Cole and Lancucki, 1974) the Ca polyhedra are directly and strictly linked to each other to form chains, connected in their turn by SO_4 groups to form sheets. In peretaite on the contrary the Ca polyhedra are isolated and form chains by the connection with SO_4 tetrahedra.

The sulfate group shows the usual tetrahedral configuration, slightly distorted. The longest S–O distance involves O(1), which is further "bonded" twice

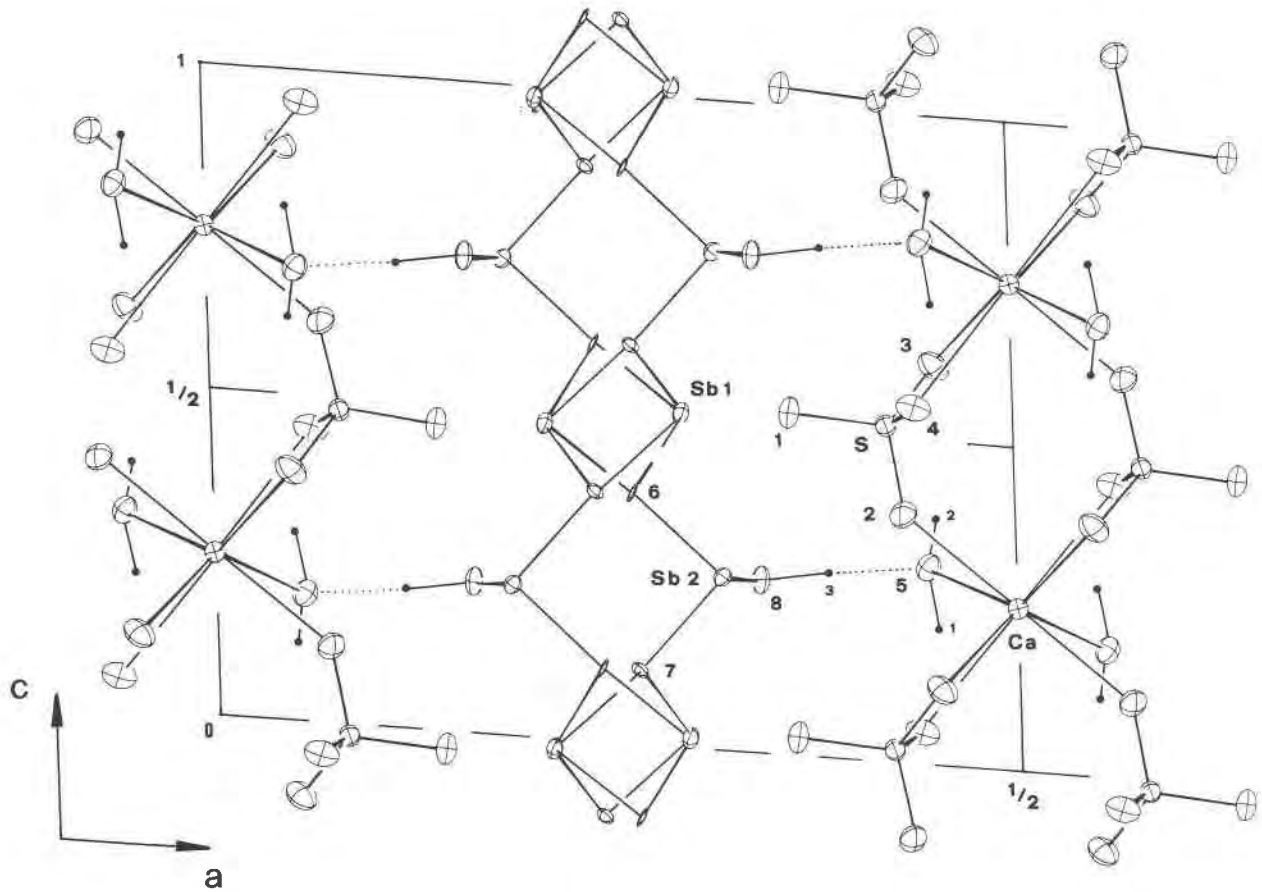

Fig. 2. The structure of peretaite projected down the *b* axis. Thermal ellipsoids are scaled at the 50% probability.

to the Sb(2) atom. Since these Sb(2)–O(1) distances (2.778 and 2.796Å) are to be considered very weak bonds, a shorter S–O(1) distance would be expected. The charge deficiency of O(1) is clearly shown by the electrostatic valence balance (Table 4), computed according to Brown and Kun Wu (1976). A similar imbalance was also observed for the sulfate oxygens of klebelsbergite.

As already said, the hydrogen atoms of the water molecule make two H-bonds among the Ca polyhedra. The water oxygen O(5) in turn is the recipient of a third H-bond from the donor O(8). The hydroxyl oxygen belongs to the Sb–O sheet, and its role is particularly relevant for the cohesion of the structure. In fact this H-bond is the only "strong" bond between Sb–O sheets and Ca–S chains. The antimony–oxygen interaction due to Sb(2)–O very weak bonds (2.778, 2.796, and 2.938Å) and some van der Waals interactions further contribute to hold the structure together.

This kind of three-dimensional connection, based on two-dimensional Sb–O elements, is different from that found in the structures of the known Sb sulfates. The structure of $Sb_2O_3 \cdot 2SO_3$ (Mercier *et al.*, 1975) consists of molecular units linked to each other by van der Waals interactions and can then be considered as a molecular structure. The atomic arrangement of $Sb_2(OH)_2(SO_4)_2 \cdot 2H_2O$ (Douglade *et al.*, 1978) is also organized in "molecular units," but the linkage among them is assured by H-bonds. The structures of $Sb_2O_3 \cdot 3SO_3$ (Mercier *et al.*, 1976) and $Sb_6O_7(SO_4)_2$ (Bovin, 1976), on the contrary, are characterized by one-dimensional elements: a sort of double chain built by both SbO_3 and SO_4 polyhedra in the first instance and a "cylindrical unit" of SbO_3 polyhedra in the second. These one-dimensional elements are held together by Sb–O weak interactions and by van der Waals forces. As in peretaite, the arrangement of Sb–O polyedra in klebelsbergite takes place according to two-dimensional elements; the sheets of klebelsbergite however are built in a different way and their connection is made directly by

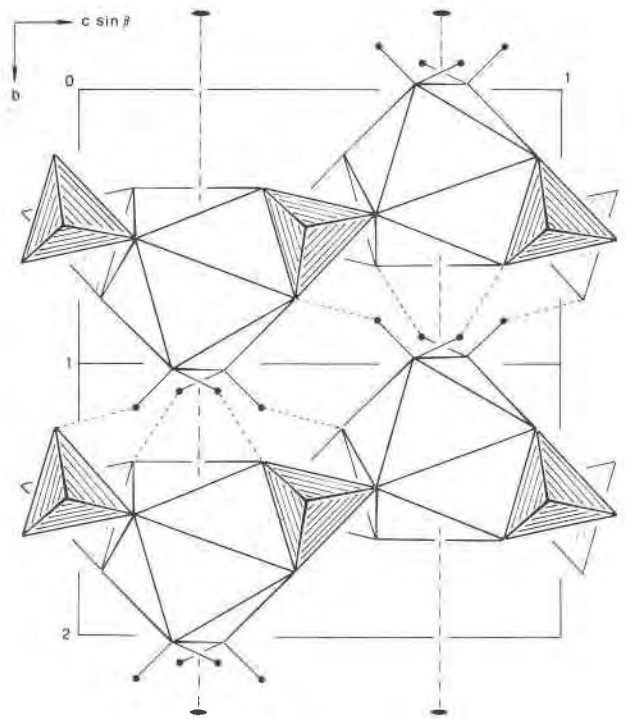

Fig. 3. A projection of peretaite down the *a* axis. Zig-zag Ca–S chains running in the *c* direction are shown.

means of SO_4 groups. In addition to the above sulfates, many other Sb synthetic compounds are structurally known. Some of these, such as the chloride oxide $Sb_4O_5Cl_2$ (Särnstrand, 1978), show Sb^{3+}–O polyhedra arranged in two-dimensional nets, as in the peretaite and klebelsbergite structures.

Table 4. Peretaite: electrostatic valence balance

Atom	Sb(1)	Sb(2)	Ca	S	H(1)	H(2)	H(3)	Sum
O(1)		0.20 0.19		1.40				1.79
O(2)		0.15	0.26	1.56				1.97
O(3)			0.22	1.52	0.22			1.96
O(4)			0.25	1.52		0.20		1.97
O(5)			0.27		0.78	0.80	0.23	2.08
O(6)	0.85 0.43	0.78						2.06
O(7)	0.80 0.56	0.76						2.12
O(8)	0.21 0.15	0.92					0.77	2.05
Sum	3.00	3.00	1.00 (x2)	6.00	1.00	1.00	1.00	

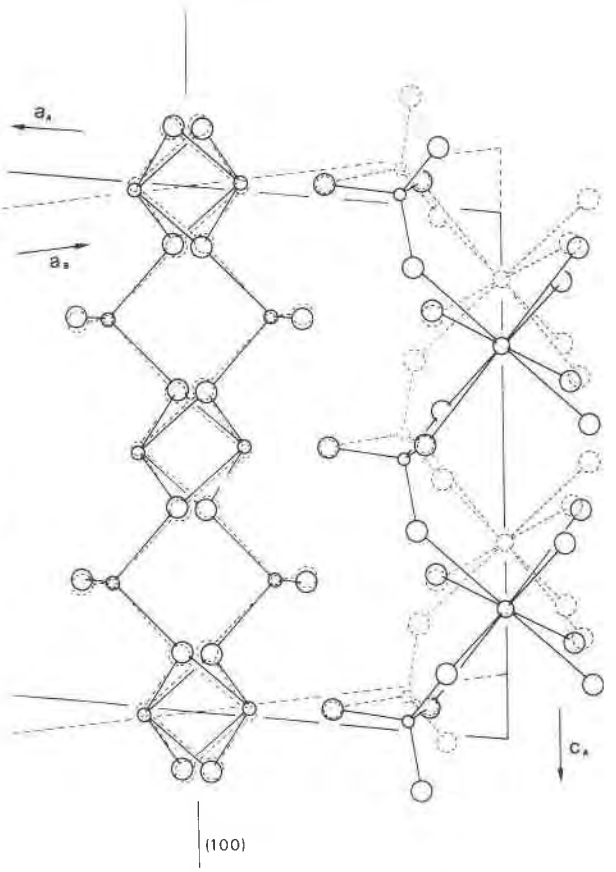

Fig. 4. A view of twinned peretaite: the A and B individuals of the twin are drawn with solid and dashed lines respectively. The unit cells are also outlined.

As concerns the change of the atomic arrangement responsible for the twinning, it seems clear that the (100) twin plane pre-exists as a "pseudo" symmetry operator in the Sb–O sheet, owing to the particular coordinates of atoms involved. These "rigid" structural slabs of an individual of the twin are practically interchangeable with those of its mate. As Figure 4 illustrates, the real change in the atomic arrangement takes place in the "soft" part of the structure, starting from the SO_4 tetrahedron and affecting mainly the Ca polyhedra.

References

Andersson, S., A. Åström, J. Galy and G. Meunier (1973) Simple calculation of bond lengths and bond angles in certain oxides, fluorides or oxide fluorides of Sb^{3+}, Te^{4+} and Pb^{2+}. *J. Solid State Chem., 6,* 187–190.

Bovin, J.-O. (1976) The crystal structure of the antimony (III) oxide sulfate $Sb_6O_7(SO_4)_2$. *Acta Crystallogr., B32,* 1771–1777.

Brown, I. D. and K. Kun Wu (1976) Empirical parameters for calculating cation–oxygen bond valences. *Acta Crystallogr., B32,* 1957–1959.

Cipriani, N., S. Menchetti, P. Orlandi and C. Sabelli (1980) Peretaite, $CaSb_4O_4(OH)_2(SO_4)_2 \cdot 2H_2O$, a new mineral from Pereta, Tuscany, Italy. *Am. Mineral., 65,* 936–939.

Cole, W. F. and C. J. Lancucki (1974) A refinement of the crystal structure of gypsum $CaSO_4 \cdot 2H_2O$. *Acta Crystallogr., B30,* 921–929.

Douglade, J., R. Mercier and H. Vivier (1978) Structure cristalline de $Sb_2(OH)_2(SO_4)_2 \cdot 2H_2O$. *Acta Crystallogr., B34,* 3163–3168.

Friedel, G. (1926) *Leçons de Cristallographie.* Berger-Levrault, Paris.

Galy, J., G. Meunier, S. Andersson and A. Åström (1975) Stéréochimie des éléments comportant des paires non liées: Ge(II), As(III), Se(IV), Br(V), Sn(II), Sb(III), Te(IV), I(V), Xe(VI), Tl(I), Pb(II) et Bi(III) (oxydes, fluorures et oxyfluorures). *J. Solid State Chem., 13,* 142–159.

International Tables for X-ray Crystallography, Vol IV (1974) Kynoch Press, Birmingham, England.

Main, P., M. M. Woolfson, L. Lessinger, G. Germain and J. P. Declercq (1974) *MULTAN 74. A System of Computer Programs for the Automatic Solution of Crystal Structures from X-ray Diffraction Data.* Universities of York, England, and Louvain-la-Neuve, Belgium.

Menchetti, S. and C. Sabelli (1980) The crystal structure of klebelsbergite, $Sb_4O_4(OH)_2SO_4$. *Am. Mineral., 65,* 931–935.

Mercier, R., J. Douglade and J. Bernard (1976) Structure cristalline de $Sb_2O_3 \cdot 3SO_3$. *Acta Crystallogr., B32,* 2787–2791.

———, ——— and F. Theobald (1975) Structure cristalline de $Sb_2O_3 \cdot 2SO_3$. *Acta Crystallogr., B31,* 2081–2085.

North, A. C. T., D. C. Phillips and F. S. Mathews (1968) A semi-empirical method of absorption correction. *Acta Crystallogr., A24,* 351–359.

Särnstrand, C. (1978) The crystal structure of antimony (III) chloride oxide $Sb_4O_5Cl_2$. *Acta Crystallogr., B34,* 2402–2407.

Manuscript received, April 2, 1980;
accepted for publication, April 22, 1980.

American Mineralogist, Volume 65, pages 947–952, 1980

Tiragalloite, $Mn_4[AsSi_3O_{12}(OH)]$, a new mineral and the first example of arsenatotrisilicate

CARLO MARIA GRAMACCIOLI

Istituto di Chimica fisica, Università, Milano
I-20133 Milano, Italy

WILLIAM L. GRIFFIN

Mineralogisk–Geologisk Museum
N-Oslo 5, Norway

AND ANNIBALE MOTTANA

Istituto di Mineralogia, Università
Città Universitaria, I-00185 Roma, Italy

Abstract

Tiragalloite occurs as small orange grains in veinlets cutting black massive aggregates of braunite and quartz from an abandoned manganese mine at Molinello near Chiavari, Liguria, Italy. The veinlets also contain quartz, manganiferous calcite, parsettensite, albite, and at least one other new mineral related to tiragalloite but containing essential vanadium instead of arsenic. Tiragalloite is optically biaxial, positive, $\alpha = 1.745(5)$, $\beta = 1.751(3)$, $\gamma = 1.760(5)$, $2V_\gamma = 38–46°$, non-pleochroic. The theoretical formula, derived from crystal-structure determination, is $Mn_4[AsSi_3O_{12}(OH)]$, and the formula derived from 29 microprobe analyses is $(Mn_{3.909}Ca_{0.077}Fe_{0.013})[(As_{0.844}V_{0.116})Si_3O_{12}(OH)]$. Density (meas.) 3.84(6); (calc.) 3.829 g cm^{-3}. The crystals are monoclinic, $P2_1/n$, with $a = 6.66(1)$, $b = 19.92(2)$, $c = 7.67(1)$Å, $\beta = 95.7(1)°$; the most intense lines in the powder pattern are (as d, *I*, *hkl*) 6.299 (24) 110; 4.742 (60) 101,130; 3.267 (71) 210,032,12$\bar{2}$; 3.149 (50) 220; 3.042 (66) 061,151; 3.006 (100) 22$\bar{1}$,042,122; 2.496 (64) 062,17$\bar{1}$,013. In the crystal structure, the most characteristic feature is the presence of an arsenatotrisilicate ion $(AsSi_3O_{12}OH)^{8-}$, comprising four tetrahedra linked together to form a chain fragment. This new ion is an extension of the trisilicate $(Si_3O_{10})^{8-}$ ion with an additional As-centered tetrahedron linked to it. This example is the first of a new series of minerals. The name is for Paolo Tiragallo (b. 1905), a distinguished amateur mineralogist.

Introduction

The manganese mines in Eastern Liguria, Italy, are well known to mineralogists and mineral collectors for their wealth of fine specimens of colorful and interesting minerals, such as rhodonite, tinzenite, parsettensite, and sursassite (Di Colbertaldo, 1970, p. 172–175; Cortesogno *et al.*, 1979). Recently, Mr. Mario Antofilli, an enthusiastic mineral collector from Genoa, gave the authors a few interesting samples which had been found several years ago in a manganese mine at Molinello, near Chiavari, Liguria. The mine is now abandoned.

A preliminary examination of the powder pattern, and a microprobe analysis, indicated the possibility that this was a new species; however, more information was necessary (Gramaccioli *et al.*, 1979a). For this purpose, after much effort, a single crystal splinter was isolated from the matrix and an X-ray crystal structure analysis was completed (Gramaccioli *et al.*, 1979b). The crystal structure confirmed the nature of a new mineral, and this paper reports the full mineralogical data. We have named the new mineral tiragalloite in honor of Mr. Paolo Tiragallo, a distinguished amateur mineralogist and dean of the Mineral Collector Group in Liguria, an enthusiastic group of amateurs, whose activity led to the discovery of tiragalloite and other interesting species.

0003–004X/80/0910–0947$02.00

The mineral and the name have been approved by the IMA Comission on New Minerals and Mineral Names. Type material is preserved in the collections of the Institutes of Mineralogy at the University of Rome (Italy) and Oslo (Norway); a fine specimen, from which the analyzed samples have been derived, has been deposited at the City Museum of Natural History, Milan.

Occurrence

Tiragalloite occurs as small orange grains enclosed in brownish to orange veinlets, about one millimeter thick, cutting a black Mn ore made up mainly of quartz and braunite, with traces of serpentine. In these veins, which have almost no cavaties, tiragalloite practically never shows idiomorphic crystals. The grains, measuring up to 1.5 mm in length but usually much smaller (0.2–0.4 mm) are either isolated, surrounded nearly invariably by quartz, or grouped together into small aggregates measuring up to 4–6 mm in diameter. The grains occasionally show an elongated shape. They are intimately associated with a number of other minerals, especially quartz, manganiferous calcite, parsettensite, and other new silicates related to tiragalloite but containing essential vanadium. For one of these, medaite, $Mn_6[VSi_5O_{18}(OH)]$, we have solved the crystal structure and have found that it is related to tiragalloite. This name has also been approved by the IMA Commission on New Minerals and Mineral Names, and final refinement of the crystal structure is in progress. The association of all these minerals is often so intimate that considerable difficulty is encountered in obtaining X-ray diffraction powder patterns free from lines due to impurities (see below), and obtaining a pure crystal fragment for X-ray analysis has been difficult.

Only fresh unaltered boundaries between tiragalloite and the other minerals are observed, except against manganiferous calcite, where a fine spongy rim shows alteration of tiragalloite grains.

Physical properties

Tiragalloite is orange to yellow in thin section. Hand specimens of the mineral are decidedly orange, sometimes with a tendency towards brownish (in the latter case, some intergrowth with similar species containing vanadium occurs, and the brown color might not be actually due to the tiragalloite). The mineral has a subadamantine luster. It is transparent in thin section and translucent in small splinters. There is a good cleavage along {100} and a distinct parting normal to the elongation.

The density, measured by flotation in dilute Clerici solution at room temperature, is 3.84±0.06 g cm^{-3}. This value compares favorably with a calculated value of 3.829 g cm^{-3} from unit-cell and chemical analysis data; for the pure end member (*i.e.* with no substitution for As and Mn) the calculated value is 3.860 g cm^{-3}.

Tiragalloite is only slightly soluble in HNO_3, giving the solution a light pink color, and insoluble in HCl or H_2SO_4.

Tiragalloite is biaxial, positive, with $2V_\gamma$ = 38–46°; these values for the axial angle have been obtained from measurements on the universal stage (6 determinations with the stage in orthoscopic setting). The indices of refraction are: α = 1.745±0.005, β = 1.751±0.003, γ = 1.760±0.005; these have been measured in white light, using small flakes oriented for β on the universal stage. From this value and the measured birefringence (obtained from a thin section, using a Berek compensator) α and γ have been obtained.

The orientation of the indicatrix is approximately parallel to the crystallographic axes, with $a \simeq \alpha$, $b = \beta$, $c \simeq \gamma$. The angle between α and the cleavage pole is 5–6°; the elongation is positive.

No pleochroism has been observed. In some cases, twinning has been detected under the microscope; it is symmetric, with the twin plane coincident with the cleavage plane. The axial dispersion is inclined, in agreement with the monoclinic symmetry.

The geometric mean of the refraction indices, 1.752, is in substantial agreement with the calculated value (1.763) according to the Gladstone–Dale rule, using the new constants proposed by Mandarino (1976); there is consequently good agreement between data from X-ray crystallography, chemical analysis, and optical measurements.

X-ray data

The unit-cell dimensions of tiragalloite are a = 6.66(1), b = 19.92(2), c = 7.67(1)Å, β = 95.7(1)°. These data have been determined and refined from 60 reflections given by a single crystal, mounted on a Syntex $P\bar{1}$ automatic diffractometer, with 2θ around 50°, using Mo$K\alpha$ radiation (λ = 0.7107Å). For this refinement a least-squares procedure was followed, and the standard deviations reported above are derived from the residuals and the inverse matrix of the normal equations.

From the Laue symmetry of the reciprocal lattice ($2/m$), and extinctions ($0k0$: $k = 2n + 1$ and $h0l$: $h + l = 2n + 1$) $P2_1/n$ symmetry is indicated unambiguously. This symmetry has been confirmed by solving the crystal structure. The number of formula units per cell is 4, and all the atoms are in general positions.

The crystal structure has been solved and refined to an R index of 0.049 for 1777 independent reflections; the procedure and the results have been reported elsewhere (Gramaccioli *et al.*, 1979b). The most interesting feature is the presence of an arsenatotrisilicate ion $(AsSi_3O_{12}OH)^{-8}$ composed of four tetrahedra linked together to form a chain fragment. This new ion is an extension of the trisilicate $(Si_3O_{10})^{8-}$ ion with an additional AsO_4 tetrahedron. This example is the first of a new series of minerals allied to sorosilicates, where the length of the chain fragments is considerably extended. Curiously enough, there are other atoms besides Si at the center of the tetrahedra; such tetrahedra are found only at one extremity of the chain fragment. The new mineral medaite represents a second example of these ions [*i.e.* a vanadopentasilicate $(VSi_5O_{18}OH)^{12-}$ with five SiO_4 tetrahedra joined together into a chain fragment, plus an additional tetrahedron with central vanadium, in part replaced by As]. In the crystal structure of these minerals, there are a series of hydrogen bonds linking the chain fragments to each other (from end to end), and this may be an essential stabilizing factor for this kind of species.

X-ray powder diffraction data are reported in Table 1. The indices in Table 1 have been assigned on the basis of comparison with single-crystal data, and when a peak is a superposition of several reflections, only the three most intense peaks (if more than 5 percent of the total) are listed, in order of importance. In such cases, the recalculated distance in the third column is a weighted average of these peaks. In view of the large absorption factor, the agreement between observed and calculated data must be considered satisfactory. Note that, with complex structures of low symmetry such as the present case, only a procedure of this kind can insure correct indexing.

In all the powder patterns obtained thus far, moderately strong lines at 12.440 and 2.93–2.95Å are present. The single exception is the pattern obtained from a Gandolfi camera, which does not show the line at 12.440Å; even in this pattern, however, the line at 2.93Å persists. They are surely due to the presence of impurities, such as parsettensite (Mn-stilpnomelane) and manganoan calcite, because they do not match any significantly strong reflection recalculated from single-crystal data.

Crystal chemistry

Electron-microprobe analyses were made using a LINK system model 860 energy-dispersive analyzer, with on-line matrix corrections by the ZAF-4 program. The system is mounted on an ARL-EMX probe at Geologisk Museum, Oslo. The analyses are based on metal standards (for As, V, Fe, Mn), wollastonite (for Ca), and quartz (for Si). Twenty-one spot analyses were completed on one grain, and 8 additional analyses were made of randomly chosen spots on as many grains in the same thin section. The results (Table 2) show within-grain variation to be as large as inter-grain variation.

The ideal formula of tiragalloite as derived from crystal structure analysis is $Mn_4[AsSi_3O_{12}(OH)]$. The collected data are accurate enough to detect and locate the hydrogen atom, and the presence and nature of water in the mineral is therefore completely clarified. If partial substitution of Mn by Ca and Fe and of As by V is assumed on the basis of the analytical results, then from the experimental ratios Mn/Ca, Mn/Fe and As/V a formula such as $(Mn_{3.909}Ca_{0.077}Fe_{0.013})[(As_{0.844}V_{0.116})Si_3O_{12}(OH)]$ can be deduced. Unless otherwise specified, the physical properties reported here for the new mineral are calculated from this formula.

The agreement between the analyzed composition and that derived from X-ray data is quite satisfactory. A still better agreement might be obtained if one assumes partial replacement of (As,V) by Si, since the analytical data are relatively too high in Si and too low in As or V. However, there are three good reasons for considering such replacement to be unlikely: (1) the final difference Fourier does not show any evidence of substitution of As atoms by much lighter atoms (Gramaccioli *et al.*, 1979b); (2) the As–O and Si–O bond length averages in tiragalloite (1.693 and 1.627Å, respectively) are in close agreement with the average values (1.686 and 1.623Å, respectively) reported by Ferraris (1970) and Smith and Bailey (1963) for arsenates and metasilicates with no substitution of As for Si; the partial substitution of vanadium for arsenic should not affect these considerations, since the As–O and V–O bond lengths are very similar; (3) there is apparently no way to reestablish charge balance, unless some oxygen around As is replaced by OH or F, or some

Table 1. X-ray powder diffraction data for tiragalloite

(1)		(2)		(3)		
d	I	d	I	d	I	hkl
6.298	14			6.299	24	110
4.979	18	4.97	m	4.991	16	031,040
4.779	21	4.77	m	4.742	60	101,130
				4.114	7	$13\bar{1}$
3.514	34	3.53	m	3.523	30	051,022
		3.43	w	3.420	16	150,141
3.258	100	3.28	s	3.267	71	$210,032,12\bar{2}$
3.151	73	3.15	s	3.149	50	220
3.118	25			3.115	27	$21\bar{1}$
3.034	72	3.03	m	3.042	66	061,151
3.003	72	3.00	s	3.006	100	$22\bar{1}$,042,122
2.889	31	2.89	s	2.904	43	211
2.846	30	2.85	w	2.845	35	$132,23\bar{1}$
2.782	40	2.78	w	2.804	24	$16\bar{1}$
2.736	54	2.74	s	2.738	39	052
2.695	31			2.685	14	231
2.657	25			2.663	24	$071,24\bar{1}$
2.608	65	2.60	w	2.606	49	$21\bar{2},20\bar{2},152$
2.529	29	2.53	w	2.530	21	$241,22\bar{2}$
2.499	45	2.49	s	2.496	64	$062,17\bar{1},013$
2.489	58					
				2.472	14	$25\bar{1}$,152
2.440	29			2.437	20	$023,10\bar{3},171$
				2.348	18	260,033
				2.316	11	$222,24\bar{2}$
2.296	17			2.272	16	072,113,103

(1)		(2)		(3)		
d	I	d	I	d	I	hkl
2.189	21			2.183	28	$30\bar{1}$,310
2.157	22			2.160	11	320,270
				2.112	13	$27\bar{1}$,172
2.062	21			2.074	16	143,082
				2.008	10	$191,18\bar{2},063$
1.993	10*			1.991	17	$280,31\bar{2}$
1.975	8*			1.979	7	153
1.853	16			1.852	11	$34\bar{2},024,19\bar{2}$
1.822	10			1.825	10	$272,36\bar{1},312$
1.756	28			1.761	16	0.11.1,044
1.742	11*			1.744	11	$14\bar{4}$,124,1.11.0
1.718	10*			1.721	10	$342,32\bar{3},253$
				1.709	12	$134,2.10.0,1.11.\bar{1}$
				1.692	18	$27\bar{3}$
1.691	18			1.688	22	$1.11.1,183,2.10.\bar{1}$
				1.674	9	371
1.659	40			1.661	14	400,0.12.0,263
1.654	27			1.653	16	$410,34\bar{3}$
				1.621	22	$0.12.1,24\bar{4},292$
1.605	21			1.590	16	193,381
1.413	17	(?)				
1.408	18			1.409	21	135,442,392
				1.386	9	471,145,373
				1.379	11	$452,480,2.13.\bar{1}$
				1.297	11	$32\bar{5}$,354,1.15.0

1) Diffraction pattern obtained from a powdered sample, using Cu K_α radiation.

2) Diffraction pattern obtained from a single grain, using Fe K_α radiation, and a Gandolfi camera.

3) Recalculated diffraction pattern from single-crystal data, assuming Cu K_α radiation and a resolving power of 0.1° in θ angles, using a program written by C.M.G.

* *Reflections marked with an asterisk are relative to another nearly identical powder pattern, obtained using a Niskanen specimen holder instead of a Schliephake specimen holder.*

The symbols s, m, and w for the intensity refer to strong, medium, and weak, respectively.

vacancies are present. However, if some OH replaces oxygen, some variation in bond length should appear, and this is not observed. A Si–F bond is unlikely in non-fumarolic minerals. The energy of formation of oxygen vacancies in structures of this kind is usually so high as to preclude them in substantial number.

For all these reasons, we believe that no substantial replacement of (As,V) by Si occurs in tiragalloite, and some overestimation of silicon and underestimation of arsenic (and vanadium?) has occurred in the chemical analysis. Note, however, that these over- or underestimates are well within the limits of a reasonable uncertainty even in the best analytical results of this kind.

Conditions of formation

Tiragalloite is the only known example of a mineral containing non-isolated AsO_4 groups; no such examples are known in nature even for phosphates, with the possible exception of kehoeite (McConnell, 1964). This probably depends on the ease of hydrolysis of polyphosphate or polyarsenate ions relative to complex silicates, polyarsenates being even more unstable than polyphosphates (Emeleus and Sharpe, 1978, p. 314–315). The conditions nearly universally

Table 2. Electron microprobe analyses for tiragalloite. All results are in weight percent

	On 1 grain (n spot=21)		On 8 grains (n spot=8)		Average (σ)	Theoretical (1-2)	
SiO_2	32.27	(31.85-33.36)	32.68	(31.94-33.28)	32.38±0.19	30.86	30.66
FeO	0.14	(0.00- 0.38)	0.25	(0.00- 0.54)	0.17±0.05	0.16	-
MnO	48.47	(47.83-49.58)	48.01	(47.36-48.71)	48.34±0.21	47.49	48.26
CaO	0.79	(0.63- 1.02)	0.66	(0.42- 0.79)	0.75±0.06	0.74	-
As_2O_5	16.00	(15.06-17.28)	16.27	(15.76-16.84)	16.07±0.12	17.40	19.54
V_2O_5	1.73	(1.17- 2.26)	1.53	(1.19- 1.82)	1.67±0.09	1.81	-
H_2O						1.54	1.53
Total	99.39		99.40		99.38	100.00	100.00

The theoretical results are relative to calculated formula (1),or to the As-rich end member (2),respectively.

encountered in the earth's crust apparently favor the existence of crystal structures with isolated AsO_4 or PO_4 groups.

Consequently, the physicochemical conditions leading to formation of tiragalloite must be quite exceptional (the mineral is rare, even at Molinello), and they should especially disfavor hydrolysis. Such requirements point to relatively low temperatures and high concentrations in solution (or, in other words, relatively low fugacity of water). The low temperature is indirectly confirmed by the absence of mutual substitution between As and Si, which might be important in other arsenate–silicate minerals but is probably insignificant for tiragalloite.

There are, of course, several stabilizing factors besides the network of hydrogen bonds. The presence of vanadium might be important, since this element is even more likely than As or P to form complex ions by joining up VO_4 tetrahedra. Such ions can also be found in nature [*i.e.* in the mineral chervetite, $Pb_2V_2O_7$, described by Bariand *et al.* (1963) and Kawahara (1967)]. From this point of view, it might be interesting to know whether the pure As-containing tiragalloite is stable enough to be found in nature. Another favorable condition can be recognized by considering that the AsO_4 group is linked to an SiO_4, instead of to another AsO_4 tetrahedron, thereby forming an intermediate structure between complex arsenates (unstable in nature) and complex silicates (very stable in natural conditions). The difficulty for the AsO_4 group to link with the other tetrahedra is shown by its presence at one extremity, rather than in the middle of the chain segment (a similar situation occurs in medaite).

Ardennite is another manganese silicate occasionally present in some alpine and subalpine deposits. It also contains Ca,Mg,Al, and essential As and V, the last two elements substituting for each other. In its crystal structure a trisilicate group $(Si_3O_{10})^{8-}$ is present, together with isolated $(As,V)O_4$ and SiO_4 tetrahedra (Donnay and Allmann, 1968); water is present in amounts around 5 percent.

In view of the similarity in crystal structures and chemical composition, it might be inferred that these two minerals can be formed in lieu of one another, the determining factor very probably being connected with conditions which favor or disfavor hydrolysis.

Acknowledgments

We thank Professor Giuseppe Schiavinato of the Institute of Mineralogy, University of Milan, for constant help and encouragement. The friendly assistance of Drs. M. Bondi, G. Liborio, and T. Pilati is also gratefully acknowledged.

References

Bariand, P. B., F. Chantret, R. Pouget and A. Rimsky (1963) Une nouvelle espèce minérale: la chervetite, pyrovanadate de plomb $Pb_2V_2O_7$. *Bull. Soc. fr. Minéral. Cristallogr., 86,* 117–120.

Cortesogno, L., G. Lucchetti and A. M. Penco (1979) Le mineralizzazioni a Mn nei diaspri delle ofioliti liguri: mineralogia e genesi. *Rend. Soc. Ital. Mineral. Petrol., 35(1),* 151–197.

Di Corbertaldo, D. (1970) *Giacimenti minerari. Vol. II: Giacimenti di Fe, Mn, Cr, Co, Ni, Ti, V.* Padua, C.E.D.A.M.

Donnay, G. and R. Allmann (1968) Si_3O_{10} groups in the crystal structure of ardennite. *Acta Crystallogr., B24,* 845–855.

Emeleus, H. J., and A. G. Sharpe (1978) *Modern Aspects of Inorganic Chemistry.* Routledge and Kegan Paul, London.

Ferraris, G. (1970) Considerazioni sulla configurazione del gruppo $(AsO_4H)^{2-}$. *Rend. Soc. Ital. Mineral. Petrol., 26,* 589–598.

Gramaccioli, C. M., W. L. Griffin and A. Mottana (1979a) Dati preliminari su un probabile nuovo minerale nella miniera di Molinello (Genova). *Rend. Soc. Ital. Mineral. Petrol., 35(1),* 145–149.

———, T. Pilati and G. Liborio (1979b) Structure of a manga-

nese(II) arsenatotrisilicate $Mn_4|AsSi_3O_{12}(OH)|$: the presence of a new tetrapolyphosphate-like anion. *Acta Crystallogr., B35,* 2287–2291.

Kawahara, A. (1967) La structure cristalline de la chervetite. *Bull. Soc. fr. Minéral. Cristallogr., 90,* 279–284.

Mandarino, J. A. (1976) The Gladstone–Dale relationship. Part I: derivation of new constants. *Can. Mineral., 14,* 498–502.

McConnell, D. (1964) A zinc phosphate analogue of analcime: kehoeite. *Mineral. Mag., 33,* 799–803.

Smith, J. V. and S. W. Bailey (1963) Second review of Al–O and Si–O tetrahedral distances. *Acta Crystallogr., 16,* 801–811.

Manuscript received, February 27, 1980;
accepted for publication, May 8, 1980.

American Mineralogist, Volume 65, pages 953-956, 1980

Alunite and crandallite: a structure derived from that of pyrochlore

MICHEL GOREAUD AND BERNARD RAVEAU

Laboratoire de Cristallographie et Chimie du Solide, L.A. 251
Institut des Sciences de la Matière et du Rayonnement
Université de Caen, Esplanade de la Paix
14032 Caen CEDEX, France

Abstract

The structures of the minerals alunite $KAl_3(SO_4)_2(OH)_6$ and crandallite $CaAl_3(OH)_6[PO_3(O_{1/2}(OH)_{1/2})]_2$ have been investigated from a geometric standpoint. The similarity of this structural type with the pyrochlores $A_{1+x}M_2O_6$ or $A_2M_2O_7$ is shown. The framework $KAl_3(OH)_6O_6$ is strongly related to the host lattice M_2O_6, *i.e.* M_4O_{12}: it is built up from distorted hexagonal tungsten bronze layers $Al_3(OH)_6O_3$ similar to the M_3O_9 layers observed for pyrochlores, and from KO_3 layers which correspond to the MO_3 layers of pyrochlores. The stacking sequence of the $Al_3(OH)_6O_3$ and M_3O_9 layers is however different in both structures; it yields, due to the tilting of the octahedra, a coordination number 12 for K^+ in the KO_3 layers, while M of the MO_3 layers is characterized by an octahedral coordination.

The crystal structure of the mineral alunite $KAl_3(SO_4)_2(OH)_6$ has formed the subject of several publications (Hendricks, 1937; Pabst, 1947; Rong Wang *et al.*, 1965). Crandallite $CaAl_3(OH)_6[PO_3(O_{1/2}(OH)_{1/2})]_2$ (Blount, 1974) has a structure analogous to alunite. Recently Moore and Araki (1977) have shown that the structure of mitridatite $Ca_6(H_2O)_6[Fe^{III}_9O_6(PO_4)_9] \cdot 3H_2O$ is topologically distinct from, but related to, alunite. Although this structure is now definitely established, no relation with other structural types has been observed. The present paper describes the relations between this structure and that of pyrochlore, $A_2M_2O_7$, which forms an important group of minerals whose classification and nomenclature has recently been revised by Hogarth (1977).

The comparison of the hexagonal cell of alunite ($a_H \simeq 7$Å and $c_H \simeq 17$Å) with the cubic cell of pyrochlore ($a_c \simeq 10$Å) admits the relations:

$$a_H \simeq a_c/\sqrt{2} \simeq 7\text{Å and } c_H \simeq a_c\sqrt{3} \simeq 17\text{Å}$$

The symmetry of alunite is in fact rhombohedral $R\bar{3}m$ with α close to 60°. Note that the cubic pyrochlores ($Fd3m$) can be equivalently described in a rhombohedral cell with the same dimensions as those of alunite and characterized by the same space group $R\bar{3}m$. From these considerations, it appears that the formula $KAl_3(OH)_6(SO_4)_2$, related to the rhombohedral cell of alunite, should be compared with $A_4M_4O_{14}$ for pyrochlores, where A is a large cation ($R > 1$Å) and M is a metal in octahedral coordination.

The atomic parameters of pyrochlores AM_2O_6, referred to the corresponding hexagonal cell, are listed in Table 1. They demonstrate that there is a similarity between the frameworks $KAl_3(OH)_6O_6$ and M_4O_{12}, where Al and M atoms both have the same octahedral coordination. Previous studies on nonstoichiometric pyrochlores $A_{1+x}M_2O_6$ (Babel *et al.*, 1967; Michel *et al.*, 1973) have shown that the seventh oxygen atom of the $A_2M_2O_7$ compounds is not indispensable to the stability of the structure. This can be considered as built up from a host lattice M_2O_6, *i.e.* M_4O_{12} (M = W, Ta, or Nb) based on octahedra, where the A cations (K^+, Rb^+, Tl^+) are inserted. This host framework can also be described as built up from two sorts of layers, M_3O_9 and MO_3, which are normal to the ⟨111⟩ direction of the cubic cell. The M_3O_9 layers, made from corner-sharing octahedra, are in fact distorted hexagonal tungsten bronze sheets previously described by Magneli (1953). The examination of the (001) planes of the hexagonal cell of alunite shows that the latter type of layer is also observed in alunite and crandallite (Fig. 1a) and has the composition $Al_3(OH)_6O_3$. The MO_6 and $Al(OH)_4O_2$ octahedra are almost regular in both the pyrochlore and alunite structures; they are tilted about c_H or $\langle 111 \rangle_c$ with approximately the same in-

0003–004X/80/0910–0953$02.00

Table 1. Atomic parameters for alunite (Rong Wang *et al.*, 1965) and pyrochlore AB_2O_6 (Michel, 1974) referred to the hexagonal cell of the $R\bar{3}m$ space group

	Alunite (a = 6.97 Å, c = 17.27 Å)				Pyrochlore (a = 7.28 Å, c = 17.84 Å)			
Position	Atom	x	y	z	Atom	x	y	z
3 (a)	K	0.	0.	0.	M	0.	0.	0.
9 (d)	Al	0.5	0.	0.5	M	0.5	0.	0.5
6 (c)	S	0.	0.	0.3030	A	0.	0.	0.375
6 (c)	O(1)	0.	0.	0.3844				
18 (h)	O(2)	0.2180	-0.2180	-0.0588	O	0.2067	-0.2067	-0.2717
18 (h)	OH	0.1247	-0.1247	0.1416	O	0.1267	-0.1267	0.1883

clination with respect to that direction (18° for alunite, 17° for crandallite, and 15° for pyrochlore), differing from the hexagonal tungsten bronzes layers (Fig. 1b), whose octahedra are not (or only slightly) tilted about the c axis. The hexagonal tungsten bronze layers (HTB) are lying at levels $z = 1/6$, $3/6$, and $5/6$ of the hexagonal cell and, in a particular structure, correspond one with another by the translation vectors of the $R\bar{3}m$ space group. Therefore, in each compound, there are three different states α, β, and γ for the HTB layers, according to their configuration with respect to the $O\vec{x}$ and $O\vec{y}$ reference axes of the hexagonal cell. The three states are shown in Figure 1a.

Thus, the structural analysis and comparison of the structures of alunite type and pyrochlore type can be achieved in two different ways. The projections of the HTB layers at the same level z are identical in both structures but the tiltings of the octahedra about the $\vec{c}_H$ axis are in the opposite direction, so that both host lattices cannot be superimposed. Another way of comparison by means of HTB layer types (α, β, or γ), with the same tilting direction, shows a different stacking order along $\vec{c}_H$: $\alpha\ \beta\ \gamma$ sequence in the pyrochlore and $\gamma\ \beta\ \alpha$ sequence in alunite type.

Thus, the stacking of the $Al_3(OH)_6O_3$ or M_3O_9 layers along $\vec{c}_H$ or $\langle 111 \rangle_c$ is comparable: two consecutive layers are derived one from the other by a gliding of $a_H/\sqrt{3}$; the gliding directions are however different in both structures (Fig. 2): they are oriented at 180° one from the other. Starting from a HTB layer, chosen as a reference, a pyrochlore type structure is obtained from the stacking HTB; HTB $(+\vec{t})$; HTB $(-\vec{t})$, while the alunite type structure agrees with HTB; HTB

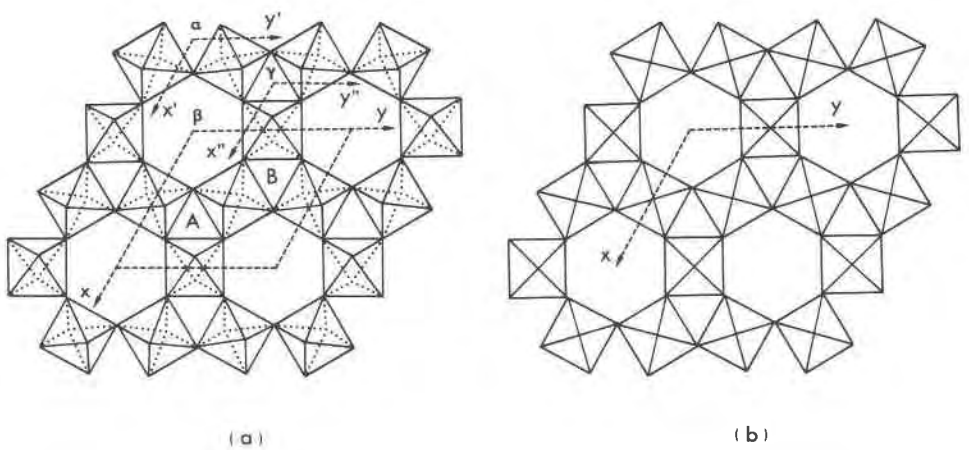

Fig. 1. Comparison of the M_3O_9 and $Al_3(OH)_6O_3$ octahedral layers of (a) alunite and pyrochlore with that of (b) hexagonal tungsten bronze (HTB). The references α, β, and γ show the three possible positions of the distorted HTB layers in the alunite and pyrochlore structures.

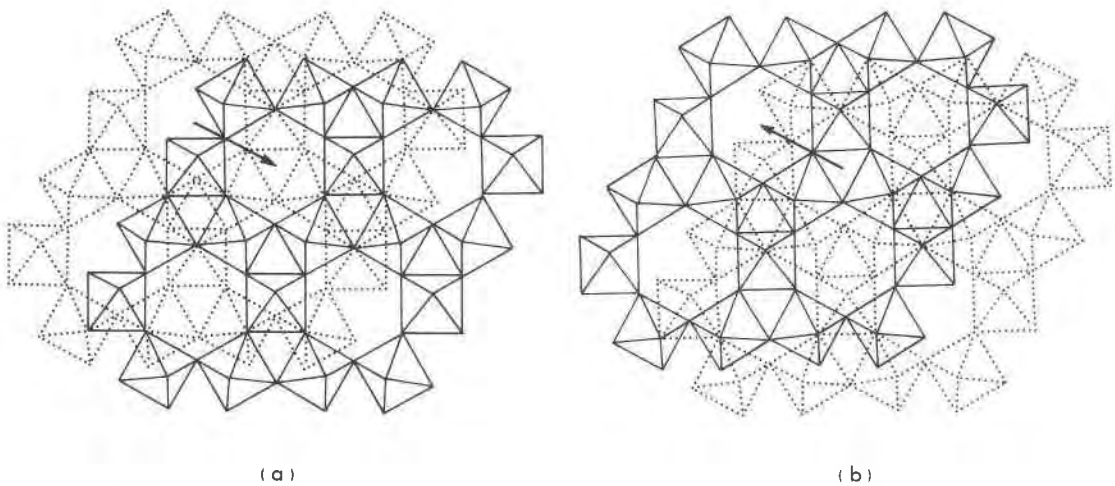

Fig. 2. Stacking of two adjacent distorted HTB layers (a) in pyrochlore (b) in alunite and crandallite.

$(-\vec{t})$; HTB $(+\vec{t})$ where $\vec{t} = (1/3)\vec{a}_H + (2/3)\vec{b}_H$. As a consequence, the main difference appears on the KO_3 and MO_3 layers connecting two consecutive M_3O_9 or $Al_3(OH)_6O_3$ layers. The tilting about $\vec{c}_H$ in the blocks "M_3O_{15}" of three corner-sharing octahedra defines two sorts of triangles whose apices are oxygen atoms located at the surface of a layer—small triangles noted A and large triangles noted B (Fig. 1a); this is in contrast to the ideal hexagonal bronze structure, where all the triangles are equivalent (Fig. 1b). The different stacking modes generate two sorts of sites which are available for M and K cations. In pyrochlore, two A triangles belonging to neighboring M_3O_9 sheets are one above the other, forming an octahedron (Fig. 3a) whose ternary axis is parallel to the $\langle 111 \rangle_c$ direction, where the M ion is located. An analogous disposition is obtained for the B triangles in alunite, forming trigonal antiprisms (Fig. 3b) where the K^+ ions (or Ca^{2+} in crandallite) are located. In fact, the opposite directions of the tilting of octahedra in Figures 3a and 3b lead to a six-coordinated M cation in pyrochlore, while K^+ (or Ca^{2+}) is twelve-coordinated in alunite, since the oxygen atoms which are common to the octahedra of a "M_3O_{15}" group are not at the same z level in both structures: they are neighbors for K^+, but not for M. The polyhedra KO_{12} can be considered as built from flattened octahedra KO_6 (antiprisms) having the same disposition in KO_3 layers as the MO_6 octahedra in MO_3 layers. Both structural families can thus be regarded as forming strongly related host lattices which are built up from the stacking of MO_3 and M_3O_9 layers along $\langle 111 \rangle_c$ for the M_4O_{12} framework (Fig. 4a) and from the stacking of KO_3 and $Al_3(OH)_6O_3$ layers along c_H for the alunite framework (Fig. 4b).

These frameworks delimit cavities which are different in each structure. In the case of pyrochlore, a large triangle B is sited directly above and below the hexagon formed by six octahedra (Fig. 2a), while for alunite such a hexagon is surrounded on both sides by small triangles A (Fig. 2b). Hence the cavities of the pyrochlore structure, bounded by 18 oxygen atoms, are limited by the hexagonal crowns of six octahedra and the "M_3O_{15}" blocks of two successive M_3O_9 layers (Fig. 5a) and share their distorted hexagonal faces, forming tunnels parallel to the $\langle 110 \rangle_c$ direction. In the non-stoichiometric pyrochlores $A_{1+x}B_2O_6$, the large A cations (K, Rb, Cs, Tl, *etc.* . . .) are located inside these cavities, whereas they are located on the common faces in $A_2M_2O_7$ pyrochlores,

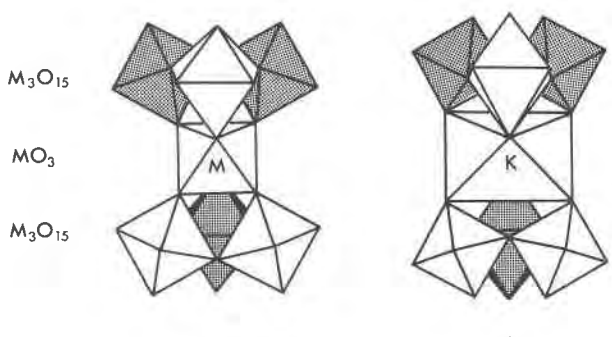

Fig. 3. Coordination of M and K^+ respectively in MO_3 and KO_3 layers: (a) the MO_6 octahedron of pyrochlore; (b) the KO_6 antiprism of alunite; the K^+ ion has however six additional close neighbors at equal distances, belonging to the "M_3O_{15}" blocks above and under the antiprism.

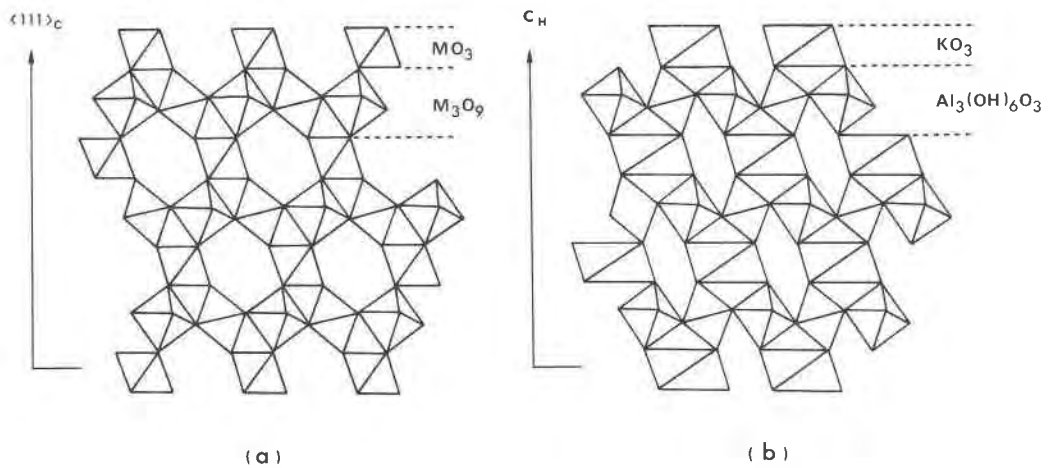

Fig. 4. Stacking of (a) the MO_3 and M_3O_9 layers in pyrochlore as seen along $[110]_H$, (b) the KO_3 and $Al_3(OH)_6O_3$ layers in the alunite as seen along $[\bar{1}10]_H$.

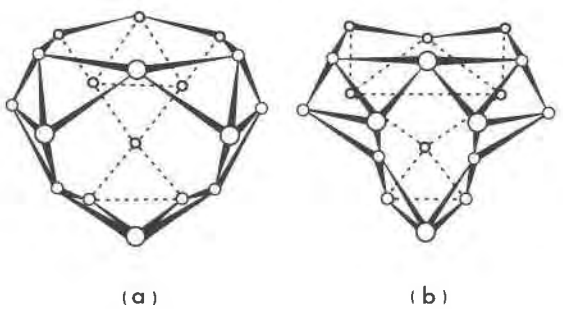

Fig. 5. The cavities bounded by 18 oxygen atoms and (or) hydroxyl groups (a) in pyrochlore (b) in alunite.

the seventh oxygen atom being situated at the center of the cavities.

The cavities of alunite are less open so that the tunnels no longer exist. Among the 18 oxygen atoms, we can consider that 9 have nearly the same disposition as in pyrocholore (Fig. 5b). The other nine atoms belong to the A and B triangles which are permuted from one structure type to the other. Each cavity contains one "SO" or "PO" group. The oxygen atom of this group is directed towards the distorted hexagonal face so that it forms, with the three oxygen atoms of the A triangle, a tetrahedron where the sulfur or phosphorus atom is located.

These structural relations show the importance of the hexagonal tungsten bronze framework, which can be considered as an elementary part of the structure of a great number of compounds. The possibility of intergrowths of alunite and pyrochlore structures, corresponding to different stackings of the M_3O_9 and $Al_3(OH)_6O_3$ layers, should be considered.

References

Babel, D., G. Pausewang and W. Wiebahn (1967) Die Struktur einiger Fluoride, Oxide und Oxidfluoride AMe_2X_6: der $RbNiCrF_6$-Typ. *Z. Naturforsch., B22,* 1219–1220.

Blount, A. M. (1974) The crystal structure of crandallite. *Am. Mineral., 59,* 41–47.

Hendricks, S. B. (1937) The crystal structure of alunite and the jarosites. *Am. Mineral., 22,* 773–784.

Hogarth, D. D. (1977) Classification and nomenclature of the pyrochlore group. *Am. Mineral., 62,* 403–410.

Magneli, A. (1953) Studies on the hexagonal tungsten bronzes of potassium, rubidium and cesium. *Acta Chem. Scand., 7,* 315–324.

Michel, C. (1974) Etude cristallochimique, évolution thermique et propriétés d'échanges d'ions de quelques oxydes ternaires de type pyrochlore. *Thèse,* Caen (France).

——— and B. Raveau (1973) Etude de la distribution des ions thallium dans les pyrochlores non-stoechiométriques $Tl_{1+\alpha}(Ta_{1+\alpha}W_{1-\alpha})O_6$. *Mater. Res. Bull., 8,* 451–458.

Moore, P. B. and T. Araki (1977) Mitridatite, $Ca_6(H_2O)_6[Fe^{III}_9O_6(PO_4)_9] \cdot 3H_2O$. A noteworthy octahedral sheet structure. *Inorg. Chem., 16,* 1096–1106.

Pabst, A. (1947) Some computations on svanbergite, woodhouseite and alunite. *Am. Mineral., 32,* 16–30.

Rong Wang, W. F. Bradley and H. Steinfink (1965) The crystal structure of alunite. *Acta Crystallogr., 18,* 249–252.

Manuscript received, December 20, 1979; accepted for publication, April 3, 1980.

American Mineralogist, Volume 65, pages 957–960, 1980

Kraisslite and mcgovernite: new chemical data

PETE J. DUNN AND JOSEPH A. NELEN

Department of Mineral Sciences
Smithsonian Institution
Washington, D. C. 20560

Abstract

Chemical analytical data have been obtained for kraisslite and mcgovernite. Kraisslite contains both trivalent and pentavalent arsenic in the weight ratio of 3:4. Specimens from different parageneses have relatively invariant chemical compositions, which suggests some degree of ordering of Mg, Mn, and Zn. The average of five analyses yields MgO 2.6, MnO 52.0, ZnO 8.6, Fe_2O_3 2.0, As_2O_3 6.69, Al_2O_3 0.2, As_2O_5 10.35, SiO_2 12.9, H_2O 3.68 percent, totalling 98.9 percent, and yielding the empirical formula $Fe_2^{3+}Mg_4Mn_{44}Zn_6(AsO_3)_4(AsO_4)_6(SiO_4)_{12}(OH)_{36}$. Ferric iron is present in both kraisslite and mcgovernite. Additional analyses of mcgovernite give the average MgO 11.5, MnO 42.2, ZnO 9.3, Fe_2O_3 1.7, As_2O_3 4.6, As_2O_5 12.5, SiO_2 9.2, H_2O 9.1 percent, totalling 100.1 percent.

Introduction

Kraisslite and mcgovernite are both very complex magnesium manganese zinc arsenosilicates which are known only from Sterling Hill, New Jersey. Kraisslite was described by Moore and Ito (1978), who proposed the tentative formula $(Mn^{2+}_{0.89}Mg_{0.08}Fe^{2+}_{0.03})_{24}Zn_4(AsO_4)_4(SiO_4)_8(OH)_{12}$. While obtaining chemical analyses of schallerite (another complex arsenosilicate composed of the same elements) for a separate study, we included samples of kraisslite and mcgovernite as control samples. Our results are at variance with existing data concerning the chemical composition of kraisslite.

Analytical methods

The samples were chemically analyzed with an ARL-SEMQ electron microprobe, utilizing an operating voltage of 15 kV and a beam current of 0.15 μA. The standards were manganite for Mn, synthetic ZnO for Zn, olivenite for As, and hornblende for Mg, Fe, Al, and Si. The data were corrected with a modified version of the *MAGIC-4* program.

Special attention was given to the determination of arsenic and its state of oxidation. Separate samples were used to determine trivalent and total As. Pentavalent As was calculated by difference. The trivalent As was distilled directly as the trichloride, followed by titration with iodine (Lundell *et al.*, 1951, p. 374–378). To obtain total As, $FeSO_4$, used as the reductant, was added to the sample before distillation with HCl. The iodine solution for the titration of the distilled As was standardized against known quantities of As carried through the procedure in a manner like that used for the unknowns. The procedure was checked against solutions containing 0.5 mg/ml As, either in the trivalent or pentavalent state. Recoveries from standards of 4.00, 4.02, 4.01, 4.07 and 4.02 mg As^{3+} were 4.00, 4.00, 4.03, 4.08 and 4.00 mg As, respectively.

We tested for reduction of pentavalent As during distillation without the reductant and it appeared to be minimal. Variation between duplicate samples of unknowns was usually 0.2 percent or less. The procedure we used is as follows: Transfer a sample containing 3–5 mg As to the distilling flask together with 175 ml HCl. For total As, also add 15 g $FeSO_4$. With the condenser outlet immersed in 100 ml distilled water, distill over 100 ml of the acid. During this process, keep the distillate cold by means of a surrounding ice-water bath. Remove the distillate and neutralize with cold concentrated NaOH solution. One drop of methyl red will serve as a good indicator. Cool again and just reacidify with 1:1 HCl. Add 20 ml saturated $NaHCO_3$ solution, 5 ml starch, and 4–5 g solid KI. Titrate with 0.01 normal standardized iodine to the first pink endpoint. Correct the titration for a blank run on the same reagents.

0003–004X/80/0910–0957$02.00

Kraisslite

Subsequent to its original description, kraisslite has been found in a number of different parageneses, indicating a broader range of associations than the original thin films and lenses. We briefly describe these parageneses for the analyzed samples, all from Sterling Hill, which remains the only locality for kraisslite. It was not determined whether or not kraisslite is in equilibrium with the associated minerals.

NMNH 144262. The sample consists of very thin foliae in fractures in willemite–franklinite ore which contains up to 10 percent holdenite by volume. Kraisslite occurs in contact with willemite and franklinite and also as sprays and warped foliae in massive holdenite. It was found between the 1200 and 1300 levels in the 1340 undercut pillar.

NMNH 146199. The sample consists of randomly oriented "booklets" of kraisslite in contact with franklinite, calcite, primary and secondary willemite, and a highly zincian adelite (containing approximately 14 percent ZnO). It was found at the 800 level in the 1220 pillar.

NMNH 143983. The sample consists of abundant irregular segregations of kraisslite in low-grade willemite–calcite–franklinite ore. The massive segregations of kraisslite are abundant in this material and locally comprise up to 20 percent of the ore. Kraisslite is in contact with all the minerals in this assemblage. The sample was found on the 700 level in the 1010 stope.

All samples were characterized by X-ray powder diffraction and the results are in excellent agreement with the X-ray powder diffraction patterns of the holotypes. The powder diffraction pattern of kraisslite, although similar to that of mcgovernite, is sufficiently distinct to permit unambiguous identification of the species. NMNH 137017 and 137018 are the holotype specimens for kraisslite; the former is the specimen that provided the original analysis.

Discussion

The analytical data in Table 1 indicate a number of significant points concerning the chemical composition of kraisslite. Zinc is in tetrahedral coordination in most of the secondary minerals of Franklin and Sterling Hill. The rather constant concentration of zinc near a value of 6 Zn per cell (consistent with equipoint ranks in space group $P6_322$; Moore and Ito, 1978) suggests that it may well be ordered in tetrahedral sites. Likewise, the nearly constant value of approximately 4 Mg per cell suggests that Mg may be ordered relative to Mn, but this is more problematical. The different parageneses and spatial separation of the occurrences suggest more than chance significance to these compositional similarities between samples.

Of special interest is the presence of ferric iron in kraisslite. All samples were subjected to microchemical tests which gave a positive reaction for ferric iron. Care was taken to use fresh unaltered material where possible. We note that ferric iron is present in mcgovernite as well and is also found in dixenite, which Moore and Araki (1978) have noted as being related to kraisslite. Hence, ferric iron may play some role in the crystal chemistry of kraisslite.

Of paramount significance, however, is the fact that the As exists in two oxidation states. Although Ito (in Moore and Ito, 1978) found only 0.87 percent As_2O_3 and predominantly pentavalent As in kraisslite, our analytical work clearly demonstrates that the As exists in two oxidation states with $As^{3+}:As^{5+} = 3:4$, and is relatively constant from sample to sample, including the holotype (reanalyzed). Other minerals with As in dual roles also exist at Sterling Hill; mcgovernite was the first arsenate–silicate to be described (Palache and Bauer, 1927), and synadelphite also occurs here (Moore and Ito, 1978) in contact with kraisslite.

Calculation of the number of atoms per unit cell in kraisslite with the unit-cell dimensions and density of Moore and Ito (1978) indicates that, on initial inspection, the numbers of Si, As^{5+}, Fe^{3+}, and Al atoms do not conform to the requirements of space group $P6_322$, which requires 12, 6, 4, or 2 equivalent atoms in the various sites. However, we note that the sum of As^{5+} and Si approximates 18 atoms, implying that there may be some substitutions involving these elements.

An idealized formula of $Fe_2^{3+}Mg_4Mn_{44}Zn_6(AsO_3)_4(AsO_4)_6(SiO_4)_{12}(OH)_{36}$ yields a calculated density of 3.918 g/cm^3, in reasonable agreement with the observed value of 3.876 g/cm^3, if we assume limited substitutions among Si and As^{5+}. This formula, however, must be considered tentative. Moore and Ito (1978) have noted streaks parallel to the *c* axis which suggest stacking faults in the structure. We agree with Moore and Ito that no unambiguous chemical formula can be proposed for this complex mineral in the absence of a complete crystal structure determination. Hence, the crystal chemistry of kraisslite

Table 1. Chemical analyses of kraisslite

	Sample number	MgO	MnO	FeO	ZnO	Fe_2O_3*	Al_2O_3	As_2O_3	As_2O_5	SiO_2	H_2O	Total
1.	Moore and Ito (1978)	2.53	51.6	1.92	8.47		0.21	0.87	17.7	13.8	3.68	100.78
2.	NMNH 137017	2.3	51.4		8.0	2.2	0.2	6.48†	10.06†	13.2	3.68**	97.5
3.	NMNH 146199	2.7	52.5		8.8	1.7	0.1	6.88†	10.25†	12.9	3.68**	99.5
4.	NMNH 143983	2.4	53.5		8.2	1.6	0.1	6.72†	10.74†	13.1	3.68**	100.0
5.	NMNH 137018	2.5	50.6		8.9	2.3	0.3	7.08††	10.96††	12.8	3.68**	99.1
6.	NMNH 144262	2.9	51.8		9.1	2.1	0.1	6.99††	10.84††	12.5	3.68**	100.0
7.	Average of 2,3,4,5,6	2.6	52.0		8.6	2.0	0.2	6.69Ψ	10.35Ψ	12.9	3.68	99.0
	Theory***	2.66	51.5		8.06	2.63		6.53	12.64	11.90	4.08	100.0
						Number of atoms per unit cell †††						
2.	NMNH 137017	3.42	43.43		5.89	1.65	0.23	3.92	5.24	13.16		
3.	NMNH 146199	4.01	44.36		6.48	1.27	0.11	4.16	5.34	12.87		
4.	NMNH 143983	3.57	45.21		6.04	1.20	0.11	4.07	5.60	13.07		
5.	NMNH 137018	3.72	42.76		6.55	1.73	0.35			12.77		
6.	NMNH 144262	4.31	43.77		6.70	1.58	0.11			12.47		
	Average	3.81	43.91		6.33	1.49	0.18	4.05Ψ	5.39Ψ	12.87		

* Iron determined as total iron; calculated as Fe_2O_3.

** Water taken from analysis by Ito in Moore and Ito (1978).

*** Theory for $Fe^{3+}_2Mg_4Mn_{44}Zn_6(AsO_3)_4(AsO_4)_6(SiO_4)_{12}(OH)_{36}$.

† Oxidation state of arsenic determined as described in text.

†† Calculated from the As^{3+}:As^{5+} ratio derived from analyses 2, 3, and 4. Total arsenic determined by microprobe.

Ψ Average of only analyses 2, 3, and 4.

††† Calculated on the basis of the unit-cell dimensions and density of Moore and Ito (1978) ($\underline{a}$ = 8.22, $\underline{b}$ = 43.88 Å, D = 3.876 g/cm^3).

Accuracy of data:± 3 percent of the amount present (for microprobe analyses).

Table 2. Chemical analyses of mcgovernite

	Sample Number	MgO	MnO	FeO	ZnO	Fe_2O_3†	As_2O_3	As_2O_5	SiO_2	H_2O	Total
1.	Palache and Bauer (1927)	11.27	42.72	1.53	10.22		4.45	12.48	8.92	8.49	100.08
2.	Moore and Ito (1978)	11.02	42.5	1.49	10.58		4.78	13.15	8.83	8.30	100.77*
3.	NMNH R3556	11.7	39.9		9.6	1.6	4.49***	12.59***	9.2	10.92**	100.0
4.	NMNH C6220-2	10.9	43.8		9.2	1.6	4.58††	12.11††	9.3	8.51**	100.0
5.	NMNH R14830	11.6	43.5		9.1	1.7	4.65††	12.60††	9.3	7.55**	100.0
6.	NMNH 104166	11.7	40.8		9.5	1.7	4.70††	12.73††	9.2	9.67**	100.0
7.	NMNH 137837	11.4	42.8		9.2	1.7	4.59††	12.46††	9.2	8.65**	100.0
8.	(Average of #3,4,5,6,7)	11.5	42.2		9.3	1.7	4.6	12.5	9.2	9.1	100.1

* Includes 0.12 % Al_2O_3.

** Water by difference.

*** Oxidation state of arsenic determined as described in text. Accuracy of data ±3 percent of the amount present, for microprobe determinations.

† Determined as total iron, calculated as Fe_2O_3.

††Calculated from the As^{3+}:As^{5+} ratio 3:7 derived from analyses 1, 2 and 3.

Arsenic determined as total arsenic by electron microprobe.

might be much more complex than indicated by our analytical study.

Mcgovernite

Mcgovernite was originally described by Palache and Bauer (1927). Its symmetry has been discussed by Wuensch (1960, 1968) and Moore and Araki (1978). Its chemical constituents are the same as those of kraisslite but are present in different ratios. We present new analyses of mcgovernite, together with those of Bauer (Palache and Bauer, 1927) and Ito (Moore and Ito, 1978), in Table 2. The analyzed samples have all been identified by X-ray diffraction.

Of special interest is the presence of ferric iron in mcgovernite, in concentrations similar to those in kraisslite, but with less variance. It is present in all samples, although not previously reported. Our determination of the oxidation states of the As substantiates the determinations by Bauer and Ito. We have calculated the ratio of $As^{3+}:As^{5+}$ for the microprobe analyses using the 3:7 ratio determined empirically by analysis (Table 2), rather than the simpler 1:3 ratio suggested by the formula of Moore and Araki (1978).

As with kraisslite, the relative concentrations of Mg, Mn, and Zn suggest some ordering of these elements in the crystal structure. We present additional analyses as evidence of the relatively invariant composition of this mineral. We offer no chemical formula for mcgovernite; calculation of cell contents yields results not in conformity with the space group requirements. The presence of over 1200 atoms in the unit cell, combined with the probability of complex substitutions such as are likely in kraisslite, precludes any simple formula.

Acknowledgments

We thank Drs. Michael Fleischer, Peter Leavens, Joseph Mandarino, Donald Peacor, Frederick Wicks, and Carl Francis for critical readings of the manuscript. Samples for study were donated by John Kolic, a miner in the Sterling mine who first noted the various parageneses. We thank Mr. Richard Johnson and Mr. Frank Walkup for the preparation of polished sections, and Mr. Charles Obermeyer for technical assistance. Mrs. Esther Claffy provided literature assistance. This project was supported in part by a grant from Mrs. E. Hadley Stuart, Jr.

References

Lundell, G. E. F., J. I. Hoffman and H. A. Bright (1951) *Chemical Analysis of Iron and Steel.* Wiley, New York.

Moore, P. B. and T. Araki (1978) Hematolite: a complex dense-packed sheet structure. *Am. Mineral., 63,* 150–159.

——— and J. Ito (1978) Kraisslite, a new platy arsenosilicate from Sterling Hill, New Jersey. *Am. Mineral., 63,* 938–940.

Palache, C. and L. H. Bauer (1927) McGovernite, a new mineral from Sterling Hill, New Jersey. *Am. Mineral., 12,* 373–374.

Wuensch, B. J. (1960) The crystallography of mcgovernite, a complex arsenosilicate. *Am. Mineral., 45,* 937–945.

——— (1968) Comparison of the crystallography of dixenite, mcgovernite and hematolite. *Z. Kristallogr., 127,* 309–318.

Manuscript received, March 14, 1980;
accepted for publication, May 8, 1980.

American Mineralogist, Volume 65, pages 961–967, 1980

Hydrated sulfates from Sydney Coalfield, Cape Breton Island, Nova Scotia, Canada: the copiapite group

ERWIN L. ZODROW

Department of Geology, College of Cape Breton
Sydney, Nova Scotia, Canada B1P 6L2

Abstract

Selected samples of copiapite from locations in the Sydney Coalfield are classified according to atomic proportions in the X position of the structural formula of copiapite. In particular, the metal content in the position is calculated by purely algebraic means, *i.e.,* by solutions of linear simultaneous equations. Proportions in the X and R positions of the structural formula are assumed 1 : 4 on the basis of substitution which at the same time serves as a check on obtained solutions. Identified species of the copiapite group include aluminocopiapite, copiapite, magnesiocopiapite, and even ferroan magnesiocopiapite. It appears that different parts in the coalfield represent different environments as judged by the chemical composition of the sampled copiapites.

Introduction

Over the last four years many hydrated sulfate specimens have been collected from the Sydney Coalfield, leading to several studies by Zodrow and McCandlish (1978a, b; 1979). Among these sulfates are certain minerals of the copiapite group, with aluminocopiapite being predominant. Minerals of this group have a wide geographical distribution in the coalfield; Figure 1 shows the locations of samples.

The copiapite group consists of hydrated sulfates with the general formula $XR_4(SO_4)_6(OH)_2 \cdot nH_2O$, where X is one oxygen equivalent (with a total charge of 2+). The X position contains one or more of Cu (cuprocopiapite), Fe (copiapite), Mn, Zn, Na, K, Co, Ca, Mg (magnesiocopiapite), Al, and others; R is mainly Fe^{3+} and some Al. The upper limit of n is 20 for fully hydrated minerals (Fanfani *et al.,* 1973); Berry (1947) proposed 21 on the basis of statistical averages. The substitutional possibilities are large and diversified in the X position; they are fully explainable by the weak bonding of the coordination polyhedra to the structural chain motif (Fanfani *et al.,* 1973). In aluminocopiapite (Berry, 1947, p. 25, 29), Al is the dominant metal in the X position.

The Al-rich nature of the sediments in the Sydney Coalfield is reflected in the composition of the hydrated sulfate minerals (Zodrow and McCandlish, 1978a, 1979), in the acid run-offs, and in shales and pyrite (Zodrow, in preparation); see Table 1. Copiapite group minerals occur on practically every outcrop of coal, on coal faces in the older mines, as precipitates from acid run-offs, and in shale in the proximity of coal.

Of all the hydrated sulfates observed in their natural environment, copiapite minerals are the most resistant to seasonal changes. For example, on the Emery seam in Glace Bay (Zodrow and McCandlish, 1978a, their Fig. 2) pickeringite [$MgAl_2(SO_4)_4 \cdot 22H_2O$], halotrichite [$FeAl_2(SO_4)_4 \cdot 22H_2O$], and other hydrated sulfates "bloom" only in the summer; a similar situation exists in the Point Aconi area (Fig. 1), where the predominant hydrated sulfate is sideronatrite [$Na_2Fe(SO_4)_2(OH) \cdot 3H_2O$]. These minerals vanished during winter but copiapite survived.

This paper, part of an environmental study of hydrated sulfates in the Sydney Coalfield, attempts to classify selected copiapite group minerals from the unit-cell content as calculated by Berry (1947, p. 30): ". . . an analysis is placed in one of the . . . five groups if the oxygen equivalent of the principal constituent of X exceeds 0.5." Berry's five groups are ferri-, alumino-, magnesio-, ferro-, and cuprocopiapites. In this study the number of atoms in the X and R positions are estimated by solutions of simultaneous linear equations based on the assumptions of substitutions in the general copiapite formula.

0003–004X/80/0910–0961$02.00

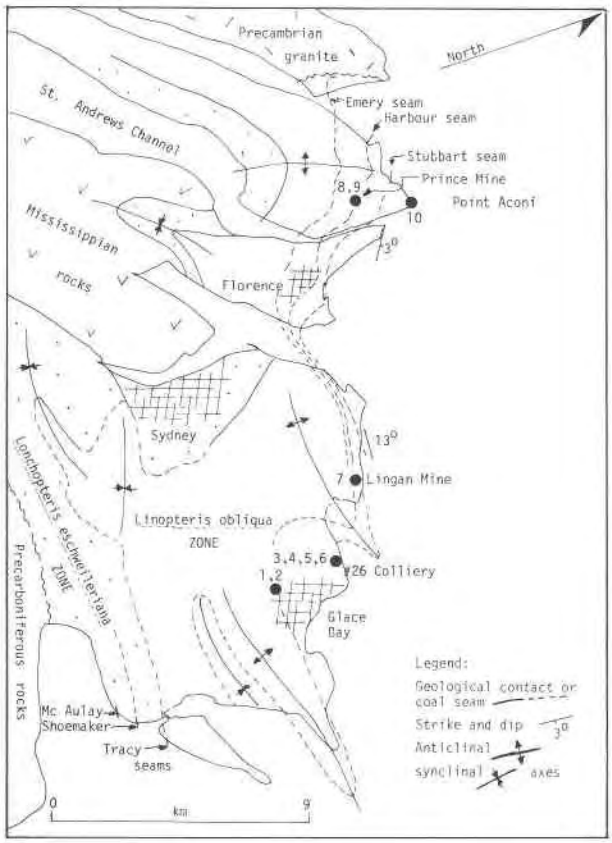

Fig. 1. Sample locations of copiapites ● 1,2 in Sydney Coalfield, Cape Breton Island, Nova Scotia, Canada

Analytical procedures

Samples for this study were hand-picked under a binocular microscope at 30× magnification. The purity of the samples is estimated to be in the range 96–100%. Standard chemical methods were employed for the quantitative analyses (Zodrow and McCandlish, 1979). In the X-ray identification of the specimens Fe-filtered Co*K* radiation was used. The samples were not ground, in order to avoid poor X-ray diffraction patterns owing to broadening of lines (Jolly and Foster, 1967, p. 1221). Portions of the samples [accession numbers 978GM-514(2), 977GF-682(2), 978GM-481, 366, 371, 346, 273, 282 and 524 of the Nova Scotia Museum in Halifax, Nova Scotia, numbered 1 to 10 in Table 2, respectively] are deposited with the National Museums of Canada in Ottawa, Ontario. Some of these samples are also deposited with the Smithsonian Institution, Washington, D. C., U.S.A., and the Musée de Minéralogie, Paris, France.

Experimental data

Table 2 indicates that minerals of the copiapite group vary greatly in composition; this is characteristic of the group. Sample #7 from Lingan has the lowest "Fe," but concomitantly the highest values of Al, Mg, Na, Mn, and Ni. A high Zn content reported for the Point Aconi sample (#10) is the second instance of high-Zn hydrated sulfates found in this general area. The other high Zn example was found in the aluminocopiapite from the Prince mine (Zodrow and McCandlish, 1979, p. 67). The lowest Al content is associated with #9 (collected from the coal face), whereas the other sample from this mine (#8) with an Al content of 2.46% was collected as a precipitate in the mine-drainage system close to the surface.

It is possible to predict the environment of formation of the copiapite group minerals, subsurface or surface, by color. Specimens of light lemon (canary) hue most likely crystallized on the surface, *e.g.*, on the Emery seam, the Point Aconi seam, and mine dumps, and in locations by the sea. Specimens of deep yellow hue are generally found underground, *e.g.*, in the Prince and 1-B mines. There is also a remarkable difference in reactivity of these minerals from the Prince mine as compared with copiapite samples from sample points 3, 4, 5, and 6 (Fig. 1), *i.e.*, the 1-B mine of #26 Colliery. The latter speci-

Table 1. Aluminum concentrations in the Sydney Coalfield, Cape Breton Island, Nova Scotia

Background concentrations	
Groundwater: well holes[1]	
Lonchopteris eschweileriana zone	*Linopteris obliqua* zone
0.05 ppm and less	0.05 ppm and less
Mc Askill Brook[2]	
water column	stream sediments
0.16 to 0.30 ppm	1,300 ppm
Shales	
argillaceous	carbonaceous
11.14 to 14.83 per cent	15.37 per cent
Coal and Pyrite	
Phalen seam: 465 ppm	pyrite (Mc Aulay seam): 475 ppm
Acid Run-Offs	
Lingan mine, coal storage:	4,350 (2,000)[3] ppm
Lingan mine, coal storage:	90 ppm, recent accumulation
Prince mine, coal storage:	680 (1,090) ppm

1 uncontaminated wells scattered about the coalfield.
2 sampled over a range of discharges and over all four seasons; leached from -60 mesh grain size of sediments. This stream is regarded as a standard because of its uncontaminated water. 3 resampled after four weeks with the last week having heavy rains.

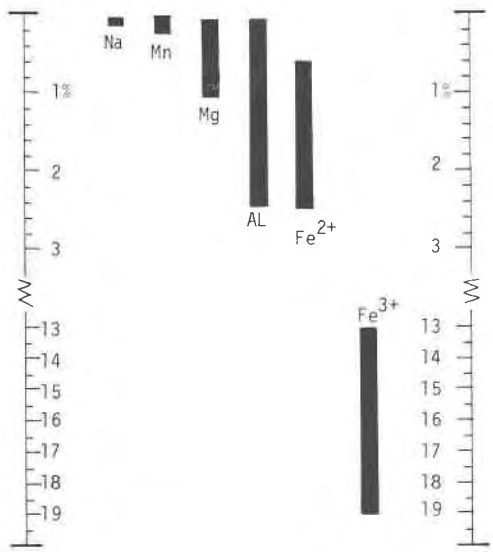

Fig. 2. Range of chemical elements in copiapite samples studied over which Model 1 in Table 4 applies.

mens show no alteration reactions after two years of storage under ambient conditions, whereas some specimens from the Prince mine show these reactions *in vitro* while stored under the same conditions as the 1-B mine samples:

Aluminocopiapite →
- natrojarosite, $NaFe_3(SO_4)_2(OH)_6$
- roemerite, $Fe^{2+}Fe^{3+}(SO_4)_4 \cdot 14H_2O$
- paracoquimbite, $Fe_2(SO_4)_3 \cdot 9H_2O$
- amarantite, $Fe(SO_4)(OH) \cdot 3H_2O$

The reactions leading to natrojarosite and amarantite need confirmation.

A linear substitution model

On the assumption that Na, Ca, Mg, Mn, Fe^{2+}, and Al substitute in the X position and some Al for Fe^{3+} in the R position of the structural formula, a model of substitution in copiapite, ignoring Zn in sample #10 and K for all of the samples, can be proposed:

$$[Na_vCa_wMg_xMn_Y\,Fe^{2+}_Z Al_{1-(V+W+X+Y+Z)}]$$
$$[Fe^{3+}_G Al_{1-G}]_4(SO_4)_6(OH)_2 \cdot nH_2O$$

The molecular weight (= MW), correct to two decimal places, is given by MW = a − bV − cX + dY + hZ + fG + jW, where a = 1105.59, b = 3.99, c = 2.66, d = 27.95, h = 28.86, f = 115.46 and j = 13.09. V, W, X, Y, Z, and G are stoichiometric coefficients that are numerically evaluated by the solution of a set of simultaneous linear equations. Table 3 shows a generalized form of the linear equations in matrix format. There are no numerical restrictions on the coefficients, but the proportions of X to R or 1:4 in the structural formula of the copiapite group require that each coefficient lie between zero and unity, that G be between zero and unity, and that the sum of the coefficients be less than unity:

$$(0 < V, W, X, Y, Z < 1); (0 \leq G \leq 1)$$
$$(V + W + X + Y + Z) < 1 \qquad (1)$$

The mathematical existence of the V, ... , G coefficients is dependent on a non-zero determinant of the matrix shown in Table 3. Al and SO_4 percentages may be predicted and compared with experimentally obtained values of Table 2. To predict Fe and SO_4 percentages, interchange subscripts of Al and Fe; a new matrix must now be formed (that in Table 3 must be rearranged).

Table 2. Chemical analyses of copiapite samples from the Sydney Coalfield, Cape Breton Island

No.[1]	1	2	3	4	5	6	7	8	9	10
Total Fe%	18.64	18.72	13.28	18.72	16.24	18.88	8.00	14.24	21.60	17.60
Fe^{3+}	18.02	17.83	13.01	17.92	15.62	18.68	3.18	13.26	19.06	16.53
Fe^{2+}	0.62	0.89	0.27	0.80	0.62	0.20	4.82	0.98	2.54	1.07
SO_4	52.74	47.78	45.97	48.70	45.77	46.68	47.07	48.40	47.84	49.61
Al	1.10	1.87	1.66	1.63	1.40	0.98	3.62	2.46	0.10	1.45
Mg	0.64	0.57	2.36	0.17	1.58	1.54	2.76	1.08	0.10	0.56
Ca	0.06	0.07	0.02	0.02	0.02	0.02	0.09	0.03	0.04	0.19
Na	0.10	0.12	0.96	0.11	0.92	0.16	2.12	0.16	0.14	0.19
Mn	0.26	0.16	0.38	0.06	0.29	0.20	0.92	0.22	0.07	0.04
K	0.02	0.04	0.01	0.01	0.01	0.01	0.01	0.01	0.02	0.02
ppm										
Cu	176	160	82	82	64	22	274	269	85	80
Ni	376	416	328	136	240	120	520	400	128	408
Zn	84	84	428	124	204	48	640	560	92	3300
Insol.	*0.10	0.50	nil	nil	nil	nil	0.16	nil	0.08	0.08
Total (less H_2O and OH)	73.56	69.33	64.63	69.42	66.23	68.47	64.59	66.60	59.91	59.66

*Coal

[1] For locations of samples see Fig. 1.
Samples No. 1 and 2 are from the exposed coalface of the Emery seam in Glace Bay; No. 3,4,5 and 6 from various locations in 1-B mine, #26 Colliery; No. 7 is a mine water precipitate from open air storage of coal at Lingan mine; No. 8 and 9 were collected from the Prince mine: 9 is a direct alteration product of pyrite in situ (in coal), while 8 is a precipitate from an underground drainage ditch; No. 10 originated from an outcrop of the Point Aconi seam.

Table 3. Model of substitution of copiapite in matrix format

$$\begin{array}{lllllll}
(\mathrm{Na} + \underline{\mathrm{Na}}\cdot b)V & + \underline{\mathrm{Na}}\cdot c\cdot X & - \underline{\mathrm{Na}}\cdot d\cdot Y & - \underline{\mathrm{Na}}\cdot h\cdot Z & - \underline{\mathrm{Na}}\cdot f\cdot G & - \underline{\mathrm{Na}}\cdot j\cdot W & = a\underline{\mathrm{Na}} \\
\underline{\mathrm{Mg}}\cdot b\cdot V & + (\mathrm{Mg} + \underline{\mathrm{Mg}}\cdot c)X & - \underline{\mathrm{Mg}}\cdot d\cdot Y & - \underline{\mathrm{Mg}}\cdot h\cdot Z & - \underline{\mathrm{Mg}}\cdot f\cdot G & - \underline{\mathrm{Mg}}\cdot j\cdot W & = a\underline{\mathrm{Mg}} \\
\underline{\mathrm{Mn}}\cdot b\cdot V & + \underline{\mathrm{Mn}}\cdot c\cdot X & + (\mathrm{Mn} - \underline{\mathrm{Mn}}\cdot d)Y & - \underline{\mathrm{Mn}}\cdot h\cdot Z & - \underline{\mathrm{Mn}}\cdot f\cdot G & - \underline{\mathrm{Mn}}\cdot j\cdot W & = a\underline{\mathrm{Mn}} \\
\underline{\mathrm{Fe}^{2+}}\cdot b\cdot V & + \underline{\mathrm{Fe}^{2+}}\cdot c\cdot X & - \underline{\mathrm{Fe}^{2+}}\cdot d\cdot Y & + (\mathrm{Fe}^{2+} - \underline{\mathrm{Fe}^{2+}}\cdot h)Z & - \underline{\mathrm{Fe}^{2+}}\cdot f\cdot G & - \underline{\mathrm{Fe}^{2+}}\cdot j\cdot W & = a\underline{\mathrm{Fe}^{2+}} \\
\underline{\mathrm{Fe}^{3+}}\cdot b\cdot V & + \underline{\mathrm{Fe}^{3+}}\cdot c\cdot X & - \underline{\mathrm{Fe}^{3+}}\cdot d\cdot Y & - \underline{\mathrm{Fe}^{3+}}\cdot h\cdot Z & + (\ 4\mathrm{Fe} - \underline{\mathrm{Fe}^{3+}}\cdot f)G & - \underline{\mathrm{Fe}^{3+}}\cdot j\cdot W & = a\underline{\mathrm{Fe}^{3+}} \\
\underline{\mathrm{Ca}}\cdot b\cdot V & + \underline{\mathrm{Ca}}\cdot c\cdot X & - \underline{\mathrm{Ca}}\cdot d\cdot Y & - \underline{\mathrm{Ca}}\cdot h\cdot Z & - \underline{\mathrm{Ca}}\cdot f\cdot G & + (\mathrm{Ca} - \underline{\mathrm{Ca}}\cdot j)W & = a\underline{\mathrm{Ca}}
\end{array}$$

Where Na, Mg, Mn, Fe and Ca are atomic weights; $\underline{\mathrm{Na}}$, $\underline{\mathrm{Mg}}$, $\underline{\mathrm{Mn}}$, $\underline{\mathrm{Fe}^{2+}}$, $\underline{\mathrm{Fe}^{3+}}$ and $\underline{\mathrm{Ca}}$ are analytical values (TABLE 2) of sodium, magnesium, manganese, iron and calcium, respectively. The coefficients from the molecular-weight formula (MW) are b, c, d, h, f, j and a. The stoichiometric coefficients to be computed are V, X, Y, Z, G *and* W. ($a\underline{\mathrm{Na}}$, $a\underline{\mathrm{Mg}}$, $a\underline{\mathrm{Mn}}$, $a\underline{\mathrm{Fe}^{2+}}$, $a\underline{\mathrm{Fe}^{3+}}$, $a\underline{\mathrm{Ca}}$) is the constant matrix vector.

NOTE: divide the MW coefficients by 100 because of percentage calculations before solving for the stoichiometric coefficients.

Other substitutional schemes may be derived by adding (subtracting) metals to the model. This necessitates a new MW and subsequently a new matrix. The latter is formed from that in Table 3 by adding (subtracting) appropriate rows (columns), manipulating the coefficients and their signs consistently; see the appended derivation.

Values in Table 4 were obtained by computing V to G on the basis of the chemical data in Table 2, then calculating weight percentages shown. Not all solved systems satisfy the conditions in (1), but all numerical solutions satisfying the algebraic equations are valid. Model 1 in Table 4 is a direct mathematical realization of the expanded structural formula; in Model 2 calcium is deleted, and Model 3 is characterized not only by deleting calcium but also by assuming that all Al is in the X site. The Fe% values are reproduced from solutions of the systems of simultaneous linear equations and thus afford an evaluation of the mathematical efficiency (numerical accuracy).

Table 5 summarizes those formulae, according to Model 1, in which (1) is satisfied. The water content for each representation was obtained from a deterministic simulation process under the assumption of constant $(OH)_2$ content. Decreasing $n = 20$ by 0.1, that number of water molecules was selected subjectively when calculated metal totals plus sulfate compared well with those in Table 2. As the copiapite group minerals may readily lose several "free" molecules of water without significant damage to the framework (Fanfani *et al.*, 1973, p. 321), the range of simulated values of n is theoretically defensible.

Discussion of results

Although Table 2 shows diversity of composition of the copiapite samples studied, they may be classified in the copiapite group with ease, as shown in Table 5: #8 is a magnesiocopiapite, #9 is a copiapite, #10, 2, and 1 are magnesian aluminocopiapite, and #4 is an aluminocopiapite. Thus the only aluminocopiapite identified so far originated from the 1-B mine, followed closely by #1 from the Emery seam in Glace Bay. It is amazing to observe that the coal face and its mine-drainage ditch represent such different environments as to produce copiapite and magnesiocopiapite, samples #9 and 8, respectively. It appears that the copiapite minerals precipitated from acid mine-waters are relatively enriched in Al, Mg, Mn, Ni, Zn and Cu, but relatively depleted in "Fe," *e.g.*, samples #7 and 8.

Table 4 shows that if all Al is assumed to be in the X position of the copiapite structure and Ca is deleted as a substituting metal, Model 3 gives the relative worst-predicted values of Al and SO_4, the relative worst-reproduced Fe%, and three instances of negative Al content. Definite improvements are offered by Models 1 and 2 in these respects. Solutions by simultaneous linear equations satisfying proportions in the general formula X to R as 1:4, according to the preferred Model 1, are observed only over particular ranges of analytical values (Fig. 2). This ratio

Table 4. Comparison between predicted and observed values of Al and SO_4 according to different assumptions in the substitutional model of copiapite

Sample No.	1	2	3	4	5	6	7	8	9	10
MODEL 1: $(Na_V Ca_W Mg_X Mn_Y Fe^{2+}_Z Al_{1-(V+W+X+Y+Z)})(Fe^{3+}_G Al_{1-G})_4 (SO_4)_6 (OH)_2 \cdot 20.0H_2O$										
Al% Predicted Value	1.04	1.10	0.95+	1.62	0.30+	-0.09+	3.33+	2.91	0.08	1.71
Al% Observed, TABLE 2	1.10	1.87	1.66	1.63	1.40	0.98	3.62	2.46	0.10	1.45
SO_4% Predicted Value	47.07	47.07	48.64	47.08	47.82	47.10	49.96	48.30	46.30	47.30
SO_4% Observed, TABLE 2	52.74	47.78	45.97	48.70	45.77	46.68	47.07	48.40	47.84	49.61
Fe% Reproduced Value*	18.67	18.75	13.39	18.73	16.35	18.85	8.08	14.28	21.62	17.63
Fe% Observed, TABLE 2	18.64	18.72	13.28	18.72	16.24	18.88	8.00	14.24	21.60	17.60
MODEL 2: $(Na_V Mg_X Mn_Y Fe^{2+}_Z Al_{1-(V+X+Y+Z)})(Fe^{3+}_G Al_{1-G})_4 (SO_4)_6 (OH)_2 \cdot 20.0H_2O$										
Al% (Predicted Value	1.04	1.11	0.95+	1.62	0.30	0.15+	3.34+	2.91	0.09+	1.71
SO_4% (Predicted Value	47.08	47.08	48.64	47.09	47.82	47.22	49.98	48.30	46.31	47.42
Fe% (Reproduced Value*	18.67	18.75	13.39	18.73	16.35	18.40	8.08	14.28	21.60	17.63
MODEL 3: $(Na_V Mg_X Mn_Y Fe^{2+}_Z Al_{1-(V+X+Y+Z)})\ Fe^{3+}_4 \cdot (SO_4)_6 (OH)_2 \cdot 20.0H_2O$										
Al% (Predicted Value	0.94	0.92	-1.89+	1.47	-1.09+	0.16	-6.29+	0.23	0.64	0.84
SO_4% (Predicted Value	47.08	46.99	47.25	47.01	47.14	47.22	46.11	46.98	46.58	46.98
Fe% (Reproduced Value*	18.45	19.10	18.58	19.02	18.89	18.40	22.76	19.19	20.60	19.28

*Total Fe computed from corresponding molecular weight formula. +Stoichiometric requirements not satisfied.

is not satisfied for any value that falls outside its range. The possibility that certain pure end-members in the group, *e.g.*, Mn or Mg, are mathematically not feasible is thus implied.

The failure of the model in certain instances, as for example if (Na + Mg) > 1.70 or when Fe^{2+} is rather low, and an apparent excess of sulfate (average observed are larger than average predicted values), are problems demanding attention. The excess sulfate is marginally decreased but the spread between predicted and observed Al values widens considerably when residual positive charges of the X position of the stoichiometric formulae in Table 5 are algebraically eliminated; this may be seen from Table 6, in which the average of 47.30 percent of predicted sulfate is marginally higher than the 47.19 percent average of predicted values from stoichiometric formulae in Table 4, as compared with the observed average value of 49.18 percent (Table 2). Aluminum predictions in Table 6 are definitely inferior to those in Table 4.

Whether the excess of sulfate is a characterizing

Table 5. Stoichiometric formulae of minerals from the copiapite group, Sydney Coalfield, Cape Breton Island

$(Na_{0.083}\ Ca_{0.009}\ Mg_{\underline{0.531}}\ Mn_{0.048}\ Fe^{2+}_{0.210}\ Al_{0.119})$	$(Fe^{3+}_{0.710}\ Al_{0.290})_4$	$(SO_4)_6\ (OH)_2 \cdot \approx 20.0H_2O$	Sample No. 8
$(Na_{0.076}\ Ca_{0.012}\ Mg_{0.051}\ Mn_{0.016}\ Fe^{2+}_{\underline{0.566}}\ Al_{0.280})$	Fe^{3+}_4	$(SO_4)_6\ (OH)_2 \cdot \approx 18.5H_2O$	Sample No. 9
$(Na_{0.100}\ Ca_{0.058}\ Mg_{\underline{0.280}}\ Mn_{0.009}\ Fe^{2+}_{0.233}\ Al_{\underline{0.320}})$	$(Fe^{3+}_{0.902}\ Al_{0.098})_4$	$(SO_4)_6\ (OH)_2 \cdot \approx 18.0H_2O$	Sample No. 10
$(Na_{0.064}\ Ca_{0.021}\ Mg_{\underline{0.287}}\ Mn_{0.035}\ Fe^{2+}_{0.195}\ Al_{\underline{0.398}})$	$(Fe^{3+}_{0.979}\ Al_{0.021})_4$	$(SO_4)_6\ (OH)_2 \cdot \approx 18.5H_2O$	Sample No. 2
$(Na_{0.053}\ Ca_{0.018}\ Mg_{\underline{0.323}}\ Mn_{0.058}\ Fe^{2+}_{0.136}\ Al_{\underline{0.412}})$	$(Fe^{3+}_{0.989}\ Al_{0.011})_4$	$(SO_4)_6\ (OH)_2 \cdot \approx 16.0H_2O$	Sample No. 1
$(Na_{0.058}\ Ca_{0.006}\ Mg_{0.085}\ Mn_{0.013}\ Fe^{2+}_{0.175}\ Al_{\underline{0.663}})$	$(Fe^{3+}_{0.983}\ Al_{0.017})_4$	$(SO_4)_6\ (OH)_2 \cdot \approx 18.4H_2O$	Sample No. 4

Note: charge-balanced formulae have these Al coefficients, by (2 - V - 2(W + X + Y + Z))/3:
0.107, 0.211, 0.246, 0.286, 0.292, and 0.461, respectively.

Sample No. 8 is a magnesiocopiapite; No. 9 the species' name, copiapite; Nos. 10, 2, and 1 are magnesian aluminocopiapite, and No. 4 is aluminocopiapite.

Table 6. Comparison between predicted and observed values of Al and SO_4 according to Model 1: residual positive charge of stoichiometric formulae in Table 5 is eliminated

Sample No.	1	2	3	4	5	6	7	8	9	10
Al%[1]	0.74	0.82	1.91+	1.17	1.00+	-.08+	5.49+	2.86	-.09	1.42
TABLE 4	1.04	1.10	0.95+	1.62	0.30+	-.09+	3.33+	2.91	0.08	1.71
Observed TABLE 2	1.10	1.87	1.66	1.63	1.40	0.98	3.62	2.46	0.10	1.45
SO_4%	47.19	47.18	48.16	47.29	47.48	47.09	48.82	48.31	46.37	47.46
TABLE 4	47.07	47.07	48.64	47.08	47.82	47.10	49.96	48.30	46.30	47.30
Observed TABLE 2	52.74	47.78	45.97	48.70	45.77	46.68	47.07	48.40	47.84	49.61

AVERAGES

	This TABLE	TABLE 4	Observed (TABLE 2)
Al%[2]	1.153	1.410	1.435
SO_4%[2]	47.300	47.187	49.178
SO_4%[3]	47.535	47.664	48.056

+Stoichiometric requirements not satisfied.

[1]Let the coefficient of Al in TABLE 4 be: (2 - V - 2(W+X+Y+Z))/3 and also substitute this expression in the molecular weight formula (MW) to obtain a new formula weight and hence the values; see TABLE 5.

[2]Average of 6 samples, or samples of +Stoichiometric requirements not satisfied are excluded.

[3]Average of all 10 samples.

feature of copiapite samples from the Sydney Coalfield, or a problem of mathematical manipulation in the prediction process, is not known at this juncture without further investigation. Fanfani *et al.* (1973), however, show well the problem between the relationship of chemical data and atomic arrangements in some copiapite samples.

Continuing research is concentrated on possible (OH) substitutions and recognition of additional anions, and sulfate content. Unit-cell refinements are in progress.

Appendix

Derivation of a system of simultaneous linear equations

The MW is obtained directly from Model 1, Table 4, by expanding: $Na_v + Ca_w + Mg_x + Mn_y + Fe_z + 4Fe_G + [4Al - 4Al_G + Al - Al(V + W + X + Y + Z)] + 6(SO_4) + 2(OH) + 20H_2O$ which upon evaluation in terms of atomic weights of the components leads directly to $(a - bV - cX + dY + hZ + fG + jW) = MW$. To reproduce Ca% from Table 2 we consider that $Ca\% = Ca_w/MW$ which when rearranged becomes the last equation (row) in Table 3.

$$Ca = Ca_w/(a - bV - cX + dY + hZ + fG + jW)$$

Exchange the constant term a Ca with Ca_w, collect terms to obtain

$$-CabV - CacX + CadY + CahZ + CafG - (Ca - Caj)W = -aCa$$

when multiplied by -1 the last row of the matrix in Table 3 is realized. This procedure is systematically followed for the remaining elements.

To add a metal, say Cu, to the substitutional model would necessitate (a) augmenting the number of subscripts and calculating a new MW, and (b) forming a new Table 3 according to the above developments. The sign of the Cu component in MW is "+" as Cu has a larger atomic weight than Al, *the metal value to be predicted.* However, in the matrix format the "+" changes to a "−". To delete a metal component, put zero in the appropriate term of MW (and delete the corresponding row and column in the matrix).

Note added in proof

Aluminocopiapite, according to X-ray analysis, collected from a coal seam in Smithers, B.C., Canada, by Keith McCandlish in 1979 with composition 11.92% Fe^{3+}, 2.23% Fe^{2+}, 42.75% SO_4, 1.54% Al, 1.05% Mg, 0.13% Ca, 0.02% Na, and 0.04% Mn does not satisfy the stoichiometric conditions, *i.e.*, Fe^{3+} and Na contents appear to be too low according to the empirical criteria in Figure 2.

Acknowledgments

This investigation is wholly supported by N. R. C. (Canada), Grant A6125. I thank Dr. J. K. Sutherland, Research and Productivity Council of New Brunswick, for identification and chemical analyses of the samples. I acknowledge valuable help from the computer center at Dalhousie University, Halifax, N. S., in executing by remote entry the program of simultaneous linear equations. Dr. R. F. Martin, Geological Sciences, McGill University, Montreal, P. Q., is thanked for constructive critique of the manuscript. F. Baechler, Nova Scotia Department of Environment, Water Planning and Management Division, Sydney, N. S., supplied information on aluminum in the Sydney Coalfield, Table 1; this cooperation is appreciated. The use of the algebraic expression for the elimination of residual positive charges was suggested by Professor G. A. Chao, Department of Geology, Carleton University, Ottawa, Ontario.

References

Berry, L. G. (1947) Composition and optics of copiapite. *Univ. Toronto Stud., Geol. Ser., 21,* 21–34.

Fanfani, L., A. Nunzi, P. F. Zanazzi and A. R. Zanzari (1973) The copiapite problem: the crystal structure of a ferrian copiapite. *Am. Mineral., 58,* 314–322.

Jolly, J. H. and H. L. Foster (1967) X-ray diffraction data of aluminocopiapite. *Am. Mineral., 52,* 1221–1223.

Zodrow, E. L. and K. McCandlish (1978a) Hydrated sulfates in the Sydney Coalfield, Cape Breton, Nova Scotia. *Can. Mineral., 16,* 17–22.

——— and ——— (1978b) Roof weakness: fossilization and cyclic regenerative hydrated sulfates. Discussion. *Can. Inst. Min. Met. Bull., 71(796),* 90–91.

——— and ——— (1979) Hydrated sulfates in the Sydney Coalfield of Cape Breton, Nova Scotia. II. Pyrite and its alteration products. *Can. Mineral., 17,* 63–70.

Manuscript received, October 22, 1979;
accepted for publication, January 29, 1980.

American Mineralogist, Volume 65, pages 968–969, 1980

Nickeloan melanterite from Sudbury Basin

MARTIN S. RUTSTEIN

Department of Geological Sciences
State University of New York
College at New Paltz
New Paltz, New York 12561

Abstract

Locomotive heat discharge on nickel sulphide ore and slag northwest of Sudbury, Ontario has formed nickeloan melanterite. The uncommon Ni–Fe substitution is the result of the unusual "weathering" of an atypical source material. The existence of the septahydrate rather than the tetrahydrate is due to the elevated temperatures and humidities of the locomotive steam.

Introduction

A visually most striking "outcrop" of an efflorescent bloom was observed in 1978 at a railroad locomotive switching site on Rt. 144 in Levack, 25 km northwest of Sudbury, Ontario. The material was identified as nickeloan melanterite [$(Fe,Ni)SO_4 \cdot 7H_2O$] by X-ray diffraction and energy-dispersive spectra techniques.

This particular occurrence is notable for three reasons. The end-members melanterite ($FeSO_4 \cdot 7H_2O$) and morenosite ($NiSO_4 \cdot 7H_2O$) are not uncommon weathering products of suitable protoliths, the latter especially in mines of the Sudbury, Ontario area (Hawley, 1963, Table 2). However, while Fe–Mg and Ni–Mg substitution have been documented, no natural occurrences of Fe–Ni solid solution in sulphates are noted in any of the standard descriptive mineralogy references. Second, the local climate is conducive to the formation of rozenite ($FeSO_4 \cdot 4H_2O$) rather than the septahydrate (Ehlers and Stiles, 1965). Third, the paragenesis brings into question whether or not the phase is "naturally occurring" and thus a mineral according to most common definitions. This note describes the composition and paragenesis of the material and suggests a modification of the definition.

Description

Bright green to blue–green concretionary and stalagmitic masses occur as individual and aggregate clusters up to 15–20 cm in diameter on gossan-like material. The iron gossan appears to have formed from ore which dropped off trains as well as from weathering of slag fill. Clusters are most dense in the central portion of a railroad switching site where ore cars from mines to the northwest are shunted onto tracks to Sudbury. From the center of the site, cluster concentrations decrease to zero longitudinally within 25 m and laterally within 5 m. Sparser concentrations occur within track sets and between sets. The spacial limitation is not due to lack of adequate source material since the gossan-like material extends beyond the zone of accumulation.

Optical study of this material revealed the occasional presence of fine-grained disseminated silicate impurities in the sulphate. These iron-bearing silicate impurities did not yield a recognizable X-ray pattern because of their low concentration and amorphous nature.

The results of qualitative energy-dispersive spectra studies of the concretionary material are consistent with the identification from X-ray diffraction of $(Fe,Ni)SO_4 \cdot 7H_2O$. The following elements were identified (with peak heights approximately normalized to S): S (100), Fe (75), P (25), Si (30), Ni (20), Al (15), Cu (5), K (tr), Ca (tr), Co (tr), Cr (tr). Since such intensities are only crude approximations of relative elemental abundances, spectra were also obtained for pure samples of hydrous iron and nickel sulphates. Assuming a linear relationship between metal/sulphur peak intensities and bulk composition, comparison of the spectra of the unknown sample with the pure end members yields a composition of 8 wt% nickel sulphate and 80 wt% iron sul-

0003-004X/80/0910–0968$02.00

phate. The lack of summation to 100% suggests that the intensity:composition relationship might not be linear, but instead might display a negative deviation. Evaluation of various slopes and consideration of analytical errors indicates a composition of 80–90% iron end members and 10–20% nickel end member.

The X-ray pattern of the slag matrix was identified as consisting mainly of a clinopyroxene-like phase. Energy-dispersive analysis of slag matrix material revealed the following elements (given with peak heights here approximately normalized to Si): Si(100), S(80), Fe(70), P(50), Al(45), Cl(30), K(15), Ca(10), Mg(5), Ni(tr), As(tr). The physical state of the phosphorus, probably added during smelting, could not be determined. The chlorine may be a residue from salts used to melt snow. Copper was not detected in the matrix, although the sulphate has an Fe–Cu energy dispersive intensity ratio of 15:1.

These data are consistent with the efflorescent bloom having formed from oxidative alteration and hydration of, and on, iron silicate slag in the intimate presence of Cu–Ni–Fe sulfide ore. Retgers as well as Wyrouboff (in Palache *et al.,* 1951, p. 517) reported that in experimental studies on Mg–Fe–Ni sulphate hydrates, "Fe substitutes for Mg up to at least Fe–Ni = 1:5." The lack of such compositions in natural environments is due to the rarity of suitable protoliths for weathering. In this occurrence, the lack of Mg and the availability of Fe and Ni have produced this unusual solid solution.

Initially, the laboratory hydration–dehydration of the sulphate was readily reversible. However, after a few months of storage in a water-containing dessicator, the reversible reaction could no longer be demonstrated since the iron had oxidized and the sulphate was partially converted to limonite. Before this oxidation had started, the dehydrated material exhibited an X-ray diffraction pattern interpreted as due to a single phase similar to the tetrahydrate rozenite ($FeSO_4 \cdot 4H_2O$). Thus, the conversion of this partial nickeliferous–ferrous solid solution suggests that a Ni tetrahydrate analogue to $FeSO_4 \cdot 4H_2O$ may be possible. However, the natural occurrence of this as a pure phase has not yet been reported.

Discussion

Ehlers and Stiles (1965) conclude that the stability field of rozenite and melanterite is a simple function of temperature and relative humidity. Under drier conditions, the tetrahydrate is stable. The amount of Ni solid solution in the materials studied here is believed unlikely to have a pronounced effect on these stability relations. Thus, it is unusual to observe the septahydrate in a mid-continental region of moderate humidity, where rozenite is more likely to form (see Jambor and Traill, 1963). On the other hand, a source for elevated relative humidity (and temperature to speed the reaction) is locally available. At the switching site, cooling motors discharge heated air laterally from the engines. Reaction with moderately humid air produces a steam which "weathers" the ore and slag rubble. This causative agent restricts the sulphate formation longitudinally and laterally along the right-of-way in the switching area. Thus, even though similar source material is available outside of the immediate area of bloom formation, the limited "artificial climate" localizes formation of the septahydrate. Further, in 1979 when the switching site was unused because of a labor strike, no bloom formation was observed.

The hydrated sulphate formed not as the result of man's willful action, but as a by-product of or incidental to man's direct and deliberate activities. The oft-quoted definition of Berry and Mason (1959, p. 3–4) notes that a mineral is "naturally occurring," although exceptions are often made which tend to be largely dependent upon the degree of human *vs.* natural (non-human) activity involved. To accommodate anthropogenic phases, the following formalized redefinition is proposed: "a mineral . . . should have formed by natural processes which are not the result of man's willful or deliberate actions . . ." Then, the nickeloan melanterite discussed herein is clearly not a synthetic analogue to a mineral, but is a mineral in the strict sense.

Note added in proof

By July 1980, the "outcrop" no longer exists, having been removed by bulldozing and the site covered with grass planted as part of a reforestation project.

Acknowledgments

The constructive comments of W. G. White are appreciated.

References

Berry, L. G. and B. Mason (1959) *Mineralogy: Concepts, Descriptions, Determinations.* Freeman, San Francisco.

Ehlers, E. G. and D. V. Stiles (1965) Melanterite–rozenite equilibrium. *Am. Mineral., 50,* 1457–1461.

Hawley, J. E. (1963) The Sudbury ores: their mineralogy and origin. *Can. Mineral., 7,* 1–207.

Jambor, J. L. and R. J. Traill (1963) On rozenite and siderotil. *Can. Mineral., 7,* 751–763.

Palache, C., H. Berman and C. Frondel (1951) *The System of Mineralogy,* Vol. II. Wiley, New York.

Manuscript received, June 18, 1979;
accepted for publication, April 18, 1980.

American Mineralogist, Volume 65, pages 970–980, 1980

The low-temperature inversion in sub-potassic nephelines

C. M. B. HENDERSON

Department of Geology, The University
Manchester M13 9PL, England

AND ALAN BRUCE THOMPSON

Institut für Kristallographie und Petrographie, ETH
Zürich CH-8092, Switzerland

Abstract

Differential scanning calorimetric (DSC) and high-temperature X-ray diffraction studies on seven nephelines belonging to the system $NaAlSiO_4$(Ne)–$KAlSiO_4$(Ks) show that samples with less than 2.5 mol percent Ks (sub-potassic nephelines) exhibit complex relations. A Type-C nepheline containing 1.6 percent Ks has a single sharp DSC peak near 360 K; this temperature is close to that at which extra X-ray reflections characteristic of an orthorhombic 3*c* superstructure disappear (365 K) and marks an inversion to hexagonal symmetry. Type-B nephelines containing 0 to 0.36 percent Ks have two DSC peaks below 480 K which are separated by 20° to 40°. The two peaks confirm the existence of two phases in Type-B nephelines and the presence of two inversions. For each sample, the lower-temperature DSC peak coincides with the disappearance of the orthorhombic superstructure (*cf.* Type-C) and the higher-temperature peak with the disappearance of extra X-ray reflections typical of a low-symmetry second phase. Type-B and -C nephelines have DSC scans similar to that for tridymite which suggests that the low-temperature inversions in sub-potassic nephelines are caused by the collapse of the 'tridymite-like' framework about the relatively small Na^+ in the larger cation sites. In contrast, nephelines with more than 2.5 percent Ks are hexagonal at room temperature and show no inversions. Thus a Type-H nepheline containing 27 percent Ks does not have extra X-ray reflections and does not show any peaks on DSC scans between 340 and 520 K.

The heat capacity (C_p°) data for A.407 (pure-Na, Type-B) above 500 K show excellent agreement with the C_p° equation fitted to the drop calorimetric data of Kelley *et al.* (1953) on synthetic pure Na nepheline between 467 and 1180 K and can be used for thermochemical calculations on Ks-bearing nephelines *above about 500* K.

Introduction

Although the natural occurrence of nepheline minerals is restricted, they have been the subject of many detailed experimental studies. In particular, the nepheline ($NaAlSiO_4$, Ne)–kalsilite ($KAlSiO_4$, Ks) system has served as a useful analogue for modelling activity–composition relations of other immiscible Na–K phases (*e.g.* feldspars, micas, and halides). In addition, nepheline solid solution towards SiO_2 has provided necessary information on defect solid solutions, and the $Na_6K_2Al_8Si_8O_{32}$ phase is an excellent example of what may be an ordered compound within a solid-solution series. However, nephelines of the same composition may crystallize in different space-groups under different conditions and these forms may be related by phase transitions of higher than first-order. Very little is known generally of how such transitions affect phase equilibria in mineral systems, but the large amount of information available for nephelines makes them suitable candidates for such studies.

Henderson and Roux (1977) showed that nephelines synthesized in the system Ne–Ks have different structures, depending upon composition and method of synthesis. At room temperature those with between 25 and 2.5 percent Ks (all compositions are given as mol percent) are hexagonal (Type-H). This

0003–004X/80/0910–0970$02.00

composition range has $x = 2.0$ to 0.2, where x is the number of K atoms in the unit cell $Na_{8-x}K_xAl_8Si_8O_{32}$. All X-ray peaks in this type of nepheline can be unequivocally indexed using the Hahn and Buerger (1955) cell (HBC). In contrast, Henderson and Roux (1977) showed that nephelines with <2.5 percent Ks [sub-potassic nephelines (Donnay *et al.*, 1959)] have extra reflections that cannot be indexed with the HBC, have anomalous pseudohexagonal cell parameters, and show multiple twin lamellae. Nephelines with between 2.5 and ~0.7 percent Ks ($x = 0.2$ to 0.06) were believed to be orthorhombic (Type-C) with a_h, $\sqrt{3}a_h$, $3c_h$ superstructures, where a_h and c_h refer to hexagonal cell parameters. Hydrothermally synthesized nephelines with 0 to ~0.7 percent Ks (Type-B) were shown to contain two phases, one with an orthorhombic $3c$ superstructure and a second with even lower symmetry. Pure-Na nephelines synthesized dry from gels at 1 atm were found to be single-phase (Type-A), with a different set of extra reflections from those characterizing pure-Na, Type-B nephelines.

Henderson and Roux (1977) showed that Type-B and -C nephelines inverted to hexagonal symmetry at ≤473 K; the inversion temperature decreased as the Ks content increased. The extra reflections and twin lamellae disappeared at the inversion, and the cell parameters became consistent with those expected for nephelines having the HBC structure. The specimens showed ~30° hysteresis, with inversion temperatures during cooling being lower than those on heating; however, the effect of cooling rate on the degree of hysteresis was not studied. All pure-Na, Type-B nephelines (A.72, A.88, A.407, and the Schairer sample) showed small steps in the a parameter at the low-temperature inversion with some specimens also having distinct steps in c, and hence discontinuities in volume (see Fig. 6, Henderson and Roux, 1977). A Type-C nepheline (N.233) showed inflections, but no steps in a and c at the inversion; the displacements in a and c were in the opposite sense so that no discontinuity in V was detected. A Type-A specimen (N.10) showed a rather different behavior. Although there was an inflection in a (but no step) at 453 K, and no apparent inflection in c, the extra reflections only disappeared above 873 K. The temperature of 453 K was equated with the low-temperature inversion observed in the other sub-potassic nephelines.

Henderson and Roux (1977) related the differences in the inversion behavior of the samples to varying degrees of collapse of the framework about the small Na cations that must occupy the larger cation site (Foreman and Peacor, 1970; Dollase, 1970). In addition it was suggested that superstructures observed in natural nephelines could also be related to framework collapse at the low-temperature inversion.

Because the thermal effects of the low-temperature inversion in nepheline are detectable by differential thermal analysis (*e.g.* Cohen and Klement, 1976), the inversion could be further characterized by differential scanning calorimetry (DSC). Because the inversion is *displacive* (in the sense of Buerger, 1951), it is important to correlate the presence or absence of a discontinuity in V, or in the coefficient of thermal expansion at the inversion, with possible changes in heat capacity or its integrated thermodynamic functions.

We have studied at least one sample of Type-A, -B, -C, and -H nephelines by DSC and the results are presented here. DSC measurements on Type-B nephelines show two heat effects at ≤473 K, consistent with the presence of two phases, but Henderson and Roux (1977) only identified one inversion at <473 K in such nephelines. We have, therefore, reconsidered the results of their X-ray experiments and have further studied the low-temperature inversion with several new samples using high-temperature X-ray diffraction methods.

X-ray investigations

Sample preparation and X-ray procedures

Several of the samples are those studied by Henderson and Roux (1976, 1977), namely: A.417, N.4, NE. Schairer, and A.407. Unfortunately, there were insufficient quantities of some of Henderson and Roux' samples for heat capacity measurements, so new samples (NE.12, NE.17, and NE.1289) were synthesized hydrothermally from gels of the appropriate compositions. The compositions and synthesis conditions for the nephelines studied are summarized in Table 1. Because the nepheline type is crucially related to Ks content, the compositions for some of the synthesized samples were confirmed by determination of K_2O by atomic absorption spectrophotometry. The quoted compositions (Table 1) are believed to be accurate to ±5 percent (relative).

Cell parameters were determined at room temperature (293 K) using a conventional Philips PW 1050 diffractometer with Cu$K\alpha$ radiation (Cu$K\alpha$ 1.54178, Cu$K\alpha'$ 1.54051Å) and a scanning rate of 0.5°2θ/min. Si was added as internal standard (a = 5.43065Å) and cell parameters were calculated by least squares.

Cell parameters at elevated temperatures were determined using the method of Henderson and Taylor (1975) in which the Pt sample holder peaks were used for internal standardization. The 2θ values for the peaks were measured with a vernier rule and are reproducible to within $\pm 0.005°$ 2θ.

The room temperature cell parameters (Table 1) for the sub-potassic nephelines refer to a pseudo-hexagonal cell, whereas those for Type-B nephelines are averaged values for the two phases present (Henderson and Roux, 1977, p. 293). This averaging is reflected in the relatively high standard errors for these samples.

The low-temperature inversion was studied with a heating stage mounted on an X-ray diffractometer, using a heating rate of ~3° min^{-1} and a cooling rate of ~5° min^{-1}.

Table 1. Synthesis conditions, composition and room temperature (293 K) cell parameters for different types of synthetic nephelines

Specimen	Ks mol %	T, K	P	Time days	a, A	c, A	V, A^3
Type-A							
N.4*	0	1390	1 atm	1	9.968(1)**	8.341(2)	717.7(2)
Type-B							
Schairer*+	0	1370 / 1320	1 atm	5 / 24	9.969(3)	8.361(4)	719.6(5)
A.407*	0	870	2.5 kbar	50	9.977(2)	8.339(4)	718.9(5)
NE.12	0.36	1170	1 kbar	4	9.931(6)	8.339(9)	719.5(9)
NE.1289	0.30	1240	2 kbar	3	9.995(3)	8.275(6)	715.9(5)
Type-C							
NE.17	1.6	990	1 kbar	3	9.990(1)	8.329(2)	719.9(2)
Type-H							
A.417	27	873	2 kbar	40	10.004(2)	8.390(3)	727.2(3)

* Data from Henderson and Roux (1977).
\+ Glass starting material; others synthesized from gel.
** Numbers in parentheses are estimated standard deviations of parameters : a, c x 10^3, V x 10^1.

X-ray results

The room-temperature X-ray patterns for the three new specimens show that NE.17 (1.6 percent Ks) is Type-C whereas NE.12 (0.36 percent Ks) and NE.1289 (0.30 percent Ks) are clearly Type-B. All three specimens have anomalous cell parameters at room temperature (Table 1) and plot below the 'normal nepheline line' defined in Figure 3 of Henderson and Roux (1977). Note that the average *c* parameter for the two phases in NE.1289 is substantially smaller than the *c* parameters for the specimens studied previously.

The inversion in NE.17 was monitored using the extra reflection at ~28.2° 2θ Cu$K\alpha$ which is characteristic of the orthorhombic 3*c* superstructure of Type-C nephelines. The reflection decreased in intensity and eventually disappeared over the temperature range 358–368±5 K, but it reappeared on cooling with a hysteresis of ~15°.

Type-B nephelines have split (002) reflections, indicating the presence of two phases. The presence of an extra reflection at ~28.2°2θ Cu$K\alpha$ confirms that one of the phases has the orthorhombic 3*c* superstructure whereas extra reflections at 22.6°, 29.2°, and 30.2° 2θ Cu$K\alpha$ presumably belong to the lower-symmetry second phase (Henderson and Roux, 1977, p. 293). Thus the inversions in NE.12 and NE.1289 (both Type-B) were monitored using the extra reflections at 28.2° and 30.2° 2θ, and the split (002) reflection. On heating NE.12, the 28.2° 2θ reflection decreased and disappeared over the temperature range 413–428±5 K. The (002) peak was broad and asymmetric at 448 K, showing that two phases were still present. The 30.2° 2θ reflection disappeared over the range 428–468±5 K. On cooling, the extra reflections reappeared at about 15° below these temperatures. On heating NE.1289, the 28.2° 2θ reflection disappeared over the range 413–428±5 K, (002) was comparatively sharp at 425 K, and the 30.2° 2θ extra reflection disappeared over the range 423–444±5 K. On cooling, all of the extra reflections reappeared at ~410 K but broadening of (002) could only be detected at ~365 K.

In NE.12 and NE.1289 the 28.2° 2θ reflection disappeared before there was any major decrease in the intensity of the 30.2° 2θ reflection. Further study of X-ray charts from heating experiments on Type-B nephelines N.1042 (0.2 percent Ks) and N.1040 (0.5 percent Ks) (Henderson and Roux, 1977) also showed that the extra reflections at ~28.2° 2θ disappeared ~10 K before the 30.2° 2θ reflection began to decrease. The same relationship was reported for the pure-Na, Type-B nephelines (*e.g.* A.72, Henderson and Roux, 1977, p. 289). The implication is that the two phases present in Type-B nephelines invert to hexagonal symmetry over different temperature ranges (see later discussion).

The X-ray patterns for NE.12, NE.17, and NE.1289 above their respective inversion temperatures are entirely consistent with hexagonal symmetry and can be fully indexed using the HBC. Cell parameters determined above the inversions are: NE.17 (408 K) a = 9.981 *esd* 0.001, c = 8.360 *esd* 0.002; NE.12 (500 K) a = 9.992 *esd* 0.001, c = 8.366 *esd* 0.002; NE.1289 (448 K) a = 9.983 *esd* 0.001, c = 8.360 *esd* 0.001Å. These values plot close to the 'normal nepheline line' and in this respect the new speci-

Table 2. Change in proportions of the two phases present in Type-B nephelines after annealing near the low-temperature inversion

Specimen	Mol. % Ks	% of phase with lower c parameter	
		Before annealing	After annealing
NE. Schairer	0	30	45
A.407	0	30	30
NE.12	0.36	30	50
NE.1289	0.30	80	50
A.72	0	40	80

mens are similar to other sub-potassic nephelines immediately above their inversion temperatures (Henderson and Roux, 1977, Fig. 3). Note that NE.1289 shows an increase of 0.085Å in c relative to the room temperature value.

Henderson and Roux (1977, p. 290 and 293) reported that the proportions of the two phases in Type-B nephelines at room temperature changed with thermal treatment. We have attempted to quantify this effect by comparing the peak heights of the split components of the (002) and (004) reflections before and after annealing the samples near the low-temperature inversion for 2 to 3 hours (Table 2). Because the split components substantially overlap, the estimated proportions are not better than ±20 percent (relative). After thermal treatment, A.72 and NE. Schairer (both pure-Na) and NE.12 (0.36 percent Ks) show *increased* proportions of the phase with the lower c parameter whereas this phase *decreased* in proportion in NE.1289 (0.30 percent Ks). All heat-treated samples show a marked increase in the intensities of the 30.2° 2θ extra reflection; thus it is the low-symmetry second phase that increases in amount. These relations allow the relative c parameters of the two phases in Type-B nephelines to be deduced for all samples except A.407. Thus in A.72, NE. Schairer, and NE.12 the low-symmetry second phase has the lower c parameter while the phase with the orthorhombic $3c$ superstructure has the higher c parameter. In NE.1289 the converse is true. Note that the c parameters for the low-symmetry phases in A.72 and NE.1289, estimated from the split (002) and (004) reflections, are very similar, with values of 8.325 and 8.315Å, respectively.

Differential scanning calorimetric study

DSC procedures with the Perkin Elmer DSC-2

DSC analysis is a comparative technique involving electrical–thermal balance between a sample sealed in a gold pan against an empty reference gold pan in the twin platinum holders of an adiabatic enclosure (O'Neill, 1966). The temperature scans with the DSC were performed at a rate of 10° min^{-1} with an instrument RANGE setting of 5 mV sec^{-1} cm^{-1}. Temperature and energy calibrations were made relative to the melting of indium metal (429.8 K) and the α–β quartz inversion (844.0 K) (Table 3). Because of the limited amounts of material available, only one aliquot was studied for some nepheline samples. However, two different aliquots studied for each of NE.12, NE.1289, and NE.17 showed that the DSC scans were reproducible.

Because the voltage displacement on a DSC scan is a function of mass, the weights of empty gold pans, sapphire reference disc, and the powdered nepheline samples in their gold pans were determined with a digital microbalance before and after each scan. Al-

Table 3. Experimental heat capacities of pure-Na, Type-B nepheline A.407 (g.f.w. = 142.055 g) determined by differential scanning calorimetry

Temp. T Kelvin	Heat capacity C_p^o J/(mol. K)	Temp. T Kelvin	Heat capacity C_p^o J/(mol. K)
367.8	135.5	466.8	165.5
372.8	136.3	471.7	157.6
377.7	137.7	476.7	152.9
382.7	138.4	481.6	148.1
387.6	139.6	486.6	147.8
392.6	140.5	496.1	145.2
397.5	141.6	501.1	145.6
402.5	142.2	506.1	148.9
407.4	143.5	511.1	146.7
412.3	144.9	521.1	147.0
417.3	146.3	531.1	147.6
422.2	149.4	541.0	149.1
427.2	150.9	551.0	149.2
432.1	155.2	561.0	150.0
437.1	159.6	571.0	151.0
		581.0	151.2
442.0	161.5	591.0	152.4
447.0	159.0	601.0	153.1
451.9	161.3	610.0	153.6
456.9	169.7	621.0	154.0
461.8	178.0	630.9	154.5
		640.9	154.9
		650.9	155.9
		660.9	156.4
		670.9	157.8
		680.9	158.6
		690.9	159.3
		700.9	160.7

Heat capacity was determined with reference to α-Al_2O_3 (Ditmars and Douglas, 1971) and is believed to be accurate to within 1 percent on the basis of alternate scans on a sapphire disc and α-Al_2O_3 powder.
Temperatures were calibrated against peak onset for indium melting at 429.8 K and the α-β quartz inversion at 844.0 K and have a precision of ~0.2°.

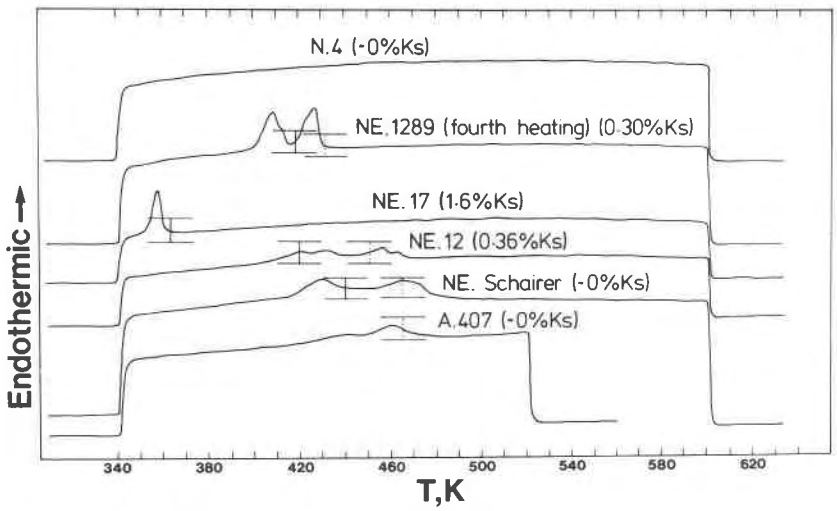

Fig. 1. Tracings of DSC scans for various nepheline samples in the temperature interval 340 to 600 K. Scans were made at 10 K min^{-1}, with a RANGE setting of 5 mcal sec^{-1} cm^{-1}, chart range 10 mV (= 25 cm) and chart speed 20 mm min^{-1}. The scan for NE.1289 is the fourth heating scan (after the three scans in Fig. 2). Sample weights are between 20 and 30 mg. The solid vertical lines refer to the temperatures (±10 K) at which the extra X-ray reflections at ~28.2°θ Cu$K\alpha$ disappear, and the dotted vertical lines to those (±10 K) at which the 30.2°2θ Cu$K\alpha$ extra X-ray reflections disappear. The displacements are a function of sample mass and heat capacity of sample and enclosing gold pans, and are measured relative to the low- and high-temperature isothermals bracketing the scans.

lowance was made for the small amounts of powdered samples that were lost during removal of the gold pans with a vacuum tool. Chart measurements were used as input for a computer program (originally written by K. Krupka, U.S. Geological Survey, Reston, and modified at ETH, Zürich) to make the necessary corrections for temperature calibration, differences in sample pan weights, energy calibration constant for the DSC instrument, and differences in low- and high-temperature isothermal baselines. The program was also used to compute the sample heat capacity relative to corundum (the sapphire reference disc), using data of Ditmars and Douglas (1971).

DSC results

Tracings of the chart recorder output for various nepheline specimens are shown in Figure 1. A scan interval of 340 to 600 K was used for N.4 (pure-Na, Type-A), NE. Schairer (pure-Na, Type-B), NE.1289 and NE.12 (both Type-B, 0.3 and 0.36 percent Ks, respectively), and NE.17 (1.6 percent Ks, Type-C). The scan interval for A.407 (pure-Na, Type-B) was 340–700 K and that for A.417 (27 percent Ks, Type-H) was 340–520 K.

The DSC scans for the Type-A, pure-Na nepheline (N.4) show only a smooth, continuous displacement without peaks over the temperature range 340 to 600 K (Fig. 1); Type-H nepheline (A.417) has a similar behavior between 340 and 520 K. The DSC scan for the Type-C nepheline (NE.17) has a single peak near 360 K (Fig. 1). The scans for the Type-B nephelines are more complex. NE. Schairer (pure-Na) shows two broad peaks, of approximately equal intensity, near 430 and 470 K; the other pure-Na, Type-B nepheline (A.407) shows a similar overall behavior, but the lower temperature peak is less pronounced. The scan for NE.12 (0.36 percent Ks) also shows two broad double peaks some 5° below those of NE. Schairer. The scan shown in Figure 1 for NE.1289 (0.3 percent Ks) is the fourth successive heating scan for this specimen and shows two distinct peaks near 370 and 390 K, each having a shoulder possibly concealing a second peak.

The nature of the DSC scans is noticeably dependent on temperature cycling, as is well illustrated for Type-B specimen NE.1289 (Fig. 2). The first scan, made without initially cycling between the low- and high-temperature isothermals so that the sample was not annealed, produced a strong split peak near 410 K with a minute irregularity near 425 K. The second heating scan on NE.1289 included cycling the sample across the full temperature interval, thus annealing it, and showed two distinct peaks. The lower-temperature peak contains shoulders corresponding to the split peak of the first scan. The higher-temperature peak, near 425 K, corresponds to the minute irregularity near this temperature observed in the first scan. Note that the combined area under the two peaks of

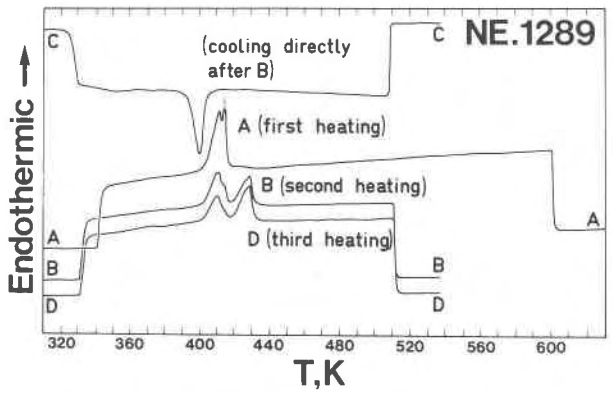

Fig. 2. Traces of DSC scans for Type-B nepheline sample NE.1289, made under the same machine conditions as for Fig. 1. Trace A represents the first heating without cycling the sample through the inversion. Curve B represents the second heating, including cycling the sample through the temperature range to adjust lower and upper isothermals. Curve C represents a cooling scan made directly after B. Curve D represents the third heating, including isothermal adjustments, made after C. See Fig. 1 for the fourth heating trace.

the second scan is similar to that under the single peak of the first scan. A cooling scan from 510 to 330 K was made directly after the second heating scan. This cooling scan revealed a single peak about 10° below and of comparable area to that of the first (unannealed) scan, and a small feature near 355 K. After the cooling scan, a third heating scan (again annealing between the low- and high-temperature isothermals) was performed and also revealed the two peaks. There was an apparent increase in the area under the higher temperature (~425 K) peak at the expense of the area under the lower peak (~410 K). The fourth heating scan on NE.1289 (Fig. 1) is similar to the third scan (Fig. 2) in terms of peak area and shape.

The presence of peaks in the DSC scans confirms the occurrence of crystallographic inversions in these nephelines, some of which may be lambda transitions (Rao and Rao, 1978, p. 22). However, it is not clear whether the broad DSC peaks in some specimens represent lambda transitions, proceeding more slowly than the α–β quartz inversion, or whether they reflect the superposition of transitions due to different composition domains in chemically zoned crystals (see later discussion). If the temperature scanning rate keeps pace with the rate of the nepheline inversion, the temperatures and areas under the DSC peaks could be used to obtain quantitative values for the heats of transition relative to the α–β quartz inversion and indium melting peaks (see later).

Discussion

Relationship between DSC and X-ray results

The absence of DSC peaks in Type-H nepheline A.417 (27 percent Ks) and the absence of discontinuities in its thermal expansion behavior (Henderson and Roux, 1976) confirm that such nephelines have the normal HBC structure at room temperature.

The absence of DSC peaks in Type-A nepheline (N.4, pure-Na) between 340 and 600 K is significant because an equivalent specimen (N.10) showed an inflection in a at 453 K. Henderson and Roux (1977) correlated this temperature with the low-temperature inversion shown by pure-Na, Type-B nephelines, but the extra X-ray reflections in N.10 did not disappear until above 873 K. The DSC results confirm that Type-A nephelines do not show the same transition near 473 K as the pure-Na, Type-B nephelines.

The single DSC peak near 360 K for Type-C nepheline NE.17 (1.6 percent Ks) can be correlated with the temperature (365±5 K) at which the extra X-ray reflection near 28.2°2θ disappears (Fig. 1). In addition, Type-C nepheline N.233 (0.3 percent Ks) showed inflections, but not discontinuities, in the thermal expansion of the cell edges close to the temperature at which the 28.2°2θ peak disappears (Henderson and Roux, 1977, Fig. 6). It seems clear that the single DSC peak is caused by the inversion of the orthorhombic 3c superstructure, characteristic of Type-C nephelines, to hexagonal symmetry.

The occurrence of two peaks in the DSC scans for Type-B nephelines is consistent with the presence of two phases, as suggested by the split (002) and (004) X-ray reflections. The temperatures of the lower-temperature DSC peaks in Type-B nephelines are within ~10 K of those at which the extra X-ray reflection at 28.2°2θ disappears (Fig. 1). By analogy with Type-C nephelines, this DSC peak is presumably caused by inversion of one of the phases from orthorhombic (3c superstructure) to hexagonal symmetry. The higher-temperature DSC peaks in Type-B nephelines can be correlated with the temperatures at which the 30.2°2θ extra X-ray reflection disappears (Fig. 1); this reflection is characteristic of the lower-symmetry phase. Type-B nephelines also show discontinuities in cell volumes at this temperature (*e.g.* NE. Schairer, Fig. 6, Henderson and Roux, 1977). The higher-temperature DSC peak can, therefore, be correlated with inversion of the low-symmetry (second) phase to hexagonal symmetry.

The assignments of the DSC peaks in Type-B nephelines are consistent with the proportions of the

phases deduced from X-ray and DSC scans for NE.1289. The increase in intensity of the higher-temperature DSC peak for NE.1289 after temperature cycling suggests that the phase producing this peak increased in proportion. This effect is also seen in the high-temperature X-ray results, which show that the phase with the higher c parameter increased in amount during annealing (Table 2). We have already deduced that in NE.1289 the low-symmetry second phase has the higher c parameter and, therefore, the higher-temperature DSC peak can be correlated with the inversion shown by this phase.

The DSC trace obtained on cooling NE.1289 immediately after the second heating (Fig. 1, scan C) shows only a single peak near 400 K. This behavior is consistent with the reappearance of both the 28.2° and 30.2°2θ extra X-ray reflections at 400±5 K upon cooling. Thus both inversions in NE.1289 appear to be indistinguishable on cooling. In addition, broadening, and ultimately splitting, of the (002) reflection can only be detected at ~363 K; this broadening may be correlated with the small feature on the DSC scan near 355 K (Fig. 2, scan C).

Dependence of inversion temperature on composition

The work of Henderson and Roux (1977) and the results of our X-ray and DSC studies demonstrate a clear relationship between increasing Ks content of nepheline and decreasing temperature of the inferred orthorhombic to hexagonal inversion. In Type-B nephelines this inversion has been correlated with the lower DSC peak (Fig. 1). The upper DSC peak also appears to be displaced to lower temperatures with increasing Ks.

The identification of two inversion peaks in the DSC study of Type-B nephelines could imply that the two phases in these samples coexist stably and have different Ks contents. Henderson and Roux (1977) considered this possibility for Ks-bearing Type-B nephelines but pointed out that it could not be the case for the supposed pure-Na, Type-B specimens. They concluded that the two phases in the latter specimens had the same composition, that the orthorhombic $3c$ superstructure was metastable, and that the lower-symmetry phase was the stable low-temperature form. Our results are not inconsistent with this interpretation, but the presence of small amounts of impurity K_2O in the nominally pure-Na nephelines could have an important effect. Partial analyses of A.407 and NE. Schairer gave <0.005±0.005 wt. percent and 0.008±0.005 wt. percent K_2O, respectively, for these specimens (equivalent to maximum values of ~0.03 and ~0.04 mol. percent Ks). The Schairer nepheline specimen, after annealing, contains approximately equal proportions of the two phases. If we assume that one of these was K-free, the other would contain ~0.08 percent Ks, which leads to a downward displacement of only ~8° in the inversion temperature for the Ks-bearing phase. In fact, the two DSC peaks in NE. Schairer are ~35° apart, suggesting that the existence of the two heat effects in Type-B nephelines cannot be primarily due to the two phases having different Ks contents. It is noteworthy, however, that the two DSC peaks in the Ks-bearing Type-B nephelines NE.12 and NE.1289 both have shoulders or split peaks (Fig. 1). The fine structure of the DSC scans, including split peaks and shoulders, were reproducible in repeated scans on the same sample and in second aliquots taken from NE.1289 and NE.12. These complexities may indicate the presence of phases having slightly different Ks contents in at least these samples. However, in view of the findings of Ishibashi and Takagi (1975), it is not certain whether the complexities are the result of sample configuration and thermal properties rather than due to the presence of two discrete phases.

Although Type-B nephelines NE.12 and NE.1289 have almost identical bulk compositions (0.36 and 0.30 percent Ks, respectively) they show significantly different DSC behavior on both heating and cooling (Figs. 1 and 2). These two nephelines could have different degrees of Na and K ordering between the two cation sites, but the limited amount of ordering possible for such K-poor compositions would be unlikely to cause such different behavior. In addition, both specimens are members of the $NaAlSiO_4$–$KAlSiO_4$ series and should not contain any excess Si, which precludes the possibility that the samples may have different degrees of vacancy disorder in the larger cation site. The reason for the different behavior of NE.12 and NE.1289 is not fully understood, but it presumably is related to their very different states of framework collapse below the low-temperature inversion (see Table 1, especially the c parameters). One of the factors controlling the state of collapse is believed to be variation in the degree of Si,Al ordering in the framework of the different samples (Henderson and Roux, 1977, p. 296).

The possibility that the coexisting phases in Type-B nephelines could have different bulk Si/Al ratios cannot be excluded, but the reasons adduced by Henderson and Roux (1977, p. 295) against this possibility still seem valid to us. Although the room-tem-

perature c parameters for the orthorhombic $3c$ superstructures in A.72 and NE.1289 differ by as much as 0.12Å, the lower-symmetry phases, which increase in amount on annealing in both specimens, have almost identical room-temperature c parameters (8.320±0.005Å, based on HBC-indexing). Thus phases with the orthorhombic $3c$ superstructure occur in very different states of framework collapse. These structures are almost certainly metastable, and the low-symmetry phase therefore appears to be the stable low-temperature form.

Relations between low-temperature inversions in nepheline and tridymite

Henderson and Roux (1977) related the occurrence of the low-temperature inversion in sub-potassic nephelines to the collapse of the 'tridymite-type' framework about the small Na atoms occupying the larger cation sites (Dollase, 1970; Foreman and Peacor, 1970). They also drew attention to the similar behavior of tridymite, which exhibits displacive transformations near 470 K and which forms various lower-symmetry (pseudohexagonal) cells below 470 K (Sato, 1963a,b, 1964; Dollase, 1967; Kihara, 1977; Nukui *et al.,* 1978).

Thompson and Wennemer (1979) measured the heat capacities of synthetic tridymite, cristobalite, and tridymite–cristobalite 'mixed phases' by DSC. Tridymite showed a sharp peak at 390 K and two broad, overlapping peaks in the range 436–470 K. These heat effects were correlated with the monoclinic to low-orthorhombic and low-orthorhombic to intermediate-orthorhombic tridymite inversions of Nukui *et al.* (1978).

The DSC traces for sub-potassic nephelines and tridymite are broadly similar in that DSC peaks occur within similar ranges of temperature. The single DSC peak occurring in Type-C nephelines (NE.17) has a similar form to the 390 K peak in tridymite. The two peaks occurring in Type-B nephelines (*e.g.* A.407) are similar in form and temperature range to the broad heat effects between 436 and 470 K in tridymite. These similarities support the suggestion (Henderson and Roux, 1977) that the low-temperature inversions in sub-potassic nephelines are primarily a property of framework collapse and that the interframework cations play a relatively subordinate role. Further correlation between nepheline and tridymite is not possible because we do not fully understand either the nature of the structures of the stable low-temperature forms or the role of 'structural cavities' (defects) in determining the structure. In addition, the nature of tridymite–cristobalite 'mixed phases' is not yet known (Thompson and Wennemer, 1979), but their occurrence suggests the possible existence of analogous nepheline–carnegieite 'mixed phases.' If such structural modulations exist as domains in sub-potassic nephelines (*e.g.* in the two-phase Type-B nephelines) the problem of characterizing the stable low-temperature form of nephelines will become even more complex.

Correlation of heat capacity measurements with previous data

Our data for the heat capacity (C_p°) of nepheline A.407 (pure-Na, Type-B) are shown as a function of temperature in Figure 3. Also shown are the low-temperature (50–298 K) adiabatic calorimetric measurements for synthetic nepheline ($NaAlSiO_4$) and kaliophilite ($KAlSiO_4$) from Kelley *et al.* (1953). (Note that the nepheline sample used by these workers was synthesized by J. F. Schairer and presumably is similar to our specimen NE. Schairer.) Kelley *et al.* also measured the heat contents for the same synthetic nepheline sample from 387 to 1509 K by drop calorimetry and presented three linear equations of C_p° *vs.* T for the ranges 298–467 K (the low-temperature inversion), 467–1180 K (the high-temperature inversion), and 1180–1525 K. These equations were adopted by Robie *et al.* (1978) in their recent compilation of thermochemical data. The fits for the 298–467 K and 467–1180 K ranges are shown by short-dashed lines in Figure 3. Our C_p° data for A.407 *above 500* K agree well with the 467–1180 K equation of Kelley *et al.* (1953, p. 15). However, their equation for the range 298–467 K represents only an average of measurements for sample A.407 because of the complex behavior of C_p° at the inversions. The DSC measurements (summarized in Table 3) suggest that the peaks at 439 K and 462 K may represent lambda-type transitions (see also Kelley *et al.,* 1953, p. 15).

The difficulties in evaluation of $H_T^\circ - H_{298}^\circ$ and $S_T^\circ - S_{298}^\circ$ from heat capacity measurements across broad transitions are well known (see Rao and Rao, 1978). However, the C_p° data obtained for nepheline A.407 (Table 3) have been fitted to polynomial equations covering various temperature ranges. The smoothed values of C_p° and the integrated functions, $H_T^\circ - H_{298}^\circ$ and $S_T^\circ - S_{298}^\circ$ are presented in Table 4. The heat involved in the transition (Fig. 3) for the inversions in A.407 was estimated by subtracting 14229 J mol^{-1}, the area between 400 K and 500 K below the extrapolated 467–1180 K C_p° equation of Kelley *et al.,* from the integrated areas in Table 4 (15397 J mol^{-1}). The

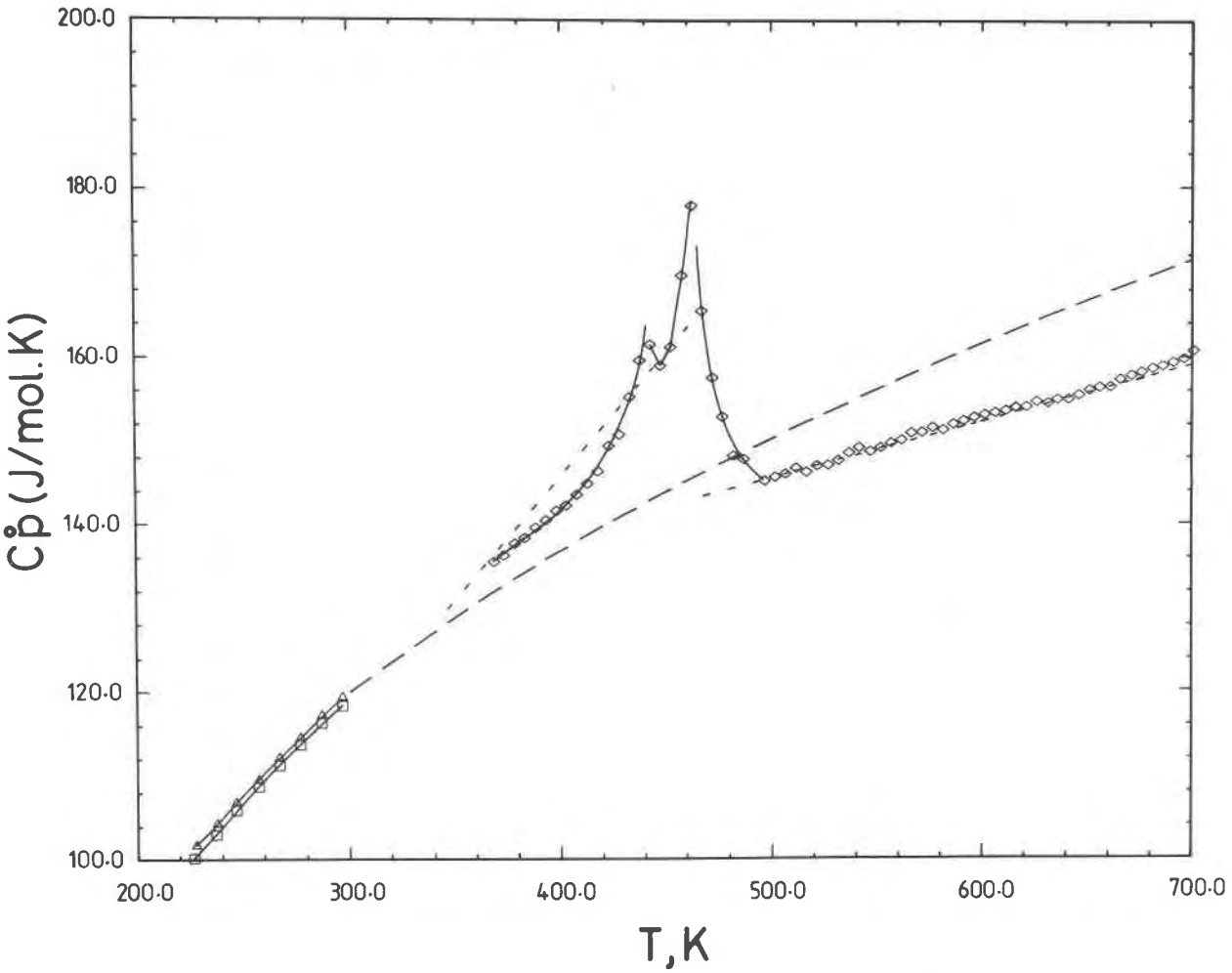

Fig. 3. Heat capacity (C_p°) in joules mol^{-1} K^{-1} as a function of temperature for the specimen of pure-Na, Type-B nepheline A.407 measured by DSC (◇ symbols between 370 and 700 K); note the presence of two peaks near 440 and 460 K. Also shown are data points for synthetic nepheline (□, $NaAlSiO_4$) and kaliophilite (△, $KAlSiO_4$) to 298 K determined by adiabatic calorimetry (Kelley *et al.*, 1953). The short-dash lines, passing approximately through the transitions to 467 K and from 467 to 700 K, refer to the fits to the drop calorimetric data for $NaAlSiO_4$ (Kelley *et al.*, 1953). The long-dash curve refers to equivalent fits for $KAlSiO_4$ (see Robie *et al.*, 1978, p. 405–416).

resulting value for the heat of transition (1168 J $mole^{-1}$) is not noticeable on the scale of Figure 4 of Kelley *et al.*, and has not been used to introduce discontinuities into the integrated functions $H_T^\circ - H_{298}^\circ$ and $S_T^\circ - S_{298}^\circ$ presented in Table 4.

Although the 298–467 K C_p° equation of Kelley *et al.* represents an average of our measurements for sample A.407, it will only be valid for nominally pure-Na, Type-B nephelines because the heat capacity relationships for Ks-bearing Type-B and -C nephelines will clearly be different from those for the specimen of Kelley *et al.* (*cf.* NE. Schairer with Ks-bearing nephelines in Fig. 1). In addition, we have shown that Type-H nephelines do not exhibit any DSC peaks between 340 and 520 K; the only nephelines likely to show such peaks in this temperature range are those with <2.5 percent Ks. The natural nephelines occurring in igneous and metamorphic rocks (*e.g.* Dollase and Thomas, 1978) and meteorites (*e.g.* Allende; Grossman and Steele, 1976) invariably contain more than 2.5 percent Ks and should show smooth curves of C_p° *vs.* temperature with no discontinuities. Therefore, although the equation of Kelley *et al.* between 467 and 1180 K can be used as a reference in thermochemical calculations applied to *natural* nephelines, the equation below 467 K will normally not be valid. Similar reasoning can be used to justify the extrapolation of the equation of Kelley *et*

Table 4. Smoothed molar thermodynamic properties for nepheline A.407 ($NaAlSiO_4$)

T	C_p^o	$H_T^o - H_{298}^o$	$S_T^o - S_{298}^o$
Kelvin	J/(mol. K)	J/(mol.)	J/(mol. K)
298.15	119.2	0	0
300.0	119.7	221	0.7
350.0	131.4	6501	20.1
360.0	133.5	7826	23.8
370.0	135.7	9172	27.5
380.0	137.9	10540	31.2
390.0	140.0	11930	34.8
400.0	142.0	13340	38.3
405.0	142.1	14056	40.1
410.0	142.9	14775	41.9
415.0	144.3	15499	43.6
420.0	146.3	16231	45.9
425.0	149.0	16976	47.1
430.0	152.3	17735	48.9
435.0	156.3	18513	50.7
440.0	160.9	19312	52.5
445.0	158.8	20119	54.4
450.0	160.6	20913	56.1
455.0	166.2	21727	57.9
460.0	174.8	22579	59.8
470.0	160.4	24263	63.4
480.0	150.2	25811	66.7
490.0	145.5	27285	69.7
500.0	145.7	28737	72.7
510.0	146.4	30197	75.5
520.0	147.1	31664	78.4
540.0	148.5	34620	84.0
560.0	149.9	37604	89.4
580.0	151.3	40616	94.7
600.0	152.7	43657	99.8
620.0	154.2	46726	104.9
640.0	155.6	49823	109.8
660.0	157.0	52949	114.6
680.0	158.4	56103	119.3
700.0	159.8	59285	123.9

The low temperature adiabatic data for nepheline (Kelley et al., 1953) was included in the smoothing of the data and thus 298.15 K is the chosen reference temperature. It is, therefore, assumed that no further transitions occur between 298 and 370 K. Note that the integrated functions have not been adjusted for heat or entropy of transition.

al. over the range 467–1180 K to temperatures above 1180 K, because the high-temperature inversion in nepheline only occurs in specimens with <5 wt. percent Ks (Tuttle and Smith, 1958).

Conclusions

Both DSC and X-ray studies indicate that the inversion characteristics of sub-potassic nephelines are dependent upon nepheline type. Type-C nephelines (0.7 to 2.5 percent Ks) have a single, sharp DSC peak between 340 and 600 K. The temperature at which this transition occurs may be correlated with the orthorhombic (3*c* superstructure)–hexagonal inversion. Type-B nephelines (<0.7 percent Ks) have two DSC peaks below 480 K. The lower-temperature transition may be correlated with the orthorhombic–hexagonal inversion (*cf.* Type-C) and the upper-temperature transition with the low-symmetry (second phase)–hexagonal inversion. In contrast, Type-H nephelines (>2.5 percent Ks) show no DSC peaks indicative of transitions or inversions between 340 and 520 K; they are hexagonal at room temperature. Type-A nephelines (pure-Na) also have no transitions between 340 and 600 K.

Similarities between the DSC scans of sub-potassic nephelines and tridymite support the suggestion that low-temperature inversions in nepheline are primarily caused by collapse of the framework. The interframework cations appear to have only a modifying effect.

In experimental studies of nephelines, the proportions of $NaAlSiO_4$–$KAlSiO_4$–$\square SiSiO_4$ (tridymite) and the amount of framework or interframework order–disorder will influence the inversion characteristics and possibly the phase relations, especially if metastable structures occur. These complicating factors should be considered when natural nephelines from igneous and metamorphic rocks are studied. For studies attempting to obtain thermochemical properties for nepheline solid-solutions, the equation of Kelley *et al.* (1953) fitting the heat capacity data for pure-Na nepheline above 467 K can be applied to Ks-bearing nephelines. However, the Kelley *et al.* equation between 298 and 467 K is an averaged fit which, because of complexities introduced by the occurrence of the low-temperature inversions, is specific to pure-Na, Type-B nephelines.

Acknowledgments

We thank Dr. J. Roux for supplying the sample of NE.1289. The differential scanning calorimeter is supported by the ETH Special Project Funds. We also thank K. Krupka for an extremely helpful review of the original manuscript. The work at Manchester was supported by the Natural Environment Research Council.

References

Buerger, M. G. (1951) Crystallographic aspects of phase transformations. In R. Smoluchowski, Ed., *Phase Transformations in Solids,* p. 183–211. Wiley, New York.

Cohen, L. H. and W. Klement, Jr. (1976) Effect of pressure on reversible solid–solid transitions in nepheline and carnegieite. *Mineral. Mag., 40,* 487–492.

Ditmars, D. A. and T. B. Douglas (1971) Measurements of the relative enthalpy of pure α-Al_2O_3 (NBS Heat capacity and enthalpy standard reference material No. 720) from 273 to 1173 K. *J. Res. Natl. Bur. Stands., 75A,* 401–420.

Dollase, W. A. (1967) The crystal structure at 220°C of orthorhombic high tridymite from the Steinbach meteorite. *Acta Crystallogr., 23,* 617–623.

——— (1970) Least-squares refinement of the structure of a plutonic nepheline. *Z. Kristallogr., 132,* 27–44.

——— and W. M. Thomas (1978) The crystal chemistry of silica-rich, alkali-deficient nepheline. *Contrib. Mineral. Petrol., 66,* 311–318.

Donnay, G., J. F. Schairer and J. D. H. Donnay (1959) Nepheline solid solutions. *Mineral. Mag., 32,* 93–109.

Foreman, N. and D. R. Peacor (1970) Refinement of the nepheline structure at several temperatures. *Z. Kristallogr., 132,* 45–70.

Grossman, L. and I. M. Steele (1976) Amoeboid olivine aggregates in the Allende meteorite. *Geochim. Cosmochim. Acta, 40,* 149–155.

Hahn, T. and M. J. Buerger (1955) The detailed structure of nepheline $KNa_3Al_4Si_4O_{16}$. *Z. Kristallogr., 106,* 308–338.

Henderson, C. M. B. and J. Roux (1976) The thermal expansions and crystallographic transformations of some synthetic nephelines. *Prog. Exp. Petrol., N.E.R.C. Rep. 3,* 60–69.

——— and ——— (1977) Inversions in sub-potassic nephelines. *Contrib. Mineral. Petrol., 61,* 279–298.

——— and D. Taylor (1975) Thermal expansion by X-ray diffraction: the use of the specimen holder as the internal standard and the expansion of MgO (periclase) and $MgAl_2O_4$ (spinel). *Trans. Brit. Ceram. Soc., 74,* 55–57.

Ishibashi, Y. and Y. Takagi (1975) Comments on specific heat measurements. *Jap. J. Appl. Phys., 14,* 637–642.

Kelley, K. K., S. C. Todd, R. L. Orr, E. G. King and K. R. Bonnickson (1953) Thermodynamic properties of sodium–aluminum and potassium–aluminum silicates. *U.S. Bur. Mines, Rep. Invest. 4955.*

Kihara, K. (1977) An orthorhombic superstructure of tridymite coexisting between about 105 and 180°C. *Z. Kristallogr., 146,* 185–203.

Nukui, A., H. Nakazawa and M. Akao (1978) Thermal changes in monoclinic tridymite. *Am. Mineral., 63,* 1252–1259.

O'Neill, M. J. (1966) Measurement of specific heat functions by differential scanning calorimetry. *Anal. Chem., 38,* 1331–1336.

Rao, C. N. R. and K. J. Rao (1978) *Phase Transitions in Solids.* McGraw-Hill, New York.

Robie, R. A., B. S. Hemingway and J. R. Fisher (1978) Thermodynamic properties of minerals and related substances at 298.15 K and one bar (10^5 pascals) pressure and at higher temperatures. *U.S. Geol. Surv. Bull. 1452.*

Sato, M. (1963a) X-ray study of tridymite (1). On tridymite M and tridymite S. *Mineral. J. (Japan),* 4, 115–130.

——— (1963b) X-ray study of tridymite (2). Structure of low tridymite, type M. *Mineral. J. (Japan), 4,* 131–146.

——— (1964) X-ray study of tridymite (3). Unit cell dimensions and phase transition of tridymite, type S. *Mineral. J. (Japan), 4,* 215–225.

Thompson, A. B. and M. Wennemer (1979) Heat capacities and inversions in tridymite, cristobalite, and tridymite–cristobalite mixed phases. *Am. Mineral., 64,* 1018–1026.

Tuttle, O. F. and J. V. Smith (1958) The nepheline–kalsilite system II. Phase relations. *Am. J. Sci., 256,* 571–589.

Manuscript received, April 2, 1979;
accepted for publication, April 4, 1980.

American Mineralogist, Volume 65, pages 981-985, 1980

The role of cationic hydrogen in pyroxenoid crystal chemistry

FRIEDRICH LIEBAU

Mineralogisches Institut der Universität
D-2300 Kiel, Federal Republic of Germany

Abstract

In pyroxenoids containing cationic hydrogen [pectolite, schizolite, serandite, unnamed $Ca(Sc,Fe^{3+})H[Si_3O_9]$, synthetic $Cd_2NaH[Si_3O_9]$, nambulite, Li-hydrorhodonite, santaclaraite, and babingtonite] the identity periods of the silicate chains are approximately 0.25Å shorter than those of corresponding non-acid pyroxenoids with similar mean cation size (wollastonite, bustamite, rhodonite). This observation is interpreted as caused by the reduction of repulsive forces between $[SiO_4]$ tetrahedra of the silicate chains due to an increase of the average electronegativity of the cations when cationic hydrogen is present. This effect (which exists also in polyphosphates and probably polygermanates) is an extreme case of the general effect that anionic tetrahedral chains will be less stretched when the average electronegativity of the cations is higher, which compensates the valence of the chains. The theory explains why acid chain silicates are common in pyroxenoids but not observed in pyroxenes.

Introduction

Pyroxenoids are silicates containing unbranched single chains $\{U, {}^{1}_{\infty}\}[Si_pO_{3p}]$ with periodicities $p = 3$, 5, 7, 9, *i.e.* with an odd number of $[SiO_4]$ tetrahedra in the repeat unit of the chains. Although the pyroxenes have a crystallographic periodicity $p_{cryst} = 2$, they can be regarded as end members of the pyroxenoid series with a formal periodicity $p_{formal} = 2n + 1$ with $n \rightarrow \infty$ (Liebau, 1972).

In pyroxenes as well as in pyroxenoids cation–oxygen octahedra share edges to form octahedral slabs that can be regarded as one-dimensionally infinite parts of the hexagonal or pseudo-hexagonal octahedral layers characteristic of the hydroxides $M(OH)_2$, M = Mg, Zn, Mn, Ca, and of most of the clay minerals. Takéuchi and Koto (1977) have pointed out that, based on the structure of the octahedral slabs, two groups of pyroxenoids can be distinguished. Using the most common members of each group, wollastonite and pectolite, they named the two groups of pyroxenoids the w-p series and the p-p series, respectively. Table 1 shows that the known members of the w-p series are anhydrous while those of the p-p series contain hydrogen atoms bonded to $[SiO_4]$ tetrahedra, *i.e.* they are acid silicates.

Ohashi and Finger (1978), in their discussion of the role of octahedral cations in pyroxenoid crystal chemistry, point out that "the role of hydrogen would be at least as important as that of the alkali atoms in making the structures of hydrous pyroxenoids distinct from those of anhydrous ones." However, since the positions of the hydrogen atoms have not yet been accurately determined, no further discussion of their crystal-chemical role was offered.

A regression analysis of 54 single-chain silicates (Liebau and Pallas, in preparation) revealed a strong negative correlation between the degree of stretching of the silicate chains, measured by a stretching factor $f_s = I_{chain}/l_e \cdot p$, and the average values $\bar{\chi}$ and $\bar{\nu}$ of the electronegativities and valences of the cations. I_{chain} is the chain period in Å, $l_e = 2.70$Å is the length of the tetrahedral edge in shattuckite, $Cu_5[Si_2O_6]_2(OH)_2$, the silicate with the most stretched chain known (Evans and Mrose, 1977), and p is the periodicity of the chain. For pyroxenes and pyroxenoids, for which $\bar{\nu}$ hardly deviates from 2, an additional positive correlation between stretching factor and the average cation radius is observed.

Observations

Table 1 gives the lattice parameter along the chain direction, I_{chain}, for the known p-p series silicates. Also given are the chain periods for those w-p series silicates which have a similar average cation radius as the p-p series silicates (hydrogen not considered). Where the acid–non-acid pairs are known, the chain

0003–004X/80/0910–0981$02.00

Table 1. Comparison of the chain periods of acid pyroxenoids (p-p series) with those of corresponding non-acid pyroxenoids (w-p series)

periodicity	acid compounds: name	formula	ref.	I_{chain} [Å]	ΔI_{chain} [Å]	non-acid compounds: I_{chain} [Å]	formula	name	ref.
3	pectolite	$Ca_2NaH[Si_3O_9]$	1	7.040	0.28	7.320	$Ca_3[Si_3O_9]$	parawollastonite	2
	schizolite	$(Ca,Mn)_2NaH[Si_3O_9]$	3	6.978	0.25	7.231	$Ca_{2.35}(Mn,Fe,Mg)_{0.65}[Si_3O_9]$	Ca-bustamite	3
	serandite	$Mn_2NaH[Si_3O_9]$	4	6.889	0.20	7.091	$Ca_{0.95}(Mn,Fe,Mg)_{2.05}[Si_3O_9]$	Mn-bustamite	3
		$Ca(Sc,Fe^{3+})H[Si_3O_9]$	5	7.076					
	synthetic	$Cd_2NaH[Si_3O_9]$	6	6.980					
	synthetic	$Na_2H[P_3O_9]$	7	6.76	0.24	7.00	$Na_3[P_3O_9]$	Maddrell's salt	8
5	Li-hydrorhodonite	$Mn_4LiH[Si_5O_{15}]$	9	12.039	0.20	12.235	$Mn_5[Si_5O_{15}]$	synthetic	10
	nambulite	$Mn_4(Na,Li)H[Si_5O_{15}]$	11	12.016	0.22	12.233	$(Mn,Fe,Mg)_{4.21}Ca_{0.79}[Si_5O_{15}]$	rhodonite	12
	santaclaraite	$Mn_4CaH[Si_5O_{15}](OH)\cdot H_2O$	13	12.001	0.23				
	babingtonite	$Ca_2Fe^{2+}Fe^{3+}H[Si_5O_{15}]$	14	12.18					
			15	12.245					
	synthetic	$Cd_4LiH[Ge_5O_{15}]$	16	12.673					
	synthetic	$Cd_4NaH[Ge_5O_{15}]$	16	12.591					

References:

1 Prewitt, 1967
2 Trojer, 1968
3 Ohashi & Finger, 1978
4 Takéuchi et al., 1976
5 Mellini, 1978
6 Belokoneva et al., 1974
7 Jost, 1962
8 Jost, 1963
9 Murakami et al., 1977
10 Narita et al., 1977
11 Narita et al., 1975
12 Peacor & Niizeki, 1963
13 Ohashi & Finger, 1980
14 Kosoi, 1976
15 Araki & Zoltai, 1972
16 Simonov et al., 1978

periods of the p-p silicates are approximately 0.25Å shorter than those of the corresponding w-p silicates, independent of the periodicity of the silicate chains. The same amount of shrinkage has been observed in acid $Na_2H[P_3O_9]$ in comparison with Maddrell's salt, $Na_3[P_3O_9]$, which is isostructural with disordered wollastonite, $Ca_3[Si_3O_9]$. The period of a pyroxenoid chain consists of n double tetrahedra and a single off-set tetrahedron sticking out from the chain like a nose, adding up to $p = 2n + 1$ tetrahedra per period. Independent of the periodicity of the chains, the shrinkage of the chains in the acid compounds takes place mainly by rotation of the two tetrahedra attached to a single off-set tetrahedron. Figure 1 compares the structures of manganoan wollastonite, $(Ca,Mn)_3[Si_3O_9]$, and serandite, $(Ca,Mn)_2NaH[Si_3O_9]$, (Ohashi and Finger, 1978) as typical representatives of the two series of pyroxenoids. Whereas in the acid compounds the three tetrahedral edges designated A–A′, B–B′, and A′–B′ in Figure 1 form an approximate open square, they form an open trapezoid in the phases containing no cationic hydrogen. In almost all the acid phases of Table 1 the presence of hydrogen bonds A–H–B has been proposed because of short A···B distances between 2.41Å and 2.60Å or because residual electron-density maxima have been found between the atoms A and B on difference Fourier syntheses. These hydrogen bridges form the fourth sides of the squares A–A′–B′–B.

Crystal-chemical discussion

Rather than a geometric description of the differences between atomic structures of the acid and non-acid pyroxenoid phases and their isotypes, a chemical explanation is desirable. Such an explanation based on the nature of the chemical bonds would not be restricted to crystalline single-chain silicates but would also be valid for single-chain silicates in the vitreous and liquid states as well as in solution. A chemical explanation should even be applicable to corresponding silicates containing geometries other than single-chain anions. Such an explanation along very simple and general lines is offered here.

Highly electropositive cations such as Na^+, K^+, Ca^{2+}, Ba^{2+} transfer their valence electrons almost completely to the nearest anions. In silicates of such

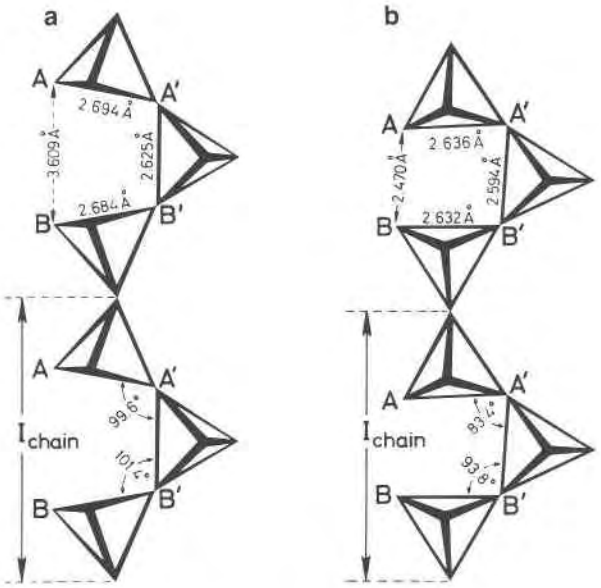

Fig. 1. Conformation of the tetrahedral single chains in corresponding acid and non-acid silicates: (a) manganoan wollastonite, $(Ca,Mn)_3[Si_3O_9]$; (b) serandite, $(Ca,Mn)_2NaH[Si_3O_9]$.

cations with the general formula $M_s[Si_pO_{3p}]$ each $[SiO_4]$ tetrahedron carries a negative charge of almost two electrons. Such high negative charges cause strong repulsive forces between the tetrahedra and, therefore, lead to a stretching of the silicate chains. As the electronegativity of the cations increases, fewer electrons are transferred from the cations to the silicate anions. This reduces the average charge per $[SiO_4]$ tetrahedron and thereby the degree of stretching of the chains.

The results of a regression analysis of single-chain silicates (Liebau and Pallas, in preparation) also support the above electrochemical explanation by giving a negative correlation between the stretching factor f_s and the average electronegativity $\bar{\chi}$ of the cations. Hydrogen with its very high electronegativity (χ = 2.1) represents an extreme case for this correlation. The existence of cationic hydrogen considerably reduces the repulsive forces between silicate tetrahedra along the chain, allowing less stretched chain conformations to be favored.

It seems reasonable to assume that the reduction of negative charges on the silicate chain will be largest at those tetrahedra to which the cationic hydrogen is bonded and that the shrinkage of the chain is most pronounced in the vicinity of these tetrahedra. This is in agreement with the observations described in the last section.

Due to the general influence of electropositive cations on the repulsive forces of chain anions, the shrinkage effect of cationic hydrogen is not restricted

Table 2. Hypothetical acid and non-acid pyroxenoids and isotypic phases together with the phases from which they are predicted

periodicity	predicted phase: formula	predicted phase: I_{chain} [Å]	predicted from: I_{chain} [Å]	predicted from: formula	ref.
3	$Ca_2NaH[Ge_3O_9]$	7.30	7.57	$Ca_3[Ge_3O_9]$	1
	$Na_2H[As_3O_9]$	7.20	7.44	$Na_3[As_3O_9]$	2
	$Na_2H[Be_3F_9]$	6.90	7.17	$Na_3[Be_3F_9]$	1
	$(Ca,Cd)_3[Si_3O_9]$	7.23	6.98	$Cd_2NaH[Si_3O_9]$	3
	$(Ca,Sc,Fe^{3+},Na)_3[Si_3O_9]$	7.32	7.076	$Ca(Sc,Fe^{3+})H[Si_3O_9]$	4
5	$Cd_5[Ge_5O_{15}]$	12.90	12.673	$Cd_4LiH[Ge_5O_{15}]$	5
			12.591	$Cd_4NaH[Ge_5O_{15}]$	5
	$Ca_2Fe^{2+}Fe^{3+}(Li,Na)[Si_5O_{15}]$	12.45	12.2	$Ca_2Fe^{2+}Fe^{3+}H[Si_5O_{15}]$	6,7
7	$(Ca,Fe)_6(Li,Na)H[Si_7O_{21}]$	17.15	17.381	$(Ca,Fe)_7[Si_7O_{21}]$	8
	$(Ca,Mn)_6(Li,Na)H[Si_7O_{21}]$	17.20	17.45	$(Ca,Mn)_7[Si_7O_{21}]$	9

1 Liebau, 1960
2 Liebau, 1956
3 Belokoneva et al., 1974
4 Mellini, 1978
5 Simonov et al., 1978
6 Araki & Zoltai, 1972
7 Kosoi, 1976
8 Burnham, 1971
9 Liebau, 1959

to single-chain silicates but also works in other compounds such as polyphosphates, polygermanates, *etc.*

Conclusions

In general, acid hydrogen tends to form hydrogen bonds. In chain silicates these may bridge either between oxygen atoms of $[SiO_4]$ tetrahedra of the same chain (intra-chain hydrogen bonds) or between $[SiO_4]$ tetrahedra of different chains (inter-chain hydrogen bonds). The latter would most probably disrupt the infinite slabs of cation–oxygen polyhedra and require a major rearrangement of the structure. On the other hand, intra-chain hydrogen bonds will not have to change the cation–oxygen clusters substantially and are therefore energetically easier to achieve. The hydrogen bonds will be formed more easily if the non-acid chains are already folded so that two tetrahedra of the chain are sufficiently close that slight rotation of these tetrahedra allows formation of a hydrogen bridge between them.

This requirement is fulfilled in the structures of the non-acid pyroxenoids and their isotypic polygermanates and polyphosphates but fails for the pyroxenes and their isotypes, although their structures are closely related to those of the pyroxenoids (end members of the pyroxenoid series). In fact, pyroxenes containing cationic hydrogen have not been reported in the literature while acid pyroxenoids are quite common. In conclusion, if acid pyroxenes should be discovered, they would contain inter-chain rather than intra-chain hydrogen bonds and would be less stable than the acid pyroxenoids.

Some hypothetical pyroxenoid-type phases and their approximate chain periods are further predicted (Table 2) from the information on known pyroxenoids.

At first glance one would expect that acid analogues of multiple-chain silicates could also exist for xonotlite, $Ca_6\{2^1_\infty\}$ $[Si_6O_{17}](OH)_2$ (Mamedov and Belov, 1956), inesite, $Ca_2Mn_7\{2^1_\infty\}$ $[Si_{10}O_{28}](OH)_2 \cdot 5H_2O$ (Wan and Ghose, 1978), canasite, $Ca_5Na_4K_2\{4^1_\infty\}$ $[Si_{12}O_{30}](OH,F)_4$ (Shiragov *et al.*, 1969), and miserite, $Ca_{10}K_2[Si_2O_7]_2\{4^1_\infty\}$ $[Si_{12}O_{30}](OH,F)_2$ (Scott, 1976). However, since in multiple chains the freedom of rotation of the tetrahedra is considerably reduced, more energy would be required to shorten a multiple chain by 0.25Å per chain period as compared with the case of single chains. Therefore, only in favorable cases could acid multiple-chain silicates with intra-chain hydrogen bridges be formed. One such case might be canasite, which has a chain period of only 7.19Å for the non-acid chains.

Note added in proof

The crystal structure of an unnamed acid silicate, $(Mn^{2+}, Mn^{3+})_5Na_{1.15}H\{B^1_\infty\}(Si_{5.5}V_{0.5})O_{18}](OH)$, has been published by R. Basso and A. Della Giusta (*Neues Jahrb. Mineral. Abh., 138,* 333–342, 1980). This silicate contains open-branched *fünfer* single chains with I_{chain} = 11.962Å. In agreement with the other acid pyroxenoids discussed this period is 0.27Å shorter than that of the corresponding non-acid rhodonite.

Acknowledgment

I thank Professors M. Mellini and Y. Ohashi for providing unpublished results on $Ca(Sc,Fe^{3+})H[Si_3O_9]$ and santaclaraite respectively, and the latter for a critical review of the manuscript.

References

Araki, T. and T. Zoltai (1972) Crystal structure of babingtonite. *Z. Kristallogr., 135,* 355–373.

Belokoneva, E. L., P. A. Sandomirskii, M. A. Simonov and N. V. Belov (1974) Crystal structure of cadmium pectolite $NaHCd_2[Si_3O_9]$. *Sov. Phys. Dokl., 18,* 629–630.

Burnham, C. W. (1971) The crystal structure of pyroxferroite from Mare Tranquillitatis. *Proc. Second Lunar Sci. Conf., 1,* 47–57.

Evans, Jr., H. T. and M. E. Mrose (1977) The crystal chemistry of the hydrous copper silicates, shattuckite and planchéite. *Am. Mineral., 62,* 491–502.

Jost, K.-H. (1962) Die Struktur eines sauren Natriumpolyphosphates. *Acta Crystallogr., 15,* 951–955.

——— (1963) Zur Struktur des Maddrellschen Salzes. *Acta Crystallogr., 16,* 428.

Kosoi, A. L. (1976) The structure of babingtonite. *Sov. Phys. Crystallogr., 20,* 446–451.

Liebau, F. (1956) Über die Kristallstruktur des Natriumpolyarsenats, $(NaAsO_3)_x$. *Acta Crystallogr., 9,* 811–817.

——— (1957) Über die Struktur des Schizoliths. *Neues Jahrb. Mineral. Monatsh.,* 227–229.

——— (1960) Zur Kristallchemie der Silikate, Germanate und Fluoberyllate des Formeltyps ABX_3. *Neues Jahrb. Mineral. Abh., 94,* 1209–1222.

——— (1972) Crystal Chemistry of Silicon. In K. H. Wedepohl, Ed., *Handbook of Geochemistry,* Vol. II, 3, 14-A. Springer-Verlag, Berlin.

Mamedov, K. S. and N. V. Belov (1956) Crystal structures of minerals of the wollastonite group. I. Structure of xonotlite. *Zap. Vses. Mineralog. Obshch., 85,* 13–38.

Murakami, T., Y. Takéuchi and T. Tagai (1977) Lithium-hydrorhodonite. *Acta Crystallogr., B33,* 919–921.

Narita, H., K. Koto and N. Morimoto (1977) The crystal structures of $MnSiO_3$ polymorphs (rhodonite- and pyroxmangite-type). *Mineral. J., 8,* 329–342.

Ohashi, Y. and L. W. Finger (1978) The role of octahedral cations in pyroxenoid crystal chemistry. I. Bustamite, wollastonite, and the pectolite–schizolite–serandite series. *Am. Mineral., 63,* 274–288.

——— and ——— (1980) The crystal structure of santaclaraite, $CaMn_4HSi_5O_{15}(OH) \cdot H_2O$: the role of hydrogen atoms in the pyroxenoid structure. *Am. Mineral.,* in press.

Peacor, D. R. and N. Niizeki (1963) The redetermination and refinement of the crystal structure of rhodonite, $(Mn,Ca)SiO_3$. *Z. Kristallogr., 119,* 98–116.

Prewitt, C. T. (1967) Refinement of the structure of pectolite, $Ca_2NaHSi_3O_9$. *Z. Kristallogr., 125,* 298–316.

Scott, J. D. (1976) Crystal structure of miserite, a Zoltai type 5 structure. *Can. Mineral., 14,* 515–528.

Shiragov, M. I., K. S. Mamedov and N. V. Belov (1969) The crystal structure of canasite—$Ca_5Na_4K_2[Si_{12}O_{30}](OH,F)_4$. *Dokl. Akad. Nauk SSSR, 185,* 672–674.

Simonov, M. A., E. L. Belokoneva, Yu. K. Egorov-Tismenko, and N. V. Belov (1978) The crystal structures of natural rhodonite $CaMn_4[Si_5O_{15}]$ and synthetic $NaHCd_4[Ge_5O_{15}]$ and $LiHCd_4[Ge_5O_{15}]$. *Sov. Phys. Dokl., 22,* 241–242.

Takéuchi, Y. and K. Koto (1977) A systematics of pyroxenoid structures. *Mineral. J., 8,* 272–285.

Trojer, F. J. (1968) The crystal structure of parawollastonite. *Z. Kristallogr., 127,* 291–308.

Wan, C. and S. Ghose (1978) Inesite, a hydrated calcium manganese silicate with five-tetrahedral repeat double chains. *Am. Mineral., 63,* 563–571.

Manuscript received, November 19, 1979;
accepted for publication, March 13, 1980.

American Mineralogist, Volume 65, pages 986–995, 1980

Low albite: an X-ray and neutron diffraction study

GEORGE E. HARLOW

Department of Mineral Sciences
American Museum of Natural History
New York, New York 10024

AND GORDON E. BROWN, JR.

Department of Geology, Stanford University
Stanford, California 94305

Abstract

Least-squares refinements of the structure of low albite from Amelia, Virginia with three-dimensional neutron and X-ray diffraction intensity data sets yield weighted *R* factors of 0.024 and 0.035, respectively, with anisotropic thermal models. The two methods result in essentially identical positional parameters, though slight differences in thermal parameters may be due to the variation in relative scattering powers. Direct refinement of Al/Si occupancy of tetrahedral sites was possible for the neutron data but not for the X-ray data, resulting in the following values of $\langle\overline{T\text{–}O}\rangle$ (in Å) and Al occupancy (associated errors in parentheses): T_1O 1.743(1)Å, 0.97(2) Al; T_1m 1.609(1)Å, 0.04(2) Al; T_2O 1.614(1)Å, 0.0 Al; T_2m 1.616(1)Å, 0.0 Al. The difference between the refined T_1O occupancy and an Al-filled T_1O site is significant at a 90% confidence. When these data are combined with other neutron diffraction estimates of order/disorder for a low sanidine and Himalaya orthoclase, a non-linear plot of $\langle\overline{T\text{–}O}\rangle$ *vs.* Al content results, which is best fit with a 3rd-order polynomial. This curve differs from the linear plot by as much as 0.016Å in the high-Al region. However, direct comparison of average T–O bond lengths between ordered and disordered tetrahedra includes an apparent shortening in disordered feldspars (comparable to a thermal motion effect) which may amount to 0.003Å. Analysis of the apparent-thermal-motion anisotropy of the Na site with displacive split-site models yields a splitting distance of 0.39Å for both data sets, but a single-Na, anisotropic thermal model is preferred.

Introduction

Since Barth (1934) first suggested that the polymorphism of K-feldspars resulted from order–disorder of Al and Si atoms, a considerable effort has been made by crystallographers, mineralogists, and petrologists to characterize Al–Si distributions in natural and synthetic feldspars. The primary reasons for the intense interest in this subject are (1) the natural abundance of alkali feldspars in the Earth's crust and (2) their potential for geothermometry from a detailed knowledge of the composition-, temperature-, and pressure-dependence of intracrystalline Al–Si distributions. Smith's (1954) important synthesis of available structural data for feldspars provided the basis for all subsequent optical and cell-parameter methods for determining the degree of ordering of Al and Si among the tetrahedral sites. He used the simple idea that Al-containing tetrahedra are larger than Si-containing ones and correlated mean T–O distances (T = Si,Al) with Al content of a tetrahedron. Later revision of Smith's study (Smith and Bailey, 1963) and statistical analyses of the correlation between mean T–O distance and % Al (Jones, 1968; Ribbe and Gibbs, 1969) have provided linear regression equations for this correlation. However, serious doubts about the linear relationship between mean T–O distance and Al content of tetrahedra were raised by Brown *et al.* (1969) and Ribbe *et al.* (1974), who pointed out a number of other factors which affect individual T–O distances in framework aluminosilicates. Because of these findings, the currently-used feldspar structural-state indicators, such as the lat-

0003–004X/80/0910–0986$02.00

tice-parameter method of Stewart and Wright (1974) for alkali feldspars, are in need of revision when enough new data become available. Ribbe (1975) has since proposed a method for estimating approximate Al contents of K-rich feldspars based on individual bond-length differences and which, according to Ribbe, eliminates concern about whether the correct Al content *vs.* T–O distance relationship is linear or nonlinear. This problem could be eliminated entirely if future structural-state determinations were based on direct measurements of Al–Si site distributions. However, such determinations have proven possible only by neutron diffraction experiments (see Prince *et al.*, 1973; Brown *et al.*, 1974), which are not feasible for more than a few samples.

Our study of the structure of a low albite with both X-ray and neutron-diffraction methods has been undertaken to help elucidate the relationship between Al–Si occupancy and T–O bond distances for this important end-member feldspar composition. In addition, we have examined general structural features, in particular the nature of apparent thermal motion of the Na atom, and have compared results from our independent X-ray and neutron structure refinements.

Table 1. Composition and cell constants of Amelia low albite

Composition:	wt.%[1]	cat./8 ox	wt.%[2]	cat./8 ox
SiO_2	69.4	3.024	68.06	2.976
Al_2O_3	19.0	0.976	20.00	1.031
Fe_2O_3	0.0	0.0	0.04	0.001
CaO	0.02	0.001	0.15	0.007
Na_2O	11.5	0.969	11.49	0.974
K_2O	0.10	0.006	0.15	0.009
	100.0	4.976	99.89	4.998
Ab	99.3		98.5	
Or	0.6		0.7	
An	0.1		0.8	

Cell Constants:

a	8.142(2) Å	α	94.19(2) deg.
b	12.785(2)	β	116.61(2)
c	7.159(2)	γ	87.68(2)
V	664.5(9) Å^3		

1 microprobe analysis

2 analysis of Morey and Fournier (1961)

Experimental technique

Samples

Samples of low albite from Amelia County, Virginia were obtained from the late D. R. Waldbaum (for sample description see Waldbaum and Robie, 1971, sample no. 6306). For the neutron work a clear glassy rhomb of cleavelandite habit with a volume of 15.4 mm^3 was selected from a larger piece; an alternate crystal was chosen from a fragment cleaved from the same large piece. The X-ray sample, cleaved from the alternate neutron crystal, had a volume of 2.04×10^{-3} mm^3 with largest edge dimension of 0.4 mm. Sample composition from wet-chemical analysis and a microprobe analysis are listed in Table 1. Cell parameters were calculated with Burnham's LCLSQ IV least-squares program using X-ray powder data collected with a powder diffractometer on material identical to that examined in this experiment (see Table 1).

Neutron experiment

Neutron diffraction data for a half sphere of reciprocal space with $0.15 \leq \sin\theta/\lambda \leq 0.69$ were collected at the Brookhaven National Laboratories Hi Flux Beam Reactor on an automated (Brookhaven Multispectrometer Control System) four-circle diffractometer. The θ–2θ step incremental scan technique with a BF_3 proportional counter was used. The reactor had a thermal neutron flux of 7×10^{14} neutron/cm^2 sec at the end of the beam tube and a flux of $\sim 10^7$ neutron/cm^2 sec at the crystal (the low energy flux relative to that used in X-ray diffraction necessitates the large crystal size). A total of 1781 reflections was measured and after correction for background (by the method of Lehmann *et al.*, 1972), absorption, and dispersion (the last two both nil), averaging of equivalent reflections, and examination of peak shapes, 1633 reflections were selected for the initial least-squares refinement. The initial refinement was performed with a modified version of ORFLS on the BNL computer system with constant scattering factors: Na, 0.362; K, 0.370; Ca, 0.466; Si, 0.415 Al, 0.345; O, 0.5803; all $\times 10^{-12}$ cm/atom. Further refinements examining tetrahedral site occupancies and the alkali site were performed on the Princeton IBM 360/91 computer system using L. W. Finger's RFINE and RFINE II.

X-ray experiment

X-ray diffraction data for a half sphere of reciprocal space with $0.05 \leq \sin\theta/\lambda \leq 0.76$ were collected on

an automated Picker FACS-1 four-circle single-crystal diffractometer with Mo$K\alpha$ radiation (Zr filter). Data were collected using θ–2θ scan with a scan speed of 1° 2θ per minute, a 2° base width compensated for dispersion; background was measured at high and low 2θ limits for a total of 20 seconds. The initial data were corrected for background, set to a uniform level relative to standard reflection intensities (2 measured every 20 reflections), corrected for Lorentz polarization and absorption, and their extinction β's calculated by a modified version of C. T. Prewitt's ACACA that employed the Gaussian quadrature technique ($4 \times 4 \times 4$ grid) for absorption. A total of 2603 reflections were used for least-squares refinement, of which 2441 were not rejected on the criterion of the counting statistics standard deviation being less than F_{obs}. RFINE II was used for the least-squares refinements, refining on a single scale factor, isotropic extinction parameter (Zachariasen, 1967), positional parameters, and first isotropic and then anisotropic thermal parameters.

The neutron refinements, which preceded the X-ray ones, yielded a weighted R factor (R_w) and unweighted R factor (R_u) of 0.076 and 0.069 for the isotropic case and 0.024 and 0.021 for the anisotropic case (standard deviation of a unit weight observation = 1.29). We assumed fully ordered tetrahedral sites (T_1O occupied by Al, the excess in T_1m); initial parameters were those of low albite from Ribbe *et al.* (1969). Positional parameters (Table 3), tetrahedral bond lengths (Table 6), and O–T–O and T–O–T angles (Table 7) were taken from the anisotropic case; anisotropic β's, isotropic B's, and R.M.S. equivalent amplitudes are listed in Tables 4 and 5. At this stage, refinements on Al/Si occupancy of the four tetrahedral sites were performed using various chemically constrained and unconstrained models. The results are noted in Table 2 with the weighted R factors for each case.

The least-squares refinement of the X-ray data yielded isotropic R factors of 0.053 R_w and 0.071 R_u and anisotropic R factors of 0.035 R_w and 0.040 R_u (standard deviation of a unit weight observation = 5.36), with relativistic Dirac–Slater atomic scattering factors calculated by Cromer and Waber (1965) for neutral atoms and Al/Si ordering as determined in the neutron refinements. Similar results were obtained on fully ionized atoms (except oxygen—O^{-1}) with scattering factors calculated by Cromer and Mann (1968); differences are noted in the text. The scattering factor for the alkali site was a compositionally weighted average of the scattering factors for Na, Ca, and K. Positional parameters (Table 3), tetrahedral bond lengths (Table 6), and temperature factors (Tables 4 and 5) are listed with the values from the neutron refinements. An attempt to refine Al/Si occupancies of the tetrahedral sites resulted in unrealistic total site occupancies for neutral atoms and realistic occupancies but excessively large errors for ionized atoms. Consequently only T occupancies as determined by the neutron refinements are listed for the X-ray refinement results.

Two models employing split isotropic Na sites were refined for each data set; one uses two half atoms and the other uses two partial atoms, with one's occupancy refined and the other's occupancy constrained so that the total occupancy of both sites is equal to 1.0. The results are listed in Tables 3 and 8.

Table 2. Results for T-site occupancy refinements including significance levels

Model	Variables	Refinement Type	Al in T Sites				Rw
1	119	Occupancy I (chemistry constrained)	0.970 .019	0.035	0.0	0.0	0.021367
2	122	Occupancy II (unconstrained)	0.970 .027	0.035 .028	-0.003 .028	-0.022 .061	0.021342
3	121	Occupancy III (chemistry constrained)	0.975 .023	0.039 .023	0.021 .023	-0.017	0.0213465
4*	120	Occupancy IV (chemistry constrained)	0.973 .03	0.009 .04	0.0	0.0	0.021389
5	118	Constrained I (fully ordered)	1.00	0.05	0.0	0.0	0.021384
6	118	Constrained II (95% Al in T_{1O})	0.95	0.10	0.0	0.0	0.021373
7	118	Constrained III (90% Al in T_{1O})	0.90	0.15	0.0	0.0	0.021461
8	118	Constrained IV (80% Al in T_{1O})	0.80	0.25	0.0	0.0	0.021928

R Factor Significance Tests

$R_{i,j} = R_{wi}/R_{wj}$

$R_{5,1} = 1.000810$

$R_{6,1} = 1.000287$

$R_{7,1} = 1.004393$

$R_{8,1} = 1.026279$

$R_{1,3} = 1.00095$

$R^*_{b,n-m,\alpha} = [\frac{b}{n-m} \cdot F_{b,n-m,\alpha} + 1]^{\frac{1}{2}}$

$R_{1,1504,0.005} = 1.00271$

$R_{1,1504,0.010} = 1.0022$

$R_{1,1504,0.10} = 1.00088$

$R_{1,1504,0.25} = 1.00048$

$R_{1,1504,0.50} = 1.00016$

$R_{2,1501,0.75} = 1.00095$

* Not totally converged

Results and discussion

General comparison of neutron and X-ray refinements

The two independently-derived sets of structural parameters (positions and apparent thermal motions)

Table 3. Atomic positional coordinates

Site		Occupancy	Spec.	X	Y	Z
T_1O	neutron	0.030(20)	Si	0.00901(10)	0.16862(6)	0.20806(11)
	x-ray	0.030	Si	0.00878(11)	0.16864(6)	0.20805(13)
T_1m	neutron	0.965	Si	0.00386(8)	0.82062(5)	0.23728(9)
	x-ray	0.965	Si	0.00382(10	0.82064(5)	0.23734(11)
T_2O	neutron	1.0	Si	0.69209(8)	0.11036(5)	0.31508(9)
	x-ray	1.0	Si	0.69210(10)	0.11040(5)	0.31507(12)
T_2m	neutron	1.0	Si	0.68152(8)	0.88195(5)	0.36078(9)
	x-ray	1.0	Si	0.68175(10)	0.88189(5)	0.36071(12)
Na	neutron	0.986	Na	0.26849(13)	0.98870(10)	0.14672(18)
	x-ray			0.26839(18)	0.98867(12)	0.14628(24)
Na_1	neutron	0.526(17)	"Na"	0.27098(28)	0.97765(36)	0.16218(55)
	x-ray	0.533(26)	"Na"	0.27033(45)	0.97800(57)	0.16219(92)
Na_2	neutron	0.474	"Na"	0.26561(32)	0.00168(41)	0.12859(62)
	x-ray	0.467	"Na"	0.26617(45)	0.00103(64)	0.12793(101)
O_{A1}	neutron	1.0	O	0.00490(7)	0.12115(4)	0.96638(7)
	x-ray	1.0	O	0.00481(27)	0.12120(14)	0.96610(30)
O_{A2}	neutron	1.0	O	0.59229(6)	0.99755(4)	0.28053(7)
	x-ray	1.0	O	0.59166(24)	0.99766(14)	0.27967(30)
O_BO	neutron	1.0	O	0.81231(7)	0.11013(4)	0.19056(8)
	x-ray	1.0	O	0.81285(26)	0.11039(15)	0.19124(32)
O_Bm	neutron	1.0	O	0.82027(7)	0.85114(4)	0.25876(9)
	x-ray	1.0	O	0.82061(27)	0.85121(15)	0.25942(34)
O_CO	neutron	1.0	O	0.01342(6)	0.30252(4)	0.27026(8)
	x-ray	1.0	O	0.01348(25)	0.30276(14)	0.27023(31)
O_Cm	neutron	1.0	O	0.02398(7)	0.69389(4)	0.22991(8)
	x-ray	1.0	O	0.02402(26)	0.69390(14)	0.22938(32)
O_DO	neutron	1.0	O	0.20770(7)	0.10901(4)	0.38910(7)
	x-ray	1.0	O	0.20765(26)	0.10922(15)	0.38898(30)
O_Dm	neutron	1.0	O	0.18364(7)	0.86819(4)	0.43609(8)
	x-ray	1.0	O	0.18316(27)	0.86825(15)	0.43555(31)

Estimated standard errors in parentheses refer to the last digits.

have been compared for consistency of error by the method of half-normal probability plot analysis (Abrahams and Keve, 1971). Figure 1 shows two plots of ranked observed-parameter deviates Δ_i *vs.* ranked normal deviates X_i for all parameters and positional parameters only, as determined from equations and tables in Section 4.3 of Volume IV of *International Tables for X-ray Crystallography* (1974). The treatment and results are similar to those of Higgins and Ribbe (1979) for sapphirine. A scatter of points about a line of unit slope would indicate a correct estimate of error with no obvious contributions due to systematic error. The observed scatter approaching a line with a slope of two for all parameters suggests that there is little distinguishable systematic error but an underestimation of pooled standard deviations by a factor of about two. In the positional parameters alone there is more scatter, which either is insignificant and only a function of the small number of points (39), or is an indication of compounded real and systematic errors of roughly the same magnitude (Abrahams and Keve, 1971). The slope of the trend for positional parameters is about 1.2, which suggests a realistic estimation of standard deviations. Hence, as might be expected, the estimation of error is more subject to bias and misevaluation for the anisotropic temperature factors than for positional parameters alone.

For the most part the refinements of the two data sets are identical within 1 or 2 standard errors of all parameters for the X-ray results. As indicated above, the largest variations occur for the thermal parameters. The neutron data, compared to the X-ray data, yield larger values of equivalent isotropic temperature factor (B) and anisotropic factor β_{33} for T and Na sites and yield smaller root-mean-squared (R.M.S.) displacements for oxygen sites. This is likely due in large part to the difference in relative scattering powers of Si, Al, Na, and O between X-ray and neutron diffraction. While it is tempting to use differences in the nature of the diffraction interaction between neutrons and X-rays to examine the asymmetry of bonding-electron distributions relative to nuclei, the variations in positional parameters and bond lengths and the evaluation of pooled errors suggest there are no measurable asymmetries.

Table 4. Thermal parameters

Site		Equivalent B	R.M.S. Amplitudes in Å Axis 1	Axis 2	Axis 3
T_1O	neutron	0.599(11)	0.0759(20)	0.0851(18)	0.0988(17)
	x-ray	0.436(12)	0.0728(25)	0.0747(23)	0.0972(19)
T_1m	neutron	0.512(9)	0.0711(17)	0.0803(15)	0.0891(15)
	x-ray	0.436(12)	0.0759(24)	0.0659(25)	0.0892(18)
T_2O	neutron	0.532(9)	0.0768(15)	0.0792(15)	0.0898(15)
	x-ray	0.464(12)	0.0615(24)	0.0772(21)	0.0889(19)
T_2m	neutron	0.532(9)	0.0768(15)	0.0792(16)	0.0898(15)
	x-ray	0.462(12)	0.0623(24)	0.0808(21)	0.0845(20)
Na	neutron	2.663(20)	0.1221(16)	0.1311(15)	0.2628(15)
	x-ray	2.529(29)	0.1169(28)	0.1306(25)	0.2557(22)
O_{A1}	neutron	0.946(7)	0.0739(13)	0.1149(9)	0.1314(8)
	x-ray	0.917(30)	0.0733(58)	0.0987(43)	0.1404(35)
O_{A2}	neutron	0.720(7)	0.0775(12)	0.0915(10)	0.1139(9)
	x-ray	0.754(28)	0.0748(52)	0.0936(44)	0.1196(39)
O_BO	neutron	1.040(8)	0.0791(13)	0.1162(9)	0.1405(8)
	x-ray	1.030(31)	0.0930(48)	0.1086(44)	0.1367(37)
O_Bm	neutron	1.319(8)	0.0787(13)	0.1410(9)	0.1551(8)
	x-ray	1.258(33)	0.0862(51)	0.1323(38)	0.1512(37)
O_CO	neutron	0.918(8)	0.0805(12)	0.1102(10)	0.1276(9)
	x-ray	0.945(31)	0.0800(50)	0.1165(41)	0.1262(40)
O_Cm	neutron	0.935(8)	0.0823(12)	0.1087(10)	0.1302(9)
	x-ray	0.981(31)	0.0776(52)	0.1083(42)	0.1397(37)
O_DO	neutron	1.020(8)	0.0868(12)	0.1180(9)	0.1316(9)
	x-ray	1.051(31)	0.0824(54)	0.1091(42)	0.1458(36)
O_Dm	neutron	1.153(8)	0.0868(12)	0.1180(9)	0.1316(9)
	x-ray	1.190(33)	0.0842(53)	0.1152(41)	0.1517(36)

Estimated standard errors in parentheses refer to the last digits.

Refinement of Al/Si order

As there is a uniform 18.5% difference in the scattering power of Al and Si in neutron diffraction (compared with an average 9% for X-rays) a meaningful refinement of the occupancy of the four T sites in low albite was possible. Many models involving either unconstrained or constrained occupancy of the T sites were refined (see Table 2). Those models involving variation of T_2O and T_2m occupancies led to results requiring Si occupancies either in excess of or insignificantly different from 1.0, as in model 2. Consequently final tetrahedral occupancy refinements involved variation in the T_1 sites only. However, it is encouraging to note that cases like model 2 are essentially identical to model 1 when errors are considered.

The *R*-factor ratio test of Hamilton (1965) was used to examine the constrained and unconstrained models of T_1O and T_1m occupancy; the results are shown in Table 2. The unconstrained case (model 1) is shown to be superior at better than the 75% significance level for all but model 6, which is within the standard error of the refined occupancy. In Figure 2, a diagrammatic curve has been drawn with the standard error in occupancy and the *R*-test significance levels marked along the ordinate and the Al content of the T_1O site along the abscissa, to show the nature of the data refinements upon tetrahedral occupancies. The results indicate that there is not much difference between completely-ordered low albite and the partially-disordered one achieved by refinement with chemical constraints, but that in any case there is a high degree of ordering.

Table 5. Root-Mean-Square amplitudes of apparent thermal vibration

Site	*	B	β_{11}	β_{22}	β_{33}	β_{12}	β_{13}	β_{23}
				$\beta \times 10^5$				
T_1O	n	0.597(36)	326(12)	98(4)	314(15)	-29(5)	163(11)	10(6)
	x	0.555(19)	333(14)	70(4)	263(17)	-20(6)	128(13)	2(7)
T_1m	n	0.601(31)	266(9)	87(3)	278(12)	15(4)	147(9)	14(5)
	x	0.450(17)	277(12)	56(4)	219(15)	21(5)	114(11)	13(6)
T_2O	n	0.607(31)	259(10)	73(3)	381(13)	-12(4)	143(9)	19(5)
	x	0.473(17)	246(12)	46(4)	306(15)	-2(5)	90(11)	0(6)
T_2m	n	0.636(31)	228(9)	79(3)	380(13)	5(4)	138(9)	25(5)
	x	0.464(17)	250(12)	49(4)	318(16)	11(5)	116(11)	15(6)
Na	n	2.510(59)	580(15)	591(8)	1548(25)	-100(9)	400(15)	-515(1)
	x	1.972(40)	620(24)	524(11)	1468(40)	-80(12)	356(25)	-516(1)
Na_1	n	1.356(64)						
	x	1.374(81)						
Na_2	n	1.413(71)						
	x	1.285(94)						
O_{A1}	n	0.979(27)	641(8)	159(3)	368(10)	-11(4)	304(7)	37(4)
	x	0.974(4)	716(36)	121(11)	333(42)	27(15)	296(33)	23(17)
O_{A2}	n	0.758(25)	311(7)	78(2)	581(10)	-5(3)	165(7)	43(4)
	x	0.763(4)	336(30)	69(9)	585(44)	-4(13)	127(31)	28(16)
O_BO	n	1.098(27)	461(8)	174(3)	805(11)	-92(4)	419(8)	-29(4)
	x	1.083(5)	518(34)	146(11)	788(49)	-67(15)	406(35)	-31(1)
O_Bm	n	1.330(28)	542(8)	233(3)	1076(12)	89(4)	582(8)	40(5)
	x	1.267(5)	593(36)	174(11)	1051(55)	97(16)	531(38)	28(20)
O_CO	n	0.971(27)	404(8)	98(2)	754(11)	-57(3)	237(8)	-20(4)
	x	0.984(4)	523(34)	82(10)	661(47)	-25(15)	217(34)	-27(17)
O_Cm	n	0.995(26)	421(8)	92(2)	701(10)	39(3)	167(7)	33(4)
	x	0.970(4)	485(33)	82(10)	672(47)	48(14)	128(33)	14(17)
O_DO	n	1.040(27)	476(8)	175(3)	409(10)	39(4)	84(7)	44(4)
	x	1.072(5)	564(35)	145(11)	403(45)	66(15)	55(33)	47(18)
O_Dm	n	1.177(27)	542(8)	180(3)	431(10)	-55(4)	12(7)	-15(4)
	x	1.213(5)	634(36)	152(11)	436(46)	-40(16)	-2(34)	-26(18)

Estimated standard errors in parentheses refer to the last digits.
* n - neutron; x - X-ray

Table 6. T–O and tetrahedral O–O bond distances

T_1O- O	neutron	x-ray	T_1m- O	neutron	x-ray
O_{A1}	1.7472(9)	1.749(2)	O_{A1}	1.5955(8)	1.594(2)
O_BO	1.7446(10)	1.739(2)	O_Bm	1.6000(9)	1.599(2)
O_CO	1.7348(9)	1.737(2)	O_Cm	1.6214(8)	1.621(2)
O_DO	1.7448(10)	1.744(2)	O_Dm	1.6179(8)	1.614(2)
Average	1.7429	1.742	Average	1.6087	1.607

T_2O- O	neutron	x-ray	T_2m- O	neutron	x-ray
O_{A2}	1.6322(8)	1.633(2)	O_{A2}	1.6448(8)	1.650(2)
O_BO	1.5918(8)	1.592(2)	O_Bm	1.6205(8)	1.617(2)
O_Cm	1.6171(8)	1.617(2)	O_CO	1.5957(8)	1.594(2)
O_Dm	1.6152(8)	1.619(2)	O_DO	1.6015(8)	1.603(2)
Average	1.6141	1.615	Average	1.6156	1.616

T_1O	neutron	x-ray	T_1m	neutron	x-ray
O_{A1}- O_BO	2.7310(9)	2.732(3)	O_{A1}- O_Bm	2.6010(9)	2.610(3)
- O_CO	2.9528(10)	2.955(3)	- O_Cm	2.6747(8)	2.671(3)
- O_DO	2.7525(8)	2.753(3)	- O_Dm	2.5883(8)	2.583(3)
O_BO- O_CO	2.881(8)	2.886(3)	O_Bm- O_Cm	2.6100(8)	2.612(3)
- O_DO	2.8783(10)	2.874(3)	- O_Dm	2.6570(10)	2.651(3)
O_CO- O_DO	2.8518(8)	2.852(3)	O_Cm- O_Dm	2.6210(8)	2.620(3)
Average	2.8424	2.842	Average	2.6253	2.625

T_2O	neutron	x-ray	T_2m	neutron	x-ray
O_{A2}- O_BO	2.6595(9)	2.662(3)	O_{A2}- O_Bm	2.6258(8)	2.631(3)
- O_Cm	2.5653(7)	2.563(3)	- O_CO	2.5875(7)	2.585(2)
- O_Dm	2.6115(8)	2.618(3)	- O_DO	2.6349(8)	2.543(3)
O_BO- O_Cm	2.6612(9)	2.660(3)	O_Bm- O_CO	2.6367(10)	2.636(3)
- O_Dm	2.6524(8)	2.652(3)	- O_DO	2.6428(8)	2.640(3)
O_Cm- O_Dm	2.6533(9)	2.659(3)	O_CO- O_DO	2.6884(9)	2.687(3)
Average	2.6339	2.636	Average	2.6365	2.637

Estimated standard errors in parentheses refer to the last digits.

T–O bond distances and Al/Si ordering

With the completion of these refinements, four more points are available for determination and refinement of the relationship between tetrahedral bond distance and Al/Si occupancy in the alkali feldspars. With values determined in other neutron diffraction experiments for a Himalaya orthoclase (Prince *et al.*, 1973) and a low sanidine (Brown *et al.*, 1974) (see Table 8), least-squares refinements of the data to fit polynomial curves of the form

$$\mathrm{Al}/(\mathrm{Al}+\mathrm{Si}) = \sum_{i=0}^{n} \langle \overline{\mathrm{T\text{–}O}} \rangle^i$$

Table 7. O–T–O and T–O–T angles

O -T_1O-		neutron	x-ray	O -T_1m-O		neutron	x-ray
O_{A1}-	-O_BO	102.91(5)	103.1(1)	O_{A1}-	-O_Bm	109.50(5)	109.6(1)
	-O_CO	115.99(5)	115.9(1)		-O_Cm	112.50(5)	112.3(1)
	-O_DO	104.04(5)	104.0(1)		-O_Dm	108.23(5)	108.4(1)
O_BO-	-O_CO	112.21(5)	112.3(1)	O_Bm-	-O_Cm	108.23(5)	108.4(1)
	-O_DO	111.16(5)	111.2(1)		-O_Dm	111.31(5)	111.2(1)
O_CO-	-O_DO	110.08(5)	110.0(1)	O_Cm-	-O_Dm	108.02(5)	108.2(1)
Average		109.40	109.4	Average		109.48	109.5

O -T_2O-O		neutron	x-ray	O -T_2m-O		neutron	x-ray
O_{A2}-	-O_BO	111.15(5)	111.3(1)	O_{A2}-	-O_Bm	107.21(4)	107.3(1)
	-O_Cm	104.23(4)	104.1(1)		-O_CO	105.96(4)	105.7(1)
	-O_Dm	107.06(4)	107.2(1)		-O_DO	108.51(4)	108.7(1)
O_BO-	-O_Cm	112.06(5)	112.0(1)	O_Bm-	-O_CO	110.14(5)	110.3(1)
	-O_Dm	111.60(5)	111.4(1)		-O_DO	110.22(5)	110.2(1)
O_Cm-	-O_Dm	110.34(5)	110.6(1)	O_CO-	-O_DO	114.46(5)	114.4(1)
Average		109.42	109.4	Average		109.42	109.4

	neutron	x-ray
T_1O-O_{A1}-T_1m	141.45(5)	141.5(1)
T_2m-O_{A2}-T_2O	130.08(4)	129.7(1)
T_1O-O_BO-T_2O	139.66(5)	129.8(1)
T_1m-O_Bm-T_2m	161.20(5)	161.5(2)
T_1O-O_CO-T_2m	129.88(5)	129.8(1)
T_1m-O_Cm-T_2O	135.85(5)	135.8(1)
T_1O-O_DO-T_2m	133.95(5)	133.9(1)
T_1m-O_Dm-T_2O	151.84(5)	151.8(2)
Average	140.49	140.5

Estimated standard errors in parentheses refer to the last digits.

were performed, where Al/(Al + Si) is the fraction of Al in a site and $\langle\overline{T\text{–}O}\rangle$ is the average inter-atomic distance between the T site and its surrounding four oxygens. Though there was little difference between the fully-ordered and partially-disordered low-albite models refined, both were used in polynomial curve fitting. Results are shown in Table 9 and Figure 3.

To test for the best fit, three criteria were used. First, is the fit physically realistic? Fits with significant negative curvatures or fits that require excess Al or Si beyond known limits were considered unrealistic and, hence, were discarded. Second, the standard error of any of the polynomial coefficients must be less than that coefficient itself. Third, a variance ratio test (Hamilton, 1964) was used to discriminate among polynomials of successive degrees. Consequently, polynomials of degree three are preferred, but the curve for the constrained model is more realistic as it does reach full Al occupancy [Al/(Al + Si) = 1.0]. The results show that there can be a large discrepancy in predicted bond lengths between linear and non-linear models; there is a difference of 0.016Å at Al/(Al + Si) ≃ 0.9. The net effect is an increase in the apparent amount of Al in a T site with $\langle\overline{T\text{–}O}\rangle$ lengths between 1.65 and 1.74Å for the non-linear model. However, these curves should not be considered determinative and, hence, have not been plotted. ⟨T–O⟩ and refined occupancy data for alkali feldspars with a structural state between that of orthoclase and low albite are needed before determinative plots may be usable. Even then, other factors (Ribbe *et al.*, 1974) must be considered. Presently, the indication is that such plots may not be linear.

One important point that has been overlooked is the effect of disorder on T–O distances. Examination of the refinements of a number of feldspar structures shows that disordered feldspars generally have shorter grand-mean-average T–O bond lengths than do ordered ones. In Table 9 the grand-mean-average of T–O bond lengths for ordered alkali feldspar structures are 0.001 to 0.003Å longer than for the disordered ones. A comparison has also been made for the $\langle\overline{T\text{–}O}\rangle$ values calculated from the Ribbe–Gibbs linear model and our 3rd-degree polynomial model; the differences in average bond lengths are less for the polynomial model but are still significant. The displacement of the individual Al and Si atoms from

Table 8. Polynomial regressions for neutron-determined feldspar occupancy data. Equations for the polynomial and the variance ratio test (V_R) are listed

$$Al/(Al+Si) = \sum_{i=0}^{n} a_i \langle T\text{-}O\rangle^i$$

A	Partially Disordered (T_1O=0.970Al; T_1m=0.035)			
	1st Order	2nd Order	3rd Order	4th Order
a_0	12.176±0.063	-45.493±130.0	4115.563±8.0x10^5	257089.983±5.2x10^4
a_1	7.559±0.023	47.393±186.0	-7432.206±2.6x10^6	-616138.021±1.8x10^5
a_2	-	-11.895± 16.6	4467.471±9.4 10^5	553563.260±1.6x10^5
a_3	-	-	-893.744±3.7x10^4	-220974.678±6.1x10^5
a_4	-	-	-	33069.047 1.3x10^4
$\Sigma\varepsilon_i^2$	0.01197	0.00889	0.00379	0.00194
V_R	-	2.043	6.714	3.828

B	Fully Ordered (T_1O=1.0Al; T_1m=0.05)		
	1st Order	2nd Order	3rd Order
a_0	-12.619±0.203	-43.698± 8.60	3203.074± 625.0
a_1	7.828±0.124	44.986±10.30	-5791.239±1120.0
a_2	-	-11.095± 3.07	3484.116± 670.0
a_3			- 697.382± 134.0
$\Sigma\varepsilon_i^2$	0.00786	0.00517	0.00192
V_R	-	3.127	8.486

$$V_R = (N-n)\frac{\Sigma\varepsilon_i^2(n-1) - \Sigma\varepsilon_i(n)}{\Sigma\varepsilon_i^2(n)}$$

the averaged T sites yields an underestimate of the T–O distances relative to a simple average of the individual Si–O and Al–O bond lengths. The effect is much the same for evaluating the effect of thermal motion on bond lengths. Consequently, since disorder displacements are included in the thermal parameter, $\langle\overline{T\text{–}O}\rangle$ values should be corrected for some model of thermal motion, probably something between riding motion and noncorrelated motion (see Ohashi and Finger, 1974; Harlow, 1977). It would be better to use some common correction scheme for thermal (and disordering) effects in calculating a regression against Al/(Al + Si), but this is not possible for lack of such information on the other neutron refinements. However, it is likely that the points for disordered feldspars would be increased to higher $\langle\overline{T\text{–}O}\rangle$ values relative to those of low albite in Figure 3.

Na site—anisotropy vs. splitting

The Na site in both low and high albite displays a large apparent thermal motion anisotropy (*e.g.* Ferguson *et al.*, 1958; Williams and Megaw, 1964; Ribbe *et al.*, 1969; Quareni and Taylor, 1971). Ribbe *et al.* (1969) examined a model with two split isotropic atoms to approximate the anisotropy, in order to see whether there might really be two loci for Na in the structure. Based on detailed calculations by Megaw in their paper, they could not distinguish between the time-average and the space-average models for their data, because there was inadequate separation between the split atoms. We have used a similar approach for our data, as earlier described. These results are listed in Table 10 along with the significance calculations for comparison of the various models.

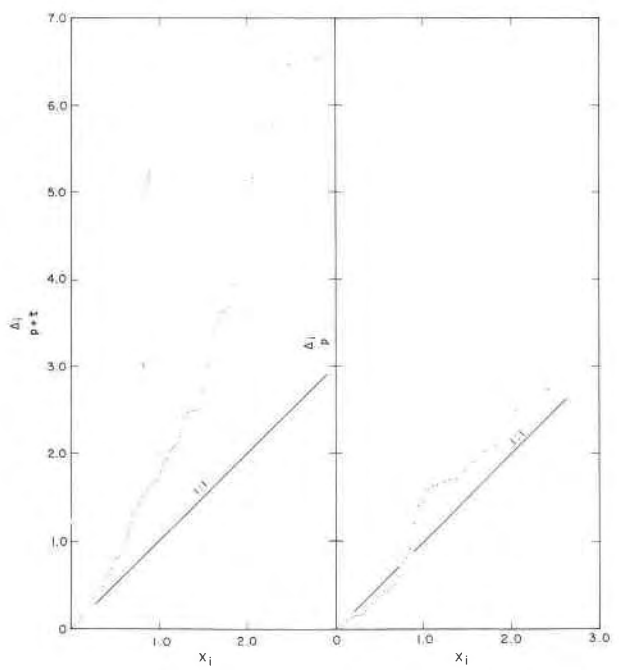

Fig. 1. Half-normal probability plots comparing positional and thermal (left) and only positional (right) parameters between the X-ray and neutron refinements of low albite.

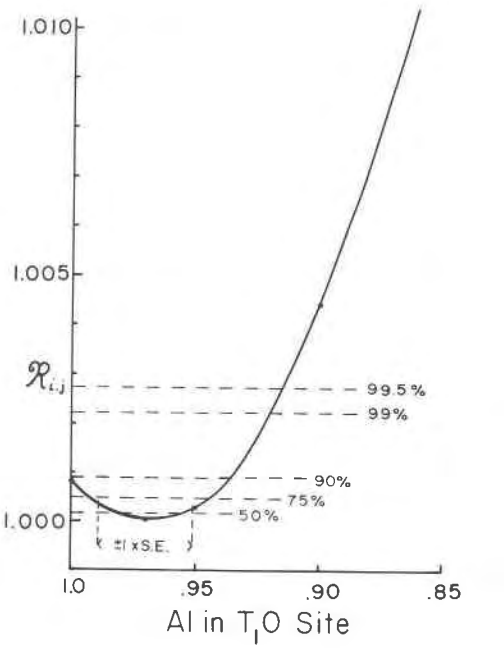

Fig. 2. Plot of R_{ij}, the R-factor ratio between the fixed T-site occupancy and refined occupancy models, and the amount of Al in the T_1O site. The significance levels and the standard error in refined T_1O occupancy are shown with dashed lines.

Among the space-average models, the refined-occupancy model is preferred statistically for both neutron and X-ray data, though there are not large differences between the models. A direct comparison of *R* factors can be made between the anisotropic (time-average) model and the refined-occupancy split-atom (space-average) model, as they have the same number of refineable parameters. For both the neutron and X-ray data, the anisotropic model yields a smaller weighted *R* factor and hence appears to be a better model. In comparison with the Na-site modelling for low albite of Ribbe *et al.* (1969), the anisotropic models are very similar within the limits of error, though errors here are lower. Differences for the split-site modelling are greater, though not much more than 1 or 2 standard errors; in particular the Na–O distances are very similar though the Na_1–Na_2 splitting distances here are larger, 0.39 *vs.* 0.36Å for

Table 9. Comparison of T–O bond distances between ordered and disordered alkali feldspars

	Total Al per Formula Unit	Or Content	Observed and Calculated $\overline{T\text{-}O}$ and differences ($\Delta \times 10^4$) in Å					
			$\langle\overline{T\text{-}O}\rangle_O^*$	$\langle\overline{T\text{-}O}\rangle_{C1}$	Δ_1	$\langle\overline{T\text{-}O}\rangle_{C2}$	Δ_2	
Ordered								
Low Microcline	1.00	99.	1.6442	1.6430	12	1.6443	- 1	Brown and Bailey (1964)
Low Microcline	1.00	100.	1.644	1.6430	10	1.6443	- 3	Finney and Bailey (1964)
Low Albite (X-ray)	1.001	0.6	1.6451	1.6430	21	1.6443	8	This study
Low Albite	1.00	0.	1.6444	1.6430	14	1.6443	1	Wainwright and Starkey (1968)
Microcline (CA1E)	1.015	88.6	1.6454	1.6436	18	1.6446	8	Dal Negro et al. (1978)
Microcline (RC20C)	1.012	88.5	1.6443	1.6434	9	1.6445	- 2	Dal Negro et al. (1978)
			Av. 1.6446		Av. 14		Av. 2	
Partially Disordered								
Orthoclase (neutron)	0.99	90.	1.6419	1.6430	-11	1.6443	-23	Prince et al. (1973)
Orthoclase	1.012	90.	1.6419	1.6434	-15	1.6446	-27	Colville and Ribbe (1968)
Adularia	1.00	88.1	1.6433	1.6430	3	1.6443	-10	Phillips and Ribbe (1973)
Adularia	1.001	88.	1.6427	1.6430	- 3	1.6443	-16	Harlow (unpublished)
Low Sanidine	1.00	85.	1.6431	1.6430	1	1.6443	-12	Phillips and Ribbe (1973)
Low Sanidine	1.00	85.	1.6408	1.6430	-22	1.6443	-35	Ohashi and Finger (1974)
Microcline (P1C)	1.012	90.0	1.6425	1.6434	- 9	1.6445	-20	Dal Negro et al. (1978)
Microcline (CA1B)	1.015	88.6	1.6438	1.6436	2	1.6446	- 8	Dal Negro et al. (1978)
Microcline (A1D)	1.011	90.4	1.6423	1.6434	-11	1.6445	-22	Dal Negro et al. (1978)
Microcline P17C)	1.001	87.1	1.6419	1.6430	-11	1.6443	-24	Dal Negro et al. (1978)
Microcline (CA1A)	1.015	88.6	1.6441	1.6436	5	1.6446	- 5	Dal Negro et al. (1978)
Microcline (P2A)	1.014	93.1	1.6443	1.6435	8	1.6446	- 3	Dal Negro et al. (1978)
Microcline	1.014	84.6	1.6428	1.6435	- 7	1.6446	-18	Bailey (1969)
Sanidine	1.018	87.	1.6438	1.6437	1	1.6447	- 9	Weitz (1972)
			Av. 1.6428		Av. - 5		Av. -16	
Disordered								
Sanidine (P2B)	1.014	93.1	1.6443	1.6435	8	1.6446	- 3	Dal Negro et al. (1978)
Heated Sanidine	1.018	87.	1.6428	1.6437	- 9	1.6447	-19	Weitz (1972)
High Sanidine (heated orthoclase)	1.025	92.	1.6421	1.6439	-18	1.6449	-28	Ribbe (1963)
High Albite	1.007	1.6	1.6434	1.64333	1	1.6444	-10	Ribbe et al. (1969)
High Albite	1.00	0.	1.6434	1.6430	4	1.6443	- 9	Wainwright (see Smith, 1974)
Anorthoclase	1.008	32.5	1.6418	1.6433	-15	1.6445	-17	Harlow (in prep.)
Anorthoclase	1.069	22.3	1.6437	1.6456	-19	1.6460	-23	Harlow (in prep.)
Anorthoclase	1.025	13.8	1.6434	1.6439	- 5	1.6449	-15	Harlow (in prep.)
			Av. 1.6431		Av. - 7		Av. -17	

$^*O$ Observed grand mean average
C_1 Calculated from total Al using $\langle\overline{T\text{-}O}\rangle$ = Al/(4x6.58)+1.605 (Ribbe and Gibbs, 1969)
C_2 Calculated using 3rd order polynomial (fully ordered albite)

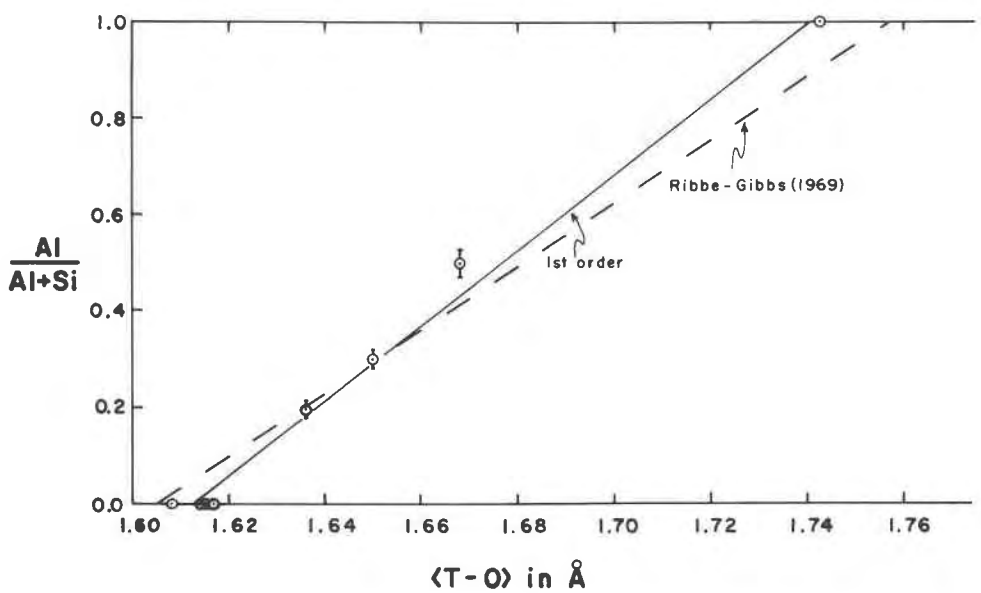

Fig. 3. Plot of average tetrahedral bond lengths for individual tetrahedra vs. occupancy, Al/(Al+Si), of the site as determined by direct refinement of neutron diffraction data. Points include low albite (constrained, full occupancy of T_1O), Himalaya orthoclase (Prince *et al.*, 1973), and sanidine (Brown *et al.*, 1974). A linear model for the data is shown.

Table 10. Results for anisotropic and split-site modelling of Na site including Na–O bond distances

Model		R_w	Occupancy Na_1	Splitting (Å)	Direction of Splittling* to a	to b	to c
1†	neutron	0.02138			101.0(8)	145.4(5)	51.9(5)
	x-ray	0.03541			103.5(13)	142.9(5)	49.1(5)
2	neutron	0.02237	0.5	0.392(3)	101.1	145.3	51.7
	x-ray	0.03599	0.5	0.387(4)	102.9	143.3	49.6
3	neutron	0.02235	0.526(17)	0.393(3)	101.2	145.3	51.7
	x-ray	0.03597	0.533(26)	0.393(3)	101.2	145.3	49.5

† 1-Anisotropic; 2-Split half atom; 3-split site, refine occupancy
*for the anisotropic case this refers to the direction of the major axis of the anisotropic ellipsoid

			Significance Level (90%)	(75%)
		$R = R_{w2}/R_{w3}$	$R_{1,n,0.10}$	$R_{1,n,0.25}$
neutron	(n=1515)	1.00083	1.00087	1.00048
x-ray	(n=2322)	1.0004	1.0057	1.00031

Na - O Bond Distances (Å)

	Na(0000)		Na_1		Na_2	
	neutron	x-ray	neutron	x-ray	neutron	x-ray
O_{A1}(0000)	2.671(1)	2.671(2)	2.801(2)	2.797(4)	2.527(2)	2.535(4)
O_{A1}(000C)	2.537(1)	2.537(2)	2.458(2)	2.456(4)	2.644(2)	2.643(4)
O_{A2}(0000)	2.372(1)	2.369(2)	2.380(2)	2.381(4)	2.381(2)	2.372(4)
O_{A2}(000C)	3.724(1)	3.719(3)	3.837(3)	3.837(5)	3.600(3)	3.590(5)
O_{A2}(000C)	3.725(1)	3.733(3)	3.623(3)	3.627(5)	3.853(3)	3.863(5)
O_B(000C)	2.461(1)	2.464(2)	2.492(2)	2.499(4)	2.442(2)	2.438(4)
O_B(m00C)	3.465(2)	3.466(3)	3.640(3)	3.641(5)	3.261(3)	3.265(5)
O_C(0zi0)	2.961(L)	2.959(2)	2.835(2)	2.839(4)	3.116(2)	3.106(4)
O_C(mzi0)	3.266(1)	3.267(2)	3.390(3)	3.390(5)	3.127(3)	3.131(4)
O_D(0000)	2.437(1)	2.440(2)	2.451(2)	2.447(4)	2.438(2)	2.449(4)
O_D(m000)	2.996(2)	2.997(3)	2.835(3)	2.834(4)	3.188(3)	3.188(5)

Estimated errors in parentheses refer to last digits

the Ribbe *et al.* model. With Megaw's theoretical approach to distinguish the models, for our data the lower limit for splitting is 0.36Å for the neutron data and 0.33Å for the X-ray data; these limits are slightly smaller than those for the refined splittings. These results tend to support the time-average position model, though not with any great certainty. Using data collected at 300° and 600°C, Quareni and Taylor (1971) concluded that anisotropic thermal motion was the correct solution for Na in low albite. More recently Winter *et al.* (1977) examined the Na anisotropy of a Tiburon, California low albite at various elevated temperatures; they found that their measured apparent-thermal-motion magnitudes extrapolate to zero at 0K, which indicates that real thermal motion is the source of the large Na-site anisotropic delocalization. Since our results agree, we conclude that thermal motion is the most reasonable interpretation for the Na-site anisotropy.

Acknowledgments

This work was initiated while both authors were at the Department of Geological and Geophysical Sciences at Princeton University and was partially supported by NASA grant NGL-31-001-283. We acknowledge the late Walter C. Hamilton of Brookhaven National Laboratory for providing reactor port time during the summer of 1972 and for many stimulating discussions. We also thank Thomas F. Koetzle (BNL) and Mogens S. Lehmann (CEDEX) for assisting us with data collection, and Paul H. Ribbe for his constructive review.

References

Abrahams, S. C. and E. T. Keve (1971) Normal probability plot analysis of error in measured and derived quantities and standard deviations. *Acta Crystallogr., A27,* 157–165.

Bailey, S. W. (1969) Refinement of an intermediate microcline structure. *Am. Mineral., 54,* 1540–1545.

Barth, T. F. W. (1934) Polymorphic phenomena and crystal structure. *Am. J. Sci., 27,* 273–286.

Brown, B. E. and S. W. Bailey (1964) The structure of maximum microcline. *Acta Crystallogr., 17,* 1391–1400.

Brown, G. E., G. V. Gibbs and P. H. Ribbe (1969) The nature and variation in length of the Si–O and Al–O bonds in framework silicates. *Am. Mineral., 54,* 1044–1061.

———, W. C. Hamilton and C. T. Prewitt (1974) Neutron diffraction study of Al/Si ordering in sanidine: a comparison with X-ray diffraction data. In W. S. MacKenzie and J. Zussman, Eds., *The Feldspars,* p. 68–80. Manchester University Press, Manchester, England.

Colville, A. A. and P. H. Ribbe (1968) The crystal structure of an adularia and a refinement of the structure of orthoclase. *Am. Mineral., 53,* 25–27.

Cromer, D. T. and J. B. Mann (1968) X-ray scattering factors computed from numerical Hartree–Fock wave functions. *Acta Crystallogr., A24,* 321–324.

——— and J. T. Waber (1965) Scattering factors computed from relativistic Dirac–Slater wave functions. *Acta Crystallogr., 18,* 104–109.

Dal Negro, A., R. De Pieri, S. Quareni and W. H. Taylor (1978) The crystal structures of nine K feldspars from the Adamello massif (northern Italy). *Acta Crystallogr., B34,* 2699–2707.

Ferguson, R. B., R. J. Traill and W. H. Taylor (1958) The crystal structures of low-temperature and high-temperature albites. *Acta Crystallogr., 11,* 331–348.

Finney, J. J. and S. W. Bailey (1964) Crystal structure of an authigenic maximum microcline. *Z. Kristallogr., 119,* 413–436.

Hamilton, W. C. (1964) Section 4–6. Multivariate linear hypotheses. In W. C. Hamilton, Ed., *Statistics in Physical Science,* p. 139–142. Ronald Press Company, New York.

——— (1965) Significance tests on the crystallographic R factor. *Acta Crystallogr., 18,* 502–510.

Harlow, G. E. (1977) *The Anorthoclase Structures: a Room and High-temperature Study.* Ph.D. Dissertation, Princeton University, Princeton, New Jersey.

Higgins, J. B. and P. H. Ribbe (1979) Sapphirine II: A neutron and X-ray diffraction study of $(Mg–Al)^{VI}$ and $(Si–Al)^{IV}$ ordering in monoclinic sapphirine. *Contrib. Mineral. Petrol., 68,* 357–368.

International Tables for X-ray Crystallography, Vol. 4. (1974) Kynoch Press, Birmingham, England.

Jones, J. B. (1968) Al–O and Si–O tetrahedral distances in aluminosilicate framework structures. *Acta Crystallogr., B24,* 355–358.

Lehmann, M. S., W. C. Hamilton and F. K. Larsen (1972) Background determination for step-scan Bragg reflections. *Am. Crystallogr. Assoc. Meeting, Albuquerque, N.M.,* Abstract 09, 87.

Morey, G. W. and R. O. Fournier (1961) The decomposition of microcline, albite, and nepheline in hot water. *Am. Mineral., 96,* 688.

Ohashi, Y. and L. W. Finger (1974) Refinement of the crystal structure of sanidine at 25° and 400°. *Carnegie Inst. Wash. Year Book 73–74,* 539–544.

Phillips, M. W. and P. H. Ribbe (1973) The structures of monoclinic potassium-rich feldspars. *Am. Mineral., 58,* 495–499.

Prince, E., G. Donnay and R. F. Martin (1973) Neutron structure refinement of an ordered orthoclase. *Am. Mineral., 58,* 500–507.

Quareni, S. and W. H. Taylor (1971) Anisotropy of the sodium atom in low albite. *Acta Crystallogr., B27,* 281–285.

Ribbe, P. H. (1963) A refinement of the crystal structure of sanidinized orthoclase. *Acta Crystallogr., 16,* 426–427.

——— (1975) The chemistry, structure, and nomenclature of feldspars. In P. H. Ribbe, Ed., *Feldspar Mineralogy,* p. R1–R72. Mineral. Soc. Am. Short Course Notes, Vol. 2.

——— and G. V. Gibbs (1969) Statistical analysis of mean Al/Si–O bond distances and the aluminum content of tetrahedra in feldspars. *Am. Mineral., 54,* 85–94.

———, M. W. Phillips and G. V. Gibbs (1974) Tetrahedral bond length variations in feldspars. In W. S. MacKenzie and J. Zussman, Eds., *The Feldspars,* p. 25–48. Manchester University Press, Manchester, England.

———, H. D. Megaw, W. H. Taylor, R. B. Ferguson and R. J. Traill (1969) The albite structures. *Acta Crystallogr., B25,* 1503–1518.

Smith, J. V. (1954) A review of Al–O and Si–O distances. *Acta Crystallogr., 7,* 479–481.

——— and S. W. Bailey (1963) Second review of Al–O and Si–O tetrahedral distances. *Acta Crystallogr., 16,* 801–811.

Stewart, D. B. and T. L. Wright (1974) Al/Si order and symmetry of natural alkali feldspars, and the relationship of strained cell parameters to bulk composition. *Bull. Soc. fr. Minéral. Cristallogr., 97,* 356–377.

Waldbaum, D. R. and R. A. Robie (1971) Calorimetric investigation of Na–K mixing and polymorphism in the alkali feldspars. *Z. Kristallogr., 134,* 381–420.

Wainwright, J. E. and J. Starkey (1968) Crystal structure of a metamorphic low albite (abstr.). *Geol. Soc. Am. Abstracts with Programs,* 310.

Weitz, G. (1972) Die Struktur des Sanidins bei verschiedenen Ordnungs graden. *Z. Kristallogr., 136,* 418–426.

Williams, P. P. and H. D. Megaw (1964) The crystal structures of high and low albites at −180°C. *Acta Crystallogr., 17,* 882–890.

Winter, J. K., S. Ghose and F. P. Okamura (1977) A high-temperature study of the thermal expansion and the anisotropy of the sodium atom in low albite. *Am. Mineral., 62,* 921–931.

Zachariasen, W. H. (1967) A general theory of X-ray diffraction in crystals. *Acta Crystallogr., 23,* 558–564.

Manuscript received, November 23, 1979;
accepted for publication, March 31, 1980.

American Mineralogist, Volume 65, pages 996–1001, 1980

Amphiboles on the join pargasite–ferropargasite

ROBERT W. CHARLES

Los Alamos Scientific Laboratory
P. O. Box 1663
Los Alamos, New Mexico 87545

Abstract

Amphiboles have been grown across the join $NaCa_2Mg_4AlSi_6Al_2O_{22}(OH)_2$–$NaCa_2Fe_4AlSi_6Al_2O_{22}(OH)_2$ on QFM and CCH_4 oxygen buffers to gain insight into the Fe–Mg substitution in an amphibole without the local charge imbalance caused by Na in the $M(4)$ site. Oxygen fugacity was found to have no effect upon the unit-cell dimensions of amphibole. Unit-cell parameters ($C2/m$) for amphibole grown across the series are [a, b, c(Å), β, V(Å^3)]:

Mg_4	9.892(1),[1]	17.941(2),	5.277(1),	105°33′(1),	902.2(3)
Mg_3Fe	9.904(1),	17.989(5),	5.291(2),	105°27′(1),	908.6(5)
Mg_2Fe_2	9.915(3),	18.031(7),	5.301(3),	105°24′(1),	913.6(1.0)
$MgFe_3$	9.930(5),	18.104(6),	5.320(2),	105°16′(1),	922.6(9)
Fe_4	9.953(5),	18.152(3),	5.330(2),	105°16′(2),	928.8(4)

No change in cell parameters is observed with temperature on a given buffer. The essentially linear trend indicates disorder of Mg and Fe in $M(1)$, $M(2)$, and $M(3)$ sites. Plagioclase and pyroxene were present in all charges. The amount ranged from a few percent to greater than 30 percent, without affecting the unit-cell parameters of coexisting amphibole.

Introduction

Pargasites are monoclinic amphiboles having high Ca, moderate Na, and high Al. The ideal chemical formula is $NaCa_2(Mg,Fe)_4AlSi_6Al_2O_{22}(OH)_2$. The structure consists of double chains of silica and alumina tetrahedra linked by $M(1)$, $M(2)$, and $M(3)$ octahedra and by the larger 6- to 8-coordinated $M(4)$ sites (Papike *et al.*, 1969). The larger 6–12-coordinated A site completes this strip of cations. In pargasite the A site, 12-coordinated, is occupied by Na whereas the two $M(4)$ sites, 8-coordinated, are occupied by Ca. The Mg, Fe, and Al^{VI} are distributed in the remaining five M sites.

No natural occurrences of the end members pargasite and ferropargasite exist. Intermediate compositions are common in metamorphosed impure limestones, fresh and metamorphosed mafic rocks, and less commonly in altered ultramafic rocks. Ferric iron substitution for octahedral aluminum is common, placing most natural pargasites in the body of the quadrilateral bounded by the binaries pargasite–ferropargasite and magnesiohastingsite–hastingsite. Natural occurrences of pargasite with >0.9 Al^{VI} lie between $Ca_2NaMg_3FeAlSi_6Al_2O_{22}(OH)_2$ and $Ca_2NaFe_3MgAlSi_6Al_2O_{22}(OH)_2$. Amphiboles grown experimentally on the pargasite–ferropargasite pseudobinary should be compositionally comparable to natural analogues.

In contrast to pargasites, the richterite series (Charles, 1974) has one Na in $M(4)$, and the five total $M(1)$, $M(2)$, and $M(3)$ sites are occupied entirely by Mg and Fe. The local charge imbalance caused by Na in $M(4)$ is not found in pargasites. Consequently, one of the objectives of this study was to synthesize intermediate and end-member pargasites in order to contrast some of the physical properties of the two series.

Experimental procedure

Five oxide mixes were prepared along the pargasite–ferropargasite join: Mg_4, Mg_3Fe, Mg_2Fe_2, $MgFe_3$, and Fe_4. As a shorthand notation only the Mg and Fe will be written: $NaCa_2Mg_3FeAlSi_6Al_2O_{22}(OH)_2$ = Mg_3Fe. Iron was added as hematite, Al as γ-Al_2O_3,

[1] Parenthesized figures represent the estimated deviation *(esd)* in terms of least units cited for the value to their immediate left, thus 9.892(1) indicates an *esd* of 0.001.

0003–004X/80/0910–0996$02.00

Table 1. Average refractive indices for the pargasite series

Phase	R. I.
Pargasite(Mg_4)	1.624 ± .003
Mg_3Fe	1.655 ± .003
Mg_2Fe_2	1.672 ± .003
$MgFe_3$	1.694 ± .003
Ferropargasite(Fe_4)	1.715 ± .005

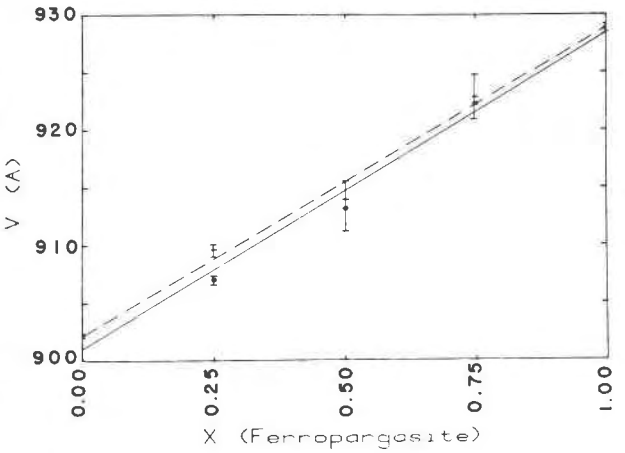

Fig. 1. Unit-cell volume *vs.* composition for pargasite grown on CCH_4 (solid line) and QFM (dashed line). 1.00 is ferropargasite. Error bars = 1σ for all figures.

Mg as periclase, Si as cristobalite, and Na as $Na_2Si_2O_5$ prepared after the method of Schairer and Bowen (1955). After the mixes were ground in an automortar for 2 hr, a portion of each mix was reduced to Fe^0 under H_2. Results were consistent regardless of the initial state of iron; only kinetics were affected.

Oxygen fugacities were buffered with solid oxygen buffers (Eugster, 1957) and the graphite–methane buffer (Eugster and Skippen, 1967). The charges were sealed with excess water in precious-metal capsules and subjected to temperature and pressure in standard cold-seal hydrothermal apparatus.

Experimental results

Microscopic examination revealed some pyroxene and plagioclase in each charge. Amounts varied from a few percent to about 30 percent by volume, depending upon the experimental conditions. Intermediate compositions did not nucleate well. Amphibole in these charges appeared as crystalline aggregates only about 5μm in diameter. Mean refractive indices of these aggregates are tabulated in Table 1.

The unit-cell parameters were determined using a Norelco powder X-ray diffraction goniometer. Scans of 1°/min at a strip-chart recorder rate of 1 cm/min were satisfactory to fix the peak positions of amphibole to ±0.01°, standardized against BaF_2 (a = 6.1971±0.0002Å) which has four usable reflections between 24° and 49°. BaF_2, in turn, was standardized against diamond (a = 3.56703±0.00018Å). The amphiboles ($C2/m$) were indexed and cell parameters calculated using a program developed by Appleman and Evans (1973). Twenty-five usable reflections for pargasite decreased to sixteen reflections for ferropargasite due to ambiguous indexing and poor crystallization. Pargasite and ferropargasite grown in this study are compared in Table 2 with that grown by Boyd (1959) and Gilbert (1966).

Unit-cell data for the pargasites are found in Table 3. For a given bulk composition, cell parameters are uniform with pressure and temperature. No variation was seen with oxygen fugacity (Fig. 1). Amphibole grown on CCH_4 and QFM show no difference in unit

Table 2. Unit-cell parameters of pargasite and ferropargasite

Reference	a(A)	b(A)	c(A)	β	V(A^3)
		Pargasite			
Boyd (1959)	9.906(10)	17.986(17)	5.265(8)	105°30'(8)	904.7(1.9)
This Study	9.892(1)	17.941(2)	5.277(1)	105°33'(1)	902.2(3)
		Ferropargasite			
Gilbert (1966)	9.95	18.14	5.33	105°18'	928
This Study	9.953(5)	18.152(3)	5.330(2)	105°16'(2)	928.8(4)

Table 3. Unit-cell dimensions

P (bars)	T (°C)	Duration (h)	Amphibole Yield (Percent)	Buffer	a (A)	b (A)	c (A)	Beta	V_3 (A^3)	asinß
				Pargasite $NaCa_2Mg_4AlSi_6Al_2O_{22}(OH)_2$						
5000	750	527	95+	---	9.888(5)*	17.943(7)	5.280(3)	105°33'(1)	902.5(5)	
2000	750	333	95+	---	9.891(4)	17.932(6)	5.275(4)	105°30'(2)	901.5(6)	
2000	750	330	80	---	9.890(3)	17.935(6)	5.277(2)	105°32'(1)	901.9(4)	
2000	750	330	85	---	9.891(8)	17.953(22)	5.280(10)	105°38'(7)	902.8(1.0)	
2000	750	330	90	---	9.895(2)	17.939(5)	5.280(2)	105°34'(2)	902.8(3)	
2000	750	330	60	---	9.887(5)	17.940(14)	5.271(6)	105°31'(4)	900.9(9)	
1000	850	336	95+	---	9.893(2)	17.941(5)	5.276(1)	105°33'(1)	902.1(2)	
1000	850	331	99+	---	9.899(2)	17.946(3)	5.278(1)	105°35'(1)	903.1(2)	
Average					9.892(1)	17.941(2)	5.277(1)	105°33'(1)	902.2(2)	9.530
				$NaCa_2Mg_3FeAlSi_6Al_2O_{22}(OH)_2$						
2000	750	127	90	HMt**	9.901(3)	17.982(7)	5.296(2)	105°28'(2)	908.9(4)	
2000	750	1095	95+	QFM	9.904(3)	17.991(6)	5.290(2)	105°27'(2)	908.5(3)	
2000	625	1008	80	QFM	9.911(5)	18.006(10)	5.283(8)	105°30'(5)	908.6(1.3)	
2000	625	1008	80	QFM	9.907(5)	18.011(11)	5.288(8)	105°27'(4)	909.5(1.0)	
1000	850	1006	95	QFM	9.906(3)	18.002(6)	5.297(2)	105°26'(1)	910.6(4)	
1000	850	332	90	QFM	9.908(2)	18.003(4)	5.300(4)	105°28'(1)	911.1(2)	
2000	800	666	90	CCH_4	9.898(4)	17.963(10)	5.289(3)	105°27'(3)	906.4(5)	
2000	700	1015	90	CCH_4	9.905(2)	17.976(5)	5.286(2)	105°31'(2)	906.9(3)	
2000	750	499	90	CCH_4	9.898(3)	17.979(7)	5.290(2)	105°24'(2)	907.6(4)	
2000	650	120	95	IW	9.903(3)	17.979(6)	5.291(2)	105°27'(1)	908.1(3)	
Average					9.904(1)	17.989(5)	5.291(2)	105°27'(1)	908.6(5)	9.546
				$NaCa_2Mg_2Fe_2AlSi_6Al_2O_{22}(OH)_2$						
5000	650	784	60	QFM	9.919(8)	18.031(20)	5.299(4)	105°26'(4)	913.5(1.0)	
2000	750	2463	60	QFM	9.917(2)	18.048(4)	5.309(2)	105°19'(1)	916.5(3)	
2000	750	1618	85	QFM	9.906(4)	18.044(7)	5.307(2)	105°19'(2)	914.9(4)	
1000	850	1650	50	QFM	9.907(4)	18.016(8)	5.292(5)	105°25'(5)	910.7(6)	
2000	750	1015	50	CCH_4	9.916(5)	18.007(10)	5.294(5)	105°32'(3)	910.7(7)	
2000	700	498	85	CCH_4	9.925(3)	18.039(7)	5.304(2)	105°23'(2)	915.5(4)	
Average					9.915(3)	18.031(7)	5.301(3)	105°24'(2)	913.6(1.0)	9.559
				$NaCa_2MgFe_3AlSi_6Al_2O_{22}(OH)_2$						
5000	650	1367	90	QFM	9.918(3)	18.088(5)	5.319(2)	105°13'(1)	920.8(3)	
2000	750	427	60	QFM	9.940(4)	18.113(9)	5.326(3)	105°18'(2)	924.9(5)	
2000	625	672	95	CCH_4	9.927(4)	18.106(9)	5.315(3)	105°18'(2)	921.4(5)	
2000	700	1178	90	CCH_4	9.934(3)	18.110(16)	5.319(2)	105°15'(2)	923.1(4)	
Average					9.930(5)	18.104(6)	5.320(2)	105°16'(1)	922.6(9)	9.580
				Ferropargasite $NaCa_2Fe_4AlSi_6Al_2O_{22}(OH)_2$						
2000	600	368	90	QFM	9.947(3)	18.154(7)	5.332(2)	105°15'(2)	928.8(4)	
2000	700	673	95	CCH_4	9.958(4)	18.149(7)	5.328(2)	105°18'(3)	928.8(4)	
Average					9.953(5)	18.152(3)	5.330(2)	105°16'(2)	928.8(4)	9.602

* Parenthesized figures represent the estimated standard deviation (esd) in terms of least units cited for the value to their immediate left, thus 9.888(5) indicates an esd of 0.005.

** Buffer notation is as follows: HMt = hematite - magnetite, QFM = quartz - fayalite - magnetite, CCH_4 = graphite - methane, and IW = iron - wustite.

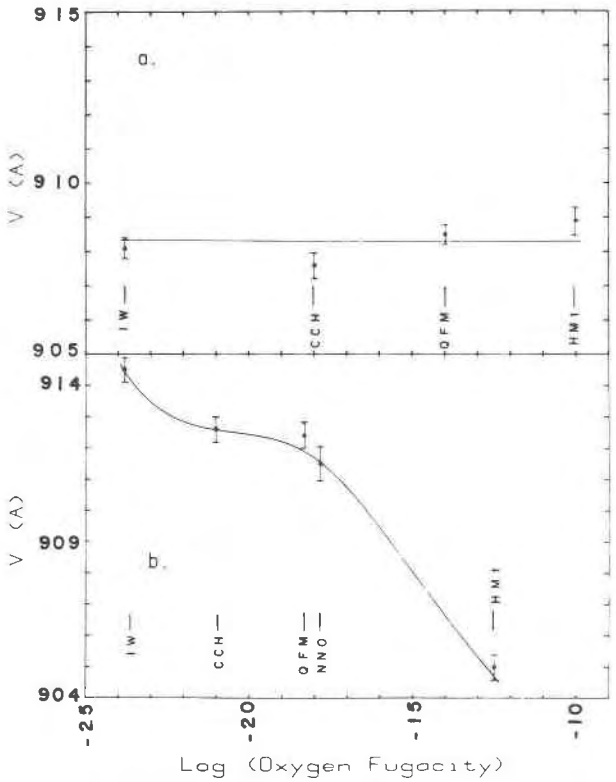

Fig. 2. (a) Unit-cell volume of pargasite $Ca_2NaMg_3FeAlSi_6Al_2O_{22}(OH)_2$ *vs.* oxygen fugacity. (b) Unit-cell volume of richterite $CaNa_2Mg_4FeSi_6O_{22}(OH)_2$ *vs.* oxygen fugacity (Charles, 1974).

cell at the 2-sigma level. The curves are fitted by least squares to a straight line,

CCH_4: V (Å^3) = 27.49 X(ferropargasite) + 900.97; $r^2 = 0.99$

QFM: V (Å^3) = 26.58 X(ferropargasite) + 902.18; $r^2 = 0.99$

Most experiments were done on QFM and CCH_4, but those done on HMt and IW substantiate this observation. This is in agreement with the study by Gilbert (1966), which shows essentially no variation in ferropargasite unit cell with oxygen fugacity.

Figure 2 compares the effects of oxygen fugacity on unit-cell parameters for analogous compositions in the pargasite and richterite series. The richterite is from Charles (1974). Within two sigma no trend is seen in the pargasite, whereas a dramatic decrease in cell volume is seen in the richterite with increase in oxygen fugacity.

Yields of amphibole down to about 60 percent of the charge by volume had no effect on the unit-cell parameters. Either charges with low amphibole yield nonstoichiometric pargasite with fortuitously similar cell dimensions to that of purer charges, or the amphibole is on composition. Experience with other amphibole systems indicates the latter case is more probable.

Figure 3 shows all the unit-cell data for the pargasite series. The dashed curves are similar measurements for the richterite series (Charles, 1974). All data are fitted with a linear curve by the least-squares method (Table 4). Some of the data suggest a nonlinear fit, but not at a two-sigma confidence level.

Discussion

Pargasites are more stable than richterites, $Na_2Ca(Mg,Fe)_5Si_8O_{22}(OH)_2$ (Boyd, 1959; Gilbert, 1966; Charles, 1975). A number of structural obser-

Table 4. Straight-line fit to unit-cell parameters y = ax + b, r^2 = degree of fit, where y = cell parameter and x = mole fraction of iron-bearing end member

Cell Parameters	Pargasite a	Pargasite b	Pargasite r^2	Richterite a	Richterite b	Richterite r^2
a	0.06A	9.89A	0.97	0.10A	9.90A	0.99
b	0.21A	17.94A	0.99	0.26A	17.97A	0.99
c	0.05A	5.28A	0.99	0.04A	5.27A	0.99
β	- 18'	105° 32'	0.94	- 17'	104° 12.5'	0.99
V	26.8A^3	901.8A^3	0.99	30.7A^3	908.5A^3	1.00
asinβ	0.07A	953A	0.99	0.11A	9.60A	1.00

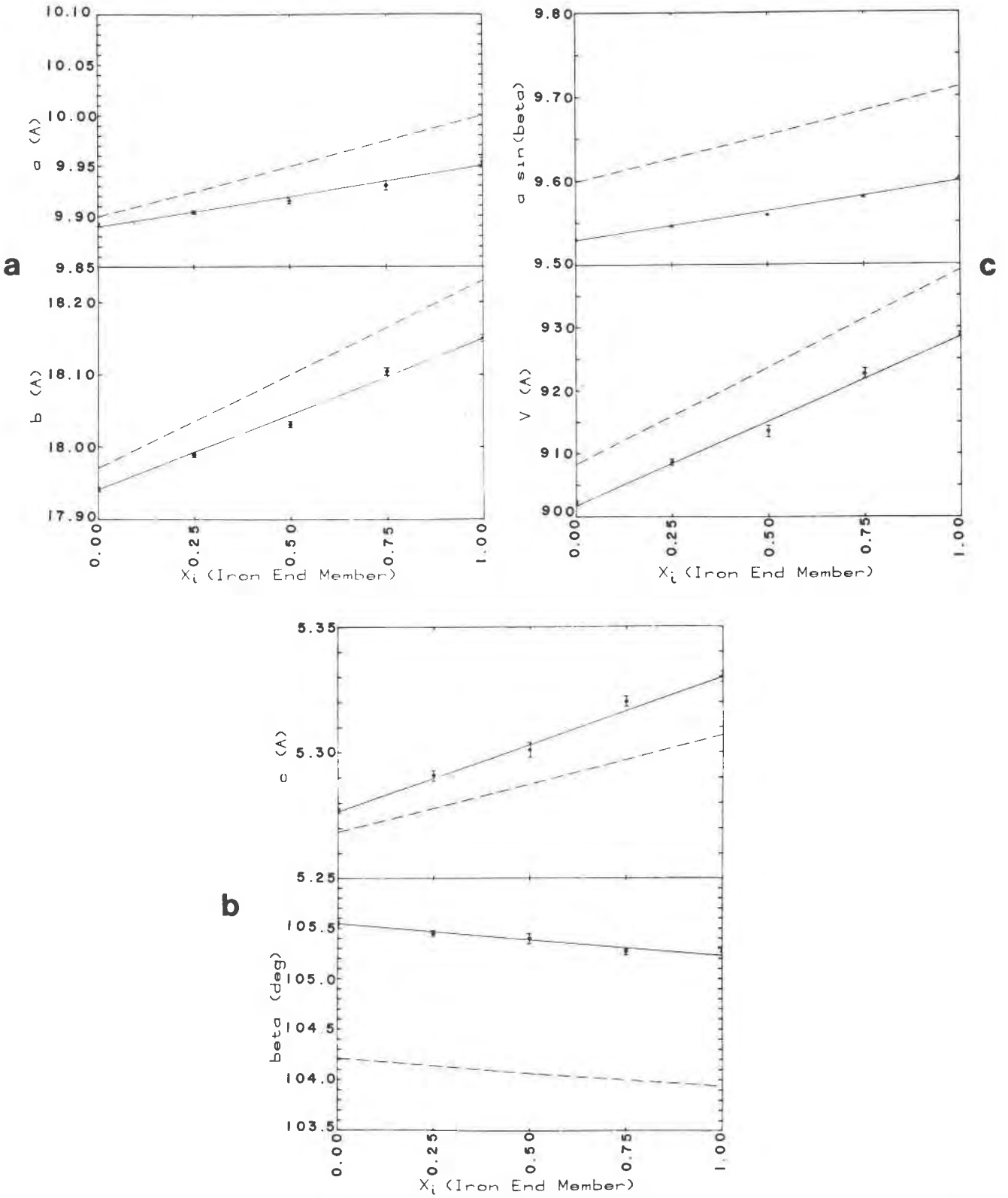

Fig. 3. Variation of average unit-cell parameters with composition (1.00 = ferropargasite) for pargasite (this study) and richterite grown on IW (Charles, 1974).

vations contrast the two amphibole series. The richterite structure has a local charge imbalance because one sodium must occupy an $M(4)$ site and be coordinated by six oxygens (Ghose, 1966; Whittaker, 1949, 1960). This is compensated by addition of a small amount of ferric iron in $M(2)$ which is nearest to $M(4)$ in the iron-bearing richterites. In pargasite $M(4)$ and A are occupied by Ca and Na respectively. The interior M sites contain Al and 4(Mg,Fe). Should some Na be present in $M(4)$, Al in $M(2)$ would alleviate any charge imbalance. This observation and the closer proximity of the adjacent double chains caused by a smaller mean cation size in the M sites indicate why pargasite is thermally more stable than richterite.

Figure 2 shows one effect of local charge imbalance. Pargasite shows a more uniform cell volume with respect to oxygen fugacity than does richterite. The local charge imbalance in richterite is enhanced at higher oxygen fugacities, presumably causing more ferric iron to enter $M(2)$. At the higher oxygen fugacities of the HMt buffer, richterite unit-cell parameters deviate from those observed at lower buffers toward magnesioriebeckite (Ernst, 1968), which is known to have Fe^{3+} occupying $M(2)$ (Bancroft and Burns, 1969).

The unit-cell parameters of pargasite are linear with composition in contrast to richterite (Charles, 1974). The variation in unit-cell parameters with composition can be interpreted in terms of amphibole structure. The parameters a and $a\sin\beta$ depend upon the mean size of cations linking the double chains of silica and alumina tetrahedra (Ernst, 1968; Huebner and Papike, 1970; Cameron and Papike, 1979). One would expect a linear change with addition of iron. This is observed in the pargasite series. Parameter b depends upon the occupancy of $M(4)$ and $M(2)$ which actually link the chains of silica–alumina tetrahedra. $M(4)$ is occupied by Ca and Na in all cases. If iron and magnesium are randomly distributed in $M(1)$, $M(2)$, and $M(3)$, a linear increase would result as is observed. Parameter c, chain length, reflects the occupancy of the chain and the $M(1)$ and $M(3)$ sites. Six Si and two Al are the tetrahedral cations for all pargasites. Linear increase in chain length reflects random mixing of Fe and Mg in $M(1)$ and $M(3)$. Beta mirrors changes in A site size. In all cases A is occupied by Na and possibly Ca. However, the structure around A becomes increasingly larger due to addition of iron. The net effect is that of placing a relatively smaller cation in A, causing β to decrease. Combining these effects for pargasite, one sees a linear increase in volume within the scatter of the data.

The nonlinearities seen in richterite due to preferential filling of $M(1)$ and $M(3)$ with ferrous iron over $M(2)$ are not seen in the pargasites. A more complete discussion of richterite unit-cell parameter is presented in Charles (1974).

Acknowledgments

I thank Professor H. J. Greenwood, The University of British Columbia, and Department of Energy for most of the support for the research presented here, and Marcella Kramer for the careful preparation of this manuscript.

References

Appleman, D. E. and H. T. Evans, Jr. (1973) Indexing and least squares refinement of powder diffraction data. *Natl. Tech. Inf. Serv., U.S. Dep. Commerce, Springfield, Virginia.* Document PB-216 188.

Bancroft, G. M. and R. G. Burns (1969) Mossbauer and absorption spectral study of alkali amphiboles. *Mineral. Soc. Am. Spec. Pap., 2,* 137–148.

Boyd, F. R. (1959) Hydrothermal investigations of amphiboles. In P. H. Abelson, Ed., *Researches in Geochemistry,* p. 377–396. Wiley, New York.

Cameron, M. and J. J. Papike (1979) Amphibole crystal chemistry: a review. *Fortschr. Mineral., 57,* 28–67.

Charles, R. W. (1974) The physical properties of the Mg–Fe richterites. *Am. Mineral., 59,* 518–528.

——— (1975) The phase equilibria of richterite and ferrorichterite. *Am. Mineral., 60,* 367–374.

Ernst, W. G. (1968) *Amphiboles.* Springer-Verlag, New York.

Eugster, H. P. (1957) Heterogeneous reactions involving oxidation and reduction at high pressures and temperatures. *J. Chem. Phys., 26,* 1760–1761.

——— and G. B. Skippen (1967) Igneous and metamorphic reactions involving gas equilibria. In P. H. Abelson, Ed., *Researches in Geochemistry,* p. 492–520. Wiley, New York.

Ghose, S. (1966) A scheme of cation distribution in amphiboles. *Mineral. Mag., 35,* 46–54.

Gilbert, M. C. (1966) Synthesis and stability relations of the hornblende ferropargasite. *Am. J. Sci., 264,* 698–742.

Huebner, J. S. and J. J. Papike (1970) Synthesis and crystal chemistry of sodium–potassium richterite, (Na,K) $NaCaMg_5Si_8O_{22}(OH,F)_2$: a model for amphiboles. *Am. Mineral., 55,* 1973–1992.

Papike, J. J., M. Ross and J. R. Clark (1969) Crystal chemical characterization of clinoamphiboles based on five new structure refinements. *Mineral. Soc. Am. Spec. Pap., 2,* 117–136.

Schairer, J. F. and N. L. Bowen (1955) The system K_2O–Al_2O_3–SiO_2. *Am. J. Sci., 253,* 681–745.

Whittaker, E. J. W. (1949) The structure of Bolivia crocidolite. *Acta Crystallogr., 2,* 312–317.

——— (1960) The crystal chemistry of the amphiboles. *Acta Crystallogr., 13,* 291–298.

Manuscript received, November 13, 1979;
accepted for publication, March 12, 1980.

American Mineralogist, Volume 65, pages 1002–1011, 1980

Rapid-quench hydrothermal experiments in dilute chloride solutions applied to the muscovite–quartz–sanidine equilibrium

ROBERT P. WINTSCH, ENRIQUE MERINO AND ROBERT F. BLAKELY

Department of Geology, Indiana University
Bloomington, Indiana 47405

Abstract

We have conducted a series of experiments in 0.01-molal chloride solutions at 200°C and 2 kbar on the muscovite–quartz–sanidine equilibrium for variable solid/fluid ratios, which in these experiments are proportional to the surface area of the solids. The quench pH decreases with increasing solid/fluid ratios for runs with starting solution compositions in the sanidine field (*i.e.*, relatively alkaline solutions), but increases with increasing solid/fluid ratios for runs with starting solutions in the muscovite field (*i.e.*, relatively acid). The two trends intersect at a solid/fluid ratio of ~1/16, which is the ratio that yields the narrowest equilibrium reversals; in turn these reversals agree well with the independently-calculated log K (200°C, 2 kbar).

For the same reaction in 0.01-molal chloride solutions at 205°C and 17 bar vapor pressure, the same trend of quench pH-*vs.*-solid/fluid ratio is observed for the runs approaching equilibrium from the muscovite field as for the 2 kbar runs, but no clear trend emerges from the runs approaching equilibrium from the sanidine field. Taken together, the experiments at 2 kbar and 17 bar indicate that surface reactions cannot account for the two trends in quench pH; if they did, the trends observed on approaching equilibrium from both sides would be the same, which they are not. We conclude that dilute solutions are appropriate for collecting high-temperature/high-pressure equilibrium data provided one uses the rapid-quench technique with solid/fluid mass ratios of ~1/16.

The rapid-quench, dilute chloride solution technique was also used to determine log K *vs.* T for the muscovite–quartz–sanidine reaction at 2 kbar and solid/fluid ~1/16 over the interval 200–500°C. The log K's, determined *via* aqueous-speciation calculations for each T and P, coincide with the log K's calculated independently from the thermodynamic properties of the reactants and products.

Introduction

Experimental studies of solid–fluid equilibria have traditionally employed concentrated (1–2 molar) chloride solutions. Although these studies have generally been successful, the technique has several drawbacks. First, the amount of solid that must react in order to buffer the solution is relatively large, which increases the time necessary to establish equilibrium. Second, the use of concentrated chloride solutions causes activities of aqueous species to depart from the corresponding molalities and the activity of H_2O to depart from unity.[1] Both of these departures can alter the values obtained for the equilibrium constant of the reaction under investigation. The use of dilute solutions eliminates these problems, but introduces the uncertainty of interpreting quench pH because of the possible effect of surface reactions. In spite of the successful use of dilute chloride solutions in autoclave experiments (Usdowski and Barnes, 1972), no systematic study has yet been carried out of the possible distorting effects of surface reactions on quench pH. These effects might be more important in dilute than in concentrated solutions. We report the results of our experiments of reaction 1, along with an assessment of the rapid-quench pH technique in dilute chloride solution.

The reaction studied is:

$$3/2\text{K-feldspar} + H^+_{aq} \rightleftarrows 1/2\text{muscovite} + 3\text{quartz} + K^+_{aq} \qquad (1)$$

[1] The standard state adopted here for aqueous species is one of unit activity in a hypothetical one-molal solution referenced to infinite dilution at any temperature and pressure. The standard state chosen for H_2O and for minerals is one of pure liquid H_2O and pure solids, respectively, at any temperature and pressure.

0003-004X/80/0910-1002$02.00

For the standard states chosen here (see footnote 1), the equilibrium constant is

$$K_1 = a_{K^+}/a_{H^+} \quad (2)$$

This reaction was chosen because (1) it has been studied experimentally over a large range of temperature, pressure, and salinity (Hemley, 1959; Shade, 1968, 1974; Usdowski and Barnes, 1972; Gunter, 1974; Wintsch, 1975); (2) equilibrium constants may be calculated from the thermodynamic properties of the reactants and products (Helgeson and Kirkham, 1976; Helgeson *et al.,* 1978); (3) dissociation constants for the aqueous complexes of interest in the final solution are well known (Helgeson and Kirkham, 1976; Walther and Helgeson, 1977); and (4) the quench molalities of H^+ and K^+ may be easily measured with specific-ion electrodes (Usdowski and Barnes, 1972).

Many of our experiments have been designed to determine if surface reactions of the type discussed by Garrels and Howard (1959),

$$\text{K-mica} + H^+ = \text{H-mica} + K^+ \quad (3)$$

$$\text{K-feldspar} + H^+ = \text{H-feldspar} + K^+ \quad (4)$$

occur in rapid-quench experiments during the quench. Because these are surface reactions, the amount of hydrogen ion adsorbed will be proportional to the surface area of the minerals present. In order to vary the surface area in each experiment, the mass of the starting solids has been varied, keeping constant the mass of starting fluid. The particle size of the solids was always the same. Thus, the total mineral surface area is proportional to the mass of solids, and also to the solid/fluid ratio. Both high pressure and vapor pressure experiments have been carried out at 200°C for the purpose of contrasting the two different quenching techniques involved (see below).

Methods

Starting materials

Only synthetic quartz, muscovite and K-feldspar have been used in this study. They were prepared by using oxide mixes of reagent-grade H_2SiO_3, $AlCl_3 \cdot 6H_2O$, and K_2CO_3. The $AlCl_3 \cdot 6H_2O$ was heated at about 900°C for several hours to produce X-ray amorphous Al_2O_3. Appropriate mixtures of these materials were sealed in gold capsules with 0.05 g distilled–deionized H_2O, and starting materials were synthesized in standard cold-seal pressure vessels.

The grain size and unit-cell dimensions of the synthetic starting materials are listed in Table 1 along with the experimental conditions of synthesis. The X-ray technique suggested by Wright and Stewart (1968) using copper radiation ($\lambda Cu K\alpha_0 = 1.540562$Å) has been followed, except that U.S. Bureau of Standards silicon ($a = 5.43088$Å at 25°C) has been used as an internal standard instead of CaF_2 and that samples have been run at slower scanning rates (1/4° 2θ/min). Unit cell parameters were calculated from the measured 2θ values by the computer program of Burnham (1962). In all cases both 1M and $2M_1$ muscovite have been synthesized together, but intensity of 1M muscovite peaks is considerably larger than that of $2M_1$ muscovite. The relatively large errors in the refinements of the muscovite structures are a consequence of the overlapping 1M and $2M_1$ peaks. Synthetic K-feldspar is high sanidine with slightly anomalous cell dimensions. Unit-cell parameters for quartz are identical to those for α-quartz and are not included in Table 1. Aqueous chloride solutions of variable m_{KCl}/m_{HCl} ratios but constant chlorinity were prepared by mixing 10^{-2} molal KCl and 10^{-2} molal HCl solutions. All rapid-quench experiments were conducted in sealed gold capsules. A constant 0.30 g of solution was used in each run, and different amounts of muscovite + sanidine + quartz (always in the mass ratio of 1:1:1) were weighed as required to vary the mineral surface area.

High-pressure experiments

High-pressure experiments were carried out in rapid-quench cold-seal pressure vessels of the type figured by Rudert *et al.* (1976). The pressure and extension vessels were 30 and 25 cm long respectively. An 8-cm filler rod was used in each run to limit convection of the H_2O pressure medium. Temperatures were measured with sheathed chromel–alumel thermocouples standardized against the melting point of NaCl (800.5°C). Rudert *et al.* report temperature gradients in rapid-quench bombs which they believe are unacceptably large. We report our measured temperature gradients in some detail because so little is known about them and because our results are significantly smaller than those of Rudert *et al.*

Temperature gradients between the thermocouple well and the charge were determined by comparing the temperature measured in the thermocouple well with the melting temperature of tin (231.9°C), zinc (419.6), and antimony (630.7). These metals were sealed in evacuated silica tubes (5 to 6 cm long and 6 mm O.D.) of dimensions close to those of the gold

Table 1. Conditions of synthesis, grain size, and unit-cell dimensions of synthetic starting materials

Mineral	T°C	P(Kb)	Run duration (days)	Crystal dimensions (microns)	a (Å)	b (Å)	c (Å)	β (deg)	$\bar{V}$ (Å^3)	no. unique observations
San 3	520	2	14	30x30x40	8.6146 ±0.0060	13.0139 ± 0.0039	7.1699 ±0.0039	116.195 ± 0.033	721.26 ± 0.93	15
San 8	600	2	14	30x30x40	8.5877 ±0.0033	13.0116 ± 0.0029	7.1711 ±0.0022	116.101 ± 0.018	719.548 ± 0.485	16
Musc 12 (1M)	600	2	20	1x10x10	5.2036 ±0.0072	8.9822 ± 0.0029	10.2427 ±0.0053	101.710 ± 0.064	468.78 ± 0.73	13
Musc 12 ($2M_1$)	600	2	20	1x10x10	5.1787 ±0.0027	8.9840 ± 0.0019	20.1651 ±0.0056	95.865 ± 0.059	933.272 ± 0.66	16
Musc 14 (1M)	570	2	12	1x10x10	5.1984 ± .0089	8.9769 ± 0.0039	10.2504 ±0.0073	101.655 ± 0.085	468.47 ± 0.97	14
Musc 14 ($2M_1$)	570	2	12	1x10x10	5.1832 ±0.0039	8.9828 ± 0.0033	20.1779 ± .0105	95.620 ± 0.094	934.961 ± 0.96	12

capsules used. The amount of metal melted as a function of distance from the hot end could readily be measured by viewing the metal through the glass. Temperature gradients so measured are shown in Figure 1. They are smaller than those reported by Rudert *et al.*, particularly at higher temperatures.

The errors of precision, thermal gradient, and furnace temperature fluctuation combine to give an estimated temperature uncertainty of between 5 and 10°C. Pressures were monitored on a Heise 7kbar temperature-compensated pressure gauge. Because all bombs were isolated from line pressure during most of the run time, temperature fluctuations led to pressure fluctuations. The maximum pressure error this causes is ±50 bar.

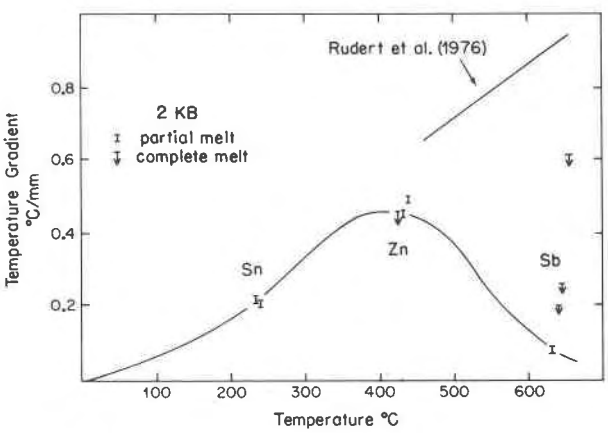

Fig. 1. The change in temperature gradient with temperature as determined by comparing the melting temperature of tin, zinc, and antimony (sealed in evacuated silica glass tubes) with the measured temperature in the thermocouple well. The data of Rudert *et al.* (1976) have been included for comparison. The temperature reported for each run is equal to the temperature given by the thermocouple minus a quantity which equals the temperature gradient (as given by this curve) multiplied by the distance between the thermocouple well and the gold reaction tube.

Vapor pressure experiments

In these experiments the sealed gold capsules were placed in a drying oven, and the temperature monitored with a thermocouple placed adjacent to the capsules on the same shelf in the oven. Pressure was the vapor pressure of the aqueous solution at the temperature of the experiment. Rapid quench was achieved by immersing the capsule in an ice bath.

Activity measurements

Both pH and pK of the final, quenched aqueous solutions were measured with specific-ion electrodes. A Beckman flat bulb combination pH electrode #39507 was used with a lithium trichloroacetate internal filling solution to prevent KCl contamination. The uncertainty in pH measurement is ±0.05. Orion's 93 series potassium-ion electrode was used in conjunction with the reference portion of the combination pH electrode to measure pK with an error of ±0.02. Orion digital pH meters were standardized to read KCl molality directly with the slope adjusted to 100%. Both electrodes were standardized before and after each experimental measurement.

All measurements were made in a glove box flushed with compressed air bubbled through NaOH solutions to remove CO_2 and through distilled water to ensure H_2O saturation. This process minimized CO_2 contamination and evaporation of the quenched solution during the measurement of activity. Approximately 4 minutes elapsed between the quench and insertion of the electrodes into the solution, and another ½ and 3 minutes were required to achieve

stable pK and pH readings respectively. The response of the pH electrode was monitored on a strip chart recorder, so that the rate of approach to a stable reading could be accurately assessed.

Run products

Following each experiment the silicates were examined by optical and X-ray techniques. The solutions were so dilute that very little new muscovite or sanidine precipitated during the experiment, and textural evidence was often insufficient to determine reaction direction. However, the growth of muscovite on sanidine crystals and the inclusion of muscovite and sanidine in quartz are taken as evidence of sanidine dissolution in solutions of low starting m_{KCl}/m_{HCl} ratio. Muscovite inclusions could be occasionally detected in sanidine crystals, indicating sanidine growth at the expense of muscovite + quartz. Euhedral quartz crystals about 10 × 50 microns crystallized in runs whose initial starting compositions were either in the muscovite or the sanidine field. In view of the irregular distribution of these textures, the direction of change in pH and pK provides a more reliable monitor of reaction direction and extent of reaction. X-ray scans of all run products have been made, but in no instance could a change in the polymorph of a phase be detected. In two runs, however, a peak at ~14Å was identified, and in both runs the amount of sanidine was much reduced.

Calculation of speciation

In order to obtain the ratio a_{K^+}/a_{H^+} (= K_{eq} for reaction 1) from the measured $m_{K,tot}$, the distribution of aqueous species must first be calculated for the aqueous solution from each run. We have calculated the speciation by solving the following nonlinear system of four mass-action-law equations (one each for the complexes KCl, HCl, KOH, and H_2O) and three mass balances (for K, H, and Cl):

$$m_{K^+}\,\gamma_{K^+}\,m_{Cl^-}\,\gamma_{Cl^-} = K_{KCl}\,m_{KCl^\circ}\,\gamma_{KCl} \quad (5)$$

$$m_{H^+}\,\gamma_{H^+}\,m_{Cl^-}\,\gamma_{Cl^-} = K_{HCl}\,m_{HCl^\circ}\,\gamma_{HCl} \quad (6)$$

$$m_{K^+}\,\gamma_{K^+}\,m_{OH^-}\,\gamma_{OH^-} = K_{KOH}\,m_{KOH^\circ}\,\gamma_{KOH} \quad (7)$$

$$m_{H^+}\,\gamma_{H^+}\,m_{OH^-}\,\gamma_{OH^-} = K_{H_2O}\,a_{H_2O} \quad (8)$$

$$m_{K,tot} = m_{K^+} + m_{KCl^\circ} + m_{KOH^\circ} \quad (9)$$

$$m_{Cl,tot} = m_{Cl^-} + m_{HCl^\circ} + m_{KCl^\circ} \quad (10)$$

$$m_{H,tot} = m_{H^+} + m_{HCl^\circ} \quad (11)$$

The seven unknowns are the molalities of K^+, H^+, OH^-, Cl^-, KCl°, HCl°, and KOH°. The activity of H_2O (see footnote 1) is a function (though a very insensitive one) of the molalities of those seven species, and it can be calculated by solving a system with the 7 equations above plus one similar to that of Wood (1975, eq. 14, p. 1150) which yields a_{H_2O} as a function of the molalities of individual aqueous species. (Wood's eq. 14 yields a_{H_2O} in terms of the stoichiometric molalities of neutral salts.) If we do this for all our runs a_{H_2O} comes out to be > 0.997, and therefore, to simplify matters, it has been set to 1.0 at any T, P.

In solving the system of equations we have calculated also (by iteration on the ionic strength) the individual-ion activity coefficients with the Stokes–Robinson equation modified by Helgeson (1969, eq. 43):

$$\log \gamma_i^*(T, P, \bar{I}) = \frac{-A(T, P)z_i^2\,\bar{I}^{1/2}}{1 + \mathring{a}_i(T)B(T, P)\bar{I}^{1/2}} + \dot{B}(T)\bar{I} \quad (12)$$

and the activity coefficients for neutral complexes with the equation (Helgeson, 1969, eq. 36):

$$\log \gamma^\circ\,(T, \bar{I}) = \sigma\bar{I} \quad (13)$$

where γ_i^* and γ° are the individual activity coefficients; $\mathring{a}_i$ and z_i the distance of closest approach and charge for each species; A, B the Debye-Hückel coefficients; $\bar{I}$ the true ionic strength; and $\dot{B}$ and σ coefficients dependent on T. The temperature and pressure dependence of γ_i^* are incorporated in the coefficients A and B which were calculated from the dielectric constant and density of H_2O at the P, T of interest (Helgeson and Kirkham, 1974, their eqs. 2 and 3). Values for $\dot{B}$ at vapor pressure were taken from Helgeson (1969) without a pressure correction. Values of σ (eq. 13) up to 300°C were obtained from the data in Helgeson (1969, Table 2); for higher-temperature experiments, the 300°C value was used, and no pressure correction was made for the experiments at 2 kbar. Errors introduced by these approximations are very small. Note in particular that the quantities $\dot{B}\bar{I}$ and $\sigma\bar{I}$ in eqs. 12 and 13 are very small, insofar as $\dot{B}$ and σ are multiplied by true ionic strengths of less than $10^{-2}m$—another minor advantage of performing quench equilibrium experiments in dilute chloride solutions.

The input needed to solve the system of equations consists of four dissociation constants (taken for each T, P of interest from Helgeson and Kirkham, 1976, p. 110–111) and the total molalities for Cl, K, and H. Chloride was assumed unchanged from the starting molality, and the last two total molalities were measured directly in the quench solution at the end of each run. We have not made the assumptions of Montoya and Hemley (1975), who took the total con-

centrations of potassium in the initial and final solutions to be equal (which ignores take-up or release of potassium by the minerals), or of Shade (1968) and Usdowski and Barnes (1972), who took the activities of K^+ and Cl^- to be equal (which is probably inaccurate on account of the differences in molalities and activity coefficients for the two ions).

The actual solving was performed by the subroutine ZSYSTM (of the International Mathematical and Statistical Library), which requires a set of initial guesses for all the unknowns. The output for each solution consists of the molalities, activities, and activity coefficients for each species in the solution, the true ionic strength, and an echo of all the constants and initial guesses used. Four-significant-figure solutions were remarkably stable, never requiring more than six iterations.

Calculated equilibrium constants

Equilibrium constants for reaction 1 were calculated using the thermodynamic properties of the solids from Helgeson *et al.* (1978), and the partial molal volumes, heat capacity T, P functions, and entropies of ions from Helgeson and Kirkham (1976). The values obtained are shown in Figures 2, 3, 4 and 6. The calculations were performed with the computer program SUPCRT described by Helgeson *et al.* (1978, p. 202) and kindly provided by them. We do not know the error of these calculated equilibrium constants, but the effect of replacing the thermodynamic properties of sanidine by those of microcline in these calculations is shown in Figures 4 and 6.

Results

Initial and final experimental concentrations and calculated equilibrium constants for all experiments are given in Tables 2 and 3. Table 2 summarizes the experiments conducted at 205°C and 17 bar vapor pressure for a variety of solid/fluid ratios. Figure 2 illustrates the relationship between solid/fluid ratio and the calculated log (a_{K^+}/a_{H^+}) ratio for these experiments. Table 3 summarizes the results of experiments conducted at 2 kbar. Experiments 1 through 24 were run at temperatures near 200°C, 2 kbar, and at various solid/fluid ratios, and their relationship is shown in Figure 3. Experiments 25–32 were conducted at various temperatures at a solid/fluid ratio of 1/16 (see below), and are summarized in Figure 4.

Discussion

Effect of solid/fluid ratio

A variety of trends are established by the series of experiments in which the solid/fluid ratio is variable. Figures 2 and 3 show that log (a_{K^+}/a_{H^+}) increases with solid/fluid ratio, and thus with surface area, for experiments whose initial solution compositions were in the muscovite field (*i.e.*, relatively acidic). The data in Tables 2 and 3 show that these trends are caused primarily by increases in the pH in the runs, and that smaller increases in pK tend to lower the effect of pH on the activity ratio. For the experiments whose starting solution compositions were in the sanidine field (*i.e.*, were relatively alkaline), (a_{K^+}/a_{H^+}) decreases with increasing solid/fluid ratio at 2 kbar, but follows no clear trend at 17 bar (Figs. 2 and 3). The 2 kbar results are also shown in Figure 5 to depict the relationship between the calculated pH and pK as the solid/fluid ratio varies. For experiments approaching equilibrium from the muscovite field the pH and pK generally vary linearly with a slope of ~1 and an intercept of pH ~4.8. For runs in which

Table 2. Results of 45-day experiments at 205°C and 17 bar (vapor pressure), and calculated values of log (a_{K^+}/a_{H^+}), $\gamma_{K^+}/\gamma_{H^+}$, and ionic strength

run #	log solid/fluid	Initial pK	Initial pH	Initial log m_K/m_H	Final (Quench) pK	Final (Quench) pH	Final (Quench) log (m_{K^+}/m_{H^+})	Calculated log (a_{K^+}/a_{H^+})	Calculated $\gamma_{K^+}/\gamma_{H^+}$	Calculated $\bar{I}^{-1} \times 10^4$
5	-2.72	2.00	4.05	2.05	2.05	5.70	3.65	3.60	0.975	87
6	-2.05	2.00	4.05	2.05	2.03	6.42	4.39	4.34	0.975	89
7	-0.99	2.00	4.05	2.05	1.96	6.22	4.26	4.21	0.973	96
8	-0.48	2.00	4.05	2.05	1.65	6.39	4.74	4.69	0.962	145
9	-2.60	2.00	9.21	7.21	2.05	5.96	3.91	3.86	0.975	87
10	-2.07	2.00	9.21	7.21	2.08	7.16	5.03	5.03	0.976	85
11	-1.00	2.00	9.21	7.21	1.97	6.15	4.18	4.13	0.973	94
12	-0.48	2.00	9.21	7.21	1.79	7.25	5.46	5.41	0.968	119
16	-1.75	2.00	10.02	8.02	1.92	5.57	3.65	3.60	0.972	100
17	-1.53	2.00	10.02	8.02	1.88	5.24	3.36	3.31	0.971	105

[1] *Molal units*

Table 3. Experimental results at 2 kbar total pressure, and calculated values of log (a_{K^+}/a_{H^+}), $\gamma_{K^+}/\gamma_{H^+}$, and ionic strength

run #	T°C	Run duration days	Log solid/fluid	Starting pK	Starting pH	Starting log (m_{K^+}/m_{H^+})	Final pK	Final pH	Final log (m_{K^+}/m_{H^+})	Calculated log (a_{K^+}/a_{H^+})	Calculated $(\gamma_{K^+}/\gamma_{H^+})$	Calculated $\bar{I}^5 \times 10^4$
1[1]	189 ± 5	55	-2.98	2.00	4.05	2.05	1.97	6.40	4.43	4.33	0.981	83
2	195 ± 2	55	-2.06	2.00	4.05	2.05	2.07	6.95	4.88	4.77	0.982	78
3	195 ± 2	55	-1.01	2.00	4.05	2.05	2.12	6.95	4.83	4.72	0.983	85
4	197 ± 3	55	-0.48	2.00	4.05	2.05	2.28	7.28	5.12	4.88	0.983	71
13	192 ± 3	42	-1.92	2.00	3.09	1.09	2.00	6.78	4.78	4.68	0.982	82
14	192 ± 3	42	-1.51	2.00	3.09	1.09	1.90	6.73	4.83	4.73	0.980	91
15	192 ± 4	45	-1.20	2.00	3.09	1.09	1.77	6.72	4.95	4.86	0.977	107
19[2]	200 ± 4	47	-2.67	2.00	10.02	8.02	2.00	8.46	6.46	6.33	0.965	179
20	209 ± 5	27	-1.92	2.00	10.02	8.02	2.00	7.51	5.51	5.40	0.979	91
21	199 ± 2	46	-1.58	2.00	10.02	8.02	1.98	7.60	5.62	5.51	0.979	94
22	201 ± 3	42	-1.31	2.00	10.02	8.02	1.82	7.08	5.26	5.16	0.977	102
23	203 ± 4	27	-0.96	2.00	9.75	7.75	1.72	6.46	4.74	4.65	0.975	114
24	201 ± 3	42	-0.48	2.00	10.02	8.02	1.38	5.28	3.90	3.83	0.960	209
25	262 ± 4	20	-1.22	2.00	3.08	1.08	1.89	6.48	4.59	4.47	0.976	90
26	362 ± 10	27	-1.20	2.00	3.24	1.24	1.72	6.58	4.80	4.67	0.968	96
27	476 ± 10	20	-1.24	2.00	3.08	1.08	1.92	5.96	4.04	3.87	0.969	63
28[3,4]	612 ± 4	20	-1.20	2.00	3.08	1.08	1.89	4.57	2.68	3.20	0.972	41
29	260 ± 6	20	-1.22	2.00	9.21	7.21	2.00	6.78	4.72	4.66	0.978	82
30	356 ± 3	20	-1.22	2.00	9.21	7.21	2.09	6.67	4.58	4.36	0.977	66
31	486 ± 2	20	-1.22	2.00	9.21	7.21	1.96	6.12	4.16	3.99	0.969	61
32[3]	623 ± 2	21	-1.24	2.00	9.21	7.21	1.94	4.61	2.67	3.20	0.974	38

[1] *No solid products present*
[2] *Too little solid products to allow x-ray analysis*
[3] *Solid products include a peak at 14 Å (= Al-montmorillonite?)*
[4] *No sanidine in run products*
[5] *Molal units*

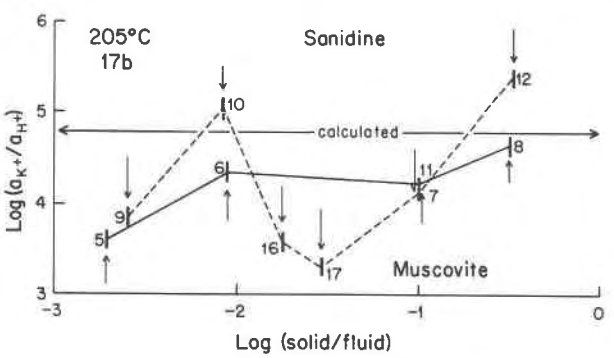

Fig. 2. Variation of log (a_{K^+}/a_{H^+}) with log (solid/fluid mass ratio) at 17 bar and 205°C. Each run is represented by a short vertical bar. The arrows show the direction of approach to equilibrium, and each number identifies a run in Table 2. Arrows pointing up and joined by the solid line refer to experiments in which the starting solution had a low a_{K^+}/a_{H^+} ratio, which is equivalent to saying that the solution was acid and that it was initially in the muscovite field. Arrows pointing down and joined by the dashed line refer to runs in which the starting solution had a high a_{K^+}/a_{H^+} (*i.e.*, a starting solution that was alkaline and in the sanidine field). The a_{K^+}/a_{H^+} for each run was calculated from quench measurements *via* the speciation of the final solution. The horizontal line at log $(a_{K^+}/a_{H^+}) \sim 4.8$ indicates the equilibrium constant for reaction 1 calculated from thermodynamic data in Helgeson *et al.* (1978) and Helgeson and Kirkham (1976).

equilibrium was approached from initially alkaline solutions a very steep trend is obtained in which the increase in a_{H^+} is much larger than that in a_{K^+}.

Surface reactions

Surface reactions like 3 and 4 could, in principle, affect the quench pH and produce the trends of Figures 3 and 4 if their exchange constants changed with temperature and pressure. However, these constants may either increase or decrease with temperature and thus only one trend at most could be explained by surface exchange. For example, if the exchange constants decreased, and especially if they become less than 1 at high P and T, these surfaces would begin to adsorb K^+ and desorb H^+. During the quench K^+ would be desorbed and H^+ adsorbed, causing m_{K^+}/m_{H^+} ratio to increase in the quench solution. This increase would be greater the greater the surface area, and could produce the trend established by the acid approach experiments of Figures 2 and 3. If, on the other hand, the exchange constants increased with increasing T and P, then the opposite pattern of surface exchange (*i.e.*, that obtained in the alkaline approach experiments, Fig. 3) would take place.

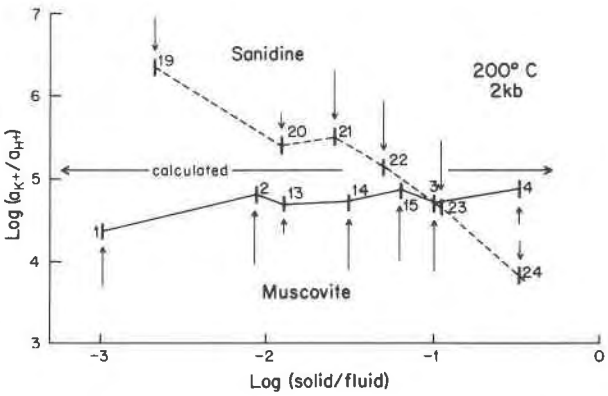

Fig. 3. Variation of log (a_{K^+}/a_{H^+}) *vs.* log (solid/fluid mass ratio) for reaction 1 at 200°C and 2 kbar total pressure. The horizontal line indicates the equilibrium constant for reaction 1 calculated from thermodynamic data—see caption to Fig. 2 for more details.

Which trend (if either) is more likely to be caused by surface reactions is determined by how and how much the exchange constants vary with changes in temperature and pressure. Considerations based on estimates of ΔS_r and ΔV_r for reactions 3 and 4 point to increasing exchange equilibrium constants, K_{ex}, with increasing temperature, and therefore only the trend of decreasing m_{K^+}/m_{H^+} with increasing solid/fluid (Fig. 3) could, in principle, be explained by surface adsorption. The experimental results of Dugger *et al.* (1964) for the surface exchange gel–SiOK + H^+_{aq} = gel–SiOH + K^+_{aq} tend to confirm the above prediction of increasing K_{ex} with increasing T. Actual values for K_{ex} of reactions 3 and 4 are only available at low temperatures. At 25°C and 1 bar, $K_3 = 10^{7.4}$ and $K_4 = 10^{9.5}$ (Garrels and Howard, 1959). The only high T–P data bearing on the problem are those of Currie (1968), who measured the solubility of albite in pure H_2O at 400–600°C and 0.75–3.5 kbar. He showed that Na/Al in the experimental solutions was always higher than in albite, and that the pH of the final solutions varied between 9.64 and 10.63, depending on the experimental conditions. The high Na^+_{aq} and low H^+_{aq} content of the experimental solutions imply that at these large temperature–pressure conditions H^+ was strongly preferred to Na^+ on the feldspar surface. Hydrolysis of ions released by congruent dissolution of the albite also changes the pH, but not by several pH units, as in Currie's experiments. Thus all the experimental evidence, though scant, suggests that these silicate surfaces strongly prefer H^+ to K^+ (or Na^+) over a wide range of temperatures and pressures.

Given, therefore, that the K_{ex}'s for surface exchange reactions 3 and 4 are $\gg 1$ at both low and high temperatures, how much would surface exchange reactions change the m_{H^+} upon quench? Order-of-magnitude calculations of such an effect yield changes in the m_{H^+} in solution of $\sim 10^{-13}$ moles/liter for the lowest solid/fluid ratio and $\sim 10^{-10}$ moles/liter for the highest solid/fluid ratio, even allowing the high-temperature K_{ex} to increase or decrease by three orders of magnitude with respect to its value at low temperature. [The calculations involved averages of particle size and surface charge density, the actual masses of the solids and fluid in our experiments (Tables 2 and 3), and the actual experimental water compositions.] Because these quantities (10^{-13}–10^{-10} mole H^+/liter) are so much smaller than the actual pH changes measured (up to three pH units, see alkaline trend, Fig. 3), it can safely be concluded that neither of the quench pH trends of Figure 3, not even the trend established by the alkaline approach experiments, can result from the surface reactions.

Approach to equilibrium

The approach of these experiments to equilibrium can only be assessed by the degree of approach of

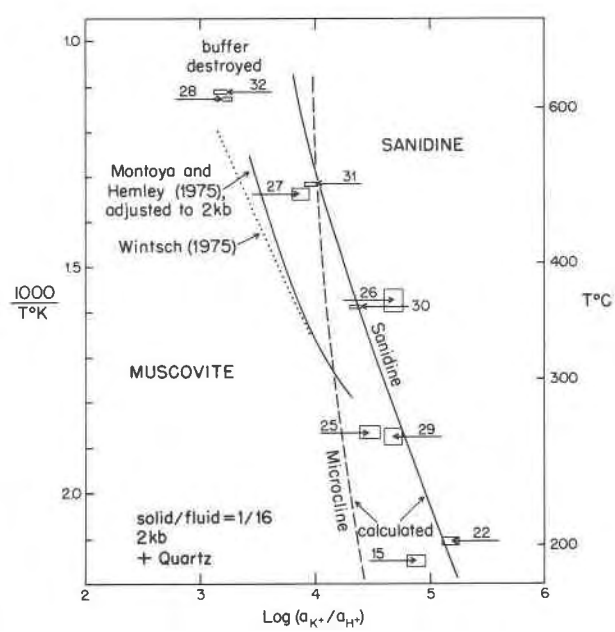

Fig. 4. The variation with temperature of the log (a_{K^+}/a_{H^+}) calculated (*via* the speciation) from experiments conducted at 2 kbar in 10^{-2} molal Cl^- solutions at a solid/fluid ratio of 1/16. Boxes give uncertainty limits, and arrows indicate the direction of approach to equilibrium (see caption to Fig. 2). The solid curve was independently calculated from thermodynamic data for minerals and aqueous species in Helgeson *et al.* (1978), Helgeson and Kirkham (1976), and Walther and Helgeson (1977).

a_{K^+}/a_{H^+} ratios at similar solid/fluid ratios. The systematic trends of Figure 3 show that the closest approach to equilibrium of initially very different starting solutions is obtained at a solid/fluid ratio of $\sim 10^{-1.2} = 1/16$. The experiments at 17 bar (Fig. 2) suggest an optimum solid/fluid ratio of ~1/10, but because they are more erratic than those at 2 kbar, 1/16 appears to be the most favorable solid/fluid ratio to approach equilibrium most closely.

Higher-temperature experiments

Experiments investigating reaction 1 have been conducted at ~260, 360, 480, and 620°C at 2 kbar, and at a solid/fluid ratio of 1/16. Figure 4 shows that all experiments between 200° and 500°C except #26 form tight reversals of reaction 1. Comparison of these reversals with the calculated equilibrium constant *vs.* temperature curve shows good agreement between the two. Two experiments (28 and 32) above 600°C on Figure 4 fall to the left of the calculated line but very close to each other. In each case a 14Å phase (aluminum montmorillonite?) was produced, destroying the buffer assemblage of reaction 1. Thus these two points should not plot with the lower-temperature results because a different assemblage buffers these experiments. These two experiments are nevertheless compatible with what is known about this chemical and mineralogical system, because all theoretically calculated equilibrium constants for muscovite–aluminosilicate lie to the left of the muscovite–sanidine line. The convergence of the solution compositions of these two runs suggests that a close approach to (probably metastable) equilibrium has been achieved. Thus these 600°C results further support the reliability of the rapid-quench technique, because they yield solution compositions in general agreement with theoretical prediction and because they are closely reversed.

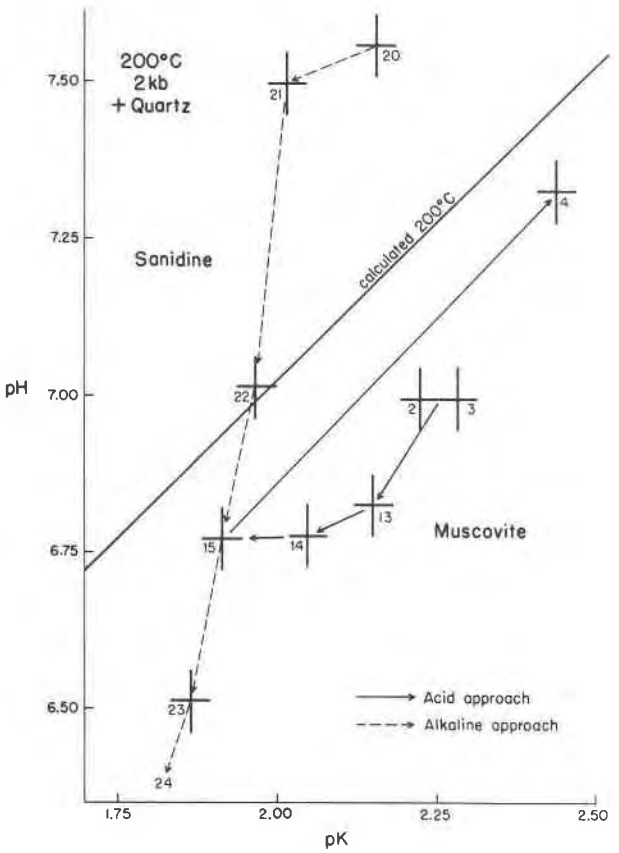

Fig. 5. Calculated ($-\log a_{H^+}$) *vs.* calculated ($-\log a_{K^+}$) for experiments conducted near 200°C at 2 kbar. The crosses indicate the uncertainties in the activities. The equilibrium constant calculated from thermodynamic data for minerals and aqueous species at 200°C is given by the slope of the solid line. See caption to Fig. 2 for more details.

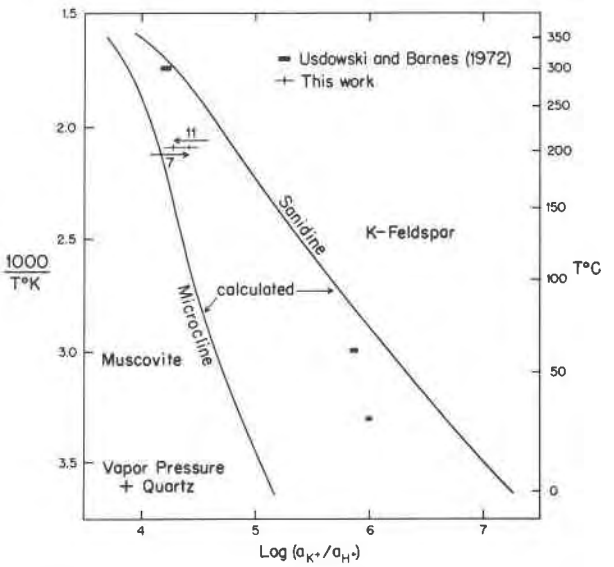

Fig. 6. The variation with temperature of the log (a_{K^+}/a_{H^+}) calculated from experiments of this study and from Usdowski and Barnes (1972). The equilibrium constants calculated theoretically for reaction 1 using alternatively microcline and sanidine are included for comparison.

Comparison with other work

Our results at 200°C and 17 bar are compared in Figure 6 to the work of Usdowski and Barnes (1972) and to the calculated equilibrium constants for microcline and sanidine. In view of the different experimental techniques and starting materials used in these two experimental studies, the results are in re-

markable agreement with each other. Also, the experimental data are in reasonable agreement with the calculated curves.

Higher-pressure experiments have been conducted on reaction 1 by Hemley (1959), Shade (1968, 1974), Gunter (1974), and Wintsch (1975). Most of these results are difficult to compare with the present study because the experiments were conducted at different pressures or chlorinities from those reported here. The study of Wintsch (1975) includes five experiments run at 2 kbar in 10^{-2} molal solutions. This curve lies at activity ratios approximately 0.4 log units smaller than the results reported here. These experiments involved solid/fluid ratios of between 1/30 and 1/60, and the data in Table 3 show that half of the discrepancy between the two experimental studies could be a consequence of this smaller solid/fluid ratio. The error in the activity ratio of these experiments is ±0.2 log units. Thus within the uncertainty of the data, the results of this study and of Wintsch (1975) are in agreement.

It is difficult to compare the calculated activity ratios of Shade (1968, 1974) and Montoya and Hemley (1975) with our calculations, because the former studies do not include the computation of activity coefficients, the calculations of Shade (1968, 1974) involve the simplifying assumption that $a_{K^+} = a_{Cl^-}$, which is not strictly valid, and the calculations of Montoya and Hemley (1975) are for 1 kbar. We have, however, adjusted the activity ratios of Montoya and Hemley to 2 kbar. The corrected ratios are included in Figure 4 for comparison. In view of the different methods involved in these calculations, they are in reasonable agreement.

The data in Figure 4 are thus significant because the equilibrium constant for reaction 1 at 2 kbar as a function of temperature has been obtained by a variety of methods that yield similar results. Within the limits of the errors involved, the equilibrium constants calculated from Hemley's (1959) experiments at 1 kbar in 2-molar solutions are indistinguishable from those calculated in this study from experiments at 2 kbar in 10^{-2} molal solutions. Both of these results agree with the equilibrium constants calculated from the thermodynamic data of Helgeson *et al.* (1978) which were, in turn, calculated from other experimental studies involving the synthetic minerals of reaction 1. We conclude, therefore, that the thermodynamic properties of synthetic muscovite, sanidine, and quartz are uniform from laboratory to laboratory.

Conclusions

From the data summarized in Figures 2 and 3 it appears that surface reactions do not affect quench pH in dilute solutions. Although we have no explanation for the observed trends of pK and pH *vs.* the solid/fluid ratio, they suggest that the narrowest reversals are obtained at solid/fluid ratios of 1/16. Significantly, these narrowest reversals are also the ones closest to the calculated log K.

We recommend that the aqueous concentrations of all elements be measured after quench for two reasons: to better monitor the approach to equilibrium of the solutions with the whole assemblage, and to allow for a more thorough calculation of the speciation of the final solution (in this case the addition of silica and aluminum species).

The agreement of our equilibrium constants, determined from experiments in dilute solutions, with the constants determined by others from experiments in concentrated solutions, and with constants calculated from an internally-consistent set of thermodynamic properties is remarkable. Clearly, accurate high-temperature/high-pressure solid–fluid equilibrium data can be obtained from experiments involving dilute chloride solutions.

Acknowledgments

It is a pleasure to thank H. C. Helgeson and G. C. Flowers of the University of California at Berkeley for their prompt and enlightening answers to many queries and for the computer program SUPCRT. We also thank E. Inouye, C. Moore, and B. Ransom for assistance in the laboratory, W. Moran and B. Moore for drafting, and T. F. Brown and S. Douthitt for typing. We acknowledge the support of the National Science Foundation (grant EAR 76-22560), of the Indiana University Foundation, and of the Indiana Geological Survey. The IMSL subroutines are a proprietary package of the International and Statistical Libraries. We acknowledge computer time given by Indiana University's Wrubel Computing Center, which also obtained the routines.

References

Burnham, C. W. (1962) Lattice constant refinement. *Carnegie Inst. Wash. Year Book, 61,* 132–135.

Currie, K. L. (1968) On the solubility of albite in supercritical water in the range 400 to 600°C and 750 to 3500 bars. *Am. J. Sci., 266,* 321–341.

Dugger, D. L., J. H. Stanton, B. N. Irby, B. L. McConnell, W. W. Cummings and R. W. Maatman (1964) The exchange of twenty metal ions with the weakly acidic silanol group of silica gel. *J. Phys. Chem., 68,* 757–760.

Garrels, R. M. and P. Howard (1959) Reactions of feldspar and mica with water at low temperature and pressure. In A. Swineford, Ed., *Clays and Clay Minerals,* p. 68–88. Pergamon Press, New York.

Gunter, W. D. (1974) *An experimental study of mineral-solution*

equilibria applicable to metamorphic rocks. Ph.D. Thesis, The Johns Hopkins University, Baltimore, Maryland.

Helgeson, H. C. (1969) Thermodynamics of hydrothermal systems at elevated temperatures and pressures. *Am. J. Sci., 267,* 729–804.

——— and D. H. Kirkham (1974) Theoretical prediction of the thermodynamic behavior of aqueous electrolytes at high pressures and temperatures: II. Debye-Hückel parameters for activity coefficients and relative partial molal properties. *Am. J. Sci., 274,* 1199–1261.

——— and ——— (1976) Theoretical prediction of the thermodynamic behavior of aqueous electrolytes at high pressures and temperatures: III. Equation of state for aqueous species at infinite dilution. *Am. J. Sci., 276,* 97–240.

———, J. M. Delany, H. W. Nesbitt and D. K. Bird (1978) Summary and critique of the thermodynamic properties of rock-forming minerals. *Am. J. Sci., 278-A,* 1–229.

Hemley, J. J. (1959) Some mineralogical equilibria in the system K_2O–Al_2O_3–SiO_2H_2O. *Am. J. Sci., 257,* 241–270.

Montoya, J. W. and J. J. Hemley (1975) Activity relations and stabilities in alkali feldspar and mica alteration reactions. *Econ. Geol., 70,* 577–583.

Rudert, V., I-M. Chou and H. P. Eugster (1976) Temperature gradients in rapid-quench cold-seal pressure vessels. *Am. Mineral., 61,* 1012–1015.

Shade, J. W. (1968) *Hydrolysis Equilibria in the System K_2O-Al_2O_3-SiO_2-H_2O.* Ph.D. Thesis, The Pennsylvania State University, University Park, Pennsylvania.

——— (1974) Hydrolysis reactions in the SiO_2-excess portion of the system K_2O–Al_2O_3–SiO_2–H_2O in chloride fluids at magmatic conditions. *Econ. Geol., 69,* 218–228.

Usdowski, H. E. and H. L. Barnes (1972) Untersuchungen über das Gleichgewicht zwischen K-Feldspat, Quarz und Muskovit und die Anwendung auf Fragen der Gesteinsbildung bei tieferen Temperaturen. *Contrib. Mineral. Petrol., 36,* 207–219.

Walther, J. V. and H. C. Helgeson (1977) Calculation of the thermodynamic properties of aqueous silica and the solubility of quartz and its polymorphs at high pressures and temperatures. *Am. J. Sci., 277,* 1315–1351.

Wintsch, R. P. (1975) Muscovite, sanidine, sillimanite, quartz and H_2O equilibria as a function of chloride concentration (abstr.). *EOS, 56,* 465–466.

Wood, J. R. (1975) Thermodynamics of brine–salt equilibria—I. The systems NaCl–KCl–$MgCl_2$–$CaCl_2$–H_2O and NaCl–$MgSO_4H_2O$ at 25°C. *Geochim. Cosmochim. Acta, 39,* 1147–1163.

Wright, T. L. and D. B. Stewart (1968) X-ray and optical study of alkali feldspar. I. Determination of composition and structural state from refined unit-cell parameters and 2*V*. *Am. Mineral., 53,* 38–87.

Manuscript received, September 17, 1979;
accepted for publication, January 30, 1980.

American Mineralogist, Volume 65, pages 1012–1019, 1980

Crystallization of mordenite from aqueous solutions

SATORU UEDA, HIROSHI MURATA, MITSUE KOIZUMI

Institute of Scientific and Industrial Research
Osaka University, Yamadakami, Suita, Osaka 565, Japan

AND HIROSHI NISHIMURA

College of General Education, Osaka University
Toyonaka, Osaka 560, Japan

Abstract

Mordenite was formed directly at 100°C, 1 atm from clear aqueous Na–Al–Si solutions containing an extremely small quantity of Al. In seeded and unseeded systems, mordenite crystals up to 4μm × 2μm with acicular or prismatic habit were grown. They were elongated along the *c* axis of the orthorhombic cell with the prism zone formed predominantly by the (110) plane.

In the seeded systems, rapid crystallization of mordenite occurred because the seed surface provided nucleation sites. Mordenite grew on the seed surfaces, whether or not the morphology and the composition and structure of the seed differed widely from mordenite. Such growth phenomena were different from those observed with analcime grown in seed systems.

The chemical composition of mordenite was governed by the initial ratios of soda, alumina, and silica in the initial gels and was independent of the depletion of nutrient with reaction time.

These results probably can be explained by the crystallization mechanism for analcime proposed by Ueda and Koizumi (1979).

Introduction

Most zeolites have been synthesized from active alkaline aluminosilicate gels consisting of heterogeneous phases in which amorphous solid and aqueous solutions coexist. The amorphous material decreases as the crystallization of zeolite proceeds, and consequently two solid phases, amorphous solid and crystalline material, coexist with solution until the reaction is completed. The crystallization mechanism in such heterogeneous phases is complicated and is not yet fully understood, but both the nature of the nutrient solid gel and the aqueous solution contribute directly to the zeolite formation.

Two hypotheses have been proposed for zeolite crystallization, namely, in the gel phase or from the solution phase. The former was postulated by Breck and Flanigen (1968), and later by McNicol *et al.* (1971, 1972), and Aiello *et al.* (1971a,b), and the latter was proposed by Kerr (1966, 1968), and later by Ciric (1968), Culfaz and Sand (1973), Cournoyer *et al.* (1975), and Ueda and Koizumi (1979).

In 1979 we reported that analcime, hydroxysodalite, and zeolite B crystallized from clear aqueous solutions. In the present study, the crystallization of mordenite from a low-Al solution phase in the Na_2O–Al_2O_3–SiO_2–H_2O system was investigated at 1 atm.

Barrer (1948) first synthesized mordenite, and there are many studies of its mineralogy, geology and chemistry: Barrer and White (1952), Sand *et al.* (1957, 1971), Ames and Sand (1958), Coombs *et al.* (1959), Ellis (1960), Ames (1963), Domine and Quobex (1968), Sand (1968), Senderov (1968), Kranich *et al.* (1971), Senderov and Khitarov (1971), Whittemore (1972), Culfaz and Sand (1973), and Nakajima (1973). Mordenite syntheses were made under hydrothermal conditions in various types of high-pressure reaction vessels.

In our experiments, the following problems were examined: (1) the effect of added seed crystals on the crystallization and morphology of synthesized mordenite, (2) the selectivity of seed materials for morde-

0003–004X/80/0910–1012$02.00

Table 1. Variation of SiO_2/Al_2O_3 ratios of synthetic mordenites in seeded systems

Sp. nos.	Run (days)	Seed (g/l)	Wt. % of seed(*1)	Apparent ratios(*2)	Corrected ratios(*3)
821	2	0.4	11.48	14.35	15.00
822	4	0.4	4.98	14.74	15.03
823	6	0.4	2.99	14.89	15.06
824	8	0.4	2.61	14.96	15.11
831	2	0.6	14.14	14.26	15.07
832	4	0.6	6.53	14.60	14.97
833	6	0.6	4.51	14.75	15.01
834	8	0.6	3.98	14.84	15.07
861	2	1.2	18.49	14.05	15.12
862	4	1.2	9.64	14.47	15.02
863	6	1.2	6.55	14.64	15.01
864	8	1.2	5.80	14.67	15.00

The SiO_2/Al_2O_3 ratio of natural mordenite used as seed was 9.32. Initial composition of gels corresponds to C2. (*1) weight % of seed in crystal aggregates, (*2) SiO_2/Al_2O_3 ratios of crystal aggregates, and (*3) the ratios calculated using the data of columns 4 and 5.

nite crystallization, and (3) the effect of reaction time and amount of added seed on the SiO_2/Al_2O_3 ratio of synthesized mordenite.

Experimental

Gels with three fixed batch compositions (C1) $10Na_2O{\cdot}0.1Al_2O_3{\cdot}34SiO_2{\cdot}440H_2O$, (C2) $10Na_2O{\cdot}0.15Al_2O_3{\cdot}36SiO_2{\cdot}440H_2O$, and (C3) $10Na_2O{\cdot}0.15Al_2O_3{\cdot}32SiO_2{\cdot}440H_2O$ were prepared from a 10M solution of sodium hydroxide (90.0 volume percent H_2O), sodium aluminate (35.05 weight percent Na_2O and 42.36 weight percent Al_2O_3), aqueous colloidal silica sol (0.3687g/ml SiO_2 and 83.5 volume percent H_2O), and distilled water. The total volume of each gel was adjusted to 250 ml in a 500 ml polypropylene bottle, which was used as a reaction vessel.

After the preparation of gels, milky turbidity was observed, which disappeared within 3 hrs by stirring and heating at 100°C in a water bath. Crystallization was observed in the clear solution systems after 30 hrs or longer at 100°C. Runs ranged in duration from 2 to 25 days.

In seeded systems, natural mordenite and quartz, synthesized mordenite, analcime, hydroxysodalite, and calcium carbonate were added to gels as seeds. The natural minerals were first ground to minus 200 mesh. After each run, the product was separated from the solution through a teflon microfilter, and washed thoroughly with hot water. The residue was dried at 110°C for 48 hrs, exposed to saturated water vapor at 25°C in a desiccator, weighed, and analyzed by X-ray powder diffraction (Cu$K\alpha$ radiation), optical microscopy, scanning electron microscopy (SEM), and DTA. Chemical analysis was made on several samples by gravimetric methods. The results are given in Table 1.

Results and discussion

Crystallization of mordenite

The crystallization of mordenite was characterized by a long induction period followed by a slow initial crystallization. In Figure 1, the amounts of mordenite synthesized from clear solutions of the batch compositions C1, C2, and C3 are plotted as a function of reaction time. The induction period was reduced as the initial SiO_2/Al_2O_3 ratio of gels increased.

Analcime, in addition to mordenite, appeared initially as a minor phase but increased with reaction time. The quantity of analcime was determined by an intensity ratio of X-ray diffraction peaks using a calibration curve.

The values on the longitudinal axis in Figure 1 indicate the absolute amounts of products per liter of gel. A relative indication such as weight percent was not used because accurate compositions of synthesized mordenite and analcime could not be determined.

As shown in Figure 2(a,b), acicular or prismatic crystals correspond to mordenite, and the spherical crystals are analcime. Electron diffraction analysis of the mordenite crystals showed that elongation of a crystal is parallel to the *c* axis of the orthorhombic cell, and the prism zone is formed by (100), (010), and (110) planes. As crystals grew, the (110) plane

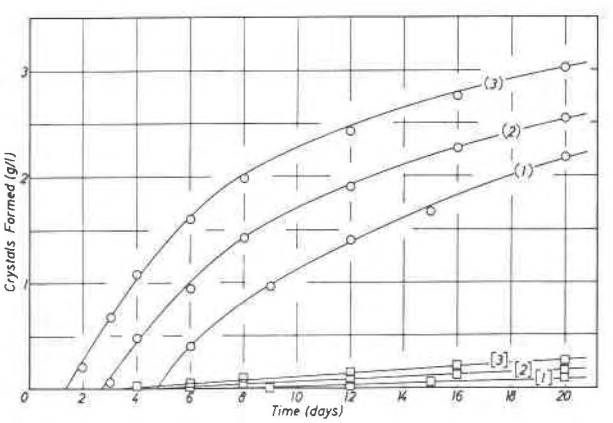

Fig. 1. Variation of the amounts of crystals formed from clear aqueous solutions as a function of time. Symbols for mordenite and analcime are circles and squares, respectively. Batch compositions of gels for curves 1, 2, and 3 correspond to C1, C2, and C3, respectively.

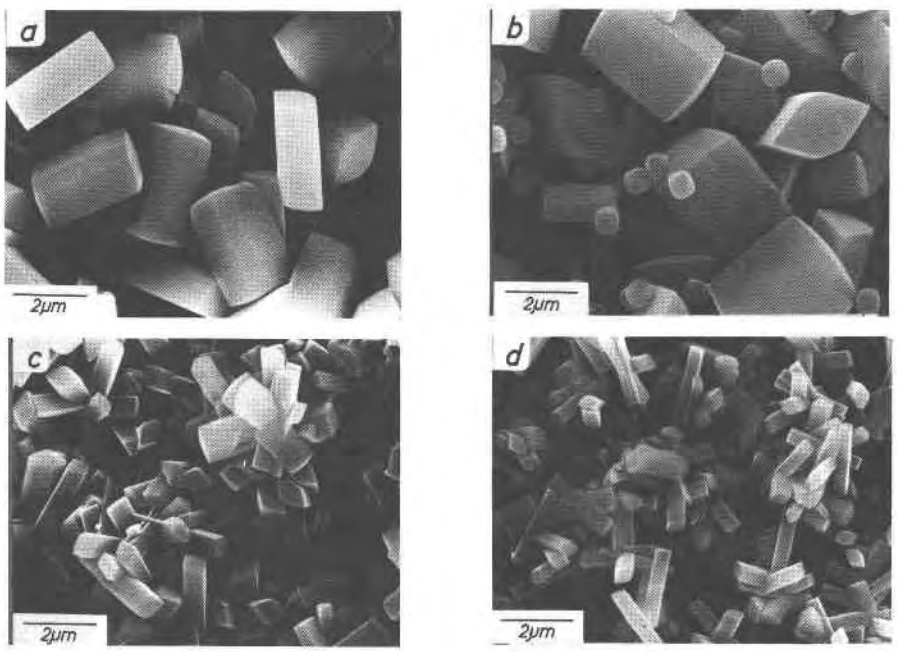

Fig. 2. SEM photographs of mordenite and analcime crystals: a and b: unseeded systems; c and d: seeded systems. Acicular or prismatic crystals are mordenite, and spherical ones are analcime. Batch compositions of gels are C2 for a, c, and d, and C3 for b. The weights of natural mordenite seed added to gels for c and d were 0.2g and 1.2g per liter of gel, respectively. Runs were 8 days for all cases.

became predominant, but the prism zone of the larger crystals increasingly deviated from the (110) plane. There was no regularity for such deviation even in the crystals produced from the same solution phase.

Effect of seeds

Mordenite crystals from Shiroishi, Miyagi, Japan, were added to prepared gels with batch compositions C1, C2, and C3 (0.1 to 1.2g per liter of gel). In Figure 3, the weight of mordenite obtained in a constant time is plotted as a function of weight of seed crystals; the plotted values do not contain the weight of seed.

The suspension of seed crystals in solutions resulted in rapid crystallization, and the addition below 0.2g/liter was particularly effective. Mordenite crystallized and grew rapidly on seed surfaces. The crystals became smaller in size and larger in number with an increase of the quantity of seed, as represented in Figure 2(c,d). Analcime could no longer be observed in the products. Probably the mordenite crystallization was so fast that the nucleation of analcime was hindered.

Synthesized mordenite with a uniform size (1 to 3μm), previously prepared from gels of batch composition C2, was added to freshly prepared gels of batch composition C3. In Figure 4, the amount of mordenite formed with a constant weight of synthetic seed is plotted as a function of time. As can be seen in Figure 4, curves 1 and 2 shift upward beyond curve N for an unseeded system. However, the synthetic seed is less effective in promoting crystallization than the natural mordenite seed shown in Figure 3. This indicates that shape and size of seed have an effect on crystallization, because a larger euhedral crystal provides a smaller total surface area for nucleation.

These results agree with those of Culfaz and Sand (1973), who investigated extensively the nucleation and crystallization of mordenite from heterogeneous gels. They concluded that, in the unseeded system, the rate-determining step in the overall process is nucleation, and in the seeded system the diffusion of soluble species, which are readily available at the crystal–liquid interface, is the rate-limiting step.

Selectivity of seeds

Synthesized analcime (12 to 14μm) and calcium carbonate (below 1μm) were used as seed for the growth experiment of mordenite. The results are represented in Figure 4, and show that these substances played a significant role in seeding for mordenite crystallization, because curves 3 to 6 in Figure 4 shift upward beyond curve N for the unseeded system.

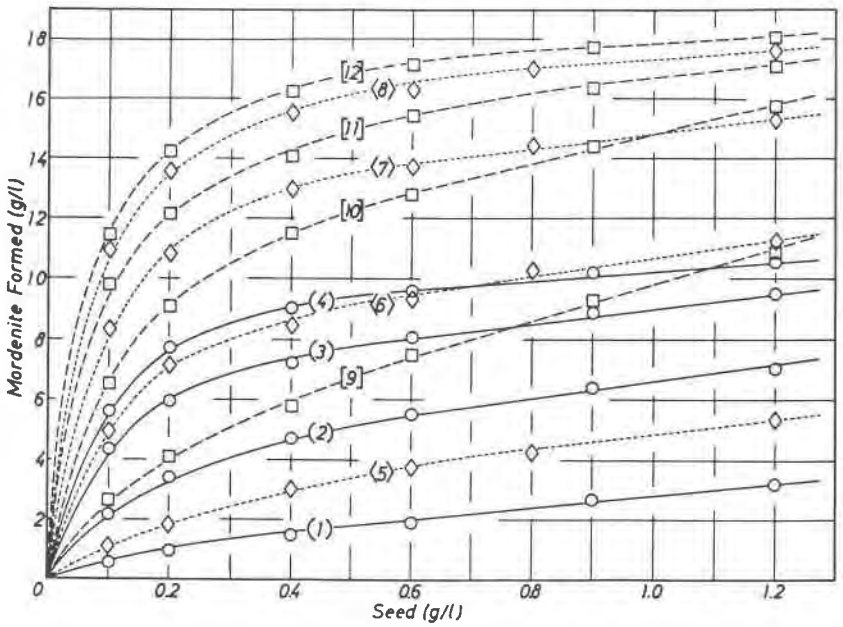

Fig. 3. Variation of the amounts of mordenite formed in natural mordenite seed system as a function of weight of seed. Batch compositions of gels are C1 for circles, C2 for diamonds, and C3 for squares. Runs were 2 days for curves 1, 5, and 9; 4 days for curves 2, 6, and 10; 6 days for curves 3, 7, and 11; and 8 days for curves 4, 8, and 12.

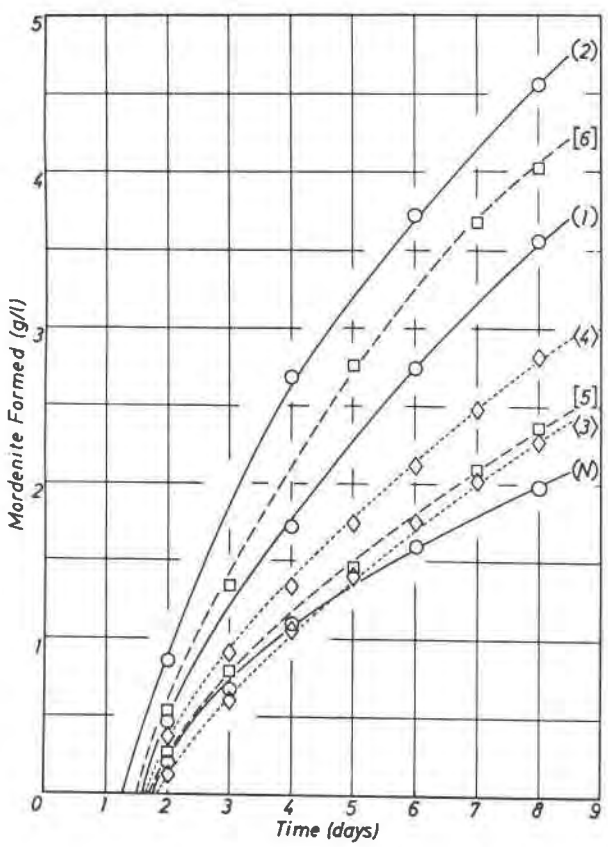

SEM photographs of the mordenite crystals grown on the surface of analcime crystals are shown in Figure 5(a,b), but no regularity of the growth habit which depends on the morphological features of analcime could be found. Although the crystal structure and composition of mordenite differ widely from the seeds, the latter surfaces are able to provide the nucleation sites for the mordenite crystallization.

On the other hand, whereas analcime also crystallized from the unseeded solution phase, in seeded systems its crystallization and growth were remarkably different from those of mordenite. With synthetic analcime (12 to 14μm), synthetic hydroxysodalite (3 to 4μm), and natural mordenite as seed, the growth experiment of analcime was carried out in clear solutions with the composition $10Na_2O{\cdot}0.075$

Fig. 4. Variation of the amounts of mordenite formed in three kinds of seeded systems as a function of time. (i) Synthetic mordenite seed for solid lines 1 and 2; (ii) synthetic analcime seed for dashed lines 3 and 4; and (iii) calcium carbonate seed for broken lines 5 and 6. However, curve N illustrates the results in unseeded systems, and corresponds to curve (3) in Fig. 1. The weight of seeds added were 0.2g per liter of gel for curves 1, 3, and 5, and 0.4g for curves 2, 4, and 6. In all cases, gels with batch composition C3 were used.

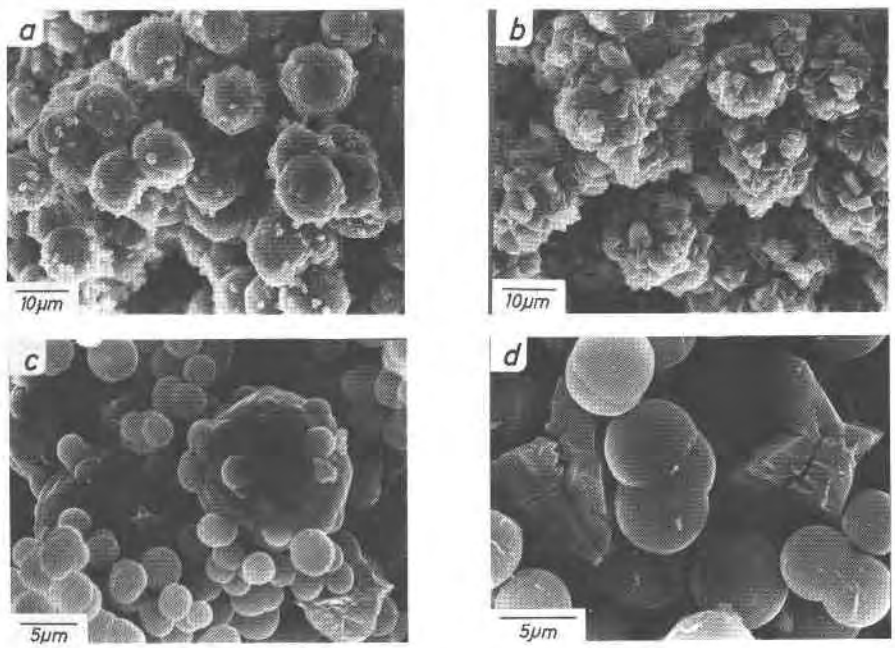

Fig. 5. SEM photographs of mordenite and analcime crystals formed in seeded systems: a and b illustrate prismatic mordenite crystals grown on the surface of analcime seed in the solution of batch composition C3; runs were 2 days for a and 4 days for b. c and d show spherical analcime crystals formed in synthetic analcime and natural mordenite seed systems, respectively. For c and d, the initial composition of gels used was $10Na_2O \cdot 0.075Al_2O_3 \cdot 10SiO_2 \cdot 370H_2O$; runs were 2 days for c and 4 days for d. In the case of c, the growth of seed (large particles) is observed. The weight of seeds added was 0.4g per liter of gel in all cases.

$Al_2O_3 \cdot 10SiO_2 \cdot 370H_2O$, which was an optimum composition for the synthesis of analcime.

In Figure 6, the amounts of analcime formed with a constant weight of seed are plotted as a function of time. Seeds other than analcime proved to be inert in the crystallization of analcime, because the observed values except for curves 1 and 2 in Figure 6 deviate downward from curve N for the unseeded system. From the fact that the deviation from curve N, especially in an early stage of reaction, increases with increasing weight of the inert seeds, we conclude that they interfered with the diffusion of soluble species of analcime in crystal–solution interface.

These results can be also explained using the SEM photographs shown in Figure 5. In analcime seeded systems (5c), large crystals are grown from seed, and small ones are newly-formed analcime. However, in the case of the natural mordenite seed system (5d), no definitive correlation between the formed crystals and the topology of seed surfaces is observed.

These results demonstrate the selectivity of seeds to crystallization and growth of analcime or mordenite, as follows. Analcime is spherical in shape at an early stage of crystal growth, and preserves a cubic trapezohedral crystal form. Accordingly, growth on the surface of seed crystals is difficult unless the seed is isostructural to analcime. On the contrary, mordenite is acicular or prismatic, and tends to elongate parallel to the *c* axis; in addition, the prism zone is not always formed by a definite plane such as the (110) plane. As the growth direction is more random, as represented in Figure 5(a,b), the topology of the seed surface is not a critical factor in the nucleation, crystallization, and growth of mordenite crystals.

Compositions of mordenites

The composition of synthetic mordenite is characterized by the SiO_2/Al_2O_3 ratio, which varies over a relatively narrow range according to the conditions of synthesis. In most cases, the ratio varies between 9 and 10 for an ideal composition (Barrer and White, 1952; Nakajima, 1973). In some mordenites prepared by special methods, however, a ratio higher than 10 has been reported (Sand, 1968; Kranich *et al.,* 1971; Whittemore, 1972).

In our study, the accurate compositions of mordenites obtained in both seeded and unseeded systems were not determined directly, because the added seed in the seeded systems and the analcime phase in the unseeded systems were coexistent in the products.

However, in the natural mordenite seeded systems comparatively good results were obtained, as a large

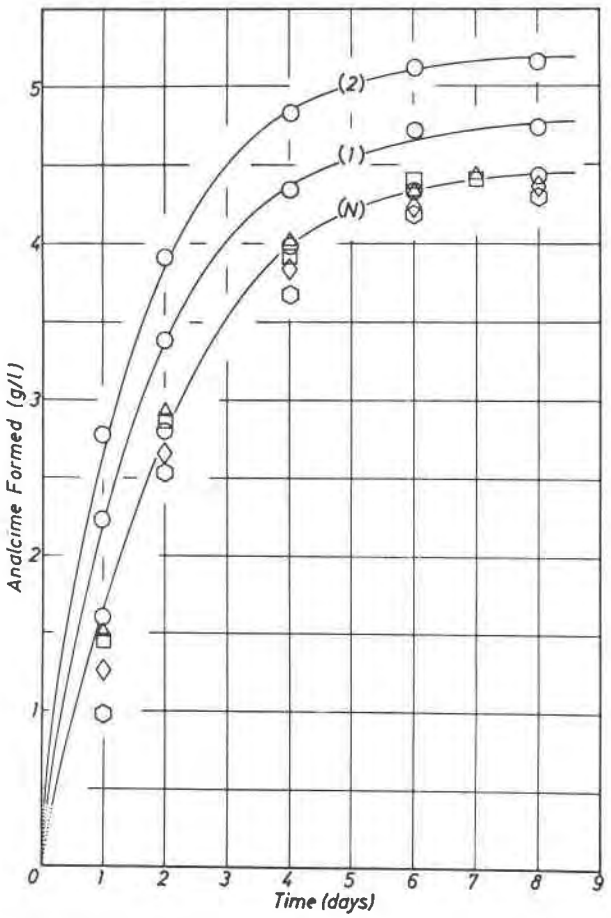

Fig. 6. Variation of the quantities of analcime formed in three kinds of seeded systems as a function of time. (i) Synthetic analcime seed for curves 1 (0.2g per liter of gel), 2 (0.4g), and N (unseeded), (ii) synthetic hydroxy-sodalite seed for triangles (0.2g) and squares (0.4g), and (iii) natural mordenite seed for diamonds (0.2g) and hexagons (0.4g). The initial gel composition was $10Na_2O \cdot 0.075Al_2O_3 \cdot 10SiO_2 \cdot 370H_2O$.

amount of mordenite was produced and the distribution of seed crystals was homogeneous in the crystal aggregates. In Figure 7, the apparent SiO_2/Al_2O_3 ratios of synthetic mordenites from solutions with the batch composition C2 are plotted as a function of time.

The solid lines in Figure 7 correspond to the variation of the ratios for the crystal aggregates. The ratio increases with reaction time and depends on the amount of seed. On the other hand, in Figure 8, the weight percent of seed in the crystal aggregates is plotted as a function of time. The SiO_2/Al_2O_3 ratio of the seed was 9.32. Accordingly, the values plotted on the solid lines in Figure 7 were corrected using the data represented in Figure 8, and the corrected values are plotted along broken lines in Figure 7. The

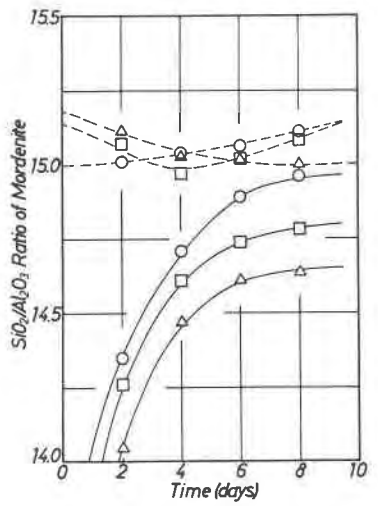

Fig. 7. Relationship between SiO_2/Al_2O_3 ratios of mordenite synthesized in natural mordenite seed systems and reaction time. The weights of seed added were 0.4g per liter of gel for circles, 0.6g for squares, and 1.2g for triangles. Solid lines illustrate the variation of SiO_2/Al_2O_3 ratio for crystal aggregates consisting of formed mordenite and seed. Dashed lines represent the corrected ratios which were calculated by considering the weight percent of seed in the crystal aggregates (see Fig. 8). In all cases, gels with batch composition C2 were used.

average value thus obtained was 15.0, and similarly, in seeded systems, the average SiO_2/Al_2O_3 ratios of mordenites crystallized from clear solutions with batch compositions C1 and C3 were 13.7 and 13.1, respectively.

As can be seen from the three batch compositions,

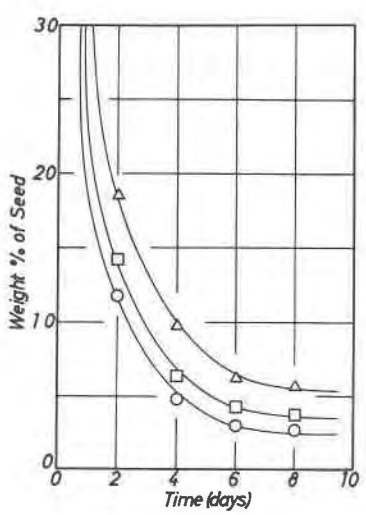

Fig. 8. Relationship between weight percent of seed contained in crystal aggregates and reaction time. Symbols of circles, squares, and triangles correspond to those in Fig. 7.

the alumina content was much lower than soda and silica contents, and consequently, owing to the formation of mordenite, the concentration of alumina in the solution phase decreased rapidly with reaction time as compared with those of other two components. Provided the SiO_2/Al_2O_3 ratio of the crystallizing mordenite varies with the change of the SiO_2/Al_2O_3 ratio of mother liquor, one might expect that the ratio in mordenite increases with reaction time. However, the corrected values along the broken lines in Figure 7 remain approximately constant regardless of the duration of reaction. Since the different batch compositions of starting materials led to different SiO_2/Al_2O_3 ratios of mordenites, it is obvious that the compositions of mordenites were governed by the initial ratio of soda, alumina, and silica in starting materials.

When mordenite crystallization occurs in clear aqueous solutions, its mechanism can probably be explained on the basis of the crystallization mechanism for analcime proposed by Ueda and Koizumi (1979).

Conclusions

Mordenite crystallized directly from aqueous clear solutions containing no amorphous solid at 100°C at 1 atm. The addition of seed to the solutions resulted in the rapid crystallization and growth of mordenite, even on the surface of seeds whose compositions and structures differ widely from those of mordenite. The composition of growing mordenite was unchanged in the overall process and was independent of the depletion of soda, alumina, and silica contents of the solution phase during the formation of crystals. From these results, we conclude that the crystallization and growth probably can be explained by assuming a complex building block model in solution for the soluble chemical species. We suggest that such species possess fixed compositions and incipient ordered structures which are identical to those of mordenite and that they polymerize to form mordenite crystals. However, their physicochemical properties have not yet been determined directly, and remain a difficult subject to be investigated in future.

Acknowledgments

The authors thank Professor L. B. Sand of Worcester Polytechnic Institute, who read the manuscript and made useful comments, and Professor D. B. Hawkins of the University of Alaska for helpful suggestions.

References

Aiello, R., R. M. Barrer and I. S. Kerr (1971a) Stages of zeolite growth from alkaline media. In R. F. Gould, Ed., *Molecular Sieve Zeolites,* p. 44–50. American Chemical Society, Washington, D.C.

———, C. Collella and R. Sersale (1971b) Zeolite formation from synthetic and natural glasses. In R. F. Gould, Ed., *Molecular Sieve Zeolites,* p. 51–61. American Chemical Society, Washington, D.C.

Ames, L. L. (1963) Synthesis of a clinoptilolite-like zeolite. *Am. Mineral., 48,* 1374–1377.

——— and L. B. Sand (1958) Hydrothermal synthesis of wairakite and calcium mordenite. *Am. Mineral., 43,* 476–480.

Barrer, R. M. (1948) Syntheses and reaction of mordenite. *J. Chem. Soc.,* 2158–2163.

——— and E. D. A. White (1952) The hydrothermal chemistry of silicates, Part II. Synthetic crystalline sodium alumino-silicates. *J. Chem. Soc.,* 1561–1571.

Breck, D. W. and E. M. Flanigen (1968) Synthesis and properties of Union Carbide zeolites L, X and Y. In R. M. Barrer, Ed., *Molecular Sieves,* p. 47–61. Society of Chemical Industry, London.

Ciric, J. (1968) Kinetics of zeolite A crystallization. *J. Colloidal Interface Sci., 28,* 315–324.

Coombs, D. S., A. J. Ellis, W. S. Fyfe and A. M. Taylor (1959) The zeolite facies with comments on the interpretation of hydrothermal syntheses. *Geochim. Cosmochim. Acta, 17,* 53–107.

Cournoyer, R. A., W. L. Kranich and L. B. Sand (1975) Zeolite crystallization kinetics related to dissolution rates of quartz reactant. *J. Phys. Chem., 79,* 1578–1581.

Culfaz, A. and L. B. Sand (1973) Mechanism of nucleation and crystallization of zeolites from gels. *Adv. Chem. Ser., 121,* 141–151.

Domine, D. and J. Quobex (1968) Synthesis of mordenite. In R. M. Barrer, Ed., *Molecular Sieves,* p. 78–87. Society of Chemical Industry, London.

Ellis, A. J. (1960) Mordenite synthesis in a natural hydrothermal solution. *Geochim. Cosmochim. Acta, 19,* 145–146.

Kerr, G. T. (1966) Chemistry of crystalline aluminosilicates. I. Factors affecting the formation of zeolite A. *J. Phys. Chem., 70,* 1047–1050.

——— (1968) Chemistry of crystalline aluminosilicates. IV. Factors affecting the formation of zeolites X and B. *J. Phys. Chem., 72,* 1385–1386.

Kranich, W. L., Y. H. Ma, L. B. Sand, A. H. Weiss and I. Zwiebel (1971) Properties of aluminum-deficient mordenites. In R. F. Gould, Ed., *Molecular Sieve Zeolites,* p. 502–512. American Chemical Society, Washington, D.C.

McNicol, B. D., G. T. Pott, K. R. Loos and N. Mulder (1971) Spectroscopic studies of zeolite synthesis: evidence for a solid state mechanism. In R. F. Gould, Ed., *Molecular Sieve Zeolites,* p. 152–161. American Chemical Society, Washington, D.C.

———, ——— and ——— (1972) Spectroscopic studies of zeolite synthesis. *J. Phys. Chem., 76,* 3388–3390.

Nakajima, W. (1973) Mordenite solid solution in the system $Na_2Al_2Si_{10}O_{24}$–$CaAl_2Si_{10}O_{24}$–H_2O. *Bull. Fac. Education, Kobe Univ., 48,* 91–98.

Sand, L. B. (1968) Synthesis of large-port and small-port mordenites. In R. M. Barrer, Ed., *Molecular Sieves,* p. 71–77. Society of Chemical Industry, London.

———, R. Roy and E. F. Osborn (1957) Stability relations of some minerals in the Na_2O–Al_2O_3–SiO_2–H_2O system. *Econ. Geol., 52,* 169–183.

Sand, M. L., W. S. Coblenz and L. B. Sand (1971) Synthesis of lithium and lithium, sodium mordenites. In R. F. Gould, Ed., *Molecular Sieve Zeolites,* p. 127–134. American Chemical Society, Washington, D.C.

Senderov, E. E. (1968) Crystallization of mordenite under hydrothermal conditions. *Geochemistry, 9,* 848–859.

——— and N. I. Khitarov (1971) Synthesis of thermodynamically stable zeolites in the Na_2O–Al_2O_3–SiO_2–H_2O system. *Adv. Chem. Ser., 101,* 279–310.

Ueda, S. and M. Koizumi (1979) Crystallization of analcime solid solutions from aqueous solutions. *Am. Mineral., 64,* 172–179.

Whittemore, O. J. (1972) Synthesis of siliceous mordenites. *Am. Mineral., 57,* 1146–1151.

Manuscript received, December 13, 1979; accepted for publication, March 31, 1980.

American Mineralogist, Volume 65, pages 1020–1025, 1980

Uranium- and thorium-rich vesuvianite from the Seward Peninsula, Alaska

GLEN R. HIMMELBERG

U. S. Geological Survey
Department of Geology, University of Missouri
Columbia, Missouri 65211

AND THOMAS P. MILLER

U. S. Geological Survey
1209 Orca Street
Anchorage, Alaska 99501

Abstract

Vesuvianite rich in U, Th, and REE occurs in a syenite and nepheline syenite in southeastern Seward Peninsula, Alaska. The vesuvianite occurs as large (up to 1.5 cm) tabular crystals; in thin section it is brownish-yellow and commonly zoned with an isotropic (metamict) core and an anisotropic (non-metamict) rim. The chemical composition can be approximated by the formula $(Ca,Na,La,Ce,Pr,Nd,U,Th)_{18.1}(Al,Ti,Fe,Mn,Mg)_{12.9}Si_{18}(O,OH,F)_{76}$. UO_2 content ranges from 0.39 (non-metamict) to 0.84 weight percent (metamict), and ThO_2 ranges from 0.72 (non-metamict) to 2.70 weight percent. Coexisting allanite has UO_2 and ThO_2 contents that range from 0.29 to 0.40 and 0.77 to 1.30 weight percents, respectively. The vesuvianite probably formed by metasomatic activity prior to intrusion of subsilicic alkaline dikes.

Introduction

Vesuvianite occurs in a variety of environments, principally in metamorphosed limestone but also in veins associated with mafic and ultramafic rocks and in nepheline syenite and other alkalic rocks. Inoue and Miyashiro (1951) have shown that compositional variations of vesuvianite are related to its occurrence. The mineral generally does not contain appreciable amounts of uranium and thorium nor is it metamict. To our knowledge, the only previously-reported occurrence of U- and Th-rich vesuvianite contained 1.00 weight percent U_3O_8 and 0.53 weight percent ThO_2 and occurred in a nepheline syenite in the USSR (Kononova, 1960). We report a recent finding of a U- and Th-rich metamict vesuvianite in syenite and nepheline syenite from the southeastern Seward Peninsula, Alaska (Fig. 1). The mineral was earlier reported to be allanite (Miller *et al.*, 1976), but more detailed study has shown that it is vesuvianite; locally, allanite is abundant and in hand specimen is indistinguishable from vesuvianite. The identification of vesuvianite is based on optical properties, chemical composition, and the powder X-ray diffraction pattern of a heated sample.

Geologic setting and petrography

The vesuvianite-bearing syenite occurs in the center of the Kachauik pluton, which is a large composite body of monzonite, syenite, and granodiorite of mid-Cretaceous age (Miller and Bunker, 1976). The pluton occupies an upland region west of the Darby Mountains and has an outcrop area of about 530 km^2. A N40°E-trending alkaline dike swarm consisting of pulaskite and pseudoleucite porphyry cuts much of the north half of the pluton.

Vesuvianite occurs in syenite boulders scattered along a ridge crest over an area approximately 1.3 by 0.4 km in the north-central part of the Kachauik pluton (Fig. 1). Extensive frost action has reduced most outcrops to rubble and talus. Due to the absence of outcrop, the relation of the vesuvianite-bearing syenite to the remaining syenite and monzonite of the pluton is uncertain. Vesuvianite-bearing syenite occurs as discrete boulders, although thin-section study indicates some gradation into adjacent vesuvianite-

0003–004X/80/0910–1020$02.00

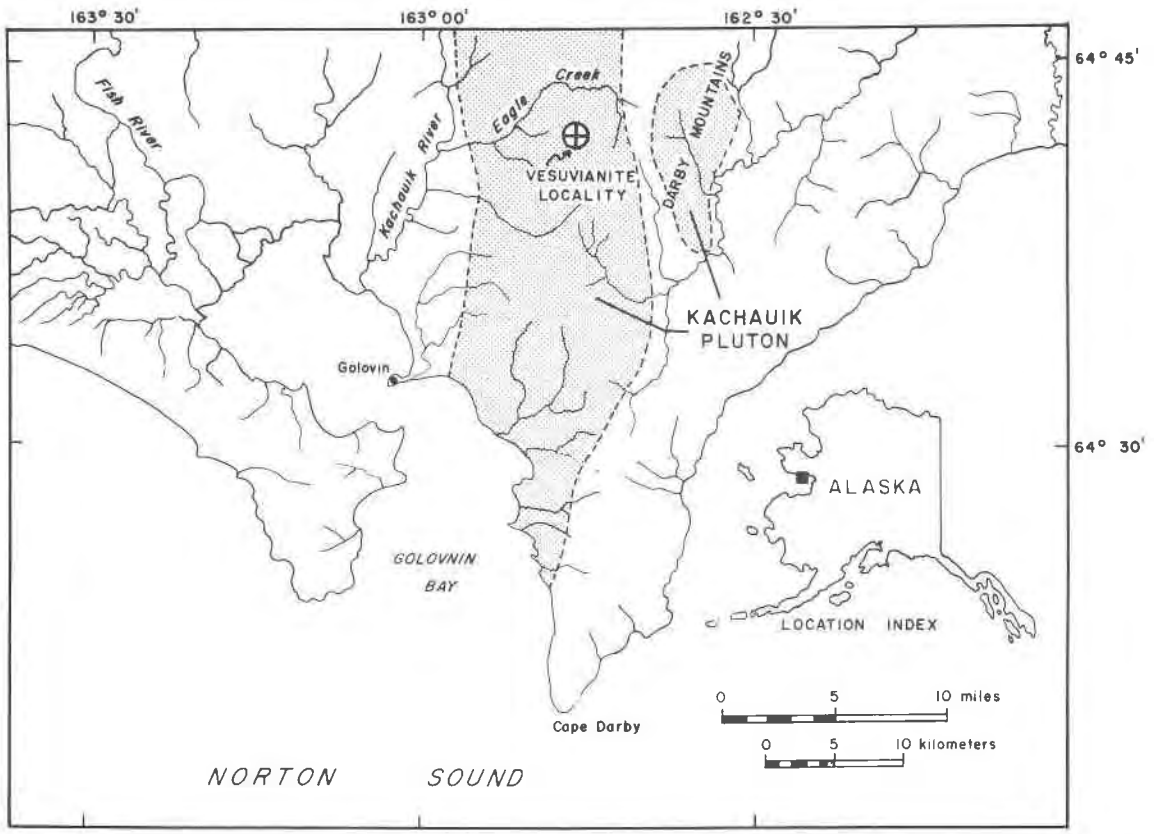

Fig. 1. Index map showing the location of uranium- and thorium-rich vesuvianite-bearing nepheline syenite (stipple pattern).

free syenite and monzonite. These boulders occur within 250 m of a pulaskite dike which is approximately 10 m wide and over 3 km long and strikes N40°E. Although the absence of outcrops makes determination of attitudes difficult, the vesuvianite-bearing syenite boulders also appear to occur discontinuously along a N40°E trend.

The monzonite and syenite are porphyritic; phenocryst minerals, set in a medium-grained groundmass, are perthitic potassium feldspar, hornblende, and clinopyroxene. Groundmass minerals are dominantly potassium feldspar and subordinate plagioclase (An_{30-45}); quartz ranges up to 5 volume percent. Biotite is rare, and melanite garnet is locally present in border phases. Nepheline is rare except in and near vesuvianite-bearing syenite. Ubiquitous sphene, apatite, zircon, and sporadically distributed magnetite and allanite are accessory minerals. Alignment of potassium feldspar phenocrysts imparts a trachytoid texture.

The vesuvianite-bearing syenite contains perthitic potassium feldspar and either nepheline or plagioclase (An_{30}), but not both in the same specimen. Plagioclase is unaltered or sericitized, and in some samples nepheline is altered to cancrinite. Mafic minerals are vesuvianite, hornblende, and lesser amounts of green clinopyroxene; biotite is present in minor amounts, generally as a replacement of hornblende. Zircon, sphene, and apatite are the most common accessory minerals; zircon occurs as large euhedra as much as 10 mm across and locally constitutes 2 to 3 percent of the rock. Melanite garnet and allanite are less common, although allanite does occur locally in amounts of a few percent. The vesuvianite-bearing syenite is medium- to coarse-grained and porphyritic, commonly with a trachytoid alignment of potassium feldspar phenocrysts.

Individual blocks of the vesuvianite-bearing syenite are highly radioactive; a hand-held scintillometer yielded a counting rate up to 8000 counts per second (total counts). Delayed neutron and gamma-ray spectrometric analyses were obtained on rock samples showing the highest radioactivity and containing an estimated 30–50 volume percent vesuvianite. Uranium in the samples reaches a maximum of 1545 ppm as compared to a maximum of over 9000 ppm

thorium (Table 1). Semiquantitative spectrographic analysis of the same samples indicates a rare-earth element (REE) content of over 2 weight percent, principally consisting of La, Ce, Pr, Nd, Sm, Gd, and Y (Miller *et al.*, 1976).

Vesuvianite

Description and powder X-ray diffraction pattern

The vesuvianite occurs as euhedral tabular crystals as long as 1.5 cm. These crystals may constitute up to 50 volume percent of individual syenite boulders. On weathered surfaces vesuvianite is altered to an unidentified bright orange material. In hand specimen the vesuvianite is black, in thin section it is brownish-yellow with anastomosing fractures. Both isotropic (metamict) and anisotropic (non-metamict) vesuvianite are present in the same thin section. Zoning of vesuvianite crystals is common; inner parts are generally isotropic, have low relief, and are darker-colored than the anisotropic, higher relief, lighter-colored rims. Contacts between zones are abrupt and irregular, and some grains show more than two zones. The anisotropic material is uniaxial negative, nonpleochroic with low birefringence. Vesuvianite contains inclusions of all other major minerals in its host rock and is one of the last minerals to have crystallized. Relict ragged grains of allanite are commonly enclosed in vesuvianite.

Because of the metamict character of most of the vesuvianite crystals, it was not possible to obtain a powder X-ray diffraction pattern of the material in its natural state. Following the method of Kononova (1960), we heated the vesuvianite to a temperature of 800°C for 1 hour. The diffraction pattern obtained from the annealed material is compared to the more intense lines of the JCPDS vesuvianite pattern 22-533 and to Kononova's analysis No. 1 (Table 2). The Alaskan vesuvianite pattern is generally comparable to the JCPDS pattern, although the interplanar spacings of the Alaskan vesuvianite are invariably larger than those of the JCPDS pattern, as are those of Kononova's sample. The differences in interplanar spacings are probably related to differences in chemical composition of the Alaskan and USSR vesuvianites relative to the more standard chemical composition.

Table 1. Uranium and thorium analyses in parts per million (ppm) of selected samples of vesuvianite-bearing syenite, Kachauik pluton, Alaska

Sample No.	U ppm*	(CV)	U ppm**	Th ppm*	(CV)	Th ppm**
76 AMm 112	1107	(1)	1000	6619	(2)	5700
76 AEr 23	1162	(1)	1050	7692	(1)	6400
76 AMm 112B	1486	(1)	--	9240	(1)	--
76 AEr 23B	1545	(1)	1500	8408	(2)	7000
77 AMm 62	1411	(3)	--	9355	(5)	--

**Delayed neutron determination. CV = Coefficient of variation = one standard deviation, expressed as percentage of concentration. Analysts: A. J. Bartel and R. J. Vinnola.*

***Gamma-ray spectrometric analysis. Analysts: C. M. Bunker and C. A. Bush.*

--not determined

Table 2. Interplanar spacing of Alaskan vesuvianite, USSR vesuvianite, and JCPDS vesuvianite 22-533

Alaskan I/I_1	Alaskan d(Å)	U.S.S.R. I/I_1	U.S.S.R. d(Å)	JCPDS 22-533 I/I_1	JCPDS 22-533 d(Å)
40	3.29			30	3.25
50	3.018	40	3.01	60	2.948
100	2.803	100	2.77	100	2.759
80	2.646	80	2.61	80	2.599
30	2.513	60	2.48	60	2.465
		10	2.39	10	2.354
10	2.187			50	2.128
10	1.935			30	1.892
				50	1.767
10	1.704			30	1.682
		40	1.677	50	1.666
70	1.658	70	1.647	80	1.625
10	1.585	10	1.590	40	1.562

Alaskan vesuvianite (sample 77 AMm 70) heated at 800°C for 1 hour. U.S.S.R. vesuvianite is analysis no. 1 from Knononova (1960).

Chemical composition

The chemical composition of the Alaskan vesuvianite was determined with an ARL EMX-SM electron microprobe, and representative analyses of a zoned crystal are given in Table 3; each analysis is an average of 5 spots. Standards were as follows: U metal for uranium; natural thorite for Th; synthetic glass for REE; and natural and synthetic pyroxenes for all other elements. Characteristic X-ray lines measured were; U$M\beta$, Th$M\alpha$, REE$L\alpha$, and $K\alpha$ for the remainder of the elements. The La$L\beta$ peak overlaps with the Pr$L\alpha$ peak, and thus in analyses for Pr the X-ray intensity obtained at the Pr$L\alpha$ wavelength setting must be corrected for the La$L\beta$ contribution. According to Åmli and Griffin (1975), this correction is approximately 12.7 percent. Although this correction is substantial and critical for many analyses of Pr, it is insignificant at the concentration levels of Pr in the vesuvianite. Uranium values were checked with a

Table 3. Chemical compositions and structural formulas of vesuvianite and allanite in nepheline syenite of the Kachauik pluton, Alaska

	Vesuvianite			Allanite
	Zone 1**	Zone 2	Zone 3	
SiO_2	37.4	35.6	36.4	33.6
Al_2O_3	11.3	11.8	12.0	15.7
TiO_2	2.83	3.01	3.58	0.56
FeO*	8.83	8.72	7.87	15.9
MnO	0.25	0.25	0.21	0.22
MgO	1.58	1.50	1.49	0.21
CaO	29.4	31.0	32.1	13.4
Na_2O	0.37	0.38	0.38	0.04
La_2O_3	1.40	1.16	0.78	5.84
Ce_2O_3	3.11	2.06	1.23	10.0
Pr_2O_3	0.48	0.32	0.20	1.52
Nd_2O_3	1.07	0.65	0.42	1.70
ThO_2	2.69	1.51	0.73	0.86
UO_2	0.84	0.66	0.64	0.38
Total	101.55	98.62	98.03	99.93
	Cations per 72 oxygens			Cations per 12.5 oxygens
Si	18.474	17.901	18.049	3.111
Al	--	0.099	--	--
ΣZ	18.474	18.000	18.049	3.111
Al	6.579	6.894	7.013	1.713
Ti	1.051	1.138	1.335	0.039
Fe^{2+}	3.648	3.666	3.264	1.231
Mn	0.104	0.106	0.088	0.017
Mg	1.164	1.124	1.101	0.029
ΣY	12.546	12.928	12.801	3.029
La	0.255	0.216	0.143	0.199
Ce	0.562	0.380	0.223	0.339
Pr	0.086	0.058	0.036	0.051
Nd	0.189	0.117	0.074	0.056
Th	0.303	0.173	0.083	0.018
U	0.092	0.074	0.071	0.008
Na	0.353	0.372	0.366	0.007
Ca	15.560	16.701	17.053	1.329
ΣX	17.400	18.091	18.049	2.007

Total iron as FeO

***Zone 1 is isotropic (metamict) core, Zone 2 is intermediate metamict zone of slightly higher relief than Zone 1, and Zone 3 is anisotropic (non-metamict) rim. Vesuvianite sample 77 AMm 70; allanite sample 77 AMm 62.*

UO_2 standard, and differences obtained with U metal and UO_2 as a standard were ±4 percent of the amount present. No standard check was available for the Th or REE. Matrix corrections were made by the procedure of Bence and Albee (1968) and the corrections factors of Albee and Ray (1970). There is no α-factor available for the U$M\beta$ line, so the U$M\alpha$ α-factor was used in the correction. Judging from the mass absorption coefficients given by Heinrich (1966) for U$M\alpha$ and U$M\beta$, any error introduced by using the U$M\alpha$ α-factor should be minimal.

Although the chemical formula of vesuvianite as proposed from a structural analysis by Warren and Modell (1931) can be written $Ca_{20}Mg_4Al_8Si_{18}(O,OH,F)_{76}$, vesuvianite analyses show considerable variation from this formula (Deer *et al.*, 1962, p. 116, 117). Machatschki (1932) proposed the alternate formula $X_{19}Y_{13}Z_{18}(O,OH,F)_{76}$ where X = Ca(Na,K,Mn), Y = (Al,Fe^{3+},Fe^{2+},Mg,Ti,Zn,Mn), and Z = Si, and analyses cited by Deer *et al.* (1962) fit this formula closer. Other proposed formulas (see Ito and Arem, 1970) are similar to Warren and Modell's original formula, but none agrees with all published analyses.

The Alaska vesuvianite formula was calculated anhydrous by Jackson *et al.*'s (1967) method. Total iron was calculated as Fe^{2+}, although some Fe^{3+} is certainly present. The Alaskan vesuvianite differs from other reported vesuvianite analyses in its significant content of U, Th, and REE. All these elements have ionic radii comparable to Ca and have been assigned to the X group of elements substituting for Ca. For the Alaskan vesuvianite X is close to 18, Y to 13, and Z to 18. A similar formula was determined for the USSR U- and Th-bearing vesuvianite (Kononova, 1960).

Except for the U, Th, and REE, the Alaskan vesuvianite is similar in composition to other vesuvianites. Inoue and Miyashiro (1951) reported that vesuvianites from nepheline syenites are characterized by higher contents of Al and Ti and lower contents of Ca and Mg than vesuvianites from metamorphosed calcareous rocks. They reported Al_2O_3 contents of approximately 18 and 19 weight percent for nepheline syenite vesuvianite; however, the Alaskan vesuvianite has only about 12 weight percent Al_2O_3. Similarly, the metamict vesuvianite reported by Kononova (1960) has an Al_2O_3 content of 14.5 weight percent.

The optical zonation of the vesuvianite shows a corresponding chemical zonation. The innermost metamict zone (zone 1, Table 3) is enriched in U, Th, REE, and Mg and depleted in Al, Ti, Fe, and Ca relative to the outer non-metamict zone (zone 3, Table 3). Additional U and Th analyses were made on several grains of vesuvianite in three samples. The metamict vesuvianite grains showed a range of 0.61 to 0.84 weight percent UO_2 and 1.38 to 2.70 weight percent ThO_2; non-metamict vesuvianite is lower in UO_2 and ThO_2, with approximately 0.40 weight percent UO_2 and 0.72 to 0.98 weight percent ThO_2. Spot analyses showed ThO_2 contents as high as 3.77

weight percent. The vesuvianite from the USSR contains 1.00 weight percent U_3O_8 (0.96 percent UO_2) and 0.53 percent ThO_2.

Allanite

Allanite was also analyzed, and a representative analysis is given in Table 3. The mineral formula was calculated anhydrous on the basis of 12.5 oxygens. All iron was calculated as Fe^{2+}, although a small amount of the total iron is certainly Fe^{3+}, which would adjust the calculated formula. The allanite shows smaller amounts of UO_2 (0.29 to 0.40 weight percent) relative to the coexisting vesuvianite although ThO_2 contents are similar (0.77 to 1.30 weight percent). An optically zoned allanite shows Th zoning, the core having 0.77 weight percent, an intermediate zone 1.38 weight percent, and the rim 2.00 to 2.88 weight percent ThO_2. These UO_2 and ThO_2 contents are relatively high for allanite but within the range reported by Frondel *et al.* (1967 p. 50).

Petrogenesis of the vesuvianite-bearing syenite

Although the exposures are poor and consequently interpretations are uncertain, the relation between the vesuvianite-bearing syenite and the surrounding syenite and monzonite of the Kachauik pluton appears to be gradational over a few centimeters. These observations suggest that the vesuvianite-bearing syenite is indeed a part of the enclosing syenite and monzonite and not a later intrusive phase.

Most of the vesuvianite-bearing syenite contains nepheline, whereas most of the surrounding monzonite and syenite are silica-saturated rocks with rare nepheline. Furthermore, nepheline and plagioclase are mutually exclusive in vesuvianite-bearing syenite, suggesting that nepheline may be a metasomatic product resulting from alkali-exchange reactions that converted plagioclase to perthite plus nepheline, as proposed by Rao and Murthy (1974). Textural evidence also suggests that the coarse vesuvianite was among the last minerals to form, since it contains abundant inclusions of all other minerals.

We therefore suggest that the vesuvianite and its host rocks of syenite and nepheline syenite were formed by metasomatic activity involving the introduction of alkali elements, U, Th, Zr, and REE into the syenite and monzonite of the Kachauik pluton. Chemical zonation of the vesuvianite grains suggests that the U, Th, and REE content of the metasomatic fluids decreased with time. Some allanite, which also occurs in the surrounding syenite and monzonite, was probably a primary mineral; however, local concentrations of allanite suggest that much of it was also introduced. The thorium-rich rim on some allanite grains probably grew on primary grains during metasomatism.

The metasomatic fluids may be related to the alkaline pulaskite dikes which also contain nepheline and occur in the immediate area of the vesuvianite-bearing syenite. The dikes were emplaced along a persistent N40°E joint system in the syenite and monzonite. Since the occurrence of the vesuvianite-bearing syenite boulders also appear to trend roughly N40°E, either the metasomatic fluids could have pervaded the syenite and monzonite along an incipient fracture system into which the pulaskite dikes were later emplaced, or the metasomatism may have occurred at the time of emplacement of the pulaskite dikes.

References

Albee, A. L. and L. Ray (1970) Correction factors for electron probe microanalysis of silicates, oxides, carbonates, phosphates, and sulfates. *Anal. Chem., 42,* 1408–1414.

Åmli, R. and W. L. Griffin (1975) Microprobe analysis of REE minerals using empirical correction factors. *Am. Mineral., 60,* 599–606.

Bence, A. E. and A. L. Albee (1968) Empirical correction factors for the electron microanalysis of silicates and oxides. *J. Geol., 76,* 382–403.

Deer, W. A., R. A. Howie and J. Zussman (1962) *Rock-Forming Minerals,* Vol. 1, *Ortho- and Ring Silicates.* Wiley, New York.

Frondel, J. W., M. Fleischer and R. S. Jones (1967) *Glossary of uranium- and thorium-bearing minerals* (fourth ed). U. S. Geol. Surv. Bull. 1250.

Heinrich, K. F. J. (1966) X-ray absorption uncertainty. In T. D. McKinley, K. F. J. Heinrich and D. B. Wittry, Eds., *The Electron Microprobe,* p. 296–377. Wiley, New York.

Inoue, T. and A. Miyashiro (1951) Occurrence of vesuvianite in nepheline–syenitic rocks of the Fukushinzan district, Korea, with general consideration of the relation between the composition and occurrence of vesuvianite. *J. Geol. Soc. Japan, 57,* 51–57.

Ito, J. and J. E. Arem (1970) Idocrase: synthesis, phase relations, and crystal chemistry. *Am. Mineral., 55,* 880–912.

Jackson, E. D., R. E. Stevens and R. W. Bowen (1967) A computer-based procedure for deriving mineral formulas from mineral analyses. *U. S. Geol. Surv. Prof. Pap., 575-C,* C23–C31.

Kononova, V. A. (1960) On a metamict variety of vesuvianite from an alkaline pegmatite in southwest Tuva. *Dokl. Akad. Nauk. SSSR, 130,* 400–403. [transl. *Dokl. Acad. Sci. SSSR, 130,* 129–132 (1961)].

Machatschki, F. (1932) Zur Formel des Vesuvian. *Z. Kristallogr., 81,* 148–152.

Miller, T. P. and C. M. Bunker (1976) A reconnaissance study of the uranium and thorium contents of plutonic rocks of the

southeastern Seward Peninsula, Alaska. *J. Res. U. S. Geol. Surv., 4,* 367–377.

———, R. L. Elliott, W. I. Finch and R. A. Brooks (1976) Preliminary report on uranium-, thorium-, and rare-earth-bearing rocks near Golovin, Alaska. *U. S. Geol. Surv. Open-file Rep. 76-710.*

Rao, Y. J. and I. S. N. Murthy (1974) Nepheline as a metasomatic product. *Am. Mineral., 59,* 690–693.

Warren, B. E. and D. I. Modell (1931) The structure of vesuvianite $Ca_{10}Al_4(Mg,Fe)_2Si_9O_{34}(OH)_4$. *Z. Kristallogr., 78,* 422–432.

Manuscript received, December 21, 1979;
accepted for publication, March 13, 1980.

American Mineralogist, Volume 65, pages 1026–1030, 1980

The stereochemistry of iron sulfides—a structural rationale for the crystallization of some metastable phases from aqueous solution[1]

PETER TAYLOR

Research Chemistry Branch, Atomic Energy of Canada Limited
Whiteshell Nuclear Research Establishment
Pinawa, Manitoba, R0E 1L0

Abstract

Stereochemical and topological arguments are used to rationalize the metastable occurrence of mackinawite and marcasite in laboratory experiments. The dimeric species, $(FeS)_2$ and $(FeS_2)_2$, are postulated as intermediates in the crystallization of mackinawite and marcasite, respectively.

Introduction

The only stable binary solids in the Fe-S system above 200°C and near ambient pressure are the pyrrhotites, $Fe_{1-x}S$ (including troilite, FeS) and pyrite, FeS_2. Several other phases, at least some of which are metastable, occur widely at lower temperatures in both natural and artificial environments (Ward, 1970; Power and Fine, 1976). Many workers have studied the synthesis and interconversion of these phases (*e.g.* Berner, 1962, 1964, 1967; Rickard, 1969; Takeno *et al.*, 1970; Rising, 1973; Taylor *et al.*, 1979a,b; Shoesmith *et al.*, 1980; Wikjord *et al.*, 1980). In this paper, stereochemical arguments are used to postulate crystallization mechanisms for some iron sulfides. Intermediates proposed in these mechanisms may exist in solution, or they may occur only at surfaces. Similar concepts were first proposed by Bloom (1939). This work was part of an investigation of corrosion and deposition phenomena in Canadian Girdler-Sulfide heavy-water production plants.

Discussion

Iron monosulfides—mackinawite, troilite, and cubic FeS

A striking feature of the low-temperature formation of iron sulfides from aqueous solution is the frequent occurrence of mackinawite. It is typically the sole crystalline product of precipitation of ferrous ions by H_2S or its salts below 100°C, in the absence of oxidants (Berner, 1964, 1967; Rickard, 1969). It also occurs widely in nature (*e.g.* Evans *et al.*, 1964; Schot *et al.*, 1972) and as a corrosion product on iron or carbon steel exposed to aqueous H_2S (Berner, 1962, 1964; Takeno *et al.*, 1970; Wikjord *et al.*, 1980; Shoesmith *et al.*, 1980). Pyrrhotites are not readily prepared from aqueous solution below 100°C, although troilite does occur as a low-temperature corrosion product (Takeno *et al.*, 1970; Wikjord *et al.*, 1980; Shoesmith *et al.*, 1980). Cubic FeS is known only as a corrosion product (Médicis, 1970a,b; Takeno *et al.*, 1970; Wikjord *et al.*, 1980; Shoesmith *et al.*, 1980).

The sluggish nature of most phase transformations in this system at low temperatures hinders the determination of equilibrium phase relations. One exception is the transformation of cubic FeS to mackinawite, which occurs spontaneously at room temperature, demonstrating that cubic FeS is not a stable phase (Médicis, 1970a,b; Takeno *et al.*, 1970; Shoesmith *et al.*, 1980).

The upper limit of thermal stability of mackinawite is about 130°C; small amounts of Ni and Co incorporated in the structure tend to enhance its stability (Takeno, 1965; Clark, 1966; Takeno and Clark, 1967). It is not known whether this limit reflects a true thermodynamic stability field, or kinetic limits on the transformation of a metastable phase.

Solubility studies (Berner, 1967; Tewari and Campbell, 1976; Tewari *et al.*, 1978) demonstrate that solutions which are saturated with respect to H_2S and synthetic mackinawite at ambient temperature and pressure are supersaturated with respect to troil-

[1] Issued as Atomic Energy of Canada Limited Report No. AECL 6645.

0003-004X/80/0910-1026$02.00

ite. However, since mackinawite usually has a metal:sulfur ratio greater than 1.00, the possible existence of a low-temperature stability field is not ruled out. Nonetheless, mackinawite is frequently formed under conditions where it is metastable with respect to troilite and/or more sulfur-rich sulfides.

Figure 1a shows the crystal structure of mackinawite (Berner, 1962; Taylor and Finger, 1971). Iron atoms occupy every site in alternate layers of tetrahedral interstices in a cubic close-packed (c.c.p.) sulfur sub-lattice. The Fe–S bonding network consists of interconnected Fe_2S_2 rings, and Fe–Fe bonding also occurs within the metal-atom layers. The Fe_2S_2 rings, and similar structural units discussed below, are not discrete moieties, but they are recognizable elements of the structural network.

Cubic FeS (Fig. 1b) is isostructural with sphalerite (Médicis, 1970; Takeno *et al.*, 1970), and differs from mackinawite in the distribution of iron atoms, which occupy one half of each layer of tetrahedral holes in the c.c.p. sulfur sub-lattice. The close structural relationship between these phases accounts for the ease of conversion of cubic FeS to mackinawite, cited above. Cubic FeS contains Fe_3S_3 but not Fe_2S_2 rings, and there are no Fe–Fe bonds.

The structure of troilite is derived from the NiAs type. Both Fe and S are six-coordinate, and iron atoms are drawn together into triangular clusters. The topology of the structure is complex; both Fe_2S_2 and Fe_3S_3 rings can be discerned (Fig. 2) (Evans, 1970).

The ease of precipitation of fine-grained (<1 μm) mackinawite demonstrates that homogeneous nucleation of this phase is facile. This nucleation presumably proceeds by complexation of Fe^{2+} and SH^- (1),

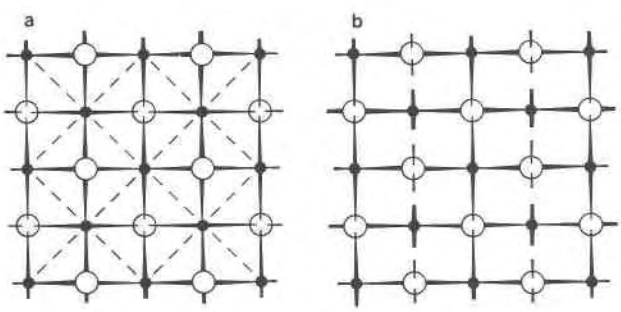

Fig. 1. (a) Projection of four unit cells of the crystal structure of mackinawite down the *c* axis. Large open and small closed circles represent S and Fe atoms, respectively; this convention is used in all figures. Dashed lines delineate Fe–Fe interactions. (b) Projection of the crystal structure of cubic FeS down the *a* axis. Broken bonds proceed to Fe atoms above and S atoms below those shown.

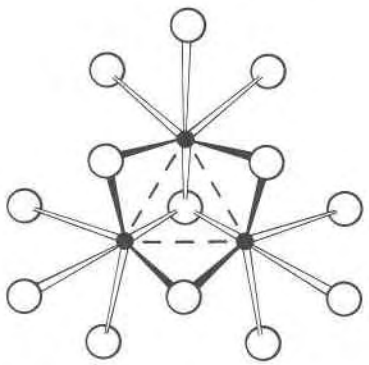

Fig. 2. Part of the crystal structure of troilite, showing the environment of one Fe_3 cluster. Interactions with neighboring Fe_3 clusters are omitted. The solid bonds delineate an Fe_3S_3 ring which may be a precursor to troilite crystallization. Dashed lines show Fe–Fe interactions.

and subsequent polymerization of $FeSH^+$ with elimination of protons and water of solvation. A similar mechanism has been proposed for the growth of thioferrite salts from aqueous solution (Taylor and Shoesmith, 1978). Few SH^- complexes of transition metals are known, but $CrSH^{2+}$ has been reported (Ramasami and Sykes, 1976). If the initial polymerization step is a dimerization (2), then further association of the dimer is readily envisaged to lead to the layer structure of mackinawite by a simple tessellation, with formation of additional bonds.

$$Fe^{2+} + SH^- \longrightarrow FeSH^+ \quad (1)$$

$$2FeSH^+ \longrightarrow Fe_2S_2 + 2H^+ \quad (2)$$

$$nFe_2S_2 \longrightarrow \text{mackinawite} \quad (3)$$

Although Fe_2S_2 rings are also present in the troilite structure, the greater complexity of their interconnection may account for the evident difficulty of troilite nucleation. Analogous situations, in which phases with high coordination numbers and complex structural networks are more difficult to crystallize than metastable polymorphs with simpler structural networks, are common, *e.g.*, GeO_2 (Rochow, 1973, p. 26), $NaFeO_2$ (Okamoto, 1968).

When troilite occurs as a corrosion product on iron or carbon steel in aqueous H_2S at low temperatures, it appears to arise from high local iron concentrations at the corroding surface (Shoesmith *et al.*, 1980). A trimeric precursor, Fe_3S_3, may be involved in its nucleation.

The absence of close Fe–Fe contacts in cubic FeS

probably results in a low activation energy for its nucleation, but its low stability confines its occurrence to conditions of high supersaturation and short reaction times. Like troilite, its formation as a corrosion product is associated with high local supersaturation. There is evidence for competition between these two phases as sinks for dissolved iron at corroding surfaces (Shoesmith *et al.*, 1980).

Iron disulfides—pyrite and marcasite

Both pyrite and marcasite have compositions very close to $FeS_{2.00}$. Buerger (1934) suggested that an apparent slight sulfur-deficiency of marcasite (*ca.* $FeS_{1.985}$) might be related to its mechanism of formation. However, Kullerud and Yoder (1959) concluded that the two phases are true dimorphs of $FeS_{2.00}$. Although the possible occurrence of a low-temperature stability field for marcasite cannot be completely ruled out, there is evidence that it is often formed under conditions where it is metastable with respect to pyrite. It may well be metastable under all conditions (Rising, 1973).

Recent work by Shoesmith *et al.* (1979), Taylor *et al.* (1979b), and Wikjord *et al.* (1980) showed that pyrite is the sole ultimate product of reaction of aqueous H_2S with iron, carbon steel, troilite, or mackinawite at 100–160°C, in the absence of oxidants other than H_2S. However, in the presence of oxygen or sulfur, or under the application of an anodic current at the crystallization site, marcasite is formed in addition to pyrite. Formation of a metastable phase under these enhanced oxidizing conditions is not unexpected. These observations are consistent with the literature, as reviewed by Rising (1973).

Both the pyrite and marcasite crystal structures are three-dimensional networks of inter-linked Fe and S_2 moieties (Brostigen and Kjekshus, 1969; Brostigen *et al.*, 1973 and references therein). In each structure, iron has approximate octahedral coordination by sulfur, and sulfur has a distorted tetrahedral coordination by three iron atoms and the second sulfur atom of the S_2 unit. The two structures differ in their network geometries, and can be described in terms of fused Fe–S ring systems (Rising, 1973).

The pyrite structure consists entirely of Fe_2S_3 rings, I (Figs. 3a and 4), whereas marcasite contains Fe_2S_2 and Fe_2S_4 rings, II and III (Figs. 3b and 4) as well. There is no significant Fe–Fe bonding in either structure. Clearly, a crystallization mechanism which favors the formation of rings II or III will favor formation of marcasite rather than pyrite, as outlined by equations (4) to (6).

$$Fe^{2+} + S_2^{2-} \longrightarrow {}^{+}Fe\text{–}S\text{–}S^{-} \quad (4)$$

$$2\ {}^{+}Fe\text{–}S\text{–}S^{-} \longrightarrow \text{II or III} \quad (5)$$

$$\text{n(II or III)} \longrightarrow \text{marcasite} \quad (6)$$

Although $(FeS_2)_2$ could have any of the structures I to III, III is most likely on the basis of the structural chemistry of related species. Six-membered polysulfide rings are known in $(NH_4)_2Pt(S_5)_3{\cdot}2H_2O$ (Jones and Katz, 1967) and $(\pi\text{-}C_5H_5)_2TiS_5$ (Koepf *et al.*, 1968). Units of the type R–S–S–R are generally more stable than R_2 S=S, with the exception of S_2F_2 (Schmidt and Siebert, 1973, p. 843–844). An example of a solution species containing an M–S–S–M linkage, $[Cr\text{–}S\text{–}S\text{–}Cr]^{4+}$, has recently been reported (Ramasami *et al.*, 1976). If III has a chair configuration, as do the rings in the compounds mentioned above and in S_6 (Donohue *et al.*, 1961), then a simple

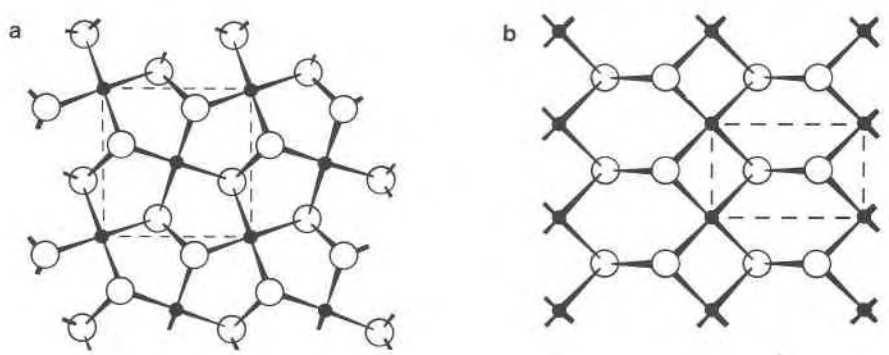

Fig. 3. (a) Part of the crystal structure of pyrite, viewed in projection down the *a* axis, showing the system of fused Fe_2S_3 rings. Bonds nearly vertical to the projection are omitted for clarity. The dashed lines delineate the unit cell. (b) Part of the crystal structure of marcasite, viewed in projection down the *a* axis, showing the system of fused Fe_2S_2 and Fe_2S_4 rings. Some bonds are omitted for clarity, as in Fig. 3a. The dashed lines delineate the unit cell; *b*- and *c*-axis projections closely resemble Fig. 3a.

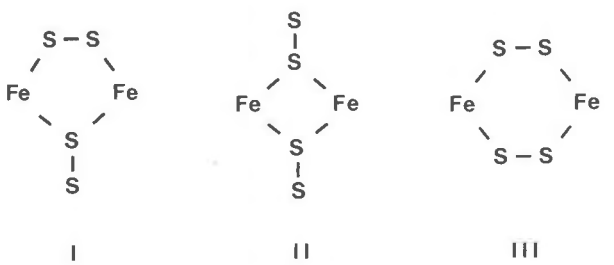

Fig. 4. Possible structures for an $(FeS_2)_2$ dimer.

three-dimensional tessellation of such units leads directly to the marcasite structure (Fig. 3b). This involves the formation of additional Fe–S bonds, but no further rearrangement of the structural net.

High concentrations of S_2^{2-} would favor the reaction sequence (4) to (6), although not necessarily to the exclusion of pyrite precipitation. This is consistent with the observations that oxidizing conditions, which favor polysulfide generation, also favor marcasite formation. It is noted that the equilibrium concentration of S_2^{2-} in the system H_2S–S–H_2O is extremely low at pH = 4 (Giggenbach, 1972; Teder, 1971). However, the same structural arguments apply if the S_2 moiety is generated only as a surface species at the crystallization site, or if FeS_2 monomer is produced by an alternative route.

Unfortunately, iron sulfide formation is not amenable to most probes which might test the hypotheses put forward here. Some relevant information might be obtained from a matrix isolation spectroscopic study of the reactions of Fe atoms with S atoms and S_2 molecules, or from the chemistry of other systems in which similar polymorphism occurs.

Acknowledgments

I am grateful to Drs. T. E. Rummery, D. W. Shoesmith, and A. G. Wikjord for stimulating discussions of this work.

References

Berner, R. A. (1962) Tetragonal iron sulfide. *Science, 137,* 669.

——— (1964) Iron sulfides formed from aqueous solution at low temperatures and atmospheric pressure. *J. Geol., 72,* 293–306.

——— (1967) Thermodynamic stability of sedimentary iron sulfides. *Am. J. Sci., 265,* 773–785.

Bloom, M. C. (1939) The mechanism of the genesis of polymorphous forms. *Am. Mineral., 24,* 281–292.

Brostigen, G. and A. Kjekshus (1969) Redetermined crystal structure of FeS_2 (pyrite). *Acta Chem. Scand., 23,* 2186–2188.

———, ——— and C. Rømming (1973) Compounds with the marcasite type crystal structure. VIII. Redetermination of the prototype. *Acta Chem. Scand., 27,* 2791–2796.

Buerger, M. J. (1934) The pyrite–marcasite relation. *Am. Mineral., 19,* 37–61.

Clark, A. H. (1966) Some comments on the composition and stability relations of mackinawite. *Neues Jahrb. Mineral. Monatsh.,* 300–304.

Donohue, J., A. Caron and E. Goldish (1961). The crystal and molecular structure of S_6 (sulfur-6). *J. Am. Chem. Soc., 83,* 3748–3751.

Evans, H. T., Jr. (1970) Lunar troilite: crystallography. *Science, 167,* 621–623.

——— C. Milton, E. C. T. Chao, I. Adler, C. Mead, B. Ingram and R. A. Berner (1964) Valleriite and the new iron sulfide, mackinawite. *U.S. Geol. Surv. Prof. Pap. 475-D,* 64–69.

Giggenbach, W. (1972) Optical spectra and equilibrium distribution of polysulfide ions in aqueous solution at 20°. *Inorg. Chem., 11,* 1201–1207.

Jones, P. E. and L. Katz (1967) The structure of the tris(pentasulphido) platinum (IV) anion. *Chem. Commun.,* 842–843.

Koepf, H., B. Block and M. Schmidt (1968) Di-π-cyclopentadienyltitanium (IV) pentaselenide and pentasulfide, two heterocyclohexachalcogens in fixed conformation. *Chem. Ber., 101,* 272–276.

Kullerud, G., and H. S. Yoder (1959). Pyrite stability relations in the Fe–S system. *Econ. Geol., 54,* 533–572.

Médicis, R. de (1970a) Cubic FeS, a metastable iron sulfide. *Science, 170,* 1191–1192.

——— (1970b) A new form of iron sulfide: cubic FeS. *Rev. Chim. Miner., 7,* 723–728.

Okamoto, S. (1968) Polymorphic transformation of sodium orthoferrites. *Z. anorg. allg. Chem., 363,* 222–224.

Power, L. F. and H. A. Fine (1976). The iron–sulfur system. Part 1. The structures and physical properties of the compounds of the low-temperature phase fields. *Minerals Sci. Eng., 8,* 106–128.

Ramasami, T. and A. G. Sykes (1976) Further characterization and aquation of the thiolopentaaquochromium (III) complex, $CrSH^{2+}$, and its equilibration with thiocyanate. *Inorg. Chem., 15,* 1010–1014.

———, R. S. Taylor and A. G. Sykes (1976) Synthesis and characterization of the μ-disulphido complexes CrS_2Cr^{4+} and CrS_2HFe^{4+}. *Chem. Commun.,* 383–384.

Rickard, D. T. (1969) The chemistry of iron sulphide formation at low temperatures. *Stockholm Contributions in Geology, 20,* 67–95.

Rising, B. A. (1973) *Phase relations among pyrite, marcasite and pyrrhotite below 300°C.* Ph.D. Thesis, Pennsylvania State University, University Park, Pennsylvania.

Rochow, E. G. (1973) Germanium. In J. C. Bailar, Jr., *et al.,* Eds., *Comprehensive Inorganic Chemistry,* Vol. 2, p. 1–41. Pergamon, Oxford.

Schmidt, M. and W. Siebert (1973) Sulphur. In J. C. Bailar, Jr., *et al.,* Eds., *Comprehensive Inorganic Chemistry,* Vol. 2, p. 795–933. Pergamon, Oxford.

Schot, E. H., J. Ottemann and P. Omenetto (1972) Some new observations on mackinawite and valleriite. *Rend. Soc. Ital. Mineral. Petrol., 28,* 241–295.

Shoesmith, D. W., T. E. Rummery, M. G. Bailey and D. G. Owen (1979) Electrocrystallization of pyrite and marcasite on stainless steel surfaces. *J. Electrochem. Soc., 126,* 911–919.

———, P. Taylor, M. G. Bailey and D. G. Owen (1980) The formation of ferrous monosulfide polymorphs during the corrosion of iron by aqueous hydrogen sulfide at 22°C. *J. Electrochem. Soc., 127,* 1007–1015.

Takeno, S. (1965) Thermal studies on mackinawite. *J. Sci. Hiroshima Univ., Ser. C, 4,* 455–478.

——— and A. H. Clark (1967) Tetragonal $(Fe,Ni,Co)_{1+x}S$, mackinawite. *J. Sci. Hiroshima Univ., Ser. C, 5,* 287–293.

———, H. Zoka and T. Niihara (1970) Metastable cubic iron sulfide—with special reference to mackinawite. *Am. Mineral., 55,* 1639–1649.

Taylor, L. A. and L. W. Finger (1971) Structure refinement and composition of mackinawite. *Carnegie Inst. Wash. Year Book, 69,* 318–323.

Taylor, P. and D. W. Shoesmith (1978) The nature of green alkaline iron sulfide solutions and the preparation of sodium iron (III) sulfide, $NaFeS_2$. *Can. J. Chem., 56,* 2797–2802.

———, T. E. Rummery and D. G. Owen (1979a) On the conversion of mackinawite to greigite. *J. Inorg. Nucl. Chem., 41,* 595–596.

———, ——— and ——— (1979b) Reactions of iron monosulfide solids with aqueous hydrogen sulfide up to 160°C. *J. Inorg. Nucl. Chem., 41,* 1683–1687.

Teder, A. (1971) The equilibrium between elementary sulfur and aqueous polysulfide solutions. *Acta Chem. Scand., 25,* 1722–1728.

Tewari, P. H. and A. B. Campbell (1976) Dissolution of iron sulfide (troilite) in aqueous sulfuric acid. *J. Phys. Chem., 80,* 1844–1848.

———, G. Wallace and A. B. Campbell (1978) The solubility of iron sulfides and their role in mass transport in Girdler-Sulfide heavy water plants. *Atomic Energy of Canada Limited Report No. AECL-5960.*

Ward, J. C. (1970) The structure and properties of some iron sulphides. *Rev. Pure Appl. Chem., 20,* 175–206.

Wikjord, A. G., T. E. Rummery, F. E. Doern and D. G. Owen (1980) Corrosion and deposition during the exposure of carbon steel to H_2O–H_2S solutions at elevated pressures. *Corrosion Science,* in press.

Manuscript received, October 24, 1979;
accepted for publication, May 5, 1980.

American Mineralogist, Volume 65, pages 1031-1037, 1980

Sphalerite geobarometry in Bodenmais ore, Bavaria

NABIL Z. BOCTOR

Geophysical Laboratory, Carnegie Institution of Washington
Washington, D. C. 20008

Abstract

Pressure estimates obtained by the application of sphalerite geobarometry to the ore from Bodenmais, Bavaria, vary within single specimens and are strongly dependent on the mineral assemblage with which sphalerite coexists. The pressure estimated for sphalerite coexisting with pyrite and pyrrhotite ranges from 2.1 to 2.9 kbar, in agreement with the pressure of metamorphism estimated by Blümel and Schreyer (1977) from the silicate mineral assemblage. Evidence, however, that sphalerite equilibrated at temperatures below the temperature of metamorphism at Bodenmais (650°–700°C) is demonstrated by (1) depletion of FeS in sphalerite at its contact with monoclinic pyrrhotite; (2) the large variation in the iron content of sphalerite with exsolved chalcopyrite over a scale of tens of micrometers within individual crystals even for sphalerite coexisting with pyrite and pyrrhotite, yielding pressure estimates between 2 and 7 kbar; (3) the low Cu content of sphalerite (0.0–0.4 wt. percent) and the low Zn content of chalcopyrite (0.08–0.16 wt. percent) in the assemblage pyrrhotite–pyrite–sphalerite–chalcopyrite. These features are indicative of equilibration at temperatures below 250°C. The sphalerite geobarometer may not yield reliable pressure estimates for ores that underwent low-temperature reactions, or for Cu-bearing zinc sulfide ores. Attempts to apply the sphalerite geobarometer, however, provide valuable insights on post-metamorphic low-temperature equilibration in these ores.

Introduction

Sphalerite is one of the refractory sulfide minerals (Barton, 1970) that tend to preserve the chemical equilibrium achieved at the time of their formation or metamorphism. The theoretical principles of sphalerite geobarometry were first proposed by Barton and Toulmin (1966). Scott (1973) and Scott and Barnes (1971) calibrated the sphalerite geobarometer experimentally. Hutcheon (1978) calculated the *P–T–X* relations for the univariant assemblage sphalerite–pyrite–pyrrhotite and found that the calculated isobars are in agreement with the experimental data of Scott (1973).

The sphalerite geobarometer has been widely applied by various investigators (*e.g.,* Campbell and Ethier, 1974; Grove *et al.*, 1975; Lusk *et al.*, 1975; Scott, 1976; Scott *et al.*, 1977; Brown *et al.*, 1978; Rai, 1978) to estimate pressures for metamorphosed sulfide ores.

The present investigation represents an evaluation of sphalerite geobarometry in Bodenmais ore. The ore seems most suitable for such study because the assemblage sphalerite–pyrite–pyrrhotite required for sphalerite geobarometry is well preserved in the ore, earlier studies by Schreyer *et al.* (1964) suggest that the equilibrium composition of sphalerite has been preserved, and independent estimates of pressure and temperature of metamorphism at Bodenmais are available from a study of the silicate mineral assemblages (Blümel and Schreyer, 1977).

Geological setting

The sulfide ores at Bodenmais, Bavaria, form an elongated mass in highly metamorphosed migmatitic cordierite–sillimanite gneisses. The ore extends over at least 750 m parallel to the strike of the gneissosity of its country rocks (Schreyer *et al.*, 1964). The gneisses show numerous veinlets and schlieren of granitoid and pegmatoid materials, particularly in direct contacts with the ore. The regional metamorphism and its associated migmatization took place in early Hercynian times (Davis and Schreyer, 1962), and both ore and country rock now exposed at the surface seem to have endured essentially identical metamorphic conditions (Schreyer *et al.*, 1964).

A recent study of the pelitic and psammitic

0003–004X/80/0910–1031$02.00

gneisses in the Lam–Bodenmais area by Blümel and Schreyer (1977) delineated two major metamorphic zones: a sillimanite–K-feldspar zone with coexisting biotite + sillimanite (+ K-feldspar + quartz) and a cordierite–K-feldspar zone with coexisting biotite + cordierite±sillimanite (+ K-feldspar + quartz). The two metamorphic zones are related to each other by the multivariant reaction:

biotite + sillimanite + quartz
$\rightarrow$ cordierite + K-feldspar + H_2O

The temperature and pressure of metamorphism that formed the cordierite–K-feldspar zone were estimated by Blümel and Schreyer (1977) as 650°–700°C and 2–3 kbar, assuming water pressure to be equal to total pressure.

The origin of the sulfide ores at Bodenmais is still controversial; a summary of the various hypotheses was given by Schreyer *et al.* (1964). A contact metamorphic origin was proposed by Hegemann and Maucher (1933). Fischer (1938) suggested that the ore formed by preferential mobilization from the gneisses during regional metamorphism. Schröcke (1955) concluded, on the basis of petrological and structural studies, that the ore formed earlier than the regional metamorphic episode. Schreyer *et al.* (1964) objected to a contact metamorphic origin because of the lack of discordant late granite in contact or even in the vicinity of the ore. They noted, however, that the mineral assemblages show similarities to those of certain metamorphic ore deposits in the Fennoscandian shield that are generally known as Mg-rich skarn deposits.

Methods of study

The ore specimens were studied in both reflected and transmitted light. Electron microprobe analyses of sulfides were performed using an automated MAC-500 electron microprobe. Synthetic sphalerite, pyrrhotite of different compositions, and pure Cd, Mn, and Cu were used as standards. Data reduction was performed with the computer program Magic IV (Colby, 1971). For distinction between monoclinic and hexagonal pyrrhotite, both etching and X-ray diffraction were used.

Mineralogy

The samples were collected from a massive sulfide-rich ore from Barbarastollen, Silberberg, Bodenmais. The ore is composed mainly of sphalerite, pyrite, pyrrhotite, and chalcopyrite. Sphalerite occurs as large crystals that may reach 1 cm. Where coexisting with pyrite and pyrrhotite, the three-phase assemblage forms interlocking crystal aggregates in mutual contact. In many instances, sphalerite coexists with either pyrrhotite (Fig. 1a) or pyrite. The iron sulfides occasionally display intergrowths of sphalerite and anhedral inclusions of galena. Chalcopyrite is abundant in some specimens as large discrete crystals that may enclose small crystals of sphalerite. Chalcopyrite exsolutions in sphalerite are rare. Optical examination of pyrrhotite in reflected light reveals no intergrowths. However, on etching with 50 percent HI by the technique of Schwarcz and Harris (1970), monoclinic pyrrhotite was found to coexist with hexagonal pyrrhotite in many specimens. In addition to its oc-

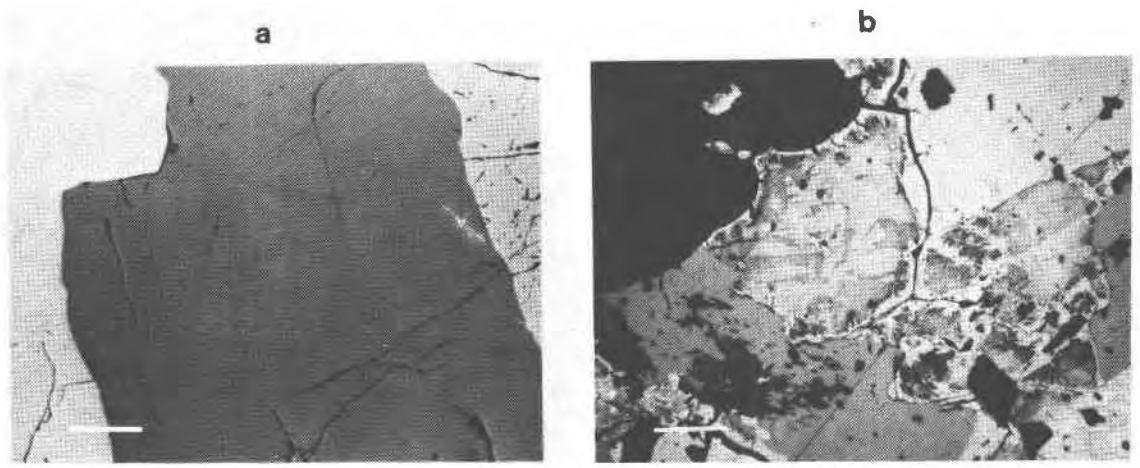

Fig. 1. (a) Large crystal of sphalerite in mutual contact with pyrrhotite. Bar = 1 mm; reflected light; oil immersion. (b) Pyrrhotite in contact with sphalerite, pyrite, and silicates etched with 50% HI. Note rims of unetched monoclinic pyrrhotite at contact with sphalerite, pyrite, and silicate and formation of monoclinic pyrrhotite along cracks. Bar = 1 mm; reflected light.

currence as discrete grains, monoclinic pyrrhotite is commonly observed as rims on hexagonal pyrrhotite, as thin veinlets along cracks, and as irregular domains within hexagonal pyrrhotite crystals (Fig. 1b). The rims of monoclinic pyrrhotite are well developed, particularly in pyrrhotite that coexists with sphalerite and pyrite as well as in pyrrhotite in contact with silicate minerals. In individual sphalerite crystals, rims in contact with monoclinic pyrrhotite are more translucent and show internal reflections that are lighter in color relative to the cores, due to variation in the iron content of sphalerite from rim to core. Pyrrhotite occasionally shows alteration to aggregates of pyrite, marcasite, or both. Magnetite is a rare mineral in some specimens, where it occurs in association with silicate minerals or pyrrhotite, but not with sphalerite. In all sulfide-rich specimens, the ore forms a matrix enclosing large granoblastic crystals of silicate minerals such as cordierite, K-feldspar, plagioclase, quartz, and biotite. Offshoots of pyrrhotite or pyrite are occasionally observed transecting the silicate minerals or following the cleavage planes in biotite.

Mineral chemistry

The average mole percent FeS in sphalerite coexisting with both pyrrhotite and pyrite varies from one sample to another, but lies within a narrow range of 15.8–16.5 (Table 1; Fig. 2). Within individual samples, the FeS content of sphalerite associated with pyrrhotite and pyrite varies from grain to grain and within individual grains as well. However, sphalerite in individual samples is essentially homogeneous (standard deviations in mole percent FeS are between 0.39 and 0.53). Sphalerite crystals in the immediate vicinity of monoclinic pyrrhotite showed a lower iron content at the rims relative to the cores (12–13 mole percent FeS at the rims *vs.* 15.5–16.5 mole percent FeS at the cores). This observation is true whether the sphalerite occurs in association with pyrrhotite alone or with pyrrhotite and pyrite.

Sphalerite in contact with either pyrite or pyrrhotite shows a slightly lower FeS content than sphalerite coexisting with both iron sulfides. The mole percent FeS in sphalerite coexisting with pyrite ranges between 15.5 and 16.0, whereas that in sphalerite coexisting with pyrrhotite ranges between 15.4 and 16.3.

Sphalerite with exsolved chalcopyrite shows a wide range in FeS content. A large crystal of sphalerite displaying exsolutions of chalcopyrite and showing mutual contacts with pyrrhotite and pyrite was analyzed. Fifteen analyses performed on this crystal show that it is inhomogeneous, having a mole percent FeS in the range 12.0 to 17.2, with an average of 14.6. This heterogeneity is real and cannot be attributed to sampling some of the chalcopyrite exsolutions during the analyses, because the concentration of copper in the fifteen sphalerite analyses is low, ranging between 0.03 and 0.38 wt. percent. Another

Table 1. Estimated pressures from sphalerite in different mineral assemblages in Silberberg ore, Bodenmais

Sample No.	Assemblage*	Mole % FeS in sphalerite		*P*, kbar**	*P*, kbar†
		Range	Average		
68919	sp, py, mpo, hpo	15.35-17.2	16.31 (0.48)††	2.3	1.7
	sp, py	15.5-15.98	15.42 (0.60)	3.4	2.7
Bo_1	sp, py, mpo, hpo	15.85-16.99	16.65 (0.31)	2.1	1.4
Bo_2	sp, py, mpo, (hpo)	14.92-16.67	15.80 (0.53)	2.9	2.1
	sp, mpo, (hpo)	14.97-15.95	15.44 (0.36)	3.5	2.7
Bo_7	sp, cp	9.63-14.41	13.49 (1.22)	6.1	5.6
Bo_8	sp, py, hpo, (mpo)	15.72-16.93	16.55 (0.39)	2.2	1.6
	sp, py, cp, hpo, (mpo)	12.00-17.20	14.57 (1.50)	4.8	4.0
	sp, hpo, mpo	15.72-16.53	16.2 (0.34)	2.4	1.8
Bo_{11}	sp, mpo, (hpo)	14.93-16.26	15.35 (0.35)	3.5	2.8

**Abbreviations: sp, sphalerite; py, pyrite; hpo, hexagonal pyrrhotite; mpo, monoclinic pyrrhotite; parentheses indicate minor amounts.*

***Pressure estimates from the experimentally determined isobars of Scott (1973, 1976).*

†Pressure estimates from the calculated isobars of Hutcheon (1978).

††Standard deviations.

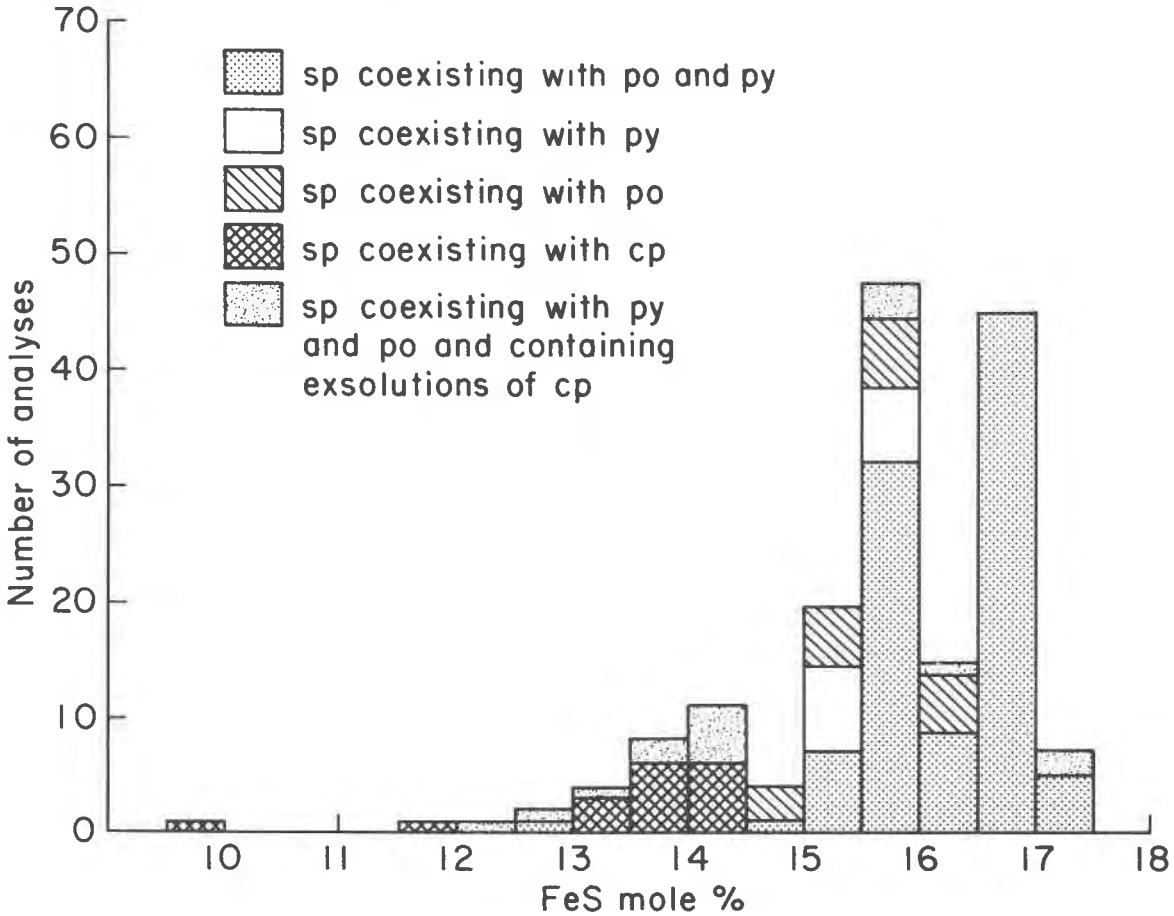

Fig. 2. Frequency distribution of mole percent FeS in sphalerite from different mineral assemblages.

large sphalerite crystal, totally surrounded by chalcopyrite and containing chalcopyrite exsolutions, was also analyzed. Pyrrhotite is present a few millimeters from the sphalerite–chalcopyrite assemblage, in direct contact with chalcopyrite but not with sphalerite. The mole percent FeS in the sphalerite crystal ranges between 9.63 and 14.4, with an average of 13.49 for 14 analyses. The Cu content of the analyzed sphalerite is in the range 0.09 to 9.32 wt. percent.

In all analyzed samples, sphalerite contains minor amounts of MnS and CdS in solid solution. The largest MnS content of sphalerite is 1.8 mole percent, whereas the CdS content does not exceed 0.3 mole percent. Representative microprobe analyses of sphalerite are given in Table 2.

The pyrrhotite composition ranges between 46.9 and 48.0 atom percent Fe. In specimens with small amounts of monoclinic pyrrhotite, the hexagonal phase shows little variation in composition, with standard deviations of the order of 0.2 atom percent Fe. In specimens where monoclinic pyrrhotite is abundant, the range for pyrrhotite composition reported above can be observed in a single polished section. Representative microprobe analyses of pyrrhotite are given in Table 3.

Sphalerite geobarometry

The mole percent FeS in sphalerite coexisting with pyrite and pyrrhotite was used to estimate the pressures from the experimentally determined isobars of Scott (1973, 1976) and from the calculated isobars of Hutcheon (1978) (Table 1). Pressures were also estimated for sphalerite coexisting with either pyrrhotite or pyrite alone and for sphalerite in chalcopyrite-bearing assemblages.

The temperature of metamorphism at Bodenmais was estimated by Blümel and Schreyer (1977) to be in the range 650°–700°C. The temperature estimate was based on the observation that the first products of anatexis at Bodenmais are found in the higher-

grade part of the sillimanite–K-feldspar zone, in which the assemblage muscovite–quartz is unstable. Therefore, the cordierite-producing reaction biotite + sillimanite + quartz → biotite + cordierite + K-feldspar + H_2O must lie below the intersection at 656°C and 3.6 kbar of the curve for the reaction muscovite + quartz → K-feldspar + Al_2SiO_5 + H_2O and the melting curve of granite. The metamorphic gradient must lie slightly above the point of intersection at 610°C and 2.25 kbar of the muscovite + quartz → K-feldspar + Al_2SiO_5 + H_2O reaction curve and the andalusite ⇄ sillimanite equilibrium. An upper temperature limit of 700°C was inferred from the reaction phlogopite + sillimanite + quartz → Mg-cordierite + K-feldspar + H_2O, which occurs at 5 kbar and 700°C but is expected to shift to lower pressures in iron-bearing rocks. A metamorphic temperature of 650°C was selected for sphalerite geobarometry. Although a change in temperature of 50°C may not always be crucial when considering silicate mineral equilibria, it is very significant in the case of the sphalerite geobarometer because there is a large change in the slope of the experimentally determined isobars in the temperature range 650°–700°C. If the upper temperature limit of 700°C is taken as the temperature of metamorphism, sphalerite compositions in the assemblage sphalerite–pyrrhotite–pyrite will fall outside the field for this ternary assemblage and plot in the pyrrhotite–sphalerite field. The pressure at 700°C will be ≃1.4 kbar lower than that estimated at 650°C.

The pressures estimated from the data of Scott (1973, 1976) for sphalerite coexisting with pyrite and pyrrhotite are in the range 2.1–2.9 kbar, in agreement with the 2–3 kbar pressure of metamorphism determined by Blümel and Schreyer (1977) from the silicate mineral assemblages. The maximum pressure estimated for sphalerite coexisting with pyrite is 3.4 kbar, whereas the minimum determined for sphalerite coexisting with pyrrhotite is 2.4 kbar.

The average mole percent FeS of sphalerite associated with chalcopyrite and pyrrhotite but not in direct contact with the latter yields a pressure of 6.1 kbar. The wide range in mole percent FeS for such sphalerite, however, corresponds to a pressure range of 5 to ~10 kbar. Similarly, the pressures determined for chalcopyrite-bearing sphalerite that coexists with pyrite and pyrrhotite range between 2 and 7.1 kbar, with an average of 4.7 kbar.

Pressures estimated from the calculated isobars of Hutcheon (1978) are somewhat lower than those estimated from the experimental data of Scott (1973, 1976); however, the two pressure estimates are in reasonable agreement.

Table 2. Representative electron microprobe analyses of sphalerite

	1*	2**	3†	4††	5††
Mn	0.67	0.89	0.41	0.11	...
Fe	9.75	8.91	8.68	7.98	5.71
Cu	0.01	0.01	0.05	0.16	0.32
Zn	55.96	55.72	56.13	57.16	60.34
Cd	0.24	0.38	0.26	0.47	0.31
S	33.93	34.27	34.30	33.94	34.04
	100.57	100.20	99.83	99.81	100.84

*Sphalerite coexisting with pyrrhotite and pyrite.
**Sphalerite coexisting with pyrrhotite.
†Sphalerite coexisting with pyrite.
††Sphalerite with chalcopyrite exsolutions.

Discussion

The application of sphalerite geobarometry to the ores from Bodenmais shows that the pressure estimates vary in single specimens and are dependent on the mineral assemblage with which sphalerite coexists, particularly the presence of exsolved chalcopyrite in sphalerite and its association with monoclinic pyrrhotite. Two observations suggest that the equilibrium composition of sphalerite attained during metamorphism was not preserved during the post-metamorphic history of the Bodenmais ore: (1) the depletion of sphalerite in FeS where it coexists with monoclinic pyrrhotite; (2) the large variation in the iron content of sphalerite in chalcopyrite-bearing assemblages, even within individual crystals.

During cooling of an assemblage of sphalerite, hexagonal pyrrhotite, and pyrite, monoclinic pyrrhotite forms at a temperature of 254°C. The formation of monoclinic pyrrhotite implies an increase of $f(S_2)$. Because a(FeS) is inversely proportional to $f(S_2)$, the iron content of sphalerite equilibrating with monoclinic pyrrhotite is expected to be lower than that of sphalerite in equilibrium with hexagonal pyrrhotite,

Table 3. Representative electron microprobe analyses of iron and copper sulfides

	Pyrrhotite			Pyrite	Chalcopyrite
	1	2	3	4	5
Mn	0.01	0.07	0.02	0.06	0.01
Fe	61.66	61.18	60.57	46.38	31.43
Cu	0.01	0.01	0.10	0.04	32.95
Zn	0.01	0.01	0.01	0.01	0.16
S	37.85	38.78	39.19	53.38	34.89
	99.51	100.04	99.89	99.86	99.48

as has been demonstrated experimentally (Scott and Kissin, 1973) and observed in other ores (*e.g.*, Grove *et al.*, 1975; Ethier *et al.*, 1976).

The large variation in FeS content of sphalerite-containing chalcopyrite exsolutions at Bodenmais was recently observed in other ores, *e.g.*, in Balmat-Edwards ore, New York (Brown *et al.*, 1978), and at Ducktown, Tennessee (Barton, personal communication, 1978). The addition of Cu to the system Zn–Fe–S is likely to affect sphalerite geobarometry because the solubility of FeS and CuS in sphalerite is dependent on the Fe:Cu ratio, temperature, and $f(S_2)$ (Wiggins and Craig, 1975). Hutchison and Scott (1978), however, found experimentally that Cu does not affect the geobarometer over its temperature-independent range and attributed the inhomogeneity in the FeS content of sphalerite to extensive exsolution of chalcopyrite. They interpreted the anomalous FeS content of chalcopyrite-bearing sphalerite as an indication of high temperature, former pyrrhotite–sphalerite equilibria, or disequilibrium assemblages (Hutchison and Scott, 1978). At Bodenmais, chalcopyrite-bearing sphalerite in mutual contacts with pyrrhotite and pyrite is compositionally inhomogeneous—a feature that cannot be attributed to exsolution of chalcopyrite alone (Hutchison and Scott, 1978). The exsolved phase in sphalerite from Bodenmais is always chalcopyrite, and no other Fe–Cu sulfides were observed in this ore. At the temperature of metamorphism at Bodenmais, chalcopyrite would be represented by a more-iron-rich intermediate solid solution (I_{ss}) (Barton, 1973; Cabri, 1973). Hutchison and Scott noted that in the temperature range 600°–350°C and at 5 kbar sphalerite in equilibrium with pyrrhotite, pyrite, and I_{ss} contains 0.0–0.4 wt. percent Cu in solid solution. The I_{ss} is unstable below 350°C, and chalcopyrite containing about 0.4 wt. percent Zn coexists with sphalerite, pyrrhotite, and pyrite. In the assemblage chalcopyrite–sphalerite–pyrrhotite–pyrite at Bodenmais, sphalerite contains 0.03–0.4 wt. percent Cu, while the coexisting chalcopyrite contains 0.08–0.16 wt. percent Zn in solid solution. The presence of chalcopyrite as the only exsolved Cu–Fe sulfide, its low Zn content, and the low Cu content of sphalerite suggest that the assemblage chalcopyrite–pyrrhotite–pyrite–sphalerite at Bodenmais equilibrated to temperatures below 350°C. In this assemblage the pyrrhotite that occurs as veinlets in sphalerite or at the immediate contact with sphalerite crystals is monoclinic. The presence of monoclinic pyrrhotite extends the limits of low-temperature equilibration of this assemblage to below 250°C. It also suggests that reaction with the monoclinic pyrrhotite is at least partly responsible for the inhomogeneity observed in these sphalerites.

The iron content of sphalerite coexisting with either pyrrhotite or pyrite is essentially similar to or slightly lower than that of sphalerite in the univariant assemblage sphalerite–pyrite–pyrrhotite. Under equilibrium conditions sphalerite in equilibrium with pyrrhotite alone or pyrite alone should have higher or lower iron contents, respectively, than sphalerite in equilibrium with both minerals. Scott (1976) observed that in many metamorphic terrains the equilibrium composition of sphalerite coexisting with iron-sulfide assemblages varies over a few meters or even a few centimeters. He concluded that in the absence of a fluid phase, the equilibrium domains of iron and sulfur are very small relative to the size of the ore body, and therefore several local equilibria are established in which the composition of sphalerite is buffered by the iron sulfide that occurs in its immediate vicinity. At Bodenmais, migmatization and the presence of hydrous phases strongly suggest that the $P(H_2O)$ was high during metamorphism. It is therefore possible that sulfur was mobile in the presence of a fluid phase and that the $f(S_2)$ varied within narrow ranges during the metamorphism of Silberberg ore; these factors would account for the similarity in composition of sphalerite coexisting with pyrite or pyrrhotite or both.

A different interpretation, however, was given by Barton and Skinner (1979) for the slightly lower iron content observed in sphalerite coexisting with pyrrhotite relative to sphalerite associated with pyrite and pyrrhotite in ores that underwent slow cooling, such as the Sullivan ore, British Columbia (Ethier *et al.*, 1976), and the Sulitjelma ore, Norway (Rai, 1978). Barton and Skinner interpreted this observation as an indication of metastability, which they attributed to the reluctance of pyrite to nucleate at low temperatures even under conditions of pyrite supersaturation. They suggested that the low FeS content of sphalerite in equilibrium with pyrrhotite relative to that in the three-phase assemblage pyrite–pyrrhotite–sphalerite can be explained by assuming that the composition of sphalerite can still be adjusted by reaction with pyrrhotite under conditions in which pyrite can no longer nucleate, although it may continue to grow on previously existing nuclei. Under such conditions the assemblage pyrite–pyrrhotite–sphalerite remains close to the equilibrium condition on cooling, whereas a pyrite-free assemblage undergoes

reaction, yielding a metastable assemblage of monoclinic pyrrhotite and FeS-depleted sphalerite (and possibly marcasite). In Bodenmais ore, monoclinic pyrrhotite commonly occurs in association with both hexagonal pyrrhotite and pyrite, and this association suggests that it is a metastable phase. The common occurrence of monoclinic pyrrhotite at the interface between hexagonal pyrrhotite and sphalerite and the depletion of sphalerite in the immediate vicinity of monoclinic pyrrhotite suggest that the reaction postulated by Barton and Skinner (1979) between hexagonal pyrrhotite and sphalerite apparently took place but did not proceed to completion.

In conclusion, the application of sphalerite geobarometry may not be a reliable method for estimating pressure in ores that underwent low-temperature reactions, or in Cu-bearing zinc sulfide areas. However, attempts to apply sphalerite geobarometry provide valuable insights on the post-metamorphic low-temperature equilibration in these ores.

Acknowledgments

I thank Dr. Gunnar Kullerud for kindly providing the samples used in this investigation and for useful discussions, and Dr. Paul B. Barton, Jr., for reviewing an early version of this manuscript, for stimulating discussions regarding the sphalerite geobarometer, and for providing a preprint of Barton and Skinner's article quoted in the manuscript. Critical comments on the manuscript by Dr. H. S. Yoder, Jr., and L. B. Wiggins are appreciated.

References

Barton, P. B., Jr. (1970) Sulfide petrology. *Mineral. Soc. Am. Spec. Pap., 3,* 187–198.

——— (1973) Solid solution in the system Cu–Fe–S. Part 1: The Cu–S and CuFe–S joins. *Econ. Geol., 68,* 455–465.

——— and B. J. Skinner (1979) Sulfide mineral stabilities. In H. L. Barnes, Ed., *Geochemistry of Hydrothermal Ore Deposits,* 2d ed., p. 278–403. Wiley, New York.

——— and P. Toulmin, III (1966) Phase relations in the Fe–Zn–S system. *Econ. Geol., 61,* 815–849.

Blümel, P. and W. Schreyer (1977) Phase relations in pelitic and psammitic gneisses of the sillimanite–potash feldspar and cordierite–potash feldspar zones in the Moldanubicum of the Lam–Bodenmais area, Bavaria. *J. Petrol., 18,* 431–459.

Brown, P. E., E. J. Essene and W. C. Kelly (1978) Sphalerite geobarometry in the Balmat-Edwards district, New York. *Am. Mineral., 63,* 250–257.

Cabri, J. L. (1973) New data on the phase relations in the Cu–Fe–S system. *Econ. Geol., 68,* 443–454.

Campbell, F. A. and V. G. Ethier (1974) Sulfur isotopes, iron content of sphalerites and ore textures in the Anvil ore body, Canada. *Econ. Geol., 69,* 482–493.

Colby, J. W. (1971) *Magic IV—a Computer Program for Quantitative Electron Microprobe Analysis.* Bell Telephone Laboratories, Inc., Allentown, Pa.

Davis, G. L. and W. Schreyer (1962) Altersbestimmungen an Gesteinen des ostbayerischen Grundgebirges und ihre geologische Deutung. *Geol. Rundsch., 52,* 146–169.

Ethier, V. G., F. A. Campbell, R. A. Both and N. R. Krouse (1976) Geological setting of the Sullivan ore body and estimates of temperatures and pressures of metamorphism. *Econ. Geol., 71,* 1570–1588.

Fischer, G. (1938) Über das Grundgebirge der Bayerischen Ostmark. Die Gneise nördlich des Pfahls. *Jahrb. Preuss. Geol. Landesanstalt, 59,* 289–352.

Grove, D. I., R. A. Binns, F. M. Barrett and K. G. McQueen (1975) Sphalerite compositions from Western Australian nickel deposits, a guide to equilibria below 300°C. *Econ. Geol., 70,* 391–396.

Hegemann, F. and A. Maucher (1933) Die Bildungsgeschichte der Kieslagerstätte im Silberberg bei Bodenmais. *Abhandl. Geol. Landesunters. Bayer. Oberbergamt, 11,* 4–36.

Hutcheon, I. (1978) Calculation of metamorphic pressure using sphalerite–pyrrhotite–pyrite equilibrium. *Am. Mineral., 63,* 87–95.

Hutchison, M. N. and S. D. Scott (1978) Effect of copper on the sphalerite geobarometer (abstr.). *Geol. Soc. Am. Abstracts with Programs, 3,* 426.

Lusk, J., F. A. Campbell and H. R. Krouse (1975) Application of sphalerite geobarometry and sulfur isotope geothermometry to ores of the Quemont Mine, Noranda, Quebec. *Econ. Geol., 70,* 1071–1083.

Rai, K. (1978) Micromineralogy and geochemistry of sphalerite from Sulitjelma Mining District, Norway. *Norsk Geol. Tidsskr., 58,* 17–32.

Schreyer, W., G. Kullerud and P. Ramdohr (1964) Metamorphic conditions of ore and country rock of the Bodenmais, Bavaria, sulfide deposit. *Neues Jahrb. Mineral. Abh., 101,* 1–26.

Schröcke, H. (1955) Petrotektonische Untersuchung des Cordieritgneisgebietes um Bodenmais im Bayer. Wald und der eingelagerten Kieslagerstätten. *Heidelberger Beitr. Mineral. Petrog., 4,* 464–503.

Schwarcz, E. J. and D. C. Harris (1970) Phases in natural pyrrhotite and the effect of heating on their magnetic properties and composition. *J. Geomagn. Geoelectr., 22,* 463–470.

Scott, S. D. (1973) Experimental calibration of the sphalerite geobarometer. *Econ. Geol., 68,* 466–474.

——— (1976) Application of the sphalerite geobarometer to regionally metamorphosed terrains. *Am. Mineral., 61,* 661–670.

——— and H. L. Barnes (1971) Sphalerite geothermometry and geobarometry. *Econ. Geol., 66,* 475–479.

———, R. A. Both and S. A. Kissin (1977) Sulfide petrology of the Broken Hill region, New South Wales. *Econ. Geol., 72,* 1410–1425.

——— and S. A. Kissin (1973) Sphalerite composition in the Zn–Fe–S system below 300°C. *Econ. Geol., 68,* 475–479.

Wiggins, L. B. and J. R. Craig (1975) A reconnaissance investigation of chalcopyrite–sphalerite relationships in the Cu–Fe–Zn–S system (abstr.). *Geol. Soc. Am. Abstracts with Programs, 7,* 1327.

Manuscript received, October 15, 1979;
accepted for publication, May 5, 1980.

American Mineralogist, Volume 65, pages 1038–1043, 1980

Spinodal decomposition in a titanomagnetite

PIERS P. K. SMITH

Department of Geology, Arizona State University
Tempe, Arizona 85281

Abstract

An optically homogeneous titanomagnetite from a dacite lava, containing 40 percent ulvöspinel, has been examined by transmission electron microscopy. A modulated structure is developed parallel to the {100} planes, with an average wavelength of 165Å. Electron diffraction patterns correspond to a single lattice, with pairs of satellite reflections convoluted about each reciprocal lattice point, parallel to the cube axes. The microstructure is consistent with exsolution having taken place by the mechanism of spinodal decomposition. The coherent spinodal temperature for this composition is calculated to be 95°C below the solvus temperature, at about 505°C. Application of interdiffusion data indicates a timescale for the transformation of the order of 4 hours.

Two possible implications for palaeomagnetism are: spinodal decomposition may increase the time-stability of the thermoremanent magnetization (TRM) carried by a titanomagnetite, and it may also be responsible for the partial self-reversal of TRM that has previously been reported in titanomagnetites of similar composition.

Introduction

It has been recognized for some time that a miscibility gap in the solid solution series magnetite (Fe_3O_4)–ulvöspinel (Fe_2TiO_4) leads to the development of exsolution intergrowths in titanomagnetites of intermediate composition. The resulting textures have been well documented in the literature; useful reviews have been presented by Ramdohr (1953) and Haggerty (1976). Exsolution takes place on the spinel {100} planes, giving rise to a characteristic cloth texture, the exact appearance depending on the relative proportions of the coexisting phases.

Members of the titanomagnetite series are of great importance in palaeomagnetic studies as they provide the principal carrier of thermoremanent magnetization (TRM) in most igneous rocks. A problem that has attracted considerable attention recently is the high stability of the TRM of many rocks, which requires the titanomagnetite to possess single magnetic domain properties. This may be due either to the presence of sub-micron titanomagnetite grains, small enough to exist as single magnetic domains, or to the subdivision of larger grains by means of intergrowth structures. The potential of exsolution intergrowths for imparting high magnetic stability to titanomagnetites has been demonstrated by Evans and Wayman (1974). An understanding of the relevance of this process to various rock types requires knowledge of the conditions under which the intergrowths may form. It is also important to determine the mechanism(s) by which the intergrowths form, as this controls their morphology. Knowledge of exsolution mechanisms in this system also has potential as an indicator of cooling rates (Price, 1979).

Mel'nikov and Khisina (1976) suggested from the morphology of an exsolved titanomagnetite that the intergrowths may form by spinodal decomposition. In this exsolution mechanism there is no nucleation event; phase separation proceeds by the gradual growth of sinusoidal fluctuations in composition (Cahn, 1968). These compositional waves may ultimately coarsen to give rise to distinct interfaces between two phases, but in the initial stages of decomposition no interfaces are created. The structure described by Mel'nikov and Khisina consisted of a periodic array of magnetite-rich cubes in an ulvöspinel-rich matrix, the spacing of the precipitates being about 425Å. Although this texture is indeed very similar to that produced by coarsening of spinodally-decomposed metal alloys, it does not prove that spinodal decomposition has taken place, as a similar structure could form by homogeneous nucleation.

The present contribution describes an electron mi-

0003–004X/80/0910–1038$02.00

croscopic study of a titanomagnetite with a modulated texture that has not coarsened into a two-phase structure. The results provide a strong indication that spinodal decomposition does occur in this system.

Specimen description and experimental procedure

The material examined was titanomagnetite contained in a banded andesite–dacite lava from the SE flank of Mt. Hakone, Japan (sample 15383, Manchester University collection). The titanomagnetite occurs as phenocrysts up to 1 mm across, the typical size being about 200 μm, and appears homogeneous under the reflected light microscope. Analysis with the electron microscope microanalyzer EMMA-4 gave an ulvöspinel content of 40±2 percent, assuming titanomagnetite stoichiometry. Coexisting ilmenite phenocrysts were found to have a hematite content of 9.2±1 percent. Both phases contain a trace of manganese, amounting to less than 1 weight percent MnO. Application of the Buddington and Lindsley (1964) geothermometer–oxygen geobarometer gives equilibration conditions of $T = 990°C$ and $\log f_{O_2} = -11.0$ for this pair of compositions.

Samples were thinned by ion-beam bombardment, and examined in Philips EM301 and JEOL JEM 100B electron microscopes operating at 100 kV.

Observations

In the electron microscope the titanomagnetite displays a fine-scale modulated texture on the {100} cube planes. This texture is best illustrated in micrographs taken with the electron beam axis parallel to a fourfold symmetry axis, say [001], in which case modulations are seen parallel to the traces of the (100) and (010) planes (Fig. 1). This modulated texture was developed uniformly throughout 3 ion-thinned grains which were examined. The average wavelength of the modulations as estimated from the micrographs is ~150Å.

Electron diffraction patterns in the [001] orientation were recorded, initially using a relatively small diffraction constant (~20Å mm) in order to include the whole of the zero-order Laue zone. Under these conditions the diffraction pattern corresponds to a single cubic phase with absences appropriate to spinel space-group symmetry ($Fd3m$), and slight streaking of reflections is observed parallel to the a* and b* reciprocal lattice directions (Fig. 2). When the same pattern is recorded using a somewhat greater camera length (diffraction constant ~60Å mm), two pairs of satellite reflections are resolved about each reflection, parallel to a* and b* (inset, Fig. 2). The

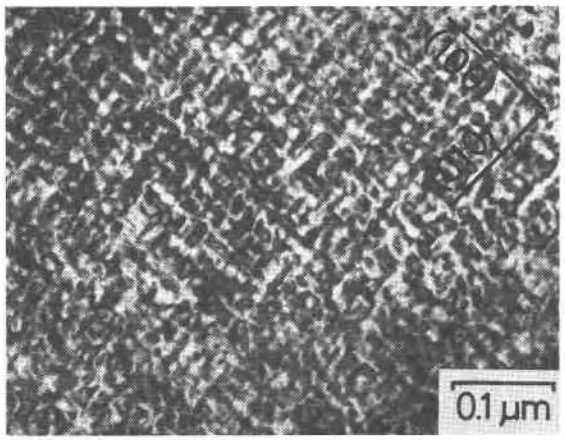

Fig. 1. Bright-field micrograph showing the modulated texture developed parallel to the {100} planes of the titanomagnetite. Beam axis parallel to [001].

presence of satellite reflections convoluted about a single reciprocal lattice point is a characteristic feature of spinodally-decomposed materials, the satellites resulting from the periodicity of the compositional waves. In the present case the spacing of the satellites indicates a modulation wavelength of 165±5Å, in agreement with that obtained from the images.

The nature of the {100} modulations was further investigated by means of dark-field imaging. Cahn (1962) showed that spinodal decomposition in crystals with cubic symmetry should lead to the development of compositional modulations with wavefronts parallel to either {100} or {111}, depending on the nature of the elastic anisotropy. No elastic constants are available for titanomagnetites, but the data given for magnetite by Birch (1966) indicate that the modulations will develop on {100}, as is the case for most cubic materials. The contrast seen in the electron microscope arises from the net strain in the lattice due to the periodic change in lattice spacing. Dark-field imaging with different diffracting vectors **g** may be used to determine the orientation of the displacement associated with each compositional wave; a displacement **R** will only lead to contrast in the image when $\mathbf{g} \cdot \mathbf{R} \neq 0$. Contrast arising from the change in structure factor can be shown to be negligible by means of a calculation similar to that described by Cadoret and Delavignette (1969) for spinodally-decomposed Cu–Ni–Fe alloys.

Figure 3 is a dark-field micrograph taken with the operating reflection 400, and the modulated contrast is only visible perpendicular to the diffraction vector. In dark-field micrographs where the diffraction vec-

tor is not parallel to one of the crystallographic axes, for example $\mathbf{g} = 440$ (Fig. 4), cross-hatched contrast is seen, indicating that $\mathbf{g} \cdot \mathbf{R} \neq 0$ for both the (100) and (010) modulations. These results are similar to those obtained by Laughlin and Cahn (1975) for spinodally-decomposed Cu–Ti alloys, and are consistent with a model involving longitudinal displacement waves along the ⟨100⟩ directions.

Discussion

There has been much consideration in the literature for both metals (Hilliard, 1970) and minerals (Champness and Lorimer, 1976) of what constitutes proof that spinodal decomposition occurs in a given system. Conclusive proof requires either a detailed study of small-angle X-ray scattering, in order to follow the development of modulations during the early stages of the transformation, or application of the microstructural time sequence method of Laughlin and Cahn (1975). A more recent approach has been to reveal the variation in lattice spacing by means of high resolution electron microscopy (Wu *et al.*, 1978).

The presence of satellite reflections in X-ray or electron diffraction patterns has long been used as an indicator of spinodal decomposition. Some authors have objected to this, pointing out that Ardell and Nicholson (1966) described a periodic structure produced by the alignment of homogeneously nucleated precipitates. However, this periodicity only developed during the coarsening of an initially random distribution of precipitates, and micrographs demonstrated the presence of two distinct phases. Thus Laughlin and Cahn (1975) concluded that "periodicity and alignment from the start of a transformation is a strong indication of spinodal decomposition." The titanomagnetite described in the present paper fulfills this criterion, since the electron micrographs and diffraction pattern show that coarsening to a two-phase structure has not taken place.

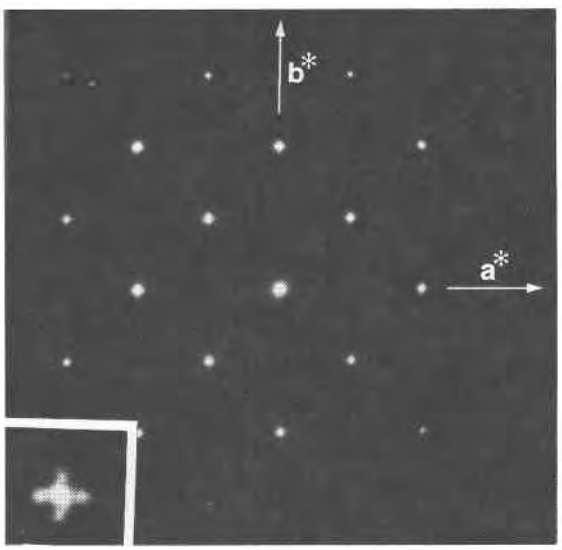

Fig. 2. A [001] electron diffraction pattern of the titanomagnetite. The inset, recorded at a higher instrumental magnification, shows the satellites about the 840 reflection.

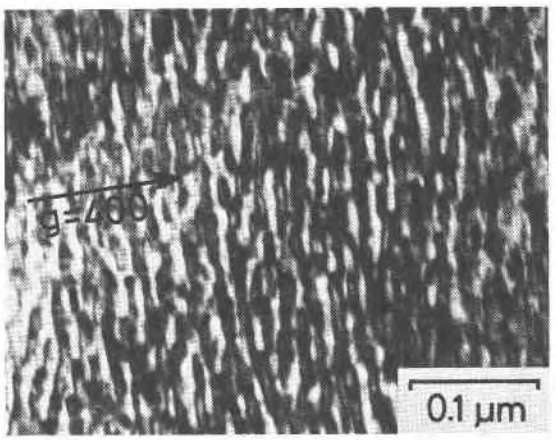

Fig. 3. Dark-field micrograph taken using the operating reflection 400. Only the modulations perpendicular to this diffracting vector are in contrast.

A similar modulated microstructure resulting from spinodal decomposition has previously been recognized in the $CoFe_2O_4$–Co_3O_4 spinel ferrites (Takahashi *et al.*, 1971). Moore and Crawford (1978) described a periodic structure in some natural chrome-rich magnesioferrite spinels and ascribed this to spinodal decomposition, but the structures were considerably coarsened. Price (1979) considered that a mottled texture seen in a titanomagnetite with $x = 0.08$[1] resulted from spinodal decomposition. However, a similar texture has been reported in TEM studies of several ion-thinned spinels, including pure Fe_3O_4 (Smith, 1979 a,b; Putnis, 1979), and it seems likely that this texture is produced during ion-thinning (Smith, 1980). In the present example the random, mottled texture is observed immediately adjacent to the thin edge of the specimen, but the directional, periodic texture dominates in thicker areas. This is consistent with the view that a thin surface layer becomes damaged during ion-thinning.

Published optical micrographs of magnetite$_{ss}$–ulvöspinel$_{ss}$ intergrowths all represent the hypabyssal or plutonic environments (Haggerty, 1976). A com-

[1] Throughout the present paper x denotes the mole fraction of ulvöspinel in the solid solution $(1 - x)Fe_3O_4$–xFe_2TiO_4.

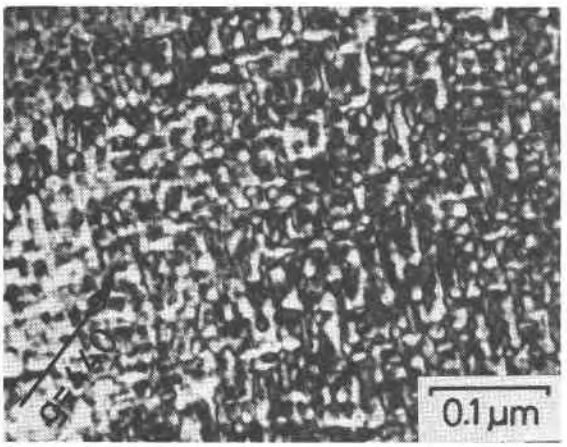

Fig. 4. Dark-field micrograph taken with the diffracting vector 440. Both sets of modulations are in contrast.

mon feature of these samples is the very uniform development of the cloth texture throughout the grain. This would be expected for spinodal decomposition, which occurs independently of any nucleation sites, and it may well be that such examples are coarsened spinodal textures. However, transformation mechanisms cannot be identified positively from coarsened microstructures, and it is also possible that homogeneous nucleation occurs at the slower cooling rates associated with these environments.

One attraction of spinodal decomposition is that a quantitative theory exists to describe it, and it thus holds considerable promise as an indicator of thermal history, at least in the initial stages of transformation. This is in contrast to exsolution mechanisms involving a nucleation step, for which the theory is less well defined. It is thus possible to estimate the temperature at which the microstructure in titanomagnetite 15383 developed, and the time taken for the transformation.

The most detailed study of the subsolidus phase diagram of the titanomagnetite system is that of Kawai (1956), giving the solvus depicted in Figure 5. The sometimes-quoted solvus of Vincent *et al.* (1957) was determined using an incorrect value for the cell parameter of ulvöspinel, leading to considerable errors in the positioning of the ulvöspinel-rich limb of the solvus. Use of the correct value for this cell parameter improves the agreement between the two studies. Kawai found difficulty in determining the low-temperature part of the diagram due to slow reaction rates, and based this part of the solvus on the compositions of natural examples. However, the crest of the solvus was determined experimentally to be at 600°C and $x = 0.42$.

The titanomagnetite from sample 15383 has a composition very close to the critical composition, and will therefore be assumed to have an equilibrium solvus temperature of 600°C. Since the equilibrium solvus and the chemical spinodal, defined by the locus of $(\partial^2 G/\partial x^2)_{T,P} = 0$, coincide at the critical composition, the chemical spinodal temperature may also be taken to be 600°C. Cahn (1968) showed that the coherent spinodal is depressed below the chemical spinodal by the amount $2\eta^2 Y/S''$, where η is the fractional misfit in cell parameter per unit change in composition, Y is a function of the elastic constants, and S″ is the second derivative with respect to composition of the entropy per unit volume. Values of η and Y may be determined using published cell parameters (Lindsley, 1965) and elastic constants (Birch, 1966). The factor S″ may be calculated using Rumble's (1977) model for the configurational entropy of titanomagnetites, and the generally accepted model of O'Reilly and Banerjee (1965) for the cation distribution in this series. For the composition $x = 0.40$ this gives a value of 95°C for the depression of the spinodal, leading to a coherent spinodal temperature of 505°C. No attempt is made here to calculate the rest of the coherent spinodal, as the low-temperature solvus data are considered insufficiently accurate to warrant this.

The time taken to form the observed microstructure may be estimated from the data of Freer

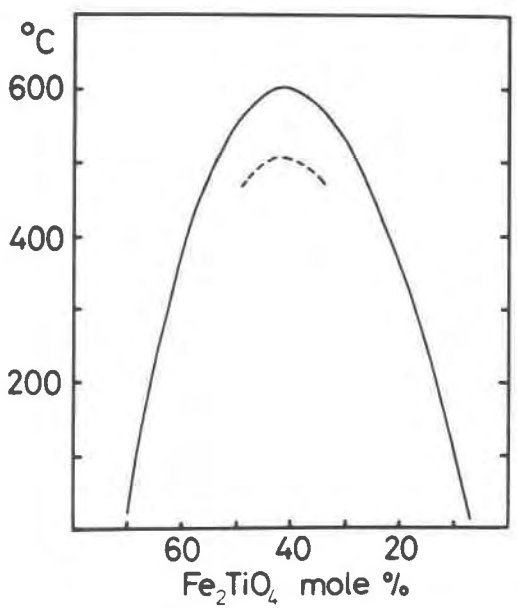

Fig. 5. Solvus for the system Fe_3O_4–Fe_2TiO_4, after Kawai (1956). The dotted line marks the crest of the coherent spinodal, as calculated in the present study.

and Hauptman (1978) for interdiffusion between pure Fe_3O_4 and titanomagnetite with $x = 0.20$. The exponential expression obtained by these authors leads to an interdiffusion constant of 1.1×10^{-17} cm^2/sec at 500°C. Freer and Hauptman showed how one may calculate the approximate time taken to create a lamellar intergrowth, given the interdiffusion constant and the scale of the microstructure. Taking the average interdiffusion distance in the spinodally-decomposed titanomagnetite to be half of the modulation wavelength, one obtains a transformation time of ~4 hours. This figure should only be treated as a rough guide, since the classical diffusion laws are not strictly applicable in the immediate vicinity of the spinodal, but it does indicate that this kind of microstructure may form in titanomagnetites on the timescale of laboratory experiments.

Implications for palaeomagnetism

Exsolution in titanomagnetites was previously considered to be restricted to the hypabyssal and plutonic environments (Haggerty, 1976); the present results show that submicroscopic exsolution may occur in volcanic titanomagnetites of suitable composition. As mentioned in the introduction, such exsolution can lead to an increased coercivity, and therefore an increased time-stability, of the TRM carried by a rock. An analogous increase in coercivity was observed in spinodally-decomposed cobalt ferrite by Takahashi *et al.* (1971). The form of the titanomagnetite solvus indicates that the coherent spinodal will be at prohibitively low temperatures for spinodal decomposition to occur in titanomagnetites from submarine tholeiites, which typically have ulvöspinel contents of ~0.6–0.7; a TEM study of such a sample did not reveal any exsolution (Smith, 1979a). Spinodal decomposition is probably restricted to titanomagnetites from intermediate and acidic volcanic suites, which have lower ulvöspinel contents.

Fine-scale exsolution in titanomagnetite may also be relevant to the problem of self-reversal of the natural remanent magnetization of rocks. Although it is now well established that reversed magnetizations of rocks are almost exclusively the result of geomagnetic field reversals, there is still some interest in possible mechanisms for the complete or partial self-reversals recorded in a few rocks.

Shcherbakov *et al.* (1975) described a partial self-reversal that occurs in some synthetic mixed ferrites and in a natural Fe_3O_4–Mg_2TiO_4 spinel. The effect is manifested as a sharp peak in the thermal demagnetization curve of a thermoremanent magnetization (TRM) near the final Curie point, implying that the partial TRM acquired by the sample over this temperature range is reversed. Bol'shakov *et al.* (1977) showed that this behavior is consistent with a model in which chemical inhomogeneities on a scale of ~100Å lead to a diffuse Curie temperature, the chemical composition being a continuous function of position. Spinodal decomposition clearly provides a possible mechanism to produce this kind of inhomogeneity. A similar partial self-reversal was observed by Petherbridge *et al.* (1974) in some partially unmixed synthetic titanomagnetites. The anomalous peak was present for samples cooled from 1350°C to room temperature over a 15-hour period, but was absent in a rapidly quenched sample. The timescale indicated for this exsolution process is thus similar to that calculated for spinodal decomposition in the present paper.

A natural example of a partially self-reversed rock is the lava from Mt. Etna, Sicily, described by Heller *et al.* (1979). The TRM of this rock is carried by optically homogeneous titanomagnetite that is zoned from $x = 0.34$ to 0.45. The self-reversal was ascribed to magnetostatic interaction between exsolved Ti-rich and Ti-poor phases, with compositions x ~0.12 and ~0.55. In view of the similar bulk composition and geological environment to the titanomagnetite from lava 15383, it is likely that the Etna material also exsolved by spinodal decomposition. Transmission electron microscopy of such thermomagnetically characterized samples would be of great value in understanding self-reversal mechanisms of the ferrimagnetic spinels.

Acknowledgments

This research was commenced at the University of Manchester during the tenure of a Natural Environment Research Council fellowship, which I gratefully acknowledge. I thank Professor J. Zussman (Department of Geology) and Professor E. Smith (Department of Metallurgy) for the provision of laboratory facilities during this period.

The study was completed in the electron microscope laboratory in the Center for Solid State Science at Arizona State University, with financial support from NSF grant EAR 77-00128. I thank David R. Veblen for reviewing the manuscript.

References

Ardell, A. J. and R. B. Nicholson (1966) On the modulated structure of aged Ni–Al alloys. *Acta Metallurgica, 14,* 1295–1309.

Birch, F. (1966) Compressibility; elastic constants. In S. P. Clark, Ed., *Handbook of Physical Constants,* p. 97–173. Geol. Soc. Am. Mem. 97.

Bol'shakov, A. S., A. K. Gapeyev, D. M. Dashevskaya, B. N. Mel'nikov and V. P. Shcherbakov (1977) Study of the thermoremanent magnetization anomaly in synthetic ferrite. *Dokl.*

Akad. Nauk SSSR, 235, 295–297. [transl. *Dokl. Earth Sci. Sections, 235,* 13–15 (1977)].

Buddington, A. F. and D. H. Lindsley (1964) Iron–titanium oxide minerals and synthetic equivalents. *J. Petrol., 5,* 310–357.

Cadoret, R. and P. Delavignette (1969) Étude de la decomposition spinoidale au microscope électronique dans les alliages CuNiFe. *Phys. Status Solidi, 32,* 853–865.

Cahn, J. W. (1962) On spinodal decomposition in cubic crystals. *Acta Metallurgica, 10,* 179–183.

——— (1968) Spinodal decomposition. *Trans. Metallurgical Soc. AIME, 242,* 166–180.

Champness, P. E. and G. W. Lorimer (1976) Exsolution in silicates. In H.-R. Wenk, Ed., *Electron Microscopy in Mineralogy,* p. 174–204. Springer-Verlag, Heidelberg.

Evans, M. E. and M. L. Wayman (1974) An investigation of the role of ultra-fine titanomagnetite intergrowths in palaeomagnetism. *Geophys. J. R. Astron. Soc., 36,* 1–10.

Freer, R. and Z. Hauptman (1978) An experimental study of magnetite–titanomagnetite interdiffusion. *Phys. Earth and Planetary Interiors, 16,* 223–231.

Haggerty, S. E. (1976) Opaque mineral oxides in terrestrial igneous rocks. In D. Rumble, III, Ed., *Oxide Minerals,* p. Hg101–Hg300. Short Course Notes, Vol. 3, Mineralogical Society of America, Washington, D.C.

Heller, F., H. Markert and E. Schmidbauer (1979) Partial self-reversal of natural remanent magnetization of an historical lava flow of Mt. Etna (Sicily). *J. Geophys., 45,* 235–257.

Hilliard, J. E. (1970) Spinodal decomposition. In *Phase Transformations,* p. 497–560. American Society for Metals, Metals Park, Ohio.

Kawai, N. (1956) Subsolidus phase relation in titanomagnetite and its significance in rock-magnetism. *Proc. 20th Int. Geol. Congr., 11A,* 103–120.

Laughlin, D. E. and J. W. Cahn (1975) Spinodal decomposition in age-hardening copper–titanium alloys. *Acta Metallurgica, 23,* 329–339.

Lindsley, D. H. (1965) Iron–titanium oxides. *Carnegie Inst. Wash. Year Book, 64,* 144–148.

Mel'nikov, B. N. and N. R. Khisina (1976) Spinodal decomposition and related partial self-reversal of magnetization in titanomagnetite from the rift zones of Africa. *Izvestiya Akad. Nauk. SSSR; Earth Physics, No. 10, 1976,* 84–92. [transl. *Izvestiya Akad. Nauk. SSSR; Phys. Solid Earth, 12,* 672–676 (1977)].

Moore, A. C. and D. Crawford (1978) Spinodal decomposition in naturally occurring non-cubic spinels. *Nature, 274,* 237–239.

O'Reilly, W. and S. K. Banerjee (1965) Cation distribution in titanomagnetites $(1-x)Fe_3O_4$–xFe_2TiO_4. *Phys. Lett., 17,* 237–238.

Petherbridge, J., A. L. Campbell and Z. Hauptman (1974) Magnetic behavior of some partially unmixed titanomagnetites. *Nature, 250,* 479–480.

Price, G. D. (1979) Microstructures in titanomagnetites as guides to cooling rates of a Swedish intrusion. *Geol. Mag., 116,* 313–318.

Putnis, A. (1979) Electron petrography of high-temperature oxidation in olivine from the Rhum Layered Intrusion. *Mineral. Mag., 43,* 293–296.

Ramdohr, P. (1953) Ulvöspinel and its significance in titaniferous iron ores. *Econ. Geol., 48,* 677–688.

Rumble, D. (1977) Configurational entropy of magnetite–ulvöspinel$_{ss}$ and hematite–ilmenite$_{ss}$. *Carnegie Inst. Wash. Year Book, 76,* 581–584.

Shcherbakov, V. P., A. S. Bol'shakov and B. N. Mel'nikov (1975) Anomalous temperature dependence of the remanent magnetization of ferromagnetics. *Dokl. Akad. Nauk, SSSR, 224,* 1315–1317. [transl. *Dokl. Earth Sci. Sections, 224,* 25–27 (1975)].

Smith, P. P. K. (1979a) The identification of single-domain titanomagnetite particles by means of transmission electron microscopy. *Can. J. Earth Sci., 16,* 375–379.

——— (1979b) The observation of enantiomorphous domains in a natural maghemite. *Contrib. Mineral. Petrol., 69,* 249–254.

——— (1980) Microstructures in titanomagnetite: discussion of a paper by G. D. Price. *Geol. Mag.,* in press.

Takahashi, M., J. R. C. Guimaraes and M. E. Fine (1971) Spinodal decomposition in the system $CoFe_2O_4$–Co_3O_4. *J. Am. Ceram. Soc., 54,* 291–295.

Vincent, E. A., J. B. Wright, R. Chevallier and S. Mathieu (1957) Heating experiments on some natural titaniferous magnetites. *Mineral. Mag., 31,* 624–655.

Wu, C. K., R. Sinclair and G. Thomas (1978) Lattice imaging and optical microanalysis of a Cu–Ni–Cr spinodal alloy. *Metallurgical Trans., 9A,* 381–387.

Manuscript received, January 4, 1980;
accepted for publication, March 7, 1980.

American Mineralogist, Volume 65, pages 1044–1049, 1980

The Mössbauer spectrum of ferrihydrite and its relations to those of other iron oxides

ENVER MURAD AND UDO SCHWERTMANN

Lehrstuhl für Bodenkunde, Technische Universität München
D-8050 Freising-Weihenstephan, Federal Republic of Germany

Abstract

The superparamagnetic Mössbauer spectra observed for ferrihydrite at room temperature are complex, and require fitting with at least two Lorentzian doublets to properly delineate the experimental data. Characteristic for such fits are a low (0.54 mm · s^{-1}) and high (0.90 mm · s^{-1}) quadrupole splitting. At 4K the Mössbauer spectrum of this mineral shows magnetic hyperfine splitting with a wide distribution of hyperfine fields, and a maximum absorption near 500 kOe.

Similar spectra are also shown by other iron oxides, especially hematite, of extremely small particle size (<100Å). This emphasizes basic structural relationships between the different iron oxides, but limits the applicability of Mössbauer spectroscopy as an analytical tool in this particle size range.

Introduction

Ferrihydrite is a naturally occurring iron oxide of bulk composition $5Fe_2O_3 \cdot 9H_2O$. Two different formulae proposed for ferrihydrite are $Fe_5HO_8 \cdot 4H_2O$ (Towe and Bradley, 1967) and $Fe_5(O_4H_3)_3$ by Chukhrov *et al.* (1972). From infrared absorption spectra Russell (1979) suggested OH to be an essential part of the structure and arrived at the formula $Fe_2O_3 \cdot 2FeOOH \cdot 2.6H_2O$.

Ferrihydrite is usually identified by X-ray diffraction which, however, is not very sensitive because this mineral yields very broad lines and often incomplete patterns due to small particle size (<100Å) and/or poor structural order. High solubility in ammonium oxalate can give an indication of the presence of ferrihydrite in natural samples (Schwertmann, 1964; 1979).

No information on the Mössbauer spectrum of this mineral from soils or sediments has been published to date. On the other hand, some earlier data on "amorphous iron oxide gels" may, in fact, refer to ferrihydrite. The Mössbauer spectrum of ferrihydrite may also be related to that of the iron core of the protein ferritin, to which it appears to be structurally similar (Harrison and Hoy, 1973).

In this study the Mössbauer spectra of synthetic and natural ferrihydrites are described and compared to published and our own (mostly unpublished) data on the other common iron oxide minerals.

Sample description

Of the synthetic samples studied, 13/0 was prepared by neutralizing a 0.5M $Fe(NO_3)_3$ solution with NH_4OH to a pH of 7.5, washing free of electrolyte, and freeze-drying. Sample DLF5 was prepared by hydrolyzing a 0.06M $Fe(NO_3)_3$ solution at 85°C, dialyzing the sol against distilled water, and freeze-drying (Towe and Bradley, 1967). Sample PT79 was prepared by passing O_2 through a 0.0125M $FeCl_2$ solution in the presence of 50 ppm SiO_2 (to suppress lepidocrocite formation) at pH 7.

The natural samples 2, 40A, 31, N162, and N196 were formed by rapid oxidation of ferriferous waters, resulting in heavy ochreous precipitates. The first three samples are from various localities in Finland (Carlson and Schwertmann, unpublished manuscript). N162 is from the vicinity of Hannover in N. Germany (Schwertmann and Fischer, 1973), and N196 is from the type locality in Kazakhstan, USSR (Chukhrov *et al.*, 1972).

X-ray diffraction shows these samples to cover a range of ferrihydrite crystallinity from a fully developed six-line pattern (31, N162, PT79, DLF5) to a very poorly ordered material which shows only the two *hk* lines at 2.5 and 1.5Å (2, 13/0). The six-line pattern is that of a well developed ferrihydrite; the two-line pattern corresponds to the most poorly ordered material, which consists only of planar arrangements of $Fe(O,OH,OH_2)_6$ octahedra without

0003–004X/80/0910–1044$02.00

any stacking perpendicular to that plane. The two lines correspond to the main Fe–Fe distances of 2.52 and 1.45Å within this structure (Feitknecht *et al.*, 1973). This material can be considered to have the most primitive arrangement of $Fe(O,OH,OH_2)_6$ octahedra, and may be a precursor of numerous other iron oxides. In nature it was found to occur in close association with ferrihydrite, feroxyhite, and other iron oxides (Carlson and Schwertmann, unpublished manuscript).

Ratios of oxalate (Schwertmann, 1964) to dithionite soluble iron (Mehra and Jackson, 1960) were over 0.9 in all samples except PT79 (0.56) and DLF5 (0.45), indicating ferrihydrite to constitute at least the dominant part of the total iron oxides.

Experimental methods

Mössbauer spectra were taken using a $^{57}Co/Rh$ source mounted on a loudspeaker-type drive system. Spectra were run at room temperature and after cooling both source and absorber to about 130 and 4K in a cryostat. Absorbers for the room-temperature spectra consisted of 11 mg sample mixed with 34 mg sugar (to improve mechanical stability), spread uniformly over an area of 2 cm^2 in a plexiglas holder. At lower temperatures 40 mg of undiluted sample were used. The transmitted radiation was registered with a proportional counter and fed into a 1024-channel analyzer. Counting proceeded until sufficiently good statistics, visually monitored with an oscilloscope, had been attained. The data were folded, plotted, and Lorentzian curve fits carried out by a computer procedure. Pure metallic iron served as a standard for velocity calibration and as reference material for isomer shifts.

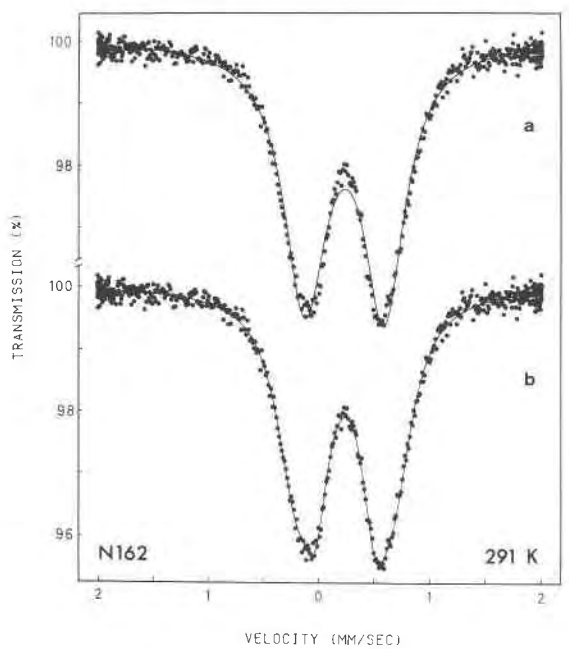

Fig. 1. Mössbauer spectrum of natural ferrihydrite N162 at room temperature, fitted with (a) one Lorentzian doublet (χ^2 = 1.41), (b) two Lorentzian doublets (χ^2 = 0.89).

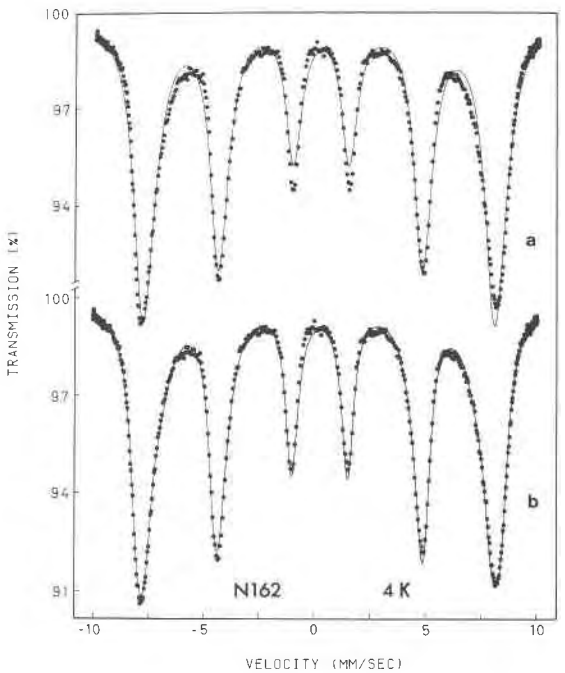

Fig. 2. Mössbauer spectrum of natural ferrihydrite N162 at 4K, fitted with (a) one sextet (χ^2 = 14.0), (b) three sextets (χ^2 = 3.4).

Results

At room temperature and 130K the Mössbauer spectra showed only a paramagnetic doublet. At 4K all spectra were completely split magnetically.

Fitting one doublet to the room temperature and 130K spectra, and one sextet to the spectra taken at 4 K resulted in only moderate coincidence with the actual line shapes (Figs. 1a, 2a). Line widths computed from such fits were exceedingly high, averaging about 0.45 $mm \cdot s^{-1}$ at room temperature, 0.53 $mm \cdot s^{-1}$ at 130K, and over 1 $mm \cdot s^{-1}$ at 4K.

Fitting two doublets to the room-temperature spectra lowered the χ^2 values (normalized by dividing χ^2 by the number of channels minus fit parameters) from an average of 1.45 to 0.95. The two doublets differ noticeably in their quadrupole splittings (0.89 and 0.54 $mm \cdot s^{-1}$) and line widths (0.45 and 0.31 $mm \cdot s^{-1}$), whereas the isomer shifts (0.34 and

0.35 mm · s^{-1}) vary significantly neither between the two doublets, nor from sample to sample.

The magnetically split spectra had to be fitted with three sextets to obtain acceptable χ^2 values. These fits, constrained to have identical isomer shifts for all sextets, showed the samples to have low and only slightly different quadrupole splittings, but a wide spread of magnetic hyperfine fields between about 445 and 510 kOe. A more realistic analysis was attained by fitting these spectra with series of up to twelve sextets, constrained to have identical line widths, isomer shifts, and quadrupole splittings. Such fits showed the ferrihydrites to possess distributions of magnetic hyperfine fields that are slightly skewed towards lower values, with maxima somewhat below 500 kOe (Fig. 3).

Parameters resulting from the individual fits of the room temperature and 4K spectra are given in Table 1. The spectra registered at 130K resemble those at room temperature (except for increased line widths), and are therefore not included in the table.

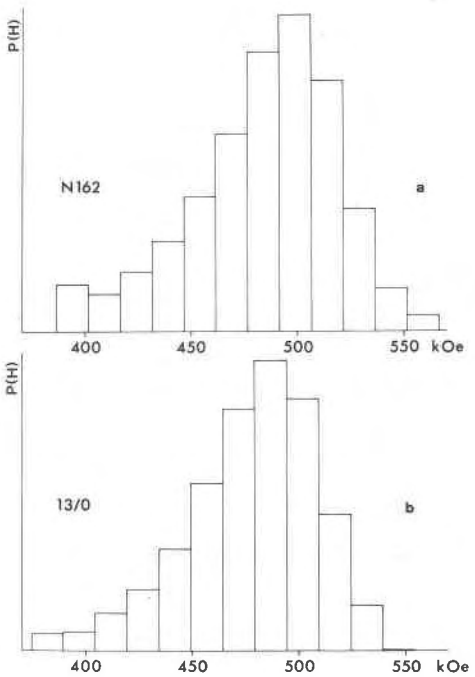

Fig. 3. Distributions of magnetic hyperfine fields at 4K for (a) natural ferrihydrite N162, and (b) synthetic ferrihydrite 13/0.

Discussion

Comparison with published values for "amorphous iron oxide gels" and ferritin

Most published quadrupole splittings of room-temperature "amorphous iron oxide" spectra (Table 2) are lower than those obtained here for a one-doublet fit of ferrihydrite (0.75 mm · s^{-1}), but higher than those of the other common iron oxides of not too small particle size (*ca.* 0.55 mm · s^{-1}). Only one of these previously described samples, which had been precipitated from an $Fe(NO_3)_3$ solution (Giessen, 1966) was, however, shown by X-ray diffraction to consist of ferrihydrite. Potvin and Greenblatt (1969) suggested that akaganéite may form when such gels are precipitated from $FeCl_3$ solutions. Impurities that gave a magnetically split spectrum at 70 K—the hyperfine field of 480 kOe indicates goethite—were observed in another case (Brady *et al.,* 1967).

Only two of the synthetic samples studied here contained significant amounts of iron oxides other than ferrihydrite. These samples (PT79, which contained some feroxyhite and lepidocrocite, and DLF5, which contained lepidocrocite and goethite), which must therefore be excluded from the calculation of average parameters, had the lowest quadrupole splittings of all.

The quadrupole splitting of 0.72 mm · s^{-1}, observed at room temperature for a natural ferric gel—possibly ferrihydrite—precipitated near freshwater springs (Coey and Readman, 1973) agrees well with our values (Table 1).

The iron-storage protein ferritin has been shown to consist of micelles of "hydrated ferric oxide" about 40–70Å in diameter, surrounded by protein shells. The X-ray and electron diffraction data are identical to those of ferrihydrite (Towe and Bradley, 1967). Correspondingly, the Mössbauer spectrum of ferritin (Blaise *et al.,* 1965; Fischbach *et al.,* 1971; Williams *et al.,* 1978) closely resembles that of ferrihydrite as described here.

Our results

Adequately good delineations of the experimental data were obtained when the room-temperature spectra were fitted with two doublets and the 4K spectra with three sextets (Figs. 1b, 2b). The different parameters resulting from these fits (Table 1) can be used to characterize the samples. They should, however, not be taken as proof for the existence of discretely different iron sites in the ferrihydrite structure. The hyperfine field distributions of the magnetically split spectra (Fig. 3) rather indicate continuous variations of parameters, and therefore of environments of the iron nuclei.

Room-temperature spectra. Our unpublished studies have shown the quadrupole splittings of super-

Table 1. Mössbauer parameters of ferrihydrite

Sample	N/S*	T(K)	δ(Fe)	ΔE_Q	W	H_i
31	N	291	*0.35(1)*	*0.71(1)*	*0.45(1)*	-
			0.35(1)	0.85(3)	0.41(1)	-
			0.36(1)	0.51(2)	0.29(2)	-
N162	N	291	*0.35(1)*	*0.71(1)*	*0.45(1)*	-
			0.34(1)	0.89(2)	0.42(1)	-
			0.35(1)	0.54(1)	0.31(1)	-
		4	*0.32(1)*	*0.05(1)*	*1.19(2)*	*492(1)*
				0.02(1)	0.74(3)	508(1)
			0.33(1)	0.08(1)	0.90(4)	484(1)
				0.03(2)	1.40(7)	444(3)
40A	N	292	*0.35(1)*	*0.78(1)*	*0.46(1)*	-
			0.35(1)	0.98(2)	0.39(1)	-
			0.35(1)	0.59(1)	0.32(1)	-
N196	N	291	*0.35(1)*	*0.78(1)*	*0.52(1)*	-
			0.34(1)	0.88(2)	0.53(1)	-
			0.35(1)	0.55(1)	0.27(5)	-
2	N	291	*0.35(1)*	*0.83(1)*	*0.52(1)*	-
			0.35(1)	0.90(2)	0.50(1)	-
			0.36(1)	0.52(1)	0.24(5)	-
PT79**	S	290	*0.34(1)*	*0.69(1)*	*0.53(1)*	-
			0.34(1)	0.86(2)	0.53(1)	-
			0.35(1)	0.51(1)	0.34(1)	-
DLF5**	S	292	*0.35(1)*	*0.64(1)*	*0.42(1)*	-
			0.33(1)	0.86(1)	0.39(1)	-
			0.35(1)	0.52(1)	0.32(1)	-
13/0	S	291	*0.34(1)*	*0.71(1)*	*0.46(1)*	-
			0.33(1)	0.87(2)	0.43(1)	-
			0.34(1)	0.54(2)	0.34(2)	-
		4	*0.34(1)*	*0.02(1)*	*1.05(2)*	*484(1)*
				-0.01(1)	0.56(3)	505(1)
			0.34(1)	0.02(1)	0.72(3)	482(1)
				0.06(1)	0.90(4)	452(2)

* Natural/synthetic sample.

** Contains noticeable amounts of other iron oxides, as determined by XRD.

Italicized values: one doublet fit (room temperature) and one sextet fit (4K), respectively.

Isomer shifts (δ), quadrupole splittings (ΔE_Q) and widths (W) given in $mm \cdot s^{-1}$, magnetic hyperfine fields in kOe

paramagnetic goethite and lepidocrocite (*ca.* 0.52–0.55 $mm \cdot s^{-1}$), minerals which are often associated with ferrihydrite in nature, to be usually lower than that obtained for a one-doublet fit of ferrihydrite (0.75 $mm \cdot s^{-1}$). Goethites of very poor crystallinity, however, were found to have higher quadrupole splittings of up to 0.63 $mm \cdot s^{-1}$. The Mössbauer spectra of such goethites should—like those of ferrihydrite—also be fitted with two doublets. Parameters of such a fit are similar isomer shifts averaging 0.35 $mm \cdot s^{-1}$, but different quadrupole splittings of 0.50 and 0.77 $mm \cdot s^{-1}$, and rather wide (FWHM 0.45 $mm \cdot s^{-1}$) outer lines.

In synthetic microcrystalline hematite decreasing particle size results in lattice expansion, as though the crystals were subjected to a "negative pressure" (Schroeer and Nininger, 1967). Decreasing pressure, however, causes the quadrupole splitting of this mineral to increase, whereas the isomer shift remains essentially unchanged (Vaughan and Drickamer, 1967). Refined analyses showed that the room-temperature Mössbauer spectra of small particles (≤70Å) of hematite can be fitted with two partly overlapping doublets that have different quadrupole splittings of 0.52 and 0.90 $mm \cdot s^{-1}$ (Kraan, 1973). These components were considered to result from well-ordered inner and poorly-ordered surface regions of the particles, respectively.

These observations correlate very well with the observed Mössbauer spectrum of ferrihydrite, which has quadrupole splittings that are practically identical to those given by Kraan (1973) for ultrafine hematite. Note in this connection that the structure of ferrihydrite may be compared to that of a disordered hematite (Towe and Bradley, 1967).

4K spectra. The magnetically split spectra shown by ferrihydrite at 4K differ from those usually observed for the other iron oxides at this temperature. Our mostly unpublished studies show that the hyperfine fields of well crystallized hematite (540 kOe) and feroxyhite (529 kOe; Carlson and Schwertmann, 1980) are distinctly higher, and that of lepidocrocite (455 kOe) is lower than the maximum of the hyperfine field distribution of ferrihydrite (*ca.* 500 kOe, see Fig. 3). The hyperfine field of goethite (505 kOe) approaches that maximum more closely, especially when lowered by aluminum substitution, but both goethite and hematite have quadrupole splittings that differ from that of ferrihydrite (0.24 and −0.41 *vs.* 0.03 $mm \cdot s^{-1}$). The Mössbauer spectrum of akaganéite comprises at least three superimposed sextets

Table 2. Mössbauer parameters of "amorphous iron oxide gels"

Author(s)	N/S*	T(K)	δ(Fe)	ΔE_Q	H_i
Giessen (1967)	S	300	0.36	0.62	-
Brady *et al.* (1968)	S	298	0.39	0.67	-
		5			455
Mathalone *et al.* (1970)	S	29x	0.33	0.65	-
		5	0.40	-	480
Coey & Readman (1973)	N	296	0.35	0.72	-
		77	0.47	0.81	-
		4	0.48	0.03	458
Loseva & Murashko (1973)	S	29x	0.32	0.62	-
Kauffman & Hazel (1975)	S	300	0.37	0.63	-
Saraswat *et al.* (1977)	S	300	0.32	0.54	-
		77	0.43	0.68	-
Okamoto & Sekizawa (1979)	S	29x		0.60	-
		4	0.5	∿ 0	494–508

* Natural/synthetic sample.

that have similar hyperfine fields between 473 and 486 kOe, but different quadrupole splittings of 0.90, 0.30, and −0.05 mm · s^{-1} (Murad, 1979).

The (poorly ordered) surface regions of small hematite particles were found to have a reduced hyperfine field (Kraan, 1973). This was considered to be the result of decreasing mutual interactions of surface ions with decreasing particle size. The particle sizes at which such effects become noticeable (70–40Å) are quite comparable to those usually observed for ferrihydrite. The hyperfine field distributions shown by this mineral are probably the outcome of particle size distributions.

Conclusions

One-doublet and one-sextet fits of room temperature and 4K Mössbauer spectra of ferrihydrite can be used to characterize this mineral. Typical parameters of such fits are a high quadrupole splitting of 0.75 mm · s^{-1} at room temperature, and a hyperfine field of about 490 kOe at 4K.

Physically sound fits require the room temperature spectra of ferrihydrite to be fitted with at least two superparamagnetic doublets of similar isomer shifts but different quadrupole splittings. At 4K hyperfine splitting with a distribution of magnetic hyperfine fields is observed. Both effects are also shown by other iron oxides of extremely small particle size, for example hematite. It thus appears that—in the microcrystal range—as particle sizes decrease, the individual characteristics of the different iron oxides gradually disappear, until finally only fundamental structural elements of short-range order common to all, *i.e.* Fe^{3+} surrounded by six O, OH, and/or OH_2, remain. This is in agreement with the conclusions from X-ray diffraction.

Acknowledgments

We are indebted to Dr. F. E. Wagner (Physics Department, Technische Universität München) for making the measurements at 130 and 4K possible, and for critically reviewing the manuscript. Natural and synthetic ferrihydrite samples were kindly provided by Dr. L. Carlson (Helsinki), Professor F. V. Chukhrov (Moscow), and Dr. D. G. Lewis (Adelaide). This study has been supported by the Deutsche Forschungsgemeinschaft under grant Schw 90/27.

References

Blaise, A., J. Chappert and J.-L. Girardet (1965) Observation par mesures magnétiques et effet Mössbauer d'un antiferromagnétisme de grains fins dans la ferritine. *C. R. Acad. Sci. Paris, 261,* 2310–2313.

Brady, G. W., C. R. Kurkjian, E. F. X. Lyden, M. B. Robin, P. Saltman, T. Spiro and A. Terzis (1967) The structure of an iron core analog of ferritin. *Biochemistry, 7,* 2185–2192.

Carlson, L. and U. Schwertmann (1980) A natural occurrence of feroxyhite (δ'-FeOOH). *Clays Clay Minerals,* in press.

Chukhrov, F. V., B. B. Zvyagin, L. P. Ermilova and A. I. Gorshkov (1972) New data on iron oxides in the weathering zone. *Proc. Int. Clay Conf. Madrid,* 333–341.

Coey, J. M. D. and P. W. Readman (1973) Characterization and magnetic properties of natural ferric gel. *Earth Planet. Sci. Lett., 21,* 45–51.

Feitknecht, W., R. Giovanoli, W. Michaelis and M. Müller (1973) Über die Hydrolyse von Eisen (III) Salzlösungen. I. Die Hydrolyse der Lösungen von Eisen (III) chlorid. *Helvetica Chim. Acta, 56,* 2847–2856.

Fischbach, F. A., D. W. Gregory, P. M. Harrison, T. G. Hoy and J. M. Williams (1971) On the structure of hemosiderin and its relationship to ferritin. *J. Ultrastructure Res., 37,* 495–503.

Giessen, A. A. van der (1966) The structure of iron (III) oxide–hydrate gels. *J. Inorganic Nuclear Chem., 28,* 2155–2159.

——— (1967) Magnetic properties of ultra-fine iron (III) oxide–hydrate particles prepared from iron (III) oxide–hydrate gels. *J. Phys. Chem. Solids, 28,* 343–346.

Harrison, P. M. and T. G. Hoy (1973) Ferritin. In G. L. Eichhorn, Ed., *Inorganic Biochemistry,* Vol. 1, p. 253–279. Elsevier, Amsterdam, London, New York.

Kauffman, K. and F. Hazel (1975) Infrared and Mössbauer spectroscopy, electron microscopy and chemical reactivity of ferric chloride hydrolysis products. *J. Inorganic Nuclear Chem., 37,* 1139–1148.

Kraan, A. M. van der (1973) Mössbauer effect studies of surface ions of ultrafine α-Fe_2O_3 particles. *Phys. Status Solidi, A18,* 215–226.

Loseva, G. V. and N. V. Murashko (1973) Use of Mössbauer spectroscopy to investigate the formation of hematite from amorphous iron hydroxide. *Inorganic Mater., 9,* 1301–1302.

Mathalone, Z., M. Ron and A. Biran (1970) Magnetic ordering in iron gel. *Solid State Comm., 8,* 333–336.

Mehra, O. P. and M. L. Jackson (1960) Iron oxide removal from soils and clays by a dithionite–citrate system buffered with sodium bicarbonate. *Clays Clay Minerals, 7,* 317–327.

Murad, E. (1979) Mössbauer and X-ray data on β-FeOOH (akaganéite). *Clay Minerals, 14,* 273–283.

Okamoto, S. and H. Sekizawa (1979) Magnetic properties of amorphous ferric hydroxide gels. *J. Phys., 40,* C2, 137–139.

Potvin, W. J. and S. Greenblatt (1969) Mössbauer study of the disintegration products of a high surface iron oxide gel. *J. Phys. Chem. Solids, 30,* 2792–2794.

Russell, J. D. (1979) Infrared spectroscopy of ferrihydrite: evidence for the presence of structural hydroxyl groups. *Clay Minerals, 14,* 109–114.

Saraswat, I. P., A. C. Vajpei and V. K. Garg (1977) Mössbauer resonance study of brown ferric oxyhydroxide gel. *Indian J. Chem., 15A,* 493–494.

Schroeer, D. and R. C. Nininger (1967) Morin transition in α-Fe_2O_3 microcrystals. *Phys. Rev. Lett., 19,* 632–634.

Schwertmann, U. (1964) Differenzierung der Eisenoxide des Bodens durch photochemische Extraktion mit sauer Ammoniumoxalat-Lösung. *Z. Pflanzenernährung, Düngung, Bodenkunde, 105,* 194–202.

——— (1979) Is there amorphous iron oxide in soils? *Agronomy Abstracts,* 228–229.

——— and W. R. Fischer (1973) Natural "amorphous" ferric hydroxide. *Geoderma, 10,* 237–247.

Towe, K. M. and W. F. Bradley (1967) Mineralogical constitution of colloidal "hydrous ferric oxides." *J. Colloid Interface Sci., 24,* 384–392.

Vaughan, R. W. and H. G. Drickamer (1967) High-pressure Mössbauer studies on α-Fe_2O_3, $FeTiO_3$, and FeO. *J. Chem. Phys., 47,* 1530–1536.

Williams, J. M., D. P. Danson and C. Janot (1978) A Mössbauer determination of the iron core particle size distribution in ferritin. *Phys. Medicine Biology, 23,* 835–851.

Manuscript received, January 29, 1980;
accepted for publication, March 7, 1980.

American Mineralogist, Volume 65, pages 1050–1052, 1980

Frequency distribution of plagioclase extinction angles: precision of the Michel-Lévy technique

ALLEN F. GLAZNER

Department of Earth and Space Sciences
University of California, Los Angeles
Los Angeles, California 90024

Abstract

The precision and accuracy of the Michel-Lévy method of plagioclase determination in thin section depend on the probability that an angle close to the maximum extinction angle will be observed in a given set of measurements. By assuming that the grains have a uniform random orientation, the probability density function of the extinction angle can be calculated. Knowledge of the density function allows one to calculate the probability of observing an angle close to the maximum angle, as a function of the number of measurements. These probabilities are surprisingly high; for most compositions, a set of ten measurements gives a 95 percent probability of predicting a composition within five mole percent An of the true value.

Introduction

The Michel-Lévy "statistical" method for thin-section determination of plagioclase composition was introduced in the last century (Michel-Lévy, 1894), and is probably the most useful optical method available. However, the method is subject to systematic errors because it depends on finding the maximum value of a randomly-distributed extinction angle. If the true maximum angle is not measured, the resulting anorthite content, as predicted from the angle, will either be too low (for compositions more calcic than An_{20}) or too high (for compositions more sodic than An_{20}). The precision and accuracy of the technique depend on the probability of observing an angle sufficiently close to the maximum angle, and thus on the frequency distribution of extinction angles. This paper discusses the statistics of plagioclase extinction angles.

Method

In this paper, the plagioclase grains are assumed to have a uniform random orientation, and only those with (010) vertical are considered. Many rocks (*e.g.* those with trachytic fabrics) do not meet this first condition, but it is a convenient starting point for discussion of the statistics of extinction angles.

The extinction angle θ, defined as the angle between the fast ray x′ and the trace of (010), can be determined on a stereonet by using the construction given in Bloss (1961, p. 228–229). Analysis of the stereonet solution shows that, for grains with (010) vertical, θ is given by

$$\theta(\rho) = \tfrac{1}{2}|\arctan[\tan\alpha_1 \sin(\beta_1 + \rho)] + \arctan[\tan\alpha_2 \sin(\beta_2 + \rho)]| \qquad (1)$$

where ρ is the angle between the crystallographic c axis and the microscope axis, and α_1, α_2, β_1, and β_2 are composition-dependent constants which depend on the orientations of the optic axes of the plagioclase grain. These constants are easily derived from the optical data of Burri *et al.* (1967; low-temperature plagioclase data abstracted in Mizutani, 1975).

Figure 1 is a plot of θ as a function of ρ for two compositions. For all compositions, θ ranges between zero and a maximum angle. The Michel-Lévy determinative curve plots this maximum extinction angle against composition. Figure 2 is such a determinative plot, derived using equation 1 and the low-temperature data cited above (19 points from An_0 to An_{90}). It agrees well with the Michel-Lévy curve, especially for intermediate compositions.

The extinction angle θ is a function of the random variable ρ, so θ is randomly distributed. ρ is uniformly distributed between 0 and 2π (under the assumption made at the start of this section), so the density function of θ can be calculated by change-of-

0003–004X/80/0910–1050$02.00

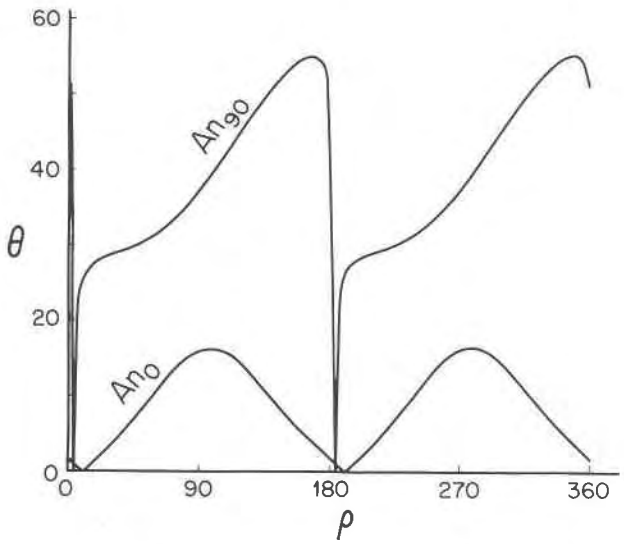

Fig. 1. Plot of the extinction angle θ as a function of the rotation angle ρ, for compositions An_0 and An_{90}.

variable techniques (Mood and Graybill, 1963, p. 220–225). Call this calculated density function $p(\theta)$. Figure 3 shows plots of $p(\theta)$ for compositions An_0 and An_{90}. For most compositions, $p(\theta)$ resembles the curve for An_0; for very calcic compositions a secondary peak is present at about half the maximum angle. Now for any composition, the probability of observing an angle between any two limits is equal to the area under $p(\theta)$ between those limits. For all compositions, $p(\theta)$ goes to infinity as θ approaches the maximum angle. Therefore, in any random observation, the probability of observing an angle near the maximum is much greater than the probability of observing an angle near any particular smaller value.

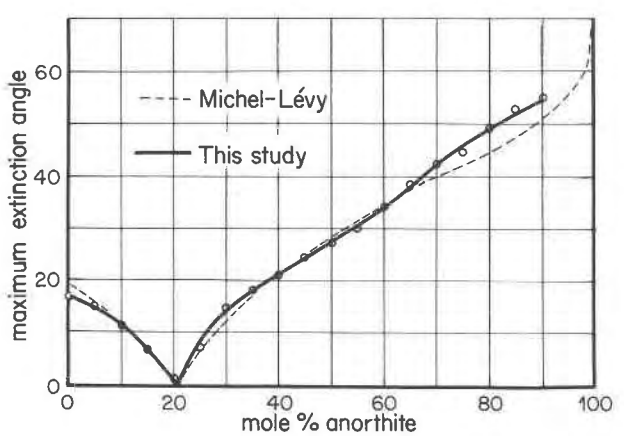

Fig. 2. Comparison of the curve plotting maximum extinction angle *vs.* composition, determined in this study, with the Michel-Lévy curve taken from Heinrich (1965, p. 364).

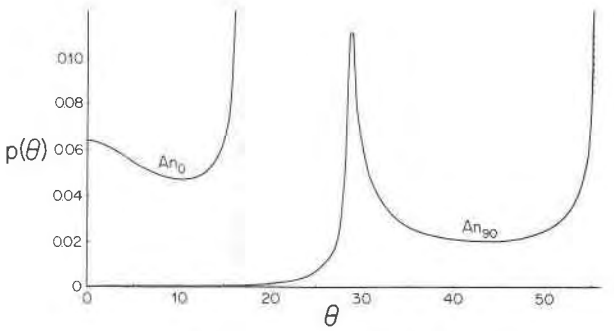

Fig. 3. Plot of the probability density function of the extinction angle θ, for compositions An_0 and An_{90}. Dashed lines are maximum angles to which the curves are asymptotic.

Now suppose that θ_{max} is the maximum extinction angle for a given composition, and θ_e is some angle less than θ_{max} which yields an apparent composition in error by e mole percent An when applied to the determinative curve of Figure 2. The probability that a randomly chosen grain will show an extinction angle less than θ_e is equal to the area under the curve $p(\theta)$ to the left of θ_e. If n randomly chosen grains are measured, the probability that *at least one* observed angle will be greater than θ_e is equal to one minus the probability that *none* of the observed angles are greater than θ_e, or

$$P = 1 - \left[\int_0^{\theta_e} p(\theta)d\theta\right]^n$$

In Figure 4 these probabilities are plotted as a function of n, for two different tolerance limits: e = 5 (Fig. 4a) and e = 10 (Fig. 4b). The probabilities are quite high; for most compositions, even as few as three measurements gives better than a 70 percent chance of being within 10 mole percent of the true composition. Ten measurements, the number recommended in most textbooks, give a very high probability of achieving the correct value. The probability of an accurate measurement reaches unity for composition near An_{20}, since for those compositions the extinction angle is so small that significant deviation from the true maximum angle is impossible.

Conclusion

If judiciously applied, the Michel-Lévy method can give highly reproducible results, in spite of its "statistical" nature. Ten measurements give a high probability of being within 5 mole percent An of the true composition, and the bias in the calculated composition is small. However, the probabilities in Figure 4 should not be used to put precise confidence

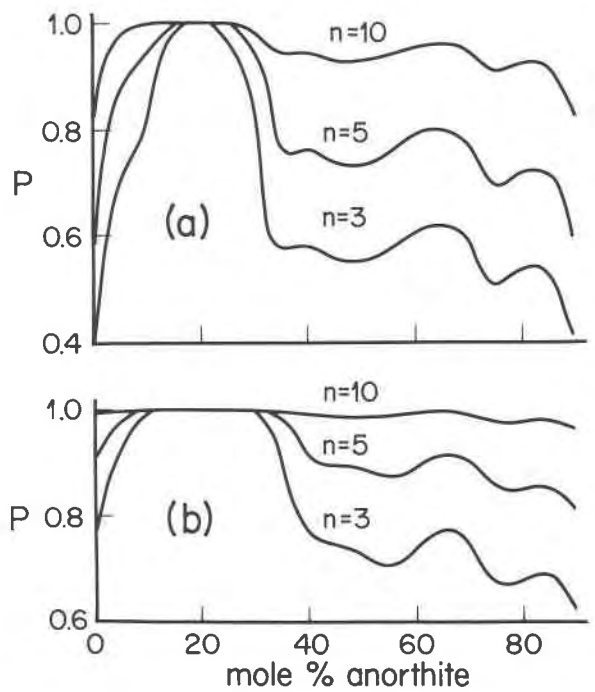

Fig. 4. Probability P of predicting a composition within (a) 5 mole % An and (b) 10 mole % An of the true composition, as a function of n (the number of measurements) and composition.

limits on optical plagioclase determinations, because several other factors enter into the true error. Some of these are: (1) non-uniform grain orientation; (2) chemical zoning; (3) change in extinction angle with change in structural state, for a given composition; (4) errors in the data used to calculate Figure 2; (5) deviations of (010) from vertical.

Acknowledgments

This study was inspired by the fascinating discussion of geometrical probability given by R. B. McCammon in Chapter 1 of his book, *Concepts in Geostatistics* (Springer-Verlag, New York, 1975). Discussions with W. A. Dollase, D. B. McIntyre, and R. L. Shreve greatly improved the manuscript. D. B. McIntyre provided a GEOREF search on the subject of extinction angles.

References

Bloss, F. D. (1961) *An Introduction to the Methods of Optical Crystallography.* Holt, Rinehart, and Winston, New York.

Burri, C., R. L. Parker, and E. Wenk (1967) *Die optische Orientierung der Plagioklase.* Birkhäuser Verlag, Basel.

Heinrich, E. W. (1965) *Microscopic Identification of Minerals.* McGraw-Hill, New York.

Michel-Lévy, A. (1894) *Étude sur la determination des feldspathes.* Lib. Polytech., Paris.

Mizutani, S. (1975) Extinction-angle distribution of plagioclase feldspars in clastic sediments. *Math. Geol., 7,* 335–348.

Mood, A. M. and F. A. Graybill (1963) *Introduction to the Theory of Statistics.* McGraw-Hill, New York.

Manuscript received, November 19, 1979;
accepted for publication, March 6, 1980.

American Mineralogist, Volume 65, pages 1053–1056, 1980

A simple rapid-quench design for cold-seal pressure vessels

GARY K. JACOBS AND DERRILL M. KERRICK

Department of Geosciences, The Pennsylvania State University
University Park, Pennsylvania 16802

Abstract

A simple rapid-quench design, utilizing conventional cold-seal pressure vessels, operates by flushing the capsule chamber with cold water injected through an axial capillary tube. Compared to a conventional air quench, improved quench rates are gained without the disadvantages associated with other rapid-quench methods (*e.g.* water-bath immersion or water-jacketed tilt mechanisms). The need for a rapid quench is illustrated by quench reactions in experiments with wollastonite-bearing equilibria in H_2O–CO_2 fluids. Upon air quenching, wollastonite reacts with CO_2 to form calcite and (presumably) silica in solution. Quenching experiments involving wollastonite and H_2O–CO_2 fluids indicate that back-reaction during cooling is minimized through use of the new rapid-quench design.

Introduction

Interpretation of hydrothermal experiments can be complicated by the precipitation of undesirable phases during quenching of conventional cold-seal pressure vessels. For example, calcite readily forms during compressed air quenches in experiments involving wollastonite equilibria in H_2O–CO_2 fluids (Kerrick and Ghent, 1980; Johannes, personal communication; Shmulovich, 1977; Ziegenbein and Johannes, 1974). Although rapid quenching of the pressure vessel through immersion into a water bath may alleviate this problem, repeated quenching by this method can shorten vessel life and lead to explosive failure. Use of water-jacketed rapid-quench vessels can be quite successful in reducing quench problems, provided precautions pointed out by Ludington (1978) and Rudert *et al.* (1976) are observed. The present paper describes a new rapid-quench design that utilizes a conventional cold-seal vessel (Tuttle, 1949) through which cool water is injected into the capsule chamber *via* an axial capillary tube; this procedure results in a rapid temperature drop in the immediate vicinity of the capsules. This new design is simple and requires little modification of a cold-seal hydrothermal laboratory.

Rapid-quench mechanism

Figure 1 is a schematic diagram illustrating the rapid-quench design used in this study. In our experiments, the pressure vessel was oriented horizontally to minimize temperature gradients (Boettcher and Kerrick, 1971). Temperatures (±2°C) were measured with an internal, inconel-sheathed, chromel–alumel thermocouple which, along with capillary A (Fig. 1), extends through the hollow filler rod to the position of the capsules. Both the thermocouple and capillary A were silver-soldered to the nipple at the top of the T-junction. Valve A is used to isolate the pressure vessel from the main pressure line after final pressure adjustments are completed. Using water as a medium, pressures were generated with an air-driven hydraulic pump (Haskel # DSXHW-903). Pressures (±20 bars) were monitored with a bourdon-tube gauge for each vessel, calibrated against a factory-calibrated standard gauge.

At the end of an experiment, pressure in the main line (Fig. 1) is equalized to that in the vessel. Valve A is then opened to connect the vessel to the main pressure line. The vessel is then removed from the furnace, placed in a stream of compressed air, and valve B is immediately opened, allowing the hot water in the vessel to exit through the T-junction, capillary B, and bleed line. Cool water, pumped in through capillary A as the hydraulic pump cycles to maintain constant pressure, flows over (and quenches) the capsules (see inset in Fig. 1). A large-volume water reservoir between each vessel and the main pressure line should help reduce momentary pressure drops which occur between each cycle of the hydraulic pump. When the vessel is cool, pumping is stopped

0003–004X/80/0910–1053$02.00

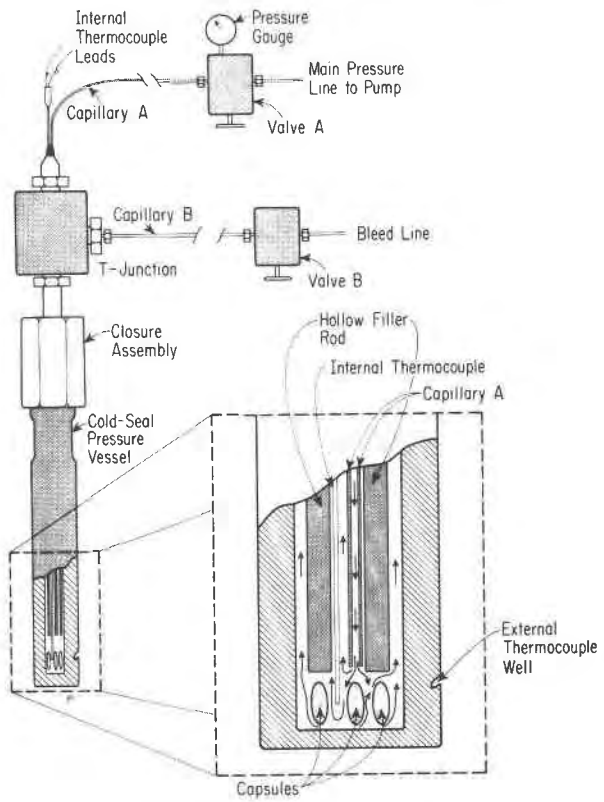

Fig. 1. Schematic diagram of the rapid-quench design. Enlarged inset shows details of hollow filler rod, internal thermocouple, and capillary A, illustrating flow of cool water (arrows) around the capsules.

and the pressure allowed to drop by closing valve A and letting the water flow out of the bleed line.

Experimental results

Quench rates

Quench rates from conventional compressed air quenches are compared to those utilizing the rapid-quench mechanism in Figure 2. The rapid-quench apparatus yields significantly larger temperature drops over the first 40 seconds of the quench. In fact, temperatures recorded with the rapid-quench mechanism averaged 150°C below those of the compressed air quench for the time span of 20–40 seconds. A temperature drop of 400° (from 600° to 200°C) occurs in about two thirds of the time with the rapid-quench design as it does with a compressed air quench. These results indicate that problems with quench reactions may be alleviated (or minimized) by utilizing the rapid-quench apparatus.

Quench reactions

The rapid-quench mechanism was used to reduce quench reactions in experiments dealing with wollastonite in H_2O–CO_2 fluids. As noted in the introduction, several authors have observed that wollastonite reacts with CO_2 during the quench to form calcite and SiO_2. X-ray analysis (Guinier camera) of some experimental charges where wollastonite reacted with CO_2 during the quench yielded patterns of wollastonite and calcite, but not quartz. This phenomenon, which was also observed in experiments by Shmulovich (1977), implies that quartz is not precipitating along with calcite; thus, silica remains in solution, and/or is present as an amorphous phase. SEM photographs of wollastonite from such experimental charges support this hypothesis. Abundant calcite rhombohedrons can be seen on the wollastonite grains; however, quartz is noticeably absent. One of the authors (D. M. Kerrick) has frequently encountered this phenomenon in thin sections of wollastonite-bearing metacarbonate rocks.

Ag_{50}–Pd_{50} capsules were loaded with equal

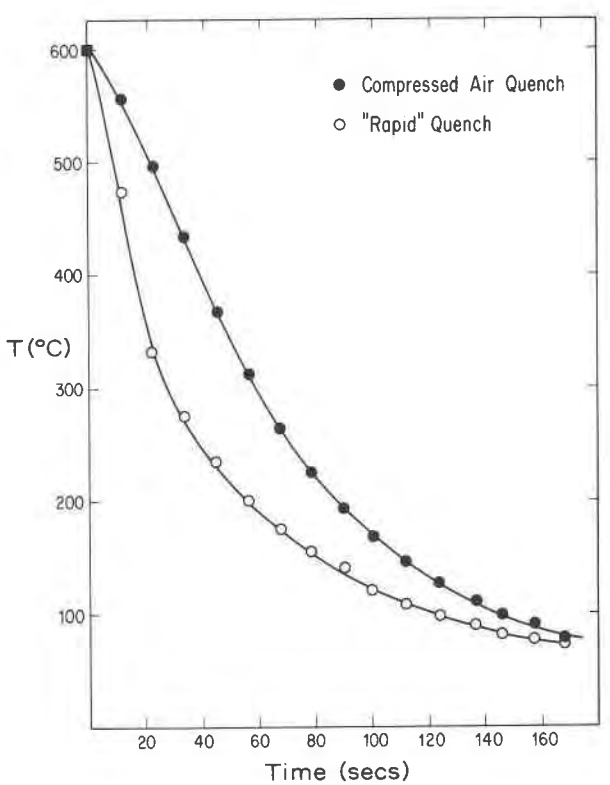

Fig. 2. Temperature–time plot comparing conventional compressed-air quench to that using the rapid-quench design. Each symbol represents an average of 3 values. Initial temperature was 600°C at a total pressure of 2.0 kbar.

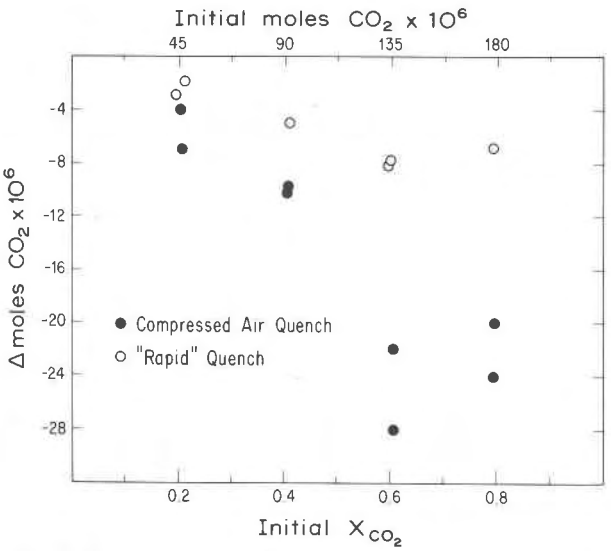

Fig. 3. Change in moles of CO_2 (final moles − initial moles) resulting from the quench reaction: wollastonite + CO_2 → calcite + SiO_2. Runs were quenched from the wollastonite + fluid field at 700°C and a total pressure of 1.0 kbar. A value of zero on the ordinate indicates no back-reaction.

amounts of −325 mesh wollastonite (for a chemical analysis of this specimen see Kerrick and Ghent, 1980) and silver oxalate + H_2O for the generation of various initial values of X_{CO_2} (Hunt and Kerrick, 1977; Slaughter *et al.,* 1975). For each capsule, the ratio of wollastonite to fluid was approximately 8:2 (by weight). To eliminate any reaction between the wollastonite and CO_2 which may have occurred during the run-up, the capsules were first subjected to 9–14 day runs at 700°C and 1 kbar—conditions well within the wollastonite stability field (Greenwood, 1967). Some vessels were then quenched with a conventional compressed air stream, while others were cooled with the rapid-quench apparatus. The final composition of the fluid phase was determined by the weight-loss method of Johannes (1969). Initial and final amounts of CO_2 in the capsules should be identical if no quench reaction occurred. However, if wollastonite reacted with CO_2 during the quench, a net loss of CO_2 should be observed. Because pressure, X_{CO_2}, and surface area of wollastonite were kept constant in sets of experiments utilizing the two quenching techniques, the change in moles of CO_2 should provide a good comparison of the degree of back-reaction of the two different quench methods for each set of runs.

Figure 3 shows the results from the quenching experiments. At all initial X_{CO_2} values, some back-reaction occurred, evidenced by the net loss of CO_2 for all data points. However, the rapid-quench technique yielded smaller CO_2 losses than the compressed air quench. This is especially evident at high initial X_{CO_2} values. For these CO_2-rich compositions, the quench path enters the calcite + quartz stability field at relatively high temperatures, where enhanced reaction kinetics cause greater losses of CO_2. Note, however, that for both quench methods the maximum loss of CO_2 occurs at initial X_{CO_2} = 0.6 rather than initial X_{CO_2} = 0.8. Apparently, quenching at initial X_{CO_2} = 0.6 represents the optimal combination of the rate-enhancing effects of H_2O and elevated temperature. Back-reaction is very limited at initial X_{CO_2} = 0.2 and 0.4 (see Fig. 3), which implies that even though the fluids are very water-rich, the temperatures at which the quench path penetrates the calcite + quartz field are too low for extensive back-reaction to occur. Thus, for this reaction, quench products are most likely to form in CO_2-rich fluids during the initial temperature drop of the quench, where the rapid-quench apparatus was shown to be most effective (see Fig. 2).

Discussion

Our rapid-quench device yields faster quench rates than conventional compressed air methods. Although quench rates with this device are not as rapid as water-immersion methods or water-jacketed tilt vessels, this new design does offer some advantages. It avoids the large temperature gradients which can be associated with some water-jacketed rapid-quench vessels (Ludington, 1978; Rudert *et al.,* 1976). In addition, with this new design it is possible to carefully check sample temperatures through use of an internal thermocouple; the design of tilt-mechanism vessels precludes the use of internal thermocouples. Our rapid-quench design should provide a safe alternative to water-immersion methods under normal operating P-T conditions for cold-seal vessels, because compared to water immersion, the relatively small mass of injected water yields smaller overall short-term strain on the vessel. No failures have occurred in approximately two dozen runs with the new design at pressures to 2 kbar and temperatures to 700°C. Actual quench rates with other pressure media such as Ar or CO_2 have not been measured; however, improved quench rates are anticipated with the rapid-quench design compared to compressed air quenches with these pressure media.

As evidenced by experiments on the back-reaction of wollastonite during quenching, the new design does not eliminate all quench problems, but it does reduce them to a more acceptable level.

Acknowledgments

We thank I-Ming Chou and D. H. Eggler for their careful review of this paper. This work represents part of G. K. Jacobs' Ph.D. research and was supported in part by NSF grants EAR 76-84199 and EAR 79-08244 (D. M. Kerrick) and an Owens-Corning Fiberglas Graduate Fellowship (G. K. Jacobs).

References

Boettcher, A. L. and D. M. Kerrick (1971) Temperature calibration in cold-seal pressure vessels. In G. C. Ulmer, Ed., *Research Techniques for High Pressure and High Temperature,* p. 179–193. Springer-Verlag, New York.

Greenwood, H. J. (1967) Wollastonite: stability in H_2O–CO_2 mixtures and occurrence in a contact-metamorphic aureole near Salmo, British Columbia, Canada. *Am. Mineral., 52,* 1669–1680.

Hunt, J. A. and D. M. Kerrick (1977) The stability of sphene: experimental redetermination and geologic implications. *Geochim. Cosmochim. Acta, 41,* 279–288.

Johannes, W. (1969) An experimental investigation of the system MgO–SiO_2–H_2O–CO_2. *Am. J. Sci., 267,* 1083–1104.

Kerrick, D. M. and E. D. Ghent (1980) P–T–X_{CO_2} relations of equilibria in the system: CaO–Al_2O_3–SiO_2–CO_2–H_2O. (in Russian) In V. A. Zharikov, V. I. Fonarev, and S. P. Korikovskii, Eds., *Problems of Physico-chemical Petrology,* p. 32–52. D. S. Korzhinskii Commemorative Volume.

Ludington, S. (1978) Temperature gradients in rapid-quench cold-seal pressure vessels—the effect of inclination (abstr.). *Geol. Soc. Am. Abstracts with Programs, 10,* 447.

Rudert, V., I-M. Chou and H. P. Eugster (1976) Temperature gradients in rapid-quench cold-seal pressure vessels. *Am. Mineral., 61,* 1012–1015.

Shmulovich, K. I. (1977) Stability limits of grossular and wollastonite in the H_2O–CO_2 system up to 6 kbar. *Geokhimiya, 12,* 1806–1816. [transl. *Geochem. Int., 14,* 126–134 (1978)].

Slaughter, J., D. M. Kerrick and V. J. Wall (1975) Experimental and thermodynamic study of equilibria in the system CaO–MgO–SiO_2–H_2O–CO_2. *Am. J. Sci., 275,* 143–162.

Tuttle, O. F. (1949) Two pressure vessels for silicate–water studies. *Geol. Soc. Am. Bull., 60,* 1727–1729.

Ziegenbein, D. and W. Johannes (1974) Wollastonitbildung aus Quarz und Calcit bei P_f = 2, 4, und 6 kb. *Fortschr. Mineral., 52,* 77–79.

Manuscript received, February 15, 1980;
accepted for publication, May 9, 1980.

American Mineralogist, Volume 65, pages 1057-1058, 1980

Hydrated aluminum hydroxy-fluoride, a ralstonite-like mineral at Big Southern Butte, Snake River Plain, Idaho

GEORGE A. DESBOROUGH AND ORA ROSTAD

U.S. Geological Survey and AMAX Exploration, Inc.
Denver, Colorado 80225

Disseminated hydrated aluminum hydroxy-fluoride, with the general formula $Al_{16}(F,OH)_{48} \cdot 12\text{–}15\ H_2O$, occurs in pale pink to pale yellow and white hydrothermally-altered rhyolitic rocks, and it may constitute 40 percent by volume. The occurrence is at an elevation of about 6,400 feet (2,130 m) above mean sea level in the NE 1/4, sec. 22, T. 1N, R. 29 E, on the northwest side of Big Southern Butte, the most prominent landmark about 60 km NW of the city of Blackfoot. This occurrence is noteworthy because it is the site of near-surface (<100 m depth) hydrothermal alteration that produced a ralstonite-like mineral without significant Na or Mg, which previously have been considered essential components of ralstonite.

Quantitative chemical data for this ralstonite-like mineral are given in Table 1, along with the cell dimensions. Quantitative electron microprobe data were obtained at 10 kV with the beam defocussed to 10 microns. Analyzed biotite, fluor-phlogopite, Al_2O_3, KCl, and CaF_2 were used as standards. The K-line intensity data for each element in specimen A50976 were processed by Magic IV, and the results were identical to those obtained without ZAF corrections. Significant chlorine and potassium are substituted for the anion and cation, respectively, in one specimen (Table 1). Quantitative analyses for Mg, Li, Be, B, and NH_3^+ (Kjeldahl method) revealed less than 0.03 weight percent of each in specimen A50976. Quartz, sanidine, and tridymite are the common associated minerals readily recognized by transmitted-light petrographic methods; these are believed to be relict from the rhyolite. Specimen Sobu-OF contains massive halite, quartz, and albite. According to X-ray diffraction studies of bulk samples, scanning electron microscopy, electron microprobe studies, and petrographic studies, we conclude that the ralstonite-like mineral, halite, and albite are of hydrothermal origin. Fluorite is sparse, and topaz was not found. The ralstonite-like mineral is optically isotropic, and occurs as compact masses of submicron-size grains. The largest crystals, shown on Figure 1, are 10- to 15-micron octahedra observed only in one of four specimens. Some rosettes of crystal aggregates occur perched on coarsely crystalline halite. Grains of

Table 1. Mineralogical data for hydrated aluminum hydroxy-fluoride in four specimens from Big Southern Butte, Snake River Plain, Idaho

Specimen no.	A50976	Sobu-A,A	Sobu-B	Sobu-OF
Element	Weight percent			
K	2.1 (0.2)	0.17 (0.04)	0.15 (0.02)	0.26 (0.10)
Na	0.27 (0.01)	0.18 (0.05)	0.16 (0.04)	0.28 (0.07)
Ca	0.08 (0.03)	<0.07	<0.07	<0.07
Al	25.9 (0.2)	27.3 (0.3)	26.8 (0.4)	27.2 (0.2)
Cl	2.8 (0.4)	0.26 (0.20)	0.23 (0.15)	0.06 (0.07)
F	33.1 (1.2)	41.2 (1.1)	40.4 (1.5)	42.2 (1.3)
OH calculated	21.4	15.3	15.0	14.4
H_2O by difference	14.3	15.6	17.3	15.6
	Atomic percent (for F+OH+Cl = 48)			
K	0.83	0.07	0.06	0.10
Na	0.18	0.08	0.11	0.19
Ca	0.03	-	-	-
Al	14.98	15.66	15.86	15.76
Cl	1.24	0.12	0.10	0.02
F	27.13	33.46	33.86	34.70
OH	19.64	14.43	14.04	13.27
H_2O	12.4	12.89	15.30	13.58
	Cell dimensions (A)			
a =	9.861(4)	9.799(3)	9.791(3)	-

Values given for weight percent are the mean, with the standard deviation in parentheses, based on 17-39 electron microprobe analyses for each element in each specimen, except for Sobu-OF which is based only on 5-7 analyses for each element. Mg is less than 0.10 in all analyses.

0003-004X/80/0910-1057$02.00

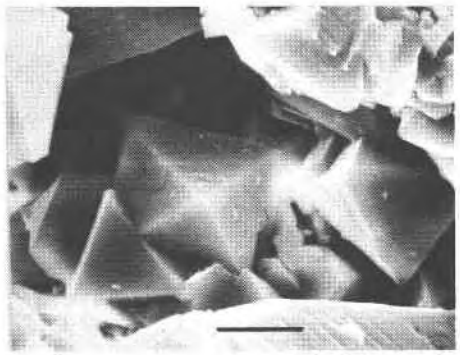

Fig. 1. Scanning electron photomicrograph of hydrated aluminum hydroxy fluoride octahedra, Sobu A, from Big Southern Butte, Snake River Plain, Idaho. Bar scale is 10 microns. (Photo by James Nishi, U.S.G.S.)

hematite and magnetite(?) 5 to 15 microns in size are present in polycrystalline aggregates.

Cell dimensions of a = 9.791(3) to 9.861(3)Å (Table 1) and the intensity of the strongest X-ray diffraction lines (Table 2) are more similar to the diffraction parameters of synthetic hydrated aluminum hydroxy-fluoride (Cowley and Scott, 1948) than to the 9.92 to 10.02Å for natural ralstonites studied by Pauly (1965). The index of refraction of the ralstonite-like mineral in specimen A50976 (Table 1), determined by Ray E. Wilcox, ranges from 1.460 to 1.464 using focal masking.

Acknowledgments

We thank James Nishi, of the U. S. Geological Survey, for use of the scanning electron microscopy laboratory and for the photomicrograph. We are also grateful to Michael Fleischer, Mary Mrose, and Ray E. Wilcox, of the U. S. Geological Survey, for their helpful suggestions, and Dr. Hans Pauly of the Technical University of Denmark for his constructive comments.

Table 2. X-ray powder diffraction data for hydrated aluminum hydroxy-fluoride (A50976), Big Southern Butte, Snake River Plain, Idaho

hkl	d,A	I
111	5.72	100
311	2.97	60
222	2.85	25
400	2.46	20
422	2.01	10
333,511	1.899	15
440	1.743	20
531	1.667	5
620	1.563	3
533	1.503	5
622	1.485	5
444	1.423	3
731,553	1.284	5
822,660	1.161	5
662	1.129	2

a = 9.861(4)

Diffractometer, scan rate 1°2 θ per inch; CuKα = 1.54178A, Ni filter

References

Cowley, J. M. and T. R. Scott (1948) Basic fluorides of aluminum. *J. Am. Chem. Soc., 70,* 105.

Pauly, H. (1965) Ralstonite from Ivigtut, South Greenland. *Am. Mineral., 50,* 1851–1864.

Manuscript received, February 4, 1980;
accepted for publication, April 2, 1980.

American Mineralogist, Volume 65, pages 1059-1060, 1980

The crystal structures and the phase transformation of Zn-Li silicates: discussion

A. R. WEST

Department of Chemistry, University of Aberdeen
Meston Walk, Old Aberdeen AB9 2UE, Scotland

Yu *et al.* (1978) reported on the preparation, polymorphism, and structure determination of a phase of composition $Zn(Zn_{0.1}Li_{0.6}Si_{0.3})SiO_4$. The purpose of this note is to point out that a considerable literature on lithium zinc silicates exists (West, 1975; West and Glasser, 1970, 1972; Villafuerte-Castrejon and West, 1979) of which the authors are apparently unaware, and to suggest, in light of this literature, some possible errors in the results of Yu *et al.*

Phase studies of the system Li_2O–ZnO–SiO_2 have shown that wide ranges of polymorphic orthosilicate solid solutions are the only equilibrium ternary phases to crystallize in this system (West and Glasser, 1970). These solid solutions cover part of the join Li_4SiO_4–Zn_2SiO_4 (Fig. 1). Of most relevance to the present discussion are solid solutions and phases that occur between Li_2ZnSiO_4 and Zn_2SiO_4; their general formula may be written $Li_{2-2x}Zn_{1+x}SiO_4 (0 < x \lesssim 0.5)$. Within this range, nine different solid solution polymorphs were encountered, named γ_0, γ_I, γ_{II}, β_I, β_I', β_{II}, β_{II}', C, and C′. Unit-cell data were obtained for most of them. Structurally, they fall into two families; the γ and C polymorphs are all derived from γ_{II} Li_2ZnSiO_4 which is isostructural with high (γ_{II}) Li_3PO_4 (Zemann, 1960), whereas the β phases are derived from β_{II} Li_2ZnSiO_4 which is isostructural with low (β_{II}) Li_3PO_4 (Keffer *et al.*, 1969). β_{II} and γ_{II} both have tetrahedral structures with approximately hexagonal close-packed oxide ions, and the structures differ mainly in the manner of occupancy of the various tetrahedral sites.

Yu *et al.* grew their crystals (called hereafter Yu crystals) from a Li_2MoO_4–MoO_3 flux and claimed a composition for them corresponding to point X, Figure 1, which is just on the silica-deficient side of the metasilicate composition. I suggest, however, that the true composition of the Yu crystals lies near point Y on the orthosilicate join, with $x \simeq 0.2$, *i.e.* at $Li_{1.6}Zn_{1.2}SiO_4$. This conclusion is based on the following.

(1) Three polymorphic forms of the Yu crystals were identified, and their cell parameters correspond fairly well to those of three of the lithium zinc orthosilicate polymorphs (Table 1). Only a rough comparison can be made because the cell parameters of γ_0, γ_{II}, and C are composition-dependent, and data are available for only one composition for each phase.

(2) The powder pattern of α (Yu) corresponds fairly well to γ_0 (West and Glasser, 1970), although the latter contains more lines. This is probably because a high-resolution focusing camera was used in the latter work to record the powder patterns.

(3) The β phase of Yu appears to be isostructural with $\gamma_{II}Li_3PO_4$ (and hence with γ_{II} Li_2ZnSiO_4). Atomic coordinates are given in Table 2. One major difference is the presence of the extra four-fold set of Li(2) sites in Li_3PO_4. I suggest that these atoms are also present in the Yu crystals but, because of the small scattering power of Li^+, they escaped detection. One effect of adding extra Li^+ to the Yu crystals would be to change the coordination of oxygen from

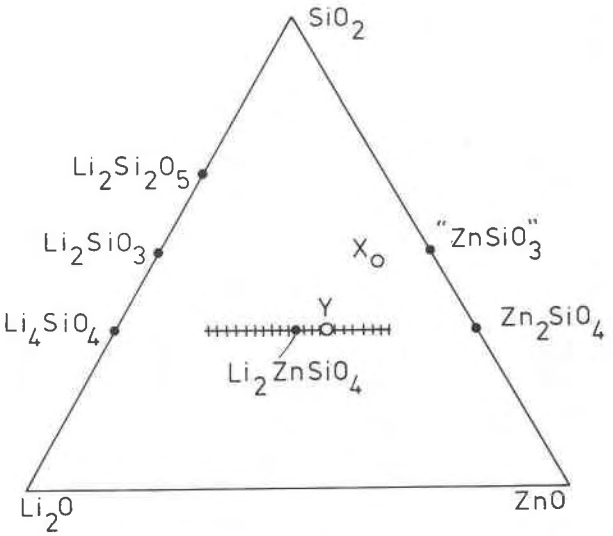

Fig. 1. Occurrence of Li_2ZnSiO_4 solid solutions (hatched) in the system Li_2O–ZnO–SiO_2. Compositions in mole percent.

0003–004X/80/0910–1059$02.00

Table 1. Comparison of cell parameters of the Yu crystals and LiZn orthosilicates (West and Glasser)

Cell parameter	α', Yu	C x = 0.24	α, Yu	x = 0	β, Yu 400°C	γ_{II} x = 0.2 700°C
a	13.01	13.16	6.340	∿6.32	6.406	6.45
b	10.41	10.6	10.516	∿10.72	10.520	10.64
c	10.07	5.06	5.011	∿5.06	5.043	5.12
γ	∿90°	∿90°	90.50°	∿91°	-	-

three cations arranged pyramidally to four arranged tetrahedrally.

(4) The Yu crystals had a density of 3.53 g cm^{-3}; in the Li,Zn orthosilicates, D varied from 3.35 ($x = 0$) to 3.63 ($x = 0.33$). If the Yu crystals are orthosilicates, then their density corresponds to $x \simeq 0.2$.

(5) The composition of the Yu crystals was determined by electron microprobe analysis, although Li^+ could not be analyzed by this technique. From emission spectroscopic analysis, a value of 10 wt% Li was obtained but rejected in favor of a value of 7 wt% obtained by difference from the microprobe results. The calculated lithium content in Li,Zn orthosilicates, $x = 0.2$ is ~6 wt%, in fair agreement with both sets of data.

In conclusion, the Yu crystals appear to be nonstoichiometric orthosilicates with $x \sim 0.2$. This x value is deduced from (1) the occurrence of a (γ_0 + C) phase assemblage, (2) the density value, and (3) the magnitude of the electron density in the Tl 8d sites. In spite of the compositional errors in the analysis of Yu *et al.*, this is a valuable piece of work since it is the first single-crystal study of Li,Zn orthosilicates and provides information on the structures of γ_{II} and γ_0 polymorphs.

Table 2. Atomic coordinates of β (Yu) and high γ_{II} Li_3PO_4 (Zemann)

		Yu		
Tl, ZnSiLi	8d	0.0004	0.1607	0.1860
T2Si	4c	0.25	0.4107	0.1834
O(1)	4c	0.25	0.4021	-0.1374
O(2)	4c	0.25	0.0575	0.2201
O(3)	8d	0.04337	0.3406	0.2954
		Zemann		
Li(1)	8d	0.005	0.162	0.196
P	4c	0.25	0.411	0.192
O(3)	4c	0.25	0.41	-0.125
O(2)	4c	0.25	0.052	0.205
O(1)	8d	0.042	0.342	0.295
Li(2)	4c	0.25	0.078	0.804

References

Keffer, C., A. Mighell, F. Mauer, H. Swanson, and S. Block (1969) The crystal structure of twinned low-temperature lithium phosphate. *Inorg. Chem., 6,* 119–125.

Villafuerte-Castrejon, M. E. and A. R. West (1979) Kinetics of polymorphic transitions in tetrahedral structures. Part I. Experimental methods and the transition $\gamma \rightarrow \beta$ Li_2ZnSiO_4. *J. Chem. Soc. Faraday Trans.* 1, *75,* 374–384.

West, A. R. (1975) Crystal chemistry of some tetrahedral oxides. *Z. Kristallogr., 141,* 422–436.

——— and F. P. Glasser (1970) Crystallisation of lithium zinc silicates. Part I. Phase equilibria in the system Li_4SiO_4–Zn_2SiO_4. *J. Mater. Sci., 5,* 557–565. Part II. Comparison of the metastable and stable phase relations and the properties of the lithium zinc orthosilicates. *Ibid., 5,* 676–688.

——— and ——— (1972) Crystallisation of lithium magnesium zinc silicates. Part 2. Phase equilibria and the crystallisation of glasses in the system Li_4SiO_4–Mg_2SiO_4–Zn_2SiO_4–SiO_2. *J. Mater. Sci., 7,* 895–908.

Yu, S. C., D. K. Smith, and S. B. Austerman, (1978) The crystal structures and the phase transformation of Zn–Li silicates. *Am. Mineral., 63,* 1241–1248.

Zemann, J. (1960) Die Kristallstruktur von Lithiumphosphat, Li_3PO_4. *Acta Crystallogr., 13,* 863–867.

Manuscript received, March 29, 1979;
accepted for publication, September 12, 1979.

American Mineralogist, Volume 65, pages 1061-1062, 1980

The crystal structures and the phase transformation of Zn-Li silicates: reply

SHU-CHENG YU,[1] DEANE K. SMITH

Department of Geosciences, The Pennsylvania State University
University Park, Pennsylvania 16802

AND STANLEY B. AUSTERMAN

Electronic Operations, Rockwell International
Anaheim, California 92803

The composition of the Zn–Li silicates reported by us (Yu *et al.*, 1978) has been questioned by West (1979) who suggests a composition closer to $Li_{1.6}Zn_{1.2}SiO_4$. The arguments raised by West require some clarification.

(1) West identified our β, α, and α' as γ_{II}, γ_0, and C respectively. West's three phases differ in composition while our β, α, and α' all have essentially the same composition. In addition, our α' is not a single phase but a twinned state of the α form at the atomic scale (Table 1).

(2) West claimed that the powder pattern of our α phase corresponds fairly well to γ_0 (West and Glasser, 1970) except that the latter has more lines. The two patterns are compared in Table 2 and Figure 1, and it is self-evident that they do not match "fairly well" as claimed. West also mentioned that the larger number of lines observed for γ_0 is probably because a high resolution focusing camera was used in West and Glasser's work to record the powder pattern. As a matter of fact, we also used the focusing camera (Guinier camera) in obtaining our X-ray pattern.

(3) West's atomic coordinates of Li_3PO_4 are identical to those of our Zn–Li silicates except that the former has an extra Li atom. If this extra Li atom in Zemann's Li_3PO_4 (Zemann, 1960) is ignored, it appears that these two structures are similar.

(4) The measured and the calculated density for our Zn–Li silicates are, respectively, 3.53 and 3.51 g/cm³. If West's composition were adopted, the calculated density would be 3.61 g/cm³, which is slightly too high when compared with the experimental value.

[1] Present address: Institute of Chemical Analysis, 341 Mugar Building, Northeastern University, Boston, Massachusetts 02115.

Table 1. Comparison of chemical compositions reported for Zn–Li silicates

Yu et al.	West		
β	γ_{II}	$(Li_{1.6}Zn_{1.2}SiO_4)$	x = 0.2
α	γ_0	(Li_2ZnSiO_4)	x = 0
α'	C	$(Li_{1.52}Zn_{1.24}SiO_4)$	x = 0.24

Table 2. Comparison of the powder patterns for α and γ_0 Zn–Li silicate

α				γ_0		
Yu et al.				West & Glasser		
d_o(A)	d_c(A)	I	hkl	d_o(A)	I	hkl
5.45	5.43	10	110	5.50	60	110
				5.40	10	020
4.23	4.52	10	011	4.60	10	011
4.07	4.05	50	120	4.09	80	120
				3.99	40	101
3.97	3.92	20	101	3.97	60	
				3.71	20	111,021
				3.69	100	
				3.19	20	200,121
				3.17	10	
3.09	3.07	40	130	3.12	40	130,210
				2.93	10	031
				2.92	20	
				2.74	60	220
2.711	2.715	30	220	2.71	80	
				2.68	80	040
2.658	2.629	30	040	2.65	40	131
2.632	2.611	30	131	2.64	10	
				2.60	10	211
				2.58	40	
				2.54	80	002
2.521	2.506	100	002	2.52	60	
2.452	2.437	30	012			
1.6282	1.6118	20	103			
1.5429	1.5338	40	260			
1.5179	1.5175	25	420			
1.3720	1.3721	25	342			

0003-004X/80/0910-1061$02.00

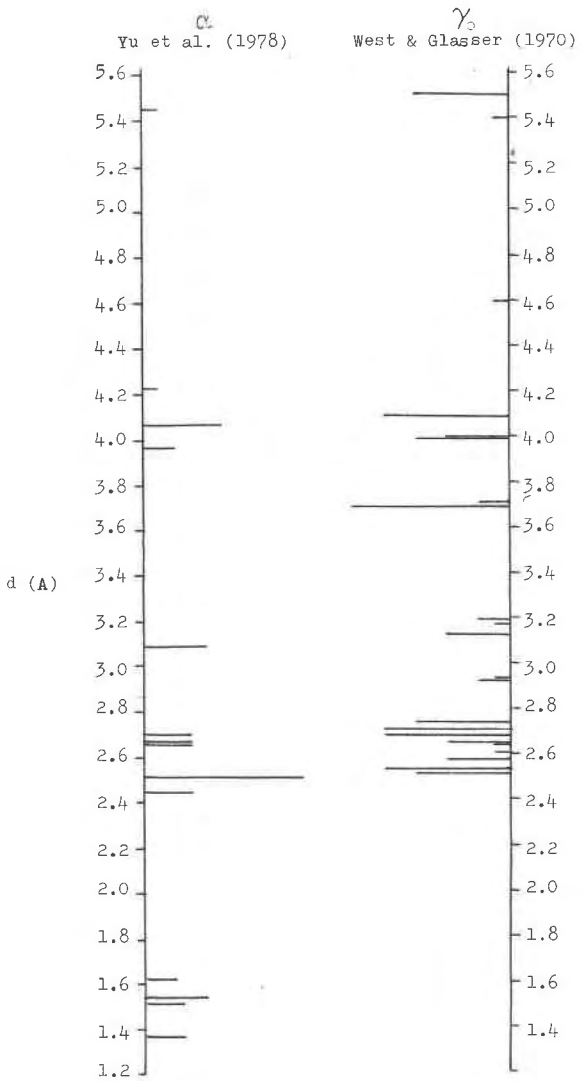

Fig. 1. Graphical comparison of two X-ray powder patterns of α and γ_0 Zn–Li silicate.

In view of the above discussion we conclude that our Zn–Li silicate appears to be a distinct phase from those reported by West. However, we appreciate West's interest and comments, and his calling to our attention to some of his valuable work on Zn–Li silicates which we did overlook in our literature review.

References

West, A. R. (1979) The crystal structures and the phase transformation of Zn–Li silicates: a discussion. *Am. Mineral., 65,* 1059–1060.

——— and F. P. Glasser (1970) Crystallisation of lithium zinc silicates. Part 1. Phase equilibria in the system Li_2SiO_4–Zn_2SiO_4. *J. Mater. Sci., 5,* 557–565.

Yu, S. C., D. K. Smith and S. B. Austerman (1978) The crystal structures and the phase transformation of Zn–Li silicates. *Am. Mineral., 63,* 1241–1248.

Zemann, J. (1960) Die Kristallstruktur von Lithiumphosphat, Li_3PO_4. *Acta Crystallogr., 13,* 863–867.

Manuscript received, August 16, 1979;
accepted for publication, September 12, 1979.

American Mineralogist, Volume 65, pages 1063-1064, 1980

Calculated phase relations for pyrite–pyrrhotite–sphalerite: correction

IAN HUTCHEON

Department of Geology and Geophysics
The University of Calgary
Calgary, Alberta, Canada T2N 1N4

Hutcheon (1978) published a calculated phase diagram for sphalerite–pyrite–pyrrhotite. In that paper it was stated that thermal expansion and isothermal compressibility data were not needed to calculate sphalerite compositions which were in agreement with experimental values given by Scott (1973). Contrary to this statement, this agreement is fortuitous because the wrong molar volume for pyrite (15.962 cm^3) was used in final calculations for the published manuscript. Using the correct volume (23.940 cm^3) results in a marked discrepancy with the experimental data. Calculations have been repeated using expansion and compressibility data.

Because of the error in the published calculations

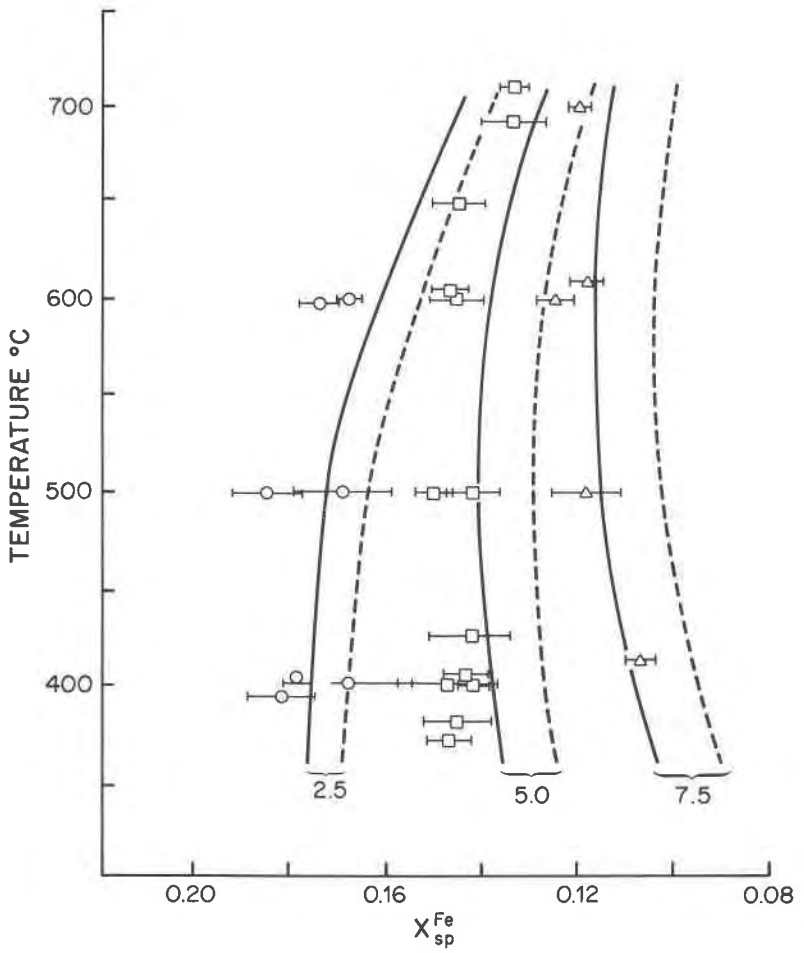

Fig. 1. Calculated phase relationships for pyrite, pyrrhotite, and sphalerite are in reasonable agreement with the experimental data of Scott (1973) if thermal expansion and isothermal compressibility data are used (solid lines). Calculated isobars which do not include expansion and compressibility data (dashed lines) do not agree with the experimental data. The curves shown are for 2.5, 5, and 7.5 kbar. The brackets represent the experimental points determined by Scott at 2.5 (circles), 5 (squares), and 7.5 (triangles) kbar.

0003–004X/80/0910–1063$02.00

the procedure is given here in more detail for 400°C and 5kbar. The composition of pyrrhotite coexisting with pyrite at any temperature between 400 and 750°C at 1 atm is obtained from a polynomial, fitted to the data of Toulmin and Barton (1964):

$$N^{po}_{FeS} = 0.9545099 + 1.019706 \times 10^{-5}(T) - 1.132749 \times 10^{7}(T^2)$$

where T = Celsius temperature.

The expressions in Toulmin and Barton are then used to calculate log fS_2 (−7.3686) and log a^{po}_{FeS} (−0.2678). From the isothermal compressibility and isobaric thermal expansion data given by Scott (1973), the volumes of pyrite (24.167 cm³), pyrrhotite (18.874 cm³), FeS sphalerite (24.092 cm³, from data for ZnS sphalerite) and sulfur with the pyrrhotite structure (15.129 cm³) are calculated at 400°C and 5kbar. If it is assumed that a^{po}_{FeS} is not pressure dependent, the equilibria:

$$\underset{\text{pyrrhotite}}{FeS} + 1/2S_2 \leftrightarrows \underset{\text{pyrite}}{FeS_2} \quad (1)$$

and:

$$\underset{\text{(in pyrrhotite)}}{S} \leftrightarrows \underset{\text{(in vapor)}}{1/2S_2} \quad (2)$$

may be used to obtain log fS_2(−7.061) and a^{po}_{FeS} (0.608) at 400°C and 5kbar, using the volumes calculated above. This procedure is described in more detail in Hutcheon (1978) and is not repeated here.

Table 1. The molar volumes of phases used in calculations

Phase	Volume (cc)	Source
Pyrite	23.94	Kullerud and Yoder (1959)
Troilite	18.20	Scott (1973)
Sphalerite (FeS)	24.033	Hutcheon (1978)
Sulfur (pyrrhotite structure)	14.456	Froese and Gunter (1976)

Having obtained a^{po}_{FeS}, at the pressure and temperature of interest, the free energy change for the equilibrium:

$$\underset{\text{pyrrhotite}}{FeS} \leftrightarrows \underset{\text{sphalerite}}{FeS} \quad (3)$$

may be calculated from:

$$G^{\circ}_{(3)} = 239 + 0.840\,T$$

The expression in Hutcheon (1978, p. 88) contains a minus (−) sign which is a typographical error. Using the molar volumes, corrected by isothermal compressibility and isobaric thermal expansion data, the procedure outlined in Hutcheon (p. 91) is then used to calculate a^{sp}_{FeS}(0.209) by iterating for X^{sp}_{FeS} (0.138) at 400°C and 5kbar. The value of γ^{sp}_{FeS} would be 1.514, using the relationship $a = \gamma \cdot X$.

On Figure 1 the results of these calculations with the expansion and compressibility data (solid lines) and without these data (dashed lines) are shown. The molar volumes at 25°C and 1 atm are shown in Table 1. As pointed out by Scott (1973), the isobaric thermal expansion data and isothermal compressibility data are necessary to obtain a reasonable fit to the published experimental values. A Fortran IV program was written to perform these calculations and copies can be obtained from the author.

References

Froese, E. and A. Gunter (1976) A note on the pyrrhotite–sulfur vapor equilibrum. *Econ. Geol., 71,* 1589–1594.

Hutcheon, I. (1978) Calculation of metamorphic pressure using the sphalerite–pyrrhotite–pyrite equilibrium. *Am. Mineral., 63,* 87–95.

Kullerud, G. and H. S. Yoder (1959) Pyrite stability relations in the Fe–S system. *Econ. Geol., 54,* 533–572.

Scott, S. D. (1973) Experimental calibration of the sphalerite geobarometer. *Econ. Geol., 68,* 466–474.

Toulmin, P., III and P. B. Barton, Jr. (1964) A thermodynamic study of pyrite and pyrrhotite. *Geochim. Cosmochim. Acta, 28,* 641–671.

Manuscript received, April 29, 1980;
accepted for publication, May 9, 1980.

American Mineralogist, Volume 65, pages 1065–1070, 1980

NEW MINERAL NAMES*

MICHAEL FLEISCHER, LOUIS J. CABRI, GEORGE Y. CHAO AND ADOLF PABST

Apachite*, Gilalite*

F. P. Cesbron and S. A. Williams (1980) Apachite and gilalite, two new copper silicates from Christmas, Arizona. *Mineral. Mag., 43,* 639–641.

Both new species are retrograde or mesogene minerals that occur in tactites at the Christmas mine, Gila County, Arizona.

For apachite the average of two closely agreeing analyses gave: CuO 43.6, FeO 0.3, MgO 1.7, CaO 1.8, SiO_2 40.8, H_2O 13.8%, sum 102.0, close to $Cu_9Si_{10}O_{29} \cdot 11\ H_2O$. Apachite is blue, H = 2, D = 2.80. Biaxial (−), 2V small, $\alpha = 1.610$, $\beta = \gamma = 1.650$. No single crystals were found, but the powder pattern was indexed on a monoclinic cell with $a = 12.89$, $b = 6.055$, $c = 19.11$Å, $\beta = 90.42°$; strongest lines of the powder pattern are 13.49(10)(100), 7.663 (7)(102), 3.168(7)(401).

For gilalite the average of two closely agreeing analyses gave: CuO 36.2, MgO 2.3, CaO 3.8, MnO 0.5, SiO_2 41.5, H_2O 14.6, sum 98.8, close to $Cu_5Si_6O_{17} \cdot 7H_2O$. Gilalite is green, H = 2, D = 2.72. Biaxial (−), 2V small, $\alpha = 1.560$, $\beta = \gamma = 1.635$. No single crystals were found but the powder pattern was indexed on a monoclinic cell with $a = 13.38$, $b = 19.16$, $c = 9.026$Å, β sensibly 90°; optics indicate the lower symmetry. Strongest lines of the powder pattern are 13.4(10)(100), 10.97(5)(110), 7.786(5)(120).

DTA shows a sharp loss of water at about 92°C for gilalite and a smooth loss curve for apachite. **A. P.**

Cadmium

B. V. Oleinikov, A. V. Okrugin and N. V. Leskova (1979) Native cadmium in traps of the Siberian Platform. *Doklady Akad. Nauk SSSR, 248,* 1426–1428 (in Russian).

Native cadmium is reported from the heavy, non-magnetic fraction of a concentrate from gabbro-dolerite of the Ust'-Khannin intrusive, eastern Siberian Platform, basin of the Vilui River. It was found as flattened grains, max. size 0.2mm, with smooth surfaces. Color tin-white with a bluish tint, luster metallic, malleable, diamagnetic. Probe analysis gave Cd 99–100% with no Zn or Sn. X-ray powder data are given (9 lines); the strongest lines are 2.79(3), 2.55(4), 2.331(10). These are slightly smaller than the lines given in JCPDS 5-0674. Unit-cell data are not given. Cadmium is hexagonal, $P6_3/mmc$, $a = 2.979$, $c = 5.617$Å.

Associated minerals listed include moissanite, native Fe, Cu, Pb, Sn, Zn, Al [*Am. Mineral., 65,* (1980)], alloys of Cu with Zn, and Sn with Sb, garnet, spinel, kyanite, corundum, rutile, and sulfides of Fe, Cu, Pb, Sb, Zn, As, Hg.

Discussion

No data are given on methods of separation or treatment. The assemblage seems highly improbable, but more data are needed. **M. F.**

Chukhrovite-(Ce), Rhabdophane-(Ce)

Kurt Walenta (1978) Chukhrovite-(Ce) and rhabdophane-(Ce) from the Clara Mine at Oberwolfach, Middle Black Forest. *Chem. der Erde, 38,* 331–339 (in German).

Chukhrovite-(Ce) occurs in white crystals up to a few mm on fluorite. X-ray data show it to be cubic with $a = 16.80 \pm 0.005$Å (surprisingly, somewhat higher than for chukhrovite). Isotropic, $n = 1.443 \pm 0.002$. The strongest X-ray lines (55 given) are 9.75(10)(111), 5.93(8)(220), 4.20(5)(400), 3.22(7)(333,511), 2.56(6)(633), 2.24(5)(642), 217(6)(731,553), 1.824(5)(842). No analysis is given. Electron microprobe analysis showed that Ce is dominant, Nd next, with La, Pr, Sm, Gd, and Eu present.

Rhabdophane-(Ce) occurs in white to pale brown crystals, aggregates of subparallel needles occurring in druses on barite, fluorite, chalcopyrite, and tetrahedrite. Optically uniaxial, positive, $\omega = 1.688$, $\epsilon = 1.744$ (both ±0.003) [both 0.03 higher than usually given for rhabdophane-(La)]. No analysis is given, but electron microprobe study showed Ce dominant, followed by Nd, La, Pr, Gd, Sm, Er, and Eu. X-ray powder data are given (28 lines); the strongest lines are 6.09(9)($10\bar{1}0$), 4.41(8)($10\bar{1}1$), 3.51(7)($11\bar{2}0$), 3.03(10)($20\bar{2}0$), 2.83(9)(2.83($10\bar{1}2$), corresponding to $a = 7.01$, $c = 6.40$Å, close to those for rhabdophane-(La).

Discussion

May be accepted provisionally. Nothing whatever is said of the presence or absence of Y in either mineral; previous analyses of chukhrovite are of chukhrovite-(Y), so the omission is a serious one. **M. F.**

Comblainite*

Paul Piret and Michel Deliens (1980) Comblainite, $(Ni_x^{2+}, Co_{1-x}^{3+})(OH)_2(CO_3)_{(1-x)/2} \cdot yH_2O$, a new mineral of the pyroaurite group. *Bull. Mineral., 103,* 113–117 (in French).

Electron microprobe analyses were made of 2 samples, giving Co_2O_3 20.80, 20.20; NiO 39.30, 38.40; UO_3 4.24, 5.20; MgO (calc.) 0.30, 0.37; P_2O_5 (calc.) 1.05, 1.29; H_2O (calc.) 1.07, 1.31, H_2O- 11.59, 8.69; ($H_2O+ + CO_2$) 21.29, 20.96, sum 99.64, 96.42%. MgO, P_2O_5, and H_2O calc. were calculated from UO_3, known to be present as metasaleeite. TGA determinations (giving CO_2, H_2O+, H_2O-, plus oxygen corresponding to $Co_2O_3 \rightarrow 2CoO$) gave 35.95, 32.79%, respectively. The valences of Ni and Co were determined by ESCA spectra. The infrared spectrum shows bands for H_2O,

* Minerals marked with asterisks were approved before publication by the Commission on New Minerals and Mineral Names of the International Mineralogical Association.

0003–004X/80/0910–1065$00.50

OH−, and $(CO_3)^{-2}$. The thermogravimetric curves show losses to 175° of 12.66 and 10.00% (molecular H_2O); the hydroxyl and CO_2 are given off 250–340°. Inflections at 480° and 710° correspond to the changes Co_2O_3 to Co_3O_4 and Co_3O_4 to CoO. The analyses give, respectively, $Ni^{2+}_{6.10}Co^{3+}_{2.90}(CO_3)_{1.315}(OH)_{18.27} \cdot 6.7\ H_2O$, and $Ni^{2+}_{6.11}Co^{3+}_{2.89}(CO_3)_{1.02}(OH)_{18.84} \cdot 9.92\ H_2O$.

The mineral is rhombohedral, $a = 7.796$Å, $\alpha = 22.47°$, $Z = 1$; in hexagonal setting $a = 3.038$, $c = 22.79$Å, space group $R\bar{3}m$, $R3m$, $R\bar{3}$, $R3$, or $R32$, D calc. for the 2 formulas above 3.16, 3.31, meas. 3.05±0.02. The strongest X-ray lines (16 given) are 7.64(100)(003), 3.808(50)(006), 2.567(70)(012), 2.778(50)(015), 1.934(40)(018). The mineral is a member of the hydrotalcite group.

The mineral occurs as turquoise-blue cryptocrystalline crusts on altered uraninite from Shinkolobwe, Zaire, associated with becquerelite, curite, rutherfordine, and heterogenite. Under the microscope, it is yellow-green, non-pleochroic, with $\omega' = 1.690$, $\varepsilon' = 1.684$ (both ±0.002).

The name is for Gordon Comblain, of the Musee Royal de l'Afrique Central, Tervuren, Belgium, who discovered the mineral. Type material is at that museum. **M. F.**

Defernite*

Halil Sarp, M. F. Taner, Jacques Deferne, Helene Bizouard and B. W. Liebich (1980) Defernite, $Ca_6(CO_3)_2(OH,Cl)_8 \cdot nH_2O$, a new calcium chloro-hydroxyl carbonate. *Bull. Mineral., 103,* 185–189 (in French).

Electron microprobe analysis (average of 18 analyses on 3 samples) gave CaO 62.9, SiO_2 1.2, CO_2 13.4, Cl 3.3, total 80.8 − (O = Cl_2) 0.74 = 80.06, H_2O 19.94% by difference, corresponding to $Ca_{5.62}(CO_3)_{1.52}(SiO_4)_{0.1}(OH)_{7.32}Cl_{0.47} \cdot 1.87\ H_2O$, or $Ca_6(CO_3)_2(OH,Cl)_8 \cdot 2H_2O$, or $Ca_3(CO_3)(OH,Cl)_4 \cdot H_2O$, for which $Z = 8$. Dissolved by cold HCl with effervescence.

Weissenberg and precession study show defernite to be orthorhombic, space group $Pna2_1$ or $Pnam$, $a = 17.860$, $b = 22.775$, $c = 3.658$Å, D calc. 2.42, meas. 2.5. The strongest X-ray lines (30 given) are 11.37(100)(020); 8.29(35)(210); 5.68(30)(040); 3.045(40)(270,141); 2.899(50)(460); 2.418(35)(531,730); 1.962(35); 1.825(40).

The mineral occurs in fan-shaped forms 100–200 microns in size. Colorless, luster vitreous. Cleavage {010} perfect, {100} distinct. Forms {001}, {100}, {010}, {101}, {201}. Optically biaxial, neg., $\alpha = 1.546$, $\beta = 1.572$, $\gamma = 1.576$ (all ±0.001), 2V = 42°; dispersion $r < v$, medium; $X = c$, $Y = b$.

The mineral occurs in skarn at the contact of granite with Cretaceous limestone near Güneyce-Ikizere, Trabson region, Turkey. Associated minerals include vesuvianite, wollastonite, andradite, diopside, calcite, rustumite, spurrite, and hillebrandite.

The name is for Jacques Deferne, Curator of Mineralogy, Museum d'Histoire Naturelle, Geneva, Switzerland, where type material is deposited. **M. F.**

Fluckite*

Hubert Bari, Fabien Cesbron, Francois Permingeat and Francois Pillard (1980) Fluckite, hydrated calcium manganese arsenate, $CaMnH_2(AsO_4)_2 \cdot 2H_2O$, a new mineral. *Bull. Mineral., 103,* 122–128 (in French).

Michele Catti, Giacomo Chiari and Giovanni Ferraris (1980) Fluckite, $CaMn(HAsO_4)_2 \cdot 2H_2O$, a structure related by pseudo-polytypism to krautite, $MnHAsO_4 \cdot H_2O$. *Bull. Mineral., 103,* 129–134.

Microprobe analyses of deep rose and pale rose varieties gave, respectively, As_2O_5 50.40, 50.49; CaO 13.01, 12.86; MnO 13.68, 16.65; FeO 0.11, 0.05; CoO 0.59, 0.03; NiO–, 0.03; MgO 0.93, –. Analysis of pale rose material by atomic absorption by B. Reynier on 80 mg gave As_2O_5 56.60, CaO 12.98, MnO 17.17, MgO 0.04, H_2O (Penfield) 13.20, sum 99.99%. Analysis by J. Hucherot on material from the Giftgrube gave As_2O_5 57.4, CaO 13.6, MnO 16.8, MgO 0.3, H_2O 13.3, sum 101.4%. All these lead to the formula $Ca(Mn,Mg,Co)(HAsO_4)_2 \cdot 2H_2O$. The DTA curve shows an endothermic break at 260° (dehydration).

The mineral is triclinic, $P\bar{1}$, $a = 8.459$±0.002, $b = 7.613$±0.001, $c = 6.98$±0.001Å, $\alpha = 82.21$±0.01, $\beta = 98.25$±0.01, $\gamma = 95.86$±0.02°; $Z = 2$; D calc. 3.11, measured 3.05±0.02. The strongest X-ray lines (36 given) are 8.323(44)(100), 7.512(100)(010), 3.767(56)($\bar{2}$10,020), 3.528(90)($\bar{1}$20,210), 3.266(91)(012), 2.975(81)(0$\bar{1}$2), 2.688(61)(220), 2.671(43)($\bar{3}$10).

The mineral is colorless to pale rose to deep rose. It occurs as radiating prismatic crystals with {100}, {110}, and {010} dominant and 6 other faces. Cleavages {010} perf., {100} easy, {$\bar{1}$01} difficult and imperfect. H = 3½–4. Optically biaxial, probably positive, $2V$ large, $\alpha' = 1.618$, $\gamma' = 1.642$.

The mineral was found at the 60 m. and 100 m. levels of the Gabe Gottes–Saint Jacques vein at Sainte Marie-aux-Mines, Vosges, France, associated with pharmacolite and picropharmacolite. The name is for Pierre Fluck, mineralogist, Louis Pasteur University, Strasbourg. **M. F.**

Giniite*

Paul Keller (1980) Giniite, $Fe^{+2}Fe^{+3}_4(H_2O)_2(OH)_2(PO_4)_4$, a new mineral from the pegmatite of Sandamab near Usakos, Namibia. *Neues Jahrb. Mineral. Monatsh.,* 49–56 (in German).

Microprobe analysis (H_2O by GA), using analyzed wyllieite as standard, gave P_2O_5 36.99, Fe_2O_3 (total Fe) 46.07, Al_2O_3 1.20, MgO 0.68, MnO 0.63, H_2O 6.45, sum 92.02%. The pleochroism and blue-green color indicate the presence of both Fe^{2+} and Fe^{3+}; the molecular weight from the unit cell dimensions suggests the formula $Fe^{2+}_xFe^{3+}_{5-x}(H_2O)_{1+x}(OH)_{3-x}(PO_4)_4$. Dehydration showed a loss of 4.0% to 330°, corresponding to $2H_2O$, and a further loss of 2.4% at 510°. The formula then becomes, with $x = 1$, $Fe^{2+}Fe^{3+}_4(PO_4)_4(OH)_2 \cdot 2H_2O$.

X-ray study showed giniite to be orthorhombic, space group $Cmm2$, $C222$, or $Cmmm$, $a = 10.365$, $b = 26.582$, $c = 5.162$Å, $Z = 4$, D calc. 3.42, meas. 3.41.

The strongest X-ray lines (22 given) are 3.36(10)(260,061), 3.20(7)(330,241), 2.80(5)(261,081), 2.28(6)(371,421), 2.04(7), 1.679(6), 1.604(7).

The mineral occurs in idiomorphic crystals with {010}, {150}, and {041} dominant, present also {310}, {001}, {100}. Crystals are up to 0.5×0.2×0.05mm. Color blackish-green to blackish-brown, streak olive, luster vitreous to greasy. No cleavage, fracture conchoidal; H 3–4. Optically biaxial neg. $2V \sim 55°$. $\alpha = 1.775$, $\beta = 1.803$, $\gamma = 1.812$; pleochroic, $X = c$, light brown, $y = b$, dark brown, $Z = a$, dark blue green.

The mineral occurs in pegmatite at Sandamab near Usakos, Namibia, associated with hureaulite, tavorite, leucophosphite, and an unknown phosphate, formed by the alteration of triphylite. The name is for the author's wife. **M. F.**

0003–004X/80/0910–1066$00.50

Helmutwinklerite*

Günter Schnorrer-Köhler (1980) Koritnigite and helmutwinklerite, two new minerals from Tsumeb, S. W. Africa. *Aufschluss, 31,* 43–49 (in German).

Microprobe analysis (H_2O by Karl Fischer method) gave (average): As_2O_5 34.35, PbO 31.28, ZnO 27.50, CuO 1.48, H_2O 6.14, sum 100.75%, corresponding to $Pb_{0.9}Cu_{0.12}Zn_{2.17}As_{1.92}O_8 \cdot 2.19H_2O$, or $PbZn_2(AsO_4)_2 \cdot 2H_2O$. Dissolved by cold concentrated HCl.

Triclinic, pseudo-monoclinic, $P1$ or $P\bar{1}$. Forms {001}, {010}, $\{1\bar{1}0\}$, and $\{11\bar{1}\}$. Color sky-blue. G = 5.3, H = 4½, $\alpha = 1.72(5)$, $\beta = 1.80(5)$, $\gamma = 1.98(5)$; biaxial positive. Luster vitreous to resinous. No cleavage. The mineral occurs in cavities in tennantite, associated with quartz and willemite.

The name is for Helmut Winkler, University of Göttingen. **M.F.**

Jungite*, Matulaite*

P. B. Moore and Jun Ito (1980) Jungite and matulaite, two new tabular phosphate minerals. *Aufschluss, 31,* 55–61 (in German).

Jungite

Analysis by J. I. gave P_2O_5 31.0, Al_2O_3 0.08, Fe_2O_3 28.4, ZnO 14.6, MgO 0.06, MnO 2.80, CaO 5.89, Na_2O 0.04, K_2O 0.01, H_2O- (180°C) 9.10, H_2O+ (loss on ign.) 8.70, sum 100.68%, corresponding to $Ca_2Zn_4Fe^{3+}_8(PO_4)_9(OH)_9 \cdot 16H_2O$.

X-ray data show it to be orthorhombic, possible space groups $Pcmm$, $Pcm2_1$, or $Pc2m$, $a = 11.98$, $b = 20.37$, $c = 9.95$Å, $Z = 2$. D calc. 2.849, meas. 2.843. The strongest lines (50 given) are 9.96(6)(10)(020), 5.09(5)(040), 3.79(4), 3.37(5)(060), 3.30(5).

The mineral occurs as rosettes up to 1 cm in diameter of very thin, tabular, bent crystals. H = 1. Cleavage perfect {010}. Color dark green, streak yellow. Luster silky to vitreous. Optically biaxial, neg.(?), $\beta = 1.658$, $\gamma = 1.664$, $2V \sim 60°$, $Y = a$, $Z = c$, $r < v$ strong. The mean n, calculated by the Gladstone–Dale rule, is stated (without comment) to be 1.703.

The mineral occurs at the Hagendorf South pegmatite, Bavaria, associated with mitridatite and manganese oxides. The name is for Dr. Gerhard Jung, who found the mineral.

Matulaite

Analysis of material from Hellertown gave P_2O_5 33.5, SiO_2 3.0, TiO_2 0.12, Al_2O_3 34.0, Fe_2O_3 1.05, ZnO 0.14, CuO 0.09, MnO 0.07, CaO 1.59, BaO 0.06, Na_2O 0.06, K_2O 0.04, H_2O- (140°C) 15.39, H_2O+ (loss on ign.) 10.64, sum 99.75%. After subtracting quartz and hematite, this gives $CaAl_{18}(PO_4)_{12}(OH)_{20} \cdot 28H_2O$. Difficultly soluble in HCl, easily in hot H_2SO_4.

Weissenberg and rotation photographs show matulaite to be monoclinic, space group probably $P2_1/c$, $a = 20.4$, $b = 16.7$, $c = 10.6$Å, $\beta = 98.2°$, $Z = 2$. The strongest X-ray lines (38 given) are 9.96(10), 6.37(4), 4.42(4), 2.395(4). A sample ground in acetone gave strongest lines 11.79(100), 10.93(90), 5.94(10), 5.51(80).

The mineral occurs in small rosettes of thin tabular crystals and botryoidal forms. Cleavage {100} very perfect. Colorless to white, luster pearly. H = 1; D = 2.330. Optically biaxial, neg., $2V \sim 60°$, $\beta = 1.576$, $\gamma = 1.582$; dispersion $r < v$ strong, $Y = b$, $Z:c = 8°$. The mean index, calc. from the Gladstone–Dale rule, is stated to be 1.542.

The mineral occurs at the Bachman iron mine, Hellertown, Pennsylvania (type locality), and from the Rotläufchen iron mine, Waldgirmes, West Germany, at both of which it occurs as incrustations on chert, the youngest mineral of the association beraunite, rockbridgeite, dufrenite, cacoxenite, strengite, wavellite. Also occurs at the LCA pegmatite, Gaston Co., N. Carolina.

The name is for Mrs. Marge Matula of Allentown, Pa., who found the Hellertown material. **M.F.**

Kolwezite*

Michel Deliens and Paul Piret (1980) Kolwezite, an hydroxycarbonate of copper and cobalt, analogous to glaukosphaerite and rosasite. *Bull. Mineral., 103,* 179–184 (in French).

Analysis (Cu, Co by X-ray fluorescence, CO_2 volumetric, H_2O + CO_2 by TGA) gave CoO 22.98, CuO 48.40, CO_2 19.44, H_2O 8.78, sum 99.60%, corresponding to $(Cu_{1.33}Co_{0.67})(CO_3)_{0.98}(OH)_{2.07}$ or $(Cu,Co)_2(CO_3)(OH)_2$ with Cu:Co = nearly 2:1. The DTA curve showed a small endothermic break at 110°, a large one at 425°, (loss of CO_2), and a small one at 560°C (conversion of Co_2O_3 to Co_3O_4). The infrared absorption curve is very similar to that of rosasite and somewhat similar to that of glaukosphaerite.

X-ray powder data are given; they correspond to a triclinic cell with $a = 9.50$, $b = 12.15$, $c = 3.189$Å, $\alpha = 93.32°$, $\beta = 90.74°$, $\gamma = 91.47°$, $Z = 4$. D 3.94 calc., 3.97 meas. The strongest lines (31 given) are 6.04(80)(020); 5.08(80)(120); 3.70(100)(220); 2.956(50)$(1\bar{1}1)$; 2.951(80)$(2\bar{1}1)$; 2.535(50)(211); 1.109(50).

The mineral occurs in the oxidized zone of the Cu–Co deposit of Kolwezi-Kamoto-Musonoi, southern Shaba, Zaire, as nodules (1–10 mm) and microcrystalline crusts. H near 4, color black to beige, $\alpha' = 1.688 \pm 0.002$, $\gamma' > 1.90$.

The name is for the locality. Type material is at the Musee Royal Afrique Centrale, Tervuren, Belgium. **M.F.**

Kuramite*

V. A. Kovalenker, T. L. Evstigneeva, N. V. Troneva and L. N. Vyal'sov (1979) Kuramite, Cu_3SnS_4, a new mineral of the stannite group. *Zap. Vses. Mineral. Obsh., 108,* 564–569 (in Russian).

Microprobe analyses of 5 samples gave Cu 36.54, 36.74, 36.25, 36.70, 40.10; Fe 2.94, 2.39, 2.84, 2.21, 1.43; Zn 1.73, 2.17, 2.50, 2.10, 0.91; Sn 30.05, 30.92, 29.50, 31.77, 28.36; In 0.21, 0.31, 0.33, 0.24, 0.51; S 28.02, 27.65, 28.04, 27.86, 27.75, sum 99.50, 100.18, 99.46, 100.87, 99.06%. These correspond to $Cu_{2.00}(Cu,Fe,Zn)SnS_4$ with Cu 2.56–2.83, Fe 0.12–0.24, Zn 0.06–0.17, Sn 1.06–1.17, In 0.01–0.02, S 3.88–3.92. This is a member of the stannite $(Cu_2^{+}Fe^{2+}SnS_4)$–kesterite$(Cu_2^{+}Zn^{2+}SnS_4)$ series, the end member being $Cu_2^{+}Cu^{2+}SnS_4$.

Kuramite is tetragonal, space group $I\bar{4}2m$, $a = 5.445 \pm 0.005$, $c = 10.75 \pm 0.02$Å, $Z = 2$. The strongest X-ray lines (11 given) are 3.13(10)(112), 1.914(8)(024,220), 1.640(6)(132), 1.108(4)(244).

Under the microscope neutral gray. Distinctly anisotropic, with color effects in brown shades. Reflectivity (R_{max} and R'e): is given at 16 wave lengths, at 460nm, 25.3, 25.2; 540, 26.5, 28.7; 580, 26.7, 29.5; 640, 26.5, 28.0%. H (20g load) 379–432, av. 390 kg/sq mm on grains of analyses 1–4; 301–372, av 333 kg/sq mm on grain 5 (highest Cu content).

The mineral occurs in gold–sulfide–quartz ores in a deposit in the Kuramin Mts., eastern Uzbekistan, as inclusions 5–80 microns in diameter within goldfieldite, which also contains inclusions of hessite, petzite, sylvanite, altaite, native Au, and other minerals.

The name is for the locality. Type material is at the Mineralogical Museum, Academy of Sciences, and in the Institute of Ore Deposits, *etc.* (IGEM), both in Moscow. **M.F.**

0003-004X/80/0910-1067$00.50

Partheite*

Halil Sarp, Jacques Deferne, Helene Bizouard and B. W. Liebich (1979) Partheite, $CaAl_2Si_2O_8 \cdot 2H_2O$, a new natural silicate of aluminum and calcium. *Schweiz. Mineral. Petrog. Mitt., 59,* 5–13 (in French).

Electron microprobe analyses (standards, analyzed vuagnatite, wollastonite, albite, orthoclase) gave SiO_2 40.24, 38.83, 38.10; Al_2O_3 31.99, 30.46, 29.68; CaO 16.38, 16.31, 16.22; Na_2O 0.32, 0.32, 0.32; K_2O 0.23, 0.23, 0.23; H_2O 10.83, 13.85, 15.45%, corresponding to the formula above.

Weissenberg photographs show partheite to be monoclinic, space group probably $C2/c$, $a = 21.59$, $b = 8.78$, $c = 9.31$Å, $\beta = 91.47°$, $Z = 8$; D calc. 2.37, meas. 2.39. The strongest X-ray lines (36 given) are 10.79(100)(200), 8.12(80)(110), 6.10(70)(111), 3.740(50)(22$\bar{1}$), 3.600(40)(31$\bar{2}$,51$\bar{1}$), 3.190(40)(022).

Partheite occurs as white fibers of vitreous luster in rodingite of the Taurus Mts., S. W. Turkey. Associated minerals are prehnite, thomsonite, and augite. The mineral is optically biaxial, positive, $2V = 48°$, $\alpha = 1.547$, $\beta = 1.549$, $\gamma = 1.559$ (all ± 0.001); $r > v$ med., elongation negative, extinction 23–30°, $X\Lambda$ elongation; cleavage distinct parallel to fibers.

The name is for Edwin Parthé, Professor of Crystallography, University of Geneva. **M.F.**

Pianlinite

Liu Changling, Liu Deye, Zhang Fu, Li Jinsheng, Sun Weijun and Lu Wenhan (1963) Pianlinite, a new clay mineral species. *Kexue Tongbao,* 10, 59–62 (in Chinese). Liu Changling (1979) New data on pianlinite. *Kexue Tongbao,* 24, 553–555 (in Chinese).

Chemical analysis gave Al_2O_3 42.63, SiO_2 50.10, TiO_2 0.32, Fe_2O_3 0.10, FeO 0.50, CaO 0.06, MgO 0.09, K_2O 0.06, Na_2O 0.03, ZrO_2 0.008, MnO tr, P_2O_5 0.005, H_2O+ 4.55, H_2O- 1.63, sum 100.083, corresponding to $Al_2O_3 \cdot 2SiO_2 \cdot H_2O$.

The mineral is almost X-ray amorphous and gives many lines on long exposures. The X-ray pattern of the better crystallized variety is characterized by the lack of very intense lines and of low-angle lines. The strongest lines (30 given) are 4.62(3, diffuse), 3.37(3), 2.56(7), 2.42(5), 2.21(6), 1.53(4), 1.48(3), 1.27(5), 1.25(3), 0.967(3), 0.846(4). Powder patterns for materials heated to 950°, 1245°, and 1385°C are also given. Powder and single-crystal electron diffraction studies show the mineral to be neither amorphous nor crystalline (no details given, GYC). The mineral is considered to be "semi-crystalline" due to strong c-axis disorder as in metakaolinite. Diffractometer tracings of coarsely crushed material (1963) show a broad peak centered at 15° 2θ and two sharp peaks at 2.016 and 2.336Å, thought to be due to preferred orientation effect.

The mineral is pure white and grayish white with vitreous luster to gray and earthy. The mineral occurs as dense massive aggregates that are brittle, hard (6–7), with uneven to subconchoidal fracture. The true density is 2.45 g/cm^3. In thin section, the aggregates are mostly phanerocrystalline, displaying colloform, myrmeketic (up to 2mm), petal-like, and fine to coarse scaly structures. The mineral is colorless. Some specimens are weakly pleochroic with X = colorless, Z = pale yellow. The mineral has a perfect (001) cleavage and shows straight extinction with the cleavage parallel to the vibration direction of the slow ray. $\alpha = 1.532(2)$, $\beta = 1.539(4)$, $\gamma = 1.541(4)$, (±) $2V = 0°$ to 5° or less. Electron microscopy shows the crystals to be irregular to nearly hexagonal plates.

DTA curve shows endothermic peaks at 144° (weak and broad) and 892° (weak and may be absent) and exothermic peaks at 950° (sharp and strong, crystallization of Al–Si-spinel) and at 1245°C (weak, crystallization of mullite and cristobalite). TGA curve shows a small initial weight loss to 100°, followed by a slow one-stage major weight loss to 500°C.

The infrared spectrum of pianlinite is similar to that of metakaolinite heated to 900°C, except the presence of the O–H stretching band at 3100–3700^{-1} and the absence of fine structures in the 600–1400cm^{-1} region of the former.

The mineral occurs as a monomineralic clay bed (less than 1m in thickness) in an Upper Carboniferous sedimentary formation in Pianling, China. Accessory minerals in the clay bed are quartz, zircon, mica, rutile, augite, garnet, epidote, ilmenite, gibbsite, halloysite, kaolinite, and ferromontmorillonite. The name is for the locality.

Discussion

The data show the mineral to be unique. The non-crystalline nature and the thermal behavior of the mineral are similar to those of allophane but it may be distinguished from allophane by its lower water content and higher refractive indices and density. It may also be distinguished from the minerals of the kaolinite group by its lower water content and the characteristic absence of a well-defined endothermic reaction at 500°–700°C on its DTA curve. However, the sharp reflections of 2.016 and 2.336Å, observed on the diffractometer tracings of the nearly amorphous material, do not match the X-ray lines given for the better crystallized material, suggesting the presence of another phase. Further study of the mineral, especially on its homogeneity and the range of composition variations, is desirable. The mineral should not have been given a name at the present stage (see Bailey, *Can. Mineral., 18,* 143–150, 1980). **G.Y.C.**

Ruarsite

Tsu-hsiang Yu and Hsueh-tsi Chou (1979) Ruarsite, a new mineral. *Science Bulletin (Ko'Hsueh Tu'ng Pao), 24,* 310–316 (in Chinese).

Ruarsite is reported as a new mineral found in heavy mineral concentrates from and in polished sections of chromium ore from an Alpine-type ultramafic, northern Tibet, as well as in placers derived from the weathered ultramafics. Eight probe analyses for seven grains gave Ru 42.45 (35.74–49.84), Os 5.94 (nil to 14.84), Ir 1.67 (nil to 2.8), Pt 0.07 (nil to 0.32), Cu 0.00 (nil to 0.01), As 36.25 (33.09–39.2), Sb 0.00 (nil to 0.01), and S 14.08 (13.7–15.0); sum 100.36 (98.3–102.3), corresponding to an average of $(Ru_{0.913}Os_{0.048}Ir_{0.018}Pt_{0.001})As_{1.050}S_{0.934}$ or, ideally, RuAsS. An X-ray powder pattern (43 lines, plus 7 lines ascribed to laurite and irarsite) of a ruarsite grain, of composition $(Ru_{0.804}Os_{0.168}Ir_{0.025}Pt_{0.003})As_{1.004}S_{0.981}$, was indexed as monoclinic, $a = 5.931$, $b = 5.915$, $c = 6.003$Å, $\beta = 112°27'$ which corresponds with data for synthetic RuAsS (Hulliger, Nature, *201,* 381–382, 1964). The strongest lines are: 3.79(50)($\bar{1}$11), 2.77(100)(002), 2.74(200), 1.890(70)($\bar{3}$02), 1.870(90)($\bar{3}$11), 1.695(90)(131) 1.660(60)(202), 1.580(50)(103) and 1.149(50)(340).

Ruarsite occurs as irregular grains or as aggregates (100–150 μm). It is lead-grey to dark-lead grey with a metallic lustre and a rough-textured surface. The streak is greyish black; it is brittle, non-magnetic and is not soluble in 1:1 HCl. In polished sections it is greyish white, pale yellow next to irarsite or laurite. The mineral

0003–004X/80/0910–1068$00.50

polishes reasonably well, better than irarsite and laurite. It is bireflectant, in oil; pleochroism varies from pale yellowish white to light greyish yellow-white. The mineral is distinctly anisotropic; with nicols 1–2° off 90° bluish grey to light-reddish. Reflectance on a grain with minor Os gave: 42.0, 43.0, 42.5 (480 nm), 42.6, 43.8, 42.73 (546 nm), 42.9, 43.3, 42.6 (589 nm), and 43.4, 44.3, 43.3 (656 nm), and on a grain with 14% Os: 43.4 (480 nm), 44.1 (546 nm), 43.8 (589 nm) and 45.1 (656 nm). VHN_{20} = 982.1–1030.2 for two low-Os grains while the grain with 14% Os gave VHN_{20} = 804, VHN_{50} = 893, and VHN_{100} = 734. Internal reflection, cleavage and twinning were not observed. In the Cr-ore associated platinum-group minerals are iridosmine, ruthenian iridosmine (= rutheniridosmine?), sperrylite, and laurite; the latter occurs as relics in ruarsite. The principal metallic minerals of the ore are Cr-spinel (85–95%) with minor pyrite, pyrrhotite, loellingite, magnetite, chalcopyrite, molybdenite, galena, and millerite found in the interstices of the Cr-spinel. Principal gangue minerals are serpentine with minor chlorite. In the placer deposits, which occur on the western part of the ultramafic, the major PGM are Os–Ir–Ru alloys, such as ruthenosmiridium (or osmiridium?), iridosmine, (Pt,Ir) alloy, (Ru,Fe) alloy, osmium, gold, trace amounts of sperrylite, and the heavy minerals chromite, magnetite, ilmenite, rutile and garnet. The ruarsite occurs on the peripheries of some Os–Ir minerals, closely associated with PG-sulfide, -sulfarsenide or -arsenides which occur as exsolutions in the Os–Ir–Ru alloys as well as inclusions in sperrylite and replacing irarsite and laurite. In addition to ruarsite, ruthenarsenite, irarsite, platinian irarsite, iridarsenite, and anduoite (*Am. Mineral., 64,* 464, 1979) occur with these sulfarsenides and sulfides.

The mineral is named after its composition, as were osarsite and irarsite. Type specimens of ruarsite are deposited in the Museum of Geology.

Discussion

A very complete description of a new mineral species. **L.J.C.**

Schlossmacherite*

K. Schmetzer and H. Bank (1979) Schlossmacherite, a new mineral, named for Prof. Dr. Karl Schlossmacher, honorary president of the German Gemmological Society. *Z. deutsch. gemmol. Ges., 28,* 131–133 (in German).

A preliminary report. Analysis gave SO_3 29.3, As_2O_5 13.4, Al_2O_3 36.3, Fe_2O_3 0.6, CaO 3.5, SrO 0.3, BaO 0.3, K_2O 0.5, Na_2O 0.5, H_2O~15, sum 100.9%, corresponding to the formula $(H_3O,Ca)Al_3(SO_4,AsO_4)_2(OH)_6$ with H_3O>Ca and SO_4>AsO_4. It is a member of the beudantite group.

The mineral is hexagonal, [trig(?)MF], a = 6.998, c = 16.67Å; strongest X-ray lines 4.92(70), 2.98(50), 2.96(100). Av. n = 1.597.

The mineral occurs with ceruleite and chenevixite at the Emma Luisa mine, Guanaco, Chile. **M.F.**

Silver-4H, Silver-2H, Silver-3C

M. I. Novgorodova, A. I. Gorshkov and A. V. Molkhov (1979) Native silver and its new structural modifications. *Zap. Vses. Mineral. Obsh., 108,* 552–563 (in Russian).

Electron diffraction patterns of native silver from northeastern USSR showed, in addition to cubic silver, a = 4.08Å, the presence of two hexagonal forms, Ag-4H (a = 2.94, 2.93, 2.88; c = 10.11, 10.18, 9.62Å; D calc. = 9.53) and Ag-2H (a = 2.94, 2.93, 2.92; c = 4.80, 4.79, 4.774; D calc. = 10.11). X-ray powder data are given. Microprobe analyses of 6 samples by A. I. Tsepin showed Ag 98.21–99.93, Au 0.04–0.33, Sb 0.04–0.37, Bi 0.18–0.26, Cu up to 0.50, and traces of Fe, Cr, and Ni. **M.F.**

Sinjarite*

Z. A. Aljubouri and S. M. Aldabbagh (1980) Sinjarite, a new mineral from Iraq. *Mineral. Mag., 43,* 643–645.

A hygroscopic, soft, pink mineral was discovered in the dry bed of an intermittent stream in Sinjar town, west of Mosul city. Wet-chemical analysis gave Ca 25.84, Cl 46.64, H_2O 26.55, Na 0.85%, sum 99.88; trace elements K 226 ppm, Mg 5 ppm, Sr 141 ppm, Fe 9 ppm. The X-ray powder pattern agrees well with that recorded for $CaCl_2 \cdot 2H_2O$ (JCPDS card 1-0989). The mineral is granular (massive), white streak, vitreous to resinous luster; H = 1½. Elongated prismatic crystals have parallel extinction and positive elongation, n = 1.54.

It may be assumed that sinjarite has been precipitated within recent sediments from the slow evaporation of ground water saturated with Ca and Cl ions. The mineral is ephemeral, and dissolves quickly during wet seasons. Alternatively, because of its hygroscopic nature it may change to the hexahydrate $CaCl_2 \cdot 6H_2O$, which melts at 30°C and will not survive hot seasons. **A.P.**

Tarnowskite (= Tarnowitzite)

Maria Czaja (1978) New data on tarnowskite (tarnowitzite) from Tarnowskie Gory. *Mineral. Polonica, 9,* 89–96.

Tarnowitzite was named by Breithaupt for the locality in Upper Silesia. The Polish name is Tarnowskie Gory. Electron microprobe analyses showed Pb 2.93–4.60%; X-ray and infrared data are given.

Discussion

Unnecessary name for plumboan aragonite. **M.F.**

Unnamed analogue of schoenfliesite

N. K. Marshukova, G. A. Sidorenko and N. I. Chistyakova (1978) On natural hydrostannates. *New Data on Minerals of the U.S.S.R., 27,* 89–95 (in Russian).

The Mushiston tin deposit, Central Asia, contains stannite–chalcopyrite–sphalerite–galena mineralization. The stannite has been altered to fine-grained earthy aggregates of brownish-green color. X-ray study showed the mineral to be cubic, a = 7.71±0.02Å. The strongest lines (17 given) are 3.840(10)(200), 2.719(8)(220), 1.722(6)(420). Microprobe analyses of 5 grains gave the formulas:

$(Cu_{0.68}Fe_{0.31}Zn_{0.14})Sn_{0.87}(OH)_6 \cdot 2.95\ H_2O$
$(Cu_{0.52}Fe_{0.40}Zn_{0.26})Sn_{0.82}(OH)_6 \cdot 2.50\ H_2O$
$(Cu_{0.41}Fe_{0.31}Zn_{0.25})Sn_{1.25}(OH)_{5.79}$
$(Cu_{0.50}Fe_{0.23}Zn_{0.41})Sn_{1.16}(OH)_{5.69}$
$(Cu_{0.28}Fe_{0.42}Zn_{0.36})Sn_{0.85}(OH)_{6.09}$

0003–004X/80/0910–1069$00.50

Discussion

Note that the first four of these have Cu dominant; the last has Fe dominant. Material with Fe dominant had previously been described by Grubb and Hannaford, *Mineralium Deposita, 2,* 148–171(1966) and by Geier and Ottemann, abstract in *Am. Mineral., 56,* 1488 (1971). **M.F.**

Unnamed chlorite

F. Radke, P. K. Schultz, and R. N. Brown (1978) Zinc-rich chlorite from Chillagoe, Queensland. *Amdel Bull., no. 23,* 25–28.

Drill cores in chloritized andesites and skarns have veins with calcite, quartz, and fibrous green chlorite. Analyses show ZnO 6.0–30.5%. Microprobe analysis by P.K.S. gave SiO_2 32.0, Al_2O_3 12.4, FeO (total Fe) 12.9, ZnO 30.5, MgO 4.6, MnO 0.15, CaO 1.0, sum 93.5%, corresponding to $(Zn_{2.47}Fe_{1.14}Mg_{0.71}Ca_{0.11}Mn_{0.01}Al_{0.19})Al(Si_{3.52}Al_{0.48})O_{10}(OH)_8$. The strongest X-ray lines (9 given) are 14.2(8), 7.15(10), 3.57(4), 2.66(3), 1.54(4). The mineral had $\alpha = 1.582$, $\gamma = 1.614$. **M.F.**

Unnamed Na_2HPO_4, unnamed $Na_2HPO_4 \cdot 2H_2O$

A. P. Khomyakov and Yu. P. Men'shikov (1979) Identification of Na_2HPO_4 and $Na_2HPO_4 \cdot 2H_2O$ in the products of alteration of natural natrophosphate. *Dokl. Akad. Nauk SSSR, 248,* 1207–1211 (in Russian).

Natrophosphate was described [see *Am. Mineral., 58,* 139 (1973)] as $Na_6H(PO_4)_2F \cdot 17H_2O$, and is here stated to be $Na_7(PO_4)_2F \cdot 19H_2O$. Material from Mt. Karnasurt, Lovozero massif, and from Yukspor and Koashva, Khibina massif, is altered to dense, porcelain-like, or friable powdery aggregates of snow-white color, with dull luster. X-ray powder data show that these consist of mixtures of villiaumite (NaF), Na_2HPO_4 (ASTM 10-184), and $Na_2HPO_4 \cdot 2H_2O$ (ASTM 1-0232). **M.F.**

Unnamed V mineral of the montmorillonite group

M. Güven and W. F. Hower (1979) A vanadium smectite. *Clay Minerals, 14,* 241–245.

Analysis of material saturated with Na, then dried to constant weight at 105°C, gave Si 18.78, V 20.90, Al 2.52, Mg 0.93, Fe 0.92, Ca 0.62, Na 3.09%. This can be calculated as V^{3+} and Fe^{2+} or as V^{4+} and Fe^{3+} respectively, giving SiO_2 40.18, V_2O_3 30.75 or V_2O_4 34.03, Al_2O_3 4.76, MgO 1.54, FeO 1.18 or Fe_2O_3 1.32, CaO 0.87, Na_2O 4.26, loss on ign. 14.92, sum 98.46 or 101.88%.

The X-ray diffraction pattern of the oriented <2 micron fraction shows a very strong reflection 15.0±0.1Å. The material saturated with Na has a basal spacing of 12.6±0.1Å, which expands to 16.7±0.1Å on saturation with glycol. Randomly oriented powder indicated $b = 9.02 \pm 0.2$Å. SEM photographs are given. **M.F.**

NEW DATA

Metavivianite = partly oxidized vivianite (?)

Jean-Francois Poullen (1979) New data on vivianite and metavivianite. *C. R. Acad. Sci. (Paris), 289D,* 51–52 (in French).

Metavivianite was described in *Am. Mineral., 59,* 896–899 (1974) as the triclinic dimorph of monoclinic vivianite. The present note, without giving any data, states that powder data, single-crystal study, and infrared study of metavivianite from the Yukon show that they are identical with those of naturally or artifically oxidized vivianite.

Discussion

Since Poullen did not examine type metavivianite from South Dakota, his conclusions have no standing. **M.F.**

DISCREDITED MINERALS

Hydrophilite

M. H. Hey (1980) What was hydrophilite? *Mineral. Mag., 43,* 682.

Hydrophilite was described by J. F. L. Hausmann (*Handb. Mineral.,* 875, 1813), as a coating on gypsum from the Lüneburg boracite deposit. He reported its constitutents to be calcium chloride and water, and that it is hygroscopic, deliquescent, very soluble in water, soluble in alcohol, and has an intensely bitter taste. Hydrophilite was evidently one of several hydrates of $CaCl_2$, and may have been an early find of antarcticite ($6H_2O$) or sinjarite ($2H_2O$), but remains undefined. **A.P.**

Slavyanskite = Tunisite

A. S. Povarennykh (1979) Slavyanskite. *Mineralog. Zhurnal, 1,* no. 2, 105–106 (in Russian).

Slavyanskite, described as $CaAl_2O_4 \cdot 8$–$8\frac{1}{2}H_2O$ (*Am. Mineral., 63,* 599, 1978) is shown by infrared spectrum to be a carbonate. Its X-ray and optical data correspond closely to those of tunisite (*Am. Mineral., 54,* 1–13, 1969), described as $HNaCa_2Al_4(CO_3)_4(OH)_{10}$. In a footnote, Povarennykh states, without giving his evidence, that the correct formula for tunisite is $CaAl_2(CO_3)_2(OH)_4$. **M.F.**

0003–004X/80/0910–1070$00.50

American Mineralogist, Volume 65, pages 1071–1073, 1980

BOOK REVIEWS

CHALCOPYRITE—ITS CHEMISTRY AND METALLURGY. By Fathi Habashi. McGraw-Hill, Inc., New York, 1978. 165 pages. $24.50.

This book, as stated by the author, is meant to serve as a literature review restricted to the chemical behavior and treatment of the most abundant copper-bearing mineral, chalcopyrite. It contains twelve chapters of which the first (7 pages) mentions the natural occurrence of this mineral, the present methods of its treatment, the drawbacks inherent in these methods, and the attempts being made to improve copper extraction. It concludes that hydrometallurgical methods must be developed to avoid air pollution. Chapter 2 (5 pages) discusses flotation, chapter 3 (10 pages) deals with structure and physical properties, chapter 4 (17 pages) cites data pertaining to the thermal stability of this mineral. Chapter 5 (17 pages) discusses thermal oxidation and chapters 6 and 7 (48 pages) deal with aqueous oxidation. Chapter 8 (12 pages) is devoted to reduction, chapter 9 (2 pages) to chlorination, chapter 10 (5 pages) to electrolytic reactions and chapter 11 (5 pages) to minor and trace metals in chalcopyrite. The final chapter (1 page) concludes that future chalcopyrite metallurgy will be directed toward acid pressure leaching of flotation concentrates at about 110°C and lists nine advantages of such procedures over other methods such as conventional smelting. The book also contains two appendices; the first (5 pages) lists world primary copper smelters and the second (2 pages) provides references to discussions of the chemistry and metallurgy of copper in the eight-volume (System Number 60) Gmelin's Handbook of Inorganic Chemistry.

The book in addition has a 5-page author index and a 9-page subject index. Although the list of references includes about 400 items, it is by no means complete. Much information in print has not been included, for instance pertaining to the thermal stability and solid solution field of the chalcopyrite phase. There are no data on the effect of pressure on polymorphic inversions and structural stabilities. The reader might understand why the author could not present detailed information on copper and iron sulfides such as covellite, blue-remaining covellites, anilite, digenite, djurleite, chalcocite, pyrrhotite, pyrite, and even bornite, one or more of which frequently coexist with chalcopyrite in ores. It is, however, not easy to understand why cubanite is not described in detail, why practically nothing is said about talnakhite, and why mooihoekite and haycockite are not even mentioned in the text. The latter four minerals are all stable in the temperature range of the hydrometallurgical procedures suggested by the author. Some, or all, of these phases may form as intermediate products during acid pressure leaching or may occur with chalcopyrite in flotation concentrates. The book in at least two places contains statements to the effect that chalcopyrite only during the last 10 to 15 years has been realized to be the most abundant copper-bearing mineral. This has been known to mineralogists at least since the turn of the century. The author also states that "It (chalcopyrite) is mined as cupriferous pyrite and pyrrhotite which contain copper in solid solution, or as disseminated grains of chalcopyrite." Chalcopyrite forms negligible solid solution with pyrite, and although chalcopyrite occurs in solid solution in pyrrhotite at high temperatures, it is rapidly exsolved on cooling and is not found in solid solution in pyrrhotite in ores. Many statements are misleading; for instance the legend to one figure says "Chalcopyrite—a major source of rhenium." Rhenium occurs in solid solution in molybdenite which, particularly in porphyry copper ores, commonly occurs with chalcopyrite. Some of the discussions, for instance that on the thermal stability of chalcopyrite, show that the author did not read the reference material in detail. Some discussions are rather interesting, for instance those pertaining to thermal and aqueous oxidation and to reduction, chlorination, and electrolytic reactions, but depth and detail are lacking.

The book is quite useful as a source of references to the published literature. It was printed with considerable care and is well bound. The illustrations are of good quality.

GUNNAR KULLERUD
Purdue University

PETROLOGY OF THE METAMORPHIC ROCKS. By Roger Mason. George Allen and Unwin, London, 1979. 254 pages. Cloth $29.75, paperback $14.95.

This book, which is the current volume 3 of the classic Hatch and Wells petrology text, is described on the cover as follows: "The style of treatment should make the book useful to a wide readership among geologists and earth scientists. It should be particularly suited to the needs of undergraduates who are not necessarily petrology specialists but need an authoritative introduction to metamorphic rocks at an intermediate level. It may also be of value to teachers and senior school students of geology, and to others needing a comprehensive introduction" [to metamorphic petrology]. In the opinion of this reviewer (note, unrelated to the author), this aim has been admirably and concisely obtained.

The author describes himself as a field petrologist, and throughout much of the book he uses the "case history" approach, describing the different types of metamorphism in the light of specific areas. Most of these are European—the Scottish Highlands, the Swiss Alps, the Scandinavian Caledonides—which may be a minor drawback (or perhaps an advantage) for a teacher in North America. However, the descriptions are fresh and illuminating, and are supported by critical references. Metamorphism is interpreted widely, and includes discussion of shock metamorphism associated with meteorite craters, and shock metamorphism in lunar rocks. Descriptions of metamorphic rocks are illustrated with excellent drawings of these rocks as seen in thin sections. The descriptive petrography is complemented by a final section, "Metamorphic Rocks in the Laboratory," which summarizes the application of laboratory studies of mineral syntheses and metamorphic reactions, and of isotope geology, to metamorphic petrogenesis.

This is a brief but comprehensive book which achieves the goals outlined above.

BRIAN MASON
Smithsonian Institution

SEDIMENTARY ENVIRONMENTS AND FACIES. Edited by H. G. Reading. Elsevier, New York, 1978. 557 pages. $24.00 (soft cover) $45.00 (hard cover).

Within the past decade a number of valuable review volumes, both new publications and revised editions, have treated the evo-

0003–004X/80/0910–1071$00.50

lution and genesis of sediments and sedimentary rocks. It would be a mistake to consider the work under review as merely another text in sedimentology since it is, in this reviewer's opinion, the best available summary of information and theory treating current concepts in the complex relationships which exist between sediments and the environmental conditions under which they accumulate. The treatment of these environments by ten contributors provides an equal balance between terrestrial situations (glacial, alluvial, lake, and desert—25% of the text) and coastal aspects (deltas, clastic shorelines, and arid/evaporite coasts—25%), and the whole spectrum of depositional regimes in the marine environment (50%).

General discussions of an introductory nature, the concept of facies in historical perspective, and present problems and prospects are provided by the editor, and the penultimate chapter on sedimentation and tectonics brings the reader a concise summary of the renewed interest in deep-sea and continental-margin sedimentation as it relates to plate tectonic theory. The volume contains 65 pages of references, some as late as 1978, which are keyed to the chapter sections—a welcome device which facilitates tracing a particular author's contribution to the subject matter. A concise index, featuring boldface type for figure references, rounds out the volume.

The value of this volume to practitioners and students of sedimentology lies in the approach taken by each author in addressing a specific sedimentary environment. Each contribution first addresses the historical development of concepts which have led to current perceptions in sediment controls in space and time, then a statement of environmental agents and processes which yield the various facies within each situation, and finally the application of our present knowledge to the interpretation of paleo-environments as displayed by structures and facies in the rock record.

The organization of the volume reflects a concern for those who wish to use it as a reference tool. Each chapter format includes numerical headings and further subheadings which facilitate location of specific elements within each topic. To those accustomed to consulting references at the end of each chapter, the collection of all citations in one listing near the end of the volume may prove a minor annoyance.

Visual materials complementing the text are of the highest quality, both in the artistic sense and in their reproduction by the printer. Numerous maps, diagrams, and cross-sections have been redrafted in a common format which provides continuity between each chapter. Some reductions have resulted in rather fine print, but all are sharp and in general a delight to the eye.

If one must seek a shortcoming in this excellent volume, it would be in the brief treatment of estuarine environments. Only four pages, two of which are full-page graphics, address this complex and important domain within the coastal zone. However, abundant information on these regions is available elsewhere, and the serious reader can refer to several excellent texts devoted to estuaries.

It is heartening to see the trend of alternative binding on the rise, since most readers find the price of hard-bound volumes well beyond their library budgets. The soft-cover version should find the wide circulation this work deserves, and it should stand for many years as the definitive summary of sedimentary facies and environmental sedimentology.

HAROLD D. PALMER
Dames and Moore
Washington, D. C.

ANCIENT SEDIMENTARY ENVIRONMENTS, 2nd edition. By Richard C. Selley. Cornell University Press, Ithaca, N. Y., 1978. xii + 287 pages, 93 figures, 9 tables. $6.95 (paperback).

Selley's book was not written for the specialist sedimentologist but for the general reader with a basic knowledge of geology. It can be read, however, with profit by anyone—even a mineralogist.

This book begins with a succinct and very perceptive summary of the principles of environmental analysis. The treatment is twofold: analysis based on data collected from outcrops and analysis based on subsurface data obtained from cores and by geophysical logging techniques. This dual treatment reappears throughout the book and is, in fact, the main difference between the first and the second editions. This difference reflects Selley's own experience, first as a geologist in an academic environment and then as one involved in oil and gas exploration and having to make interpretations mainly from subsurface data and having sophisticated tools available to collect such data. Some of the statements made in the introduction are judgemental and may raise the hackles of a few—in particular the statement (p. 6) on the value of grain size analyses.

In the introduction the author also defines the concepts of environment and facies and presents a simplified classification of each. The remainder of the book consists of short chapters dealing with each category: river deposits, wind-blown sediments, lake deposits, deltas, linear clastic shorelines, shelf deposits: carbonates and terrigeneous, reefs, flysch and turbidites, and pelagic deposits. In each chapter there is a short summary of modern or Recent examples followed by one or two well-documented ancient examples.

Two aspects of Selley's treatment of ancient environments are noteworthy and different from much of the older literature, namely his use of the vertical profile and of paleocurrents. The vertical profile or cyclic concept is not new but the understanding of autocyclic (internally generated cycles) patterns is a recent development—a development greatly furthered by the Shell Research group at Houston in the fifties and subsequently promulgated by J. R. L. Allen, DeRaaf, Reading, and Walker, Visher, and others. Selley utilizes this approach with great skill. Paleocurrent analysis is another tool of recent origin, stemming particularly from the work of Potter and Olson in the fifties. Selley himself has made a significant contribution to the subject, especially the environmental significance of paleocurrent patterns.

Selley's book ends with a short essay on sedimentary models—mythical and mathematical. A subject and author index are included.

What is amazing is that Selley has been able to condense and convey so much in such a compact book—the new edition is no more than fifty pages longer than the first. The reviewer knows of no better-written and better-illustrated summary of the state of the art of environmental interpretation. The book is a gem and at the price a great bargain.

F. J. PETTIJOHN
The Johns Hopkins University

THE ANDES—A GEOLOGICAL REVIEW. By W. Zeil. Gebrüder Borntraeger, Berlin, 1979. viii + 260 pages, 143 figures. $75.60.

A geologic synthesis of the longest mountain range on Earth is a monumental undertaking. Prof. Zeil early acknowledges the difficulty of the task and the necessity of being selective in dealing

0003-004X/80/0910-1072$00.50

with sources of uneven geographic distribution and geologic quality. His result is a book, vol. 13 of the series "Beiträge zur regionalen Geologie der Erde," with 207 pages of text, 33 pages of references, three indexes, and 143 figures that include 14 fold-out maps and sections. Owing to dubious organization and poor editing, the book is a disappointment.

Following eight pages of introductory material, six chapters make up the bulk of *The Andes—a geological review*. These are: "Crust and mantle in the Andes" (23 pages), "Igneous rocks" (45), "Sedimentary and metamorphic structural material" (48), "The Andes as a geodynamic body" (60), "The Andes as a plate tectonics model" (11), and "The mineral deposits of the Andes—a brief review" (12). References in the long bibliography, on the other hand, are grouped under "General bibliography", "Crust, mantle, plate tectonics", "Magmatic rocks", "Venezuela", "Colombia", "Ecuador", "Peru", "Bolivia", "Argentina", and "Chile". The reader will lose considerable time hunting the complex bibliography for some of the references cited in the text and, in fact, will find that a few have been left out.

The isolation of igneous rocks in a separate chapter is unfortunate. In so many Andean sedimentary sections, tephra constitute a major component and have important genetic connotations. The metamorphic basement of the Andes (cropping out as "isolated eminences" we are told on p. 77) is dealt with in an independent section 12 pages long. Regionally metamorphosed terrains in the Andes are assembled indiscriminately, yet extensive areas of rocks metamorphosed regionally in Tertiary time on the Guajira Peninsula and in the Sierra Nevada de Santa Marta, Colombia, as well as in the Cordillera Oriental, Ecuador, are supracrustal.

It was disconcerting to find many factual errors on the part of the Andes with which I am familiar firsthand. A few are: contrary to Figure 25, no plutonic igneous rocks are known on the Sta Elena Peninsula, Ecuador, nor are Late Cretaceous or younger plutonites found on the border with Peru on the Pacific; the Antioquian batholith, Colombia, is not Paleozoic (Fig. 65); the Carnegie ridge is referred to as seismically active (p. 26), which it is not, and it is mislocated geographically (Fig. 15); Sumaco, an extinct volcano in Ecuador, is cited as active (p. 58 and Fig. 98); the elevations of the upper Cauca and Magdalena grabens, Colombia, are given as between 1800 and 2500 m (p. 75), whereas they are everywhere below 1000 m; a map of the tectonic elements of the Andes in Ecuador (Fig. 98) omits large areas of basement rocks shown correctly in Figure 69; annual displacement on the Boconó fault, Venezuela, is stated to be 66 cm (p. 150), rather than 6.6 mm; high-*P*/low-*T* metamorphism in the Western Cordillera of Colombia is referred to in several places, but in fact has nowhere been documented; metamorphic basement rocks do not crop out in Ecuador solely in the Eastern Cordillera (p. 80), an extensive terrain is found west of the Andes at the Peruvian border; Pleistocene volcanic deposits near the Río Pisque, Ecuador, are wholly continental and include no marine sediments as stated in Figure 87; the Maracaibo basin is filled with "more than 10,000 m of sediments built up during the Cretaceous and the Quaternary" (p. 111)—what about the petroliferous Tertiary rocks that put Venezuela in OPEC?; Cerro Pantanos, an important Colombian copper prospect, is located in the wrong cordillera (p. 202); and contrary to "until recently only relatively small [petroleum] deposits have been exploited in sedimentation basins on the Pacific coast in Ecuador and Peru" (p. 205), the Talara field in northwestern Peru, in continuous production for a century, is the first-discovered of the world's "giant oil fields."

The usefulness of the book is further sapped by poor editing of the translation from German. A few examples: "impregnation deposits", for disseminated deposits; "sedimentation basins", for sedimentary basins; "material", for rocks, "overtilted", for overturned; "magmatic structural material", for igneous rocks; "mineworthy", for mineable; "horizontal faults", for strike–slip faults; or such unclear expressions as "violent fracture faults"; "positive and negative fracturing"; "latiandesites"; "narrow-bedded alpinotype structures"; "magmatological events"; and many others. Heavy wording and awkward sentence structure assault the reader. Two examples are: " . . . the Cambro-Ordovician series are non-metamorphically developed and contain corresponding fossils" (p. 131); and "The primary and secondary concentration of rich metals in the material constitution of the range was correctly correlated at an early date with the quantitatively high proportion of magmatic processes and rocks" (p. 200). Editing of the maps wasn't much better. The geologic map of Chile, admittedly a tough country to depict on paper, leaves a 400-km-wide gap between the northern (Fig. 79) and central (Fig. 80) portions of the country. Also, the join between the central and southern (Fig. 82) portions does not match. The geology of Ecuador depicted on Figure 69 departs markedly from that shown on Figure 98. Were two maps necessary anyway? Also, five outline maps of the continent are given, each more than a half page, solely to show the geographic locations of Colombia (Fig. 94), Ecuador (Fig. 97), Peru (Fig. 100), Bolivia (Fig. 102), and Chile (Fig. 117). Does not a reader of this book already have a firm idea of South American geography? At worst, he could be referred to a single map, preferably placed in the early pages of the book. The numerous photographs are mostly not well tied to the text. Accent marks and spelling of Spanish names and terms are meticulously correct in places, and seriously in error elsewhere.

Plate tectonic theory and its application to the Andes is treated weakly, at best. The reader is offered statements that are meaningless ("In the countries through which the Andes pass, the violent seismic activity frequently gives rise to severe catastrophes and proves that the mountain range is not yet consolidated with its substructure"—p. 4), or that suggest unfamiliarity with the theory itself ("Since seismic activity and volcanic activity are far from synchronous—frequent severe earthquakes have occurred recently in the region of Peru north of Lima which is free from any recent volcanism—one single explanation cannot easily be found for these different tectonic phenomena"—p. 76; or "The Eastern Pacific ridge has been active for about 20 m.y."—p. 191). Prof. Zeil rightly points out that some zealots have forced or even distorted geological and geophysical data to favor their arguments. Even so, recent papers that deal with the oceanography and geophysics of the Nazca plate and its dynamic boundary with the South American plate strongly support the applicability of plate tectonic theory to the Andes, although simultaneously emphasizing that the story isn't as simple as that envisioned only ten years ago.

The Andes—a geological review stresses the rich heterogeneity of the Andes, and effectively demolishes the concept of a uniform "Andean geosyncline." Nevertheless, the Andinophile will probably learn little new, as the book offers no independent geologic interpretation. The neophyte will be discouraged by the awkward organization and cumbersome prose. He would get a more coherent view of the Andes from Gansser's superb article, only 39 pages long, "Facts and theories on the Andes" (*J. Geol. Soc. London, v. 129,* 1973).

TOMAS FEININGER
Université Laval, Québec

0003–004X/80/0910–1073$00.50

American Mineralogist, Volume 65, page 1074, 1980

NOTICES

New Glossary of Geology

The *Glossary of Geology* has now appeared in an expanded up-to-date edition. It includes 36,000 terms, compared to 33,000 in the 1972 edition, and reflects changes in the geoscience vocabulary in the last decade. Changes in the *Glossary* are particularly evident in such active fields as biostratigraphy, remote sensing, plate tectonics, caves and karst, igneous petrology, paleomagnetism, remote sensing, plate tectonics, and seismic stratigraphy. The compilers added about 450 new mineral names, more than 100 abbreviations, such as GOR (Gas Oil Ratio), LVL, and PDB, and nearly 500 new references to the literature. The *Glossary of Geology* is edited by Robert L. Bates and Julia A. Jackson. Second edition, American Geological Institute (1980). 749 pages, $60 from AGI.

AGI Minority Participation Program Scholarships

The American Geological Institute will again offer scholarships for geoscience majors who are United States citizens and members of the following ethnic minority groups: American-born Blacks, American Indians, and Hispanics. Approximately 50 such awards (ranging from $500 to $1,250) were granted in 1980–1981. About the same number (and amounts) will be awarded for 1981–1982. Requests for application materials or nominations for scholarships should be addressed to:

William H. Matthews III
Director of Education
American Geological Institute
Box 10031
Lamar University Station
Beaumont, TX 77710

The deadline for filing the completed application is February 1, 1981.

0003–004X/80/0910–1074$00.50